materials

Special Issue Reprint

Computational Mechanics of Structures and Materials

Edited by
Michele Bacciocchi, Angelo Marcello Tarantino,
Raimondo Luciano and Carmelo Majorana

mdpi.com/journal/materials

MDPI

Computational Mechanics of Structures and Materials

Computational Mechanics of Structures and Materials

Editors

Michele Bacciocchi
Angelo Marcello Tarantino
Raimondo Luciano
Carmelo Majorana

MDPI

Basel • Beijing • Wuhan • Barcelona • Belgrade • Novi Sad • Cluj • Manchester

Editors

Michele Bacciocchi
University of San Marino
Dogana
Republic of San Marino

Angelo Marcello Tarantino
University of Modena and
Reggio Emilia
Modena
Italy

Raimondo Luciano
University of Napoli
Parthenope
Naples
Italy

Carmelo Majorana
University of Padova
Padua
Italy

Editorial Office
MDPI
St. Alban-Anlage 66
4052 Basel, Switzerland

This is a reprint of articles from the Special Issue published online in the open access journal *Materials* (ISSN 1996-1944) (available at: https://www.mdpi.com/journal/materials/special_issues/Comput_Mech_Struct_Mater).

For citation purposes, cite each article independently as indicated on the article page online and as indicated below:

Lastname, A.A.; Lastname, B.B. Article Title. *Journal Name* **Year**, *Volume Number*, Page Range.

ISBN 978-3-0365-9712-6 (Hbk)
ISBN 978-3-0365-9713-3 (PDF)
doi.org/10.3390/books978-3-0365-9713-3

Contents

About the Editors

Michele Bacciocchi

Michele Bacciocchi is an associate professor at the University of the Republic of San Marino (San Marino). He obtained his PhD in Civil, Chemical, Environmental, and Materials Engineering at the University of Bologna (Italy). He was a research-visiting scholar at Texas A&M University (United States). His research interests are the mechanics of solids, elasticity, and numerical modeling of structures. He co-authored more than 65 international peer-reviewed journal papers, 6 books, and more than 15 abstracts used at international and national conferences. He organized, as Conference Co-Chair, several international events on composite materials and structures.

Angelo Marcello Tarantino

Angelo Marcello Tarantino is a full professor of Structural Engineering at the University of Modena and Reggio Emilia (Italy). He is an expert in the theory of elasticity and structural engineering and the author of textbooks and 120 scientific publications, of which 90 were published in international journals, mainly with him billed as the sole author. He has carried out studies and research activities in France, England, the United States, Switzerland, and China. He is the scientist responsible for several research projects.

Raimondo Luciano

Raimondo Luciano is a full professor in Structural Mechanics at the University of Naples Parthenope and he is a member of the Comitato Nazionale dei Garanti per la Ricerca (CNGR). He was the Coordinator of the Faculty Activities of Civil and Environmental Engineering at the University of Cassino and Southern Lazio. He has been involved in many research activities since 1991 as an assistant professor at the University of Cassino. He has been the local coordinator of several research projects. He has more than 170 publications in national and international journals and conferences. He has collaborated with distinguished international scientists. He was the President of the National Committee of the MIUR for the PRIN Grants 2015. He was one of the four professors in the National Committee for Italian national qualification (ASN of MIUR) for Full and Associate professors in 08/B2 competitive sector. He collaborates for the realization of the Italian Design Guidelines CNR DT/200 and many others for the use of composite materials in Civil Engineering. He has been involved in over 20 mainly Italian consultancy projects pertaining to structures, namely in the diagnosis and strengthening of the design of bridges and buildings.

Carmelo Majorana

Carmelo Majorana is a full professor of Solid and Structural Mechanics and Engineering at the University of Padova (Italy). Expert in Computational Mechanics and Structural Engineering, he is the author of textbooks and more than 200 scientific papers, of which 100 are in international journals. He has carried out studies and research activities in Europe and the United States. He has been the scientist responsible for several research projects.

Preface

The idea of a Special Issue focused on "Computational Mechanics of Structures and Materials" arose from the enormous potential that characterizes different computational methods in many engineering fields. In particular, these methodologies, due to their ability to facilitate various tasks, have surely affected the approach to dealing with structures and materials, as can be observed from the body of pertinent literature, proving not only the attractiveness of this broad topic but also its potential in developing further advancements.

Therefore, the aim of the Special Issue is to gather innovative investigations dealing with accurate, reliable, and effective numerical approaches in the field of both structural mechanics and mechanics of materials. The collected papers present different computational techniques involving the achievement of solutions characterized by higher accuracy and reliability.

This Special Issue attracted many interesting submissions from many different countries of the world. Authors who decided to contribute and experts who reviewed the papers are all gladly acknowledged. The success of the collection has been made possible thanks to the constant support provided by Ms. Cecilia Zhang, the Section Managing Editor. The Guest Editors would like to thank her for her commitment to the Special Issue. Finally, the whole editorial team of *Materials*, including the Editors-in-Chief, must be mentioned.

Michele Bacciocchi, Angelo Marcello Tarantino, Raimondo Luciano, and Carmelo Majorana
Editors

materials

MDPI

Editorial

Special Issue: "Computational Mechanics of Structures and Materials"

Michele Bacciocchi [1,*], Angelo Marcello Tarantino [2], Raimondo Luciano [3] and Carmelo Majorana [4]

[1] Department of Economics, Science and Law, University of San Marino, Via Consiglio dei Sessanta 99, 47891 Dogana, San Marino
[2] DIEF—Department of Engineering "Enzo Ferrari", University of Modena and Reggio Emilia, Via P. Vivarelli 10, 41125 Modena, Italy; angelomarcello.tarantino@unimore.it
[3] Engineering Department, University of Napoli Parthenope, Via Ammiraglio Ferdinando Acton, 80133 Napoli, Italy; raimondo.luciano@uniparthenope.it
[4] Department of Civil, Environmental and Architectural Engineering (DICEA), University of Padova, Via F. Marzolo, 35131 Padova, Italy; carmelo.maiorana@unipd.it
* Correspondence: michele.bacciocchi@unirsm.sm

Computational methods have always affected many engineering fields due to their enormous potential and ability to facilitate various tasks. This statement is surely true as far as the research in structures and materials is concerned. In fact, it can be observed that the body of literature focused on computational and numerical methods for solving various structural problems and characterizing different constituents and materials is huge. This proves not only the attractiveness of this broad topic, but also its potential in developing further advancements in these contexts.

For these reasons, the Guest Editors decided to organize a Special Issue focused on "Computational Mechanics of Structures and Materials", to collect innovative investigations dealing with accurate, reliable, and effective numerical approaches in the field of both structural mechanics and mechanics of materials. To this aim, a broad scope has been defined, accepting not only finite element or finite-element-based methods, but also different computational techniques involving the achievement of solutions characterized by higher accuracy and reliability. The innovation demonstrated in dealing with advanced materials and constituents is a positive feature of all submitted papers that contributed to their acceptance.

Over several months, this Special Issues constantly proved to be a success, attracting and collecting many interesting submissions. The first heartfelt thanks is directed to all the authors from many different countries of the world who decided to contribute to the collection. Specifically, nineteen papers (out of the twenty-six submitted) have been published, passing through a meticulous review process. Sincere gratitude has to be expressed to the experts who reviewed the papers in spite of their many personal and academic responsibilities.

This great achievement has been made possible thanks to the constant support provided by Ms. Cecilia Zhang, the Section Managing Editor. The Guest Editors would like to thank her for the commitment given to the Special Issue. Finally, the whole editorial team of *Materials*, including the Editors-in-Chief, must be mentioned. They made the management of this Special Issue possible.

To celebrate the success of this commitment, a brief review of the works included in the collection is presented, highlighting the main advancements obtained in the field of computational mechanics.

Gawryluk presented a discussion on the appropriate choice of boundary conditions in structures subjected to a failure analysis. In particular, the research is focused on a thin-walled laminated angle column under compression. The results of both experimental and numerical tests are presented and compared, taking into account different damage criteria [1].

Citation: Bacciocchi, M.; Tarantino, A.M.; Luciano, R.; Majorana, C. Special Issue: "Computational Mechanics of Structures and Materials". *Materials* **2023**, *16*, 5617. https://doi.org/10.3390/ma16165617

Received: 31 July 2023
Accepted: 9 August 2023
Published: 14 August 2023

Klimczak and Cecot developed an innovative multiscale finite element method. Their numerical approach proved to be a fast and flexible technique suitable for dealing with heterogeneous materials. The results were obtained in the context of the steady-state heat transfer problem [2].

Bogdan and Radosław employed the finite element method (FEM), including the Johnson–Cook model and the failure parameters of a peculiar class of steel, to simulate the resistance of structures to collisions, shelling, and the impact of pressure waves caused by explosions in water and air in relation to submarines [3].

By means of the finite element method, Wang et al. proposed an investigation on the bearing capacity of high-strength steel-reinforced concrete composite columns. In particular, their analysis emphasized the effect of the confinement of stirrups and steel, highlighting the influence of several parameters and discussing the role of different regulations [4].

Lee and Han studied an infinite isotropic solid embedding different kinds of isotropic and anisotropic spheroidal inclusions. To this aim, they introduced the volume integral equation method (VIEM), which has been demonstrated to be a versatile numerical approach for the three-dimensional elastostatic inclusion problem [5].

Mucha et al. proposed a numerical method to describe a propagating instability phenomenon that effects metals, known as the Portevin–Le Chatelier (PLC) effect. They performed several studies varying the model parameters, which was then efficaciously compared with experimental results [6].

Shi et al. presented a numerical investigation to discuss the effects of the direction and scale of microstructures on the tension problem of a composite plate with a circular hole, proving that these features in solids also have a significant influence on the development of advanced materials. In this context, a micropolar continuum (Cosserat) model was considered [7].

Badea et al. highlighted the limitations of usual finite element models in dealing with tubular structures. By means of a previously developed beam T-junction model, their results provided some strategies to improve the accuracy of beam-element-type approaches, taking into account the real junction stiffness [8].

The paper by Sokołowski and Kamiński is focused on the problem of the topological optimization of corroding structures with uncertainties. They proposed a framework for the reliability-based design optimization (RBDO) of structural elements, considering a corrugated web I-girder as an example. Several numerical approaches have been compared in this context [9].

The work by Bochenek and Tajs-Zielińska also deals with topology optimization. They proposed the concept of the original heuristic topology generator, combining an algorithm with a commercial finite element software, characterized by a significant level of versatility [10].

Chan et al. investigated the mechanics of frozen particle fluid systems by means of a microscale simulation approach based on the discrete element method (DEM) and bonded-particle model (BPM) approach. The results provided by their methodology have been proven to be in good agreement with experimental results [11].

Alrayes et al. developed a numerical approach for simulating crack growth. To this aim, they used a scaled boundary finite element model (SBFEM), emphasizing the importance of simulating the fracture process zone when attempting to describe the cracking behavior of heterogeneous and quasi-brittle materials, taking concrete under monotonic and cyclic actions as an example [12].

Li et al. analyzed the behavior of a hydraulically expanded joint between a tubesheet and titanium tube by means of the finite element method. Their results highlighted the influence of several phenomena with many practical consequences [13].

Alrayes et al. studied mixed-mode crack propagation in concrete through some numerical simulations. They used the scaled boundary finite element method (SBFEM) to assess this phenomenon [14].

Kim et al. developed a nonlinear framework based on the modified couple stress theory to study the axisymmetric bending of circular and annular microplates subjected to thermal and mechanical loads. Their results, obtained via the finite element method, highlighted the effects of several parameters on the bending response [15].

Zhang et al. investigated creep at room temperature by means of a mechanical double-spring steering-gear load table. Their numerical results were successfully compared to experimental tests [16].

Andreotti et al. proposed a methodology to compute the resultant force of ballistic impacts resulting in a full fragmentation of the impactor with no penetration of the target. They discussed the accuracy of different discretization strategies for the corresponding finite element analysis. The results provide many useful suggestions to deal with this kind of problem [17].

The paper by Tahani et al. presents an investigation on the overall mechanical properties of ceramic–metal composites. This was achieved using a computational approach based on the molecular dynamics method. Their results highlighted the influence of several parameters [18].

Finally, the work by Giunta et al. deals with the free vibration analysis of variable-stiffness composite plates. They expanded Carrera's unified formulation (CUF) plate finite elements to composite laminates reinforced by curvilinear fibers. The effectiveness of the solution was proven through a comparison with results available in the literature or obtained through other commercial codes [19].

The Guest Editors would like to congratulate all the authors for the remarkable achievements illustrated in these papers.

Conflicts of Interest: The authors declare no conflict of interest.

References

1. Gawryluk, J. Impact of Boundary Conditions on the Behavior of Thin-Walled Laminated Angle Column under Uniform Shortening. *Materials* **2021**, *14*, 2732. [CrossRef] [PubMed]
2. Klimczak, M.; Cecot, W. Higher Order Multiscale Finite Element Method for Heat Transfer Modeling. *Materials* **2021**, *14*, 3827. [CrossRef] [PubMed]
3. Bogdan, S.; Radosław, K. Material Properties of HY 80 Steel after 55 Years of Operation for FEM Applications. *Materials* **2021**, *14*, 4213. [CrossRef] [PubMed]
4. Wang, J.; Duan, Y.; Wang, Y.; Wang, X.; Liu, Q. Analysis and Modification of Methods for Calculating Axial Load Capacity of High-Strength Steel-Reinforced Concrete Composite Columns. *Materials* **2021**, *14*, 6860. [CrossRef]
5. Lee, J.; Han, M. Volume Integral Equation Method Solution for Spheroidal Inclusion Problem. *Materials* **2021**, *14*, 6996. [CrossRef]
6. Mucha, M.; Wcisło, B.; Pamin, J. Simulation of PLC Effect Using Regularized Large-Strain Elasto-Plasticity. *Materials* **2022**, *15*, 4327. [CrossRef] [PubMed]
7. Shi, F.; Fantuzzi, N.; Trovalusci, P.; Li, Y.; Wei, Z. Stress Field Evaluation in Orthotropic Microstructured Composites with Holes as Cosserat Continuum. *Materials* **2022**, *15*, 6196. [CrossRef] [PubMed]
8. Badea, F.; Olazagoitia, J.; Perez, J. Validation of Alternative Beam T-Junction Fem Models for Complex Tubular Structures. *Materials* **2022**, *15*, 6468. [CrossRef] [PubMed]
9. Sokołowski, D.; Kamiński, M. Stochastic Reliability-Based Design Optimization Framework for the Steel Plate Girder with Corrugated Web Subjected to Corrosion. *Materials* **2022**, *15*, 7170. [CrossRef] [PubMed]
10. Bochenek, B.; Tajs-Zielińska, K. Cellular Automaton Mimicking Colliding Bodies for Topology Optimization. *Materials* **2022**, *15*, 8057. [CrossRef] [PubMed]
11. Chan, T.T.; Heinrich, S.; Grabe, J.; Dosta, M. Microscale Modeling of Frozen Particle Fluid Systems with a Bonded-Particle Model Method. *Materials* **2022**, *15*, 8505. [CrossRef] [PubMed]
12. Alrayes, O.; Könke, C.; Ooi, E.T.; Hamdia, K.M. Modeling Cyclic Crack Propagation in Concrete Using the Scaled Boundary Finite Element Method Coupled with the Cumulative Damage-Plasticity Constitutive Law. *Materials* **2023**, *16*, 863. [CrossRef] [PubMed]
13. Li, J.; Li, J.; Zhang, Y.; Zhou, C. Investigation on Performance of Hydraulically Expanded Joint of Titanium-Steel Clad Tubesheet. *Materials* **2023**, *16*, 1106. [CrossRef] [PubMed]
14. Alrayes, O.; Könke, C.; Hamdia, K.M. A Numerical Study of Crack Mixed Mode Model in Concrete Material Subjected to Cyclic Loading. *Materials* **2023**, *16*, 1916. [CrossRef] [PubMed]

15. Kim, J.; Nava, E.; Rakici, S. Nonlinear Finite Element Model for Bending Analysis of Functionally-Graded Porous Circular/Annular Micro-Plates under Thermomechanical Loads Using Quasi-3D Reddy Third-Order Plate Theory. *Materials* **2023**, *16*, 3505. [CrossRef] [PubMed]
16. Zhang, B.; Ren, P.; Wang, Z.; Ma, H. Research on the Spring Creep Based on the Load Simulator of the Double Torsion Spring Steering Gear. *Materials* **2023**, *16*, 3763. [CrossRef] [PubMed]
17. Andreotti, R.; Casaroli, A.; Colamartino, I.; Quercia, M.; Boniardi, M.V.; Berto, F. Ballistic Impacts with Bullet Splash—Load History Estimation for .308 Bullets vs. Hard Steel Targets. *Materials* **2023**, *16*, 3990. [CrossRef]
18. Tahani, M.; Postek, E.; Sadowski, T. Diffusion and Interdiffusion Study at Al- and O-Terminated $Al_2O_3/AlSi_{12}$ Interface Using Molecular Dynamics Simulations. *Materials* **2023**, *16*, 4324. [CrossRef] [PubMed]
19. Giunta, G.; Iannotta, D.A.; Montemurro, M. A FEM Free Vibration Analysis of Variable Stiffness Composite Plates through Hierarchical Modeling. *Materials* **2023**, *16*, 4643. [CrossRef] [PubMed]

materials

MDPI

Article

Impact of Boundary Conditions on the Behavior of Thin-Walled Laminated Angle Column under Uniform Shortening

Jarosław Gawryluk

Department of Applied Mechanics, Lublin University of Technology, Nadbystrzycka 36, 20-618 Lublin, Poland; j.gawryluk@pollub.pl; Tel.: +48-815384144

Abstract: Determining the appropriate boundary conditions of a structure is a very important aspect in the failure analysis. In experimental tests, the method of compressing composite samples significantly influences the obtained results. In numerical studies, there is a problem of correctly defining the boundary conditions applied in real object. Therefore, many numerical tests on samples should be undertaken to observe their behavior and to determine ultimate load. The present work includes study to determine the impact of boundary conditions on the thin-walled laminated angle column under compression. The phenomenon of buckling and the post-buckling bahavior of columns were investigated experimentally and numerically. First, the real simply supported angle columns subjected to uniform shortening are tested. Due to the stress concentration between the real sample and the grips, a flexible pads were used. Experimental tests are carried out on the universal testing machine. The deformations of columns were measured using the non-contact Aramis System. The composite material condition was monitored by acoustic emission using the Vallen Systeme with piezoelectric sensors. Next, the numerical calculations in Abaqus software based on the finite element method are performed to validate the empirical results. To determine the influence of the boundary conditions, two numerical models of the system with and without flexible pads are developed. To estimate damage initiation load in numerical models a different damage criteria (Tsai-Hill, Tsai-Wu, Azzi-Tsai-Hill, Hashin) are used. Based on the results specified that the model with elastic pads more accurately reflects the actual behavior of the L-profile element under compression. It was supported, i.e., by good agreement of flanges deflection (the equilibrium paths) with experimental results. Furthermore, a qualitative and quantitative agreement of damage initiation load were obtained using Hashin criteria (error 4.61%).

Keywords: flexible pad; laminated angle column; compresion; FEM; experiment

Citation: Gawryluk, J. Impact of Boundary Conditions on the Behavior of Thin-Walled Laminated Angle Column under Uniform Shortening. *Materials* **2021**, *14*, 2732. https://doi.org/10.3390/ma14112732

Academic Editors: Carmelo Majorana, Angelo Marcello Tarantino, Raimondo Luciano and Michele Bacciocchi

Received: 24 April 2021
Accepted: 17 May 2021
Published: 21 May 2021

1. Introduction

Loss of stability is an important process during operation of thin-walled structures, which can lead to the complete damage of the structure. Therefore, a detailed analysis of the structure failure under the load is extremely necessary from an engineering point of view. In particular, the problem is encountered in the aerospace industry [1,2], where isotropic materials are replaced with modern composite materials, which are characterized by excellent strength parameters with a significant weight reduction of these elements. An important issue is description the damage process of thin-walled laminated structures [3,4]. In thin-walled structures with flat walls made of composite material, the system works after the loss of stability (the system has stable equilibrium paths) [5,6]. This means that apart from knowledge the critical load value, the behaviour of the structure after loss of stability also has an important role. In most cases, the analysis of post-critical states requires taking into account non-linear relationships between displacements and deformations. Nonlinear calculations are usually performed for structures with initialized geometrical imperfections corresponding to the selected buckling mode of the structure, which was determined in the linear stability analysis. This makes it possible to determine the relationship between the load on the structure and the geometrical parameters

determining the displacement of its nodes—i.e., we will obtain post-critical equilibrium paths [7]. By carrying out nonlinear studies in a post-critical state, the moment of failure initiation in a composite structure can be determined. This is particularly important as this phenomenon exhausts the load capacity of the structure. It is quite a complicated and ambiguous problem, as the failure model depends on many factors, i.e., the type of load, geometry and size of the analyzed element, mechanical properties of the materials used, preloads and damages. Moreover, the method of producing the actual structure significantly influences the course of the destruction process. As a result, it leads to many failure mechanisms, i.e., matrix/fiber cracking, local buckling of the fibers or the entire laminate layer, and delamination. In order to describe the respective damage mechanism, many failure models have been developed and various failure criteria have been introduced into the literature. The most popular criteria in practical analyses describe the failure of the first layer: the maximum stress criterion, the maximum deformation criterion, the Tsai-Hill criterion, the Tsai-Wu criterion, and the Azzi-Tsai-Hill criterion. The destruction process occurs when at least one criteria is fulfilled [8]. All the above-mentioned criteria provide information that the moment of damage initiation has caused, but they are not able to clearly define which element of the structure was destroyed. For this purpose, the Hashin's criterion can be used, which determines the destruction of fibers or matrix [9]. Interesting research describing the influence of boundary conditions on the buckling of beams is described in [10]. The Cold-Formed Steel beams with staggered slotted perforations were analyzed. These beams are being used in light gauge steel construction aiming to enhance both the fire and energy performance. However, these web perforations affect the bending capacity. In order to determine this effect, numerical and experimental studies were carried out. It was found that the influence of staggered slotted perforations on local buckling strength of the CFS beams is relatively small (11%).

In the literature, there are a lot of papers describing destruction process of thin-walled structures [11].The analytical methods are used for the post-buckling analysis, in which the thin-walled structure is described with orthotropic material [12]. In order to verify the theoretical models, it was necessary to conduct laboratory tests [13]. One of the experimental methods allowing a description of the damage process of the laminated structure is the acoustic emission method, which enables monitoring of the damage initiation and development of damage up to the complete destruction of the element. Experimental test of thin-walled chanell section profile subjected to compression are described in the paper [14]. Six different configurations of the glass fibers arrangement in the epoxy matrix, considering only symmetrical laminates were investigated. The tests were carried out on a testing machine with the use of an environment for recording acoustic emissions. This applied method made it possible to observe the structure's behaviour, thanks to which it was possible to estimate the damage initiation load. Similar studies for carbon-epoxy laminate were presented in the work [6]. The authors experimentally tested four variants of laminate fiber arrangement. The AE method was used experimentally. From the conducted experimental studies, it was possible to estimate the loads initiating the damage of structures. Teter et al. [15] presented compression tests of a thin-walled omega profile made of carbon-epoxy laminate. Experimental tests with the use of acoustic emission were considered. Additionally strain gauges were used to record deformations of selected surfaces. This allowed estimating the damage initiation load and post-buckling equilibrium path.The research carried out in the above works has shown that the acoustic emission method is effective in monitoring structural damage. In the latest works devoted to the damage of thin-walled structures, experimental and numerical studies using the finite element method can be found [16]. Nonlinear buckling analyses have been carried out to predict the initial buckling loads of the pultruded glass reinforced plastic wide flange columns under compression in paper [17]. The authors used new criteria for the web-flange junction, because the failure behaviour of this junction is quite different from web or flanges. Numerical results were compared with experimental, and good correlation was obtained. Rozylo et al. [18] described the numerical and experimental tests of thin-walled profiles

with an omega cross-section under axial compression. The non-linear range of structures with geometrical imperfection was calculated in the Abaqus environment by the Newton-Raphson method. The Hashin criterion was used to identify the initiation of structure failure. A high agreement of numerical and experimental results was obtained. Detailed research on the post-buckling analysis of thin-walled laminated profiles with a C-section is presented in [19]. Numerical studies in the Ansys environment and experimental studies were carried out. A high agreement of the results was obtained. Samples subjected to axial compression were analyzed. Similar studies on chanell section profiles were presented in [20], where the Abaqus environment was used, and samples were tested under eccentric loading. In the experimental tests, acoustic emission was used to determine the damage initiation. Teter et al. [21] conducted detailed studies of thin-walled angular columns in various configurations of fiber arrangement under uniform compression. The nonlinear research was carried out with the analytical-numerical and finite element method. The influence of geometrical imperfection on the value of the smallest buckling load was determined. The authors proposed the $P - \Delta$ intersection method and the $P - \Delta^n$ method, thanks to which it was possible to estimate the value of the buckling load with high and small amplitude of the initial deflection with high accuracy. Similar numerical studies were compared with the semi-analytical method (SAM) based on the Byskov-Hutchinson method in [22]. The load-shortening diagrams of the column in the nonlinear range were developed as well as the influence of imperfection on the buckling load were determined.

Taking the above-mentioned into account, it can be said that there are still too few papers with results presenting the behaviour of thin-walled composite structures with L-profile subjected to compressive load. Therefore, it was decided to conduct experimental and numerical tests. This articule is a continuation of previous studies described in paper [23], where the numerical model of the elastic pad was validated and the influence of its parameters on the obtained results was determined. In the present study, the impact of boundary conditions on the thin-walled laminated angle column in post-buckling behavior is analyzed. Therefore, two numerical models with different boundary conditions were compared with the results obtained experimentally. Linear buckling and nonlinear post-buckling analysis were considered to investigate the post-buckling behavior of the beam under uniform compression. In order to estimate damage initiation load in numerical models a different damage criteria were used. Finally, the equilibrium paths for all analysed cases were determined. Based on the results, it was found that the model without elastic pads characterized a much more stiffness then the second one with pads, as shown by: a greater bifurcation load, damage initiation load in all analyzed criteria, lower shortening and less deflection of the column in its center. However, model with flexible pads shows a similar character to the experimental results, i.e., high convergence of the equilibrium paths and a small error in the damage initiation load (Hashin criteria).

2. Problem Statement

Thin-walled composite channel-section column with L-profile subject to axial compression were considered. Buckling and post-buckling of such beams were analyzed. Those investigations were mainly aimed at:

- validation of FE model of ideal column with L-profile with results of experimental tests;
- finding advantages and disadvantages of the proposed numerical models of angle column with and without pad;
- checking an influence of the flexible pad on post-buckling behavior.

The thin-walled profiles under consideration were made of a carbon-epoxy unidirectional prepreg tape using autoclaving technique. The thickness of each ply was approx. 0.045 mm. This column consist of 18 layers with following configuration: [60, 0(2), −60(2), 60(3), −60(2), 0(3), −60(2), 0, 60(2)]T. The considered beam was 300 mm long and the width of flanges was 40 mm. The material properties of the beams were determined in tensile and compression tests described in paper [6]. The following material properties (Table 1) Young's modulus in two orthogonal directions E_1 and E_2 , Poisson's ratio v_{12}, and the

shear modulus G_{12} were determined. Additionally, the limit properties of the composite, i.e., tensile strength F_{TU} in two orthogonal directions, compression strength F_{CU} in two orthogonal direction and shear strength F_{SU} were determined. These material properties are presented in Table 2.

Table 1. Properties of used material.

Composite Material	
Young's modulus E_1 (MPa)	170,000
Young's modulus E_2 (MPa)	7600
shear modulus G_{12} (MPa)	3520
Poisson's ratio v_{12} (−)	0.36
Flexible Pad	
Young's modulus (MPa)	40
Poisson's ratio (−)	0.49

Table 2. Limit properties of the composite as determined in compliance with relevant ISO standards.

$\mathbf{F_{TU}}$ **(MPa)**		$\mathbf{F_{CU}}$ **(MPa)**		$\mathbf{F_{SU}}$ **(MPa)**
0°	90°	0°	90°	45°
1601	14.4	1052	117	90.7

To eliminate the effect of stress concentration in experimental test, flexible pads between the thin-walled profile and the testing machine handle were used. To check an impact of the flexible pad on post-buckling behaviour of the thin-walled beam under consideration, numerical model with and without pads were investigated.

3. Laboratory Setup

Experimental tests consisted in static compression of the fabricated L-profiles on the universal testing machine (Figure 1). In order to eliminate the stress concentration effect between the sample and handle of testing machine, the flexible pads with a thickness of 5.2 mm were used. Laboratory test were performed at a constant velocity of the cross-bar equal to 1 mm/min. The tested columns were loaded with the force value from zero to load, in which damage initiation load was observed. The composite material condition was monitored by acoustic emission. Signals were recorded using the Vallen Systeme, provided with a two piezoelectric sensors. In AE method usually uses the following parameters: the number of hits, the number of counts, the signal amplitude or energy [6,14,15]. In addition, to determine deflection of the sample in the whole range of load, a Aramis system was employed. The ARAMIS is a non-contact measuring system based on digital image correlation doing high-precision measurements with a 3D measurement resolution in the sub-micrometer range, regardless of the specimen's geometry and temperature. For this purpose, the system used a series of digital photos done at regular intervals during measurements time by two cameras positioned at the appropriate distance from the tested object. I used this system to recording the behavior of the real object, in particular to calculate the shortening of the sample and its flange deflections. The values of the load applied to the system were obtained directly from the testing machine. This allowed to determine a post-buckling equilibrium curves for all tested samples and the value of the load at which the first layer of the laminate was damaged. The experiments were conducted under laboratory conditions at room temperature of 23 °C.

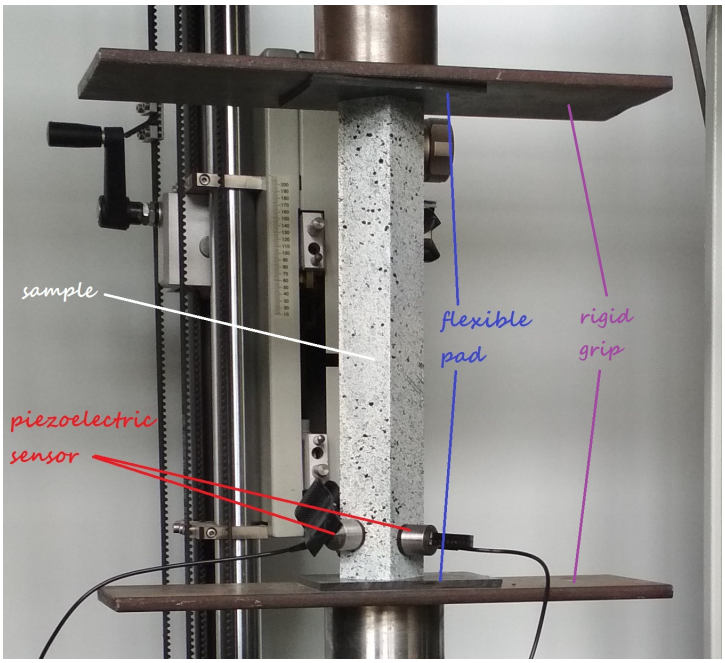

Figure 1. Experimental setup.

Additionally, verification of the material constants for the flexible pad was carried out in experimental tests. Detailed research was described in paper [23]. However, the obtained substitute material constants are presented in Table 1.

4. Numerical Nonlinear Analyses

The numerical nonlinear stability problem was solved with the finite element method (FEM)—ABAQUS software [24]. Two models with different boundary conditions were considered. The first geometrical model (denoted as M-1) consists of only a part of the column situated between the rigid grips (see Figure 2a). The second one (denoted as M-2) has flexible pads between sample and rigid grips are additionally included (Figure 2b). The second assumed model was closer to the structure tested experimentally.

The L-profile laminate column was modelled using S8R shell finite elements. They are 8-node elements with a second order shape function with reduced integration (with six degrees of freedom in each node). The layup-ply technique is used to define the sequence of the laminate layers. Each layer is made of a carbon-epoxy unidirectional prepreg with material parameters presented in the previous section. However, the model of grips are shown as a rigid body (without predefined material properties), made of 4-node, bilinear quadrilateral discrete rigid elements (R3D4) with six degrees of freedom in each node. In the second model (M-2), the flexible pad consists of C3D20R solid element with reduced integration. These are 20-node 2nd order elements (with square shape function) with three translational degrees of freedom at each node. The number of elements was assumed on the basis of the previous experience (e.g., [23]). However, the mesh density was assumed in such a way as not to limit column deformation. The convergence of the model by selecting the size of the elements used (especially the column and pad) was investigated numerically. In the case of the pad, it was determined based on simulations that the number of 3 elements in thickness is sufficient. In both FE models, the thickness of elements discretizing a part of the model corresponding to the considered laminated beam is assumed as 0.81 mm. The system of the L-profile beam with grips was simply supported at two ends. Contact relations were defined between the rigid plate and the profile edge (M-1) or between the flexible pads and the profile edge (M-2) in the normal and tangential directions (friction coefficient set equal to 0.6).

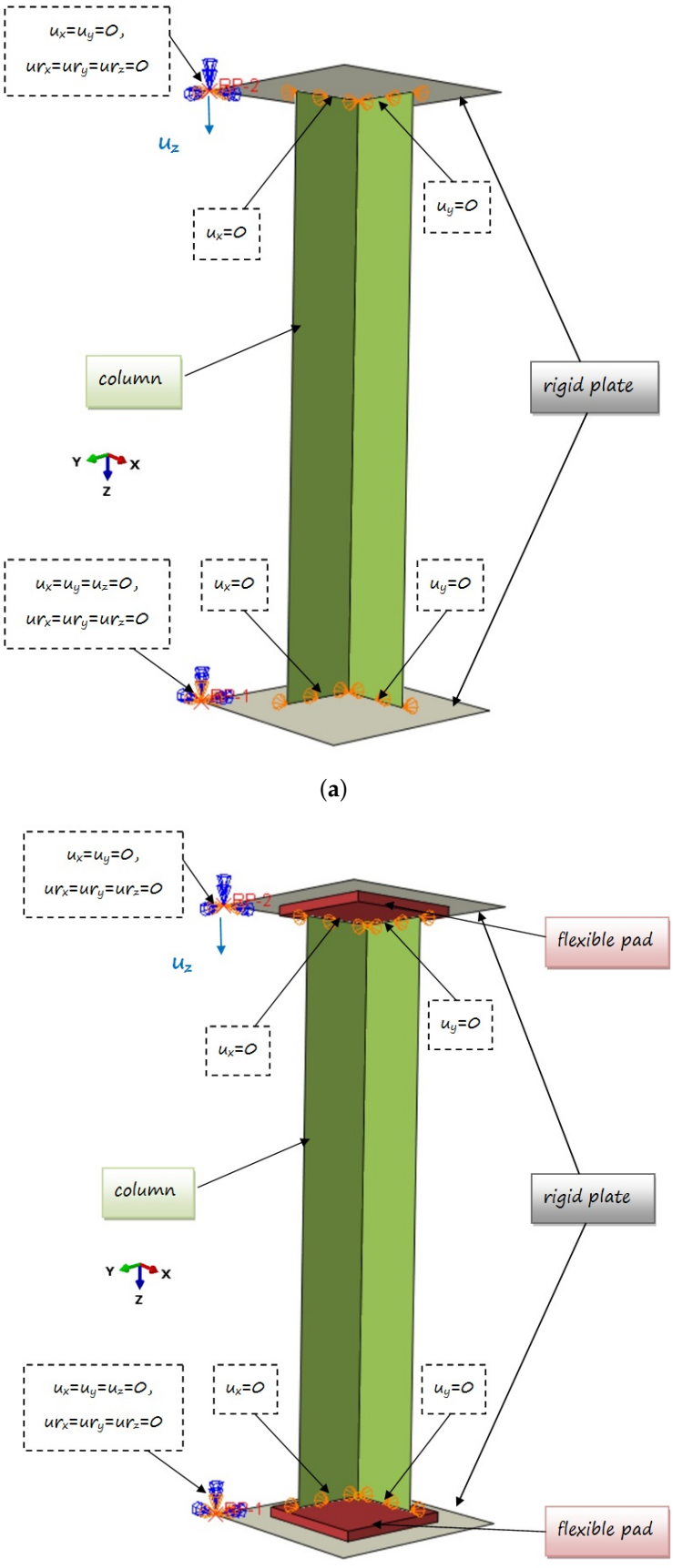

Figure 2. Numerical models of the column: (**a**) M-1; (**b**) M-2.

The top rigid plate was locked at the first reference point (RP1), while the bottom rigid plate was allowed to move in the Z direction (at the second reference point (RP2)). The compressive load was realized by displacement of bottom plate along the longitudinal axis of the column. The displacement in the directions perpendicular to the plane of the angle column is set to zero in all nodes located on the profile edges (at the contact points). The specific boundary conditions used in the models are presented in Figure 2.

The above-described numerical models were employed in the numerical calculations to perform an eigenbuckling analysis and a nonlinear buckling analysis to investigate the post-buckling behavior of the beam under consideration. To estimate the moment of the first laminate layer damage, the following initiation criteria were used: maximum stress criterion, Tsai-Hill, Tsai-Wu, Azzi-Tsai-Hill, and Hashin criterions. The value of the damage initiation load and the place where it occurred, according to the above criteria were determined.

5. Comparison of Results and Discussion

The results of the laboratory tests were used to validate the FE models employed to determine the post-buckling behavior of thin-walled structures. The results of the numerical calculations obtained with two models were compared to the results of the experimental investigations. In the linear numerical analysis, the lowest bifurcation load and the corresponding mode of buckling were determined. The same buckling mode was obtained for two models, while the bifurcation load differed by approx 14%. The first model (M-1) obtained a greater bifurcation load, which proves that this model had greater stiffness. However, when the stiffness of flexible pads significantly increased (e.g., E $\times 10^6$), the same bifurcation load was obtained in both models. Furthermore, the same mode (along the length of the column one buckling half-wave) in an experimental case was observed (Figure 3).

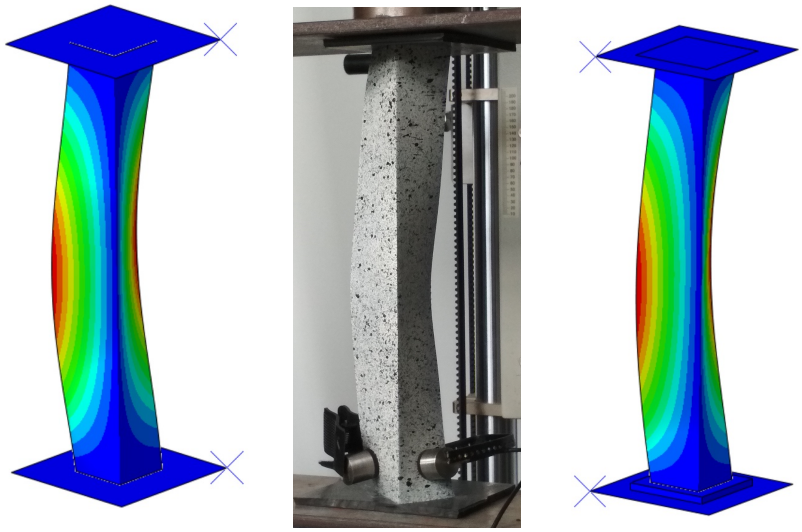

(**a**) (**b**) (**c**)

Figure 3. Modes of buckling under axial compression: (**a**) M-1; (**b**) EXP; (**c**) M-2.

The maps of the laminate failure parameter for initiation criteria obtained in the numerical calculations shows a different qualitative character in M-1 and M-2 models. Namely, in the first model, due to lack of flexible pads, the damage initiation in all criteria concerns only areas at the profile edges. However, in the second model the damage initiation concerns areas at the profile edges and additionally at the corner of the angle section in 1/2 of its height and in the middle part of one of the flanges. Using the Tsai-Hill, Tsai-Wu, Azzi-Tsai-Hill, and maximum stress criterions, it is possible to catch the moment of damage initiation, but it is not possible to determine the failure mechanism

(i.e., what elements of laminate have been damaged). Therefore, the damage initiation criteria based on Hashin theory was used,that allow independent assessment of damage initiation in individual components of the material, i.e., the fibre tensile/compressive initiation criterion (HSNFTCRT/HSNFCCRT) or the matrix tensile/compressive initiation criterion (HSNMTCRT/HSNMCCRT). The initiation of damage occurs when any of the above criteria reaches the critical value of 1. It is used to determine the composite material damage initiation load. In the analyzed sample, the obtained results demonstrate the fulfillment of the Hashin criterion when tensile the matrix (HSNMTCRT). Maps of damage parameter for M-1 and M-2 models are presented in (Figure 4). However, the condition was not achieved in the other failure parameters.

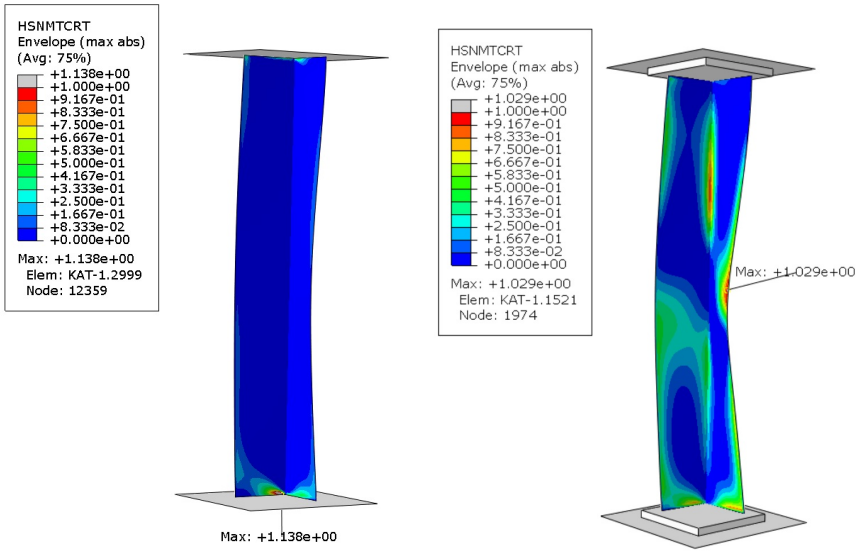

Figure 4. Maps of damage parameter for an angle column: (**a**) M-1; (**b**) M-2.

The damage initiation in M-2 model occurred mainly in the middle part of one of the flanges, while the place of damage initiation with the Hashin criterion did not change in the first model. Additionally, it was checked in the M-1 model whether the damage mechanism occurring in the M-2 model would appear in further analysis. After completing the necessary research, it was found that the damage mechanism from second model was not observed in the first model. From a practical point of view, the angle section under compression should damage closer to the center than at the edge of the profile. Furthermore, the maximall deflection in the middle of the column was observed in the experimental tests (Figure 5a). It was compared with the second numerical model Figure 5b.

Additionally, the deflection curves of two flanges (u_1 deflection in the X direction and u_2 deflection in the Y direction) from two numerical models were compared as a function of the compressive load. Moreover, the above-described curves have been compiled with the deformations recorded by the Aramis system. The deflection of the angle column near the middle, recorded from the experimental and two numerical cases are presented in Figure 6. The deflection of the flange is shown in absolute value, but it should be remembered that not every variant (real sample or numerical model) has a deflection in the same direction. The positioning of the test sample did not allow simultaneous observation of two L-profile column flanges. Therefore, the deflection only one of the sample flanges was recorded.

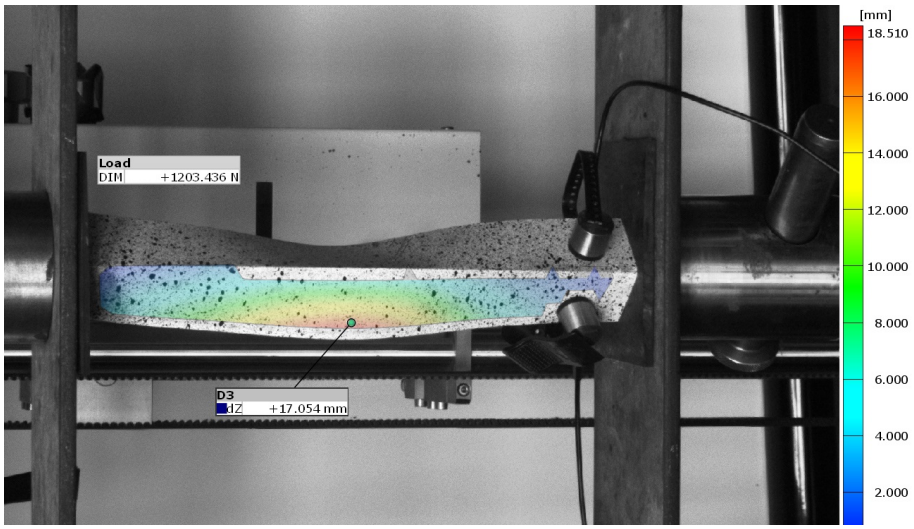

(**a**)

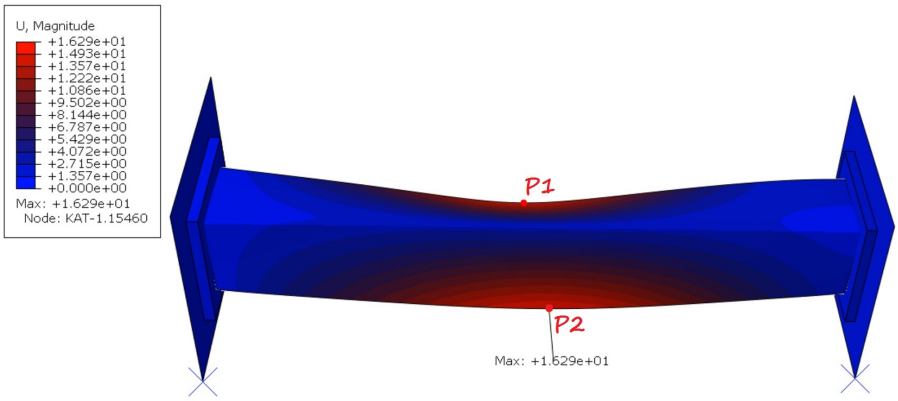

(**b**)

Figure 5. The deflection of an angle column under axial shortening: (**a**) EXP; (**b**) M-2.

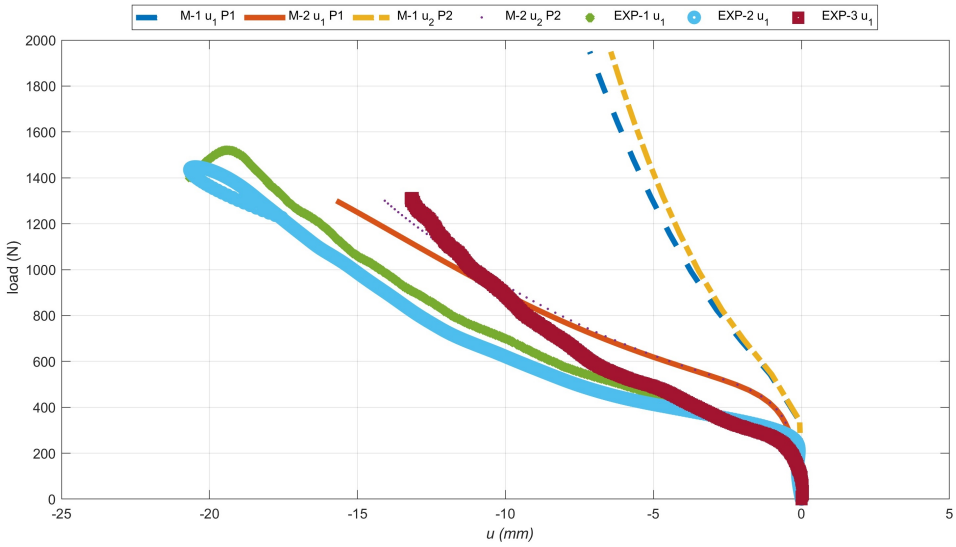

Figure 6. The equilibrium paths, i.e., load-flange deflection relations.

The equilibrium paths clearly show that the first numerical model cis haracterized by a different nature of damage. The deflection in the same node at the damage initiation load

differed by about 120%. It relate to both X and Y directions. However, comparing the M-2 model with the experiment, a much smaller error in the range of 11–31% was obtained. Furthermore, the nature of the experimental curves (EXP-1 and EXP-2) complies with that obtained in the second numerical case. In experimental tests, using the AE method, the value of the damage initiation load of the first layer was determined. According to the literature [6,14,15], this type of damage occurs at the first local increase of the acoustic signal energy, which was significantly greater than the previous ones. In Figure 7, such a situation was observed for approx. 560 s, where the energy increased almost eightfold. Thus, the damage initiation load from the load signal at 560s. was assumed. The damage initiation load for other samples in a similar way were determined. Earlier registered lower energy readings could occur as a result of matching the sample to the flexible pads.

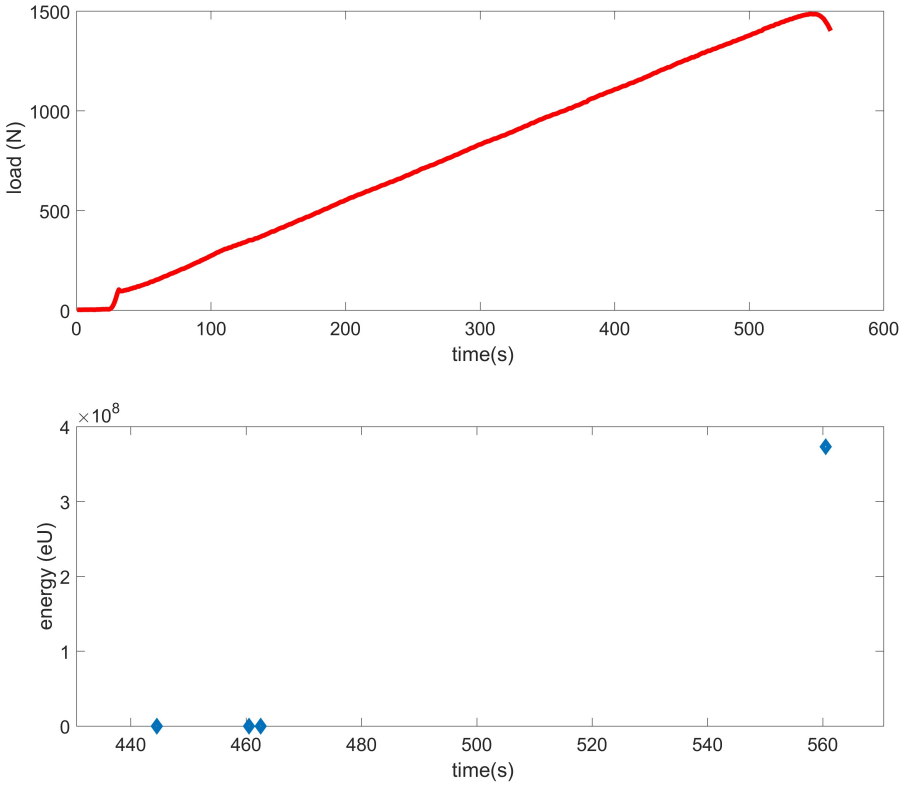

Figure 7. The load and acoustic energy signal versus time for the second real column (EXP-2): Aramis signal—red line; energy signal of AEM—blue mark.

All the values obtained from the experimental tests were presented in the collective diagram together with the results obtained from the numerical tests (Figure 8),where the following symbols have been adopted: TSAIW—Tsai-Wu criteria, TSAIH—Tsai-Hill'a criteria, AZZIT—Azzi-TsaiHill'a criteria, MSTRS—maximum stress criteria and HASHIN-Hashin's criteria.

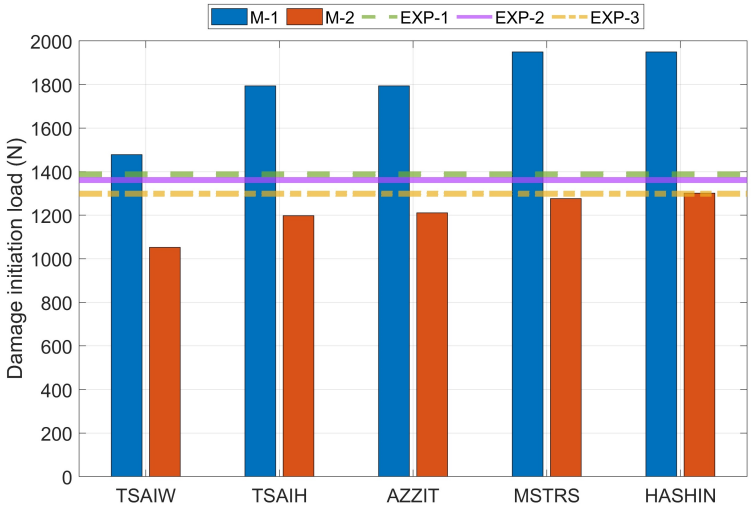

Figure 8. The damage initiation load from numerical and experimental cases.

The results obtained for the first model were about 28 to 34% higher than for the second one. This confirms the significant influence of the boundary conditions on the behavior of laminated thin-walled columns. Such a large discrepancy in the results may indicate that both numerical models do not analyze the same damage mechanism. Hashin's criterion on the second model (M-2) almost perfectly defined the damage initiation load compared to the experimental.Based on the three experimental results, the median was determined to be 1361N (EXP-2). Next, relative errors for the numerical results with respect to the median of the experimental results were calculated (Figure 9). The smallest value overestimation was for model M-1 in the case of the Tsai-Wu criterion, while in the other criteria the error increased until it obtained the highest overestimation of the value for the Hashin criteria. However, the smallest underestimation of the value was for the M-2 model in the case of Hashin criterion (4.61%), while in the other criteria the error increased until it obtained the largest underestimation of the value for the Tsai-Wu criterion. In the first case (M-1), the Tsai-Wu criterion allows identifying the damage initiation load, while in the second model, the Hashin criterion definitely helps to identify the damage initiation load. It is worth remembering that in two variants this applies to different damage mechanisms. Considering the above, Hashin's criterion most accurately describes the actual damage initiation load.

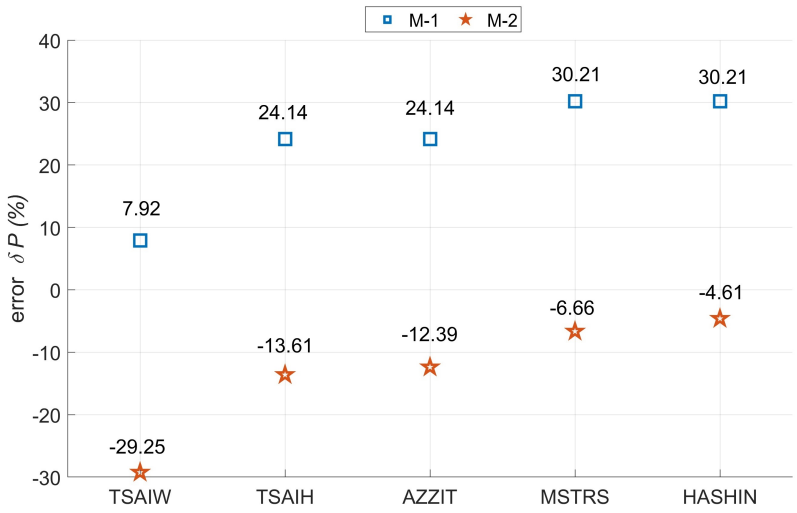

Figure 9. The relative error between numerical and experimental results: $\delta P = ((P_{MES} - P_{EXP})/P_{MES}) \times 100$ *percent*.

Dimensionless equilibrium paths determined from experimental and numerical tests are presented in Figure 10. A very good agreement of the results was obtained for the M-2 model, while the results from the M-1 model demonstrate a different damage mechanism. It is also clearly visible in Figure 11, where the equilibrium paths obtained from numerical models are presented. The shortening of the M-1 model was around 550% lower than for the second one. Moreover, the damage initiation load obtained in the first model is higher by about 50% compared to the results of the second model. In addition, it is worth noting how much influence the flexible pad (i.e., the appropriate stiffness of the support) has on the behavior of the thin-walled laminate L-shaped column. It can be suspected that, by increasing the stiffness of the pads, the equilibrium curve should be placed between the presented results.

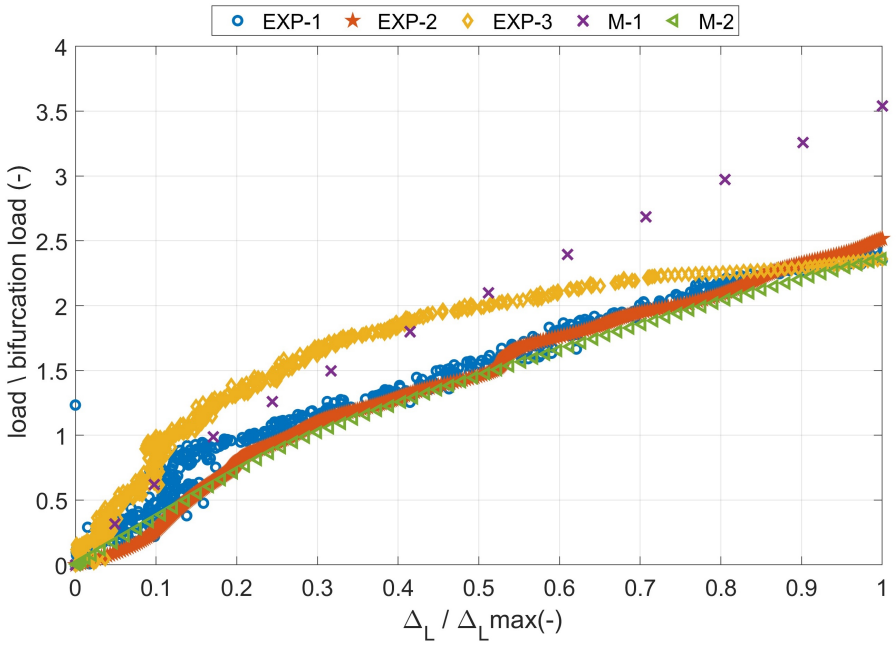

Figure 10. Dimensionless equilibrium paths of L-profile column under shortening.

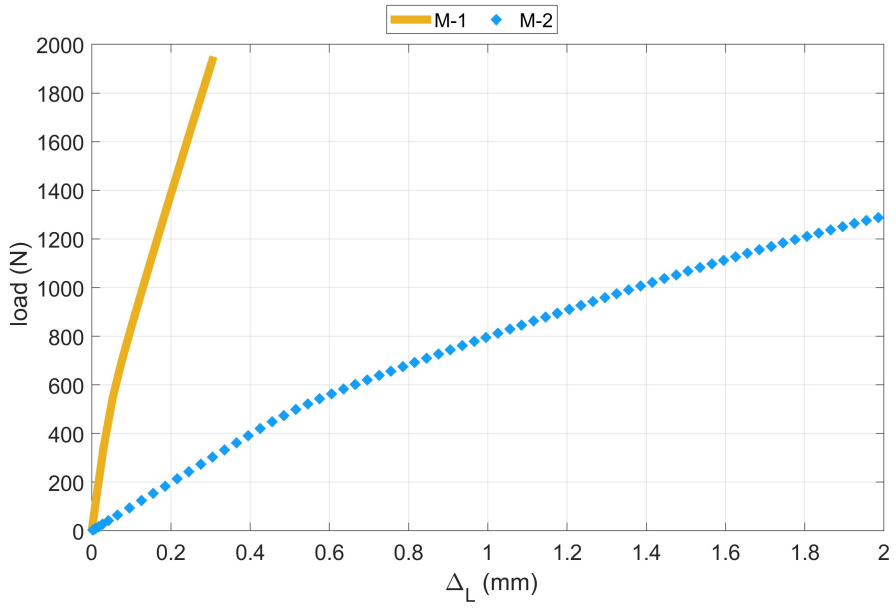

Figure 11. Equilibrium paths of L-profile column under shortening-numerical results.

6. Conclusions

The main aim of the study was to validate the numerical models (M-1, M-2) with the results of the experimental tests. The first model M-1 consists of laminated column situated between the rigid grips, while in the second model the flexible pads between sample and rigid grips are additionally included.Based on the obtained results, the following conclusions have been drawn:

- One of the main parameters (the number of half-waves) determining good correlation of the experimental and numerical results is identical.
- The signals from acoustic emissions method should be carefully analyzed, to catch those responsible for damage of the first laminate layer.
- The damage initiation in M-1 and M-2 models shows a different qualitative and quantitative character (Hashin's criteria), i.e., in the second model occurred mainly in the middle part of one of the flanges, while in the first model it concerns only areas at the profile edges.
- The first model (M-1) was characterized by much more stiffness, as shown by: a greater bifurcation load (about 14%), damage initiation load (up to 34%) in all analyzed criteria, up to 550% lower shortening and less deflection of the column in its center (up to 120%) then the second model M-2.
- The greater flange deflections obtained in real tests may result from inaccuracies in the fabrication of the samples, but they are not easy to identify. For this purpose, a three-dimensional surface analysis should be carried out (using a 3D scanner) and the quality of the actual columns, before the damage test, should be checked.
- The results obtained in the model with flexible pads show a similar character to the experimental results, i.e., the equilibrium paths shows a high convergence and a small error was obtained in the damage initiation load.

Therefore, the model with elastic pads more accurately reflects the actual behavior of the L-profile element under compression. However, further development in numerical models (especially checking more detailed boundary conditions) together with their experimental validation is necessary.

Funding: The project/research was financed in the framework of the project Lublin University of Technology—Regional Excellence Initiative, funded by the Polish Ministry of Science and Higher Education (contract No. 030/RID/2018/19).

Institutional Review Board Statement: Not applicable.

Informed Consent Statement: Not applicable.

Data Availability Statement: Data is contained within the article.

Conflicts of Interest: The author declares no conflict of interest.

References

1. Hu, D.; Song, B.; Wang, D.; Chen, Z. Experiment and numerical simulation of a full-scale helicopter composite cockpit structure subject to a bird strike. *Compos. Struct.* **2016**, *149*, 385–397. [CrossRef]
2. Smojver, I.; Ivančević, D. Numerical simulation of bird strike damage prediction in airplane flap structure. *Compos. Struct.* **2010**, *92*, 2016–2026. [CrossRef]
3. Bažant, Z.P.; Cedolin, L. *Stability of Structures: Elastic, Inelastic, Fracture and Damage Theories*; World Scientific Publishing Co.: Singapore, 2010.
4. Debski, H.; Jonak, J. Failure analysis of thin-walled composite channel section columns. *Compos. Struct.* **2015**, *132*, 567–574. [CrossRef]
5. Urbaniak, M.; Teter, A.; Kubiak, T. Influence of boundary conditions on the critical and failure load in the GFPR channel cross-section columns subjected to compression. *Compos. Struct.* **2015**, *134*, 199–208. [CrossRef]
6. Debski, H.; Teter, A.; Kubiak, T.; Samborski, S. Local buckling, post-buckling and collapse of thin-walled channel section composite columns subjected to quasi-static compression. *Compos. Struct.* **2016**, *136*, 593–601. [CrossRef]
7. Jollivet, T.; Catherine Peyrac, C.; Lefebvre, F. Damage of Composite Materials. *Procedia Eng.* **2013**, *66*, 746–758. [CrossRef]
8. Wetherhold, R. Damage and Failure of Composite Materials. *AIAA J.* **2014**, *52*, 859. [CrossRef]

9. Lapczyk, I.; Hurtado, J. Progressive damage modeling in fiber-reinforced materials. *Compos. Part A Appl. Sci. Manuf.* **2007**, *38*, 2333–2341. [CrossRef]
10. Degtyareva, N.; Gatheeshgar, P.; Poologanathan, K.; Gunalan, S.; Shyha, I.; McIntosh, A. Local buckling strength and design of cold-formed steel beams with slotted perforations. *Thin-Walled Struct.* **2020**, *156*, 106951. [CrossRef]
11. Rajanish, M.; Nanjundaradhya, N.; Ramesh, S.; Bhaskar, P. A Review Of Failure Of Composite Materials. *Int. J. Eng. Res. Appl.* **2012**, *3*, 122–124.
12. Kołakowski, Z.; Mania, R.J. Semi-analytical method versus the FEM for analysis of the local post-buckling of thin-walled composite structures. *Compos. Struct.* **2013**, *97*, 99–106. [CrossRef]
13. Debski, H.; Teter, A.; Kubiak, T. Numerical and experimental studies of compressed composite columns with complex open cross-sections. *Compos. Struct.* **2014**, *118*, 28–36. [CrossRef]
14. Kubiak, T.; Samborski, S.; Teter, A. Experimental investigation of failure process in compressed channel-section GFRP laminate columns assisted with the acoustic emission method. *Compos. Struct.* **2015**, *133*, 921–929. [CrossRef]
15. Teter, A.; Debski, H.; Samborski, S. On buckling collapse and failure analysis of thin-walled composite lipped-channel columns subjected to uniaxial compression. *Thin-Walled Struct.* **2014**, *85*, 324–331. [CrossRef]
16. Kreja, I. A literature review on computational models for laminated composite and sandwich panels. *Cent. Eur. J. Eng.* **2011**, *1*, 59–80. [CrossRef]
17. Turvey, G.J.; Zhang, Y. A computational and experimental analysis of the buckling, postbuckling and initial failure of pultruded GRP columns. *Comput. Struct.* **2006**, *84*, 1527–1537. [CrossRef]
18. Rozylo, P.; Debski, H.; Wysmulski, P.; Falkowicz, K. Numerical and experimental failure analysis of thin-walled composite columns with a top-hat cross section under axial compression. *Compos. Struct.* **2018**, *204*, 207–216. [CrossRef]
19. Kubiak, T.; Mania, R.J. Hybrid versus FR laminate channel section columns—Buckling and postbuckling behaviour. *Compos. Struct.* **2016**, *154*, 142–149. [CrossRef]
20. Wysmulski, P.; Debski, H. Post-buckling and limit states of composite channel-section profiles under eccentric compression. *Compos. Struct.* **2020**, *245*, 112356. [CrossRef]
21. Teter, A.; Kolakowski, Z. On using load-axial shortening plots to determine the approximate buckling load of short, real angle columns under compression. *Compos. Struct.* **2019**, *212*, 175–183. [CrossRef]
22. Teter, A.; Kolakowski, Z.; Jankowski, J. How to determine a value of the bifurcation shortening of real thin-walled laminated columns subjected to uniform compression? *Compos. Struct.* **2020**, *247*, 112430. [CrossRef]
23. Gawryluk, J.; Teter, A. Experimental-numerical studies on the first-ply failure analysis of real, thin walled laminated angle columns subjected to uniform shortening. *Compos. Struct.* **2021**, *268*, 114046. [CrossRef]
24. Abaqus 2019, HTML Documentation. Available online: http://130.149.89.49/v6.14/ (accessed on 5 May 2021).

materials

MDPI

Article

Higher Order Multiscale Finite Element Method for Heat Transfer Modeling

Marek Klimczak * and Witold Cecot

Faculty of Civil Engineering, Cracow University of Technology, Warszawska 24 Street, 31-155 Cracow, Poland; plcecot@cyf-kr.edu.pl
* Correspondence: mklimczak@L5.pk.edu.pl

Abstract: In this paper, we present a new approach to model the steady-state heat transfer in heterogeneous materials. The multiscale finite element method (MsFEM) is improved and used to solve this problem. MsFEM is a fast and flexible method for upscaling. Its numerical efficiency is based on the natural parallelization of the main computations and their further simplifications due to the numerical nature of the problem. The approach does not require the distinct separation of scales, which makes its applicability to the numerical modeling of the composites very broad. Our novelty relies on modifications to the standard higher-order shape functions, which are then applied to the steady-state heat transfer problem. To the best of our knowledge, MsFEM (based on the special shape function assessment) has not been previously used for an approximation order higher than $p = 2$, with the hierarchical shape functions applied and non-periodic domains, in this problem. Some numerical results are presented and compared with the standard direct finite-element solutions. The first test shows the performance of higher-order MsFEM for the asphalt concrete sample which is subject to heating. The second test is the challenging problem of metal foam analysis. The thermal conductivity of air and aluminum differ by several orders of magnitude, which is typically very difficult for the upscaling methods. A very good agreement between our upscaled and reference results was observed, together with a significant reduction in the number of degrees of freedom. The error analysis and the *p*-convergence of the method are also presented. The latter is studied in terms of both the number of degrees of freedom and the computational time.

Keywords: heat transfer; multiscale finite-element method; homogenization

Citation: Klimczak, M.; Cecot, W. Higher Order Multiscale Finite Element Method for Heat Transfer Modeling. *Materials* **2021**, *14*, 3827. https://doi.org/10.3390/ma14143827

Academic Editors: Michele Bacciocchi, Raimondo Luciano, Angelo Marcello Tarantino and Carmelo Majorana

Received: 9 June 2021
Accepted: 2 July 2021
Published: 8 July 2021

1. Introduction

Numerical modeling of the heterogeneous materials is a very active research field [1–7]. This is due to the fact that such materials are widely used in many important industry branches, e.g., civil engineering [1,2,6,7], automotive engineering [3,4], aerospace engineering [8] and many others. The composite's superior performance is due to its manifold mechanisms, among others:

- A specific composite type, e.g., laminate [9,10] or matrix-inclusion [1,5];
- The specific properties, shapes [11] and weight/volume ratios of the constituents;
- A very high adhesion between the constituents [5,11].

The major aspects, listed above, are analyzed at their respective scale, i.e., atomistic, micro-, meso- or macroscale, in order to optimize the overall composite performance at the higher scale. The design process of the new composites is enhanced with numerical analyses that are complementary to laboratory experimentsm and provide an evident speed-up. A number of numerical methods are used to model composites. The most frequent applications are based on the finite-element method [1,11], the finite-difference method [2], the discrete element method [12] and other methods [5,13]. In our research, we make use of the higher-order, finite-element method. In this paper, only the *p*-convergence is studied, i.e., we keep the same mesh and sequentially increase the approximation order

p within all elements. However, in our previous studies [14], we presented the application of the automatic *hp*-adaptivity [15,16] coupled with the multiscale finite-element method. The automatic *hp*-adaptivity enhances the whole framework due to its expected exponential convergence. In this paper, the scope is narrower concerning this aspect. The benefits of the higher-order multiscale-finite element method with the modified hierarchical shape functions in the multiscale analysis are demonstrated in Section 4.

A direct numerical analysis of the composite at the heterogeneity scale is frequently infeasible or unnecessary [17,18]. The analysis itself would be challenging in the context of the computational resources, as well as time-consuming. When completed, the results would provide an amount of data that could be impractical to present and demanding to store. Thus, a variety of upscaling methods was used to reduce the computation cost with the simultaneous incorporation of the lower-scale information in analyses carried out at the higher scale. Extensive revisions of the most popular upscaling methods can be found, for instance, in [19–22]. In our research, we made use of the multiscale finite-element method (MsFEM) in a form developed in [14,18,23,24]. A concise description of this is provided in Section 3.1. The outline and the specific features of the method are provided therein. Selected other multiscale finite-element methods [19] and similar approaches used for heat transfer analysis (or Poisson equations in general) are also presented in Section 3.1.

We mainly use MsFEM due to its flexibility. In the case of the composites' analysis, the method exhibits a very important advantage that should be stressed here. Namely, it is free of the assumption regarding the distinct separation of the bridged scales. In some applications (e.g., asphalt pavement), this feature is useful in effective multiscale analysis. This is due to the relationship between aggregate particle diameters and layer thicknesses.

The natural parallelization, without any special amendments, introduced to the independent problems solved within neighboring subdomains, guarantees a substantial speed-up to the computations. A number of observations, which are thoroughly discussed in Section 3.1, give rise to additional computational time savings, which facilitate MsFEM implementation.

The main novelty of this paper consists of the application of the higher-order, multiscale, finite-element method to the steady-state heat transfer problem. The approach is based on a modified shape function construction. The auxiliary boundary value problem was introduced, and used for the heat transfer problem. In our previous papers [14,18,23,24], we applied a higher-order MsFEM to other partial differential equations (PDEs), namely, to the elasticity and viscoelasticity.

In this paper, we demonstrate an effective MsFEM performance and also test its p-convergence in order to illustrate the benefits of the higher-order approximation in a steady-state heat transfer problem. It is additionally discussed in terms of the computational time.

Finally, the proposed method was tested on very challenging numerical problems with a large contrast in terms of its material parameters (several orders of magnitude).

Ensuring the effective and reliable heat transfer analysis of the composites is one of the challenging numerical problems. Multiscale methods are the common approach in this case, due to the reasons given in the above paragraph. State-of-the-art papers devoted to the review and classification of multiscale methods developed for the heat transfer problem are present in the literature [25–27]. The main distinction refers to the analysis scale [27]; therefore, one can distinguish:

- The microscale modeling using molecular dynamics (MD) with the motion analysis of every single atom/molecule in the domain [28,29];
- The particle-based mesoscopic modeling based on a coarse-grained analysis, e.g., Monte Carlo method, lattice Boltzmann method [30];
- The macroscale modeling with the assumption of the continuum of the domain [2,13, 31,32].

In order to avoid the problem of the excessively large amount of the information obtained in the direct composite analyses at any scale, a number of hybrid and multiscale methods are used for the heat transfer problem [27,28,30,31]. They can be classified in a

manifold manner. In [27], they are mainly grouped according to the scales they bridge, e.g., molecular dynamics—continuum description, molecular dynamics—particle-based description. Below, following the distinction used in [27], we briefly present the selected methods using a description of the respective resolution, in order to subsequently upscale this. However, it should be noted that the coupling of scales is not exclusively performed for two neighboring scales. For instance, a hierarchical bridging between several scales can be performed, as in [33]. Thus, the coupling possibilities are not limited to those presented in the next section.

In this paper, the focus is only on the macroscale modeling. Namely, at both bridged scales, the assumption of the continuum of the domain is used. The purpose of describing the methods referring to lower analysis scales is to place the multiscale, finite-element method among other approaches. In the case of micro- and mesoscale analysis, we arbitrarily selected the most representative methods. For an extensive review of these, we refer the reader to [27,28,30,31]. In the case of the macroscale modeling, the description is slightly different. We present several representative methods, as well as a group of approaches that share similar concepts, as the multiscale finite-element method used in this study.

1.1. Microscale Modeling

In molecular dynamics, we analyze the motion of every single atom. An atom's motion is described by Newton's second law and interactions between atoms are described by the potential functions [27,30]. In the case of large domains, this approach is very time-consuming and provides an excessive amount of information. Thus, the research interest was to simplify the modeling.

The first coupled MD-continuum analysis was described in [34], and referred to the flow in a channel. The whole domain was divided into an atomistic and continuum region with a hybrid solution interface (HSI), where both of the descriptions were valid. The development of the methodology presented in [34] was mainly associated with the numerical treatment of the atomistic region and its coupling with the continuum region [35] (*coupling by states*). A coupling strength parameter ξ was introduced, due to the constrained dynamics used to transfer the data at the HSI. The study on this parameter led to further improvements [36,37] in the methodology presented in [34]. In [38], these two regions (continuum and MD) were coupled, introducing the fluxes in the HSI (*coupling by fluxes*). The USHER algorithm was also proposed [39] for both types of coupling to conserve the overall energy, momentum and mass by manipulating the number of atoms at the HSI.

The methods presented above constitute a group of hybrid methods, which use two regions with a different description resolution. Although these approaches are not purely heat-transfer-oriented, their methodologies can also be applied to the leading problem of this paper and to other elliptic problems. Due to the necessity of partial MD analysis in the domain, they remain relatively computationally demanding.

In order to actually bridge the MD scale with the continuum scale, a number of methods that originated from the heterogeneous multiscale method (HMM) [40] were developed. The main analysis was carried out at the continuum level with the local transfer of information from the atomistic scale.

1.2. Mesoscale (Particle-Based) Modeling

Unlike in the molecular dynamics, where we analyze the motion of every single atom/molecule, mesoscale modeling is based on a coarse-grained analysis [26,27]. This approach can be regarded as a kind of microscale analysis upscaling. A group of molecules is represented by the computational particle, and the mechanisms of such particles' evolution were assumed. The differences between the main representatives of this group consist of a description of the particle evolution mechanism. The macroscale description was based on the continuum assumption at the higher scale, and the microscopic description at the lower scale is discrete. The mesoscale modeling is situated between these, i.e., the description is discrete but the scale of analysis (spatial and temporal) is substantially reduced.

When the particle motion is characterized by a probabilistic description, the direct simulation Monte Carlo method (DSMC) was established [27,30]. When the hydrodynamic behavior of the particles was mainly modeled by the addition of the dissipative force, dissipative particle dynamics (DPD) are used. Two other main representatives of this approach are the lattice gas automata (LGA) and the lattice Boltzmann method (LBM), which are based on the simplifications introduced to the collision term in the Boltzmann equation [27].

For the multiscale techniques bridging the microscale and mesoscale modeling, one can look at, e.g., the methods transferring the velocities between the scales [41] (MD, DPD and the continuum) or their distributions [42].

1.3. Macroscale Modeling

As far as the heat transfer modeling is concerned, the continuum assumption is typically used. It is also the main scale of interest within this paper. The methods which are most frequently [27] used to numerically solve the heat transfer problem at this scale are the finite-element method (FEM), the finite-difference method (FDM), the finite-volume method (FVM) and a number of further modifications. In our research, we make use of the higher-order finite-element method due to its expected exponential convergence, especially when combined with the automatic *hp*-adaptivity, as mentioned in Section 1.

The methods used to bridge between lower observation scales and the continuum description were mentioned in Sections 1.1 and 1.2. It is natural that the processes occurring at these scales affect the macroscale response. The scope of this paper is narrower. Namely, we are only interested in multiscale analysis at the continuum level. The constituent properties are assumed to be known (e.g., from the laboratory test), but we analyze the effective response of a composite.

The very basic engineering approach is made to assess the effective properties of the material (the conductivity, in this case) on the basis of its underlying microstructure. In further analysis, the material is numerically modeled as the homogeneous one. For instance, direct or inverse mixture rule is used for this purpose.

In the case of the periodic domains, a theoretical approach to the asymptotic homogenization [43,44] was primarily used. This is based on the auxiliary BVP solution for a unit cell. Practically, a number of such BVPs are solved for the increasing unit cell sizes. This version of the homogenization for the Poisson equation was used, e.g., in [45,46]. Unlike this method, the improved MsFEM used in this study does not require the periodicity of the domain. It needs an auxiliary BVP to be solved, but the subdomain (a coarse mesh element) used for this purpose is typically selected only once.

The most popular approach used in the numerical analyses is the computational homogenization [5,22], which is based on the representative volume element (RVE) approach. Using the auxiliary BVP solution for every RVE (typically associated with the Gauss integration point), the quantities at the macroresolution are assessed using the Hill–Mandel condition. It is also free of the assumption of domain periodicity. If the finite element method is used at both analysis levels, the approach is known as FE^2 homogenization [47,48]. The advantage of computational homogenization is that we do not need to assume a constitutive equation at the macroresolution, but can transfer the tangent stiffness tensor from the lower scale. The main limitation to this is the separation of the scales' condition in the RVE analysis. Namely, the ratio of the characteristic dimensions of the micro- and macroscale should not exceed 0.1. In some structures, this condition does not hold. The improved MsFEM, used in this study, does not require this condition to be fulfilled. The computational homogenization for the heat transfer problem is discussed, e.g., in [49]. In a recursive manner, macro- to microscale transitions are performed. The pointwise macroscale response is transferred to the lower scale in a form of the boundary conditions for the BVP solved in the RVE (and associated with this point). From this microscale level, the averaged quantities are transferred to the macroscale.

In [13,31], the multiscale seamless-domain method (SDM) is presented. It has some similarities to both the computational homogenization and the multiscale finite-element method used in this paper. The macroscale solution is sought at the so-called coarse-grained point. Its surrounding subdomain is discretized arbitrarily (regardless of the mesh generated for a subdomain associated with neighboring coarse-grained point). The solutions sought are interpolated within these subdomains. Subsequently, the final solution is obtained using the SDM scheme to "average" the solutions resulting from the overlapping subdomains. In MsFEM, discretizations for the neighboring subdomains need to be compatible. Moreover, MsFEM is the FE^2 scheme, unlike the SDM or the computational homogenization, which can be employed for any numerical method at the microscale level.

For instance, using the proper orthogonal decomposition (POD) at the RVE level constitutes the FEPOD method [50]. Therein, POD is used to reduce the basis and to speed-up the computations.

MsFEM shares a similar substructuring concept to the superelements [51]. This is a smart way of obtaining the fine mesh solution, using static condensation and solving the reduced problem only for the nodes associated with the skeleton. Consequently, the discretizations within the neighboring superelements need to be compatible. Unlike this concept, MsFEM first delivers the upscaled coarse-mesh solution, which can be transferred elementwise to the corresponding fine meshes.

As was noted in [27], not all the multiscale frameworks can be easily classified using the distinction on the bridged scales. The multiscale finite-element method improved in this paper does not fall within the above-mentioned classification. Like, e.g., the computational homogenization [22], it uses the same material description level (continuum) at both bridged scales.

The similarities between the MsFEM presented in this paper and the heterogeneous multiscale method (HMH) [40] should be underlined, since, in both cases, the microscale coupling $\boldsymbol{u}$ and macroscale $\boldsymbol{U}$ variables can be performed mutually by the respective operators. The means of their assessment constitutes the main part of the aforementioned methods. In HMH, the underlying microstructure is taken into account during the integration of the respective entries of the macroscale stiffness matrix and load vector. MsFEM enables the effective computation of these quantities through the multiplication operations of the assembled (within a coarse element) fine-mesh quantities.

A short comment on the nomenclature is necessary. There is a variety of so-called multiscale methods. The MsFEM version we use is based on a special shape function concept. There are also other approaches with a similar name. In [52], for instance, a multiscale finite-element method, based on the asymptotic expansion, is presented in applications to a periodic microstructure.

For a comprehensive description of the other existing homogenization methods, we refer to [20–22].

The remaining part of this paper is organized as follows. Section 2 constitutes a brief description of the analyzed heat transfer problem. For the sake of clarity, we limit this paper to the steady-state heat-transfer problem. In Section 3 an outline of the developed MsFEM version is presented, together with the formulation of the boundary value problem used to assess the special shape functions. Additionally, some comments on the numerical implementation are provided. In Section 4, the numerical results are shown to illustrate the performance of the introduced method. Finally, in Section 5, the findings of this paper are recapitulated and discussed.

2. Problem Formulation

We selected the steady-state heat-transfer equation as the test problem for the developed version of MsFEM. Thus, we limit our problem to the resulting Poisson equation of the following form:

$$\frac{\partial q_x}{\partial x} + \frac{\partial q_y}{\partial y} + \frac{\partial q_x}{\partial z} = f \tag{1}$$

Herein, f denotes the internal heat source; q_x, q_y and q_z denote the respective heat flux components. Using Fourier's law, the latter can be expressed in terms of the temperature $T(x, y, z)$, as:

$$\begin{aligned} q_x &= -k\frac{\partial T}{\partial x} \\ q_y &= -k\frac{\partial T}{\partial y} \\ q_z &= -k\frac{\partial T}{\partial z} \end{aligned} \tag{2}$$

where k is the thermal conductivity coefficient. We limit this study to the isotropic material, so k is independent of direction. This assumption is not necessary; therefore, we used it to simplify the description. Moreover, the materials analyzed in this study exhibit such behavior. Inserting (2) to Equation (1), we obtain:

$$-\frac{\partial}{\partial x}\left(k\frac{\partial T}{\partial x}\right) - \frac{\partial}{\partial y}\left(k\frac{\partial T}{\partial y}\right) - \frac{\partial}{\partial z}\left(k\frac{\partial T}{\partial z}\right) = f \tag{3}$$

for every subdomain with C^1-continuous k, with both temperature and normal flux component continuity on the subdomain interfaces. In this paper, we use only two types of boundary conditions, i.e.,

- Dirichlet boundary conditions: $T(x, y, z) = T_D$ on $\partial\Omega_D$;
- Neumann boundary conditions: $q_x n_x + q_y n_y + q_z n_z = q_N$ on $\partial\Omega_N$ ($\boldsymbol{n}$ is the unit outward normal vector, q_N denotes the heat flux across $\partial\Omega_N$).

3. Upscaling

In this chapter, the MsFEM outline is described and illustrated. Some comments on the implementation of the presented approach are also provided, to emphasize the potential benefits of its application in the numerical modeling of composites.

3.1. Idea

As was mentioned in the Introduction, MsFEM shares a similar concept to HMM [40]. Namely, there is a distinct hierarchy of scales. Let us name them the microscale and the macroscale. Unlike in the Introduction, they both refer to the continuum level, but the microscale resolves the heterogeneous material structure and the macroscale is the scale of the analyzed effective material response. The mappings between the micro- ($\boldsymbol{u}$) and macroscale ($\boldsymbol{U}$) degrees of freedom must be determined in the first step. As a result of the analysis, we obtain the macroscale solution, and the microscale one can be derived in the post-processing phase.

The construction of the prolongation operator $\boldsymbol{P}$, which allows us to express the microscale solution in terms of the macroscale one ($\boldsymbol{u} = \boldsymbol{P}\boldsymbol{U}$), as well as in the other way ($\boldsymbol{U} = \boldsymbol{P}^T\boldsymbol{u}$), is the core of the argued methodology.

We proceed with two sets of compatible meshes. The whole domain is discretized at the macroresolution level with a coarse mesh. Then, each of its elements is substantially refined in order to capture all the heterogeneities at the microresolution level. In this manner, the coarse mesh is naturally compatible with this set of the corresponding fine meshes. In [14], we demonstrated the potential of *hp*-adaptivity application at the macroresolution level. Thus, this is also used here.

In order to generate the prolongation operator $\boldsymbol{P}$, we modify the standard coarse-element shape functions to account for the microstructure, by the solution of the auxiliary problem in coarse elements [14,23]. In Figure 1, we present a standard bilinear shape function and its modified counterpart, which was obtained as an exemplary composite. Knowledge of the operator $\boldsymbol{P}$ is used to compute the effective stiffness matrices and load vectors. Instead of integrating the modified shape functions over the coarse elements, we can immediately compute the effective stiffness matrix $\boldsymbol{K_H}$ and load vector $\boldsymbol{f_H}$ using the

corresponding fine mesh quantities $\boldsymbol{K_h}$ and $\boldsymbol{f_h}$, which are assembled locally within a single coarse mesh element, since

$$\begin{aligned} \boldsymbol{K}_H &= \boldsymbol{P}^T \boldsymbol{K}_h \boldsymbol{P} \\ \boldsymbol{f}_H &= \boldsymbol{P}^T \boldsymbol{f}_h \end{aligned} \tag{4}$$

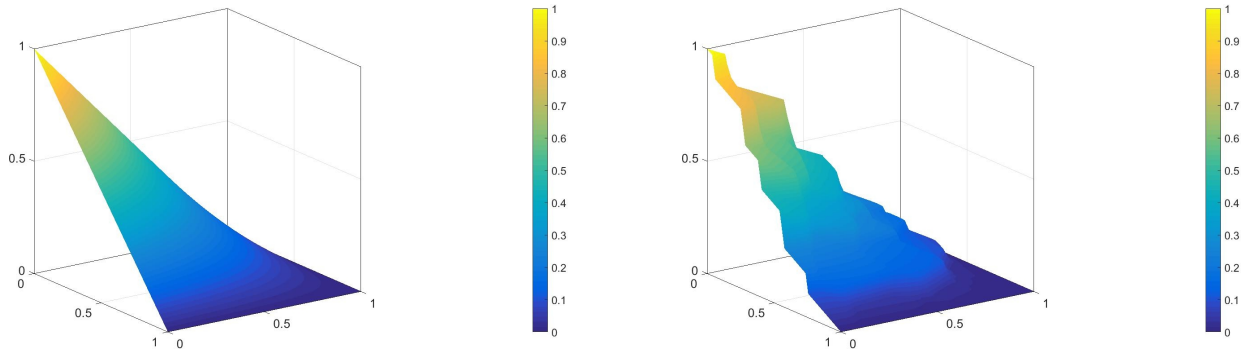

(**a**) (**b**)

Figure 1. Exemplary bilinear standard (**a**) and modified (**b**) shape functions for the unit square coarse element.

For a number of tests on the special shape functions, we refer to [18]. Therein, MsFEM was used to solve the linear elasticity and viscoelasticity problems.

The general algorithm of the MsFEM application to the steady-state heat-transfer problem is analogous to the one presented in [18] for the linear elasticity. The difference, beside the different governing partial differential equation (PDE) to be solved (Equation (3)), consists of the other auxiliary boundary value problem (Equation (5)), which was consequently used for the special shape function assessment. This is marked in blue in Algorithm 1.

Algorithm 1 Solve a heat transfer problem within a heterogeneous domain.

Require: define the problem (heterogeneous domain and boundary conditions)
Ensure: a coarse mesh and an appropriate refinement of each coarse element
  for n=1 to Nel **do** {loop over coarse mesh elements}
    for m=1 to M **do** {loop over n-th element shape functions}
      solve local problem (5) in the n-th element for the m-th shape function
    end for
    compute $\boldsymbol{K}_H$ and $\boldsymbol{f}_H$ for the n-th element
  end for
  solve the coarse mesh problem using the effective matrices $\boldsymbol{K}_H$ and vectors $\boldsymbol{f}_H$

3.2. Formulation

The problem formulation for the assessment of the modified shape function is presented below. This is solved within a subdomain Ω_s (occupied by a single coarse mesh element) of the whole analyzed domain Ω. We need to solve problem (5) for every coarse-element shape function. The degrees of freedom obtained for the m-th standard shape function Ψ are the m-th column of the prolongation operator $\boldsymbol{P}$. The problem presented below expresses the equality of the residuum of the solution (temperature) interpolant and residuum of the interpolated function Φ_m.

Given Ψ_m, which is a coarse mesh scalar-valued shape function ($m = 1, \ldots, M$), we look for its scalar-valued counterpart Φ_m, which is a discrete solution of the following Dirichlet boundary value problem

$$\begin{cases} \frac{\partial}{\partial x_i}\left(k\frac{\partial \Phi_m}{\partial x_i}\right) = -\frac{\partial^2}{\partial x_i^2}\Psi_m \quad \forall i = 1,2,3,\ \boldsymbol{x} \in \Omega_s^j \subset \Omega_s \subset \Omega \\ \Phi_m = \hat{\Phi}_m \quad \text{on} \quad \partial\Omega_s \\ + \text{interface continuity conditions} \end{cases} \tag{5}$$

where k is the thermal conductivity of the material at a given location $\boldsymbol{x}$, Ω_s^j *denotes the j-th constituent of the composite.*

For the finite-element-method computations, we need a variational formulation, which is presented below.

Find $\Phi_m \in V_0 + \hat{\Phi}$ *such that*

$$\int_\Omega k\nabla v \cdot \nabla \Phi_m d\Omega = \int_\Omega v \Delta \Psi_m d\Omega \quad \forall v \in V_0 \quad \text{where} \quad V_0 = \{v \in H^1(\Omega_s) : v = 0 \text{ on } \partial\Omega_s\} \tag{6}$$

This was obtained via the multiplication of (5) by the test function v, and the further integration of both equation sides over Ω_s (integrating by parts was also used at the left-hand side to transfer the derivative to the test function v). Practically, we additionally scaled the bubble functions in such a way that the extreme values were equal to 1.

Definition of the Dirichlet boundary conditions $\hat{\Phi}_m$ needs special treatment regarding the dimensionality of the problem:

- In 1D, we only solve the reduced Equation (5) ($i = 1$), obtaining the modified shape function. For the linear shape functions, we use 0 and 1 as the boundary conditions. For the "bubble" ones, $\hat{\Phi}_m$ is equal to zero. Exemplary standard and modified "bubble" shape functions for this case are shown in Figure 2. The horizontal thick lines represent the material distribution; thus, the standard shape function (Figure 2a) is the solution of problem (5) for the material with constant thermal conductivity in Ω_s^{1D}. The solution presented in Figure 2b was obtained using 50 finite elements, which comply with the microstructure schematically marked with the horizontal line. The green material is characterized by a thermal conductivity 10 times larger than the other one;
- In 2D, we first solve the 1D problems along all necessary Ω_s^{2D} edges, as described above. Then, we use these solutions as $\hat{\Phi}_m$ for the Equation (5) solved for $i = 1, 2$. The exemplary result of such a two-step strategy is presented in Figure 1b;
- In 3D, we need to solve reduced problems (5) along the edges and, subsequently, within the faces of the domain. Finally, Equation (5) is solved with the Dirichlet boundary conditions resulting from the lower scales auxiliary computations. A number of 3D-modified shape function examples for the linear elasticity problem can be found in [14,18].

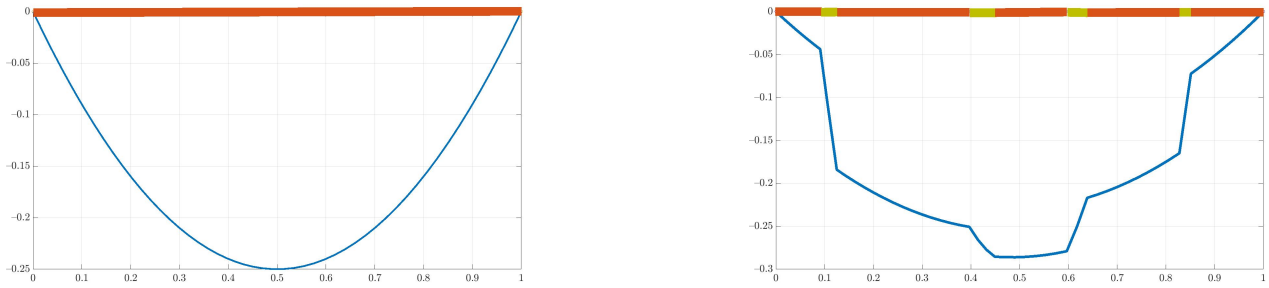

(**a**) (**b**)

Figure 2. Exemplary "bubble" (**a**) standard and (**b**) modified shape functions for the unit 1D coarse element.

3.3. Implementation

We implemented [14,18] MsFEM for the linear elasticity and viscoelasticity problems. In this paper (Section 4), we present the results of the 2D analysis of the steady-state heat transfer using modified MsFEM.

To facilitate the multiscale computations, one can take advantage of two approaches, which are almost equivalent in terms of time saved:

- For the periodic heterogeneous domains, we compute the effective stiffness matrix $\boldsymbol{K_H}$ once, and use it for every coarse mesh element—the effective load vectors $\boldsymbol{f_H}$ are different in most cases;
- For non-periodic heterogeneous domains, we can parallelize the computations of the coarse-mesh-element matrices and vectors $\boldsymbol{K_H}$ and $\boldsymbol{f_H}$.

The second option is general, and the only time losses are due to the transfer of the local fine mesh computation ($\boldsymbol{K_H}$ and $\boldsymbol{f_H}$) to the global solver.

Another advantage of MsFEM, in the context of computational efficiency, is the possible low cost of Equation (5) solution. In fact, this is the main computational cost of the whole approach, since it has to be solved for every standard coarse-element shape function Ψ_m. However, it can be observed that Equation (5) leads to a system of algebraic equations with multiple right-hand sides. Let us denote the number of the functions Ψ_m as M, and the time required for the solution of Equation (5) for a single Ψ_m as t_Ψ^m. The overall computational time T_P leading to the full operator $\boldsymbol{P}$ assessment is not, therefore, equal to $M \times t_\Psi^m$ but $T_P \ll M \times t_\Psi^m$, and it is of the order of t_Ψ^m. This is due to the fact that the computational time necessary to solve the system of linear algebraic equations with multiple right-hand sides does not significantly exceed the computational time used for a single system of linear algebraic equations.

In addition to the above discussion, one can observe that the matrix $\boldsymbol{K}_h$, present in (4), is the same as the left-hand side of (5) for the arbitrary coarse element. Thus, the assembly can be performed once and is primarily used for Equation (5), and subsequently for Equation (4), which can also provide a further speed-up to the computations.

Preserving the global continuity of the solution is necessary in the MsFEM workflow. In the case of the irregularly shaped constituents (see Figure 3a), the solution to Equation (5) along the edges of the coarse elements (denoted with numbers from 1 to 4) is straightforward. For instance, one of the modified linear shape functions for the common edge of elements 2 and 4 (marked with a red dotted line) is of the form shown in Figure 3b.

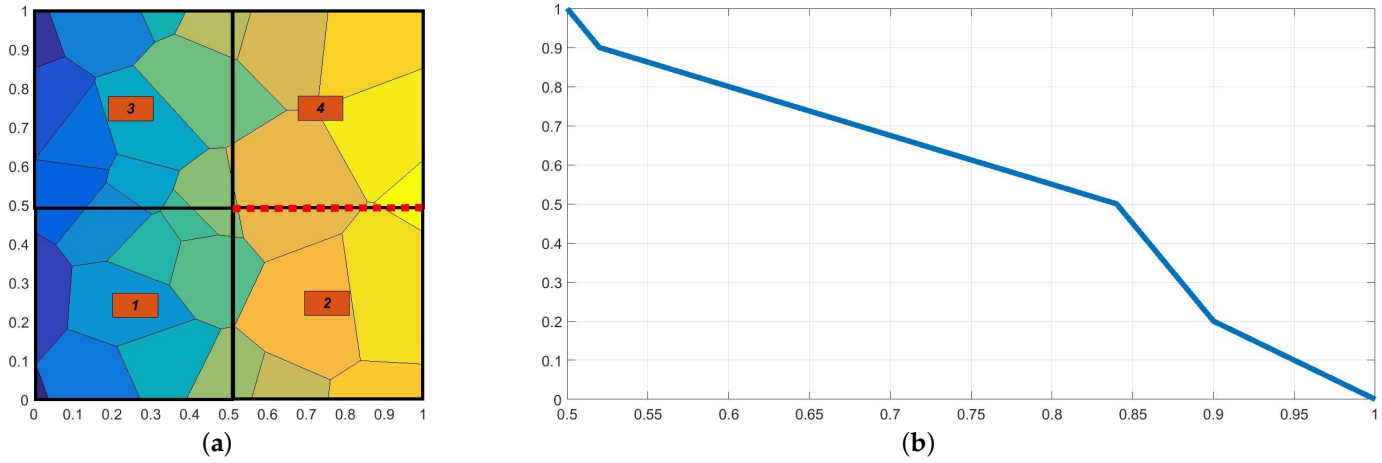

Figure 3. Exemplary shape function assessment: (**a**) analyzed domain—colors denote various thermal conductivities of the constituent, (**b**) modified linear shape function along the dotted edge.

A situation where the coarse element edge coincides with different material interfaces needs special attention. When solving Equation (5) along an edge, thermal conductivity k needs to be used for a given $\boldsymbol{x}$. Using different values for the common edge in a loop over coarse elements would not preserve the continuity of the sought function Φ within a 2D domain. To overcome this problem, we always take the average thermal conductivity at a given Gauss point ($\frac{k(\boldsymbol{x}+\boldsymbol{\varepsilon})+k(\boldsymbol{x}-\boldsymbol{\varepsilon})}{2}$, where $\boldsymbol{\varepsilon}$ is a small vector, orthogonal to the edge). This operation was performed to provide the continuity of the solution. If this was skipped, one could observe "jumps" in the solution of the interface (in the

discussed situation). The accuracy would decrease with the increasing contrast between the constituents' parameters.

4. Numerical Results

4.1. Asphalt Concrete

In this test, we analyzed a sample with the dimensions 10 cm × 15 cm, made of asphalt concrete (AC), as shown in Figure 4b. AC is a standard asphalt mixture that can be applied for all asphalt layers constituting the flexible pavement structure. It comprises two main phases: mastic (the asphalt binder mixed with the filler) and the aggregate particles. The detailed procedure of the AC microstructure generation used for this test is presented in [24]. Given the prescribed gradation curve in asphalt concrete, we used the approach based on the shrunk Voronoi cells to generate a microstructure realizing this requirement. Using the method presented in [24], we generated a non-periodic microstructure in a coarse element with "periodic boundary conditions", which enabled us to easily multiply this geometry. The temperature along the bottom edge was fixed and equal to 15 °C. The upper edge was subjected to heating with q = 30 W/m. The remaining edges were insulated (q = 0). Thermal conductivity was equal to 4 W/(mK) for the aggregate particles and 0.8 W/(mK) for the asphalt binder. In this test, we neglected the presence of the air voids.

In Figure 5, we present the temperature distributions obtained using direct FEM analysis (p = 1) and MsFEM (p = 5). The corresponding cross-section plots, performed at half the specimen height, are shown in Figure 6. The modified shape functions for the coarse elements are similar to those presented in Figure 1b. The temperature distributions for the lower approximation orders, used at the macroscale, were skipped for the sake of brevity. They are visually indistinguishable from the solution presented in Figure 5b. Instead, the convergence plots are presented in Figure 7. They illustrate the applicability of MsFEM with respect to both the number of degrees of freedom and computational time.

We measure the error using the following formula

$$\frac{|T^h - T^H|}{|T^h|} \tag{7}$$

where T^h is the value of temperature at a given position obtained using the fine mesh and T^H is the corresponding temperature obtained using the coarse mesh. By the fine mesh solution, we mean the reference solution plotted in Figure 5a. This was obtained using about 100,000 degrees of freedom.

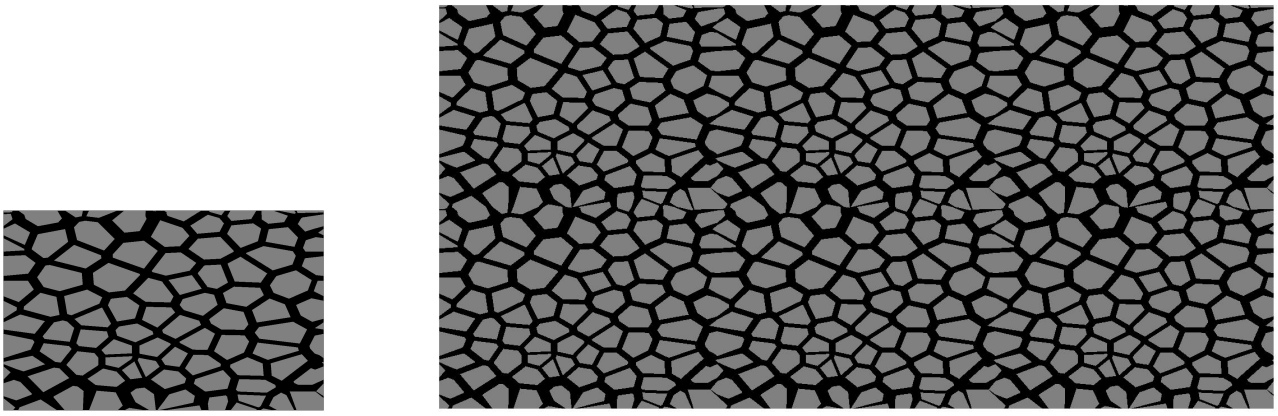

(**a**) (**b**)

Figure 4. Synthetic asphalt concrete microstructure: (**a**) within a single coarse element, (**b**) within a whole domain.

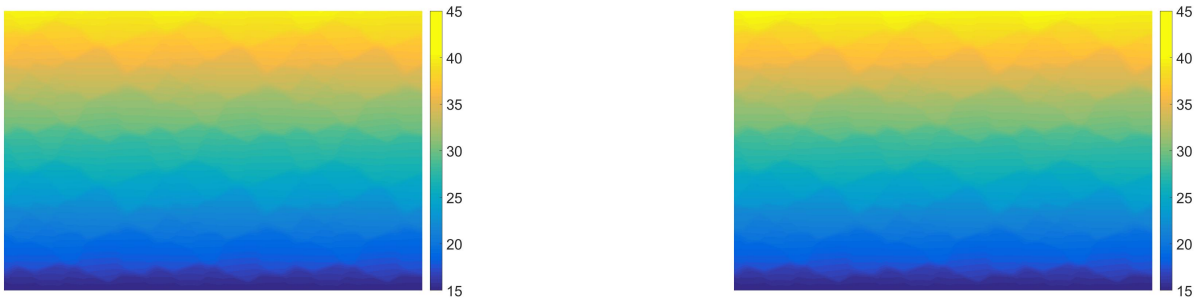

(**a**) (**b**)

Figure 5. Temperature distribution [°C]: (**a**) direct FEM solution, (**b**) upscaled solution (plotted for $p = 5$).

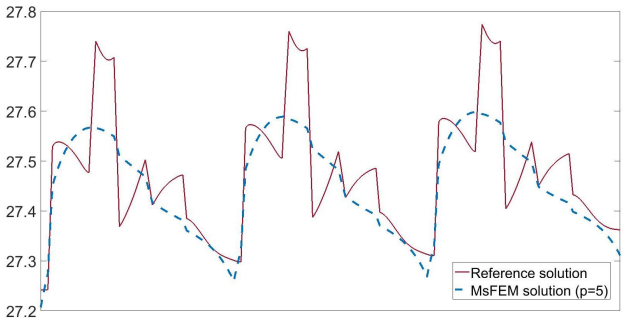

Figure 6. Temperature [°C] along the selected segment (at the half of the specimen height).

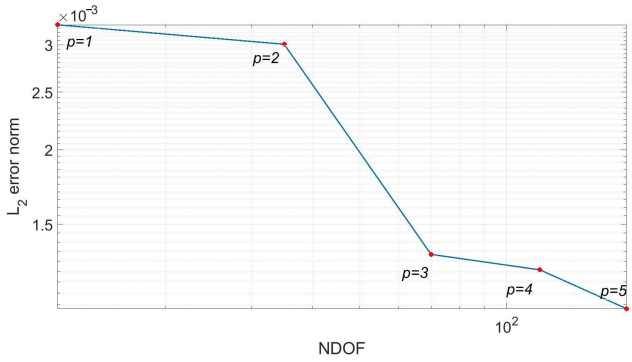

(**a**)

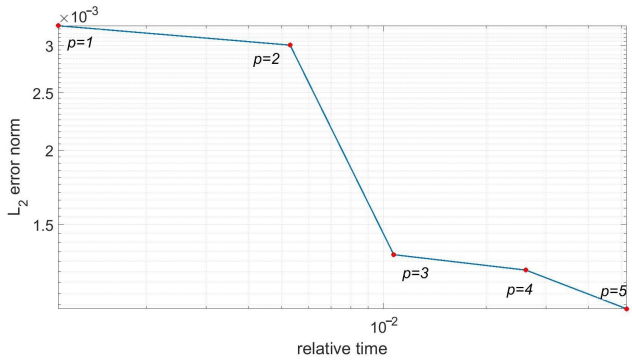

(**b**)

Figure 7. Convergence test for the increasing approximation orders at the macroscale (logarithmic scale) w.r.t. (**a**) number of degrees of freedom and (**b**) relative time (the ratio of the computational time used for the upscaled and reference solutions).

The additional modeling error introduced by the upscaling is very small; even for the bilinear shape functions used at the macroresolution its norm, it is smaller than 0.4%. It should be noted that, in this case, we used only 12 degrees of freedom. For the approximation order equal to 5 at this scale, the number of degrees of freedom (NDOF) is equal to 176 and the error norm drops to about 0.1%. The number of coarse elements is kept constant and equal to 6. The reduction in degrees of freedom between the reference and upscaled solutions range from about 570 to about 8300. The results of this test confirm the p-convergence of MsFEM. The h-convergence was not studied in this paper. The focus was on the verification of the higher-order approximation applicability at the macroscale. In our previous papers [14,23], we also tested this type of convergence for the elasticity problem.

In our academic code, we only implemented the approximation of the order p, equal up to 5, for the heat transfer problem. The code would have to be modified to numerically verify the further shape of the convergence plot for this example. It should be noted that the macroscale p-convergence is affected by the microscale, and the corresponding discretization at this scale. A theoretical example of $p \to \infty$ would be cumbersome for this method. A prohibitively expensive fine mesh would have to be generated in order to approximate, with linear shape functions (typically used at the microscale level), a macroscale shape function of a very high order. This would be the case even for a very simple geometry. Practically, the order $p = 5$ is very rarely exceeded in numerical applications.

4.2. Metal Foam

In the second test, we present the application of MsFEM in steady-state heat-transfer analysis of the metal foam. This lightweight material is used in many industry branches. In the context of the numerical modeling of heat transfer, the metal foam, analyzed with the application of any upscaling methods, can be regarded as a very challenging problem. This is due to the large difference between the constituents' thermal conductivity. In this test, we analyzed the idealized aluminum foam sample with a matrix thermal conductivity equal to 236 W/(mK) and the thermal conductivity of the air was set as 0.0262 W/(mK). The rectangular sample of dimensions 2 cm $\times$ 8 cm was heated along the upper edge with $q = 300$ W/m. Along the bottom edge, the temperature is equal to 15 °C and the remaining edges are insulated. The material distribution, as well as the reference and upscaled solutions, are presented in Figure 8. The corresponding cross-section plots, performed at half of the specimen height, are shown in Figure 9. The air voids are modeled as circles with a random radii distribution.

In this test, the reference solution was obtained using more than 69,000 degrees of freedom. The fine mesh within a single coarse element is shown in Figure 10.

The upscaled solutions were obtained using $10 \div 126$ degrees of freedom for the approximation order $p = 1 \div 5$, consecutively. The number of coarse elements is equal to 4. In Figure 11, we present the error convergence plots for the increasing approximation orders used at the macroscale. The convergence is demonstrated with respect to both the number of degrees of freedom and the computational time.

In this test, the L_2 norm of error (see Figure 11), measured according to 7, is equal to about 1.6% for $p = 1$ at the macroscale, and drops below 1.2% for the approximation order $p = 5$. The reduction in the number of degrees of freedom spans from about 550 ($p = 5$) to about 6900 ($p = 1$).

In Figure 12, we present the upscaling error distribution for this test (for $p = 1, 3, 5$). We compute the error according to Formula (7). The differences span from about 0.76% ($p = 5$) to about 2% ($p = 1$). These discrepancies are acceptable from the engineering perspective. The character of error distribution around the air voids closest to the boundary is the result of a small number of finite elements, generated between this boundary and the void (see Figure 10).

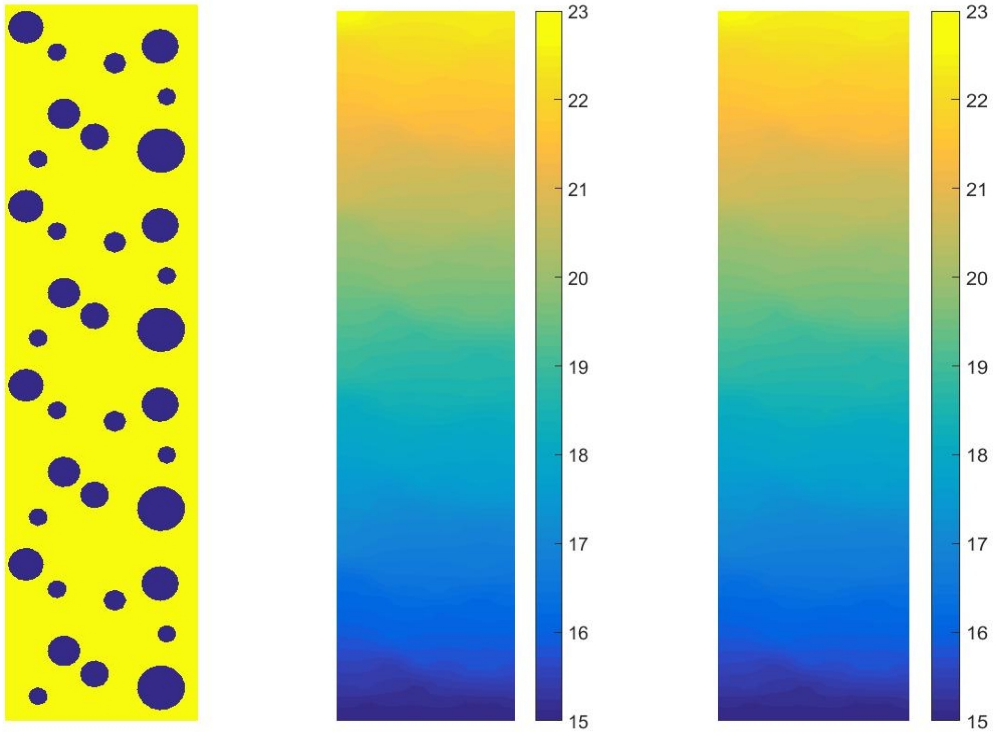

Figure 8. Material distribution (**a**) and temperature maps [°C]: (**b**) direct FEM solution, (**c**) upscaled solution (plotted for $p = 5$).

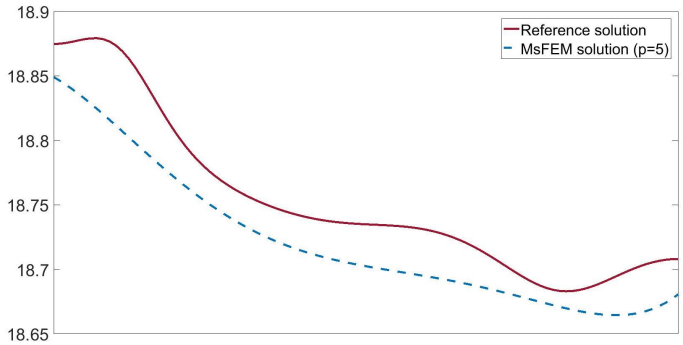

Figure 9. Temperature [°C] along the selected segment (at the half of the specimen height).

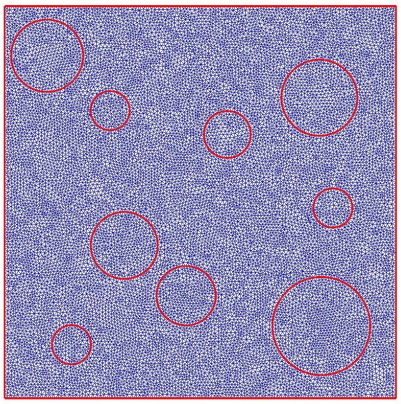

Figure 10. Fine mesh within a coarse element.

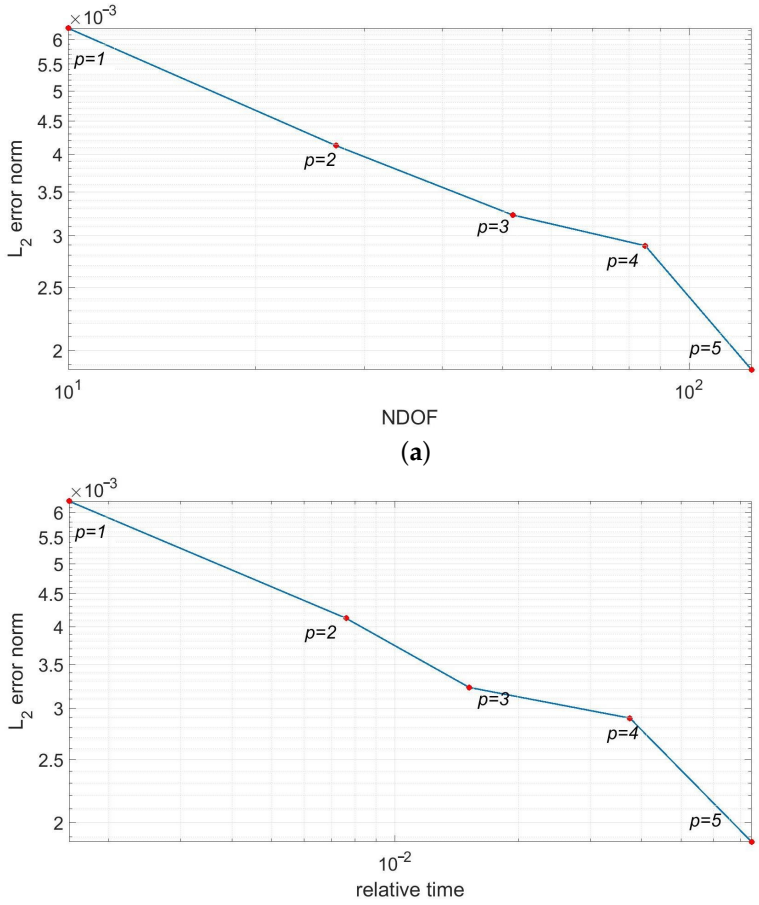

Figure 11. Convergence test for the increasing approximation orders at the macroscale (logarithmic scale) w.r.t. (**a**) number of degrees of freedom and (**b**) relative time (the ratio of the computational time used for the upscaled and reference solutions).

Both convergence plots were created using the logarithmic scale to demonstrate the impact of the higher-order approximation at the macroscale on the result correctness. Technically, the comparisons between the reference and upscaled solutions are justified, since the mesh was generated as follows. First, the mesh was generated for a single coarse element. Then, it was copied several times to model the whole domain. In this manner, we compare the solutions obtained using meshes of the same densities.

A short discussion regarding the error convergence plots shown in Figures 7b and 11b is necessary. Compared to the NDOF reduction in the upscaled solution, the observed speed-up is not equally impressive. This is due to the additional time necessary for the prolongation operator $\boldsymbol{P}$ assessment. It should be noted that this is highly affected by the implementation itself, as well as the discretizations at both scales. Moreover, MsFEM and other upscaling methods are addressed for problems, where the direct solutions are prohibitively computationally expensive or unfeasible to obtain. In this latter case, the computational time is less important than the ability to obtain the solution.

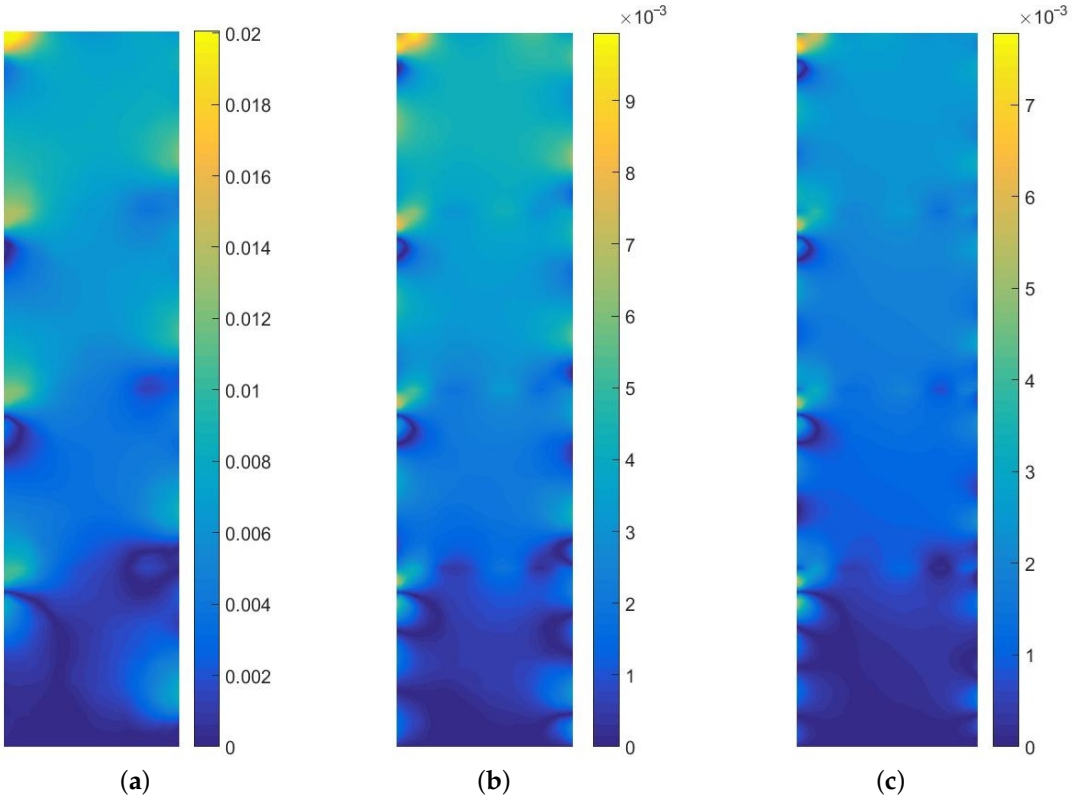

Figure 12. Error distribution for the increasing approximation order: (**a**) $p = 1$, (**b**) $p = 3$, (**c**) $p = 5$, consecutively.

5. Concluding Remarks

In this paper, we proposed a higher-order MsFEM for the steady-state heat-transfer problem. The main novelty consists of the modified shape function assessment for this problem, presented in Section 3.2, and numerical confirmation of the upscaled solution p-convergence for a very large material contrast. We demonstrated the convergence of this method with respect to both the number of degrees of freedom and the computational time.

The proposed approach was verified on two tests, which were performed for the realistic materials. The first presents the application of MsFEM to the steady-state heat-transfer analysis of the asphalt concrete sample. In this example, the focus was on the method performance for a non-trivial microstructure, and there was not a large difference between the constituent thermal conductivity. The second test presented the application of MsFEM to a very challenging numerical problem. The steady-state heat transfer analysis of the aluminum foam was presented. In order to illustrate the superiority of the method, the air voids were included in the numerical modeling. Its presence implies the necessity of special composite modeling. Namely, we deal with a material with constituent parameters varying by several orders of magnitude. This is a very difficult problem for any upscaling method.

In both of the presented tests, a large reduction in the degrees of freedom was observed for the upscaled solutions. Compared to the reference fine mesh solutions, this was equal to $570 \div 8300$ (asphalt concrete sample) and $550 \div 6900$ (metal foam sample). It should be noted that, even for the harder test (metal foam) and the bilinear approximation, the maximum error is equal to about 2%. In both tests, the p-convergence was observed. Considering the large disproportion of the material parameters and the obtained NDOF reduction, this result is acceptable.

In terms of the computational time, the applicability of MsFEM was also demonstrated. The relative time, i.e., the ratio of the computational time necessary for the upscaled and reference solutions, is much smaller than the unity for both tests. The possible speed-up is highly affected by the implementation and discretizations at both scales. Thus, this can be increased. However, this was not the focus of this study.

Our further research effort is to extend the proposed framework to thermoelastic analysis. Such an approach is necessary, e.g., in the context of asphalt concrete modeling, where the thermal effects are very significant.

Author Contributions: Conceptualization, M.K. and W.C.; methodology, M.K.; investigation, M.K. and W.C.; writing—original draft preparation, M.K.; writing—review and editing, M.K. and W.C. Both authors have read and agreed to the published version of the manuscript.

Funding: This research was funded by Narodowe Centrum Nauki (Poland) grant number UMO-2017/25/B/ST8/02752. The APC was funded by the Dean of the Civil Engineering Faculty (Cracow University of Technology).

Institutional Review Board Statement: Not applicable.

Informed Consent Statement: Not applicable.

Data Availability Statement: Data sharing is not applicable.

Conflicts of Interest: The authors declare no conflict of interest. The funders had no role in the design of the study; in the collection, analyses, or interpretation of data; in the writing of the manuscript, or in the decision to publish the results.

References

1. You, T.; Al-Rub, R.; Darabi, M.; Masad, E.; Little, D. Three-dimensional microstructural modeling of asphalt concrete using a unified viscoelastic-viscoplastic-viscodamage model. *Constr. Build. Mater.* **2012**, *28*, 531–548. [CrossRef]
2. Jia, L.; Sun, L.; Huang, L.; Qin, J. Numerical temperature prediction model for asphalt concrete pavement. *J. Tongji Univ.* **2007**, *35*, 1039–1043.
3. Israr, H.; King, W.; Rivallant, S. Numerical Modelling Strategies for Composite Structures crashworthiness: A Review. *J. Adv. Res. Mater. Sci.* **2018**, *42*, 8–23.
4. Pinho, S.; Camanho, P.; Moura, M.D. Numerical simulation of the crushing process of composite materials. *Int. J. Crashworthiness* **2004**, *9*, 263–276. [CrossRef]
5. Jaworska, I. Higher order multipoint Meshless Finite Difference Method for two-scale analysis of heterogeneous materials. *Int. J. Multiscale Comput. Eng.* **2019**, *17*, 239–260. [CrossRef]
6. Wang, Y.H.; Nie, J.G.; Cai, C. Numerical modeling on concrete structures and steel-concrete composite frame structures. *Compos. Part Eng.* **2013**, *51*, 58–67. [CrossRef]
7. Ožbolt, J.; Balabanić, G.; Kušter, M. 3D Numerical modelling of steel corrosion in concrete structures. *Corros. Sci.* **2011**, *53*, 4166–4177. [CrossRef]
8. Guinard, S.; Bouclier, R.; Toniolli, M.; Passieux, J.C. Multiscale analysis of complex aeronautical structures using robust non-intrusive coupling. *Adv. Model. Simul. Eng. Sci.* **2018**, *5*, 1–27. [CrossRef]
9. Guan, Z.; Cantwell, W.; Abdullah, M. Numerical Modeling of the Impact Response of Fiber-Metal Laminates. *Polym. Compos.* **2009**, *30*, 603–611. [CrossRef]
10. Liu, T.; Zhang, X.T.; He, N.B.; Jia, G.H. Numerical Material Model for Composite Laminates in High-Velocity Impact Simulation. *Lat. Am. J. Solids Struct.* **2017**, *14*, 1912–1931. [CrossRef]
11. Liu, P.; Hu, J.; Wang, D.; Oeser, M.; Alber, S.; Ressel, W.; Fala, G. Modelling and evaluation of aggregate morphology on asphalt compression behavior. *Constr. Build. Mater.* **2017**, *133*, 196–208. [CrossRef]
12. Liu, Y.; Dai, Q.; You, Z. Viscoelastic Model for Discrete Element Simulation of Asphalt Mixtures. *J. Eng. Mech.* **2009**, *135*, 324–333. [CrossRef]
13. Suzuki, Y. A domain decomposition technique based on the multiscale seamless-domain method. *Mech. Eng. J.* **2017**, *4*, 17–00145. [CrossRef]
14. Klimczak, M.; Cecot, W. An adaptive MsFEM for non periodic viscoelastic composites. *Int. J. Numer. Methods Eng.* **2018**, *114*, 861–881. [CrossRef]
15. Demkowicz, L.; Rachowicz, W.; Devloo, P. A Fully Automatic *hp*-Adaptivity. *J. Sci. Comput.* **2002**, *17*, 117–142. [CrossRef]
16. Demkowicz, L.; Kurtz, J.; Pardo, D.; Paszynski, M.; Rachowicz, W.; Zdunek, A. *Computing with hp-Adaptive Finite Elements. Vol 2. Frontiers: Three-Dimensional Elliptic and Maxwell Problems with Applications*; Chapman & Hall/CRC: New York, NY, USA, 2008.
17. Schüller, T.; Jänicke, R.; Steeb, H. Nonlinear modeling and computational homogenization of asphalt concrete on the basis of XRCT scans. *Constr. Build. Mater.* **2016**, *109*, 96–108. [CrossRef]
18. Klimczak, M.; Cecot, W. Towards asphalt concrete modeling by the multiscale finite element method. *Finite Elem. Anal. Des.* **2020**, *171*, 103367. [CrossRef]
19. Efendiev, Y.; Hou, T. *Multiscale Finite Element Methods*; Springer: New York, NY, USA, 2009.
20. Fish, J. (Ed.) *Multiscale Methods. Bridging the Scales in Science and Engineering*; Oxford University Press: Oxford, UK, 2009.
21. Fish, J. *Practical Multiscaling*; Wiley: Chichester, UK, 2014.

22. Geers, M.; Kouznetsova, V.; Brekelmans, W. Multi-scale computational homogenization: Trends and challenges. *J. Comput. Appl. Math.* **2010**, *234*, 2175–2182. [CrossRef]
23. Cecot, W.; Oleksy, M. High order FEM for multigrid homogenization. *Comput. Math. Appl.* **2015**, *70*, 1391–1400. [CrossRef]
24. Klimczak, M.; Cecot, W. Synthetic Microstructure Generation and Multiscale Analysis of Asphalt Concrete. *Appl. Sci.* **2020**, *10*, 765. [CrossRef]
25. Murthy, J.; Mathur, S. Computational Heat Transfer in Complex Systems: A Review of Needs and Opportunities. *J. Heat Transf.* **2012**, *134*, 031016. [CrossRef]
26. He, Y.L.; Tao, W.Q. Numerical Solutions of Nano/Microphenomena Coupled With Macroscopic Process of Heat Transfer and Fluid Flow: A Brief Review. *J. Heat Transf.* **2015**, *137*, 090801. [CrossRef]
27. Tong, Z.X.; He, Y.L.; Tao, W.Q. A review of current progress in multiscale simulations for fluid flow and heat transfer problems: The frameworks, coupling techniques and future perspectives. *Int. J. Heat Mass Transf.* **2019**, *137*, 1263–1289. [CrossRef]
28. Chantrenne, P. Multiscale simulations: Application to the heat transfer simulation of sliding solids. *Int. J. Mater. Form.* **2008**, *1*, 31–37. [CrossRef]
29. Sun, H.; Li, F.; Wang, M.; Xin, G.; Wang, X. Molecular dynamics study of convective heat transfer mechanism in a nano heat exchanger. *RSC Adv.* **2020**, *10*, 23097–23107. [CrossRef]
30. Teschner, T.; Könözsy, L.; Jenkins, K. Progress in particle-based multiscale and hybrid methods for flow applications. *Microfluid. Nanofluid.* **2016**, *20*, 68. [CrossRef]
31. Suzuki, Y. Multiscale Seamless-Domain Method for Nonperiodic Fields: Nonlinear Heat Conduction Analysis. *Int. J. Multiscale Comput. Eng.* **2019**, *17*, 1–28. [CrossRef]
32. Khan, A.A.; Bukhari, S.R.; Marin, M.; Ellahi, R. Effects of Chemical Reaction on Third-Grade MHD Fluid Flow Under the Influence of Heat and Mass Transfer With Variable Reactive Index. *Heat Transf. Res.* **2019**, *50*, 1061–1080. [CrossRef]
33. Murashima, T.; Urata, S.; Li, S. Coupling finite element method with large scale atomic/molecular massively parallel simulator (LAMMPS) for hierarchical multiscale simulations. *Eur. Phys. J.* **2019**, *92*. [CrossRef]
34. O'Connell, S.; Thompson, P. Molecular dynamics-continuum hybrid computations: A tool for studying complex fluid flows. *Phys. Rev. E* **1995**, *52*, 5792–5795. [CrossRef] [PubMed]
35. Hadjiconstantinou, N.; Patera, A. Heterogeneous Atomistic-Continuum Representations for Dense Fluid Systems. *Int. J. Mod. Phys. C* **1997**, *8*, 967–976. [CrossRef]
36. Wang, Y.C.; He, G.W. A dynamic coupling model for hybrid atomistic–continuum computations. *Chem. Eng. Sci.* **2007**, *62*, 3574–3579. [CrossRef]
37. Kamali, R.; Kharazmi, A. Investigation of multiscale fluid flow characteristics based on a hybrid atomistic–continuum method. *Comput. Phys. Commun.* **2013**, *184*, 2316–2320. [CrossRef]
38. Flekkøy, E.; Wagner, G.; Feder, J. Hybrid model for combined particle and continuum dynamics. *Europhys. Lett.* **2000**, *52*, 271–276. [CrossRef]
39. Delgado-Buscalioni, R.; Coveney, P. USHER: An algorithm for particle insertion in dense fluids. *J. Chem. Phys.* **2003**, *119*, 978–987. [CrossRef]
40. E, W.; Engquist, B.; Huang, Z. Heterogeneous multiscale method: A general methodology for multiscale modeling. *Phys. Rev. B* **2003**, *67*, 092101. [CrossRef]
41. Fedosov, D.; Karniadakis, G. Triple-decker: Interfacing atomistic-mesoscopic-continuum flow regimes. *J. Comput. Phys.* **2009**, *228*, 1157–1171. [CrossRef]
42. Liang, T.; Ye, W. An Efficient Hybrid DSMC/MD Algorithm for Accurate Modeling of Micro Gas Flows. *Commun. Comput. Phys.* **2014**, *15*, 246–264. [CrossRef]
43. Bensoussan, A.; Lions, J.L.; Papanicolaou, G. *Asymptotic Analysis for Periodic Structures*; North Holland: Amsterdam, The Netherlands, 1978.
44. Sanchez-Palencia, E. Non-homogeneous media and vibration theory. In *Lecture Notes in Physics 127*; Springer: Berlin/Heidelberg, Germany, 1980.
45. Donato, P.; Paulin, J.S.J. Homogenization of the Poisson equation in a porous medium with double periodicity. *Jpn. J. Ind. Appl. Math.* **1993**, *10*, 333–349. [CrossRef]
46. Melnyk, T. Homogenization of the Poisson Equation in a Thick Periodic Junction. *J. Anal. Its Appl.* **1999**, *18*, 953–975. [CrossRef]
47. Feyel, F.; Chaboche, L. FE^2 multiscale approach for modelling the elasto-visco-plastic behaviour of long fibre SiC/Ti composite materials. *Comput. Methods Appl. Mech. Eng.* **2000**, *183*, 309–330. [CrossRef]
48. Feyel, F. A multilevel finite element method (FE^2) to describe the response of highly non-linear structures using generalized continua. *Comput. Methods Appl. Mech. Eng.* **2003**, *192*, 3233–3244. [CrossRef]
49. Özdemir, I.; Brekelmans, W.; Geers, M. Computational homogenization for heat conduction in heterogeneous solids. *Int. J. Numer. Methods Eng.* **2008**, *73*, 185–204. [CrossRef]
50. Radermacher, A.; Bednarcyk, B.; Stier, B.; Simon, J.; Zhou, L.; Reese, S. Displacement-based multiscale modeling of fiber-reinforced composites by means of proper orthogonal decomposition. *Adv. Model. Simul. Eng. Sci.* **2016**, *3*, 1–23. [CrossRef]
51. Cook, R.D.; Malkus, D.S.; Plesha, M.E.; Witt, R.J. *Concepts and Applications of Finite Element Analysis*; Wiley: Chichester, UK, 2002.
52. Liu, X.Q. Multiscale Finite Element Methods for Heat Equation in Three Dimension Honeycomb Structure. In Proceedings of the Third International Conference on Artificial Intelligence and Computational Intelligence, AICI'11, Taiyuan, China, 24–25 September 2011; Volume 3, pp. 186–194.

materials

MDPI

Article

Material Properties of HY 80 Steel after 55 Years of Operation for FEM Applications

Szturomski Bogdan and Kiciński Radosław *

Mechanical and Electrical Engineering Department, Polish Naval Academy, 81-103 Gdynia, Poland; bsztur@gmail.com

* Correspondence: r.kicinski@amw.gdynia.pl; Tel.: +48-505-710-486

Abstract: The paper presents the results of testing the properties of HY 80 steel from the hull of a Kobben class 207 submarine after 60 years of operation in extreme sea conditions. Steels from the HY family in the post-war period were used to build American and German submarines. For the obtained fragment of steel from the hull of the Polish submarine ORP Jastrząb (ORP-Boat of the Republic of Poland), static tensile tests were performed on an MTS testing machine. Dynamic tensile tests were carried out on a rotary hammer for the strain rate in the range of 500~2000 s^{-1}. Results: Based on the obtained results, the Johnson–Cook model and the failure parameters of HY 80 steel in terms of the finite element method (FEM) were developed. Conclusion: This model can be used to simulate fast-changing processes such as resistance of structures to collisions, shelling, and the impact of pressure waves caused by explosions in water and air related to submarines.

Keywords: HY 80 steel; static tensile test; dynamic tensile test; rotary hammer; plastic characteristics; Johnson–Cook material model

Citation: Bogdan, S.; Radosław, K. Material Properties of HY 80 Steel after 55 Years of Operation for FEM Applications. *Materials* **2021**, *14*, 4213. https://doi.org/10.3390/ma14154213

Academic Editor: Michele Bacciocchi

Received: 5 July 2021
Accepted: 26 July 2021
Published: 28 July 2021

1. Introduction

Steels of increased strength have been used to construct the hulls of submarines, the structure of which is exposed to high loads caused by water pressure when submerged, impacts when lying on the bottom, and the effects of explosions of underwater mines and depth bombs. Commonly used by the United States for shipbuilding in the post-war years were HY 80, HY 100, HY 130, and HY 200 [1,2]. In 1960, HY 80 steel was used to make the hull of the first nuclear-powered submarine USS Thresher (SSN-593), which unfortunately ended its service tragically in April 1963.

The hulls of Los Angeles type units-USS Providence (SSN-719) [3] were made of HY 80 steel [4]. German shipyards also used this steel for the construction of project 205 submarines and their modifications. Until 2019, there were four Kobben-class (project 207) submarines in operational use by the Polish Navy. These were (S-306 Skolpen) ORP "Sep", (S-308 Stord) ORP "Sokol", (S-309 Swenner) ORP "Bielik", and (S-319 Kunna) ORP "Kondor" (Figure 1). The fifth submarine, (S-318 Kobben) ORP "Jastrzab", is used as a crew training simulator at the Polish Naval Academy. They are the last ships of this series worldwide. In 1964–1967, 15 such units were built at the German shipyard Rheinstahl Nordseewerke to modify the 205 project submarines for Norway's Navy. Five of them were transferred to the Polish Navy in 2002–2003 [5]. These ships end their service in the Polish Navy. Due to the decommissioning, their tactical data can be declassified, and therefore, their documentation can be used for scientific purposes.

HY 80 (High Yield 80) steel can withstand a load of 80 pounds per square inch which is equivalent to approximately 551.5 MPa. Their catalogue yield point is 552 MPa [4]. It is an iron alloy with a content of 0.12–0.2% carbon, 2–3.5% nickel with the addition of chromium, molybdenum, and copper. Owing to these additives, they are characterised by increased strength, good plasticity, impact strength, and corrosion resistance. Moreover,

steels of this type show good weldability, making it possible to build ships in sections and then join them [2].

Figure 1. Submarines of project 207 (Kobben) in the home port in Gdynia [6].

In recent years, the number of accidents to submarines made of HY80 steel has increased. As a result of this study, submarine engineers have the opportunity to analyse the strength of submarine hulls. They can decide to allow them for further use. The conducted tests will allow the properties of the steel to be assessed after 55 years of operation to discern whether they have changed, or whether the ship's hull can be further used.

2. Materials and Methods

The adaptation of ORP "Jastrząb" (S-318 Kobben, built: 1966) (Figure 2) as a submarine simulator at the Naval Academy in Gdynia required numerous modifications to the hull, including vents and air conditioning connections. The material that had been removed to make holes for conditioning purposes was obtained as strength test specimens.

The obtained material was used to make standardised samples for the quasi-static tensile test on the MTS testing machine with a diameter of 8 mm in accordance with EN ISO 6892-1: 2016 [7] (Figure 3). For the dynamic tensile test on a rotary hammer, round specimens with a thread with a working part diameter of 5 mm and a length of 40 mm were made. The samples were made along the ship's axis–axial.

Figure 2. ORP "Jastrząb" (S-318 Kobben). Places from which material was taken for test samples.

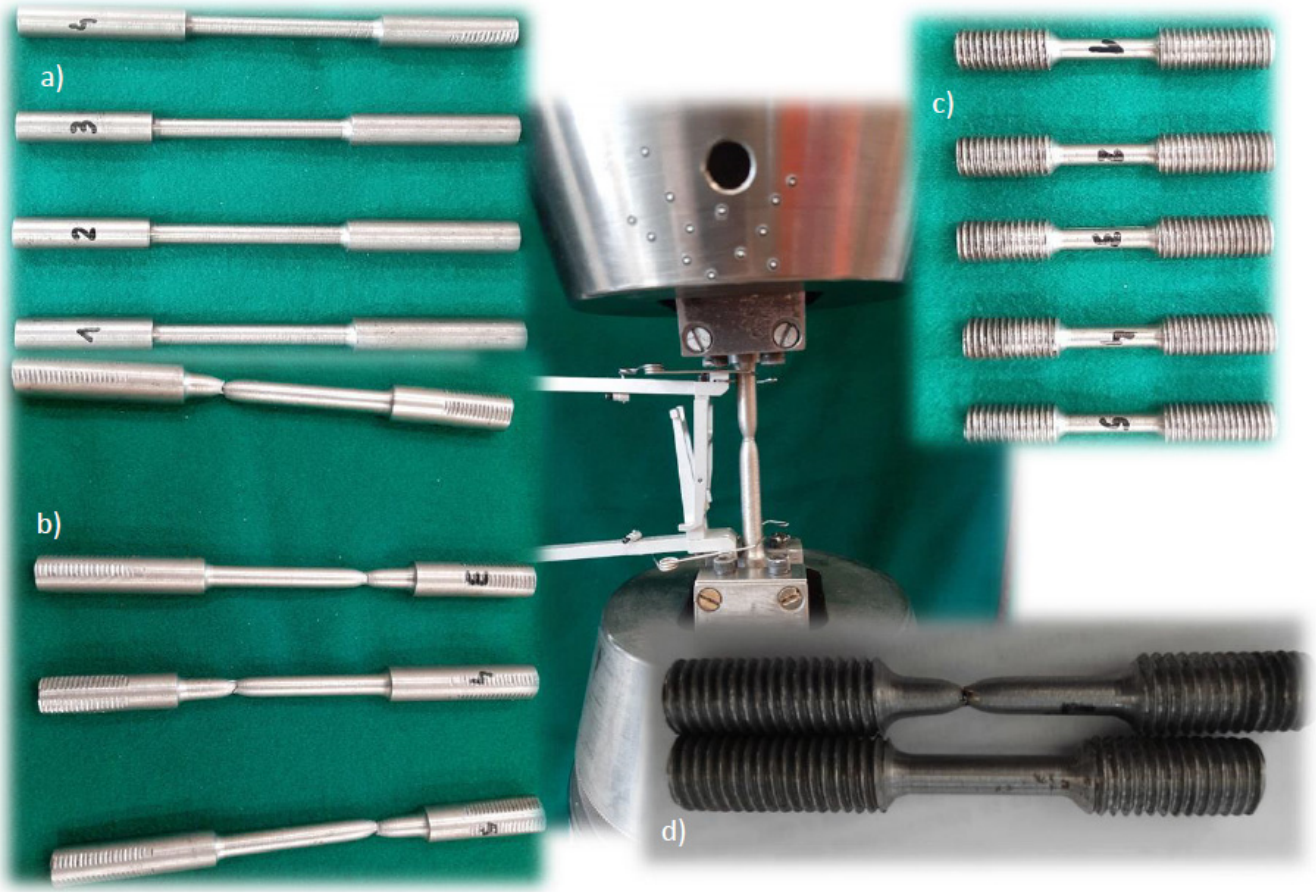

Figure 3. HY 80 steel specimens for static and dynamic tests: (**a**) samples for static tests on the MTS machine; (**b**) samples for static tests after fracture; (**c**) samples for dynamic tests on a rotary hammer; (**d**) samples for dynamic tests after fracture.

3. Results

3.1. Uniaxial Static Tensile Test

Samples were prepared from the obtained material, and a static tensile test was performed. The test was carried out on four samples. The test results are summarised in Figure 4.

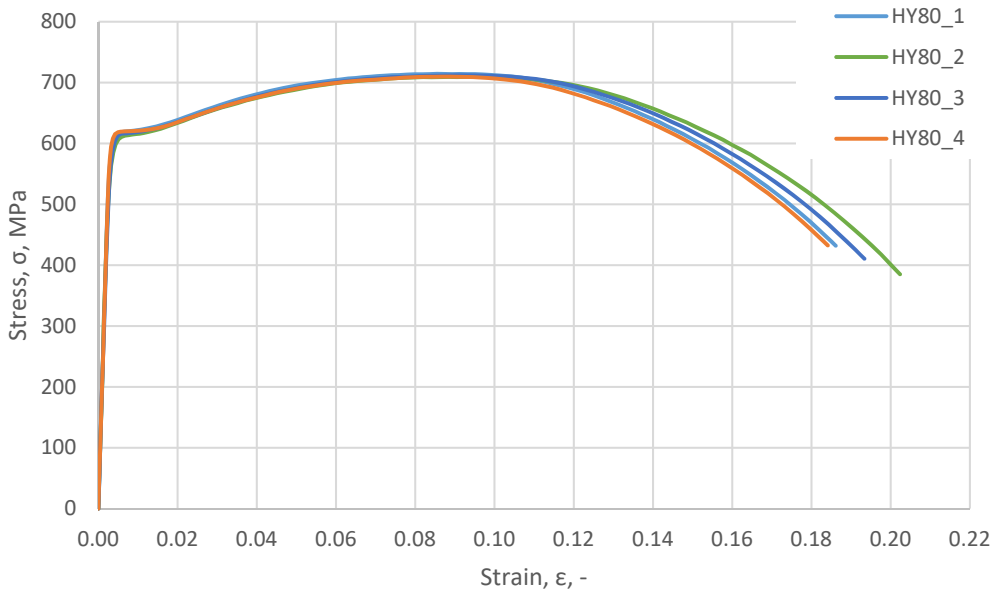

Figure 4. Tensile test results; nominal σ–ε of HY 80 steel, strain rate $\dot{\varepsilon} = 0.0001\ s^{-1}$.

3.2. The Study of Dynamic Mechanical Properties Using a Rotary Hammer

The Fundamentals of Technology Laboratory of the Naval Academy in Gdynia has a unique stand-a rotary hammer (Figure 5) that enables performing the dynamic tensile test at speeds in the range of 10–50 m/s. With a sample length of 20 mm, this allows the strain rate to be equal to 500–2000 s^{-1}. The measurement results are presented in Table 1.

At the rotary hammer laboratory stand, the sample breaking force is recorded at a given strain rate in the range of 0–2000 s^{-1}. The maximum breaking force is then converted into the stress corresponding to the ultimate strength in dynamic tensile strength. The strain rate is defined as the ratio of the tearing speed of the sample to its measured length [8] as follows:

$$\dot{\varepsilon} = \frac{d\varepsilon}{dt} = \frac{d}{dt}\left(\frac{v \cdot t}{l}\right) = \frac{v}{l} \tag{1}$$

3.3. HY 80 True Characteristics

The relationship between the true stresses σ_{true} and nominal stresses σ_{nom} obtained from the tensile test is obtained assuming that the volume of the stretched sample during stretching is constant; thus,

$$l_0 \cdot A_0 = l \cdot A(F) \tag{2}$$

Hence,

$$\sigma_{true} = \frac{F}{A(F)} = \frac{F}{A_0}\frac{l}{l_0} = \sigma_{nom}\left(\frac{l}{l_0}\right) \tag{3}$$

Since

$$\frac{l}{l_0} = 1 + \varepsilon_{nom} \tag{4}$$

we have, therefore,

$$\varepsilon_{true} = \ln(1 + \varepsilon_{nom}). \tag{5}$$

$$\sigma_{true} = \sigma_{nom}(1 + \varepsilon_{nom}) \tag{6}$$

Plastic deformation is the difference between the true deformation ε_{true}, and the elastic deformation ε_{el}.

$$\varepsilon_{pl} = \varepsilon_{true} - \varepsilon_{el} = \varepsilon_{true} - \frac{\sigma_{true}}{E} \quad (7)$$

According to the above formulas, the true and plastic characteristics for the tested HY 80 steel samples were developed (Figure 6). The basic material constants describing the tested steel are summarised in Table 2.

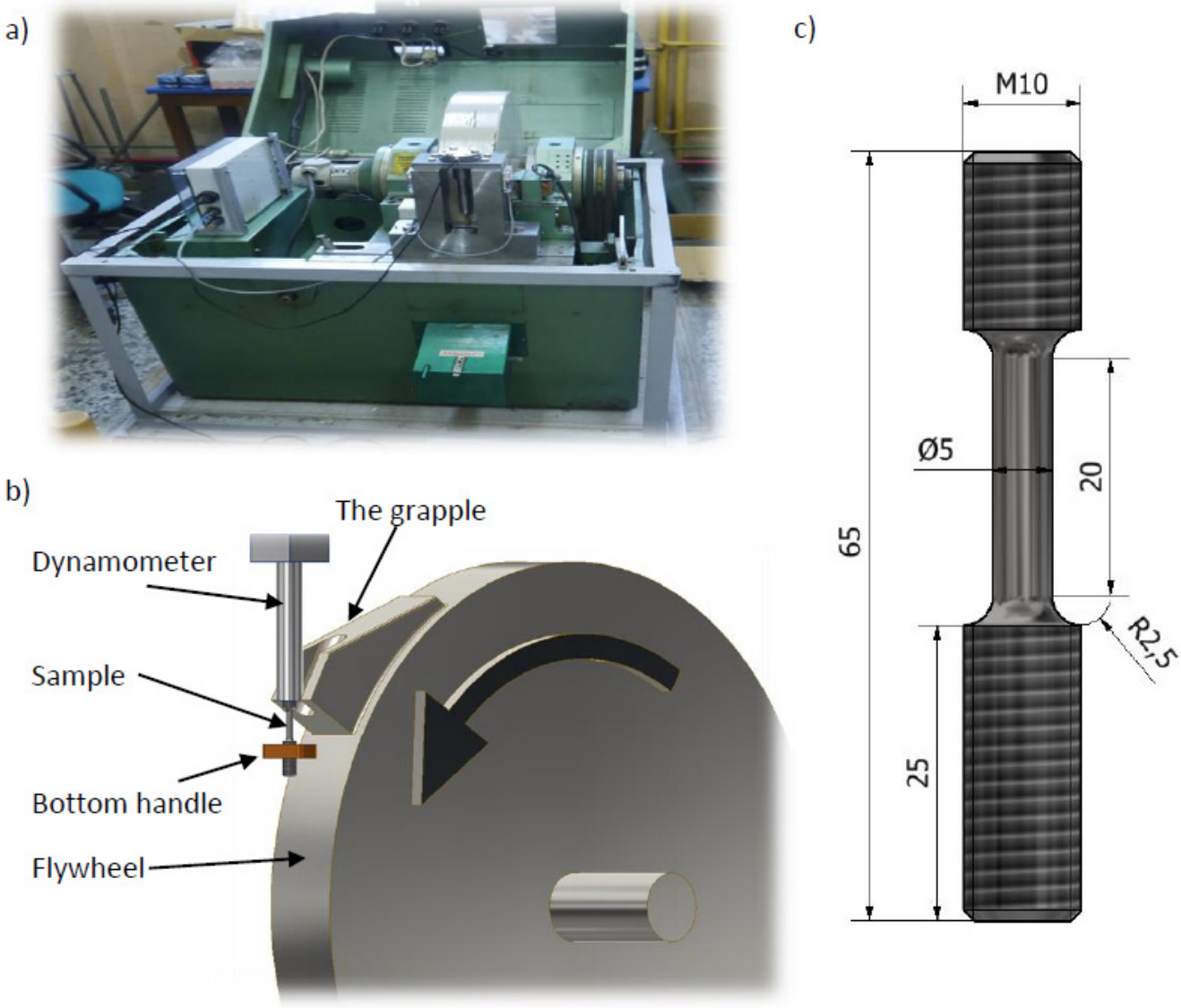

Figure 5. (**a**) Rotary hammer station (Fundamentals of Technology Laboratory, Polish Naval Academy), (**b**) scheme of dynamic tensile test on a rotary hammer, and (**c**) dimensions of a sample.

Table 1. Summary of test results on a rotary hammer.

Sample Name	φ	Measuring Length	Area A_0	Breaking Force F_m	Hammer Rotational Speed	Strain Rate	Dynamic Ultimate Strength Rm
	mm	mm	mm^2	kN	m/s	s^{-1}	MPa
HY 80_d1_v10	5.03	18.69	19.86	25.13	10.00	535	1265.28
HY 80_d2_v20	5.03	19.36	19.86	30.35	20.00	1033	1528.10
HY 80_d3_v30	5.02	19.33	19.78	30.76	30.00	1552	1554.92
HY 80_d4_v40	5.07	18.53	20.18	31.41	40.00	2159	1556.62

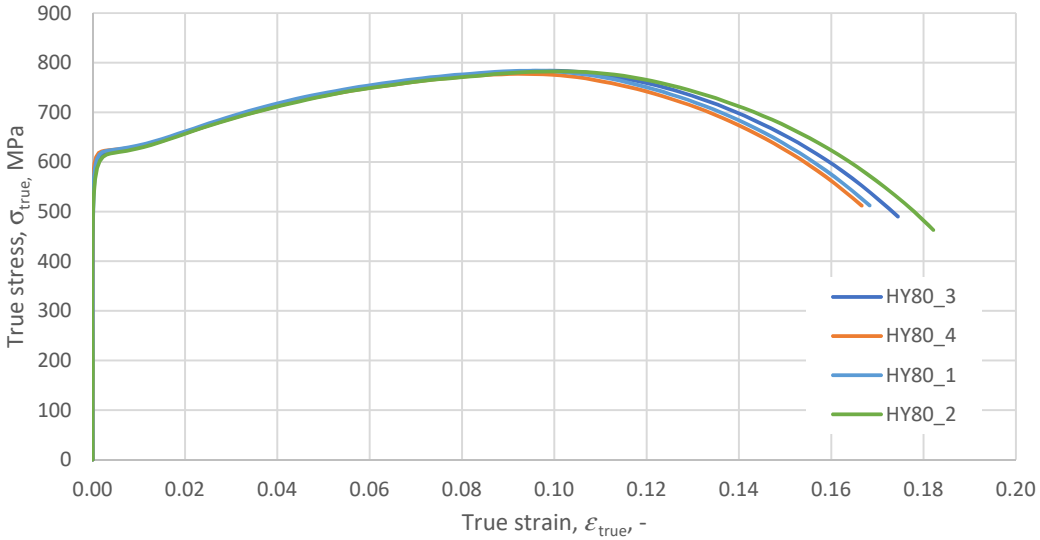

Figure 6. HY 80 σ_{true}-ε_{pl} true characteristics, strain rate $\dot{\varepsilon} = 0.0001\ s^{-1}$.

Table 2. Material constants describing HY 80 steel based on Formulas (3)–(7).

Sample Name	Young Modulus	Yield Point	Yield Strain	Ultimate Strength	Ultimate Strain	Proof Load
	E GPa	R_e MPa	ε_e -	R_m MPa	ε_m -	$A = \sigma_{pl=0}$ MPa
HY 80_1	208.6	605.9	0.0041	783.9	0.1028	563.9
HY 80_2	210.8	610.5	0.0037	777.5	0.0958	576.0
HY 80_3	214.6	604.4	0.0037	784.1	0.0996	561.2
HY 80_4	210.7	601.7	0.0044	782.6	0.1045	536.0
Average	**211.2**	**605.6**	**0.0040**	**782.0**	**0.1007**	**559.3**

The chemical composition of the breakthrough structure and the material model proposal was also considered in the paper [2]. However, in CAE programs, functions are used to describe the plastic characteristic depending on the strain rate and temperature $\sigma_{true} = \sigma_{true}\left(\varepsilon_{pl}, \dot{\varepsilon}, \theta\right)$. In the case of metals, the Johnson–Cook constitutive model has become the most frequently used standard [9]. In this model, the plastic Huber–Mises–Hencky (HMH) reduced stresses σ_{pl} are described by the following equation:

$$\sigma_{pl} = \left(A + B\varepsilon_{pl}^{n}\right)\left[1 + C\ln\left(\frac{\dot{\varepsilon}}{\dot{\varepsilon}_0}\right)\right]\left[1 - \left(\frac{\theta - \theta_0}{\theta_{melt} - \theta_0}\right)^{m}\right] \quad (8)$$

where

A–elastic range of the material $\sigma_{pl=0}$ (it is often simplified in form A = R_e);
B–hardening parameter;
n–hardening exponent;
C–strain rate coefficient;
ε_{pl}–true plastic strain;
$\dot{\varepsilon}$ –strain rate;
$\dot{\varepsilon}_0$–quasi-static strain rate (0.0001 s^{-1});
θ–current material temperature;
θ_0–ambient temperature;
θ_{tmelt}–melting temperature;
m–thermal softening exponent.

The above values for this model are determined based on the static tensile test and Hopkinson or Taylor tests [10]. However, with strain rates ranging up to 2000 s^{-1}, these data can be obtained from a rotary hammer tensile test.

The parameters A, B, C, n, and m can be determined in many other ways [11]. One of the ways is the so-called engineering formula, according to which the parameters of the first term A, B, and n are determined based on the results of the static tensile test according to the following algorithm:

R_m, ε_m, E should be determined from true characteristics, along with the values of the A point corresponding to $\sigma_{pl=0}$, $\varepsilon_{pl=0}$, which constitute the elastic range of the material behaviour; then, according to the Formulas (9)–(12), calculate the $R_{e,true}$, $R_{m,true}$, $\varepsilon_{m,true}$, $\varepsilon_{m,pl}$ values as follows:

$$A = \sigma_{pl=0} \tag{9}$$

$$R_{m,true} = R_m(1 + \varepsilon_m). \tag{10}$$

$$\varepsilon_{m,true} = \ln(1 + \varepsilon_m) \tag{11}$$

$$\varepsilon_{m,pl} = \varepsilon_{m,true} - \frac{R_{m,true}}{E} \tag{12}$$

determine the parameters B, n [11] according to the following Formulas (13) and (14):

$$n = \frac{R_{m,true} \cdot \varepsilon_{m,pl}}{R_{m,true} - A} \tag{13}$$

$$B = \frac{R_{m,true} - A}{\varepsilon_{m,pl}^{n}} \tag{14}$$

Taking the average values from Table 2 and using the Formulas (9), (13) and (14), the coefficients for the first component of the Johnson–Cook constitutive model were determined, which are the following:

A = 559 MPa;
B = 518 MPa;
n = 0.379.

Figure 7 shows the compilation of the nominal characteristic from the MTS machine (red), the true characteristic determined from Equations (5) and (6) (blue), and the JC model (the first part of the Equation (8) (green).

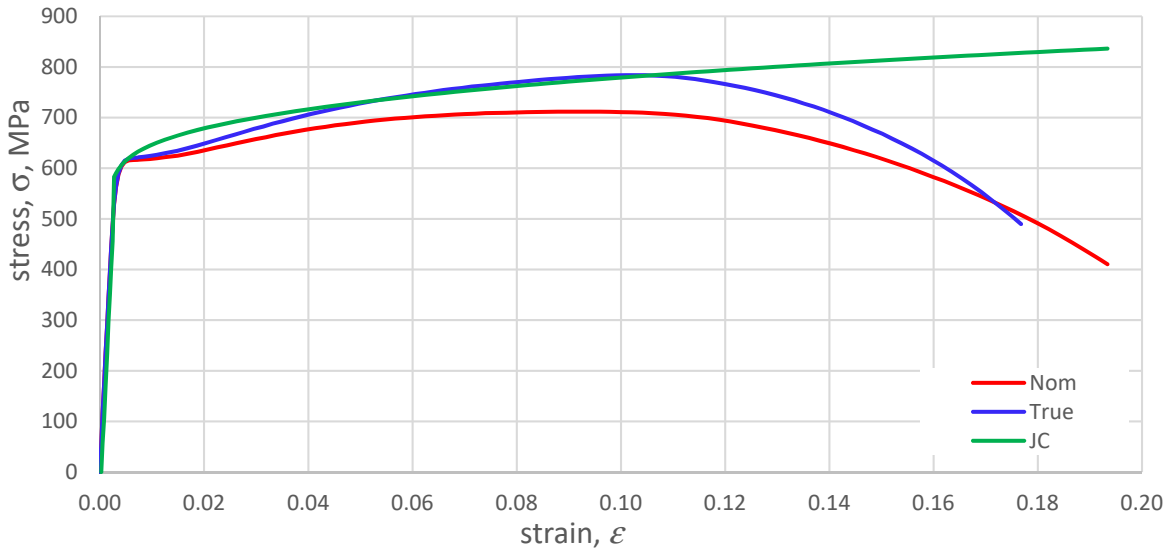

Figure 7. Comparison of the nominal, true characteristics and the proposed Johnson Cook HY 80 steel model, strain rate $\dot{\varepsilon} = 0.0001\ s^{-1}$.

To determine the C parameter, it is necessary to know the value $R_{m,\,true}(\dot{\varepsilon})$ or a given strain rate determined during the dynamic tensile test on a rotary hammer (Table 3). From transforming Equation (8), we obtain

$$C = \left(\frac{R_{m,true}(\dot{\varepsilon})}{R_{m,true}(\dot{\varepsilon_0})} - 1 \right) / \ln\left(\frac{\dot{\varepsilon}}{\dot{\varepsilon}_0} \right) \tag{15}$$

Table 3. Ultimate strength for various strain rates.

Strain Rate, $\dot{\varepsilon}$	**$\dot{\varepsilon}_0$ = 0.0001 s^{-1}**	**$\dot{\varepsilon}$ = 535 s^{-1}**	**$\dot{\varepsilon}$ = 1033 s^{-1}**	**$\dot{\varepsilon}$ = 1555 s^{-1}**	**$\dot{\varepsilon}$ = 2159 s^{-1}**
$R_{m,(\dot{\varepsilon})}$, MPa	782.00	1047	1115	1130	1140
C	-	0.021873	0.026366	0.026877	0.027108

Based on the calculations, the mean value of the C parameter was determined, C = 0.0268. In Figure 8, the influence of the C parameter on material behaviour is shown. Figure 8 shows the behaviour of the material as a function of strain rate in the Johnson–Cook model (first and second term of Equation (8) against the background of the real characterisation determined from Equation (6).

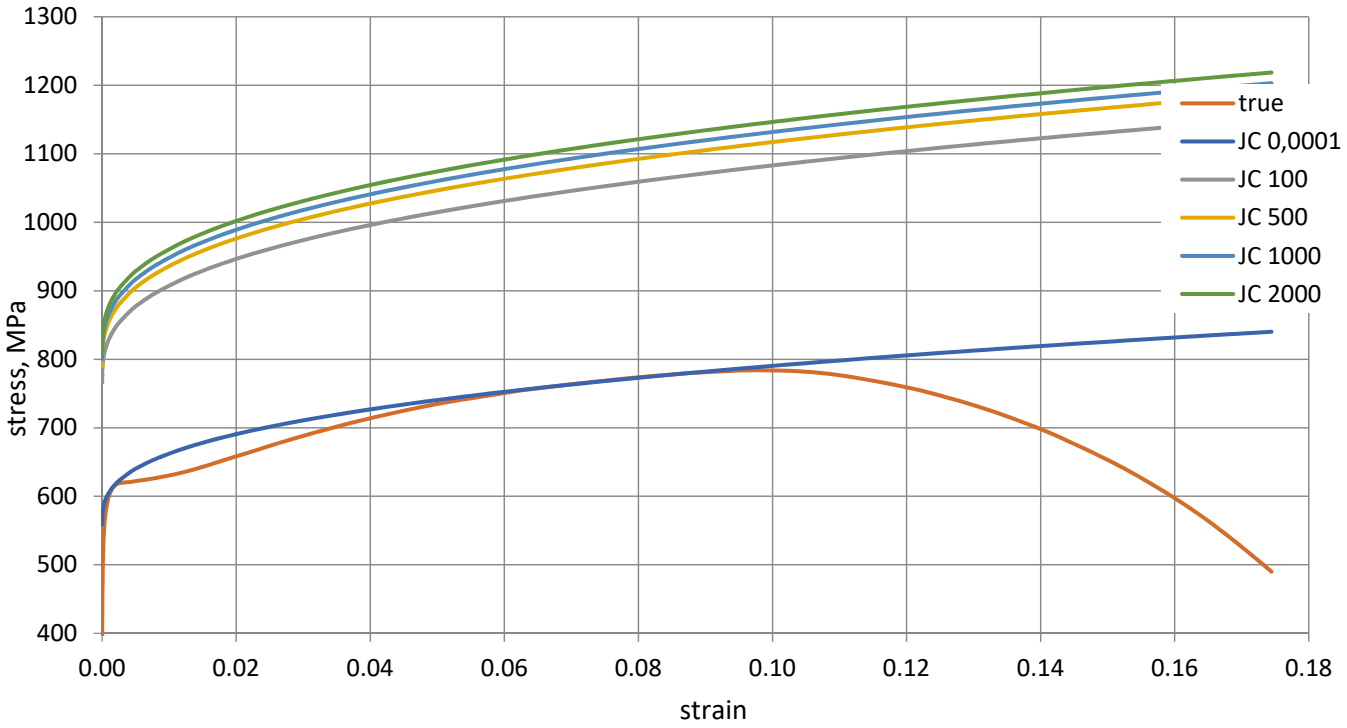

Figure 8. Johnson–Cook model of HY 80 steel as a function of strain rate, *C* = 0.0268.

The values for the temperature component can be taken based on the literature [1,4], and they are similar for most steels; thus,

Ambient temperature θ_0 = 293.15 K;
Melting temperature θ_{top} = 1733~1793;
Thermal coefficient m = 0.75 ÷ 1.15.

3.4. HY 80 Steel Failure at Uniaxial Tension

The material failure model used in CAE programs is detailed in several studies [6,8,12–14]. The value of the destructive deformation is a function of the so-called stress state indicator

η_{TRIAX} (stress triaxiality). It is the ratio of the pressure being the mean of the principal stresses to the Huber–Mises–Hencky reduced stress σ_{HMH} [12,13]

$$\eta_{TRIAX} = \frac{p}{\sigma_{HMH}} \tag{16}$$

In a three-dimensional state of stress, the pressure is

$$p = \frac{1}{3}(\sigma_1 + \sigma_2 + \sigma_3). \tag{17}$$

For the uniaxial stretching state, the value of the triaxiality coefficient is equal to 0.33 (Table 4).

Table 4. η_{TRIAX} values for selected 3D cases [3].

3D Cases	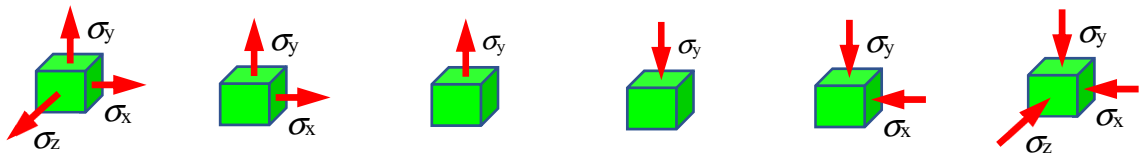					
Principal stresses	$\sigma_x = \sigma_y = \sigma_z$ >0	$\sigma_x = \sigma_y$ $\sigma_z = 0$	$\sigma_y > 0$ $\sigma_x = \sigma_z = 0$	$\sigma_y < 0$ $\sigma_x = \sigma_z = 0$	$-\sigma_x = -\sigma_y$ $\sigma_z = 0$	$\sigma_x = \sigma_y = \sigma_z$ <0
η_{TRIAX}	∞	0.66	0.33	−0.33	−0.66	$-\infty$

4. Discussion

The failure mechanism for HY 80 steel is shown in the true characteristic diagram σ_{true}-ε_{true} (Figure 9). The elastic range is between points 0 and 1. Between points 1 and 2, there is a plastic range (hardening). In point 2, the destruction process is initiated. After crossing point 2 in the material model without failure criteria, the stresses would continue to increase with the strain increase towards point 5 and further. If the loading forces disappear in point 2, then the elastic forces will reduce the deformation to point 7 along path 2~7 and parallel to path 0~1. In the model with failure, point 5 corresponds to point 3 on the curve 2~4, where strength loss (softening) occurs. The 2~4 curve is called the degradation or failure curve defined by the parameter d, which is the damage evolution coefficient taking values from 0 to 1. The stress on the degradation curve is appropriate.

$$\sigma = (1 - d)\overline{\sigma}. \tag{18}$$

The material fracture occurs in point 4 after reaching the value of the fracture deformation $\varepsilon^{pl}_{failure}$ However, if during the degradation of the material on the curve 2–4 the element breaks or the forces loading the element disappear, e.g., in point 3, then the remaining elastic forces will reduce its deformation to point 6 along the 3–6 path, which is not parallel to the 0–1 path. The evolution of failure determines the degree of degradation at which failure of the material will occur. The value of $d = 0$ means that the plastic stress has reached the value of R_m, but the material has not yet been degraded, while the value of $d = 1$ means the complete degradation of the material. The failure evolution is described as a function of the plastic displacement of the u_{pl}, defined as follows [13]:

$$u_{pl} = L \cdot \varepsilon_{pl} \tag{19}$$

where L is the characteristic length of the FEM element.

The rate of evolution of failure describes the path along which material degradation develops. In CAE programs, linear, exponential, and tabular descriptions are adopted. The linear relationship is expressed as the ratio of plastic displacement to failure displacement [13].

$$d = \frac{u_{\mathrm{pl}}}{u_{\mathrm{failure}}} \tag{20}$$

Table 5 lists the points from the diagram in Figure 9, based on which the failure parameters for tensile strength of HY 80 steel were determined.

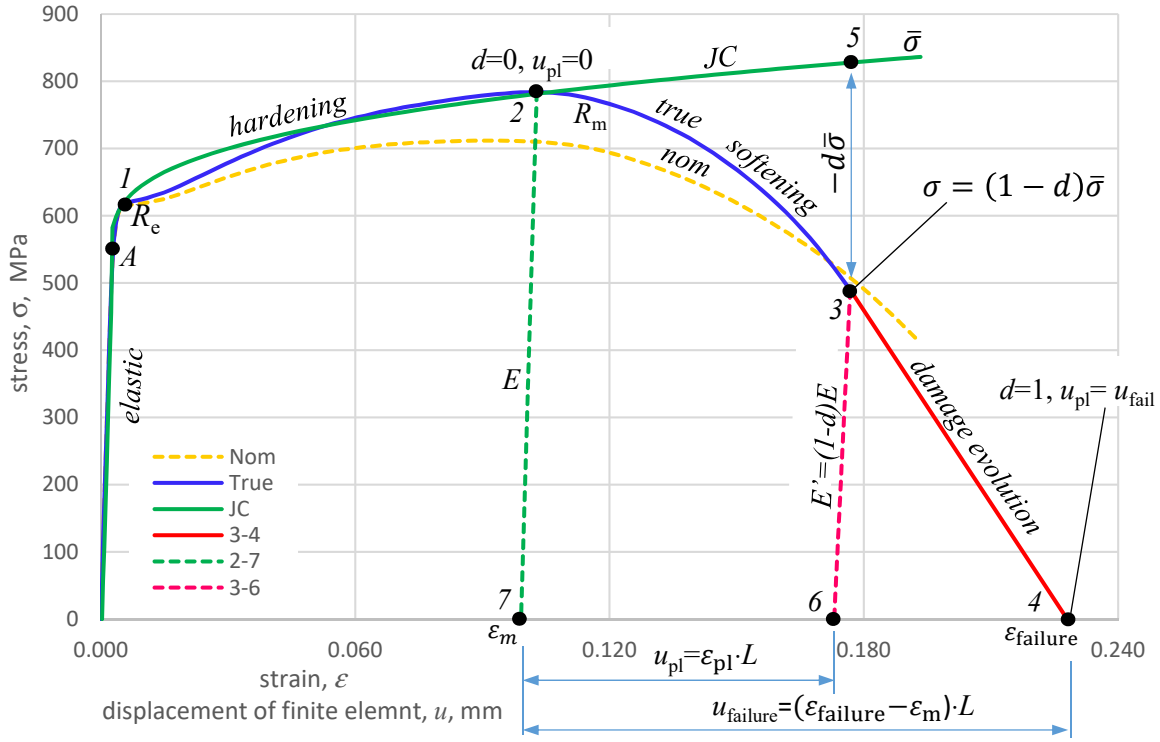

Figure 9. Failure diagram on the true characteristics of HY 80 steel (σ_{true}-$\varepsilon_{\mathrm{true}}$).

Table 5. The values in Figure 9 used in the calculations.

Point Label	Strain	Stress	Remarks
	$\varepsilon_{\mathrm{el}}$, -	σ_{true}, MPa	
1	0.0040	605.6	Yield point R_e
2	0.1028	783.8	Ultimate tensile strength R_m
3	0.1768	489.9	Sample fracture
4	0.2280	0.00	d = 1 material total degradation
5	0.1768	836.0	Stresses in the material model without failure parameters
6	0.1730	0.00	Fracture deformation
7	0.0991	0.00	Deformation at ultimate strength R_m, d = 0

Following these parameters, calculations were carried out for uniaxial stretching as follows:

$$\varepsilon_{failure} = \varepsilon_4 - \varepsilon_7 = 0.2280 - 0.0991 = 0.1289.$$

$$d\overline{\sigma} = \sigma_5 - \sigma_3 = 836.0 - 489.9 = 346.1.\ \mathrm{MPa}$$

$$\text{since } \sigma = (1-d)\overline{\sigma}.\ \text{so } d = 1 - \frac{\sigma}{\overline{\sigma}} = 1 - \frac{489.9}{836} = 0.414.$$

$$E' = (1-d)E = (1-0.414)\cdot 211 = \ 124 \text{ GPa}$$

$$u_{failure} = 0.1289 \cdot L$$

Summarising the tested HY-80 steel can be described by the following equations:
Young modulus: $E = 211$ GPa;
Johnson–Cook model:

$$\sigma = \left(559 + 518 \cdot \varepsilon^{0.379}\right)\left[1 + 0.0268 \cdot \ln\left(\frac{\dot{\varepsilon}}{0.0001}\right)\right]\left[1 - \left(\frac{\theta - 293.15}{1\,470}\right)^{1.14}\right]$$

Failure parameters:

$$d = 0.414;\ \varepsilon_{failure} = 0.1289;\ \eta_{Triax} = 0.33$$

5. Conclusions

Johnson–Cook HY 80 steel characteristics and material model were developed based on the static and dynamic tensile tests on the rotary hammer. Tensile tests performed on a rotary hammer allowed us to determine the mechanical properties of steel in the range of deformation speed 0–2000 s^{-1}. The knowledge of the behaviour of steel for increased deformation rates enables the simulation of fast-changing processes such as a collision, projectile fire, impact of a shock wave (pressure from the explosion) on the tested object, or modelling of submarine implosion. The obtained data should be verified by an appropriate simulation and experiment, which will be the subject of the subsequent study.

The results of the tests of HY 80 steel after 55 years of operation show that the several decades of exploitation of this material in challenging sea conditions did not adversely affect its mechanical properties. They are close to catalogue values. The yield point of this steel is catalogued at 80 KSI (552 MPa). From the tests performed, the yield point of R_e = 605.6 MPa (R_{02} = 444.5 MPa) was obtained, and the strength limit was R_m = 782 MPa with a deformation of 0.1, which proves that good plastic and strength properties were maintained.

By analysing the mechanical properties, it can be concluded that the ship's hull made of this steel without significant corrosion and operational losses could be used for the next years. One should be aware that it is still subject to erosive wear, which changes the overall strength of the hull. That may have an impact on limiting the maximum operational depth of the submarine.

Tests with a rotary hammer showed an increase in the strength of the steel with a reduced deformation. Unfortunately, due to the dynamic nature of the test and the possibility of potential damage to the extensometers, it was not possible to measure the deformation during the trial. This problem will be solved in the future with the use of high-speed cameras.

Increasing the strain rate in the range of up to 2000 s^{-1} increases the strength of the tested steel to 1140 MPa. That is a typical phenomenon in high-quality steel.

The study determined the failure parameters for the uniaxial tensile case (η = 0.33). The compression/tensile diagram for steel is symmetrical, which allows for the assumed failure criterion also for $\eta = -0.33$. The obtained amount of material did not qualify for a greater number of tests in which the failure parameters could be determined for the remaining characteristic values of the triaxiality coefficient.

Author Contributions: Conceptualisation, S.B. and K.R.; methodology, S.B. and K.R.; software, S.B. and K.R.; validation, S.B. and K.R.; formal analysis, K.R.; investigation, S.B. and K.R.; resources, S.B. and K.R.; data curation, S.B. and K.R.; writing—original draft preparation, S.B.; writing—review and editing, K.R.; visualisation S.B. and K.R.; supervision, S.B.; project administration, K.R.; funding acquisition, S.B. Both authors have read and agreed to the published version of the manuscript.

Funding: This research received no external funding.

Institutional Review Board Statement: Not applicable.

Informed Consent Statement: Not applicable.

Data Availability Statement: Not applicable.

Conflicts of Interest: The authors declare no conflict of interest.

References

1. Holmquist, T.J. *Strenght and Fracture Characteristics of HY-80, HY-100, and HY-130 Steels Subjected to Various Strains, Strain Rates Temperatures, Adn Pressures*; Nacal Surface Warfare Center, NSWC: Dahlgren, VA, USA, 1987.
2. Lee, J.; Lee, K.; Lee, S.; Kwon, O.M.; Kang, W.-K.; Lim, J.-I.; Lee, H.-K.; Kim, S.-M.; Kwon, D. Application of Macro-Instrumented Indentation Test for Superficial Residual Stress and Mechanical Properties Measurement for HY Steel Welded T-Joints. *Materials* **2021**, *14*, 2061. [CrossRef] [PubMed]
3. Kut, S. State of Stress Identification in Numerical Modeling of 3D Issues. *Arch. Metall. Mater.* **2009**, *54*, 628–632.
4. Konieczny, J. Materiały Konstrukcyjne Okrętów (Ship Construction Materials). *Kwartalnik Bellona* **2009**, *658*, 153–159.
5. Okręty Podwodne Typu Kobben-Defence24. Available online: https://www.defence24.pl/okrety-podwodne-typu-kobben (accessed on 8 November 2020).
6. Rajendran, A.M.; Last, H.R.; Garrett, R.K. *Plastic Flow and Failure in HY100, HY130 and AF1410 Alloy Steels under High Strain Rate and Impact Loading Conditions 1995*; NASA STI/Recon Technical Report N; NASA: Washington, DC, USA, 1995.
7. Polish Norm PN-EN ISO 6892-1:2016, Metallic Materials. In *Tensile Testing. Part 1–Method of Test at Room Temperature 2016*; Key to Metals AG: Zürich, Switzerland, 2016.
8. Szturomski, B. *Modelowanie Oddziaływania Wybuchu Podwodnego Na Kadłub Okrętu w Ujęciu Numerycznym [Modeling the Effect of the Underwater Explosion to Hull Board in a Numberic Concept]*; Akademia Marynarki Wojennej: Gdynia, Poland, 2016. (In Polish)
9. Johnson, G.R.; Cook, W.H. A Constitutive Model and Data for Metals Subjected to Large Strains, High Strain Rates. In Proceedings of the 7th International Symposium on Ballistics, The Hague, The Netherlands, 19–21 April 2009.
10. Korkmaz, M.E.; Verleysen, P.; Günay, M. Identification of Constitutive Model Parameters for Nimonic 80A Superalloy. *Trans Indian Inst. Met.* **2018**, *71*, 2945–2952. [CrossRef]
11. Leszek Flis Identyfikacja Parametrów Równania Konstytutywnego Johnsona-Cook'a w Odniesieniu Do Symulacji MES [Identification of Parameters of the Johnson-Cook Constitutive Equation for FEM Simulation]. In Proceedings of the XIII Konferencji n.t. Techniki Komputerowe w Inżynierii, Licheń Stary, Poland, 5–8 May 2014; Academy of Sciences: Warsaw, Poland, 2014. (In Polish)
12. Kohnke, P. *Ansys Theory Reference, Release 5.6*; ANSYS: Canonsburg, PA, USA, 1999.
13. Abaqus 6.14 Theory Manual. In *Simulia, Dassault Systems*; Dassault Systèmes Simulia Corp.: Providence, RI, USA, 2014.
14. Banerjee, A.; Dhar, S.; Acharyya, S.; Datta, D.; Nayak, N. Determination of Johnson Cook Material and Failure Model Constants and Numerical Modelling of Charpy Impact Test of Armour Steel. *Mater. Sci. Eng. A* **2015**, *640*, 200–209. [CrossRef]

materials

MDPI

Article

Analysis and Modification of Methods for Calculating Axial Load Capacity of High-Strength Steel-Reinforced Concrete Composite Columns

Jun Wang *, Yuxin Duan *, Yifan Wang, Xinran Wang and Qi Liu

School of Civil Engineering, Northeast Forestry University, Harbin 150000, China; sunwangyifan@163.com (Y.W.); xinran19972021@163.com (X.W.); liu_q_wangyi@163.com (Q.L.)
* Correspondence: jun.w.619@nefu.edu.cn (J.W.); yuxind666@163.com (Y.D.); Tel.: +86-188-4589-2847 (Y.D.)

Abstract: To investigate the applicability of the methods for calculating the bearing capacity of high-strength steel-reinforced concrete (SRC) composite columns according to specifications and the effect of confinement of stirrups and steel on the bearing capacity of SRC columns. The axial compression tests were conducted on 10 high-strength SRC columns and 4 ordinary SRC columns. The influences of the steel strength grade, the steel ratio, the types of stirrups and slenderness ratio on the bearing capacity of such members were examined. The analysis results indicate that using high-strength steel and improving the steel ratio can significantly enhance the bearing capacity of the SRC columns. When the slenderness ratio increases dramatically, the bearing capacity of the SRC columns plummets. As the confinement effect of the stirrups on the concrete improves, the utilization ratio of the high-strength steel in the SRC columns increases. Furthermore, the results calculated by AISC360-19(U.S.), EN1994-1-1-2004 (Europe), and JGJ138-2016(China) are too conservative compared with test results. Finally, a modified formula for calculating the bearing capacity of the SRC columns is proposed based on the confinement effect of the stirrups and steel on concrete. The results calculated by the modified formula and the finite element modeling results based on the confinement effect agree well with the test results.

Keywords: high-strength steel; steel-reinforced concrete column; axial bearing capacity; confinement effect; simulation analysis

Citation: Wang, J.; Duan, Y.; Wang, Y.; Wang, X.; Liu, Q. Analysis and Modification of Methods for Calculating Axial Load Capacity of High-Strength Steel-Reinforced Concrete Composite Columns. *Materials* **2021**, *14*, 6860. https://doi.org/10.3390/ma14226860

Academic Editors: Michele Bacciocchi, Angelo Marcello Tarantino, Raimondo Luciano and Carmelo Majorana

Received: 8 October 2021
Accepted: 11 November 2021
Published: 14 November 2021

1. Introduction

Due to enjoying the advantages of strength, plasticity, toughness and weldability, high-strength steel has become one of the most important building materials. In recent years, high-strength steel with a yield strength ranging from 460 to 960 MPa has been used in building structures [1–3], such as the Bird's Nest and Water Cube in China, and the Sony Center in Germany [4]. However, the applicability of the current design and calculation methods to high-strength steel-reinforced concrete (SRC) composite structures has become challenging since they have gradually been applied to high-rise buildings and long-span structures.

In 2014, Q460 and Q690 high-strength steel were used to replace Q345 ordinary steel in SRC composite columns in the upper part of the structure in the high-rise project of Zhengzhou Greenland Central Plaza in Henan Province, China, to enhance the bearing capacity and reduce the self-weight of the structures. Thus, it is necessary to develop the design of SRC structures. However, in Specifications for Structural Steel Buildings (AISC360-16, the USA) [5], Design of Composite Steel and Concrete Structures (EN1994-1-1:2004, Eurocode) [6] and Code for Design of Composite Structures (JGJ138-2016, China) [7], the design methods of SRC composite members are primarily based on the research on ordinary steel. Yang et al. performed model tests on Q460 high-strength SRC columns with a circular section to solve this issue and found that Q460 high-strength steel enhanced the

bearing capacity of the SRC columns remarkably. Nevertheless, the calculation results by the relevant specifications were only about 60% of the test results, which led to a waste of materials [8]. Zhao et al. conducted tests on the Q460 SRC-core columns to find the reason why calculation results are too conservative [9]. It was found that the confinement effect of steel and stirrups on bearing capacity was neglected in the methods for calculating the bearing capacity of SRC composite columns in current specifications, and only the load-bearing capacity of the steel, the concrete and the longitudinal reinforcements was taken into account. Moreover, the theoretical stress–strain model of confined concrete on concrete was developed, but neither the full verification of the model nor specific calculation suggestions was proposed for the bearing capacity of SRC structures.

In recent years, there has been some research on the confinement theory of SRC members. In 1992, Mirza and Skrabek conducted tests on slender composite beam-columns with ordinary strength materials [10]. It was found that concrete in a SRC cross-section can be divided into three parts according to the confining pressure level, that is: unconfined concrete (UCC), partially confined concrete (PCC) and highly confined concrete (HCC). For PCC, the confinement effect can be considered as normal reinforced concrete, which has been extensively studied by Sheikh and Uzumeri, Mander et al. [11,12]. For HCC, Chen and Wu proposed an analytical method for predicting the axial compressive behavior of the SRC column using a cross-shaped steel section with flanges [13]. However, Wang and Su carried out tests on slender SRC columns; 270 MPa~600 MPa steel was used in the specimens. It was found that when the confinement of steel and stirrup was calculated, the bearing capacity of slender SRC columns increased by only 2% compared with only considering the confinement of stirrups [14]. Despite all this research, there are still some codes for SRC columns which do not take into account the strength of confined concrete, leading to the calculations being too conservative, such as AISC, Eurocode 4 and JGJ138-2016. Therefore, more experiments are needed to analyze the confinement of stirrups and steel on concrete, especially when high-strength steel is used in SRC columns. The codes also need more suggestions to improve the accuracy of the calculations.

In this paper, structural tests were carried out on SRC columns under an axial load to verify the applicability of the current specifications to high-strength SRC composite columns and provide a calculation method considering the confinement effect for such composite columns. Then, the finite element models were utilized to prove the accuracy of the prediction method using the theoretical stress–strain model of confined concrete for engineering applications.

2. Experimental Investigation

2.1. Test Specimens

On the basis of the theory proposed by Zhao et al. [15] and the formulas described in EN1994-1-1:2004, Eurocode, the strength of steel, the steel ratio, the stirrups and the slenderness ratio are the primary factors influencing the bearing capacity of SRC columns. Thus, 10 high-strength SRC columns and 4 ordinary SRC columns were analyzed to verify the confinement effect and determine the magnitude of the known factors. Table 1 lists the main parameters of the specimens, and Figure 1 shows the labelling rule of specimens.

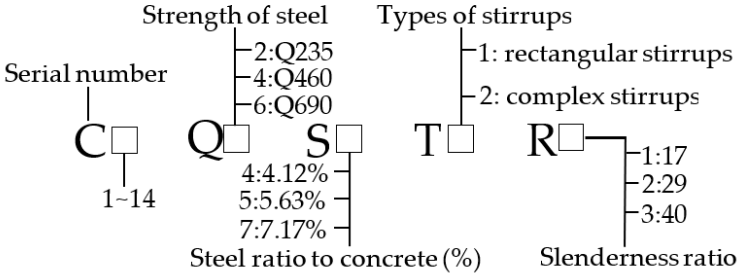

Figure 1. Labeling rule of specimens. (**C**: Serial number; **Q**: Strength of steel; **S**: Steel ratio to concrete; **T**: Type of stirrups; **R**: Slenderness ratio).

Table 1. Main parameters of specimens.

Specimen Designation	Steel Grade	Steel Ratio to Concrete	Steel Geometric Size (h × bf × t1 × t2)/mm	Stirrup Type	Slenderness Ratio	Height/mm	Stirrups Spacing
C1Q2S4T1R1 (C_1)	Q235	4.12%	130 × 70 × 5 × 5	1	17	1200	80
C2Q2S4T2R1 (C_2)	Q235	4.12%	130 × 70 × 5 × 5	2	17	1200	80
C3Q2S5T1R1 (C_3)	Q235	5.63%	140 × 75 × 5 × 8	1	17	1200	80
C4Q2S7T1R1 (C_4)	Q235	7.17%	140 × 80 × 8 × 8	2	17	1200	80
C5Q4S4T1R1 (C_5)	Q460	4.12%	130 × 70 × 5 × 5	1	17	1200	80
C6Q4S4T2R1 (C_6)	Q460	4.12%	130 × 70 × 5 × 5	2	17	1200	80
C7Q4S5T1R1 (C_7)	Q460	5.63%	140 × 75 × 5 × 8	1	17	1200	80
C8Q4S7T1R1 (C_8)	Q460	7.17%	140 × 80 × 8 × 8	2	17	1200	80
C9Q4S7T1R2 (C_9)	Q460	7.17%	140 × 80 × 8 × 8	1	29	2000	80
C10Q4S7T1R3 (C_{10})	Q460	7.17%	140 × 80 × 8 × 8	2	40	2800	80
C11Q6S4T1R1 (C_{11})	Q690	4.12%	130 × 70 × 5 × 5	1	17	1200	80
C12Q6S4T2R1 (C_{12})	Q690	4.12%	130 × 70 × 5 × 5	2	17	1200	80
C13Q6S5T1R1 (C_{13})	Q690	5.63%	140 × 75 × 5 × 8	1	17	1200	80
C14Q6S7T1R1 (C_{14})	Q690	7.17%	140 × 80 × 8 × 8	2	17	1200	80

Four kinds of sections were selected for this study, as shown in Figure 2. Moreover, stirrup encryption and reinforcement with carbon fiber cloth were performed within 1/6 height of both ends of the column to prevent local pressure failure at the upper and lower ends of the columns.

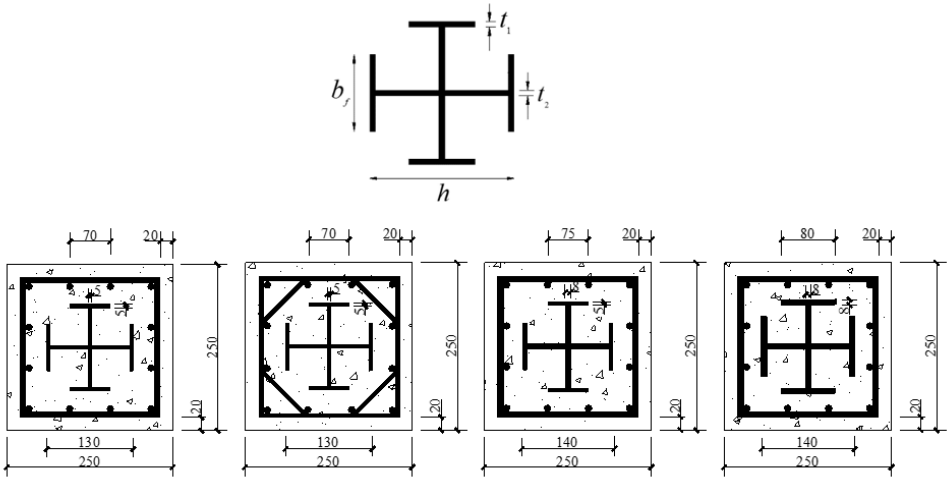

Figure 2. Sectional dimensions of specimens (millimeters).

2.2. Material Properties

Steel sheets of grade Q235, Q460, Q690, with a reinforcement of HRB400, were selected to manufacture the specimens. Tensile coupon tests were carried out to obtain the material properties of steel. According to the Chinese Standard GB/T 228-2010 [16], the measured material properties of the steel presented in Table 2 are the mean values of results.

Table 2. Mechanical properties of steel.

Grade	t/mm	fy/Mpa	fu/Mpa	δ/%
Q235	5	277	437	33.7
Q235	8	305	469	32.5
Q460	5	474	558	28.8
Q460	8	507	596	27.9
Q690	5	740	820	16.5
Q690	8	738	818	17.2
HRB400 (stirrups)	8	469	611	28.6
HRB400 (longitudinal reinforcement)	10	460	609	27.8

C50 concrete is used in this test. After finishing the preparation work, all the specimens were poured at one time and maintained for 28 days under the condition of a temperature no less than 5 °C. According to the standard for test methods of concrete structures (GB/T 50152-2012) [17], 9 concrete cubes (150 × 150 × 150 mm) were maintained under the same conditions as the specimens. The compressive strength test was carried out before the formal loading began, as shown in Figure 3. The results are listed in Table 3.

Figure 3. Concrete cubes and the failure mode of concrete tubes.

Table 3. Results of compressive strength test.

Grade of Concrete	f_{cu}^0	$f_{cu,m}^0$	f_c^0	E_c^0
C50	52.6 56.1 54.8 53.2 56.6 57.4 57.3 54.9 55.7	55.4	40.8	35,736.3

f_{cu}^0 is the cubic compressive strength of concrete by the test, respectively; $f_{cu,m}^0$ is the average cubic compressive strength; f_c^0 is the calculation of the prism compressive strength, which is used in the finite element models; E_c^0 is the elastic modulus measured by the test, respectively.

2.3. Test Setup and Procedure

A 30,000 kN servo-hydraulic testing machine was employed for loading, and the loading device is shown in Figure 4a. The accuracy of the instrument is 1/1000, which is allowed according to GB50152-2012 [17]. The specimens were subjected to multi-stage loading, and before formal loading, a 50 kN load was applied in advance to confirm whether the test apparatus functioned normally. During the formal testing, force-controlled loading was first conducted at a rate of 200 kN/min. When the load reached 60% of the estimated ultimate bearing capacity, the loading rate was reduced to 150 kN/min. When the load reached 80% of the estimated ultimate bearing capacity, the loading mode was changed from the force-controlled loading to the displacement-controlled loading, and the loading rate was set as 0.4 mm/min. After the ultimate load (ultimate bearing capacity), the testing was terminated when the load decreased to 70% of the ultimate bearing capacity. The arrangement of the measuring points is depicted in Figure 4b. The strain gauges were arranged on two adjacent sides of the steel, on the surfaces of stirrups and the longitudinal reinforcement, and four sides of concrete in the middle height of the specimens. The vertical displacement of the specimens was recorded by a displacement meter in the loading device.

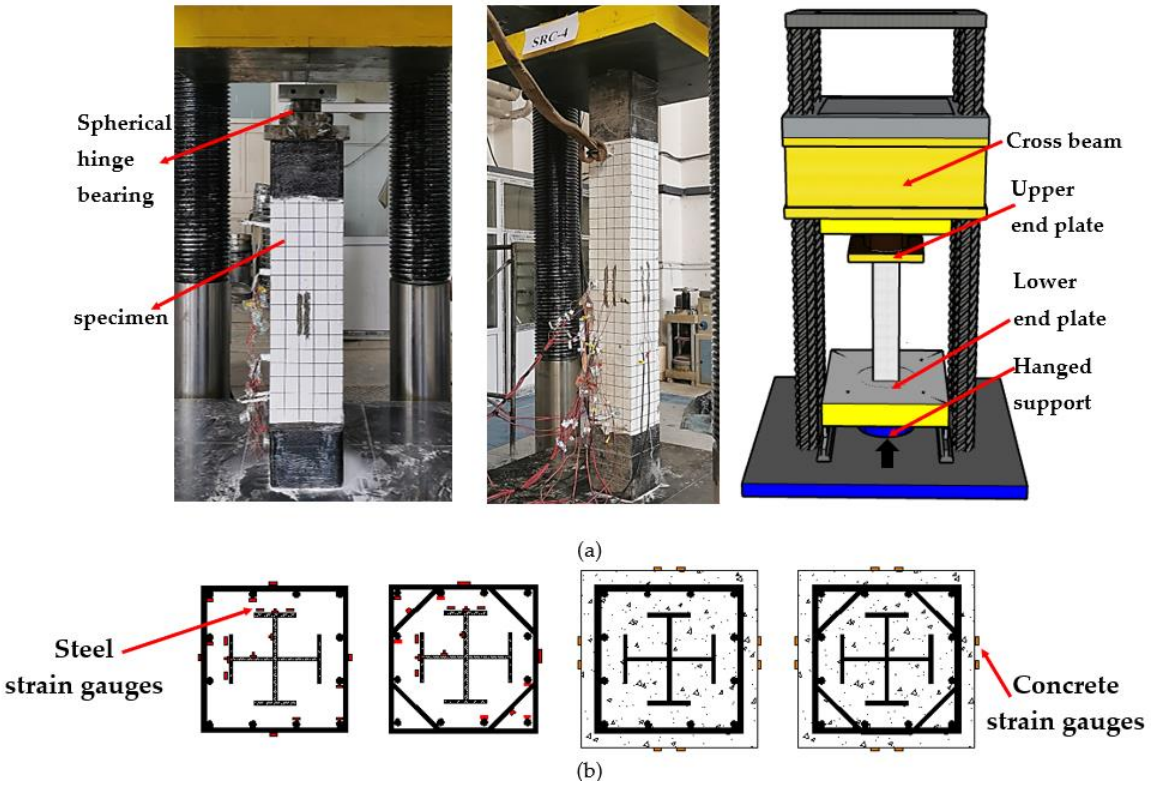

Figure 4. Test setup and arrangement of strain gauges. (**a**) test setup and instrumentations; (**b**) strain gauges position.

2.4. Test Results and Analysis

2.4.1. Failure Mode

The specimen was in the elastic deformation stage during the initial loading, and no cracks formed on its surface. With an increase in the load, apparent longitudinal cracks appeared in the middle of the specimen and continuously extended to both ends of the column. When the ultimate bearing capacity was reached, both the steel and longitudinal reinforcement of the specimen reached the yield strength, the length and width of the cracks increased rapidly. In addition, the cover concrete at the middle height of the specimen crushed and peeled off, and the longitudinal reinforcement bulged outward.

Figure 5 illustrates the failure modes of the specimens. As shown in Figure 5a, when the specimen with built-in Q235 steel failed, it had a relatively low degree of surface cracking. At a steel ratio of 7.17%, when the strength grade of the steel improved from Q235 to Q460 and Q690, the vertical displacement of the specimen during failure increased from 7.53 mm to 10.5 mm and 11.7 mm, respectively. Furthermore, the cracking and crushing degree of the cover concrete intensified accordingly, as illustrated in Figure 5b,c, respectively.

As presented in Figure 5d, specimen C9 with a slenderness ratio of 29 showed strength failure characteristics. However, when the slenderness ratio of the specimen increased to 40, specimen C10 displayed evident instability failure characteristics with a significant lateral displacement, as shown in Figure 5e.

Figure 6 demonstrates the crushing patterns of the concrete in high-strength SRC composite columns with different stirrup configurations. Compared with the specimens with complex stirrups, the concrete crushing depth of specimens C1, C5 and C11 with standard rectangular stirrups reached the stirrup confinement concrete during failure. On the contrary, the stirrup confinement concrete of specimens C2, C6, and C12 with complex stirrups remained almost intact during failure.

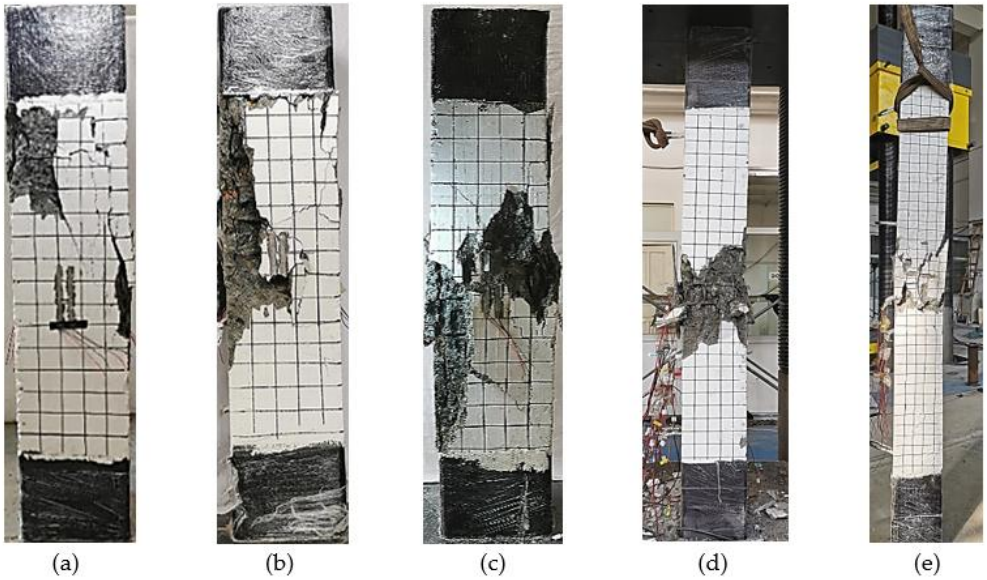

Figure 5. Failure modes of the specimens: (**a**) failure mode of the specimen with Q235 steel, steel ratio is 7.17%; (**b**) failure mode of the specimen with Q460 steel, steel ratio is 7.17%; (**c**) failure mode of the specimen with Q690 steel, steel ratio is 7.17%; (**d**) failure mode of the specimen C9; (**e**) failure mode of the specimen C10.

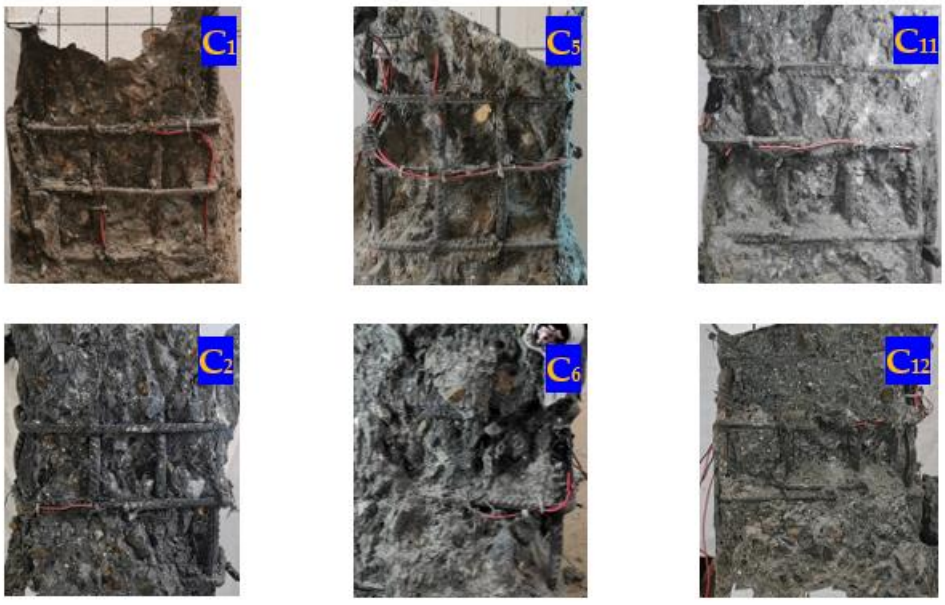

Figure 6. Concrete crushing modes of specimens with different stirrup configurations. (C_1, C_5, C_{11} are the specimens with rectangular stirrup; C_2, C_6, C_{12} are the specimens with complex stirrup).

2.4.2. Ultimate Bearing Capacity

Table 4 lists the ultimate bearing capacity of the specimens. Compared with the specimen with built-in Q235 steel, the ultimate bearing capacity of the specimens with built-in Q460 and Q690 steel increased by 17.1% and 35.3%, respectively, indicating a marked increase in the bearing capacity of the columns. Figure 7a plots the load–displacement curves of the specimens at different strength grades of the steel and steel ratios. For the specimens with the same strength grade of steel, the maximum improvement in the ultimate bearing capacity of the specimens with a steel ratio of 5.63% and 7.17% was 13.2% and 28.3%, respectively, compared with that of the specimen with a steel ratio of 4.12%,

which implied that increasing the steel ratio could noticeably enhance the ultimate bearing capacity of the members.

Table 4. Comparison of test results with calculation results calculated codes.

Specimens	Test Results	AISC360-16	$(\frac{N_{ai}}{N_u} - 1)\%$	Eurocode 4	$(\frac{N_e}{N_u} - 1)\%$	JGJ138-2016	$(\frac{N_j}{N_u} - 1)\%$
	N_u/kN	N_{ai}/kN		N_e/kN		N_j/kN	
C1Q2S4T1R1	4200	2633	37.3%	2713	35.4%	2943	29.9%
C2Q2S4T2R1	4506	2633	41.6%	2713	39.8%	2943	34.7%
C3Q2S5T1R1	4340	2887	33.5%	2968	31.6%	3166	27.1%
C4Q2S7T1R1	4596	3149	31.5%	3230	29.7%	3394	26.2%
C5Q4S4T1R1	4462	3006	32.6%	3107	30.4%	3305	25.9%
C6Q4S4T2R1	5050	3006	40.5%	3107	38.5%	3305	34.6%
C7Q4S5T1R1	4878	3398	30.3%	3505	28.1%	3660	25.0%
C8Q4S7T1R1	5383	3803	29.4%	3912	27.3%	4023	25.3%
C9Q4S7T1R2	5120	3561	30.4%	3778	26.2%	3983	22.2%
C10Q4S7T1R3	4848	3228	33.4%	3617	25.5%	3862	20.3%
C11Q6S4T1R1	4847	3666	24.4%	3810	21.4%	3954	18.4%
C12Q6S4T2R1	5407	3666	32.2%	3810	29.5%	3954	26.9%
C13Q6S5T1R1	5487	4299	21.7%	4461	18.7%	4546	17.1%
C14Q6S7T1R1	6220	4953	20.4%	5126	17.6%	5152	17.2%

Figure 7b delineates the load–displacement curves of the specimens at different slenderness ratios. Raising the slenderness ratio from 17 to 29 while keeping the other parameters unchanged reduced the ultimate bearing capacity of the column by 4.9%, implying a negligible reduction in the bearing capacity of the members. In contrast, when the slenderness ratio increased from 17 to 40, the ultimate bearing capacity of the column declined to 90.1%, indicating a remarkable reduction. Specimen C10, with a slenderness ratio of 40 experienced a small vertical displacement when the load reached the ultimate bearing capacity. Moreover, the ultimate bearing capacity of the specimen plummeted, and the specimen presented evident brittle failure characteristics.

Figure 7c draws the load–displacement curves of the specimens with different types of stirrups. When the type of stirrup was changed from standard rectangular stirrups to complex stirrups, the ultimate bearing capacity of the column with built-in Q235, Q460 and Q690 steel increased by 7.3%, 13.2% and 11.6%, respectively. The strength grade of the steel also raised the bearing capacity of the high-strength SRC composite columns with complex stirrups, which was due to the profound confinement effect of the complex stirrups, bringing the steel into full play.

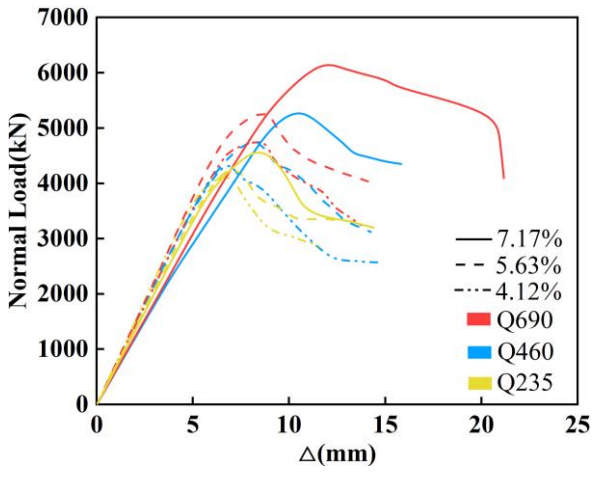

(**a**)

Figure 7. *Cont.*

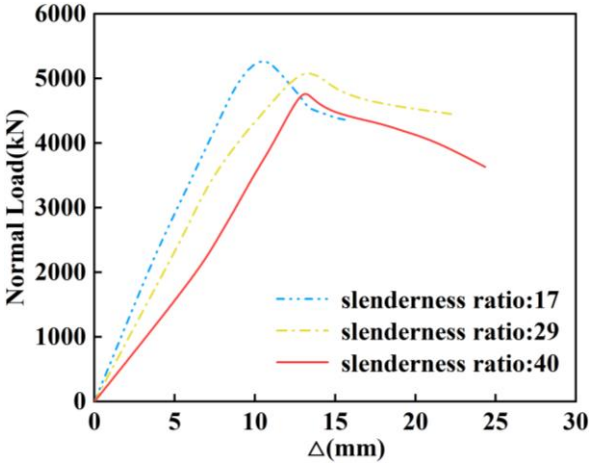

(**b**)

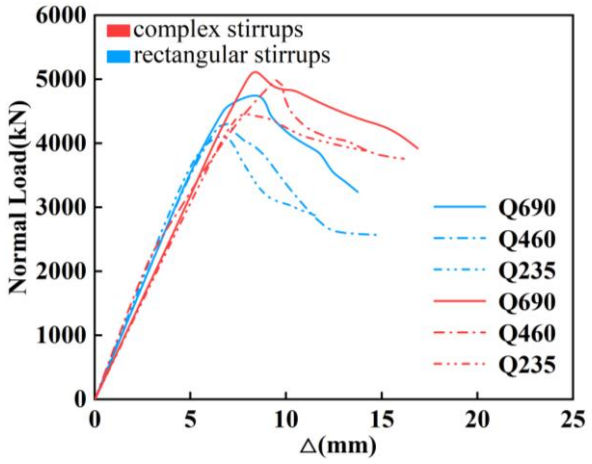

(**c**)

Figure 7. Load–displacement curves of specimens: (**a**) the load–displacement curves of the specimens at different strength grades of the steel and steel ratios; (**b**) the load–displacement curves of the specimens at different slenderness ratios; (**c**) the load–displacement curves of the specimens with different types of stirrups.

3. Modification of Bearing Capacity Calculation

3.1. Current Calculation Methods

In the American National Standard Specifications for Structural Steel Buildings (AISCI360-16), the wrapped reinforced concrete part is considered to be equivalent to the steel. Thus, the formula for calculating the axial compression by utilizing the steel structure design method is defined as:

$$P_n = \begin{cases} P_{n0}\left(0.658^{\frac{P_{n0}}{P_e}}\right) & \frac{P_{n0}}{P_e} \le 2.25 \\ 0.877P_e & \frac{P_{n0}}{P_e} > 2.25 \end{cases} \quad (1)$$

$$P_{n0} = F_y A_s + F_{ysr} A_{sr} + 0.85 f_c' A_c \quad (2)$$

$$P_e = \pi^2 (EI_{\text{eff}}) / L_c^2 \quad (3)$$

where A_s, A_{sr} and A_c are the cross-sectional area of the section steel, longitudinal reinforcement and concrete, respectively. F_y, F_{ysr} and f_c' represent the compressive strength of the steel, longitudinal reinforcement and concrete, respectively; EI_{eff} stands for the effective stiffness of the section; L_c is the effective length of the member.

The Code Design of Composite Steel and Concrete Structures (EN1994-1-1:2004), defines the formula for calculating the bearing capacity of biaxially symmetric SRC columns under axial compression as:

$$N_{Ed} \leq \chi N_{pl,Rd} \tag{4}$$

$$N_{pl,Rd} = A_a f_{yd} + 0.85 A_c f_{cd} + A_s f_{sd} \tag{5}$$

where A_a, A_c and A_s denote the cross-sectional area of the section steel, concrete and longitudinal reinforcement; f_{yd}, f_{cd} and f_{sd} are the compressive strength of the section steel, concrete and reinforcement, respectively; χ is the buckling reduction factor considering the relative slenderness ratio, and is expressed by Equation (7), as described in the Section 6.3 of Eurocode 3: Design of Steel Structures (EN 1993-1-1:2005),

$$\chi = \frac{1}{\Phi + \sqrt{\Phi^2 - \overline{\lambda}^2}}, \text{ when } \chi \leq 1 \tag{6}$$

$$\Phi = 0.5\left[1 + \alpha(\overline{\lambda} - 0.2) + \overline{\lambda}^2\right] \tag{7}$$

where α is the section type; $\overline{\lambda}$ represents the relative slenderness ratio.

The Code for Design of Composite Structures (JGJ138-2016), defines the formula for calculating the bearing capacity of axially compressed SRC columns under axial compression as:

$$N \leq 0.9\varphi(f_c A_c + f'_y A'_s + f'_a A'_a) \tag{8}$$

where A_c, A'_s and A'_a indicate the cross-sectional area of the concrete, reinforcement and section steel, respectively; f_c, f'_y and f'_a are the design value of the compressive strength of concrete, reinforcement and section steel, respectively; φ is the coefficient of axial compression stability and can be determined according to the slenderness ratio presented in a specific table in the code JGJ138-2016.

3.2. Comparison between Test Results and Calculations

Table 4 lists the test results and the calculations of the different specifications. Figure 8 compares them at various parameters. Figure 8a,b demonstrate that as the strength grade of steel improves from Q235 to Q460 and Q690 at a constant steel ratio, the results calculated by the different codes are far smaller than the test results, indicating that the calculations are too conservative. The results calculated according to code JGJ138-2016 are the closest to the test results, whereas those calculated according to code AISC360-16 are the most conservative.

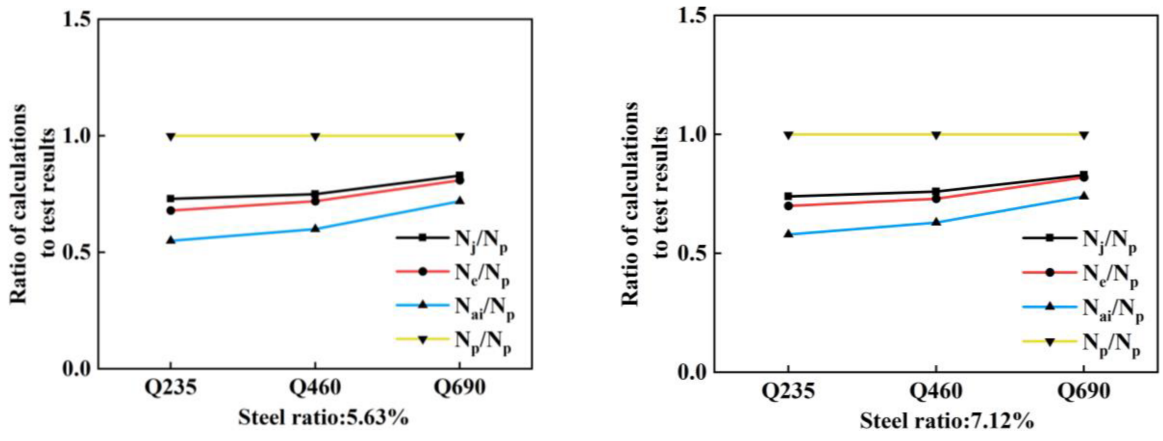

(**a**) (**b**)

Figure 8. *Cont.*

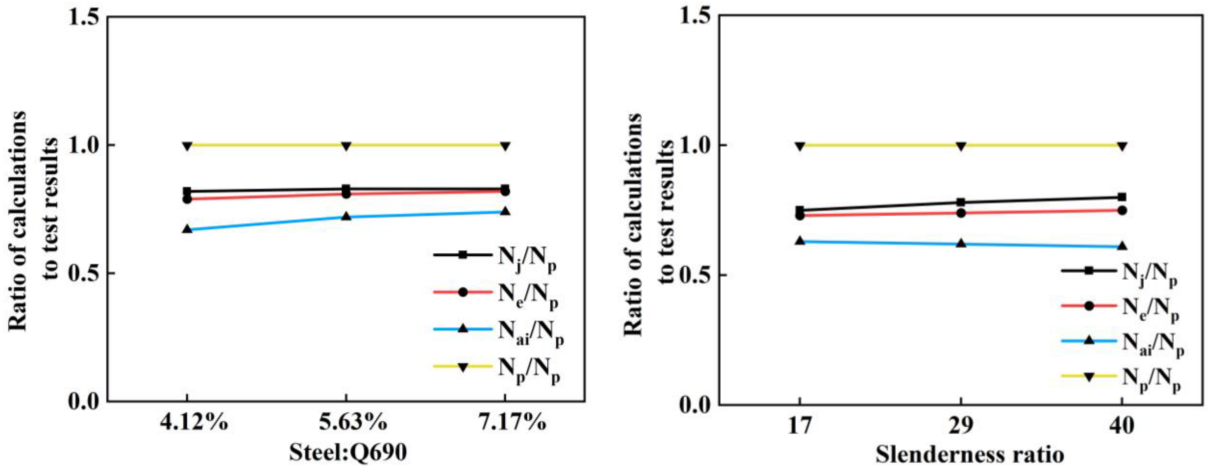

(**c**) (**d**)

Figure 8. Effect of parameters on bearing capacity of specimens: (**a**) Comparison of test results and calculations for the specimens with steel ratio 5.63%; (**b**) Comparison of test results and calculations for the specimens with steel ratio 7.17%; (**c**) Comparison of test results and calculations for the specimens with Q690 steel; (**d**) Comparison of test results and calculations for the specimens with different slenderness ratios.

Figure 8c shows that, at a constant strength grade of the steel, the slope of the growth of the test results is similar to that of the results when the steel ratio enlarges.

As shown in Figure 8d, when the slenderness ratio increases from 17 to 40, the changing trend of the bearing capacity of the column determined by the test is similar to the one calculated by code AISC360-16: the higher the slenderness ratio is, the more profound its impact on the bearing capacity of the SRC composite columns becomes. However, the calculation results of codes JGJ138-2016 and Eurocode 4 show a small decreasing trend in the bearing capacity of the SRC columns with an increase in the slenderness ratio.

According to Figure 9, since the influence of the type of stirrups on the bearing capacity of composite columns is not considered in the methods proposed by different codes, the calculations according to different codes are generally similar. Changing the types of stirrups and strengthening the stirrup confinement effect on SRC composite columns can enhance the ultimate bearing capacity of the high-strength SRC columns more than that of the ordinary SRC columns. The ultimate bearing capacity of the Q690 SRC composite columns is relatively low when rectangular stirrups are configurated.

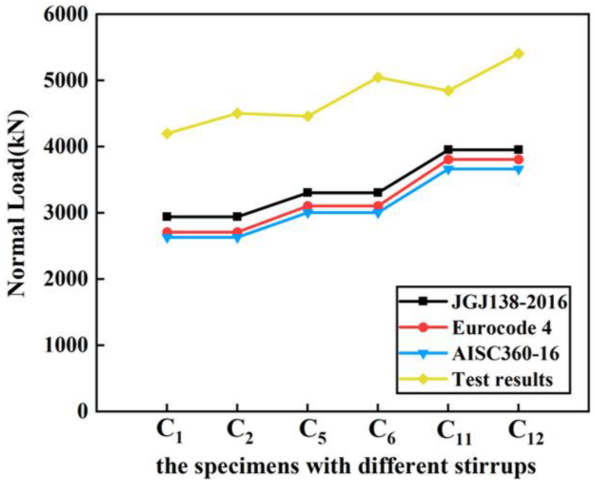

Figure 9. Effect of types of stirrups on bearing capacity of specimens. (C_1, C_5, C_{11} are the specimens with rectangular stirrup; C_2, C_6, C_{12} are the specimens with complex stirrup).

3.3. Modification of Formula for Calculating Bearing Capacity Considering Confinement Effect of Stirrup

Specifications ignore the confinement effect of the stirrups and steel on concrete when calculating the bearing capacity of reinforced concrete columns under axial compression. The bearing capacity calculated by the different specifications is smaller than the measured bearing capacity, thus they produce a conservative result. At present, there are two types of methods for analyzing the confinement effect: one only considers the confinement effect of stirrups [12], and the other takes account of the confinement effect of the stirrups and steel [15,18].

Figure 10a illustrates the section considering the confined effect of the stirrups on concrete, and Figure 10b shows the section considering the confinement effect of the stirrups and the steel on concrete. It is found that the confinement effect of the steel (open section) on concrete increases the bearing capacity of the composite columns marginally; that is, by less than about 2% [14]. Hence, this theoretical analysis only takes the confinement effect of the stirrups on the concrete strength into account. There are two methods to calculate the stress–strain relationship of stirrup confined concrete.

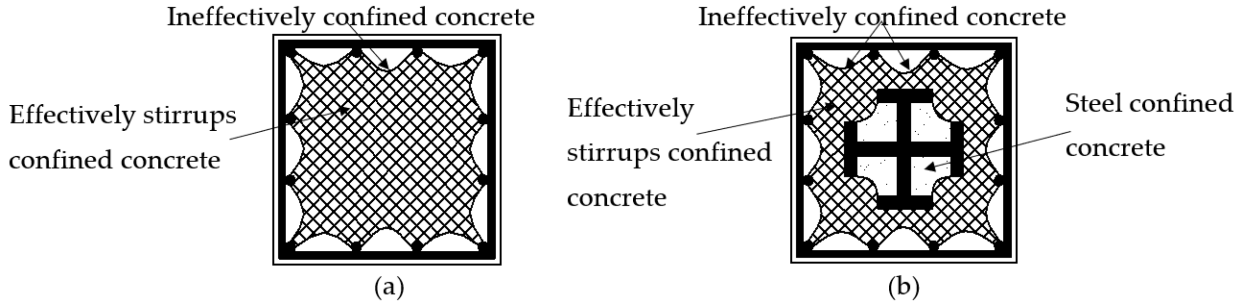

Figure 10. Effectively confined region and ineffectively confined region of concrete: (**a**) Ordinary reinforced concrete column; (**b**) SRC column with cross-section steel.

One is according to the research of Uzumeri and Mander [11,12], the maximum restraint stress on the stirrups only plays a role in the core confined area. Thus, Mander proposed the following calculation formula for the effective restraint stress on the stirrups:

$$f_l' = \frac{1}{2} k_e \rho_s f_{yh} \tag{9}$$

where ρ_s is the stirrup ratio, f_{yh} represents the yield strength of the stirrup and k_e indicates the effective restraint coefficient of the stirrup and is given by Equation (10). The effect of the stirrup on the core concrete confinement area is regarded as the one on all concrete areas within the stirrup area.

$$k_e = \frac{\left(1 - \sum \frac{(w')^2}{6 b_c d_c}\right)\left(1 - \frac{s'}{2b_c}\right)\left(1 - \frac{s'}{2d_c}\right)}{1 - \rho_{cc}} \tag{10}$$

where ω' is the net distance between the adjacent longitudinal reinforcement; b_c and d_c represent the length and width of the rectangular stirrup, respectively; s' denotes the net distance between the stirrups; ρ_{cc} stands for the ratio of the area of the longitudinal reinforcement to that of the confinement area.

Then, Mander developed the calculation method for the peak stress improvement coefficient k of concrete in the confinement area:

$$k = -1.254 + 2.254\sqrt{1 + 7.94\frac{f_l'}{f_{c0}}} - 2\frac{f_l'}{f_{c0}} \tag{11}$$

where f_{c0} is the axial compressive strength of concrete.

The other is the calculation method in the Section 7.2.3.1.6 of fib-CEB Model Code 2010 [19].

$$\sigma_2 = w_c f_{cd}(1 - \frac{s_c}{a_c})(1 - \frac{s_c}{b_c})(1 - \frac{\sum b_i^2/6}{a_c b_c}) \tag{12}$$

$$k = \frac{f_{ck,c}}{f_{ck}} = 1 + 3.5(\frac{\sigma_2}{f_{ck}})^{\frac{3}{4}} \tag{13}$$

$$\varepsilon_{c2,c} = \varepsilon_{c2}\left[1 + 5\left(\frac{f_{ck,c}}{f_{ck}} - 1\right)\right] \tag{14}$$

where $\sigma_2 (= \sigma_3)$ is the effective lateral compressive stress at the ULS due to confinement; f_{ck} stands for the characteristic compressive strength of concrete; $f_{ck,c}$ is the value of confined concrete.

In terms of application, the above equations are very complicated, especially for square section members. To simplify, Yu Xiaolai (a scholar) proposed simplified formulas through a number of tests based on Mander's theory [20]. The equations are as follows,

$$f_{cc} = f_{c0}(2.254\sqrt{1 + 3.85\lambda_v} - 0.97\lambda_v - 1.254)\ k = \frac{f_{cc}}{f_{c0}} \tag{15}$$

$$\varepsilon_{cc} = \varepsilon_{c0}(1 + 3.5\lambda_v) \tag{16}$$

$$\lambda_v = \rho_s f_{yh}/f_{c0} \tag{17}$$

where ε_{c0} is the strain corresponding to the peak stress on the unconfined concrete, ρ_s indicates the stirrup ratio; f_{c0} denotes the axial compressive strength of concrete; f_{yh} stands for the yield strength of the stirrup; λ_v stands for the stirrup eigenvalue.

Based on the research by Yu, Equations (15)–(17) also apply to circular section members. The calculations of the simplified formulas are in good agreement with those of the above two methods, so the method for calculating the bearing capacity of the SRC column of rectangular section is modified by the simplified formulas.

These test results show that the confinement effect of the stirrup on concrete is noticeable, especially when the high-strength steel is configurated. The influence coefficient of steel strength is proposed based on Mander's model. The modified calculation formula for the bearing capacity of SRC columns under axial compression according to code JGJ138-2016 is as follows:

$$N \leq 0.9\varphi(kA_c f_c + A_a f_a + A_y f_y) \tag{18}$$

For the SRC columns of circular or square section, Equations (15)–(17) can be selected to calculate. When the section is rectangular, Equations (9)–(14) should be used.

Figure 11 compares the bearing capacity of the specimens measured by the test results, with that calculated by the modified formulas, Equations (15)–(18), and calculations according to code JGJ 138-2016. The results confirm that the bearing capacity of the column calculated by Equations (15)–(18) deviates from the test results by only around 10%, and the bearing capacity calculated by code JGJ138-2016 deviates from the test results by 17–35%, respectively. Thus, the modified formula considering stirrup confinement can more accurately predict the ultimate bearing capacity of such members.

According to the work of Kim [21,22], it is necessary to ensure that the steel strain corresponding to the peak stress on concrete is not smaller than the yield strain of steel so as to achieve the full mechanical performance of high-strength steel in structures, that is:

$$\varepsilon_{cc} \geq f_a/E_a \tag{19}$$

where f_a and E_a represent the yield stress and elastic modulus of section steel, respectively.

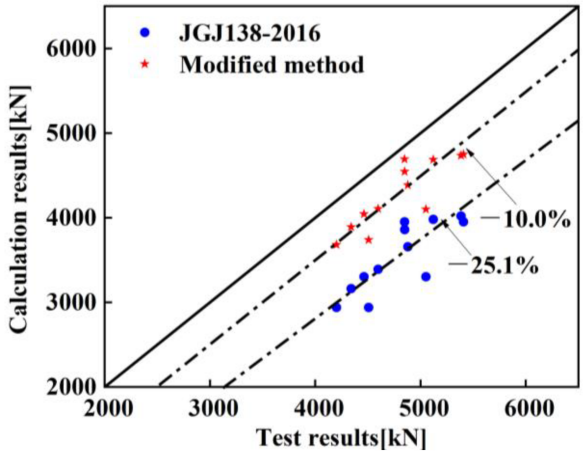

Figure 11. Comparison among test results, modified calculation results of formulas and the calculation results by JGJ138-2016.

According to Equations (16) and (17), when the high-strength steel is applied to SRC columns with a square section, this study determines the stirrup configuration conditions to ensure the full utilization of the strength of the steel as follows:

$$\lambda_v \geq \frac{f_a - E_a\varepsilon_{c0}}{3.5E_a\varepsilon_{c0}} \tag{20}$$

According to Equation (16), the minimum stirrup eigenvalues are, respectively, 0.13 and 0.35, when Q460 and Q690 steel give full play to their strength in this test. When the rectangular stirrups are configured, the stirrup eigenvalue of specimen C5 is 0.15, which is higher than the minimum stirrup eigenvalue of the SRC columns with Q460 steel, 0.13; thus, the yield strength of Q460 steel can be brought into full play. However, for specimen C11, the stirrup eigenvalue of the rectangular stirrups is far lower than 0.35, thus the effective strength of Q690 steel is only 55.1% of its yield strength.

When the complex stirrups are configured in the SRC column, the stirrup eigenvalue of the specimen C6 is 0.34, much higher than 0.13, and the stress on the Q460 steel can reach the yield strength of the Q460 steel. Nevertheless, the stirrup eigenvalue of the specimen C12 is still slightly lower than the minimum stirrup eigenvalue, 0.35. The maximum stress on the Q690 steel can only reach as high as 89% of its yield strength, as shown in Figure 12. To summarize, the test data collected in this test, the requirements in code JGJ138-2016 and the calculations of Equation (16) can provide a reference for improving the stirrup design of high-strength SRC composite columns.

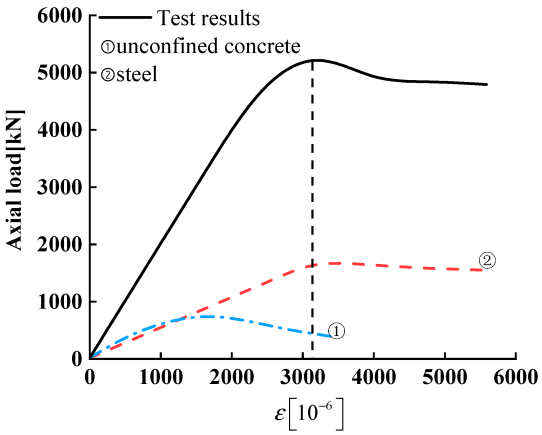

Figure 12. Axial load-strain relationships of C14.

4. Verification of Finite Element Model and Parametric Study

4.1. Establishment of Finite Element Model

In Section 3.2, the reason for Q690 steel (in the specimen C_{11}) unyielding under ultimate bearing capacity is well explained, and the design suggestion of the high-strength SRC column is put forward. However, it is found that not only the type of stirrups but also the spacing of stirrups affect the value of ρ_s and λ_v. In this test, the value of λ_v was increased by changing the stirrup type, the contribution of Q690 steel was increased, but the stirrup spacing was not considered. Therefore, the influence range of stirrup spacing on the bearing capacity of the specimens was studied by the analysis of expanding parameters with finite element models.

On the basis of the material property test, the finite element model of the test specimens was established using ABAQUS software to verify the applicability of the confinement theory to high-strength SRC columns in this test and study the influence of stirrup spacing on bearing capacity for high-strength SRC columns. Figure 13 displays the typical specimen models according to the test parameters. Moreover, eight-node hexahedral linear reduction integral stress element (C3D8R) were used for the concrete and steel in the finite element model, and two-node three-dimensional truss elements (T3D2) were employed for the reinforcement. Friction was defined at the interface between the concrete and the steel to account for their bonding. The grid was divided according to the length/Width/depth = 1.0:1.0:2.5, and the confinement effect was imposed according to the actual loading device.

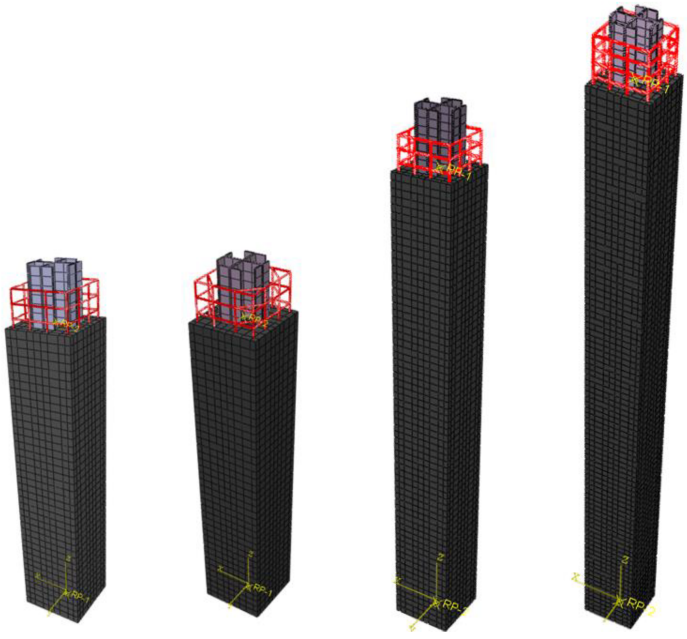

Figure 13. Typical specimen models.

Table 2 presents the material properties of the steel obtained from the coupon tests. As for the concrete, three types of confinement effects were considered. Figure 14 also presents the three types of concrete sections. Figure 14a represents the section with no confinement; Figure 14b stands the section with the confinement effect of the stirrups and Figure 14c represents the section with the confinement effect of stirrups and steel. The uniaxial compression stress–strain curve of the concrete without any confinement effect was determined using the design of Concrete Structures (GB50010-2010) [23]. The

stress–strain relationship of the concrete with confinement effect of the stirrups or of both stirrups and steel was calculated by Equation (21) [12]:

$$\sigma = \frac{f_{cc} x r}{r - 1 + x^r} \tag{21}$$

$$x = \varepsilon / \varepsilon_{cc} \cdot r = E_c / (E_c - E_{sec}) \cdot E_{sec} = f_{cc} / \varepsilon_{cc} \cdot f_{cc} = k f_{c0} \cdot \varepsilon_{cc} = [1 + 5(k-1)] \varepsilon_{c0} \tag{22}$$

where σ is the stress of confined concrete; f_{cc} is the compressive strength of confined concrete; E_c, E_{sec} are the elasticity modulus and secant modulus of concrete, respectively; f_{c0} is the axial compressive strength of the unconfined concrete; k denotes the coefficient of improvement in the strength and strain.

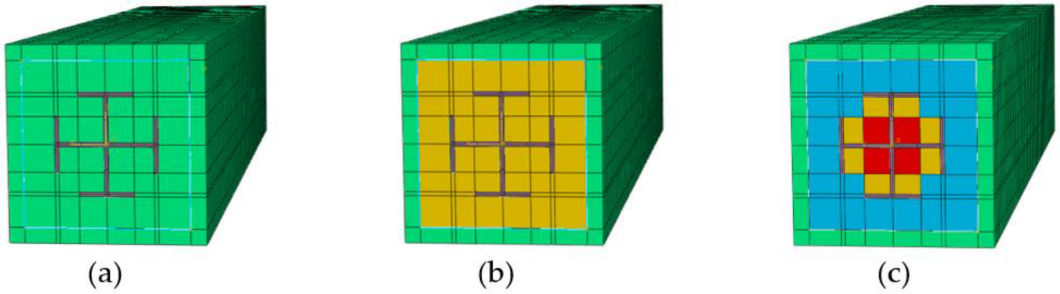

Figure 14. Three kinds of confinement effect on concrete: (**a**) the section with no confinement; (**b**) the section with the confinement effect of the stirrups (**c**) the section with the confinement effect of stirrups and steel.

4.2. Verification of Finite Element Model

Table 5 tabulates the ultimate bearing capacity of the specimens simulated by three finite element models. When the confinement effect is not taken into account, the difference between simulation data and the test results of the specimens with built-in Q235 steel is less than 5%. Figure 15a compares the simulation results with test result of C_4. Figure 15b shows the load–displacement of simulation results and test result of C_6, which also demonstrates the difference of specimens with built-in Q460 is between 4% and 8%, according to Table 5. Based on Table 5 and Figure 15c, the difference between the simulation data and the test results of Q690 high-strength SRC composite columns is in the range of 9% to 13%.

Table 5. Comparison of three simulation results with test results.

Specimens	ABAQUS Results			Test Results	N_u/N_p	N_{up}/N_p	N_{uh}/N_p
	N_u/kN	N_{up}/kN	N_{uh}/kN	N_p/kN			
C1Q2S4T1R1	4107	4183	4220	4200	97.8%	99.6%	100.5%
C2Q2S4T2R1	4341	4495	4554	4506	96.3%	99.8%	101.1%
C3Q2S5T1R1	4208	4317	4388	4340	96.9%	99.5%	101.1%
C4Q2S7T1R1	4529	4690	4721	4596	98.5%	102.0%	102.7%
C5Q4S4T1R1	4270	4641	4726	4462	95.7%	104.0%	105.9%
C6Q4S4T2R1	4649	5094	5307	5050	92.1%	100.9%	105.1%
C7Q4S5T1R1	4621	4991	5056	4878	94.7%	102.3%	103.6%
C8Q4S7T1R1	5086	5447	5531	5383	94.5%	101.2%	102.7%
C9Q4S7T1R2	4824	5283	5312	5120	94.2%	103.2%	103.8%
C10Q4S7T1R3	4707	4951	5003	4848	97.1%	102.1%	103.2%
C11Q6S4T1R1	4433	4961	5019	4847	91.5%	102.4%	103.5%
C12Q6S4T2R1	4786	5440	5536	5407	88.5%	100.6%	102.4%
C13Q6S5T1R1	5025	5729	5955	5487	91.6%	104.4%	108.5%
C14Q6S7T1R1	5682	6733	6892	6220	91.1%	108.2%	110.8%

N_u is the simulation result based on no confinement, N_{up} is the simulation result only considering the confinement effect of the stirrups, N_{uh} is the simulation result considering the confinement effect of the stirrups and steel.

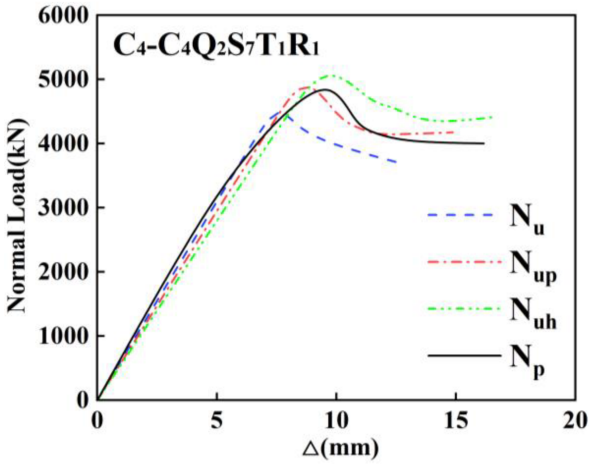

(**a**)

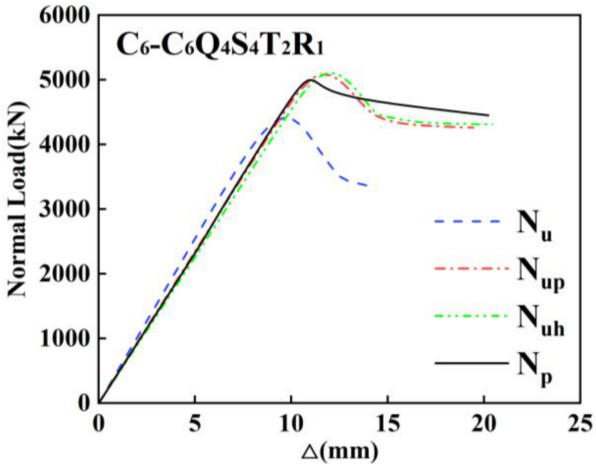

(**b**)

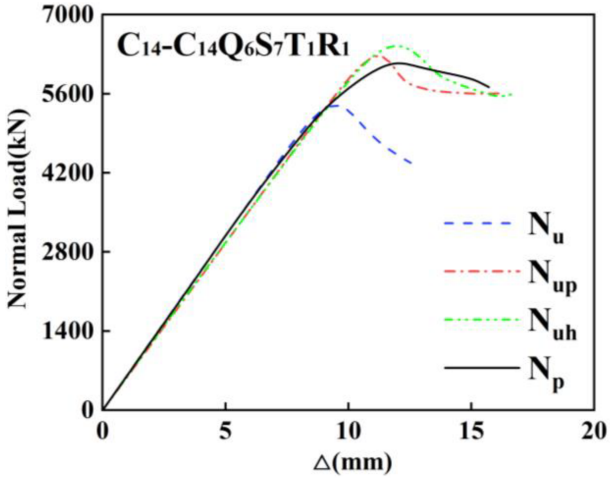

(**c**)

Figure 15. Comparison between test results and the simulation results: (**a**) the load-displacement curves of simulation results and test result for C_4; (**b**) the load-displacement curves of simulation results and test result for C_6. (**c**) the load-displacement curves of simulation results and test result for C_{14}.

In general, the difference between the simulated data and the test results are both less than 11% for the models considering only the confinement effect of the stirrups and the models considering the confinement effect of the stirrups and the steel. The simulated value of the model considering the confinement effect of both the stirrups and the steel increases by about 2% compared with that of the model only considering the confinement effect of the stirrups. Therefore, the confinement effect of the stirrups and the steel on the bearing capacity of high-strength SRC composite columns cannot be ignored.

4.3. Finite Element Parametric Study

In order to expand the parametric analysis, it is necessary to verify the accuracy and applicability of the finite element model to high-strength SRC columns; C14 and C6 were taken as examples to compare the failure mode determined by the numerical simulation with the tested one, as shown in Figures 16 and 17. It can be seen that when the ultimate bearing capacity of the SRC column is reached, the maximum stress on the reinforcement is 460 MPa. However, the maximum stress on the Q690 steel is far from its yield strength, with slight buckling. The concrete on the buckling side crushes first. For specimen C6 with complex stirrups and Q460 steel, when the bearing capacity is reached, almost the entire length of the reinforcement yields with lateral expansion. The strain of the confinement concrete increases, and it functions well together with steel, which improves the utilization of the steel, concrete and reinforcement. As a result, the maximum stress on Q460 steel exceeds its yield strength, but no apparent buckling is noticed. According to the above comparison, both the bearing capacity and the failure mode obtained from the simulation show good agreement with the test results.

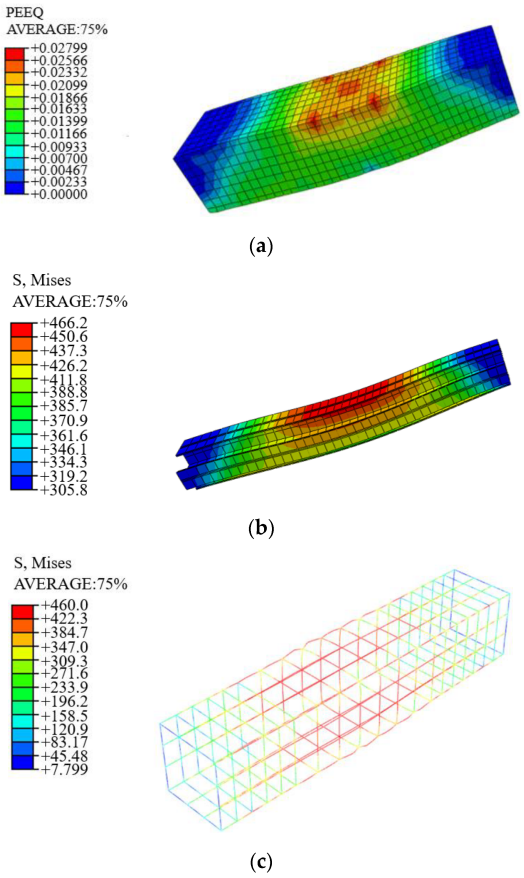

Figure 16. Stress–field nephogram of specimen C14 (considering only confinement effect of the stirrups). (**a**) Stress–field nephogram of C14, (**b**) Stress–field nephogram of Q690 steel in specimen C14 and (**c**) Stress–field nephogram of reinforcement.

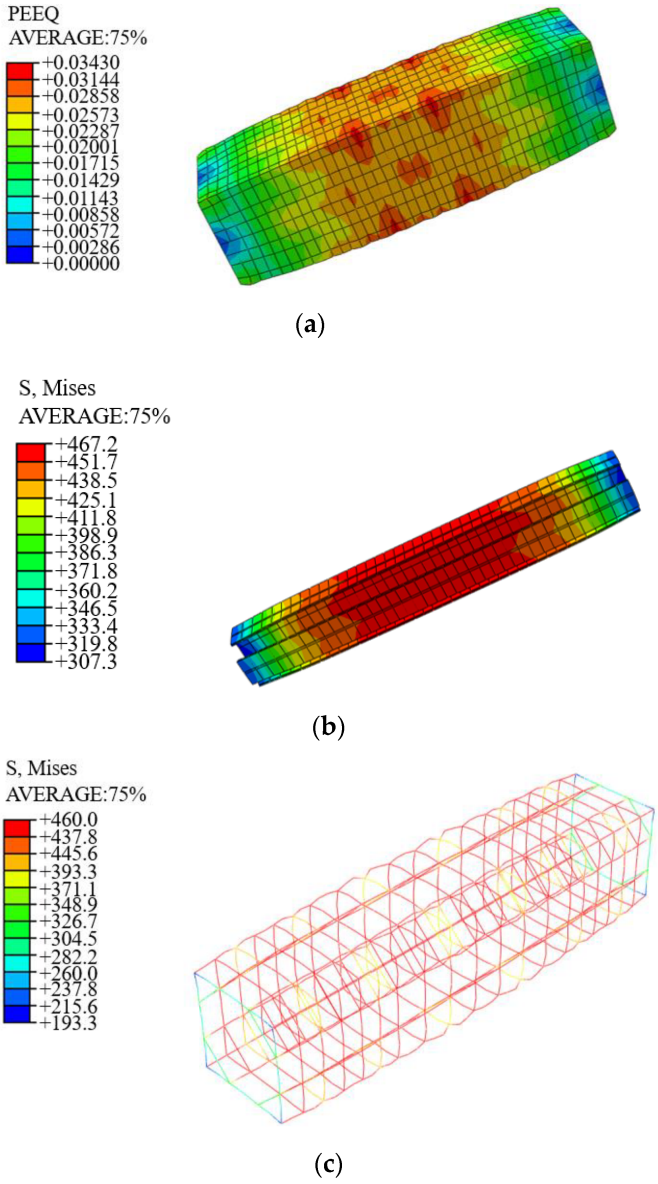

Figure 17. Stress–field nephogram of specimen C6 (considering only confinement effect of the stirrups). (**a**) Stress–field nephogram of C6, (**b**) Stress–field nephogram of Q690 steel in specimen C6 and (**c**) Stress–field nephogram of reinforcement.

Changing the stirrup type enlarges the contribution of Q690 steel effectively. Another way to improve the stirrup confinement is to reduce the spacing of stirrups. The parameters of expanded specimens and the simulation results of bearing capacity are listed in Table 6.

Table 6. Main parameters of the expanded specimens.

Specimen	Stirrup Spacing (mm)	Stirrup Type	Simulation Results (kN)	Increasing Magnitude
C11Q6S4T1R1	80	rectangular	4961	0.0%
Sp_{70}-Q6S4T1R1	70	rectangular	5197	4.8%
Sp_{60}-Q6S4T1R1	60	rectangular	5536	11.6%
Sp_{50}-Q6S4T1R1	50	rectangular	5927	19.5%
C12Q6S4T2R1	80	complex	5440	0.0%
Sp_{70}-Q6S4T2R1	70	complex	5745	5.6%
Sp_{60}-Q6S4T2R1	60	complex	5899	8.4%

For the four specimens with rectangular stirrups, the increasing magnitude of ultimate bearing capacity is similar to the increasing trend of λ_v with the reduction in stirrups spacing, as shown in Figure 18a. However, although the ultimate bearing capacity of the three specimens with complex stirrups increases as spacing reduces, the increasing magnitude of ultimate bearing capacity decreases when the stirrup spacing decreases from 70 to 60 mm, as shown in Figure 18b. In general, if the value of is λ_v, too much larger than the minimum stirrup eigenvalues, the increasing magnitude of the bearing capacity will also decrease.

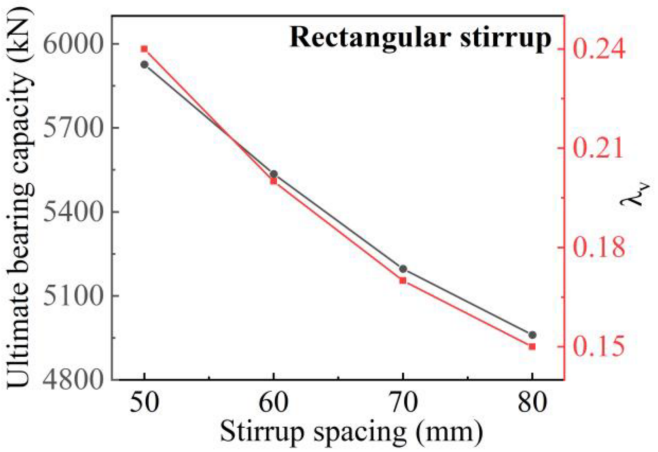

(**a**)

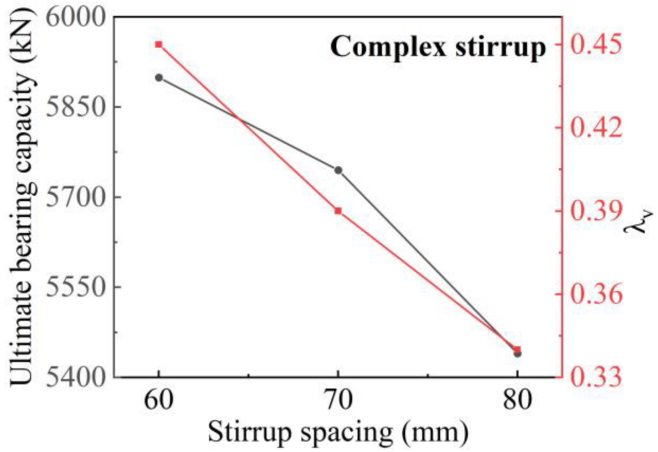

(**b**)

Figure 18. Influence of stirrup spacing on ultimate bearing capacity of the specimens: (**a**) specimens with rectangular stirrup (**b**) specimens with complex stirrup.

According to the stress Nephogram in Figure 19, the value of λ_v of the four specimens with rectangular stirrups does not reach 0.35, and the steel still does not yield under the ultimate load. However, the increasing value of ultimate bearing capacity includes both that of confined concrete and steel. For the specimens with complex stirrups, reducing the spacing from 70 to 60 mm, the increasing value of ultimate bearing capacity is mainly from the bearing capacity of confined concrete. The contribution of Q690 steel is minimal. Therefore, when the materials have been selected, the design of high-strength SRC columns should be carried out in terms of stirrup type and stirrup spacing to ensure material utilization and save materials.

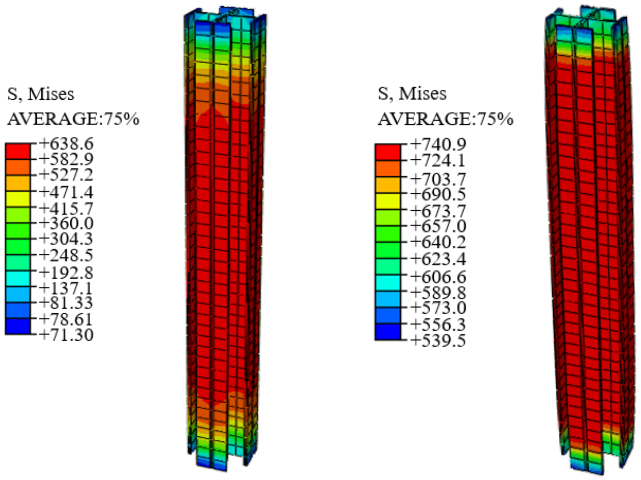

Figure 19. Q690 steel contribution of specimens with different stirrup spacing, type. (**a**) Rectangular stirrup, spacing = 50 mm (**b**) Complex stirrup, spacing = 70 mm.

5. Conclusions

An experimental study of SRC columns with high-strength steel was carried out to investigate the applicability of the formula for the bearing capacity described in specifications to high-strength SRC columns. It was concluded that the results calculated by the specifications were too conservative, and a modified formula considering the confinement effect of the stirrups was proposed. Furthermore, the comparison of the test results with results calculated according to the modified formula proved that considering the confinement effect of the stirrups on concrete for calculating the bearing capacity of high-strength SRC columns was accurate and effective. Finally, the finite element models considering different confinement levels were established, and their simulation results agree well with the test results. In general, an accurate calculation and design method for practical application was provided. The main conclusions that follow from the findings of the current work are that:

1. The bearing capacity of SRC columns can be significantly improved by high-strength steel. Compared with the bearing capacity of the Q235 SRC columns, the maximum bearing capacity of the Q460 SRC column and the Q690 SRC column increase by 13.2% and 35.3%, respectively. Further, the bearing capacity of the SRC columns was significantly improved by increasing the steel ratio.
2. When stirrups satisfy the requirements of the stirrup eigenvalues, the utilization ratio of high-strength steel increases. The bearing capacity of high-strength SRC columns with complex stirrups significantly enlarges compared with the high-strength SRC columns with rectangular stirrups.
3. The bearing capacity of the high-strength SRC columns declines with an increase in the slenderness ratio. The high-strength SRC composite columns with a large slenderness ratio experience greater buckling deformation than high-strength SRC columns with a conventional slenderness ratio.
4. Comparing of the results calculated by codes AISC360-16, Eurocode 4 and JGJ138-2016 with this test results reveals that these codes are too conservative, and the calculation results of code JGJ138-2016 are closest to the test results. A modified formula for the bearing capacity of the SRC columns considering the confinement effect of the stirrups on concrete is derived based on code JGJ138-2016.
5. The simulation results considering the confinement effect of the stirrups show great agreement with the experimental bearing capacity and failure mode of the SRC columns. The contribution of high-strength steel can be maximized, and the bearing capacity can be improved by reducing the stirrup spacing. When the stirrup eigenvalues λ_v is close to the minimum stirrup eigenvalues, the increasing magnitude of

bearing capacity is obvious. When the stirrups eigenvalues λ_v exceed the minimum stirrup eigenvalues, the improvement of bearing capacity is not apparent.

Author Contributions: Conceptualization, J.W.; methodology, J.W. and Y.D.; software, Y.D. and X.W.; validation, Y.W., Y.D. and Q.L.; formal analysis, J.W.; investigation, Y.D.; resources, J.W.; data curation, Y.D.; writing—original draft preparation, J.W. and Y.D.; writing—review and editing, Y.D.; visualization, X.W.; supervision, Q.L.; project administration, Y.W.; funding acquisition, J.W. All authors have read and agreed to the published version of the manuscript.

Funding: This research is financially supported by the Natural Science Foundation of Heilongjiang Province in China (ZD2019E001) 'Study on bearing capacity and seismic performance of Q460 high strength steel-reinforced concrete columns', and the National College Students' innovation and entrepreneurship training program 'Experimental study on mechanical properties of steel reinforced concrete columns under axial compression' (202110225185).

Institutional Review Board Statement: Not applicable.

Informed Consent Statement: Not applicable.

Data Availability Statement: The data presented in this study are available on request from the corresponding author.

Conflicts of Interest: The authors declare no conflict of interest.

References

1. Shokouhian, M.; Shi, Y.J. Flexural strength of hybrid steel I-beams based on slenderness. *Eng. Struct.* **2015**, *93*, 114–128. [CrossRef]
2. Tsutsumi, S.; Kitamura, T.; Fincato, R. Ductile behaviour of carbon steel for welded structures: Experiments and numerical simulations. *J. Constr. Steel Res.* **2020**, *172*, 106185. [CrossRef]
3. Al-azzani, H.; Yang, J.; Sharhan, A.; Wang, W.Y. A practical approach for fire resistance design of restrained high-strength Q690 steel beam considering creep effect. *Fire Technol.* **2021**, *57*, 1683–1706. [CrossRef]
4. Gang, S.; Ban, H.-Y.; Shi, Y.-J.; Yuanqing, W. Overview of research progress for high strength steel structures. *Eng. Mech.* **2013**, *30*, 1–13.
5. ANSI/AISC360-2016. *Specification for Structural Steel Buildings*; AISC Committee on Specifications: Chicago, IL, USA, 2016.
6. European Committee for Standardization. *Eurocode 4: Design of Composite Steel and Concrete Structures Part 1-1: General Rules for Buildings: EN 1994-1-1:2004*; European Committee for Standardization: Brussels, Belgium, 2004.
7. JGJ138-2016. *Code for Design of Composite Structures*; 000013338/2016-00180; Architecture and Building Press: Beijing, China, 2016.
8. Yang, Y.; Hou, Z.; Li, G.; Gong, C.; Chen, S.; Qiu, L. The bearing capacity and seismic performance of high strength steel reinforced concrete column. *Steel Constr.* **2016**, *31*, 21–31.
9. Mirza, S.A.; Skrabek, B.W. Statistical analysis of slender composite beam-column strength. *J. Struct. Eng.* **1992**, *118*, 1312–1332. [CrossRef]
10. Zhao, X.; Wen, F.; Chan, T.-M.; Cao, S. Theoretical stress–strain model for concrete in steel-reinforced concrete columns. *J. Struct. Eng.* **2019**, *145*, 04019009. [CrossRef]
11. Sheikh, S.A.; Uzumeri, S.M. Strength and Ductility of Tied Concrete Columns. *J. Struct. Div.* **1980**, *106*, 1079–1102. [CrossRef]
12. Mander, J.B.; Priestley, M.J.N.; Park, R. Theoretical stress-strain model for confined concrete. *J. Struct. Eng.* **1988**, *114*, 1804–1826. [CrossRef]
13. Chen, S.; Wu, P. Analytical model for predicting axial compressive behavior of steel reinforced concrete column. *J. Constr. Steel Res.* **2016**, *128*, 649–660. [CrossRef]
14. Wang, J.; Su, Y.; Zhao, J.; Wang, X.; Su, W. Study on axial compression performance of high strength H-section steel reinforced concrete composite column. *J. Build. Struct.* **2021**. [CrossRef]
15. Zhao, X.; Wen, F.; Chen, Y.; Hu, J.; Yang, X.; Dai, L.; Cao, S. Experimental study on the static performance of steel reinforced concrete columns with high encased steel ratios. *Struct. Des. Tall Spec. Build.* **2018**, *27*, e1536. [CrossRef]
16. GB/T228-2010. *Chinese Standard for Metallic Materials-Tensile Testing at Ambient Temperature*; Architecture and Building Press: Beijing, China, 2010.
17. GB/T50152-2012. *Standard for Test Methods of Concrete Structures*; 000013338/2012-00191; Architecture and Building Press: Beijing, China, 2012.
18. Zhao, X.-Z.; Wen, F.-P. Theoretical study on confinement mechanism and stress-strain model for steel confined concrete in SRC columns. *Eng. Mech.* **2018**, *35*, 36–46.
19. Fib. *Fib Model Code for Concrete Structures 2010*; International Federation for Structural Concrete: Lausanne, Switzerland, 2010.
20. Xiaolai, Y.; Rongxin, T.; Zhongliang, X.; Yan, L. Modification of mechanical model of confined concrete proposed by Mander. *J. Yangzhou Univ. (Nat. Sci. Ed.)* **2018**, *21*, 61–65. (In Chinese)

21. Kim, C.-S.; Park, H.-G.; Chung, K.-S.; Choi, I.-R. Eccentric axial load testing for concrete-encased steel columns using 800 MPa steel and 100 MPa concrete. *J. Struct. Eng.* **2012**, *138*, 1019–1031. [CrossRef]
22. Kim, C.-S.; Park, H.-G.; Lee, H.-J.; Choi, I.-R.; Chung, K.-S. Eccentric Axial Load Test for High-Strength Composite Columns of Various Sectional Configurations. *J. Struct. Eng.* **2017**, *143*, 04017075. [CrossRef]
23. GB 50010-2010. *Chinese Standard for Design of Concrete Structures*; 000013338/2015-00308; Architecture and Building Press: Beijing, China, 2010.

materials

MDPI

Article

Volume Integral Equation Method Solution for Spheroidal Inclusion Problem

Jungki Lee * and Mingu Han

Department of Mechanical and Design Engineering, Hongik University, Sejong City 30016, Korea; pooh9265@naver.com
* Correspondence: inq3jkl@hongik.ac.kr

Abstract: In this paper, the volume integral equation method (VIEM) is introduced for the numerical analysis of an infinite isotropic solid containing a variety of single isotropic/anisotropic spheroidal inclusions. In order to introduce the VIEM as a versatile numerical method for the three-dimensional elastostatic inclusion problem, VIEM results are first presented for a range of single isotropic/orthotropic spherical, prolate and oblate spheroidal inclusions in an infinite isotropic matrix under uniform remote tensile loading. We next considered single isotropic/orthotropic spherical, prolate and oblate spheroidal inclusions in an infinite isotropic matrix under remote shear loading. The authors hope that the results using the VIEM cited in this paper will be established as reference values for verifying the results of similar research using other analytical and numerical methods.

Keywords: volume integral equation method (VIEM); isotropic/anisotropic inclusion problems; boundary element method (BEM); standard finite element method (FEM)

Citation: Lee, J.; Han, M. Volume Integral Equation Method Solution for Spheroidal Inclusion Problem. *Materials* **2021**, *14*, 6996. https://doi.org/10.3390/ma14226996

Academic Editor: Michele Bacciocchi

Received: 27 September 2021
Accepted: 15 November 2021
Published: 18 November 2021

1. Introduction

The matrix and fibers in composites are usually made of isotropic material. However, in order to have higher strength and stiffness for commercial use, especially in the aerospace and automobile sectors, some constituents of metal matrix composites can be anisotropic. Since anisotropic materials are able to enhance mechanical properties toward orientation, certain mechanical properties (e.g., tensile strength) of anisotropic materials thus depend on orientation. As an example, in titanium-silicon carbide (Ti-SiC) composites, the matrix is nearly isotropic, but the SiC fiber has strong anisotropy and a multilayered structure including an interphase and a core.

A number of analytical techniques for solving inclusion problems are available when the inclusions are simple two-dimensional shapes (cylindrical and elliptical) or simple three-dimensional shapes (spherical and ellipsoidal) and when they are well-separated [1–5]. In particular, Eshelby developed a simple and elegant method for solving the inclusion problem in isotropic solids in 1957 [1]. Eshelby first pointed out that the resulting elastic field can be found with the help of a sequence of imaginary cutting, straining and welding operations [1]. Eshelby also found that the strain and stress field inside the ellipsoidal inclusion is uniform and has a closed-form solution, regardless of the material properties and initial eigenstrain [1]. Eshelby's findings significantly influenced the mechanics of composites.

In the micromechanical analysis of composite materials, it is often assumed that the inclusions are periodically distributed in the matrix. Then, the unit-cell model with periodic boundary conditions is used to evaluate the overall, microstructure-insensitive, material properties of the composite. However, in real composites, the distribution of the inclusions is not periodic. Thus, the unit-cell model may not provide accurate estimates of the failure and damage mechanisms in composites [6–8].

Therefore, stress analysis of heterogeneous solids often requires the use of numerical approaches based on the standard finite element or boundary element formulations. How-

ever, both methods present difficulties in dealing with problems involving infinite media or multiple anisotropic inclusions. In response to this concern, it has been demonstrated that the volume integral formulation can overcome both of these limitations in heterogeneous problems involving infinite media [9–11].

In comparison to the boundary element method (BEM), the volume integral equation method (VIEM) does not require the use of the Green's function for anisotropic inclusions and is not sensitive to the geometry of the inclusions. Moreover, as opposed to the standard finite element method (FEM), where it is necessary to discretize the full domain, the multiple inclusions only need to be discretized in the VIEM.

In this paper, three-dimensional elastostatic inclusion problems using the volume integral equation method (VIEM) will be investigated.

In order to introduce the VIEM as a versatile numerical method for the three-dimensional elastostatic inclusion problem, we first examine single isotropic/orthotropic spherical, prolate and oblate spheroidal inclusions in an infinite isotropic matrix subject to uniform remote tensile loading. Two different prolate and oblate spheroidal inclusions with an aspect ratio of 0.5 and 0.75 are considered, respectively. The matrix is assumed to be isotropic. Eight isotropic and five orthotropic inclusions with different characteristics are considered in the numerical calculation. The normalized tensile stress inside the inclusions is investigated in two different directions. Next, we examine single isotropic/orthotropic spherical, prolate and oblate spheroidal inclusions in an infinite isotropic matrix subject to remote shear loading. Two different prolate and oblate spheroidal inclusions with an aspect ratio of 0.5 and 0.75 are considered, respectively. The matrix is assumed to be isotropic. Three isotropic and two orthotropic inclusions with different characteristics are considered in the numerical calculation. The normalized shear stress inside the inclusions is investigated in two different directions.

The authors hope that the present solutions using the parallel volume integral equation method for the single isotropic/orthotropic spherical, prolate and oblate spheroidal inclusions with different material properties under uniform remote tensile loading or remote shear loading will be established as reference values for verifying the results of other analytical and numerical methods.

Since the VIEM is a combination of two powerful general-purpose numerical methods, the standard finite element method (FEM) and the boundary element method (BEM), it is also a highly beneficial tool in the field of numerical analysis and can play a very important role in solving inclusion problems. Subsequently, the purpose of this paper is to introduce the parallel volume integral equation method (PVIEM) as an accessible, versatile and powerful numerical method for solving inclusion problems in the areas of computational mechanics and mechanics of composite materials.

2. Governing Equations of Volume Integral Equation Formulation

The geometry of the general elastodynamic problem is shown in Figure 1a, where an infinite homogeneous, isotropic and linearly elastic solid containing a number of isotropic or anisotropic inclusions of arbitrary number and shape are subjected to prescribed dynamic loading at infinity.

In Figure 1a, V and S represent the volume and surface of the inclusion respectively, and n is the outward unit normal to S while V_o and S_o represent the infinite volume and surface, respectively.

The symbols $\rho^{(1)}$ and $c_{ijkl}{}^{(1)}$ denote the density and the elastic stiffness tensor of the inclusion, while $\rho^{(2)}$ and $c_{ijkl}{}^{(2)}$ denote the density and the elastic stiffness tensor of the infinite homogeneous, isotropic and linearly elastic matrix material, respectively. Therefore, $c_{ijkl}{}^{(2)}$ is a constant isotropic tensor, while $c_{ijkl}{}^{(1)}$ can be arbitrary, i.e., the inclusions may, in general, be inhomogeneous and anisotropic. The isotropic or anisotropic inclusions are assumed to be perfectly bonded to the matrix.

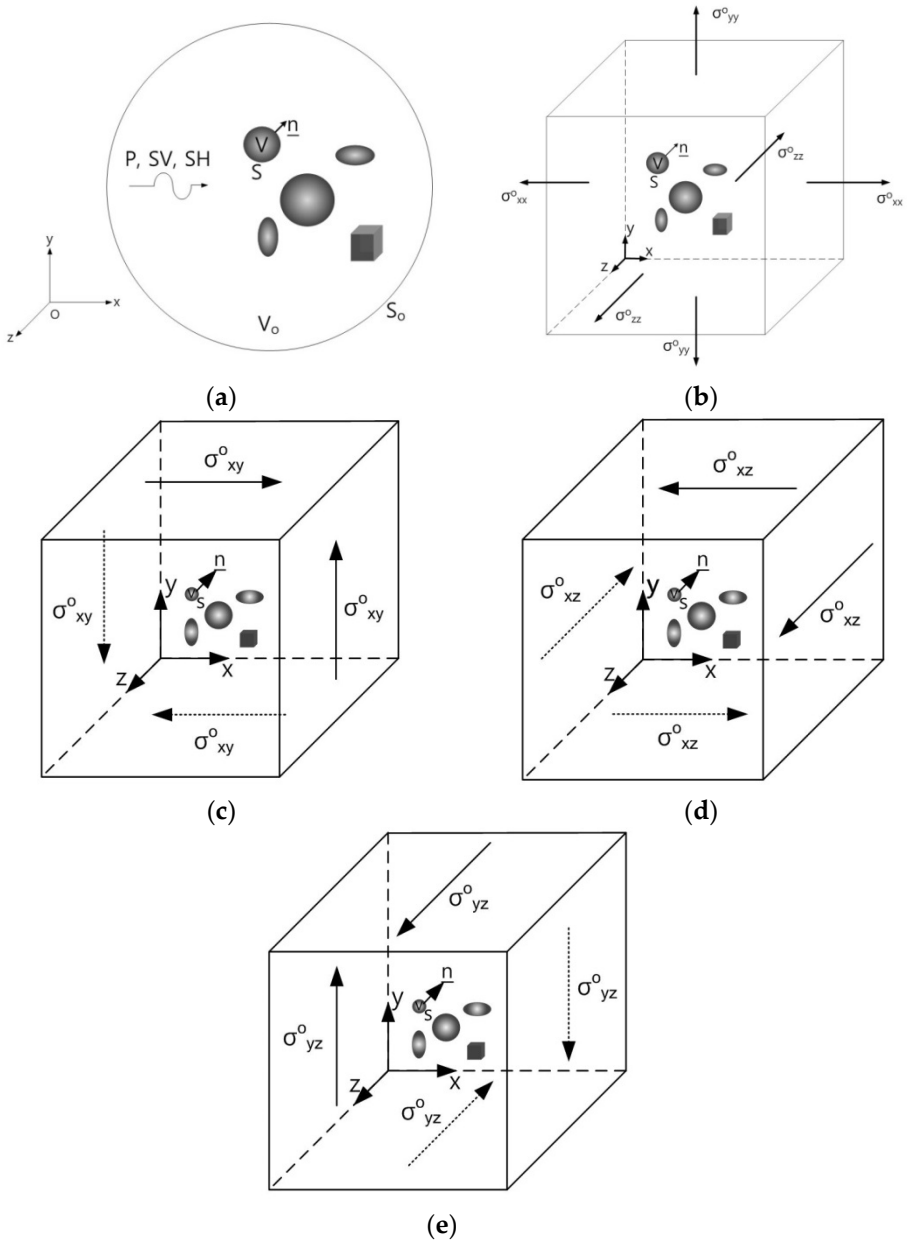

Figure 1. Geometry of the general (**a**) elastodynamic and (**b**) elastostatic problem. (**c**) A remote shear loading, σ^o_{xy}. (**d**) A remote shear loading, σ^o_{xz}. (**e**) A remote shear loading, σ^o_{yz}.

Mal and Knopoff [12] showed that the elastodynamic displacement, $u_m(\mathbf{x})$, in the composite satisfies the volume integral equation:

$$u_m(\mathbf{x}) = u^o_m(\mathbf{x}) + \int_V [\delta\rho\omega^2 g^m_i(\boldsymbol{\xi},\mathbf{x})u_i(\boldsymbol{\xi}) - \delta c_{ijkl} g^m_{i,j}(\boldsymbol{\xi},\mathbf{x})u_{k,l}(\boldsymbol{\xi})]d\boldsymbol{\xi} \quad (1)$$

where the integral is over the domain V occupied by the isotropic or anisotropic inclusions, $\delta\rho = \rho^{(1)} - \rho^{(2)}$ and $\delta c_{ijkl} = c_{ijkl}{}^{(1)} - c_{ijkl}{}^{(2)}$, and $g_i{}^m(\boldsymbol{\xi},\mathbf{x})$ is the elastodynamic Green's function for the infinite homogeneous, isotropic and linearly elastic matrix material.

In Equation (1), $u_m{}^o(\mathbf{x}, \boldsymbol{\omega})e^{-i\omega t}$ represents the mth component of the displacement vector due to the incident field at $\mathbf{x}$ in the absence of the inclusions, while $u_m(\mathbf{x}, \boldsymbol{\omega})e^{-i\omega t}$ denotes the same quantity in the presence of the isotropic or anisotropic inclusions, where $\boldsymbol{\omega}$ is the circular frequency of the waves. In what follows, the explicit dependence on the circular frequency, and the common time factor, $e^{-i\omega t}$, for all field quantities will be suppressed.

The geometry of the general elastostatic problem is shown in Figure 1b–e. It has been shown by Lee and Mal [9] that the corresponding elastostatic displacement, $u_m(\mathbf{x})$, within the composite, fulfills the volume integral equation as:

$$u_m(\mathbf{x}) = u_m^o(\mathbf{x}) - \int_V \delta c_{ijkl} g_{i,j}^m(\boldsymbol{\xi}, \mathbf{x}) u_{k,l}(\boldsymbol{\xi}) d\boldsymbol{\xi} \quad (2)$$

where the integral is over the space V occupied by the isotropic or anisotropic inclusions and $\delta c_{ijkl} = c_{ijkl}^{(1)} - c_{ijkl}^{(2)}$. The value $g_i{}^m(\boldsymbol{\xi},\mathbf{x})$ represents the elastostatic Kelvin's solution (or Green's function) for the infinite homogeneous, isotropic and linearly elastic matrix material.

In Equations (1) and (2), the differentiations are with respect to the integration variable, ξ_i, and the summation convention and comma notation have been utilized. The integrand is non-zero within the isotropic or anisotropic inclusions only, since $\delta c_{ijkl} = 0$ outside the inclusions.

If $\mathbf{x}$ lies inside the inclusions, then Equations (1) and (2) are integro-differential equations for the unknown displacement vector $\mathbf{u}(\mathbf{x})$ within the inclusions. It should be noted that an algorithm was developed by Lee and Mal [9,10] to numerically calculate the unknown displacement vector $\mathbf{u}(\mathbf{x})$ by discretizing the inclusions only using standard finite elements. Once $\mathbf{u}(\mathbf{x})$ within the inclusions is determined, the displacement field outside the inclusions can be obtained from Equations (1) and (2) by evaluating the corresponding integrals respectively, and the stress field within and outside the inclusions can also be readily determined.

The volume integral equation method (VIEM) was originated from Lee and Mal [10] in 1995. Since 1995, Lee and his co-workers (e.g., [9–11,13–17]) have been developing a more engineering-oriented VIEM, while Buryachenko (e.g., [18–20]) has been examining a more mathematically oriented VIEM since 2000. Additionally, Dong has conducted research on the volume integral equation method since 2003 [21]. Therefore, the VIEM is broadening its influence on computational fields of study.

Furthermore, Section 4.3 entitled 'Volume Integral Equation Method' of the book "Micromechanics of Heterogeneous Materials" by Buryachenko [18] also explains further mathematical formulation of the elastostatic volume integral equation method. In particular, a general description of the volume integral equation method is presented in Chapter 4 entitled 'Volume Integral Equation Method (VIEM)' of the book "Advances in Computers and Information in Engineering Research, Vol. 2" by Michopoulos et al. (eds.) [22]. In addition, complete descriptions of the fundamental numerical technique of Equation (2) can be found in [17] for three-dimensional elastostatic problems.

Although each numerical method has certain advantages, specific disadvantages have led to further discussion and research. For example, in Section 3.1 of Reference [20], Buryachenko points out that the VIEM is quite time-consuming. Moreover, no optimized commercial software exists for its application.

Firstly, in order to resolve this 'time-consuming' problem, we propose the parallel volume integral equation method and implement MPI-based code. Such method allows us not only to solve the large domain but also to speed up computation in the volume integral equation method. The FORTRAN 90 (Version 1.1, IBM, Armonk, NY, USA) source code containing about 9000 lines for the three-dimensional VIEM of the previous paper [17] was parallelized and optimized for this paper, with support from the Korea Institute of Science and Technology Information (KISTI, Daejeon, Korea). Figure 2 shows the procedures of a representative MPI parallelization approach ("pvi3ds01_sm7560xx.f90") for the sequential three-dimensional VIEM code ("svi3ds01_sm4320xx.f"). As a result, the program execution time has been greatly reduced. Furthermore, we could use more finite elements (31,857 nodes and 7560 elements) in the VIEM model of this paper than those (18,109 nodes and 4320 elements) in the VIEM model of the previous paper [17]. The parallel FORTRAN source code for the three-dimensional VIEM is presently being processed in the KISTI-5. It is referred to as "Nurion", which is a system consisting of compute nodes, CPU-only nodes, Omni-Path interconnect networks, Burst Buffer high-speed storage, a Luster-based parallel

file system and a water-cooling device based on a Rear Door Heat Exchanger (RDHx). The CPU-only nodes consist of 132 Intel Xeon 6148 2.4 GHz processors (named "Skylake"). The total theoretical performance is 25.7 petaflops, which ranked 11th in the world in June 2018 (http://www.top500.org, accessed on 3 May 2021). It should be noted that, in order to investigate three-dimensional stress problems with multiple inclusions, in addition to parallelization and optimization of the sequential three-dimensional VIEM code, a domain decomposition method (DDM) was applied to the parallel three-dimensional VIEM code, with support from the Korea Institute of Science and Technology Information (KISTI). The domain decomposition method allows decomposition of large-sized problem solutions to solutions of several smaller-sized problems [23]. Therefore, the parallel volume integral equation method (PVIEM) using the domain decomposition method enables us to investigate more complicated multiple inclusion problems elastostatically or elastodynamically.

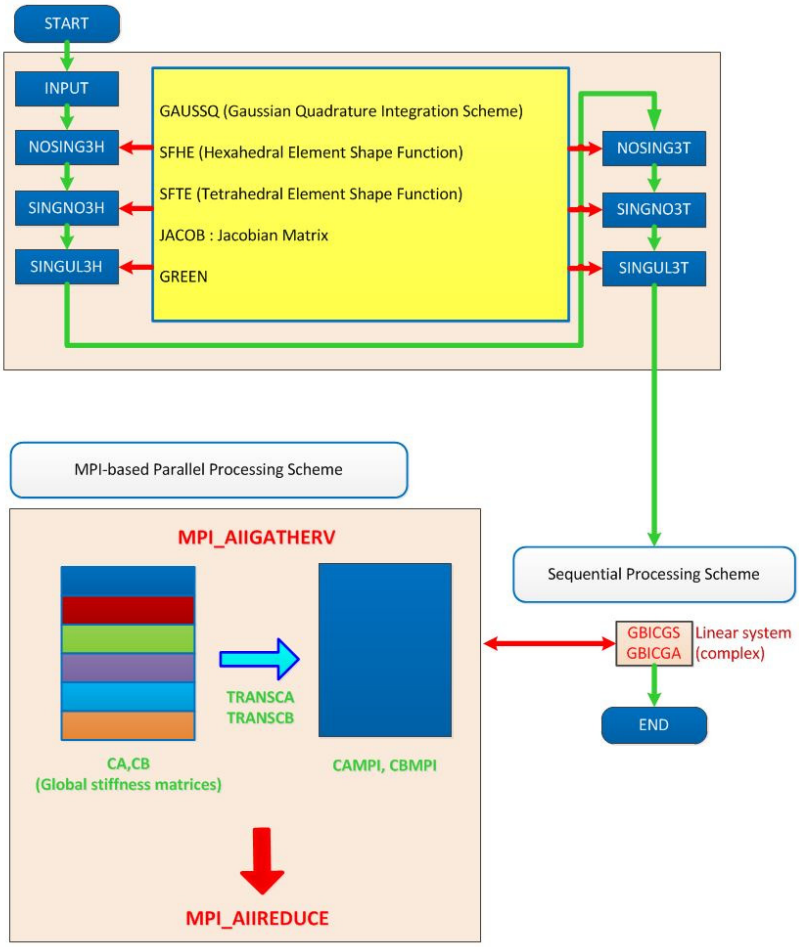

Figure 2. Procedures of 'pvi3ds01_sm7560xx.f90' using MPI parallelization.

Secondly, in order to resolve the 'no optimized commercial software' problem, we plan to develop a semi-commercial VIEM software called the "Volume Integral Equation Method Application Program" (VIEMAP). Table 1 shows the analysis capabilities of VIEMAP including a pre-processor (ViemMesh), a solver (VIEM) and a post-processor (ViemPlot) adapted to solve multiple isotropic/anisotropic inclusion problems in a computationally tractable manner. Figure 3 shows the registered trademark for the VIEMAP. The authors aim to help both university students and researchers create VIEM models using the VIEMAP more easily than using the standard finite element method (FEM), as well as solve multiple isotropic/anisotropic inclusion problems in an unbounded isotropic medium more accurately and conveniently than the boundary element method (BEM).

Table 1. Capabilities of VIEMAP.

	Two Dimensional	Three Dimensional
ViemMesh (Pre-Processor)	(1) 8-node quadrilateral finite element (2) 6-node triangular finite element	(1) 20-node hexahedral finite element (2) 10-node tetrahedral finite element
VIEM (Solver)	**Multiple Inclusion Problems** **Isotropic Inclusions** **Anisotropic Inclusions** (1) Elastostatic solver (2) Elastodynamic solver	**Multiple Inclusion Problems** **Isotropic Inclusions** **Anisotropic Inclusions** (1) Elastostatic solver (2) Elastodynamic solver
ViemPlot (Post-Processor)	(1) Displacement contour plot (2) Stress contour plot	(1) Displacement contour plot (2) Stress contour plot

Figure 3. Registered trademark for VIEMAP.

3. Three-Dimensional Elastostatic Problems Using the VIEM

In this section, we first examine single isotropic/orthotropic spherical, prolate and oblate spheroidal inclusions in an infinite isotropic matrix subject to uniform remote tensile loading, σ^{o}_{xx}, as shown in Figure 4 (also see Figures 1b and 5). The remote applied load can be arbitrarily chosen and was assumed to be σ^{o}_{xx} = 143.10 GPa for convenience purposes only. Two different prolate spheroidal inclusions were considered: (a) a/b = c/b = 0.5 and (b) a/b = c/b = 0.75 (see Figure 5). Additionally, two different oblate spheroidal inclusions were considered: (a) b/a = c/a = 0.5 and (b) b/a = c/a = 0.75 (see Figure 5).

The elastic constants for the isotropic matrix and the isotropic inclusions are listed in Table 2. The elastic constants for the isotropic matrix and the orthotropic inclusions are listed in Table 3.

We next examine single isotropic/orthotropic spherical, prolate and oblate spheroidal inclusions in an infinite isotropic matrix subject to remote shear loading, σ^{o}_{xy}, σ^{o}_{xz} or σ^{o}_{yz}, as shown in Figure 6 (also see Figures 1c–e and 5) [24]. The remote applied load can be arbitrarily chosen and was assumed to be $\sigma^{o}_{xy} = \sigma^{o}_{xz} = \sigma^{o}_{yz}$ = 75.76 GPa for convenience purposes only. We considered the same geometry of the single spherical, prolate (with an aspect ratio of 0.5 and 0.75) and oblate (with an aspect ratio of 0.5 and 0.75) spheroidal inclusions in an infinite isotropic matrix under remote shear loading (σ^{o}_{xy}, σ^{o}_{xz} and σ^{o}_{yz}).

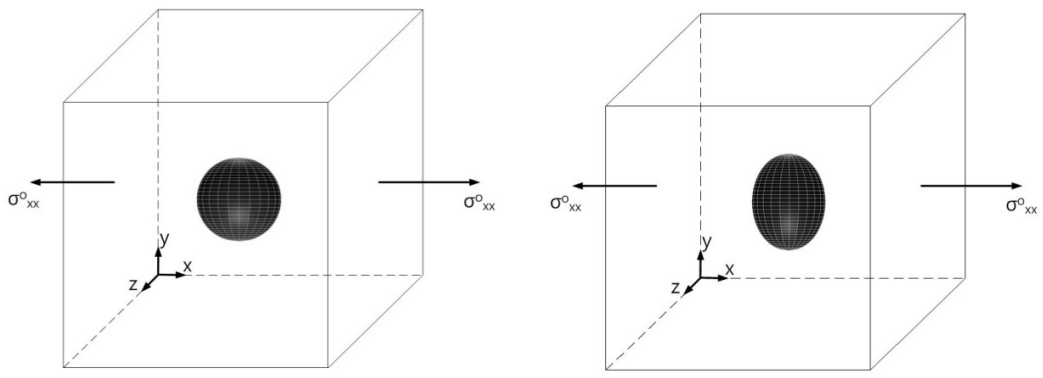

(**a**) A spherical inhomogeneity (**b**) A prolate spheroidal inhomogeneity

Figure 4. *Cont.*

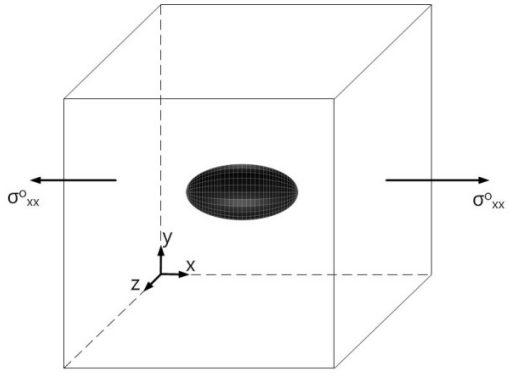

(**c**) An oblate spheroidal inhomogeneity

Figure 4. (**a**) Spherical, (**b**) prolate spheroidal and (**c**) oblate spheroidal inclusions under uniform remote tensile loading (σ^{o}_{xx}).

Table 2. Material Properties of the Isotropic Matrix and the Isotropic Inclusions.

Material	λ (GPa)	μ (GPa)	E (GPa)	ν
Matrix (Iso_01)	67.3401	37.8788	100.0	0.32
Inclusion (Iso_01)	176.060	176.060	440.15	0.25
Matrix (Iso_02)	121.154	80.7692	210.0	0.30
Inclusion (Iso_02)	83.1643	176.724	410.0	0.16
Matrix (Iso_03)	75.0	37.5	100.0	0.3333
Inclusion (Iso_03)	150.0	75.0	200.0	0.3333
Matrix (Iso_04)	75.0	37.5	100.0	0.3333
Inclusion (Iso_04)	375.0	187.5	500.0	0.3333
Matrix (Iso_05)	75.0	37.5	100.0	0.3333
Inclusion (Iso_05)	750.0	375.0	1000.0	0.3333
Matrix (Iso_06)	121.154	80.7692	210.0	0.30
Inclusion (Iso_06)	87.2202	41.0448	110.0	0.34
Matrix (Iso_07)	75.0	37.5	100.0	0.3333
Inclusion (Iso_07)	15.0	7.5	20.0	0.3333
Matrix (Iso_08)	75.0	37.5	100.0	0.3333
Inclusion (Iso_08)	52.5	26.25	70.0	0.3333

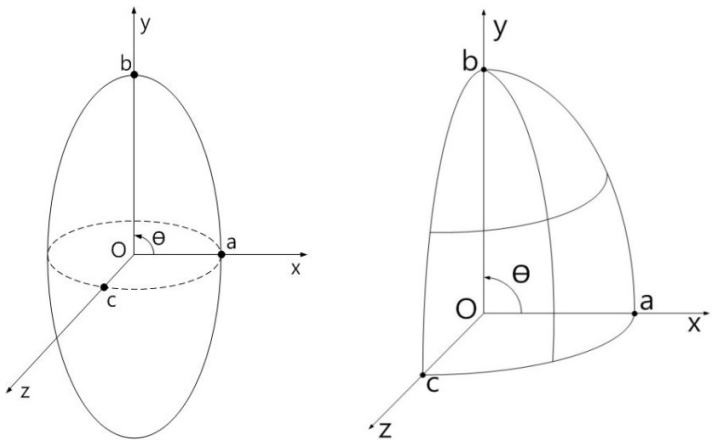

(**a**) (**b**)

Figure 5. The orientation of spherical, prolate spheroidal and oblate spheroidal inclusions. (**a**) Spheroidal coordinate system. (**b**) Cartesian coordinate system.

Three different material properties (Iso_01, Iso_05 and Iso_06) in Table 2 were used in the numerical calculation. The elastic constants for the isotropic matrix and the orthotropic inclusions are listed in Table 4. Table 5 shows various characteristics of the material properties used in the numerical calculation. In order to demonstrate the capability of the volume integral equation method for the three-dimensional anisotropic inclusion problem, three independent elastic constants, c_{44} (shear modulus in the yz plane), c_{55} (shear modulus in the xz plane) and c_{66} (shear modulus in the xy plane), were assumed to be different from each other [25].

Table 3. Material Properties of the Isotropic Matrix and the Orthotropic Inclusions.

Unit: GPa	Orthotropic Inclusions					Isotropic Matrix
	Ort_01	Ort_02	Ort_03	Ort_04	Ort_05	
c_{11}	139.54	279.08	418.61	41.86	69.77	143.10
$c_{12} = c_{21}$	3.90	7.80	11.7	1.17	1.95	67.34
$c_{13} = c_{31}$	3.90	7.80	11.7	1.17	1.95	67.34
c_{22}	15.28	30.56	45.83	4.58	7.64	143.10
$c_{23} = c_{32}$	3.29	6.59	9.88	0.99	1.65	67.34
c_{33}	15.28	30.56	45.83	4.58	7.64	143.10
c_{44}	5.90	11.80	17.70	1.77	2.95	37.88
c_{55}	5.90	11.80	17.70	1.77	2.95	37.88
c_{66}	5.90	11.80	17.70	1.77	2.95	37.88

Table 4. Material properties of the isotropic matrix and the orthotropic inclusions.

Unit: GPa	Orthotropic Inclusions		Isotropic Matrix
	Ort_06	Ort_07	
c_{11}	61.11	458.30	143.10
$c_{12} = c_{21}$	17.95	134.63	67.34
$c_{13} = c_{31}$	20.54	154.02	67.34
c_{22}	32.77	245.78	143.10
$c_{23} = c_{32}$	15.05	112.87	67.34
c_{33}	47.89	359.15	143.10
c_{44}	9.97	74.79	37.88
c_{55}	15.16	113.69	37.88
c_{66}	10.99	82.40	37.88

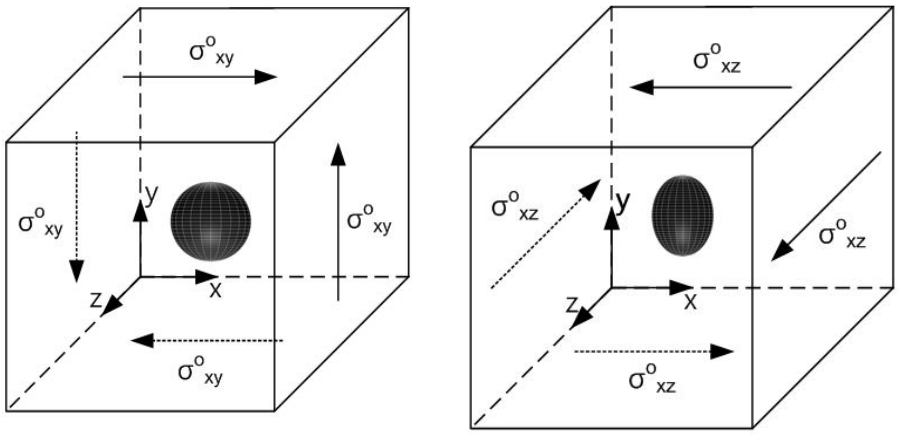

(**a**) A spherical inclusion (σ^{o}_{xy}) (**b**) A prolate spheroidal inclusion (σ^{o}_{xz})

Figure 6. *Cont.*

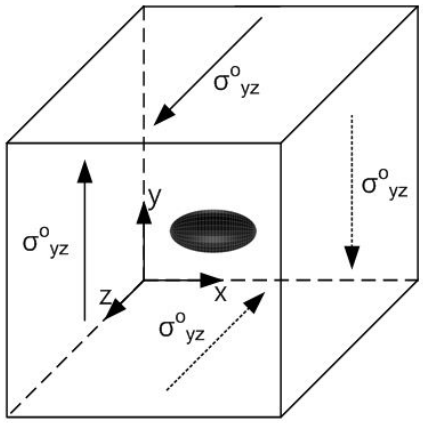

(**c**) An oblate spheroidal inclusion (σ^{o}_{yz})

Figure 6. (**a**) Spherical, (**b**) prolate spheroidal and (**c**) oblate spheroidal inclusions under remote shear loading.

Table 5. Material Property Characteristics.

Material		Characteristics	
Matrix (Iso_01)	Isotropic	No restriction in Poisson's ratio	E(Inclusion) > E(Matrix)
Inclusion (Iso_01)	Isotropic	No restriction in Poisson's ratio	
Matrix (Iso_02)	Isotropic	No restriction in Poisson's ratio	E(Inclusion) > E(Matrix)
Inclusion (Iso_02)	Isotropic	No restriction in Poisson's ratio	
Matrix (Iso_03)	Isotropic	$\nu = 1/3$	E(Inclusion) > E(Matrix)
Inclusion (Iso_03)	Isotropic	$\nu = 1/3$	
Matrix (Iso_04)	Isotropic	$\nu = 1/3$	E(Inclusion) > E(Matrix)
Inclusion (Iso_04)	Isotropic	$\nu = 1/3$; E(Iso_04) > E(Iso_03)	
Matrix (Iso_05)	Isotropic	$\nu = 1/3$	E(Inclusion) > E(Matrix)
Inclusion (Iso_05)	Isotropic	$\nu = 1/3$; E(Iso_05) > E(Iso_04)	
Matrix (Iso_06)	Isotropic	No restriction in Poisson's ratio	E(Inclusion) < E(Matrix)
Inclusion (Iso_06)	Isotropic	No restriction in Poisson's ratio	
Matrix (Iso_07)	Isotropic	$\nu = 1/3$	E(Inclusion) < E(Matrix)
Inclusion (Iso_07)	Isotropic	$\nu = 1/3$	
Matrix (Iso_08)	Isotropic	$\nu = 1/3$	E(Inclusion) < E(Matrix)
Inclusion (Iso_08)	Isotropic	$\nu = 1/3$; E(Iso_08) > E(Iso_07)	
Matrix (Ort_01)	Isotropic	No restriction in Poisson's ratio	
Inclusion (Ort_01)	Orthotropic	$c_{11} > c_{22} = c_{33}$	
Matrix (Ort_02)	Isotropic	No restriction in Poisson's ratio	
Inclusion (Ort_02)	Orthotropic	$c_{11} > c_{22} = c_{33}$; c_{11}(Ort_02) > c_{11}(Ort_01)	
Matrix (Ort_03)	Isotropic	No restriction in Poisson's ratio	
Inclusion (Ort_03)	Orthotropic	$c_{11} > c_{22} = c_{33}$; c_{11}(Ort_03) > c_{11}(Ort_02)	
Matrix (Ort_04)	Isotropic	No restriction in Poisson's ratio	
Inclusion (Ort_04)	Orthotropic	$c_{11} > c_{22} = c_{33}$; c_{11}(Ort_04) < c_{11}(Ort_01)	
Matrix (Ort_05)	Isotropic	No restriction in Poisson's ratio	
Inclusion (Ort_05)	Orthotropic	$c_{11} > c_{22} = c_{33}$; c_{11}(Ort_04) < c_{11}(Ort_05) < c_{11}(Ort_01)	
Matrix (Ort_06)	Isotropic	No restriction in Poisson's ratio	
Inclusion (Ort_06)	Orthotropic	μ (Matrix) > c_{55} (Inclusion) > c_{66} (Inclusion) > c_{44} (Inclusion)	
Matrix (Ort_07)	Isotropic	No restriction in Poisson's ratio	
Inclusion (Ort_07)	Orthotropic	c_{55} (Inclusion) > c_{66} (Inclusion) > c_{44} (Inclusion) > μ (Matrix)	

3.1. Single Spherical Inclusion Problems under Uniform Remote Tensile Loading

3.1.1. VIEM Formulation Applied to Isotropic Inclusion Problems

The displacements in the volume integral Equation (2) for isotropic spherical, prolate and oblate spheroidal inclusions can be expressed in the form:

$$\begin{aligned} u_1(x) = \; & u_1^o(x) - \int_V \{\delta(\lambda+2\mu)g^1_{1,1}u_{1,1} + \delta\lambda(g^1_{1,1}u_{2,2} + g^1_{2,2}u_{1,1}) + \delta\lambda(g^1_{1,1}u_{3,3} + g^1_{3,3}u_{1,1}) \\ & + \delta(\lambda+2\mu)g^1_{2,2}u_{2,2} + \delta\lambda(g^1_{2,2}u_{3,3} + g^1_{3,3}u_{2,2}) + \delta(\lambda+2\mu)g^1_{3,3}u_{3,3} \\ & + \delta\mu[g^1_{2,3}(u_{2,3}+u_{3,2}) + g^1_{3,2}(u_{2,3}+u_{3,2})] \\ & + \delta\mu[g^1_{1,3}(u_{1,3}+u_{3,1}) + g^1_{3,1}(u_{1,3}+u_{3,1})] \\ & + \delta\mu[g^1_{1,2}(u_{1,2}+u_{2,1}) + g^1_{2,1}(u_{1,2}+u_{2,1})]\}d\xi_1 d\xi_2 d\xi_3 \end{aligned} \tag{3}$$

$$\begin{aligned} u_2(x) = \; & u_2^o(x) - \int_V \{\delta(\lambda+2\mu)g^2_{1,1}u_{1,1} + \delta\lambda(g^2_{1,1}u_{2,2} + g^2_{2,2}u_{1,1}) + \delta\lambda(g^2_{1,1}u_{3,3} + g^2_{3,3}u_{1,1}) \\ & + \delta(\lambda+2\mu)g^2_{2,2}u_{2,2} + \delta\lambda(g^2_{2,2}u_{3,3} + g^2_{3,3}u_{2,2}) + \delta(\lambda+2\mu)g^2_{3,3}u_{3,3} \\ & + \delta\mu[g^2_{2,3}(u_{2,3}+u_{3,2}) + g^2_{3,2}(u_{2,3}+u_{3,2})] \\ & + \delta\mu[g^2_{1,3}(u_{1,3}+u_{3,1}) + g^2_{3,1}(u_{1,3}+u_{3,1})] \\ & + \delta\mu[g^2_{1,2}(u_{1,2}+u_{2,1}) + g^2_{2,1}(u_{1,2}+u_{2,1})]\}d\xi_1 d\xi_2 d\xi_3 \end{aligned} \tag{4}$$

$$\begin{aligned} u_3(x) = \; & u_3^o(x) - \int_V \{\delta(\lambda+2\mu)g^3_{1,1}u_{1,1} + \delta\lambda(g^3_{1,1}u_{2,2} + g^3_{2,2}u_{1,1}) + \delta\lambda(g^3_{1,1}u_{3,3} + g^3_{3,3}u_{1,1}) \\ & + \delta(\lambda+2\mu)g^3_{2,2}u_{2,2} + \delta\lambda(g^3_{2,2}u_{3,3} + g^3_{3,3}u_{2,2}) + \delta(\lambda+2\mu)g^3_{3,3}u_{3,3} \\ & + \delta\mu[g^3_{2,3}(u_{2,3}+u_{3,2}) + g^3_{3,2}(u_{2,3}+u_{3,2})] \\ & + \delta\mu[g^3_{1,3}(u_{1,3}+u_{3,1}) + g^3_{3,1}(u_{1,3}+u_{3,1})] \\ & + \delta\mu[g^3_{1,2}(u_{1,2}+u_{2,1}) + g^3_{2,1}(u_{1,2}+u_{2,1})]\}d\xi_1 d\xi_2 d\xi_3 \end{aligned} \tag{5}$$

where $u_1(x)$, $u_2(x)$ and $u_3(x)$ are the three-dimensional displacements, $\delta c_{\alpha\beta} = c_{\alpha\beta}(1) - c_{\alpha\beta}(2)$ (α, $\beta = 1, 6$), where $c_{\alpha\beta}(1)$ represents the elastic stiffness constants of the isotropic inclusions, while $c_{\alpha\beta}(2)$ denotes those for the isotropic matrix material: $\delta c_{11} = \delta c_{22} = \delta c_{33} = (\lambda_1 + 2\mu_1) - (\lambda_2 + 2\mu_2)$, $\delta c_{12} = \delta c_{13} = \delta c_{23} = \lambda_1 - \lambda_2$ and $\delta c_{44} = \delta c_{55} = \delta c_{66} = \mu_1 - \mu_2$.

In Equations (3)–(5), $g_i{}^m(\boldsymbol{\xi},\boldsymbol{x})$ is the Green's function for the infinite isotropic matrix material and is stated by Banerjee [26] and Pao and Varatharajulu [27] as:

$$\begin{aligned} g^1_1 &= \tfrac{1}{16\pi(1-\nu)\mu r}\left[\tfrac{(x_1-\xi_1)^2}{r^2} + (3-4\nu)\right] \\ g^1_2 = g^2_1 &= \tfrac{1}{16\pi(1-\nu)\mu r}\left[\tfrac{(x_1-\xi_1)(x_2-\xi_2)}{r^2}\right] \\ g^1_3 = g^3_1 &= \tfrac{1}{16\pi(1-\nu)\mu r}\left[\tfrac{(x_1-\xi_1)(x_3-\xi_3)}{r^2}\right] \\ g^2_2 &= \tfrac{1}{16\pi(1-\nu)\mu r}\left[\tfrac{(x_2-\xi_2)^2}{r^2} + (3-4\nu)\right] \\ g^2_3 = g^3_2 &= \tfrac{1}{16\pi(1-\nu)\mu r}\left[\tfrac{(x_2-\xi_2)(x_3-\xi_3)}{r^2}\right] \\ g^3_3 &= \tfrac{1}{16\pi(1-\nu)\mu r}\left[\tfrac{(x_3-\xi_3)^2}{r^2} + (3-4\nu)\right] \end{aligned} \tag{6}$$

where $r = |x - \xi| = \sqrt{(x_1-\xi_1)^2 + (x_2-\xi_2)^2 + (x_3-\xi_3)^2}$, ν is Poisson's ratio and μ is the shear modulus for the infinite isotropic matrix material.

3.1.2. VIEM Formulation Applied to Orthotropic Inclusion Problems

Let the coordinate axes $x_1(x)$, $x_2(y)$ and $x_3(z)$ be taken parallel to the symmetry axes of the orthotropic material, and c_{11}, c_{12}, c_{13}, c_{22}, c_{23}, c_{33}, c_{44}, c_{55} and c_{66} denote the elastic constants. The displacements in Equation (2) for orthotropic spherical, prolate and oblate spheroidal inclusions can be expressed in the form:

$$\begin{aligned} u_1(x) = \; & u_1^o(x) - \int_V \{\delta c_{11}g^1_{1,1}u_{1,1} + \delta c_{12}(g^1_{1,1}u_{2,2} + g^1_{2,2}u_{1,1}) + \delta c_{13}(g^1_{1,1}u_{3,3} + g^1_{3,3}u_{1,1}) \\ & + \delta c_{22}g^1_{2,2}u_{2,2} + \delta c_{23}(g^1_{2,2}u_{3,3} + g^1_{3,3}u_{2,2}) + \delta c_{33}g^1_{3,3}u_{3,3} \\ & + \delta c_{44}[g^1_{2,3}(u_{2,3}+u_{3,2}) + g^1_{3,2}(u_{2,3}+u_{3,2})] \\ & + \delta c_{55}[g^1_{1,3}(u_{1,3}+u_{3,1}) + g^1_{3,1}(u_{1,3}+u_{3,1})] \\ & + \delta c_{66}[g^1_{1,2}(u_{1,2}+u_{2,1}) + g^1_{2,1}(u_{1,2}+u_{2,1})]\}d\xi_1 d\xi_2 d\xi_3 \end{aligned} \tag{7}$$

$$\begin{aligned} u_2(x) = \; & u_2^o(x) - \int_V \{\delta c_{11} g_{1,1}^2 u_{1,1} + \delta c_{12}(g_{1,1}^2 u_{2,2} + g_{2,2}^2 u_{1,1}) + \delta c_{13}(g_{1,1}^2 u_{3,3} + g_{3,3}^2 u_{1,1}) \\ & + \delta c_{22} g_{2,2}^2 u_{2,2} + \delta c_{23}(g_{2,2}^2 u_{3,3} + g_{3,3}^2 u_{2,2}) + \delta c_{33} g_{3,3}^2 u_{3,3} \\ & + \delta c_{44}[g_{2,3}^2(u_{2,3} + u_{3,2}) + g_{3,2}^2(u_{2,3} + u_{3,2})] \\ & + \delta c_{55}[g_{1,3}^2(u_{1,3} + u_{3,1}) + g_{3,1}^2(u_{1,3} + u_{3,1})] \\ & + \delta c_{66}[g_{1,2}^2(u_{1,2} + u_{2,1}) + g_{2,1}^2(u_{1,2} + u_{2,1})]\} d\xi_1 d\xi_2 d\xi_3 \end{aligned} \tag{8}$$

$$\begin{aligned} u_3(x) = \; & u_3^o(x) - \int_V \{\delta c_{11} g_{1,1}^3 u_{1,1} + \delta c_{12}(g_{1,1}^3 u_{2,2} + g_{2,2}^3 u_{1,1}) + \delta c_{13}(g_{1,1}^3 u_{3,3} + g_{3,3}^3 u_{1,1}) \\ & + \delta c_{22} g_{2,2}^3 u_{2,2} + \delta c_{23}(g_{2,2}^3 u_{3,3} + g_{3,3}^3 u_{2,2}) + \delta c_{33} g_{3,3}^3 u_{3,3} \\ & + \delta c_{44}[g_{2,3}^3(u_{2,3} + u_{3,2}) + g_{3,2}^3(u_{2,3} + u_{3,2})] \\ & + \delta c_{55}[g_{1,3}^3(u_{1,3} + u_{3,1}) + g_{3,1}^3(u_{1,3} + u_{3,1})] \\ & + \delta c_{66}[g_{1,2}^3(u_{1,2} + u_{2,1}) + g_{2,1}^3(u_{1,2} + u_{2,1})]\} d\xi_1 d\xi_2 d\xi_3 \end{aligned} \tag{9}$$

where $u_1(x)$, $u_2(x)$ and $u_3(x)$ are the three-dimensional displacements, $\delta c_{\alpha\beta} = c_{\alpha\beta}(1) - c_{\alpha\beta}(2)$ (α, β = 1, 6), where = $c_{\alpha\beta}(1)$ represents the elastic stiffness constants of the orthotropic inclusions, while $c_{\alpha\beta}(2)$ denotes those for the isotropic matrix material: $\delta c_{11} = c_{11} - (\lambda_2 + 2\mu_2)$, $\delta c_{22} = c_{22} - (\lambda_2 + 2\mu_2)$, $\delta c_{33} = c_{33} - (\lambda_2 + 2\mu_2)$, $\delta c_{12} = c_{12} - \lambda_2$, $\delta c_{13} = c_{13} - \lambda_2$, $\delta c_{23} = c_{23} - \lambda_2$ and $\delta c_{44} = c_{44} - \mu_2$, $\delta c_{55} = c_{55} - \mu_2$, $\delta c_{66} = c_{66} - \mu_2$.

In Equations (7)–(9), ${g_i}^m(\boldsymbol{\xi},\boldsymbol{x})$ is the Green's function for the infinite isotropic matrix material and is stated in Equation (6). Thus, the VIEM does not require the use of the Green's function for the orthotropic material of the inclusion. In general, Green's function for an anisotropic material is much more complex than that of an isotropic material [28]. Furthermore, a closed form solution of the generalized Green's function for an anisotropic material is not available in the literature.

In contrast, in the BEM, Green's functions for both the isotropic matrix and the anisotropic inclusions must be specified in the formulation. In particular, special emphasis is placed on the fact that Green's function for the anisotropic material of the inclusions is not required in the VIEM.

3.1.3. Numerical Formulations in the VIEM

The integrands in Equations (3)–(8) contain singularities with different orders due to the singular characteristics of the Green's function at $x = \xi$ (i.e., $r = 0$). Thus, evaluation of the singular integrals requires special attention. In general, ${g_i}^m(\boldsymbol{\xi},\boldsymbol{x})$ behaves as $1/r$, while its derivatives behave as $1/r^2$ as $r \to 0$. It should be noted that only ${g_i}^m(\boldsymbol{\xi},\boldsymbol{x})$ for the isotropic matrix and its derivatives are required in the VIEM. Furthermore, in the BEM, the Green's function for anisotropic inclusions and their derivatives must also be specified. As a result, this may be a critical drawback to the BEM when solving multiple anisotropic inclusion problems.

In contrast to the BEM, the singularities in the VIEM are integrable (weak). Thus, we have decided to utilize the direct integration scheme stated by Li et al. [29]. Finally, after suitable adjustments, we have succeeded in addressing these weak singular integrands in the volume integral equation formulations.

A comprehensive elaboration for the accurate evaluation of singular integrals using the tetrahedron polar co-ordinates shown in [29] was presented in [17].

3.1.4. A Single Isotropic Spherical Inclusion

In order to examine the accuracy of the numerical results using the VIEM, the numerical results using the VIEM for a single isotropic spherical inclusion were first compared to the analytical solutions [21,30]. We considered a single isotropic spherical inclusion with a radius of 6 mm in an infinite isotropic matrix subject to uniform remote tensile loading, ${\sigma_{xx}}^o$, as shown in Figure 4a. It should be noted that the length of the radius can be arbitrarily chosen. In Figure 7, standard 20-node quadratic hexahedral elements were used in the discretization [31]. The number of hexahedral elements, 7560, was determined based on a convergence test. For the seven different material properties (Iso_2, Iso_03, Iso_04, Iso_05, Iso_06, Iso_07 and Iso_08) in Table 2, a comparison was made between the

numerical results using the volume integral equation method (VIEM) and the analytical solutions. As shown in Table 5, there was no restriction to Poisson's ratio in the inclusions and matrices of Iso_02 and Iso_06. However, Poison's ratio was 1/3 in both the inclusion and matrix of Iso_03, Iso_04, Iso_05, Iso_07 and Iso_08. Furthermore, for Iso_02, Iso_03, Iso_04 and Iso_05, Young's modulus (E) in the isotropic inclusion was greater than that in the isotropic matrix. For Iso_06, Iso_07 and Iso_08, Young's modulus (E) in the isotropic matrix was greater than that in the isotropic inclusion. Thus, seven material properties representing a diversity of materials were chosen. Excellent agreement was found between the analytical and numerical solutions using the VIEM for the seven different materials considered. It should be noted that the VIEM results represent average values of the normalized stresses in all the nodes of the VIEM model in Figure 7. It should also be noted that the normalized tensile stress ($\sigma_{xx}/\sigma^{o}{}_{xx}$) inside the isotropic spherical inclusions was found to be constant [1,30]. Tables 6–8 show that the percentage differences for the two sets of results are less than 0.1% in seven cases. Figure 8 shows numerical solution by the volume integral equation method for the normalized tensile stress ($\sigma_{xx}/\sigma^{o}{}_{xx}$) along (i) the x–axis inside (-6 mm $\leq$ x $\leq$ 6 mm) and (ii) the circumferential direction ($0^\circ \leq \theta$ (see Figure 7) $\leq 360^\circ$) of the isotropic spherical inclusions with a radius of 6 mm under uniform remote tensile loading.

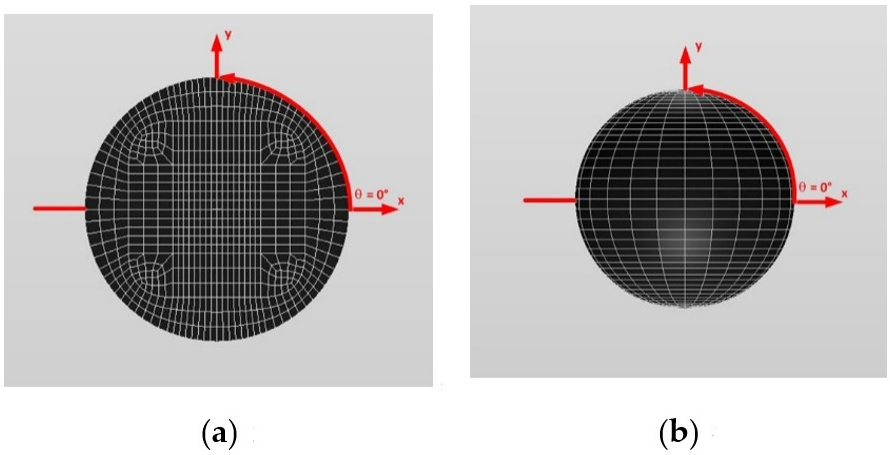

(**a**) (**b**)

Figure 7. A typical discretized spherical model in the volume integral equation method (VIEM). (**a**) An inside view of a spherical model. (**b**) A spherical model.

Table 6. Normalized tensile stress component ($\sigma_{xx}/\sigma^{o}{}_{xx}$) within the isotropic spherical inclusion due to uniform remote tensile loading ($\sigma^{o}{}_{xx}$).

Material	VIEM (Average)	Analytical Solution	Error (%)
Iso_01	1.5800	-	-
Iso_02	1.2823	1.2822	0.0078

Table 7. Normalized tensile stress component ($\sigma_{xx}/\sigma^{o}{}_{xx}$) within the isotropic spherical inclusion due to uniform remote tensile loading ($\sigma^{o}{}_{xx}$).

Material	VIEM (Average)	Analytical Solution	Error (%)
Iso_03	1.3090	1.3091	0.0076
Iso_04	1.6171	1.6173	0.0124
Iso_05	1.7582	1.7582	0.0

Table 8. Normalized tensile stress component ($\sigma_{xx}/\sigma^{o}_{xx}$) within the isotropic spherical inclusion due to uniform remote tensile loading (σ^{o}_{xx}).

Material	VIEM (Average)	Analytical Solution	Error (%)
Iso_06	0.7200	0.7200	0.0
Iso_07	0.3557	0.3556	0.0281
Iso_08	0.8343	0.8343	0.0

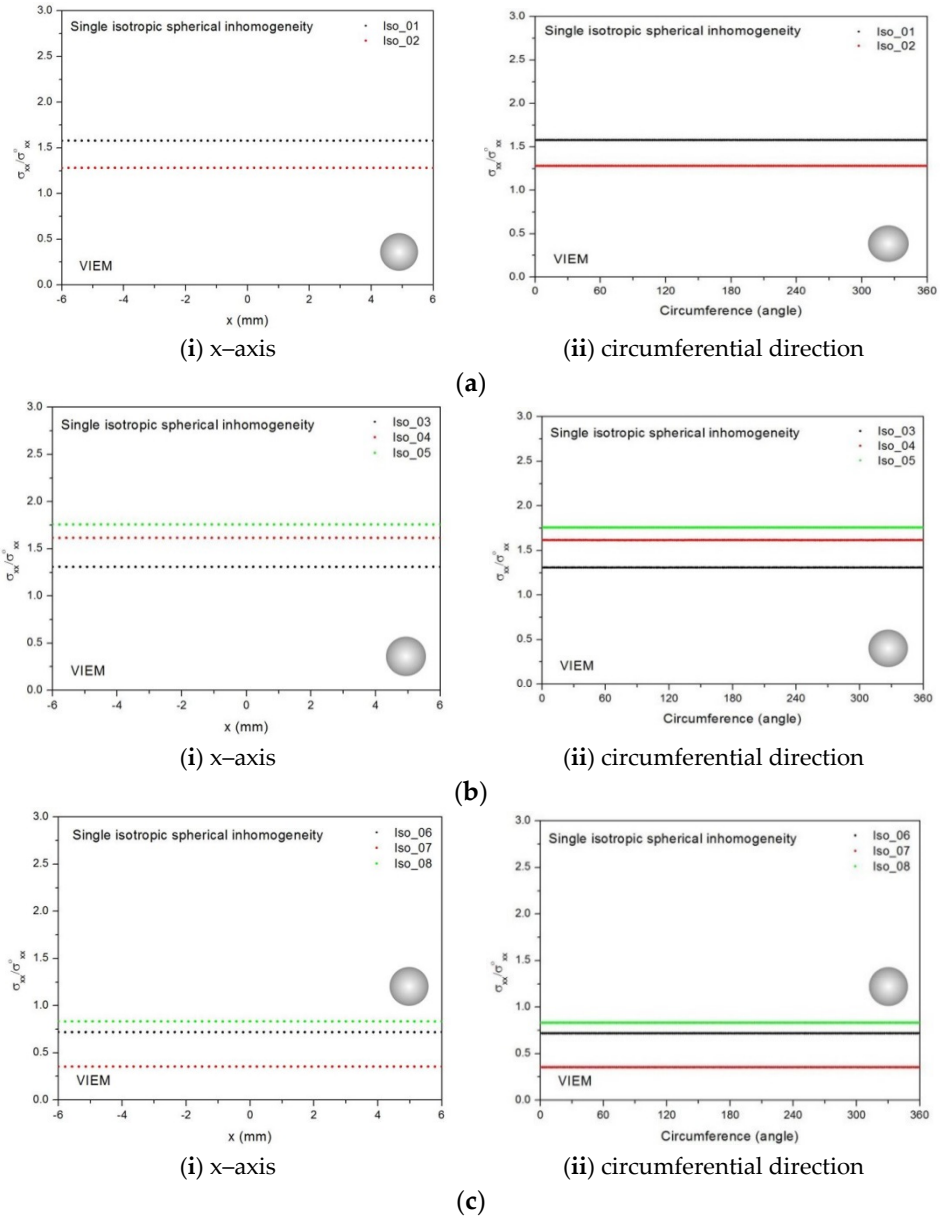

(**i**) x–axis (**ii**) circumferential direction

(**a**)

(**i**) x–axis (**ii**) circumferential direction

(**b**)

(**i**) x–axis (**ii**) circumferential direction

(**c**)

Figure 8. VIEM results for the normalized tensile stress component ($\sigma_{xx}/\sigma^{o}_{xx}$) along (**i**) the x–axis inside and (**ii**) the circumferential direction of the isotropic spherical inclusions with a radius of 6 mm under uniform remote tensile loading. (**a**) Iso_01 and Iso_02. (**b**) Iso_03, Iso_04 and Iso_05. (**c**) Iso_06, Iso_07 and Iso_08.

In most references, the numerical results for this problem were obtained in one direction. Thus, in order to show the VIEM results more thoroughly, the normalized tensile stress ($\sigma_{xx}/\sigma^{o}_{xx}$) using the VIEM was presented along (i) the x–axis inside (-6 mm $\leq$ x $\leq$ 6 mm) and (ii) the circumferential direction ($0^\circ \leq \theta$ (see Figure 7) $\leq 360^\circ$) of the isotropic spherical

inclusions. It was determined in Figure 8 that the normalized tensile stress ($\sigma_{xx}/\sigma^{o}{}_{xx}$) inside the isotropic spherical inclusions is constant in all directions considered.

3.1.5. A Single Orthotropic Spherical Inclusion

In order to show the advantages of the volume integral equation method (VIEM), we consider a single orthotropic spherical inclusion with a radius of 6 mm in an infinite isotropic matrix subject to uniform remote tensile loading, $\sigma^{o}{}_{xx}$, as shown in Figure 4a. It should be noted that the length of the radius can be arbitrarily chosen. In Figure 7, standard 20-node quadratic hexahedral elements were used in the discretization [31]. The number of hexahedral elements was 7560, determined based on a convergence test. For this problem, in comparison to the boundary element method (BEM), since the VIEM is not sensitive to the anisotropy of the inclusions, it does not require use of the Green's function for the anisotropic inclusions. Moreover, as opposed to the standard FEM, where it is necessary to discretize the full domain, the orthotropic inclusion only needs to be discretized in the VIEM.

Five different material properties (Ort_1, Ort_02, Ort_03, Ort_04 and Ort_05) in Table 5 were used in the numerical calculation. As shown in Table 5, it was assumed that $c_{11} > c_{22} = c_{33}$ for five orthotropic inclusions. Additionally, c_{11} of the inclusion in Ort_03 > c_{11} of the inclusion in Ort_02 > c_{11} of the inclusion in Ort_01. Furthermore, c_{11} of the inclusion in Ort_04 < c_{11} of the inclusion in Ort_05 < c_{11} of the inclusion in Ort_01. Thus, five material properties representing a diversity of materials were chosen. It should be noted that the VIEM results represent average values of the normalized stresses in all the nodes of the VIEM model in Figure 7. Moreover, the normalized tensile stress ($\sigma_{xx}/\sigma^{o}{}_{xx}$) inside the orthotropic spherical inclusions was found to be constant [1,30]. Table 9 shows the numerical solution by the volume integral equation method for the normalized tensile stress ($\sigma_{xx}/\sigma^{o}{}_{xx}$) inside the orthotropic spherical inclusions. For the inclusions in Ort_01, Ort_02 and Ort_03, the normalized tensile stress ($\sigma_{xx}/\sigma^{o}{}_{xx}$) inside the inclusion was greater than 1.0. However, for the inclusions in Ort_04 and Ort_05, the normalized tensile stress ($\sigma_{xx}/\sigma^{o}{}_{xx}$) inside the inclusion was less than 1.0. Figure 9 shows the numerical solution by the volume integral equation method for the normalized tensile stress ($\sigma_{xx}/\sigma^{o}{}_{xx}$) along (left) the x–axis inside (-6 mm $\leq x \leq 6$ mm) and (right) the circumferential direction ($0^{\circ} \leq \theta$ (see Figure 7) $\leq 360^{\circ}$) of the orthotropic spherical inclusions with a radius of 6 mm under uniform remote tensile loading. It was determined in Figure 9 that the normalized tensile stress ($\sigma_{xx}/\sigma^{o}{}_{xx}$) inside the orthotropic spherical inclusions is constant in all directions considered.

Table 9. Normalized tensile stress component ($\sigma_{xx}/\sigma^{o}{}_{xx}$) within the orthotropic spherical inclusion due to uniform remote tensile loading ($\sigma^{o}{}_{xx}$).

Material	VIEM (Average)
Ort_01	1.1520
Ort_02	1.4536
Ort_03	1.5910
Ort_04	0.5836
Ort_05	0.8129

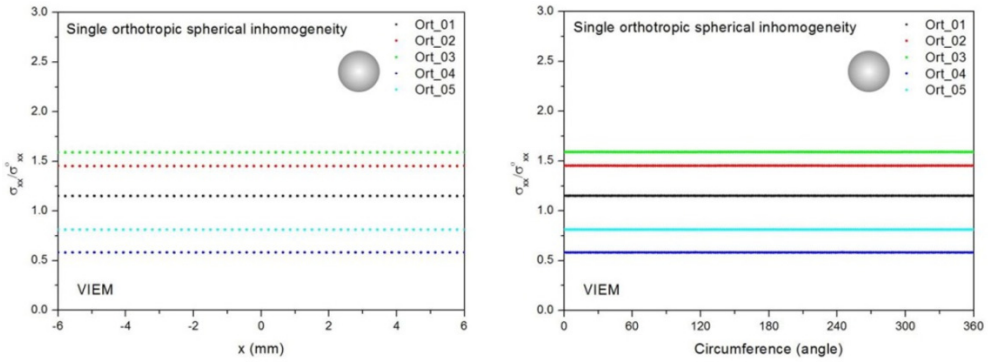

Figure 9. VIEM results for the normalized tensile stress component ($\sigma_{xx}/\sigma^{o}_{xx}$) along (**left**) the x–axis inside and (**right**) the circumferential direction of the orthotropic spherical inclusions (Ort_01, Ort_02, Ort_03, Ort_04 and Ort_05) with a radius of 6 mm under uniform remote tensile loading.

3.2. A Single Spheroidal Inclusion Problem under Uniform Remote Tensile Loading

In order to introduce the VIEM as a versatile numerical method, we considered a single isotropic/orthotropic spheroidal inclusion in an infinite isotropic matrix subject to uniform remote tensile loading, σ^{o}_{xx}, as shown in Figure 4b,c. Figure 5 shows an orientation of the spheroidal inclusion.

3.2.1. A Single Isotropic Prolate Spheroidal Inclusion

Two different prolate spheroidal inclusions are considered: (a) a/b = c/b = 0.5, where b = 6 mm, and (b) a/b = c/b = 0.75, where b = 6 mm (see Figure 5). It should be noted that the length of b (=6 mm) can be arbitrarily chosen.

Figures 10 and 11 show a typical discretized model for the single (a) prolate spheroidal inclusion (a/b = c/b = 0.5 where b = 6 mm) and (b) prolate spheroidal inclusion (a/b = c/b = 0.75 where b = 6 mm) used in the VIEM [31], respectively. A total of 7560 standard 20-node quadratic hexahedral elements were used for the single prolate spheroidal inclusion in Figures 10 and 11. The number of elements, 7560, was determined based on a convergence test.

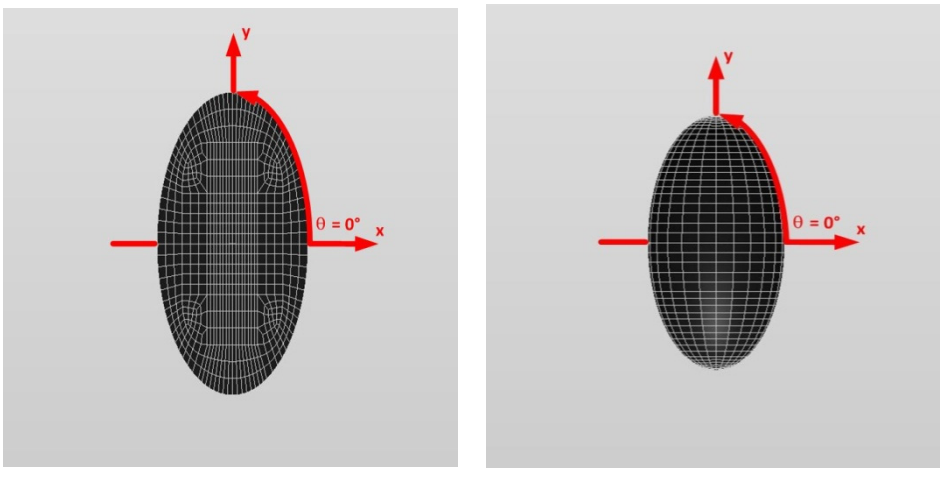

(**a**) (**b**)

Figure 10. A typical discretized prolate spheroidal model (a/b = c/b = 0.5) in the volume integral equation method (VIEM). (**a**) An inside view of a prolate spheroidal model. (**b**) A prolate spheroidal model.

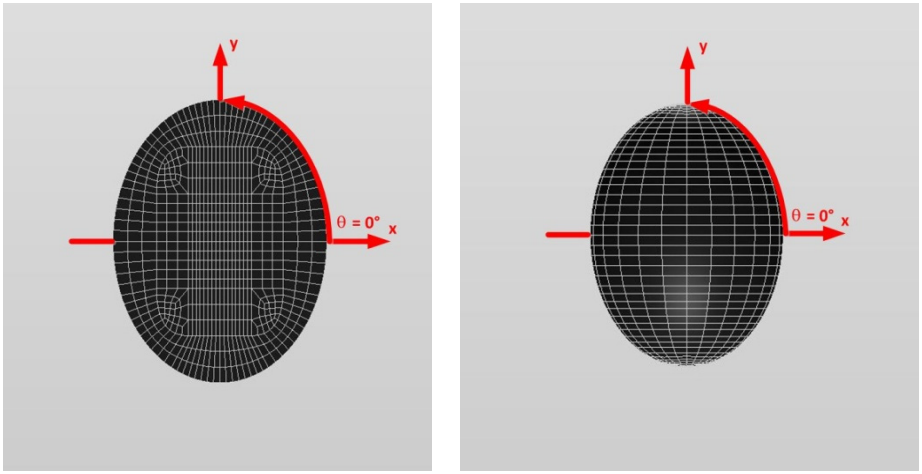

(**a**) (**b**)

Figure 11. A typical discretized prolate spheroidal model (a/b = c/b = 0.75) in the volume integral equation method (VIEM). (**a**) An inside view of a prolate spheroidal model. (**b**) A prolate spheroidal model.

Eight different isotropic inclusions (from Iso_01 to Iso_08) in Table 2 were used in the numerical calculation. It should be noted that the VIEM results represent average values of the normalized stresses in all the nodes of the VIEM model in Figures 10 and 11. It should also be noted that the normalized tensile stress ($\sigma_{xx}/\sigma^{o}_{xx}$) inside the isotropic prolate spheroidal inclusions was found to be constant [1,30].

Tables 10–12 show numerical solutions by the volume integral equation method for the normalized tensile stress ($\sigma_{xx}/\sigma^{o}_{xx}$) inside the isotropic prolate spheroidal inclusions. For the inclusions in Iso_01, Iso_02, Iso_03, Iso_04 and Iso_05, the normalized tensile stress ($\sigma_{xx}/\sigma^{o}_{xx}$) inside the inclusion was greater than 1.0. However, for the inclusions in Iso_06, Iso_07 and Iso_08, the normalized tensile stress ($\sigma_{xx}/\sigma^{o}_{xx}$) inside the inclusion was less than 1.0. Figure 12 shows numerical solutions by the volume integral equation method for the normalized tensile stress ($\sigma_{xx}/\sigma^{o}_{xx}$) along (i) the x–axis inside (-3 mm $\leq$ x $\leq$ 3 mm) and (ii) the circumferential direction ($0^\circ \leq \theta$ (see Figure 10) $\leq 360^\circ$) of the isotropic prolate spheroidal inclusions (a/b = c/b = 0.5 where b = 6 mm) under uniform remote tensile loading. Figure 13 shows numerical solutions by the volume integral equation method for the normalized tensile stress ($\sigma_{xx}/\sigma^{o}_{xx}$) along (i) the x–axis inside (-4.5 mm $\leq$ x $\leq$ 4.5 mm) and (ii) the circumferential direction ($0^\circ \leq \theta$ (see Figure 11) $\leq 360^\circ$) of the isotropic prolate spheroidal inclusions (a/b = c/b = 0.75 where b = 6 mm) under uniform remote tensile loading. It was determined in Figures 12 and 13 that the normalized tensile stress ($\sigma_{xx}/\sigma^{o}_{xx}$) inside the isotropic prolate spheroidal inclusions is constant in all directions considered.

Table 10. Normalized tensile stress component ($\sigma_{xx}/\sigma^{o}_{xx}$) within the isotropic prolate spheroidal inclusion due to uniform remote tensile loading (σ^{o}_{xx}).

Material	VIEM (Average)	
	a/b = c/b = 0.5 (see Figure 5)	**a/b = c/b = 0.75 (see Figure 5)**
Iso_01	1.4268	1.5028
Iso_02	1.2177	1.2500

Table 11. Normalized tensile stress component ($\sigma_{xx}/\sigma^{o}{}_{xx}$) within the isotropic prolate spheroidal inclusion due to uniform remote tensile loading ($\sigma^{o}{}_{xx}$).

Material	VIEM (Average)	
	a/b = c/b = 0.5 (See Figure 5)	**a/b = c/b = 0.75 (See Figure 5)**
Iso_03	1.2374	1.2736
Iso_04	1.4502	1.5330
Iso_05	1.5409	1.6477

Table 12. Normalized tensile stress component ($\sigma_{xx}/\sigma^{o}{}_{xx}$) within the isotropic prolate spheroidal inclusion due to uniform remote tensile loading ($\sigma^{o}{}_{xx}$).

	VIEM (Average)	
	a/b = c/b = 0.5 (See Figure 5)	**a/b = c/b = 0.75 (See Figure 5)**
Iso_06	0.7613	0.7397
Iso_07	0.4042	0.3780
Iso_08	0.8610	0.8471

3.2.2. A Single Orthotropic Prolate Spheroidal Inclusion

Two different prolate spheroidal inclusions are considered: (a) a/b = c/b = 0.5, where b = 6 mm, and (b) a/b = c/b = 0.75, where b = 6 mm (see Figure 5). It should be noted that the length of b (=6 mm) can be arbitrarily chosen.

Figures 10 and 11 show a typical discretized model for the single (a) prolate spheroidal inclusion (a/b = c/b = 0.5 where b = 6 mm) and (b) prolate spheroidal inclusion (a/b = c/b = 0.75 where b = 6 mm) used in the VIEM [31], respectively. A total of 7560 standard 20-node quadratic hexahedral elements were used for the single prolate spheroidal inclusion in Figures 10 and 11. The number of elements, 7560, was determined based on a convergence test.

Five different orthotropic inclusions (from Ort_01 to Ort_05) in Table 3 were used in the numerical calculation. It should be noted that the VIEM results represent average values of the normalized stresses in all the nodes of the VIEM model in Figures 10 and 11. It should also be noted that the normalized tensile stress ($\sigma_{xx}/\sigma^{o}{}_{xx}$) inside the orthotropic prolate spheroidal inclusions was found to be constant [1,30]. Table 13 shows numerical solutions by the volume integral equation method for the normalized tensile stress ($\sigma_{xx}/\sigma^{o}{}_{xx}$) inside the orthotropic prolate spheroidal inclusions. For the inclusions in Ort_01, Ort_02 and Ort_03, the normalized tensile stress ($\sigma_{xx}/\sigma^{o}{}_{xx}$) inside the inclusion was greater than 1.0. However, for the inclusions in Ort_04 and Iso_05, the normalized tensile stress ($\sigma_{xx}/\sigma^{o}{}_{xx}$) inside the inclusion was less than 1.0. Figure 14 shows numerical solution by the volume integral equation method for the normalized tensile stress ($\sigma_{xx}/\sigma^{o}{}_{xx}$) along (left) the x–axis inside (-3 mm $\leq$ x $\leq$ 3 mm) and (right) the circumferential direction ($0^{\circ} \leq \theta$ (see Figure 10) $\leq 360^{\circ}$) of the orthotropic prolate spheroidal inclusions (a/b = c/b = 0.5 where b = 6 mm) under uniform remote tensile loading.

Table 13. Normalized Tensile Stress Component ($\sigma_{xx}/\sigma^{o}{}_{xx}$) within the Orthotropic Prolate Spheroidal Inclusion due to Uniform Remote Tensile Loading ($\sigma^{o}{}_{xx}$).

Material	VIEM (Average)	
	a/b = c/b = 0.5 (See Figure 5)	**a/b = c/b = 0.75 (See Figure 5)**
Ort_01	1.1244	1.1385
Ort_02	1.3546	1.4038
Ort_03	1.4519	1.5202
Ort_04	0.6246	0.6027
Ort_05	0.8375	0.8246

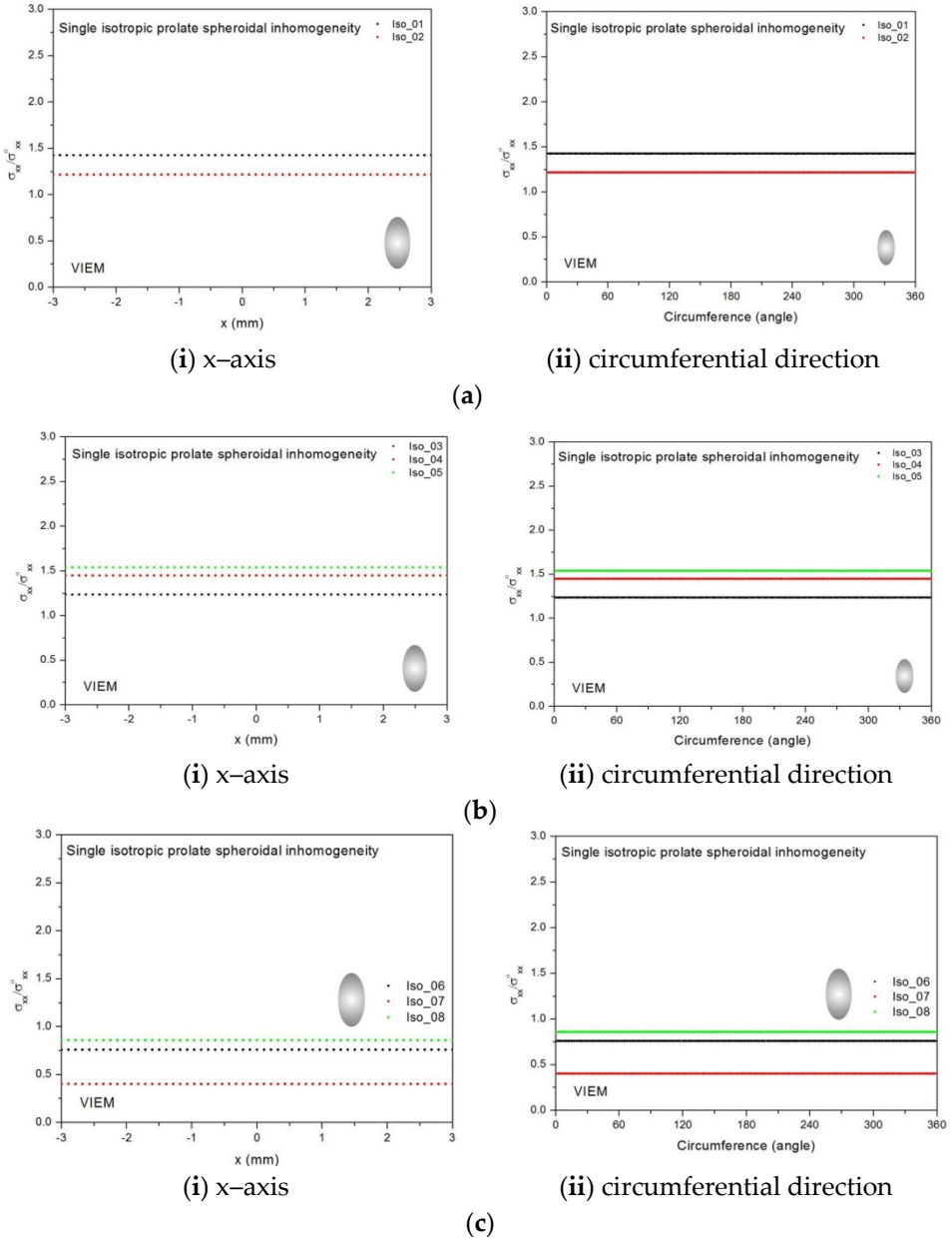

Figure 12. VIEM results for the normalized tensile stress component ($\sigma_{xx}/\sigma^{o}{}_{xx}$) along (**i**) the x–axis inside and (**ii**) the circumferential direction of the isotropic prolate spheroidal inclusions with a/b = c/b = 0.5 (b = 6 mm) under uniform remote tensile loading. (**a**) Iso_01 and Iso_02. (**b**) Iso_03, Iso_04 and Iso_05. (**c**) Iso_06, Iso_07 and Iso_08.

Figure 15 shows numerical solutions by the volume integral equation method for the normalized tensile stress ($\sigma_{xx}/\sigma^{o}{}_{xx}$) along (left) the x–axis inside (-4.5 mm $\leq$ x $\leq$ 4.5 mm) and (right) the circumferential direction ($0^\circ \leq \theta$ (see Figure 11) $\leq 360^\circ$) of the orthotropic prolate spheroidal inclusions (a/b = c/b = 0.75 where b = 6 mm) under uniform remote tensile loading. It was determined in Figures 14 and 15 that the normalized tensile stress ($\sigma_{xx}/\sigma^{o}{}_{xx}$) inside the orthotropic prolate spheroidal inclusions is constant in all directions considered.

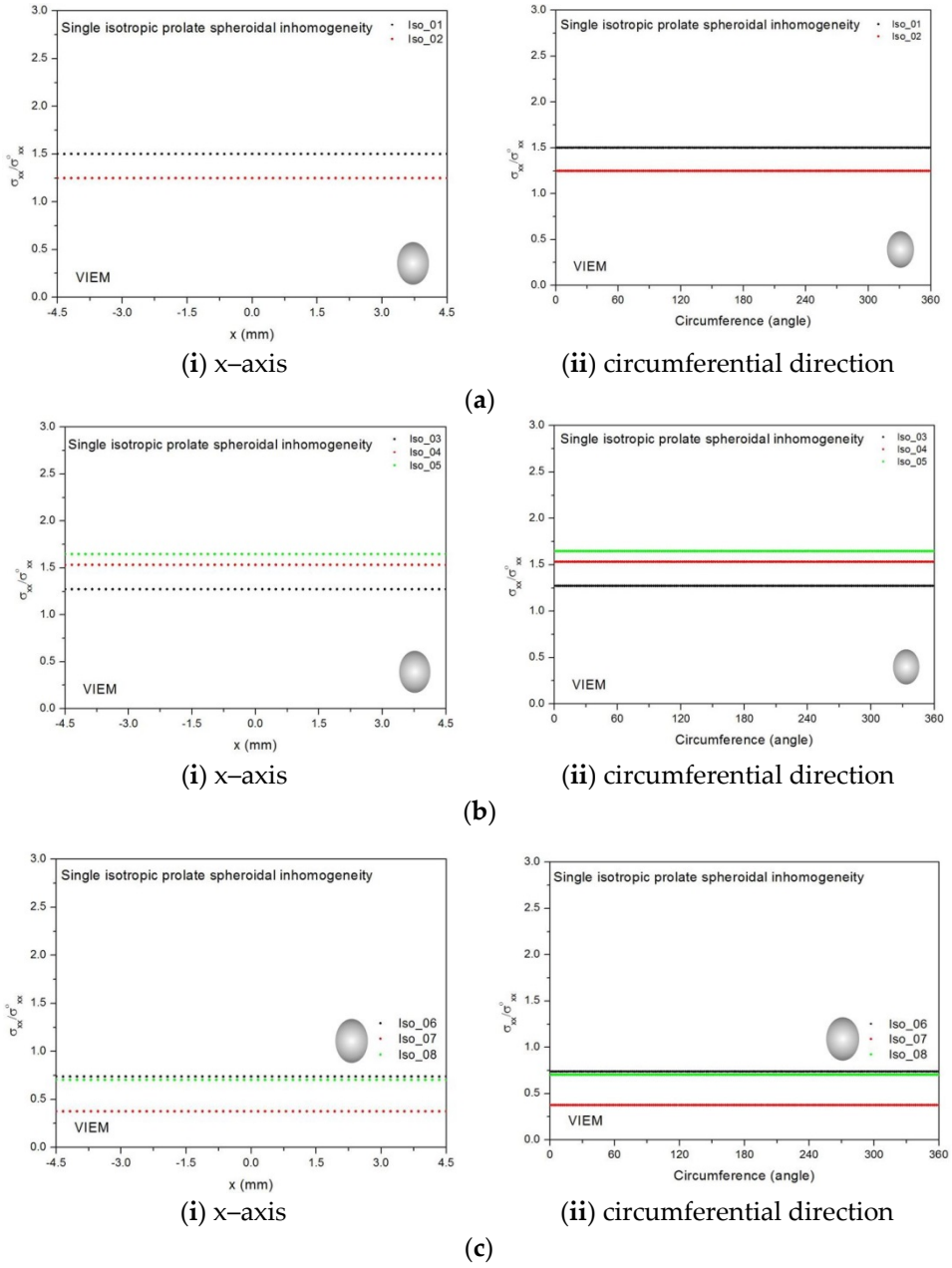

Figure 13. VIEM results for the normalized tensile stress component ($\sigma_{xx}/\sigma^{o}_{xx}$) along (**i**) the x–axis inside and (**ii**) the circumferential direction of the isotropic prolate spheroidal inclusions with a/b = c/b = 0.75 (b = 6 mm) under uniform remote tensile loading. (**a**) Iso_01 and Iso_02. (**b**) Iso_03, Iso_04 and Iso_05. (**c**) Iso_06, Iso_07 and Iso_08.

3.2.3. A Single Isotropic Oblate Spheroidal Inclusion

In this section, two different oblate spheroidal inclusions are considered: (a) b/a = c/a = 0.5, where a = 6 mm, and (b) b/a = c/a = 0.75, where a = 6 mm (see Figure 5). It should be noted that the length of a (=6 mm) can be arbitrarily chosen.

Figures 16 and 17 show a typical discretized model for the single (a) oblate spheroidal inclusion (b/a = c/a = 0.5 where a = 6 mm) and (b) oblate spheroidal inclusion (b/a = c/a = 0.75 where a = 6 mm) used in the VIEM [31], respectively. A total of 7560 standard 20-node quadratic hexahedral elements were used for the single oblate spheroidal inclusion in Figures 16 and 17. The number of elements, 7560, was determined based on a convergence test.

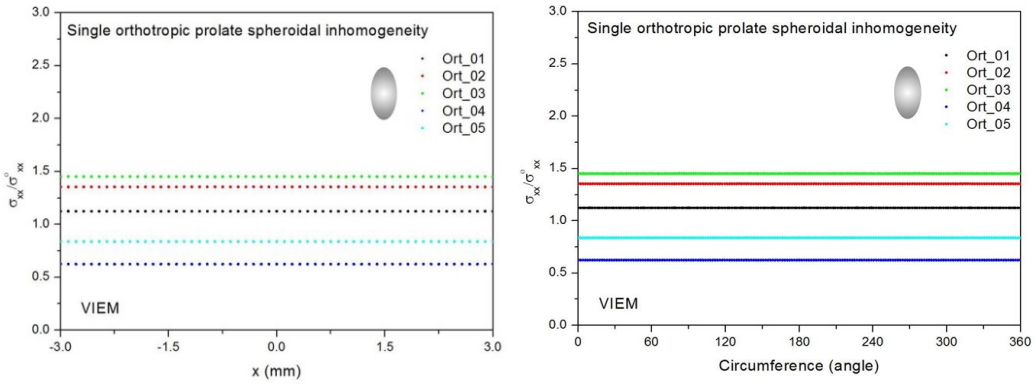

Figure 14. VIEM results for the normalized tensile stress component ($\sigma_{xx}/\sigma^{o}{}_{xx}$) along (**left**) the x–axis inside and (**right**) the circumferential direction of the orthotropic prolate spheroidal inclusions (Ort_01, Ort_02, Ort_03, Ort_04 and Ort_05) with a/b = c/b = 0.5 (b = 6 mm) under uniform remote tensile loading.

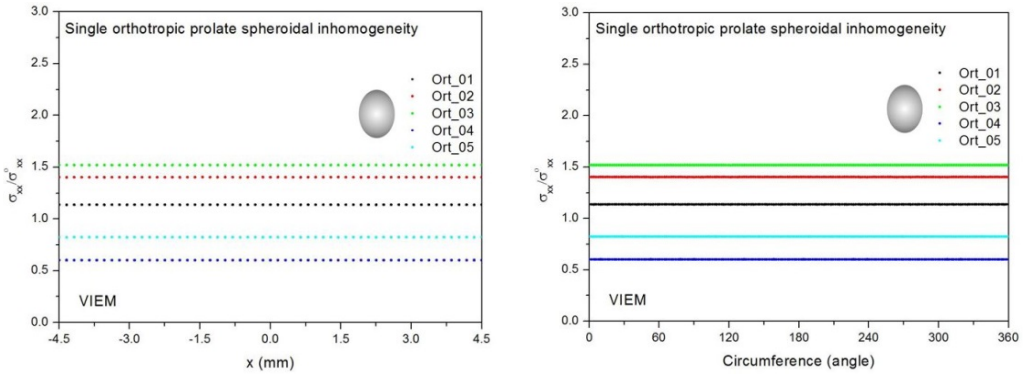

Figure 15. VIEM results for the normalized tensile stress component ($\sigma_{xx}/\sigma^{o}{}_{xx}$) along (**left**) the x–axis inside and (**right**) the circumferential direction of the orthotropic prolate spheroidal inclusions (Ort_01, Ort_02, Ort_03, Ort_04 and Ort_05) with a/b = c/b = 0.75 (b = 6 mm) under uniform remote tensile loading.

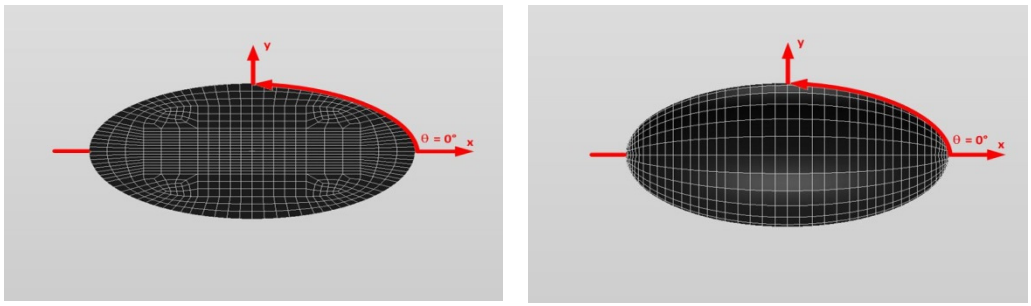

(**a**) (**b**)

Figure 16. A typical discretized oblate spheroidal model (b/a = c/a = 0.5) in the volume integral equation method (VIEM). (**a**) An inside view of an oblate spheroidal model. (**b**) An oblate spheroidal model.

Eight different isotropic inclusions (from Iso_01 to Iso_08) in Table 2 were used in the numerical calculation. It should be noted that the VIEM results represent average values of the normalized stresses in all the nodes of the VIEM model in Figures 16 and 17. It should also be noted that the normalized tensile stress ($\sigma_{xx}/\sigma^{o}{}_{xx}$) inside the isotropic oblate spheroidal inclusions was found to be constant [1,30]. Tables 14–16 show numerical solutions by the volume integral equation method for the normalized tensile stress

($\sigma_{xx}/\sigma^{o}{}_{xx}$) inside the isotropic oblate spheroidal inclusions. For the inclusions in Iso_01, Iso_02, Iso_03, Iso_04 and Iso_05, the normalized tensile stress ($\sigma_{xx}/\sigma^{o}{}_{xx}$) inside the inclusion was greater than 1.0. However, for the inclusions in Iso_06, Iso_07 and Iso_08, the normalized tensile stress ($\sigma_{xx}/\sigma^{o}{}_{xx}$) inside the inclusion was less than 1.0. Figure 18 shows numerical solutions by the volume integral equation method for the normalized tensile stress ($\sigma_{xx}/\sigma^{o}{}_{xx}$) along (i) the x–axis inside (-6 mm $\leq$ x $\leq$ 6 mm) and (ii) the circumferential direction ($0^\circ \leq \theta$ (see Figure 16) $\leq 360^\circ$) of the isotropic oblate spheroidal inclusions (b/a = c/a = 0.5 where a = 6 mm) under uniform remote tensile loading. Figure 19 shows numerical solutions by the volume integral equation method for the normalized tensile stress ($\sigma_{xx}/\sigma^{o}{}_{xx}$) along (i) the x–axis inside (-6 mm $\leq$ x $\leq$ 6 mm) and (ii) the circumferential direction ($0^\circ \leq \theta$ (see Figure 17) $\leq 360^\circ$) of the isotropic oblate spheroidal inclusions (b/a = c/a = 0.75 where a = 6 mm) under uniform remote tensile loading. It was determined in Figures 18 and 19 that the normalized tensile stress ($\sigma_{xx}/\sigma^{o}{}_{xx}$) inside the isotropic oblate spheroidal inclusions is constant in all directions considered.

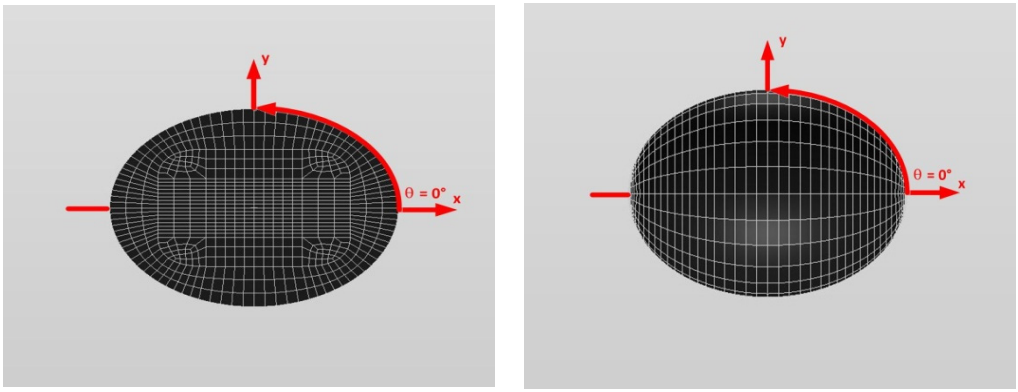

(**a**) (**b**)

Figure 17. A typical discretized oblate spheroidal model (b/a = c/a = 0.75) in the volume integral equation method (VIEM). (**a**) An inside view of an oblate spheroidal model. (**b**) An oblate spheroidal model.

Table 14. Normalized tensile stress component ($\sigma_{xx}/\sigma^{o}{}_{xx}$) within the isotropic oblate spheroidal inclusion due to uniform remote tensile loading ($\sigma^{o}{}_{xx}$).

Material	VIEM (Average)	
	b/a = c/a = 0.5 (See Figure 5)	**b/a = c/a = 0.75 (See Figure 5)**
Iso_01	2.1363	1.7790
Iso_02	1.4811	1.3599

Table 15. Normalized tensile stress component ($\sigma_{xx}/\sigma^{o}{}_{xx}$) within the isotropic oblate spheroidal inclusion due to uniform remote tensile loading ($\sigma^{o}{}_{xx}$).

Material	VIEM (Average)	
	b/a = c/a = 0.5 (See Figure 5)	**b/a = c/a = 0.75 (See Figure 5)**
Iso_03	1.5251	1.3938
Iso_04	2.2350	1.8413
Iso_05	2.6483	2.0556

3.2.4. A Single Orthotropic Oblate Spheroidal Inclusion

In this section, two different oblate spheroidal inclusions are considered: (a) b/a = c/a = 0.5, where a = 6 mm, and (b) b/a = c/a = 0.75, where a = 6 mm (see Figure 5). It should be noted that the length of a (=6 mm) can be arbitrarily chosen.

Table 16. Normalized tensile stress component ($\sigma_{xx}/\sigma^{o}{}_{xx}$) within the isotropic oblate spheroidal inclusion due to uniform remote tensile loading ($\sigma^{o}{}_{xx}$).

Material	VIEM (Average)	
	b/a = c/a = 0.5 (See Figure 5)	**b/a = c/a = 0.75 (See Figure 5)**
Iso_06	0.6310	0.6793
Iso_07	0.2695	0.3134
Iso_08	0.7733	0.8072

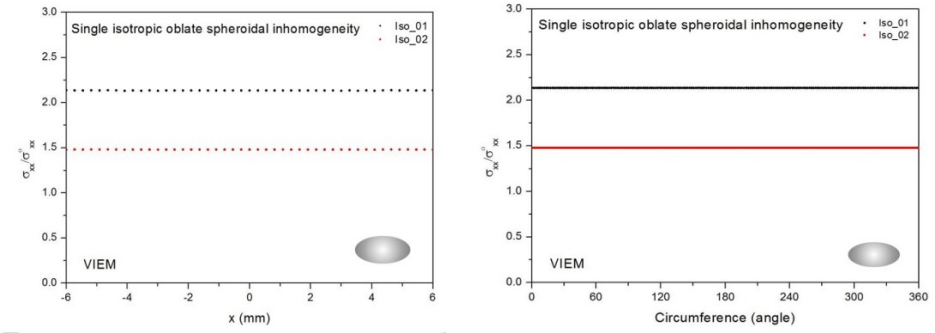

(**i**) x–axis (**ii**) circumferential direction

(**a**)

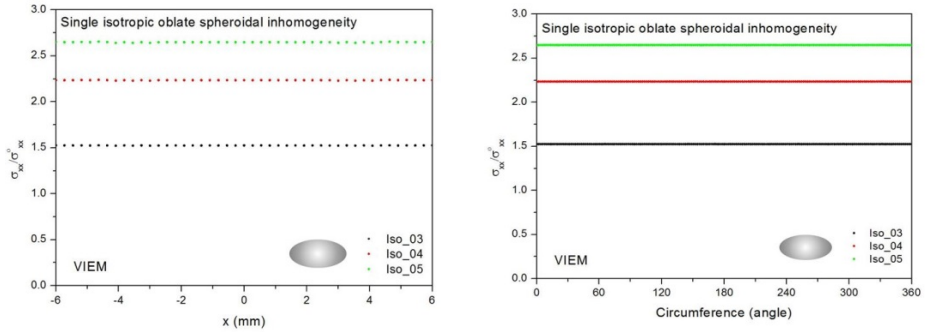

(**i**) x–axis (**ii**) circumferential direction

(**b**)

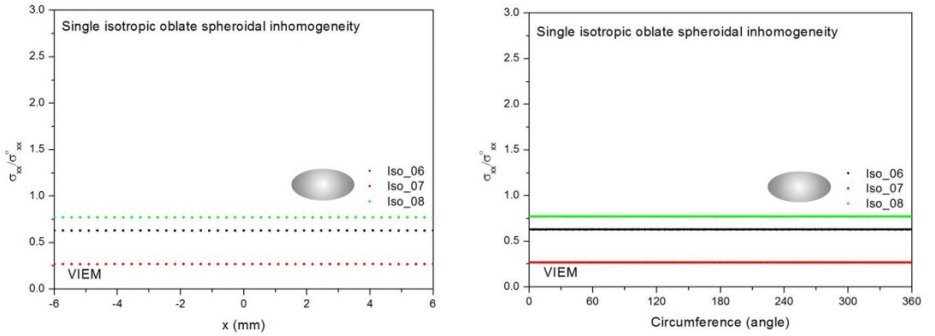

(**i**) x–axis (**ii**) circumferential direction

(**c**)

Figure 18. VIEM results for the normalized tensile stress component ($\sigma_{xx}/\sigma^{o}{}_{xx}$) along (**i**) the x–axis inside and (**ii**) the circumferential direction of the isotropic oblate spheroidal inclusions with b/a = c/a = 0.5 (a = 6 mm) under uniform remote tensile loading. (**a**) Iso_01 and Iso_02. (**b**) Iso_03, Iso_04 and Iso_05. (**c**) Iso_06, Iso_07 and Iso_08.

Figures 16 and 17 show a typical discretized model for the single (a) oblate spheroidal inclusion (b/a = c/a = 0.5 where a = 6 mm) and (b) oblate spheroidal inclusion (b/a = c/a = 0.75 where a = 6 mm) used in the VIEM [31], respectively. A total of 7560 standard 20-node

quadratic hexahedral elements were used for the single oblate spheroidal inclusion in Figures 16 and 17. The number of elements, 7560, was determined based on a convergence test.

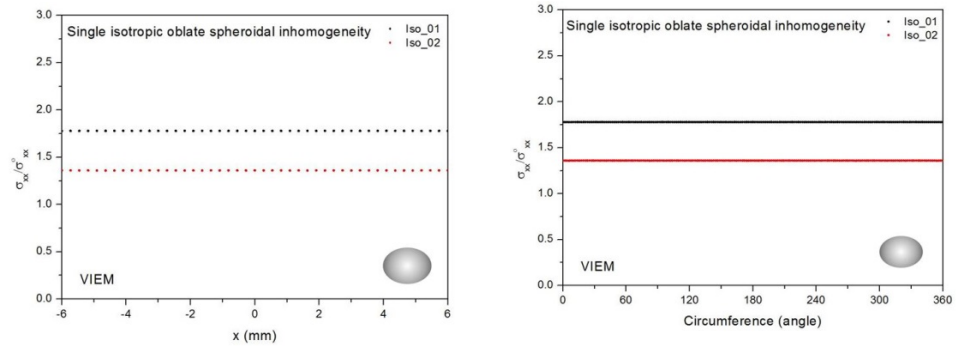

(**i**) x–axis (**ii**) circumferential direction

(**a**)

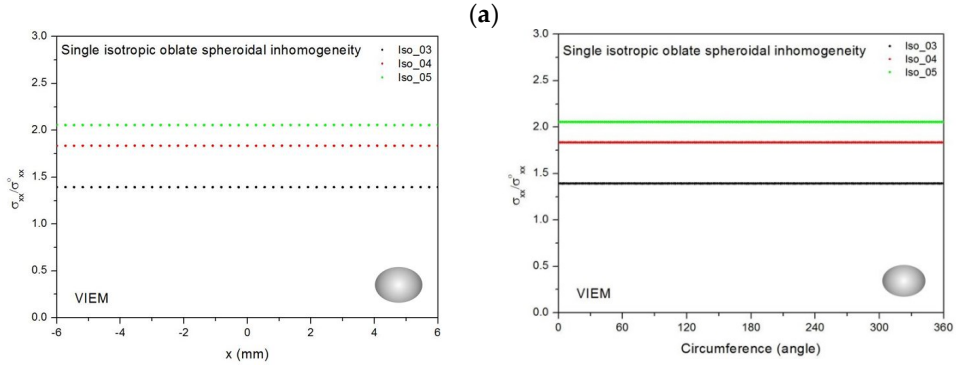

(**i**) x–axis (**ii**) circumferential direction

(**b**)

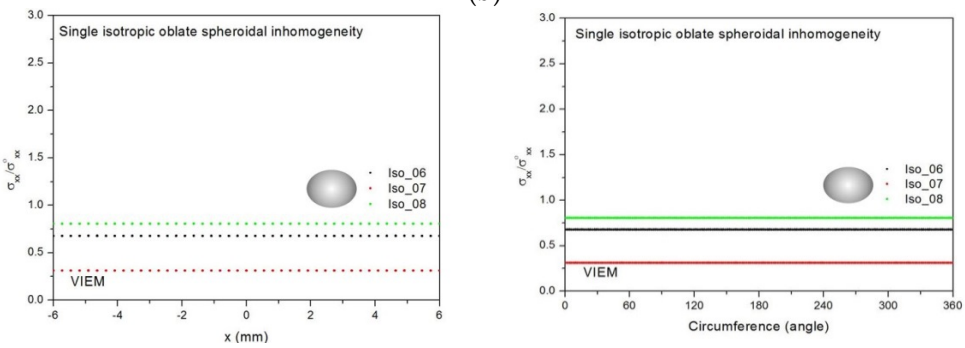

(**i**) x–axis (**ii**) circumferential direction

(**c**)

Figure 19. VIEM results for the normalized tensile stress component ($\sigma_{xx}/\sigma^{o}{}_{xx}$) along (**i**) the x–axis inside and (**ii**) the circumferential direction of the isotropic oblate spheroidal inclusions with b/a = c/a = 0.75 (a = 6 mm) under uniform remote tensile loading. (**a**) Iso_01 and Iso_02. (**b**) Iso_03, Iso_04 and Iso_05. (**c**) Iso_06, Iso_07 and Iso_08.

Five different orthotropic inclusions (from Ort_01 to Ort_05) in Table 3 were used in the numerical calculation. It should be noted that the VIEM results represent average values of the normalized stresses in all the nodes of the VIEM model in Figures 16 and 17. It should also be noted that the normalized tensile stress ($\sigma_{xx}/\sigma^{o}{}_{xx}$) inside the orthotropic oblate spheroidal inclusions was found to be constant [1,30]. Table 17 shows numerical solutions by the volume integral equation method for the normalized tensile stress ($\sigma_{xx}/\sigma^{o}{}_{xx}$) inside the orthotropic oblate pheroidal inclusions. For the inclusions in Ort_01, Ort_02 and Ort_03, the normalized tensile stress ($\sigma_{xx}/\sigma^{o}{}_{xx}$) inside the inclusion was greater than 1.0. However, for the inclusions in Ort_04 and Iso_05, the normalized tensile stress ($\sigma_{xx}/\sigma^{o}{}_{xx}$) inside the

inclusion was less than 1.0. Figure 20 shows numerical solutions by the volume integral equation method for the normalized tensile stress ($\sigma_{xx}/\sigma^{o}_{xx}$) along (left) the x–axis inside (-6 mm $\leq$ x $\leq$ 6 mm) and (right) the circumferential direction ($0^{\circ} \leq \theta$ (see Figure 16) $\leq 360^{\circ}$) of the orthotropic oblate spheroidal inclusions (b/a = c/a = 0.5 where a = 6 mm) under uniform remote tensile loading. Figure 21 shows numerical solutions by the volume integral equation method for the normalized tensile stress ($\sigma_{xx}/\sigma^{o}_{xx}$) along (left) the x–axis inside (-6 mm $\leq$ x $\leq$ 6 mm) and (right) the circumferential direction ($0^{\circ} \leq \theta$ (see Figure 17) $\leq 360^{\circ}$) of the orthotropic oblate spheroidal inclusions (b/a = c/a = 0.75 where a = 6 mm) under uniform remote tensile loading. It was determined in Figures 20 and 21 that the normalized tensile stress ($\sigma_{xx}/\sigma^{o}_{xx}$) inside the orthotropic oblate spheroidal inclusions is constant in all directions considered.

Table 17. Normalized tensile stress component ($\sigma_{xx}/\sigma^{o}_{xx}$) within the orthotropic oblate spheroidal inclusion due to uniform remote tensile loading (σ^{o}_{xx}).

Material	VIEM (Average)	
	b/a = c/a = 0.5 (See Figure 5)	b/a = c/a = 0.75 (See Figure 5)
Ort_01	1.2292	1.1833
Ort_02	1.7864	1.5780
Ort_03	2.1040	1.7745
Ort_04	0.5006	0.5453
Ort_05	0.7570	0.7882

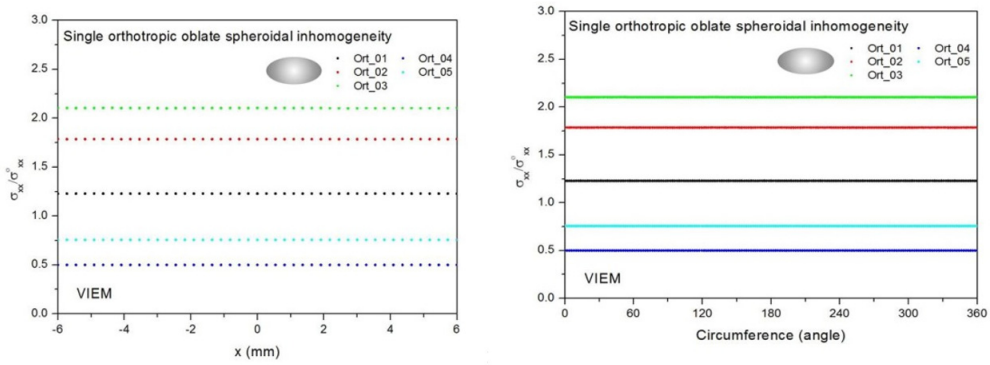

Figure 20. VIEM results for the normalized tensile stress component ($\sigma_{xx}/\sigma^{o}_{xx}$) along (**left**) the x–axis inside and (**right**) the circumferential direction of the orthotropic oblate spheroidal inclusions (Ort_01, Ort_02, Ort_03, Ort_04 and Ort_05) with b/a = c/a = 0.5 (a = 6 mm) under uniform remote tensile loading.

From Figures 8, 9, 12–15 and 18–21 and Tables 6–17, it was determined that if the inclusion is harder than the matrix, the normalized tensile stress ($\sigma_{xx}/\sigma^{o}_{xx}$) inside the inclusion is greater than 1.0. Additionally, the normalized tensile stress ($\sigma_{xx}/\sigma^{o}_{xx}$) inside the prolate spheroidal inclusion (a/b = c/b = 0.75) is greater than that inside the prolate spheroidal inclusion (a/b = c/b = 0.5). However, the normalized tensile stress ($\sigma_{xx}/\sigma^{o}_{xx}$) inside the oblate spheroidal inclusion (b/a = c/a = 0.5) is greater than that inside the oblate spheroidal inclusion (b/a = c/a = 0.75). Thus, the normalized tensile stress ($\sigma_{xx}/\sigma^{o}_{xx}$) inside the inclusion can be arranged in ascending order of magnitude: (1) prolate spheroidal inclusion (a/b = c/b = 0.5), (2) prolate spheroidal inclusion (a/b = c/b = 0.75), (3) sphere, (4) oblate spheroidal inclusion (b/a = c/a = 0.75) and (5) oblate spheroidal inclusion (b/a = c/a = 0.5). From Figures 8, 9, 12–15 and 18–21 and Tables 6–17, it was also determined that if the inclusion is softer than the matrix, the normalized tensile stress ($\sigma_{xx}/\sigma^{o}_{xx}$) inside the inclusion is less than 1.0. Additionally, the normalized tensile stress ($\sigma_{xx}/\sigma^{o}_{xx}$) inside the prolate spheroidal inclusion (a/b = c/b = 0.5) is greater than that inside the prolate spheroidal inclusion (a/b = c/b = 0.75). However, the normalized tensile stress ($\sigma_{xx}/\sigma^{o}_{xx}$) inside the oblate spheroidal inclusion (b/a = c/a = 0.75) is greater than that inside the

oblate spheroidal inclusion (b/a = c/a = 0.5). Thus, the normalized tensile stress ($\sigma_{xx}/\sigma^{o}{}_{xx}$) inside the inclusion can be arranged in ascending order of magnitude: (1) oblate spheroidal inclusion (b/a = c/a = 0.5), (2) oblate spheroidal inclusion (b/a = c/a = 0.75), (3) sphere, (4) prolate spheroidal inclusion (a/b = c/b = 0.75) and (5) prolate spheroidal inclusion (a/b = c/b = 0.5).

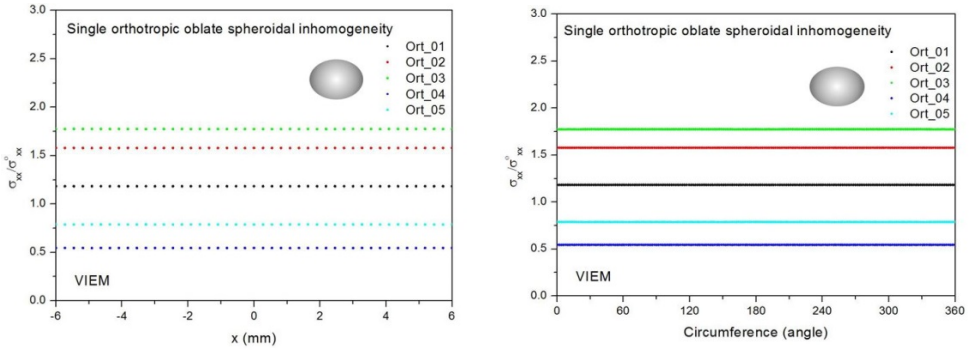

Figure 21. VIEM results for the normalized tensile stress component ($\sigma_{xx}/\sigma^{o}{}_{xx}$) along (**left**) the x–axis inside and (**right**) the circumferential direction of the orthotropic oblate spheroidal inclusions (Ort_01, Ort_02, Ort_03, Ort_04 and Ort_05) with b/a = c/a = 0.75 (a = 6 mm) under uniform remote tensile loading.

Both the standard finite element method (FEM) and the boundary element method (BEM) are powerful general-purpose tools in the field of numerical analysis. Since the VIEM is a combination of these two methods, it is also highly beneficial to the field of numerical analysis and can play a very important role in solving "inclusion problems". The authors hope that the results using the VIEM cited in this paper will be used as benchmarked data for verifying the results of similar research using other analytical and numerical methods.

3.3. Single Spherical Inclusion Problems under Remote Shear Loading

3.3.1. VIEM Formulation Applied to Isotropic/Orthotropic Inclusion Problems

The displacements for isotropic spherical, prolate and oblate spheroidal inclusions can be determined from volume integral Equations (3)–(5), while the displacements for orthotropic spherical, prolate and oblate spheroidal inclusions can be determined from volume integral Equations (6)–(8).

3.3.2. A Single Isotropic Spherical Inclusion

We considered a single isotropic spherical inclusion with a radius of 6 mm in an infinite isotropic matrix subject to remote shear loading, $\sigma^{o}{}_{xy}$, $\sigma^{o}{}_{xz}$ and $\sigma^{o}{}_{yz}$, as shown in Figure 6a [24]. It should be noted that the length of the radius can be arbitrarily chosen. In Figure 7, standard 20-node quadratic hexahedral elements were used in the discretization [31]. The number of hexahedral elements, 7560, was determined based on a convergence test. Three different material properties (Iso_01, Iso_05 and Iso_06) in Table 2 were used in the numerical calculation. It should be noted that the normalized shear stresses ($\sigma_{xy}/\sigma^{o}{}_{xy}$, $\sigma_{xz}/\sigma^{o}{}_{xz}$ and $\sigma_{yz}/\sigma^{o}{}_{yz}$) inside the isotropic spherical inclusions were found to be constant, respectively [1]. It should also be noted that the VIEM results represent average values of the normalized stresses in all the nodes of the VIEM model in Figure 7. Table 18 shows numerical solutions by the volume integral equation method for the normalized shear stresses ($\sigma_{xy}/\sigma^{o}{}_{xy}$, $\sigma_{xz}/\sigma^{o}{}_{xz}$ and $\sigma_{yz}/\sigma^{o}{}_{yz}$) inside the isotropic spherical inclusions. For the inclusions in Iso_01 and Iso_05, the normalized shear stresses ($\sigma_{xy}/\sigma^{o}{}_{xy}$, $\sigma_{xz}/\sigma^{o}{}_{xz}$ and $\sigma_{yz}/\sigma^{o}{}_{yz}$) inside the inclusion were greater than 1.0, respectively. However, for the inclusion in Iso_06, the normalized shear stresses ($\sigma_{xy}/\sigma^{o}{}_{xy}$, $\sigma_{xz}/\sigma^{o}{}_{xz}$ and $\sigma_{yz}/\sigma^{o}{}_{yz}$) inside the inclusion were less than 1.0, respectively. Figure 22 shows numerical solutions by the volume integral equation method for the normalized shear stresses ($\sigma_{xy}/\sigma^{o}{}_{xy}$, $\sigma_{xz}/\sigma^{o}{}_{xz}$ and $\sigma_{yz}/\sigma^{o}{}_{yz}$) along (i) the x–axis inside (-6 mm $\leq$ x $\leq$ 6 mm) and (ii) the circumferential

direction ($0^\circ \leq \theta$ (see Figure 7) $\leq 360^\circ$) of the isotropic spherical inclusions with a radius of 6 mm under remote shear loading.

Table 18. Normalized shear stress components ($\sigma_{xy}/\sigma^o{}_{xy}$, $\sigma_{xz}/\sigma^o{}_{xz}$ and $\sigma_{yz}/\sigma^o{}_{yz}$) within the isotropic spherical inclusion due to remote shear loading ($\sigma^o{}_{xy}$, $\sigma^o{}_{xz}$ and $\sigma^o{}_{yz}$).

Material	VIEM (Average)		
	$\sigma_{xy}/\sigma^o{}_{xy}$	$\sigma_{xz}/\sigma^o{}_{xz}$	$\sigma_{yz}/\sigma^o{}_{yz}$
Iso_01	1.7109	1.7109	1.7109
Iso_05	1.9231	1.9231	1.9231
Iso_06	0.6636	0.6636	0.6636

In most references, spherical inclusion problems under uniform remote tensile loading were considered. Thus, in order to show the VIEM results more thoroughly, the normalized shear stresses, (a) $\sigma_{xy}/\sigma^o{}_{xy}$, (b) $\sigma_{xz}/\sigma^o{}_{xz}$ and (c) $\sigma_{yz}/\sigma^o{}_{yz}$, using the VIEM were presented along (i) the x–axis inside (-6 mm $\leq x \leq 6$ mm) and (ii) the circumferential direction ($0^\circ \leq \theta$ (see Figure 7) $\leq 360^\circ$) of the isotropic spherical inclusions.

It was determined in Figure 22 that the normalized shear stresses ($\sigma_{xy}/\sigma^o{}_{xy}$, $\sigma_{xz}/\sigma^o{}_{xz}$ and $\sigma_{yz}/\sigma^o{}_{yz}$) inside the single isotropic spherical inclusions are constant in all directions considered and are identical to each other. Since isotropic materials have an infinite number of planes of symmetry, the normalized shear stresses ($\sigma_{xy}/\sigma^o{}_{xy}$, $\sigma_{xz}/\sigma^o{}_{xz}$ and $\sigma_{yz}/\sigma^o{}_{yz}$) inside the single isotropic spherical inclusions turned out to be identical to each other.

3.3.3. A Single Orthotropic Spherical Inclusion

In order to show the advantages of the volume integral equation method (VIEM), we considered a single orthotropic spherical inclusion with a radius of 6 mm in an infinite isotropic matrix subject to remote shear loading, $\sigma^o{}_{xy}$, $\sigma^o{}_{xz}$ and $\sigma^o{}_{yz}$, as shown in Figure 6a. It should be noted that the length of the radius can be arbitrarily chosen. In Figure 7, standard 20-node quadratic hexahedral elements were used in the discretization [31]. The number of hexahedral elements was 7560, determined based on a convergence test. For this problem, in comparison to the boundary element method (BEM), since the VIEM is not sensitive to the anisotropy of the inclusions, it does not require the use of the Green's function for the anisotropic inclusions. Moreover, as opposed to the standard FEM, where it is necessary to discretize the full domain, the orthotropic inclusion only needs to be discretized in the VIEM.

Two different material properties (Ort_06 and Ort_07) in Table 4 were used in the numerical calculation [25]. As shown in Table 5, it was assumed that $c_{55} > c_{66} > c_{44}$ for two orthotropic inclusions. Additionally, c_{44}, c_{55} and c_{66} of the inclusion were assumed be greater than μ of the matrix in the Ort_06 material, while μ of the matrix was assumed to be greater than c_{44}, c_{55} and c_{66} of the inclusion in the Ort_07 material. Thus, two material properties representing different characteristics were chosen. It should be noted that the VIEM results represent average values of the normalized stresses in all the nodes of the VIEM model in Figure 7. Moreover, the normalized shear stresses ($\sigma_{xy}/\sigma^o{}_{xy}$, $\sigma_{xz}/\sigma^o{}_{xz}$ and $\sigma_{yz}/\sigma^o{}_{yz}$) inside the orthotropic spherical inclusions were found to be constant, respectively [1]. Table 19 shows numerical solutions by the volume integral equation method for the normalized shear stresses ($\sigma_{xy}/\sigma^o{}_{xy}$, $\sigma_{xz}/\sigma^o{}_{xz}$ and $\sigma_{yz}/\sigma^o{}_{yz}$) inside the orthotropic spherical inclusions. For the inclusion in Ort_06, the normalized shear stresses ($\sigma_{xy}/\sigma^o{}_{xy}$, $\sigma_{xz}/\sigma^o{}_{xz}$ and $\sigma_{yz}/\sigma^o{}_{yz}$) inside the inclusion were greater than 1.0, respectively. However, for the inclusion in Ort_07, the normalized shear stresses ($\sigma_{xy}/\sigma^o{}_{xy}$, $\sigma_{xz}/\sigma^o{}_{xz}$ and $\sigma_{yz}/\sigma^o{}_{yz}$) inside the inclusion were less than 1.0, respectively. Figure 23 shows numerical solutions by the volume integral equation method for the normalized shear stresses (a) $\sigma_{xy}/\sigma^o{}_{xy}$, (b) $\sigma_{xz}/\sigma^o{}_{xz}$ and (c) $\sigma_{yz}/\sigma^o{}_{yz}$ along (i) the x–axis inside (-6 mm $\leq x \leq 6$ mm) and (ii) the circumferential direction ($0^\circ \leq \theta$ (see Figure 7) $\leq 360^\circ$) of the orthotropic spherical inclusions with a radius of 6 mm under remote shear loading. It was determined in

Figure 23 that the normalized shear stresses ($\sigma_{xy}/\sigma^{o}{}_{xy}$, $\sigma_{xz}/\sigma^{o}{}_{xz}$ and $\sigma_{yz}/\sigma^{o}{}_{yz}$) inside the orthotropic spherical inclusions are constant in all directions considered and are different from each other. Since orthotropic materials have three planes/axes of symmetry and the independent shear moduli in three planes of symmetry are different from each other ($c_{55} > c_{66} > c_{44}$), the normalized shear stresses ($\sigma_{xy}/\sigma^{o}{}_{xy}$, $\sigma_{xz}/\sigma^{o}{}_{xz}$ and $\sigma_{yz}/\sigma^{o}{}_{yz}$) inside the orthotropic spherical inclusions turned out to be different from each other. Furthermore, since c_{55} (shear modulus in the xz plane) is greater than c_{66} (shear modulus in the xy plane) and c_{66} is greater than c_{44} (shear modulus in the yz plane) in the orthotropic inclusions of the Ort_06 and Ort_07 materials, it was determined that the normalized shear stress, $\sigma_{xz}/\sigma^{o}{}_{xz}$, was greater than the normalized shear stress, $\sigma_{xy}/\sigma^{o}{}_{xy}$. Furthermore, $\sigma_{xy}/\sigma^{o}{}_{xy}$ was found to be greater than the normalized shear stress, $\sigma_{yz}/\sigma^{o}{}_{yz}$, inside the orthotropic spherical inclusions.

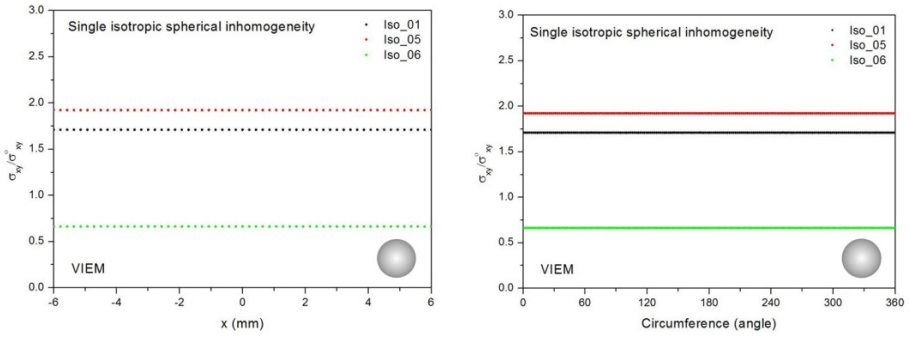

(**i**) x–axis (**ii**) circumferential direction

(**a**) Shear stress component ($\sigma_{xy}/\sigma^{o}{}_{xy}$)

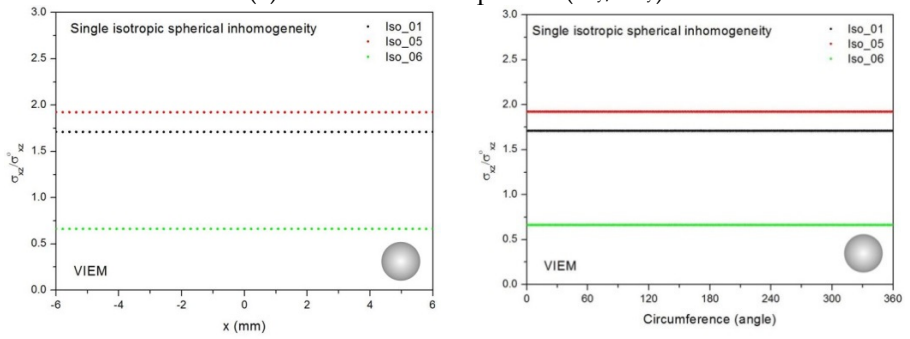

(**i**) x–axis (**ii**) circumferential direction

(**b**) Shear stress component ($\sigma_{xz}/\sigma^{o}{}_{xz}$)

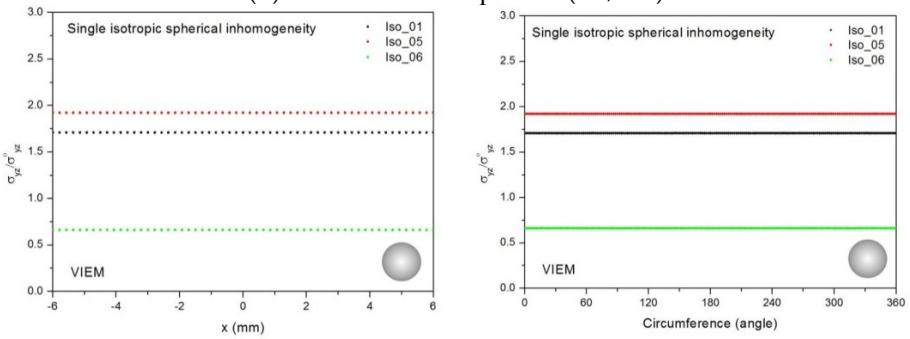

(**i**) x–axis (**ii**) circumferential direction

(**c**) Shear stress component ($\sigma_{yz}/\sigma^{o}{}_{yz}$)

Figure 22. VIEM results for the normalized shear stress components (**a**) $\sigma_{xy}/\sigma^{o}{}_{xy}$, (**b**) $\sigma_{xz}/\sigma^{o}{}_{xz}$ and (**c**) $\sigma_{yz}/\sigma^{o}{}_{yz}$ along (**i**) the x–axis inside and (**ii**) the circumferential direction of the isotropic spherical inclusions (Iso_01, Iso_05 and Iso_06) with a radius of 6 mm under remote shear loading ($\sigma^{o}{}_{xy}$, $\sigma^{o}{}_{xz}$ and $\sigma^{o}{}_{yz}$).

Table 19. Normalized shear stress components ($\sigma_{xy}/\sigma^{o}{}_{xy}$, $\sigma_{xz}/\sigma^{o}{}_{xz}$ and $\sigma_{yz}/\sigma^{o}{}_{yz}$) within the orthotropic spherical inclusion due to remote shear loading ($\sigma^{o}{}_{xy}$, $\sigma^{o}{}_{xz}$ and $\sigma^{o}{}_{yz}$).

Material	VIEM (Average)		
	$\sigma_{xy}/\sigma^{o}{}_{xy}$	$\sigma_{xz}/\sigma^{o}{}_{xz}$	$\sigma_{yz}/\sigma^{o}{}_{yz}$
Ort_06	1.4006	1.5456	1.3537
Ort_07	0.4356	0.5576	0.4030

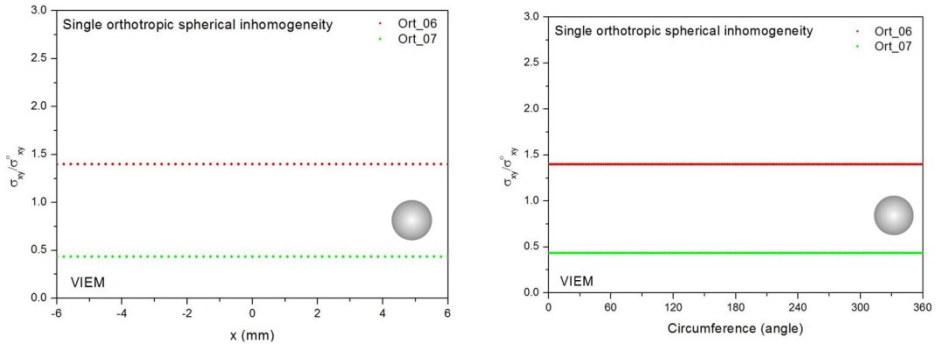

(**i**) x–axis (**ii**) circumferential direction

(**a**) Shear stress component ($\sigma_{xy}/\sigma^{o}{}_{xy}$)

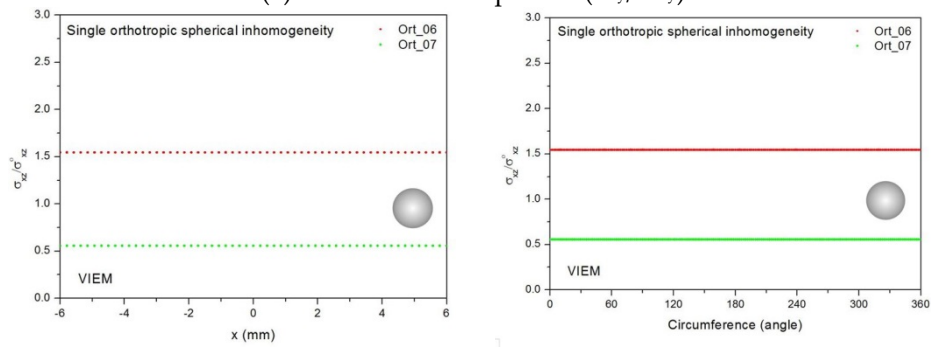

(**i**) x–axis (**ii**) circumferential direction

(**b**) Shear stress component ($\sigma_{xz}/\sigma^{o}{}_{xz}$)

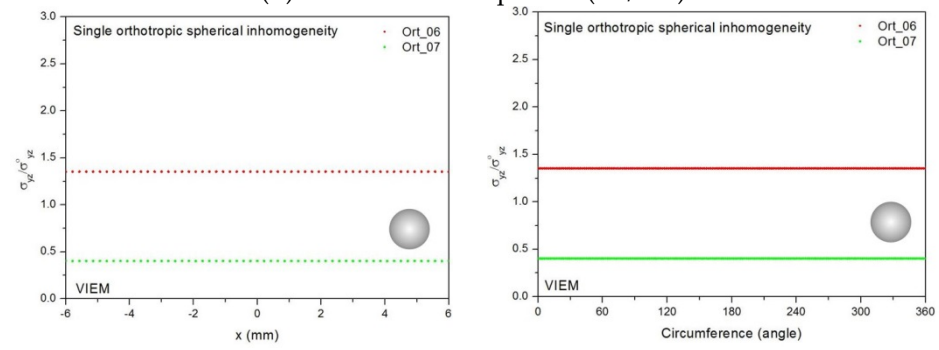

(**i**) x–axis (**ii**) circumferential direction

(**c**) Shear stress component ($\sigma_{yz}/\sigma^{o}{}_{yz}$)

Figure 23. VIEM results for the normalized shear stress components (**a**) $\sigma_{xy}/\sigma^{o}{}_{xy}$, (**b**) $\sigma_{xz}/\sigma^{o}{}_{xz}$ and (**c**) $\sigma_{yz}/\sigma^{o}{}_{yz}$ along (**i**) the x–axis inside and (**ii**) the circumferential direction of the orthotropic spherical inclusions (Ort_06 and Ort_07) with a radius of 6 mm under remote shear loading ($\sigma^{o}{}_{xy}$, $\sigma^{o}{}_{xz}$ and $\sigma^{o}{}_{yz}$).

3.4. A Single Spheroidal Inclusion Problem under Remote Shear Loading

In order to introduce the VIEM as a versatile numerical method, we considered a single isotropic/orthotropic spheroidal inclusion in an infinite isotropic matrix subject to

remote shear loading, σ^{o}_{xy}, σ^{o}_{xz} and σ^{o}_{yz}, as shown in Figure 6b,c. Figure 5 shows the orientation of the spheroidal inclusion.

3.4.1. A Single Isotropic Prolate Spheroidal Inclusion

Two different prolate spheroidal inclusions are considered: (a) a/b = c/b = 0.5, where b = 6 mm, and (b) a/b = c/b = 0.75, where b = 6 mm (see Figure 5). It should be noted that the length of b (=6 mm) can be arbitrarily chosen.

Figures 10 and 11 show a typical discretized model for the single (a) prolate spheroidal inclusion (a/b = c/b = 0.5 where b = 6 mm) and (b) prolate spheroidal inclusion (a/b = c/b = 0.75 where b = 6 mm) used in the VIEM [31], respectively. A total of 7560 standard 20-node quadratic hexahedral elements were used for the single prolate spheroidal inclusion in Figures 10 and 11. The number of elements, 7560, was determined based on a convergence test.

Three different isotropic inclusions (Iso_01, Iso_05 and Iso_06) in Table 2 were used in the numerical calculation. It should be noted that the VIEM results represent average values of the normalized stresses in all the nodes of the VIEM model in Figures 10 and 11. It should also be noted that the normalized shear stresses ($\sigma_{xy}/\sigma^{o}_{xy}$, $\sigma_{xz}/\sigma^{o}_{xz}$ and $\sigma_{yz}/\sigma^{o}_{yz}$) inside the isotropic prolate spheroidal inclusions were found to be constant, respectively [1]. Table 20 shows numerical solutions by the volume integral equation method for the normalized shear stresses ($\sigma_{xy}/\sigma^{o}_{xy}$, $\sigma_{xz}/\sigma^{o}_{xz}$ and $\sigma_{yz}/\sigma^{o}_{yz}$) inside the isotropic prolate spheroidal inclusions. For the inclusions in Iso_01 and Iso_05, the normalized shear stresses ($\sigma_{xy}/\sigma^{o}_{xy}$, $\sigma_{xz}/\sigma^{o}_{xz}$ and $\sigma_{yz}/\sigma^{o}_{yz}$) inside the inclusion were greater than 1.0, respectively. However, for the inclusion in Iso_06, the normalized shear stresses ($\sigma_{xy}/\sigma^{o}_{xy}$, $\sigma_{xz}/\sigma^{o}_{xz}$ and $\sigma_{yz}/\sigma^{o}_{yz}$) inside the inclusion were less than 1.0, respectively. Figure 24 shows numerical solutions by the volume integral equation method for the normalized shear stresses (a) $\sigma_{xy}/\sigma^{o}_{xy}$, (b) $\sigma_{xz}/\sigma^{o}_{xz}$ and (c) $\sigma_{yz}/\sigma^{o}_{yz}$ along (i) the x–axis inside (-3 mm $\leq x \leq 3$ mm) and (ii) the circumferential direction ($0^\circ \leq \theta$ (see Figure 10) $\leq 360^\circ$) of the isotropic prolate spheroidal inclusions (a/b = c/b = 0.5 where b = 6 mm) under remote shear loading, σ^{o}_{xy}, σ^{o}_{xz} and σ^{o}_{yz}. Figure 25 shows numerical solutions by the volume integral equation method for the normalized shear stresses (a) $\sigma_{xy}/\sigma^{o}_{xy}$, (b) $\sigma_{xz}/\sigma^{o}_{xz}$ and (c) $\sigma_{yz}/\sigma^{o}_{yz}$ along (i) the x–axis inside (-4.5 mm $\leq x \leq 4.5$ mm) and (ii) the circumferential direction ($0^\circ \leq \theta$ (see Figure 11) $\leq 360^\circ$) of the isotropic prolate spheroidal inclusions (a/b = c/b = 0.75 where b = 6 mm) under remote shear loading, σ^{o}_{xy}, σ^{o}_{xz} and σ^{o}_{yz}. It was determined in Figures 24 and 25 that the normalized shear stresses ($\sigma_{xy}/\sigma^{o}_{xy}$, $\sigma_{xz}/\sigma^{o}_{xz}$ and $\sigma_{yz}/\sigma^{o}_{yz}$) inside the isotropic prolate spheroidal inclusions are constant in all directions considered. Furthermore, since, as shown in Figure 26, the cross-section in the xy plane is identical to the cross-section in the yz plane in the prolate spheroidal inclusion, the normalized shear stress, $\sigma_{xy}/\sigma^{o}_{xy}$, was identical to the normalized shear stress, $\sigma_{yz}/\sigma^{o}_{yz}$, inside the isotropic prolate spheroidal inclusion under remote shear loading.

Table 20. Normalized shear stress components ($\sigma_{xy}/\sigma^{o}_{xy}$, $\sigma_{xz}/\sigma^{o}_{xz}$ and $\sigma_{yz}/\sigma^{o}_{yz}$) within the isotropic prolate spheroidal inclusion due remote shear loading (σ^{o}_{xy}, σ^{o}_{xz} and σ^{o}_{yz}).

Material	**VIEM (Average)**					
	a/b = c/b = 0.5 (See Figure 5)			**a/b = c/b = 0.75 (See Figure 5)**		
	$\sigma_{xy}/\sigma^{o}_{xy}$	$\sigma_{xz}/\sigma^{o}_{xz}$	$\sigma_{yz}/\sigma^{o}_{yz}$	$\sigma_{xy}/\sigma^{o}_{xy}$	$\sigma_{xz}/\sigma^{o}_{xz}$	$\sigma_{yz}/\sigma^{o}_{yz}$
Iso_01	1.7619	1.5329	1.7619	1.7490	1.6214	1.7490
Iso_05	1.9935	1.6765	1.9935	1.9772	1.7972	1.9772
Iso_06	0.6538	0.7036	0.6538	0.6565	0.6820	0.6565

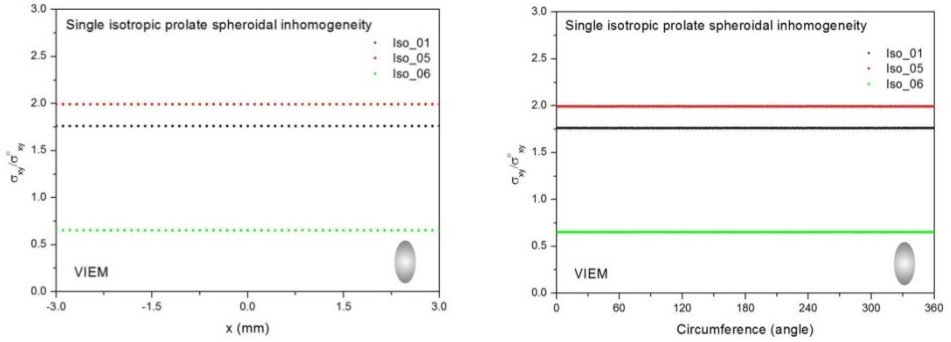

(**i**) x–axis (**ii**) circumferential direction

(**a**) Shear stress component ($\sigma_{xy}/\sigma^{o}_{xy}$)

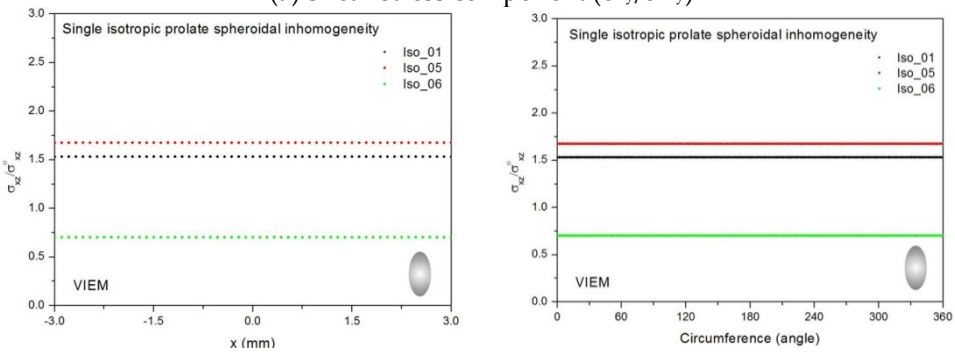

(**i**) x–axis (**ii**) circumferential direction

(**b**) Shear stress component ($\sigma_{xz}/\sigma^{o}_{xz}$)

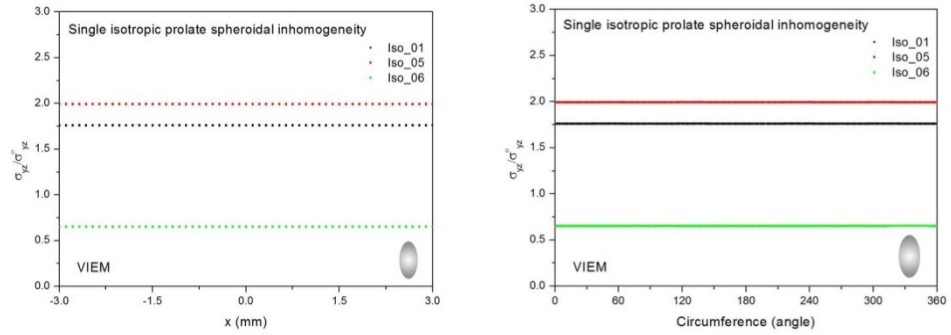

(**i**) x–axis (**ii**) circumferential direction

(**c**) Shear stress component ($\sigma_{yz}/\sigma^{o}_{yz}$)

Figure 24. VIEM results for the normalized shear stress components (**a**) $\sigma_{xy}/\sigma^{o}_{xy}$, (**b**) $\sigma_{xz}/\sigma^{o}_{xz}$ and (**c**) $\sigma_{yz}/\sigma^{o}_{yz}$ along (**i**) the x–axis inside and (**ii**) the circumferential direction of the isotropic prolate spheroidal inclusions (Iso_01, Iso_05 and Iso_06) with a/b = c/b = 0.5 (b = 6 mm) under remote shear loading (σ^{o}_{xy}, σ^{o}_{xz} and σ^{o}_{yz}).

3.4.2. A Single Orthotropic Prolate Spheroidal Inclusion

Two different prolate spheroidal inclusions are considered: (a) a/b = c/b = 0.5, where b = 6 mm, and (b) a/b = c/b = 0.75, where b = 6 mm (see Figure 5). It should be noted that the length of b (=6 mm) can be arbitrarily chosen.

Figures 10 and 11 show a typical discretized model for the single (a) prolate spheroidal inclusion (a/b = c/b = 0.5 where b = 6 mm) and (b) prolate spheroidal inclusion (a/b = c/b = 0.75 where b = 6 mm) used in the VIEM [31], respectively. A total of 7560 standard 20-node quadratic hexahedral elements were used for the single prolate spheroidal inclusion in Figures 10 and 11. The number of elements, 7560, was determined based on a convergence test.

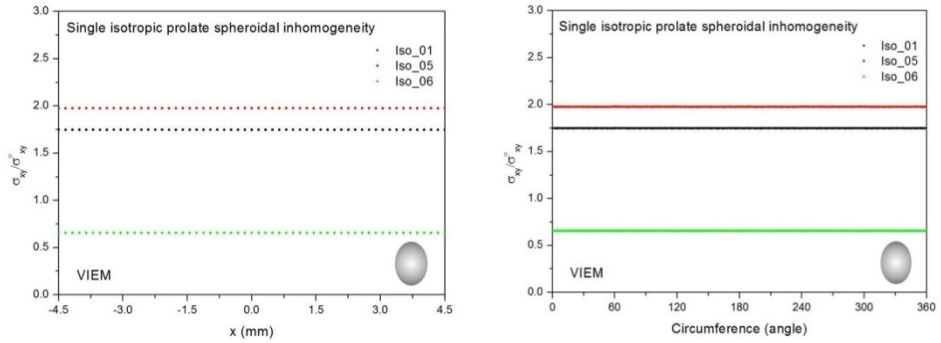

(**i**) x–axis (**ii**) circumferential direction

(**a**) Shear stress component ($\sigma_{xy}/\sigma^{o}_{xy}$)

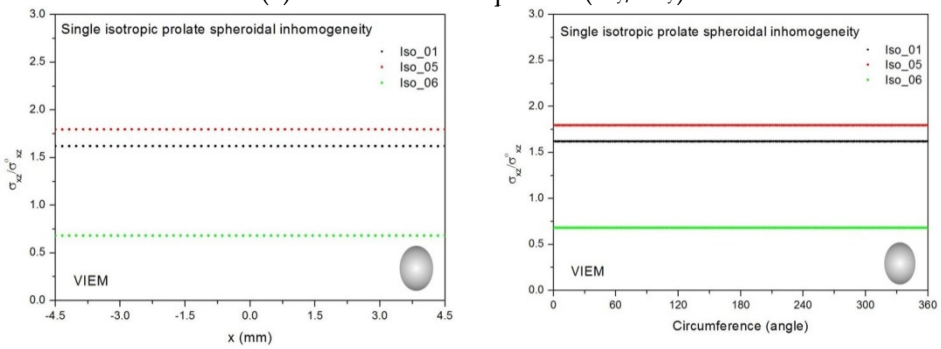

(**i**) x–axis (**ii**) circumferential direction

(**b**) Shear stress component ($\sigma_{xz}/\sigma^{o}_{xz}$)

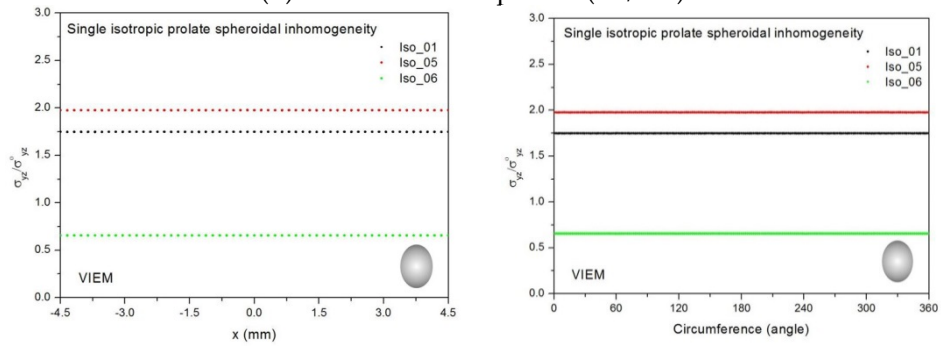

(**i**) x–axis (**ii**) circumferential direction

(**c**) Shear stress component ($\sigma_{yz}/\sigma^{o}_{yz}$)

Figure 25. VIEM results for the normalized shear stress components (**a**) $\sigma_{xy}/\sigma^{o}_{xy}$, (**b**) $\sigma_{xz}/\sigma^{o}_{xz}$ and (**c**) $\sigma_{yz}/\sigma^{o}_{yz}$ along (**i**) the x–axis inside and (**ii**) the circumferential direction of the isotropic prolate spheroidal inclusions (Iso_01, Iso_05 and Iso_06) with a/b = c/b = 0.75 (b = 6 mm) under remote shear loading (σ^{o}_{xy}, σ^{o}_{xz} and σ^{o}_{yz}).

Two different orthotropic inclusions (Ort_06 and Ort_07) in Table 4 were used in the numerical calculation. It should be noted that the VIEM results represent average values of the normalized stresses in all the nodes of the VIEM model in Figures 10 and 11. It should also be noted that the normalized shear stresses ($\sigma_{xy}/\sigma^{o}_{xy}$, $\sigma_{xz}/\sigma^{o}_{xz}$ and $\sigma_{yz}/\sigma^{o}_{yz}$) inside the orthotropic prolate spheroidal inclusions were found to be constant, respectively [1]. Table 21 shows numerical solutions by the volume integral equation method for the normalized shear stresses ($\sigma_{xy}/\sigma^{o}_{xy}$, $\sigma_{xz}/\sigma^{o}_{xz}$ and $\sigma_{yz}/\sigma^{o}_{yz}$) inside the orthotropic prolate spheroidal inclusions. For the inclusion in Ort_06, the normalized shear stresses ($\sigma_{xy}/\sigma^{o}_{xy}$, $\sigma_{xz}/\sigma^{o}_{xz}$ and $\sigma_{yz}/\sigma^{o}_{yz}$) inside the inclusion were greater than 1.0, respectively. However, for the inclusion in Ort_07, the normalized shear stresses ($\sigma_{xy}/\sigma^{o}_{xy}$, $\sigma_{xz}/\sigma^{o}_{xz}$ and $\sigma_{yz}/\sigma^{o}_{yz}$) inside the inclusion were less than 1.0, respectively. Figure 27 shows numerical solutions by the volume integral equation method for the normalized shear stresses

(a) $\sigma_{xy}/\sigma^{o}{}_{xy}$, (b) $\sigma_{xz}/\sigma^{o}{}_{xz}$ and (c) $\sigma_{yz}/\sigma^{o}{}_{yz}$ along (i) the x–axis inside (-3 mm $\leq x \leq 3$ mm) and (ii) the circumferential direction ($0^{\circ} \leq \theta$ (see Figure 10) $\leq 360^{\circ}$) of the orthotropic prolate spheroidal inclusions (a/b = c/b = 0.5 where b = 6 mm) under remote shear loading, $\sigma^{o}{}_{xy}$, $\sigma^{o}{}_{xz}$ and $\sigma^{o}{}_{yz}$. Figure 28 shows numerical solutions by the volume integral equation method for the normalized shear stresses (a) $\sigma_{xy}/\sigma^{o}{}_{xy}$, (b) $\sigma_{xz}/\sigma^{o}{}_{xz}$ and (c) $\sigma_{yz}/\sigma^{o}{}_{yz}$ along (i) the x–axis inside (-4.5 mm $\leq x \leq 4.5$ mm) and (ii) the circumferential direction ($0^{\circ} \leq \theta$ (see Figure 11) $\leq 360^{\circ}$) of the orthotropic prolate spheroidal inclusions (a/b = c/b = 0.75 where b = 6 mm) under remote shear loading, $\sigma^{o}{}_{xy}$, $\sigma^{o}{}_{xz}$ and $\sigma^{o}{}_{yz}$. It was determined in Figures 27 and 28 that the normalized shear stresses ($\sigma_{xy}/\sigma^{o}{}_{xy}$, $\sigma_{xz}/\sigma^{o}{}_{xz}$ and $\sigma_{yz}/\sigma^{o}{}_{yz}$) inside the orthotropic prolate spheroidal inclusions are constant in all directions considered. Furthermore, even though, as shown in Figure 26, the cross-section in the xy plane is identical to the cross-section in the yz plane in the prolate spheroidal inclusion, since c_{55} (shear modulus in the xz plane) is greater than c_{66} (shear modulus in the xy plane) and c_{66} is greater than c_{44} (shear modulus in the yz plane) in the orthotropic inclusions of the Ort_06 and Ort_07 materials, the normalized shear stress, $\sigma_{xy}/\sigma^{o}{}_{xy}$, was different from the normalized shear stress, $\sigma_{yz}/\sigma^{o}{}_{yz}$, inside the isotropic prolate spheroidal inclusion under remote shear loading.

Table 21. Normalized shear stress components ($\sigma_{xy}/\sigma^{o}{}_{xy}$, $\sigma_{xz}/\sigma^{o}{}_{xz}$ and $\sigma_{yz}/\sigma^{o}{}_{yz}$) within the orthotropic prolate spheroidal inclusion due remote shear loading ($\sigma^{o}{}_{xy}$, $\sigma^{o}{}_{xz}$ and $\sigma^{o}{}_{yz}$).

Material	**VIEM (Average)**					
	a/b = c/b = 0.5 (See Figure 5)			**a/b = c/b = 0.75 (See Figure 5)**		
	$\sigma_{xy}/\sigma^{o}{}_{xy}$	$\sigma_{xz}/\sigma^{o}{}_{xz}$	$\sigma_{yz}/\sigma^{o}{}_{yz}$	$\sigma_{xy}/\sigma^{o}{}_{xy}$	$\sigma_{xz}/\sigma^{o}{}_{xz}$	$\sigma_{yz}/\sigma^{o}{}_{yz}$
Ort_06	1.4239	1.4192	1.3735	1.4180	1.4828	1.3685
Ort_07	0.4258	0.6010	0.3934	0.4282	0.5774	0.3957

3.4.3. A Single Isotropic Oblate Spheroidal Inclusion

In this section, two different oblate spheroidal inclusions are considered: (a) b/a = c/a = 0.5, where a = 6 mm, and (b) b/a = c/a = 0.75, where a = 6 mm (see Figure 5). It should be noted that the length of a (=6 mm) can be arbitrarily chosen.

Figures 16 and 17 show a typical discretized model for the single (a) oblate spheroidal inclusion (b/a = c/a = 0.5 where a = 6 mm) and (b) oblate spheroidal inclusion (b/a = c/a = 0.75 where a = 6 mm) used in the VIEM [31], respectively. A total of 7560 standard 20-node quadratic hexahedral elements were used for the single oblate spheroidal inclusion in Figures 16 and 17. The number of elements, 7560, was determined based on a convergence test.

Three different isotropic inclusions (Iso_01, Iso_05 and Iso_06) in Table 2 were used in the numerical calculation. It should be noted that the VIEM results represent average values of the normalized stresses in all the nodes of the VIEM model in Figures 16 and 17. It should also be noted that the normalized shear stresses ($\sigma_{xy}/\sigma^{o}{}_{xy}$, $\sigma_{xz}/\sigma^{o}{}_{xz}$ and $\sigma_{yz}/\sigma^{o}{}_{yz}$) inside the isotropic oblate spheroidal inclusions were found to be constant, respectively [1]. Table 22 shows numerical solutions by the volume integral equation method for the normalized shear stresses ($\sigma_{xy}/\sigma^{o}{}_{xy}$, $\sigma_{xz}/\sigma^{o}{}_{xz}$ and $\sigma_{yz}/\sigma^{o}{}_{yz}$) inside the isotropic oblate spheroidal inclusions. For the inclusions in Iso_01 and Iso_05, the normalized shear stresses ($\sigma_{xy}/\sigma^{o}{}_{xy}$, $\sigma_{xz}/\sigma^{o}{}_{xz}$ and $\sigma_{yz}/\sigma^{o}{}_{yz}$) inside the inclusion were greater than 1.0, respectively. However, for the inclusion in Iso_06, the normalized shear stresses ($\sigma_{xy}/\sigma^{o}{}_{xy}$, $\sigma_{xz}/\sigma^{o}{}_{xz}$ and $\sigma_{yz}/\sigma^{o}{}_{yz}$) inside the inclusion were less than 1.0, respectively.

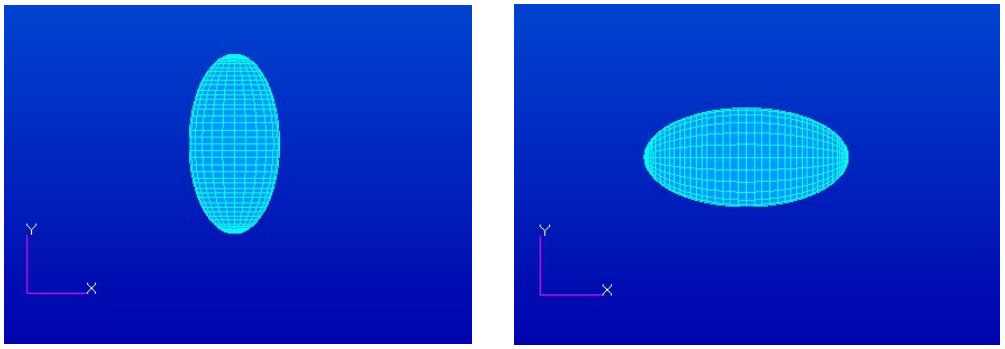

(**i**) A prolate spheroidal inclusion (**ii**) An oblate spheroidal inclusion

(**a**) Cross-section in the xy plane

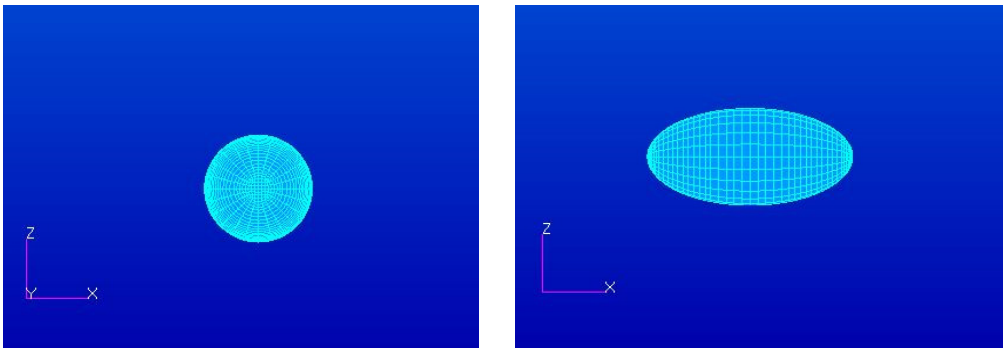

(**i**) A prolate spheroidal inclusion (**ii**) An oblate spheroidal inclusion

(**b**) Cross-section in the xz plane

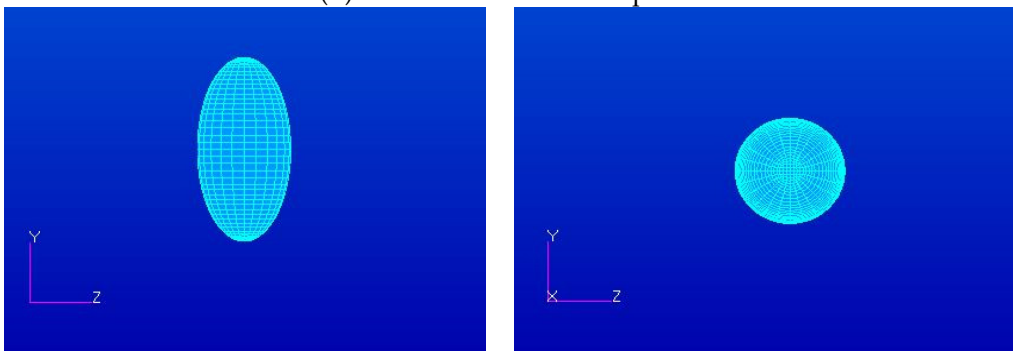

(**i**) A prolate spheroidal inclusion (**ii**) An oblate spheroidal inclusion

(**c**) Cross-section in the yz plane

Figure 26. Cross-section in the (**a**) xy plane, (**b**) xz plane and (**c**) yz plane of (**i**) prolate spheroidal (with an aspect ratio of 0.5) and (**ii**) oblate spheroidal (with an aspect ratio of 0.5) inclusions under remote shear loading.

Figure 29 shows numerical results using the volume integral equation method (VIEM) for the normalized shear stresses (a) $\sigma_{xy}/\sigma^{o}_{xy}$, (b) $\sigma_{xz}/\sigma^{o}_{xz}$ and (c) $\sigma_{yz}/\sigma^{o}_{yz}$ along (i) the x–axis inside (-6 mm $\leq x \leq 6$ mm) and (ii) the circumferential direction ($0^\circ \leq \theta$ (see Figure 16) $\leq 360^\circ$) of the isotropic oblate spheroidal inclusions (b/a = c/a = 0.5 where a = 6 mm) under remote shear loading, σ^{o}_{xy}, σ^{o}_{xz} and σ^{o}_{yz}. Figure 30 shows numerical solutions by the volume integral equation method for the normalized shear stresses (a) $\sigma_{xy}/\sigma^{o}_{xy}$, (b) $\sigma_{xz}/\sigma^{o}_{xz}$ and (c) $\sigma_{yz}/\sigma^{o}_{yz}$ along (i) the x–axis inside (-6 mm $\leq x \leq 6$ mm) and (ii) the circumferential direction ($0^\circ \leq \theta$ (see Figure 17) $\leq 360^\circ$) of the isotropic oblate spheroidal inclusions (b/a = c/a = 0.75 where a = 6 mm) under remote shear loading, σ^{o}_{xy}, σ^{o}_{xz} and σ^{o}_{yz}. It was determined in Figures 29 and 30 that the normalized shear stresses ($\sigma_{xy}/\sigma^{o}_{xy}$, $\sigma_{xz}/\sigma^{o}_{xz}$ and $\sigma_{yz}/\sigma^{o}_{yz}$) inside the isotropic oblate spheroidal inclusions are constant in all directions considered. Furthermore, since, as shown in Figure 26, the cross-section in the xy

plane is identical to the cross-section in the xz plane in the oblate spheroidal inclusion, the normalized shear stress, $\sigma_{xy}/\sigma^{o}{}_{xy}$, was identical to the normalized shear stress, $\sigma_{xz}/\sigma^{o}{}_{xz}$, inside the isotropic oblate spheroidal inclusion under remote shear loading.

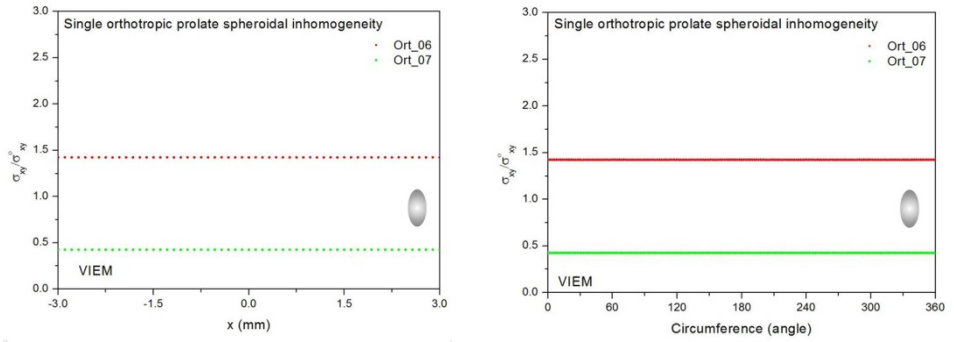

(**i**) x–axis (**ii**) circumferential direction

(**a**) Shear stress component ($\sigma_{xy}/\sigma^{o}{}_{xy}$)

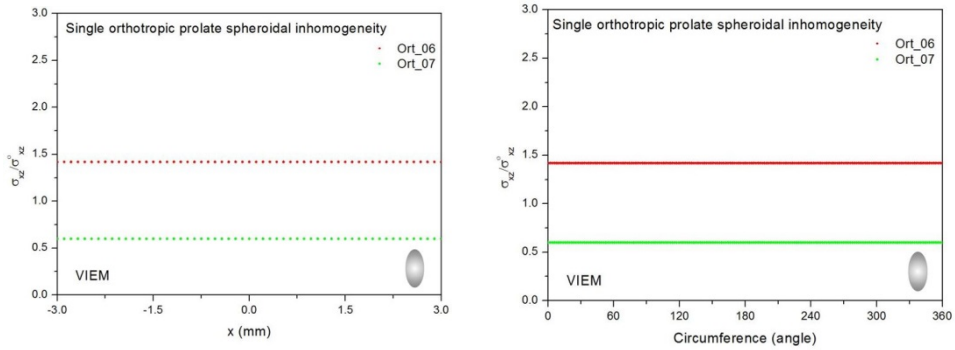

(**i**) x–axis (**ii**) circumferential direction

(**b**) Shear stress component ($\sigma_{xz}/\sigma^{o}{}_{xz}$)

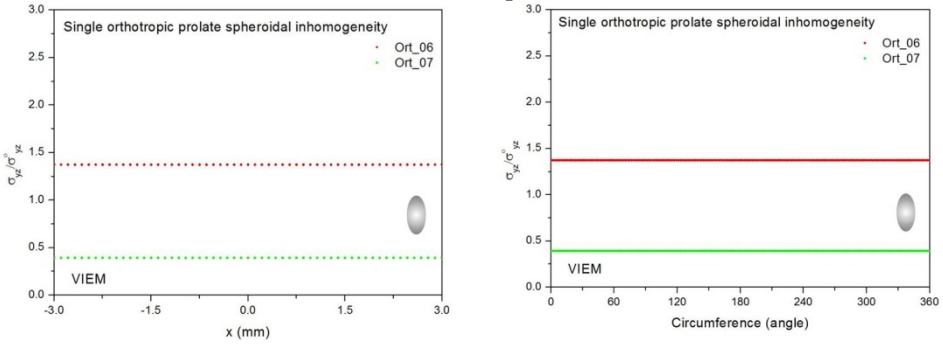

(**i**) x–axis (**ii**) circumferential direction

(**c**) Shear stress component ($\sigma_{yz}/\sigma^{o}{}_{yz}$)

Figure 27. VIEM results for the normalized shear stress components (**a**) $\sigma_{xy}/\sigma^{o}{}_{xy}$, (**b**) $\sigma_{xz}/\sigma^{o}{}_{xz}$ and (**c**) $\sigma_{yz}/\sigma^{o}{}_{yz}$ along (**i**) the x–axis inside and (**ii**) the circumferential direction of the orthotropic prolate spheroidal inclusions (Ort_06 and Ort_07) with a/b = c/b = 0.5 (b = 6 mm) under remote shear loading ($\sigma^{o}{}_{xy}$, $\sigma^{o}{}_{xz}$ and $\sigma^{o}{}_{yz}$).

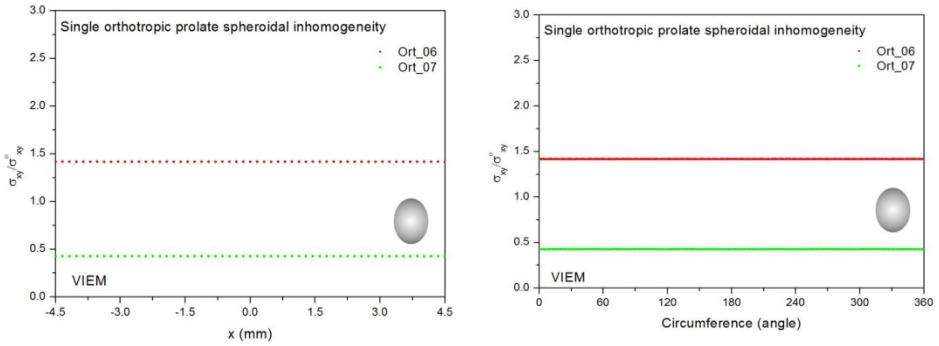

(**i**) x–axis (**ii**) circumferential direction

(**a**) Shear stress component ($\sigma_{xy}/\sigma^{o}_{xy}$)

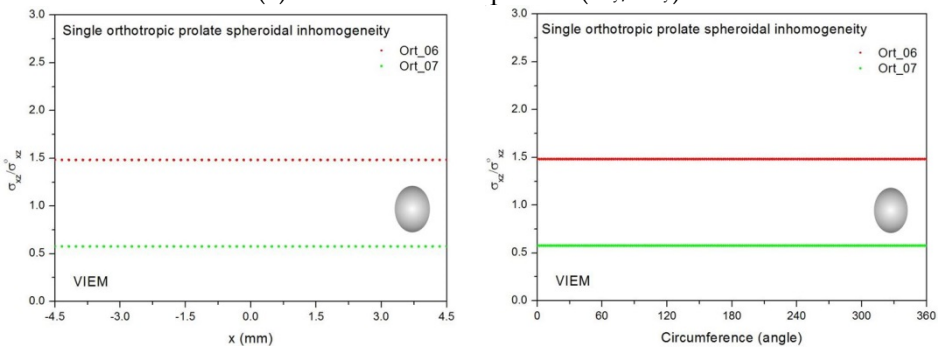

(**i**) x–axis (**ii**) circumferential direction

(**b**) Shear stress component ($\sigma_{xz}/\sigma^{o}_{xz}$)

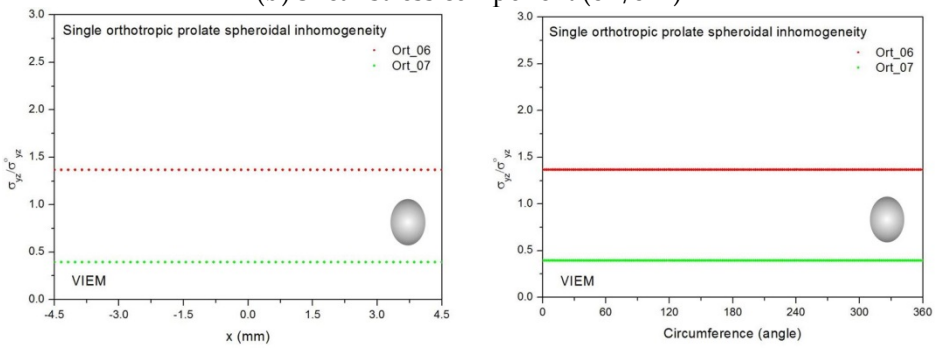

(**i**) x–axis (**ii**) circumferential direction

(**c**) Shear stress component ($\sigma_{yz}/\sigma^{o}_{yz}$)

Figure 28. VIEM results for the normalized shear stress components (**a**) $\sigma_{xy}/\sigma^{o}_{xy}$, (**b**) $\sigma_{xz}/\sigma^{o}_{xz}$ and (**c**) $\sigma_{yz}/\sigma^{o}_{yz}$ along (**i**) the x–axis inside and (**ii**) the circumferential direction of the orthotropic prolate spheroidal inclusions (Ort_06 and Ort_07) with a/b = c/b = 0.75 (b = 6 mm) under remote shear loading (σ^{o}_{xy}, σ^{o}_{xz} and σ^{o}_{yz}).

Table 22. Normalized shear stress components ($\sigma_{xy}/\sigma^{o}_{xy}$, $\sigma_{xz}/\sigma^{o}_{xz}$ and $\sigma_{yz}/\sigma^{o}_{yz}$) within the isotropic oblate spheroidal inclusion due remote shear loading (σ^{o}_{xy}, σ^{o}_{xz} and σ^{o}_{yz}).

Material	**VIEM (Average)**					
	b/a = c/a = 0.5 (See Figure 5)			**b/a = c/a = 0.75 (See Figure 5)**		
	$\sigma_{xy}/\sigma^{o}_{xy}$	$\sigma_{xz}/\sigma^{o}_{xz}$	$\sigma_{yz}/\sigma^{o}_{yz}$	$\sigma_{xy}/\sigma^{o}_{xy}$	$\sigma_{xz}/\sigma^{o}_{xz}$	$\sigma_{yz}/\sigma^{o}_{yz}$
Iso_01	1.7619	1.7619	1.5329	1.7490	1.7490	1.6214
Iso_05	1.9935	1.9935	1.6765	1.9772	1.9772	1.7972
Iso_06	0.6538	0.6538	0.7036	0.6565	0.6565	0.6820

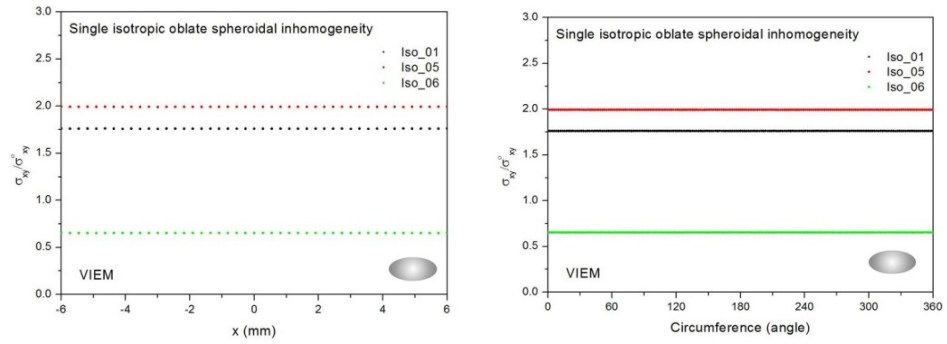

(**i**) x–axis (**ii**) circumferential direction

(**a**) Shear stress component ($\sigma_{xy}/\sigma^{o}_{xy}$)

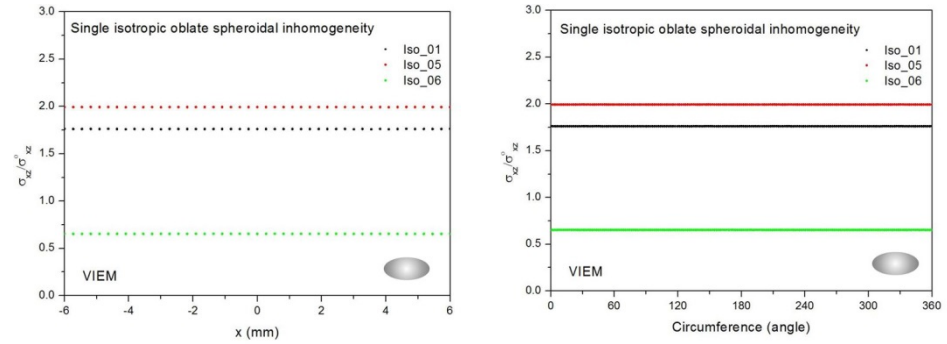

(**i**) x–axis (**ii**) circumferential direction

(**b**) Shear stress component ($\sigma_{xz}/\sigma^{o}_{xz}$)

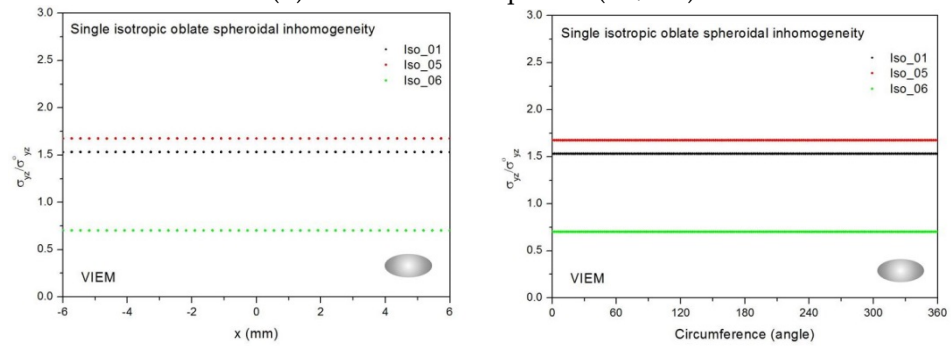

(**i**) x–axis (**ii**) circumferential direction

(**c**) Shear stress component ($\sigma_{yz}/\sigma^{o}_{yz}$)

Figure 29. VIEM results for the normalized shear stress components (**a**) $\sigma_{xy}/\sigma^{o}_{xy}$, (**b**) $\sigma_{xz}/\sigma^{o}_{xz}$ and (**c**) $\sigma_{yz}/\sigma^{o}_{yz}$ along (**i**) the x–axis inside and (**ii**) the circumferential direction of the isotropic oblate spheroidal inclusions (Iso_01, Iso_05 and Iso_06) with b/a = c/a = 0.5 (a = 6 mm) under remote shear loading (σ^{o}_{xy}, σ^{o}_{xz} and σ^{o}_{yz}).

3.4.4. A Single Orthotropic Oblate Spheroidal Inclusion

In this section, two different oblate spheroidal inclusions are considered: (a) b/a = c/a = 0.5, where a = 6 mm, and (b) b/a = c/a = 0.75, where a = 6 mm (see Figure 5). It should be noted that the length of a (=6 mm) can be arbitrarily chosen. Figures 16 and 17 show a typical discretized model for the single (a) oblate spheroidal inclusion (b/a = c/a = 0.5 where a = 6 mm) and (b) oblate spheroidal inclusion (b/a = c/a = 0.75 where a = 6 mm) used in the VIEM [31], respectively. A total of 7560 standard 20-node quadratic hexahedral elements were used for the single oblate spheroidal inclusion in Figures 16 and 17. The number of elements, 7560, was determined based on a convergence test.

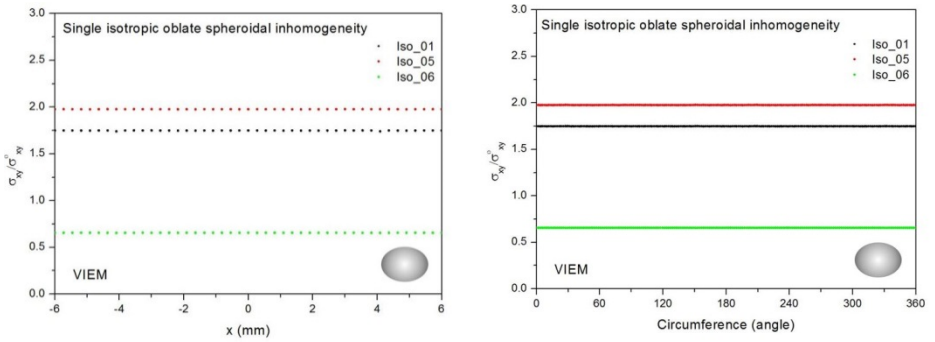

(**i**) x–axis (**ii**) circumferential direction

(**a**) Shear stress component ($\sigma_{xy}/\sigma^{o}_{xy}$)

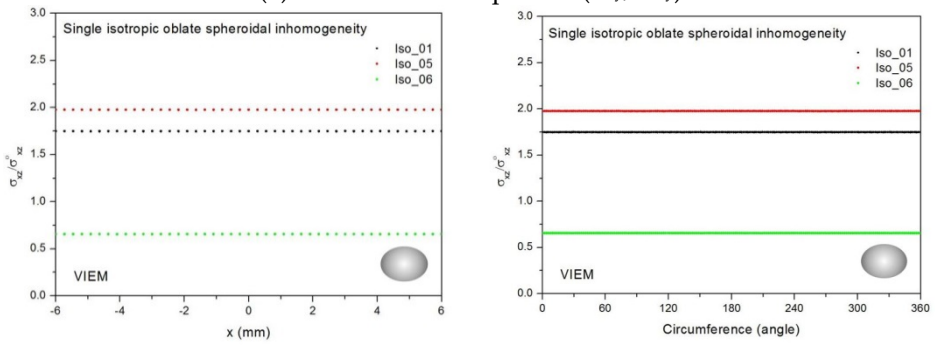

(**i**) x–axis (**ii**) circumferential direction

(**b**) Shear stress component ($\sigma_{xz}/\sigma^{o}_{xz}$)

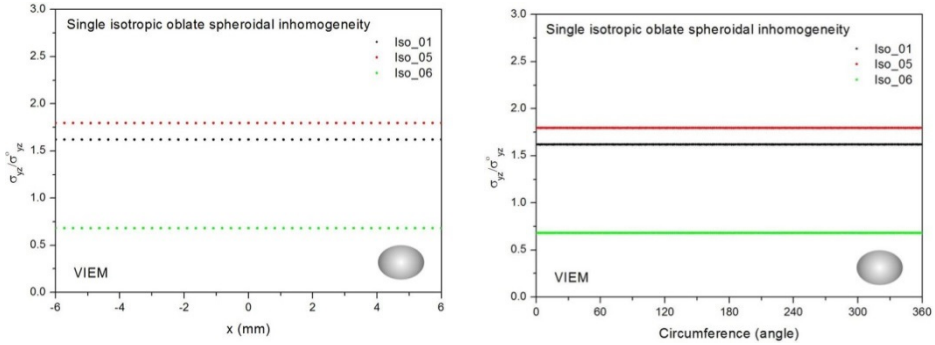

(**i**) x–axis (**ii**) circumferential direction

(**c**) Shear stress component ($\sigma_{yz}/\sigma^{o}_{yz}$)

Figure 30. VIEM results for the normalized shear stress components (**a**) $\sigma_{xy}/\sigma^{o}_{xy}$, (**b**) $\sigma_{xz}/\sigma^{o}_{xz}$ and (**c**) $\sigma_{yz}/\sigma^{o}_{yz}$ along (**i**) the x–axis inside and (**ii**) the circumferential direction of the isotropic oblate spheroidal inclusions (Iso_01, Iso_05 and Iso_06) with b/a = c/a = 0.75 (a = 6 mm) under remote shear loading (σ^{o}_{xy}, σ^{o}_{xz} and σ^{o}_{yz}).

Two different orthotropic inclusions (Ort_06 and Ort_07) in Table 4 were used in the numerical calculation. It should be noted that the VIEM results represent average values of the normalized stresses in all the nodes of the VIEM model in Figures 16 and 17. It should also be noted that the normalized shear stresses ($\sigma_{xy}/\sigma^{o}_{xy}$, $\sigma_{xz}/\sigma^{o}_{xz}$ and $\sigma_{yz}/\sigma^{o}_{yz}$) inside the orthotropic oblate spheroidal inclusions were found to be constant, respectively [1]. Table 23 shows numerical solutions by the volume integral equation method for the normalized shear stresses ($\sigma_{xy}/\sigma^{o}_{xy}$, $\sigma_{xz}/\sigma^{o}_{xz}$ and $\sigma_{yz}/\sigma^{o}_{yz}$) inside the orthotropic oblate spheroidal inclusions. For the inclusion in Ort_06, the normalized shear stresses ($\sigma_{xy}/\sigma^{o}_{xy}$, $\sigma_{xz}/\sigma^{o}_{xz}$ and $\sigma_{yz}/\sigma^{o}_{yz}$) inside the inclusion were greater than 1.0, respectively. However, for the inclusion in Ort_07, the normalized shear stresses ($\sigma_{xy}/\sigma^{o}_{xy}$, $\sigma_{xz}/\sigma^{o}_{xz}$ and $\sigma_{yz}/\sigma^{o}_{yz}$) inside the inclusion were less than 1.0, respectively. Figure 31 shows numer-

ical solutions by the volume integral equation method for the normalized shear stresses (a) $\sigma_{xy}/\sigma^{o}{}_{xy}$, (b) $\sigma_{xz}/\sigma^{o}{}_{xz}$ and (c) $\sigma_{yz}/\sigma^{o}{}_{yz}$ along (i) the x–axis inside (-6 mm $\leq x \leq 6$ mm) and (ii) the circumferential direction ($0^\circ \leq \theta$ (see Figure 16) $\leq 360^\circ$) of the orthotropic oblate spheroidal inclusions (b/a = c/a = 0.5 where a = 6 mm) under remote shear loading, $\sigma^{o}{}_{xy}$, $\sigma^{o}{}_{xz}$ and $\sigma^{o}{}_{yz}$. Figure 32 shows numerical solutions by the volume integral equation method for the normalized shear stresses (a) $\sigma_{xy}/\sigma^{o}{}_{xy}$, (b) $\sigma_{xz}/\sigma^{o}{}_{xz}$ and (c) $\sigma_{yz}/\sigma^{o}{}_{yz}$ along (i) the x–axis inside (-6 mm $\leq x \leq 6$ mm) and (ii) the circumferential direction ($0^\circ \leq \theta$ (see Figure 17) $\leq 360^\circ$) of the orthotropic oblate spheroidal inclusions (b/a = c/a = 0.75 where a = 6 mm) under remote shear loading, $\sigma^{o}{}_{xy}$, $\sigma^{o}{}_{xz}$ and $\sigma^{o}{}_{yz}$. It was determined in Figures 31 and 32 that the normalized shear stresses ($\sigma_{xy}/\sigma^{o}{}_{xy}$, $\sigma_{xz}/\sigma^{o}{}_{xz}$ and $\sigma_{yz}/\sigma^{o}{}_{yz}$) inside the orthotropic oblate spheroidal inclusions are constant in all directions considered. Furthermore, even though, as shown in Figure 26, the cross-section in the xy plane is identical to the cross-section in the xz plane in the oblate spheroidal inclusion, since c_{55} (shear modulus in the xz plane) is greater than c_{66} (shear modulus in the xy plane) and c_{66} is greater than c_{44} (shear modulus in the yz plane) in the orthotropic inclusions of the Ort_06 and Ort_07 materials, the normalized shear stress, $\sigma_{xy}/\sigma^{o}{}_{xy}$, was different from the normalized shear stress, $\sigma_{xz}/\sigma^{o}{}_{xz}$, inside the orthotropic oblate spheroidal inclusion under remote shear loading.

Table 23. Normalized shear stress components ($\sigma_{xy}/\sigma^{o}{}_{xy}$, $\sigma_{xz}/\sigma^{o}{}_{xz}$ and $\sigma_{yz}/\sigma^{o}{}_{yz}$) within the orthotropic oblate spheroidal inclusion due remote shear loading ($\sigma^{o}{}_{xy}$, $\sigma^{o}{}_{xz}$ and $\sigma^{o}{}_{yz}$).

Material	**VIEM (Average)**					
	b/a = c/a = 0.5 (See Figure 5)			**b/a = c/a = 0.75 (See Figure 5)**		
	$\sigma_{xy}/\sigma^{o}{}_{xy}$	$\sigma_{xz}/\sigma^{o}{}_{xz}$	$\sigma_{yz}/\sigma^{o}{}_{yz}$	$\sigma_{xy}/\sigma^{o}{}_{xy}$	$\sigma_{xz}/\sigma^{o}{}_{xz}$	$\sigma_{yz}/\sigma^{o}{}_{yz}$
Ort_06	1.4239	1.5808	1.2798	1.4180	1.5719	1.3175
Ort_07	0.4258	0.5477	0.4465	0.4282	0.5501	0.4226

From Figures 22–25 and 27–32 and Tables 17–22, it was determined that if the inclusion is harder than the matrix, the normalized shear stresses ($\sigma_{xy}/\sigma^{o}{}_{xy}$, $\sigma_{xz}/\sigma^{o}{}_{xz}$ and $\sigma_{yz}/\sigma^{o}{}_{yz}$) inside the inclusion are greater than 1.0, respectively. It was also determined that if the inclusion is softer than the matrix, the normalized shear stresses ($\sigma_{xy}/\sigma^{o}{}_{xy}$, $\sigma_{xz}/\sigma^{o}{}_{xz}$ and $\sigma_{yz}/\sigma^{o}{}_{yz}$) inside the inclusion are less than 1.0, respectively.

From Figure 26, notable similarities are observed for isotropic inclusions. First, the cross-section in the xy plane of the isotropic prolate spheroidal inclusion is identical to the cross-section in the yz plane and is symmetrical to the cross-sections in the xy and xz planes of the isotropic oblate spheroidal inclusion. Second, the normalized shear stress, $\sigma_{xy}/\sigma^{o}{}_{xy}$, inside the isotropic prolate spheroidal inclusion is identical to both the normalized shear stress, $\sigma_{yz}/\sigma^{o}{}_{yz}$, inside the isotropic prolate spheroidal inclusion and the normalized shear stresses, $\sigma_{xy}/\sigma^{o}{}_{xy}$ and $\sigma_{xz}/\sigma^{o}{}_{xz}$, inside the isotropic oblate spheroidal inclusion under remote shear loading. Third, the cross-section in the xz plane of the isotropic prolate spheroidal inclusion is symmetrical to the cross-section in the yz plane of the isotropic oblate spheroidal inclusion. Fourth, the normalized shear stress, $\sigma_{xz}/\sigma^{o}{}_{xz}$, inside the isotropic prolate spheroidal inclusion is identical to the normalized shear stress, $\sigma_{yz}/\sigma^{o}{}_{yz}$, inside the isotropic oblate spheroidal inclusion under remote shear loading.

In contrast, certain differences can be seen for orthotropic inclusions. First, although the cross-section in the xy plane of the orthotropic prolate spheroidal inclusion is still symmetrical to the cross-section in the xy plane of the orthotropic oblate spheroidal inclusion, it is no longer identical to the cross-section in the yz plane of the orthotropic prolate spheroidal inclusion. Second, since the cross-section in the xy plane of the orthotropic prolate spheroidal inclusion is no longer symmetrical to the cross-section in the xz plane of the orthotropic oblate spheroidal inclusion, the normalized shear stress, $\sigma_{xy}/\sigma^{o}{}_{xy}$, inside the orthotropic prolate spheroidal inclusion is only identical to the normalized shear stress, $\sigma_{xy}/\sigma^{o}{}_{xy}$, inside the orthotropic oblate spheroidal inclusion under remote shear loading.

Third, since the cross-section in the xz plane of the orthotropic prolate spheroidal inclusion is no longer symmetrical to the cross-section in the yz plane of the orthotropic oblate spheroidal inclusion, the normalized shear stress, $\sigma_{xz}/\sigma^{o}_{xz}$, inside the orthotropic prolate spheroidal inclusion is not identical to the normalized shear stress, $\sigma_{yz}/\sigma^{o}_{yz}$, inside the orthotropic oblate spheroidal inclusion under remote shear loading.

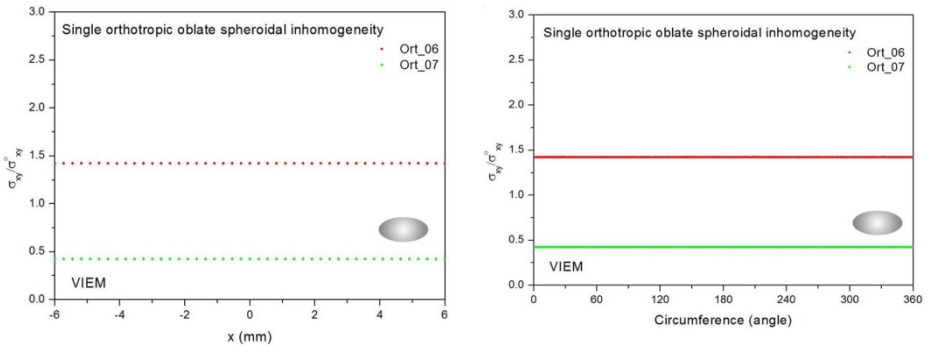

(**i**) x–axis (**ii**) circumferential direction

(**a**) Shear stress component ($\sigma_{xy}/\sigma^{o}_{xy}$)

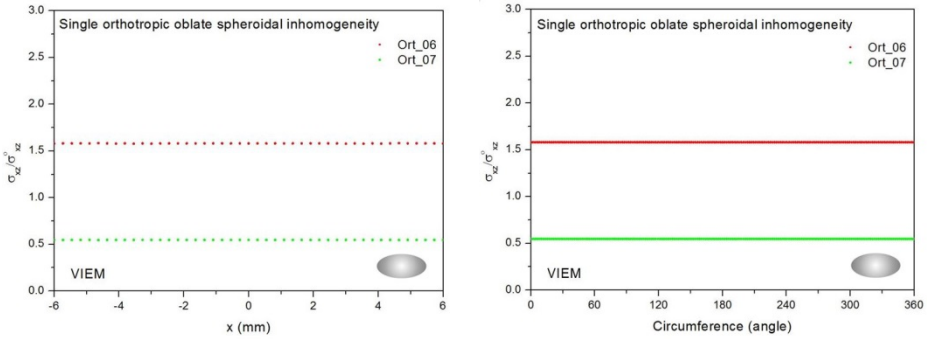

(**i**) x–axis (**ii**) circumferential direction

(**b**) Shear stress component ($\sigma_{xz}/\sigma^{o}_{xz}$)

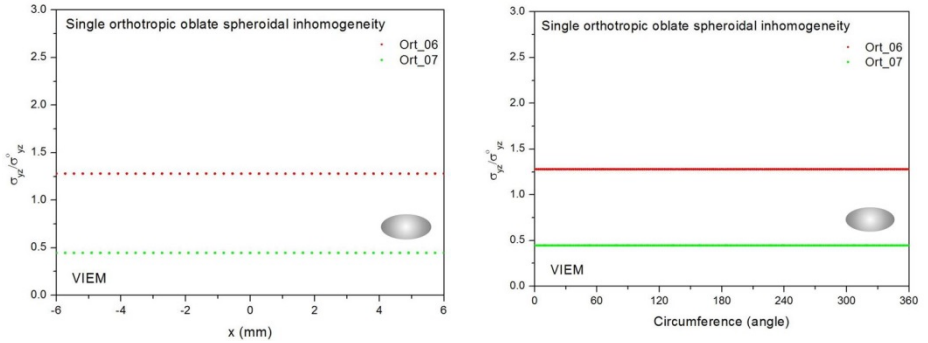

(**i**) x–axis (**ii**) circumferential direction

(**c**) Shear stress component ($\sigma_{yz}/\sigma^{o}_{yz}$)

Figure 31. VIEM results for the normalized shear stress components (**a**) $\sigma_{xy}/\sigma^{o}_{xy}$, (**b**) $\sigma_{xz}/\sigma^{o}_{xz}$ and (**c**) $\sigma_{yz}/\sigma^{o}_{yz}$ along (**i**) the x–axis inside and (**ii**) the circumferential direction of the orthotropic oblate spheroidal inclusions (Ort_06 and Ort_07) with b/a = c/a = 0.5 (a = 6 mm) under remote shear loading (σ^{o}_{xy}, σ^{o}_{xz} and σ^{o}_{yz}).

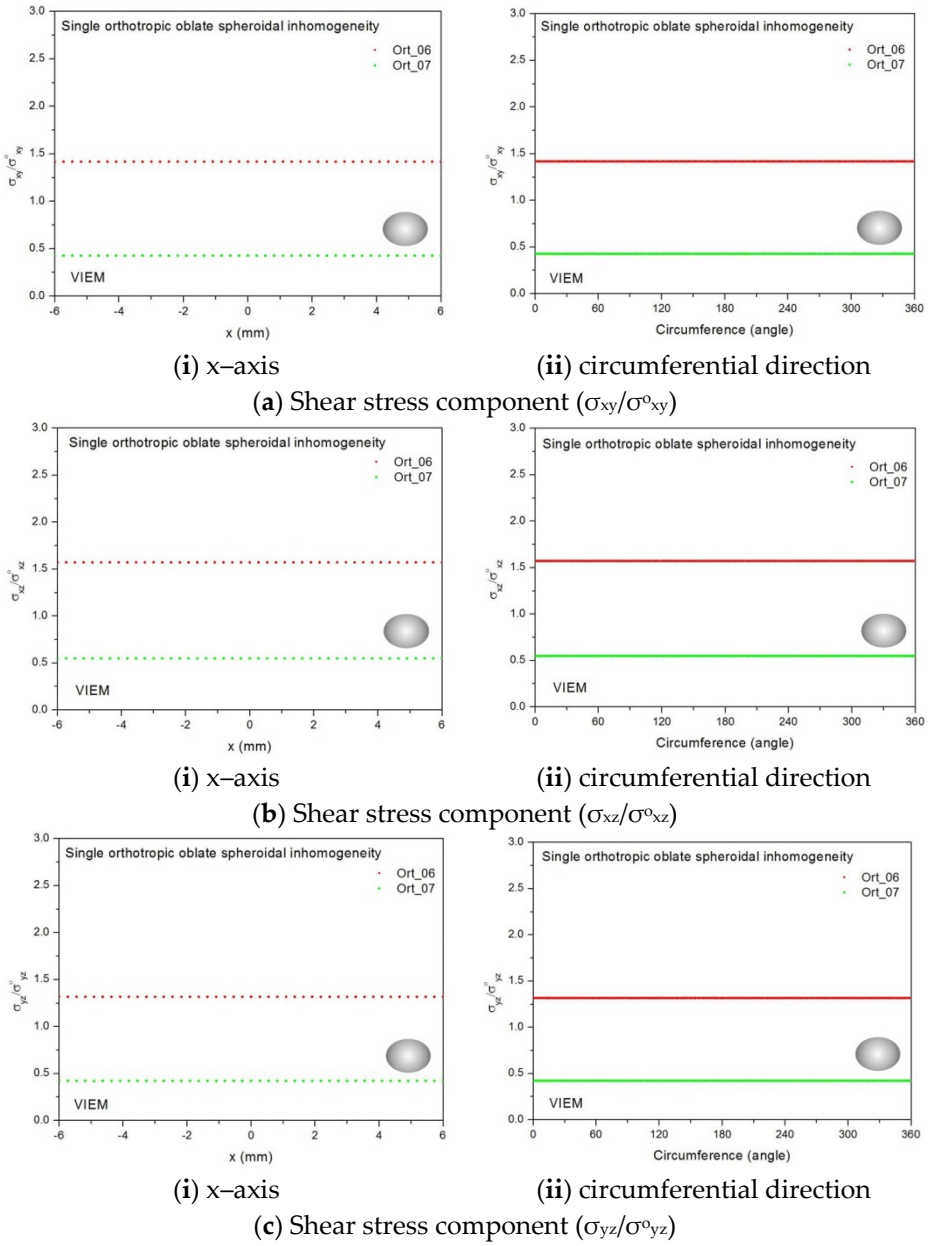

(**i**) x–axis (**ii**) circumferential direction

(**a**) Shear stress component ($\sigma_{xy}/\sigma^{o}_{xy}$)

(**i**) x–axis (**ii**) circumferential direction

(**b**) Shear stress component ($\sigma_{xz}/\sigma^{o}_{xz}$)

(**i**) x–axis (**ii**) circumferential direction

(**c**) Shear stress component ($\sigma_{yz}/\sigma^{o}_{yz}$)

Figure 32. VIEM results for the normalized shear stress components (**a**) $\sigma_{xy}/\sigma^{o}_{xy}$, (**b**) $\sigma_{xz}/\sigma^{o}_{xz}$ and (**c**) $\sigma_{yz}/\sigma^{o}_{yz}$ along (**i**) the x–axis inside and (**ii**) the circumferential direction of the orthotropic oblate spheroidal inclusions (Ort_06 and Ort_07) with b/a = c/a = 0.75 (a = 6 mm) under remote shear loading (σ^{o}_{xy}, σ^{o}_{xz} and σ^{o}_{yz}).

It should be noted that, through numerical analysis using the volume integral equation method, we could quantitatively verify two qualitative predictions: (1) the normalized shear stresses ($\sigma_{xy}/\sigma^{o}_{xy}$, $\sigma_{xz}/\sigma^{o}_{xz}$ and $\sigma_{yz}/\sigma^{o}_{yz}$) inside the orthotropic spherical inclusions are different from each other, and (2) for orthotropic spheroidal inclusions, there exists only one symmetrical cross-section when the remote loadings are shear (σ^{o}_{xy}, σ^{o}_{xz} and σ^{o}_{yz}).

It was determined that values of the normalized tensile stress ($\sigma_{xx}/\sigma^{o}_{xx}$) or the normalized shear stresses ($\sigma_{xy}/\sigma^{o}_{xy}$, $\sigma_{xz}/\sigma^{o}_{xz}$ and $\sigma_{yz}/\sigma^{o}_{yz}$) inside the isotropic spheroidal inclusions differed significantly from those inside the orthotropic spheroidal inclusions. Therefore, thorough investigation of spheroidal inclusion problems requires stress analysis for both anisotropic spheroidal inclusion problems and isotropic spheroidal inclusion problems.

We also considered multiple isotropic/anisotropic spheroidal inclusions in an infinite isotropic matrix subject to uniform remote tensile loading, σ^{o}_{xx}. In a future paper, the

authors will introduce the VIEM solutions of multiple isotropic/orthotropic spheroidal inclusions in an infinite isotropic matrix under arbitrary loading conditions. It is obvious that general characteristics of multiple isotropic/anisotropic inclusion problems cannot be fully analyzed from the basic characteristics of the corresponding single or two isotropic/anisotropic inclusion problems. Therefore, applying multiple inclusion problems to a wide class of real composite materials and structures requires extending the analysis to multiple isotropic/anisotropic inclusions of different shapes.

Both the standard finite element method (FEM) and the boundary element method (BEM) are powerful general-purpose tools in the field of numerical analysis. Since the VIEM is a combination of these two methods, it is also highly beneficial to the field of numerical analysis and can play a very important role in solving "multiple inclusion problems". The authors hope that the results using the VIEM cited in this paper will be used as benchmarked data for verifying the results of similar research using other analytical and numerical methods.

4. Conclusions

In order to introduce the VIEM as a versatile numerical method for the three-dimensional elastostatic inclusion problem, it was applied to a class of three-dimensional elastostatic inclusion problems. We first considered single isotropic/orthotropic spherical, prolate (with an aspect ratio of 0.5 and 0.75) and oblate (with an aspect ratio of 0.5 and 0.75) spheroidal inclusions in an infinite isotropic matrix under uniform remote tensile loading. Thirteen inclusions with different characteristics were considered in the numerical calculation. Excellent agreement was found between the analytical and numerical solutions using the VIEM for single isotropic spherical inclusion problems. It was determined that the normalized tensile stress ($\sigma_{xx}/\sigma^{o}{}_{xx}$) inside the isotropic/orthotropic spherical, prolate and oblate spheroidal inclusions was constant in two different directions (x–axis and circumferential direction). When the inclusion is harder than the matrix, the normalized tensile stress ($\sigma_{xx}/\sigma^{o}{}_{xx}$) inside the inclusion can be arranged in ascending order of magnitude: (1) prolate spheroidal inclusion (a/b = c/b = 0.5), (2) prolate spheroidal inclusion (a/b = c/b = 0.75), (3) sphere, (4) oblate spheroidal inclusion (b/a = c/a = 0.75) and (5) oblate spheroidal inclusion (b/a = c/a = 0.5).

We next considered single isotropic/orthotropic spherical, prolate (with an aspect ratio of 0.5 and 0.75) and oblate (with an aspect ratio of 0.5 and 0.75) spheroidal inclusions in an infinite isotropic matrix under remote shear loading. Five inclusions with different characteristics were considered in the numerical calculation. It was determined that the normalized shear stresses ($\sigma_{xy}/\sigma^{o}{}_{xy}$, $\sigma_{xz}/\sigma^{o}{}_{xz}$ and $\sigma_{yz}/\sigma^{o}{}_{yz}$) inside the isotropic/orthotropic spherical, prolate and oblate spheroidal inclusions were constant in two different directions (x–axis and circumferential direction), respectively. When the inclusion was harder than the matrix, the normalized shear stresses ($\sigma_{xy}/\sigma^{o}{}_{xy}$, $\sigma_{xz}/\sigma^{o}{}_{xz}$ and $\sigma_{yz}/\sigma^{o}{}_{yz}$) inside the inclusion were greater than 1.0, respectively. Furthermore, for isotropic spheroidal inclusions, there existed two identical or symmetrical cross-sections, while for orthotropic spheroidal inclusions, there existed only one symmetric cross-section when the remote loadings were shear ($\sigma^{o}{}_{xy}$, $\sigma^{o}{}_{xz}$ and $\sigma^{o}{}_{yz}$).

It is the authors' hope that the present solutions for various types of inclusions with different material properties under different loading conditions using the parallel volume integral equation method will be established as reference values for verifying the results of other analytical and numerical methods.

It was also determined that applying multiple inclusion problems to a wide class of real composite materials and structures requires extending the analysis to multiple isotropic/anisotropic inclusions of different numbers and shapes. The parallel volume integral equation method (PVIEM) is now generally more applicable and executable than the standard finite element or boundary element methods. Subsequently, the PVIEM can be used to calculate other quantities of practical interest in realistic models of com-

posites containing isotropic or anisotropic inclusions of arbitrary shapes under arbitrary loading conditions.

It should also be pointed out that, since the VIEM is a combination of the FEM and the BEM, it may have an unknown advantage that neither the FEM model nor the BEM model alone possess. For example, although certain VIEM models are incorrect from the point of view of the standard FEM only, they can be correctly implemented in the VIEM. In a future paper, the authors will attempt to provide more distinct examples to support this new finding. Finally, as a new machine learning-based predictive framework has been proposed for the accurate and efficient evaluation of singular integrals in the boundary element method (BEM) [32], of particular interest to researchers going forward will be the development of a general-purpose machine learning framework for predicting singular integrals [29] in the volume integral equation method.

Author Contributions: Conceptualization, J.L.; Methodology, J.L.; VIEM analysis, J.L.; Investigation, J.L. and M.H.; Validation, J.L. and M.H.; Software, J.L. and M.H.; Writing—original draft preparation, J.L.; FEM modeling, M.H.; Supervision, J.L. All authors have read and agreed to the published version of the manuscript.

Funding: This research was supported by the Basic Science Research Program through the National Research Foundation of Korea (NRF) funded by the Ministry of Science and ICT, Republic of Korea (Grant No. 2015-R1A2A2A01004531), and the 2020 Hongik University Research Fund. The authors would also like to acknowledge the support of the National Supercomputing Center with supercomputing resources, including technical support (No. KSC-2020-CRE-0107).

Institutional Review Board Statement: Not applicable.

Informed Consent Statement: Not applicable.

Data Availability Statement: The data presented in this study are available upon request from the corresponding author.

Acknowledgments: The authors would like to express their sincere appreciation to Kyunghun Lim for parallelizing and optimizing the three-dimensional VIEM code and Oh-Kyoung Kwon for applying the domain decomposition method to the parallel three-dimensional VIEM code.

Conflicts of Interest: The authors declare no conflict of interest.

References

1. Eshelby, J.D. The determination of the elastic field of an ellipsoidal inclusion, and related problems. *Proc. R. Soc. A* **1957**, *241*, 376–396.
2. Eshelby, J.D. The force on an elastic singularity. *Philos. Trans. R. Soc. A* **1951**, *244*, 87–112.
3. Bose, S.K.; Mal, A.K. Elastic waves in a fiber-reinforced composite. *J. Mech. Phys. Solids* **1974**, *22*, 217–229. [CrossRef]
4. Maslov, B.P. Stress concentration in an isotropic matrix bonded by anisotropic fibers. *Sov. Appl. Mech.* **1987**, *23*, 963–969. [CrossRef]
5. Yang, R.B.; Mal, A.K. The effective transverse moduli of a composite with degraded fiber-matrix interfaces. *Int. J. Eng. Sci.* **1995**, *33*, 1623–1632. [CrossRef]
6. Tsukrov, I.; Kachanov, M. Effective moduli of an anisotropic material with elliptical holes of arbitrary orientational distribution. *Int. J. Solids Struct.* **2000**, *37*, 5919–5941. [CrossRef]
7. Shen, L.; Yi, S. An effective inclusion model for effective moduli of heterogeneous materials with ellipsoidal inhomogeneities. *Int. J. Solids Struct.* **2001**, *38*, 5789–5805. [CrossRef]
8. Vilchevskaya, E.; Sevostianov, I. Effective elastic properties of a particulate composite with transversely-isotropic matrix. *Int. J. Eng. Sci.* **2015**, *94*, 139–149. [CrossRef]
9. Lee, J.K.; Mal, A.K. A volume integral equation technique for multiple inclusion and crack interaction problems. *J. Appl. Mech.—Trans. ASME* **1997**, *64*, 23–31. [CrossRef]
10. Lee, J.K.; Mal, A.K. A volume integral equation technique for multiple scattering problems in elastodynamics. *Appl. Math. Comput.* **1995**, *67*, 135–159. [CrossRef]
11. Lee, J.; Kim, H. Volume integral equation method for multiple circular and elliptical inclusion problems in antiplane elastostatics. *Compos. B Eng.* **2012**, *43*, 1224–1243. [CrossRef]
12. Mal, A.K.; Knopoff, L. Elastic wave velocities in two component systems. *J. Inst. Math. Appl.* **1967**, *3*, 376–387. [CrossRef]
13. Lee, J.K.; Lee, H.C.; Jeong, H.G. Multiple scattering using parallel volume integral equation method: Interaction of SH waves with multiple multilayered anisotropic elliptical inclusions. *Math. Probl. Eng.* **2015**, *2015*, 809320. [CrossRef]

14. Lee, J.K.; Oh, S.M.; Mal, A. Calculation of interfacial stresses in composites containing elliptical inclusions of various types. *Eur. J. Mech. A Solid.* **2014**, *44*, 17–40. [CrossRef]
15. Lee, J.K.; Lee, H.M.; Mal, A. A mixed volume and boundary integral equation technique for elastic wave field calculations in heterogeneous materials. *Wave Motion* **2004**, *39*, 1–19. [CrossRef]
16. Lee, J.K.; Lee, H.C.; Jeong, H.G. Numerical analysis of SH wave field calculations for various types of a multilayered anisotropic inclusion. *Eng. Anal. Bound. Elem.* **2016**, *64*, 38–67. [CrossRef]
17. Lee, J.K.; Han, M.G. Three-dimensional volume integral equation method for solving isotropic/anisotropic inhomogeneity problems. *Mathematics* **2020**, *8*, 1866. [CrossRef]
18. Buryachenko, V.A. *Micromechanics of Heterogeneous Materials*; Springer: New York, NY, USA, 2007.
19. Buryachenko, V.A.; Bechel, V.T. A series solution of the volume integral equation for multiple-inclusion interaction problems. *Compos. Sci. Technol.* **2000**, *60*, 2465–2469. [CrossRef]
20. Buryachenko, V.A. Solution of general integral equations of micromechanics of heterogeneous materials. *Int. J. Solids Struct.* **2014**, *51*, 3823–3843. [CrossRef]
21. Dong, C.Y.; Lo, S.H.; Cheung, Y.K. Numerical solution of 3D elastostatic inclusion problems using the volume integral equation method. *Comput. Methods Appl. Mech. Eng.* **2003**, *192*, 95–106. [CrossRef]
22. Michopoulos, J.G.; Rosen, D.W.; Paredis, C.J.; Vance, J.M. (Eds.) *Advances in Computers and Information in Engineering Research*; ASME Press: New York, NY, USA, 2021; Volume 2.
23. Ma, J.; Nie, Z. FEM-DDM with an efficient second-order transmission condition in both high-frequency and low-frequency applications. *Prog. Electromagn. Res. B* **2013**, *50*, 253–271. [CrossRef]
24. Jasiuk, I.; Sheng, P.Y.; Tsuchida, E. A spherical inclusion in an elastic half-space under shear. *J. Appl. Mech.—Trans. ASME* **1997**, *64*, 471–479. [CrossRef]
25. Lovald, S.T.; Wagner, J.D.; Baack, B. Biomechanical optimization of bone plates used in rigid fixation of mandibular fractures. *J. Oral. Maxillofac. Surg.* **2009**, *67*, 973–985. [CrossRef]
26. Banerjee, P.K. *The Boundary Element Methods in Engineering*; McGraw-Hill: New York, NY, USA, 1993.
27. Pao, Y.-H.; Varatharajulu, V. Huygens' principle, radiation conditions, and integral formulas for the scattering of elastic waves. *J. Acoust. Soc. Am.* **1976**, *59*, 1361–1369. [CrossRef]
28. Lee, K.J.; Mal, A.K. A boundary element method for plane anisotropic elastic media. *J. Appl. Mech.—Trans. ASME* **1990**, *57*, 600–606. [CrossRef]
29. Li, H.B.; Han, G.M.; Mang, H.A. A new method for evaluating singular integrals in stress analysis of solids by the direct boundary element method. *Int. J. Numer. Methods Eng.* **1985**, *21*, 2071–2098. [CrossRef]
30. Shibata, M.; Ono, K. Stress concentration due to a prolate spheroidal inclusion. *J. Compos. Mater.* **1978**, *12*, 132–138. [CrossRef]
31. *PATRAN User's Manual*; Version 2008 r2; MSC/PATRAN: Santa Ana, CA, USA, 2008.
32. Li, Y.; Mao, W.; Wang, G.; Liu, J.; Wang, S. A general-purpose machine learning framework for predicting singular integrals in boundary element method. *Eng. Anal. Bound. Elem.* **2020**, *117*, 41–56. [CrossRef]

materials

MDPI

Article

Simulation of PLC Effect Using Regularized Large-Strain Elasto-Plasticity

Marzena Mucha *, Balbina Wcisło and Jerzy Pamin

Chair for Computational Engineering, Faculty of Civil Engineering, Cracow University of Technology, Warszawska 24, 31-155 Cracow, Poland; balbina.wcislo@pk.edu.pl (B.W.); jerzy.pamin@pk.edu.pl (J.P.)
* Correspondence: marzena.mucha@pk.edu.pl

Abstract: The purpose of this paper is to develop a constitutive description and to numerically simulate a propagating instability phenomenon called the Portevin–Le Chatelier (PLC) effect, which is observed for metallic materials. It manifests itself by moving plastic shear bands in the sample and serrations in the stress–strain diagram. In this paper, the PLC is modeled by geometrically non-linear thermo-visco-plasticity with the hardening function of the Estrin–McCormick type to reproduce a serrated response. To regularize softening, which in this model comes from thermal, geometrical and strain-rate effects, the viscosity and heat conductivity are incorporated. Plasticity description can additionally include degradation of the yield strength, and then the model is enhanced by higher-order gradients. Simulations are performed using AceGen/FEM. Two tensioned specimens are tested: a rod and a dog-bone sample. The first specimen is used for general verification. The results obtained for the second specimen are compared with the experimental results. Studies for different values of model parameters are performed. The results of the simulations are in good agreement with the experimental outcome and the sensitivity to model parameters is in line with the expectations for the pre-peak regime. In the presented tests, the gradient enhancement does not significantly influence the results.

Keywords: PLC effect; visco-plasticity; thermo-mechanical coupling; gradient enhancement; FEM

Citation: Mucha, M.; Wcisło, B.; Pamin, J. Simulation of PLC Effect Using Regularized Large-Strain Elasto-Plasticity. *Materials* **2022**, *15*, 4327. https://doi.org/10.3390/ma15124327

Academic Editor: Raimondo Luciano, Carmelo Majorana, Angelo Marcello Tarantino and Michele Bacciocchi

Received: 12 May 2022
Accepted: 10 June 2022
Published: 18 June 2022

1. Introduction

The Portevin–Le Chatelier (PLC) effect is an instability phenomenon that manifests itself in bands of localized plastic strain rate, propagating along a stressed specimen. It is related to stress jumps (serrations) in the load-displacement diagram, which represents a specimen response under tension or shear. The source of this behaviour lies in the microstructure evolution, in particular at the level of dislocation motion. It is specifically exhibited by steel and aluminium alloys and occurs for a certain range of strain rates and temperatures. The PLC can reduce ductility and formability of alloys; hence, its analysis is of both theoretical and practical importance.

The plastic flow in metals and alloys can be explained by nucleation and motion of dislocations. The motion can be blocked by other dislocations, causing dislocation pile-up which can be unlocked by a sufficiently large strain. In solid solutions, dislocations can also be stopped by diffused solute atoms. The dislocation pinning by the solutes, repeatedly followed by unpinning, produces instabilities in the plastic flow. They occur as serrations in the stress–strain diagram, related to the motion (or repeated occurrence and vanishing) of localized strain-rate bands along a stressed specimen.

The micro-structural phenomenon responsible for the PLC effect is so-called Dynamic Strain Aging (DSA) [1,2]. As explained above, DSA is related to dynamic interactions between the motion of mobile dislocations and the diffusion of solute atoms. The recurring decrease in the concentration of solute atoms at temporarily arrested dislocations is represented by a reduction in solute contribution to the flow stress.

The PLC effect was first reported by [3]. Experimental studies and analytical models of propagative instabilities, in particular of Lueders bands and the Portevin–Le Chatelier effect, were discussed in [4]. An extensive numerical study of the phenomena using small-strain isothermal elasto-plasticity models is provided in [5,6]. Finite element models of the PLC effect are analyzed there in the context of regularized dynamics. An overview of the experiments showing the PLC phenomenon, including a classification of its types, is presented in [7]. Experimental analysis and modeling of the three types is performed in [8]. A review of modeling options for the phenomenon is provided in [9].

The PLC effect can be described, among others, by the Estrin–McCormick model [10–13]. In [10], the model is derived; in [11,12], it is applied in small-strain FE simulations of the phenomenon. In [13], the model is implemented within a large strain model of elasto-plasticity, including parameter identification for an aluminium alloy based on experiments on tensile specimens under loading with different rates.

In recent years, several scientists have considered the phenomenon in their theoretical, experimental and numerical studies. In particular, steel specimens were examined in [14–18] (the last paper covers an experimental study of the PLC phenomenon in high-strength steel) and aluminium alloys in a larger number of works; for instance, [13,19–22].

The majority of specimens used in the studies were rectangular or dog-bone shape tensile plates (see [8,13,15,19,20,23]), sometimes notched (e.g., [17]), and tensile rods with circular cross-section (see for instance [23]). Some studies concerned shear specimens [21,24,25]. Several papers compare the experimental response (in some cases monitored using the DIC technique) with simulation results; see, for instance [17,19,22,26–28]. The final failure, involving necking and fracture, was examined in [15]. Moreover, in some papers, the influence of loading/strain rate has been examined, see [8,13,20,24,29].

A few studies considered temperature dependence of the PLC effect. These were [20,25,30,31]. The simulation of the temperature-dependent process zone at the crack tip was in the focus of [14]. Finally, it is mentioned that a constitutive model of discontinuous plastic flow for materials deformed at cryogenic temperatures was developed in [32] and further considered in [33]. In fact, these papers and the present one belong to the broad field of research on thermo-mechanics of heterogeneous/composite materials and structures. The thermo-mechanical couplings are constantly a subject of intensive scientific activity; see, for instance [34–41].

In the present paper, the PLC effect is simulated using a formulation of geometrically non-linear thermo-plasticity developed in [42,43]. The model includes full thermo-mechanical coupling involving thermal expansion, plastic heating, thermal softening in the plasticity function, and Fourier's law in the deformed configuration. Following [44,45], the thermo-elastic coupling is neglected in the energy balance because it is relatively insignificant for the metallic materials under consideration.

The plasticity description is based on [46] and includes the Huber–Mises–Hencky yield criterion. This model was recently extended to visco-plasticity and was employed by the authors to simulate Lueders bands in [47]. The rate-dependent hardening function of the Estrin–McCormick type, described in [13], is used to simulate DSA and the serrations induced by strain-rate softening, but it is enhanced with temperature dependence of the characteristic time of solute diffusion.

The models are implemented in an AceGen code generator developed in [48] within Wolfram Mathematica. One of the aims of the research is to examine the influence of temperature and strain rates on the PLC phenomenon, and the importance of regularization in the models involving recurring strain-rate-softening phases. It is stressed here that the stabilizing effect is provided by viscosity and heat conduction, but can also be provided by a gradient enhancement.

The paper is organized as follows. In Section 2, the theory of large strain thermo-visco-plasticity is summarized and then extended to include the Estrin–McCormick component of the yield strength, which makes it possible to simulate the PLC effect. Interest is limited to tension and moderate temperatures (20–200 degrees Celsius). A gradient enhancement

of the model is optionally incorporated to regularize the softening involved in the model. In Section 3 the coupled balance equations are presented in local and weak forms, and then the implementation of the model in AceGen/FEM for Mathematica is briefly discussed. In Section 4, the simulation results are presented. First, a one-dimensional rod model is considered and detailed response is shown for one serration. Then, a series of simulations for a dog-bone specimen under tension is presented. The computed model is based on the experimental research on aluminium dog-bone-type specimens, presented in [49]. Comparisons with laboratory test results are made, and some parametric studies are performed. Finally, in Section 5 some conclusions are drawn and directions of future work are proposed.

2. Brief Description of Constitutive Models

2.1. Thermo-Visco-Plasticity

The material models used in this paper for the simulation of the PLC-type instabilities are described below. They are based on the large-strain description of elasto-plasticity [13,45,50,51].

The starting point of the formulation is standard. We consider a continuous deformable body and its material is assumed to be initially isotropic. Vector $\mathbf{X}$ identifies the reference location of a body particle at time $t = 0$ and in initial temperature T_0 (T_0 is assumed to be the reference temperature for a strain-free state), vector $\mathbf{x}$ points to the current position of the particle at time t and in temperature T. The motion of the body is described by function $\mathbf{x} = \boldsymbol{\varphi}(\mathbf{X}, t, T)$. The classical definition of the deformation gradient $\mathbf{F}$ is recalled:

$$\mathbf{F} = \frac{\partial \boldsymbol{\varphi}(\mathbf{X}, t, T)}{\partial \mathbf{X}}. \tag{1}$$

A multiplicative decomposition of $\mathbf{F}$ into mechanical and thermal parts denoted by $\mathbf{F}^m$ and $\mathbf{F}^\theta$, respectively, is performed [45,52]. In turn, $\mathbf{F}^m$ is decomposed into elastic and plastic factors $\mathbf{F}^e$ and $\mathbf{F}^p$ (see [53–55])

$$\mathbf{F} = \mathbf{F}^m\mathbf{F}^\theta = \mathbf{F}^e\mathbf{F}^p\mathbf{F}^\theta. \tag{2}$$

The thermal factor $\mathbf{F}^\theta$ is assumed to be purely volumetric and defined as

$$\mathbf{F}^\theta = (J^\theta)^{1/3}\mathbf{I}, \qquad J^\theta = \det(\mathbf{F}^\theta), \tag{3}$$

where $\mathbf{I}$ is the second-order identity tensor. The volumetric deformation caused by the temperature change $T - T_0$ is represented by [55]

$$J^\theta = \exp[3\alpha_T(T - T_0)], \tag{4}$$

where α_T is the coefficient of linear thermal expansion. Based on Equations (2) and (4) the mechanical part of the deformation gradient is derived as

$$\mathbf{F}^m = \exp[-\alpha_T(T - T_0)]\mathbf{F}. \tag{5}$$

For the classical thermo-plasticity theory, the Helmholtz potential calculated per unit volume in the reference configuration is decomposed into elastic, plastic, and purely thermal components (see [45,50])

$$\psi(\mathbf{b}^e, \alpha, T) = \psi^e(\mathbf{b}^e) + \psi^p(\alpha) + \psi^\theta(T). \tag{6}$$

The following definitions of the potential parts are employed.

$$\psi^e(\mathbf{b}^e) = \frac{1}{2}G\left[\mathrm{tr}(\det(\mathbf{b}^e)^{-1/3}\mathbf{b}^e) - 3\right] + \frac{1}{2}K\ln(J^e)^2, \tag{7}$$

$$\psi^p(\alpha) = (\sigma_{yf} - \sigma_{y0})\left[\alpha + \frac{\exp(-\delta\alpha)}{\delta}\right], \tag{8}$$

$$\psi^{\theta}(T) = c\left[(T - T_0) - T\ln\left(\frac{T}{T_0}\right)\right]. \tag{9}$$

In Equation (7), G and K are shear and bulk elastic moduli, $\mathbf{b}^e = \mathbf{F}^e(\mathbf{F}^e)^{\mathrm{T}}$ is the elastic left Cauchy–Green tensor, and $J^e = \det(\mathbf{F}^e)$.

The second component of the free energy represents plastic hardening and is assumed in the form relevant for saturation-type hardening with a scalar equivalent plastic strain α, σ_{y0} is an initial yield strength, σ_{yf} is a final yield strength, and δ is a saturation constant. In general, ψ^p depends on adopted hardening specification. Moreover, in Equation (9), c is the heat capacity per unit of volume. According to [46] it can be defined as $c = -T\frac{\partial^2\psi}{\partial T^2}$ and therefore for the adopted form of free energy, c is constant.

The Kirchhoff stress tensor $\boldsymbol{\tau}$ and hardening function $h(\alpha)$ are derived from the free energy potential

$$\boldsymbol{\tau} = 2\frac{\partial\psi}{\partial\mathbf{b}^e}\mathbf{b}^e, \qquad h = \frac{\partial\psi}{\partial\alpha}. \tag{10}$$

The constitutive relation for heat conduction is the classical Fourier law for isotropic materials. It is formulated according to [46] using the Kirchhoff heat flux vector $\mathbf{q}$

$$\mathbf{q} = -k\nabla T, \tag{11}$$

where k is a heat conduction coefficient specified in the reference configuration and ∇T is a spatial gradient of temperature.

Further, the plasticity formulation is specified. The yield function is defined as

$$F_p(\boldsymbol{\tau}, \alpha, \dot{\alpha}) = f(\boldsymbol{\tau}) - \sigma_y(\alpha, \dot{\alpha}) \leq 0, \tag{12}$$

where $f(\boldsymbol{\tau})$ is the Huber–Mises–Hencky (HMH) stress measure and σ_y represents the evolving yield strength (flow stress) for the rate-dependent (viscoplastic) model, which is the starting point of the derivation. The viscoplasticy formulation follows the consistency concept, cf. [5]. The particular forms of σ_y will be discussed in the next section for the Estrin–McCormick visco-plasticity model and a gradient-enhanced version of the model. The following definitions are used

$$f(\boldsymbol{\tau}) = \sqrt{2J_2}, \tag{13}$$

$$J_2 = \frac{1}{2}\boldsymbol{\tau}_{dev}^2 \cdot \mathbf{I}, \tag{14}$$

where $\boldsymbol{\tau}_{dev}$ is deviatoric part of the Kirchhoff stress tensor and $\mathbf{I}$ is the second order unit tensor.

The yield function presented in Equation (12) has a general form which can easily be modified to apply another yield criterion. The Huber–Mises–Hencky function is chosen in the work because it describes the behaviour of metals satisfactorily. This form of stress measure is independent of the hydrostatic pressure, which implies the isochoric plastic flow. In this approach, the volumetric-deviatoric split of large-strain measures does not need to be incorporated in the description. It is worth mentioning that the volume of the material can change due to thermal expansion and elastic deformation.

Following [50], the associated flow rule is adopted for the Lie derivative of $\mathbf{b}^e$

$$-\frac{1}{2}\mathcal{L}_v\mathbf{b}^e = \dot{\gamma}\frac{\partial F_p}{\partial\boldsymbol{\tau}}\mathbf{b}^e, \tag{15}$$

where $\dot{\gamma}$ denotes the plastic multiplier satisfying the standard Kuhn–Tucker conditions:

$$\dot{\gamma} \geq 0, \qquad F_p \leq 0, \qquad \dot{\gamma}F_p = 0. \tag{16}$$

According to [56], the plastic multiplier plays the role of the plastic strain measure according to the relation

$$\dot{\alpha} = \sqrt{2/3}\dot{\gamma}. \tag{17}$$

2.2. Estrin–McCormick Model with Optional Gradient Enhancement

The Estrin–McCormick model (further called the McCormick model or the EMC model in brief) is a phenomenological description of DSA based on an internal variable called effective strain aging time t_a, cf. [10,12,13]. The evolution of t_a introduces repeated negative strain-rate dependence, causing the serrations related to nucleating and propagating localization bands.

In this paper, the model is extended to include temperature dependence, cf. [9,25]. The yield function is defined as

$$F_p(\boldsymbol{\tau}, \alpha, \dot{\alpha}, t_a, T) = f(\boldsymbol{\tau}) - \sqrt{2/3}\sigma_y(\alpha, \dot{\alpha}, t_a, T) \leq 0. \tag{18}$$

It is assumed for simplicity that the standard hardening has a saturation character, viscosity does not depend on temperature, and thermal softening is linear. The yield strength σ_y depends on equivalent plastic strain α, its rate $\dot{\alpha}$, strain aging time t_a, and temperature T. It has three components related to strain hardening σ_H, strain rate sensitivity σ_V, and dynamic strain aging σ_B:

$$\sigma_y(\alpha, \dot{\alpha}, t_a, T) = \sigma_H(\alpha, T) + \sigma_V(\dot{\alpha}) + \sigma_B(\alpha, t_a, T). \tag{19}$$

The first component represents the saturation hardening scaled by a thermal softening factor

$$\sigma_H(\alpha) = \Big[\sigma_{y0} + (\sigma_{yf} - \sigma_{y0})(1 - \exp(-\delta\alpha)\Big][1 - H_T(T - T_0)]. \tag{20}$$

The part $(1 - H_T(T - T_0))$ corresponds to linear thermal softening, and H_T is a thermal softening modulus. Alternative formulae for thermal softening and their discussion in the context of strain localization simulations can be found in [57].

The second component of the yield strength introduces positive strain rate influence (ξ is viscosity parameter)

$$\sigma_V(\dot{\alpha}) = \xi\dot{\alpha}. \tag{21}$$

It is noted that the time derivative of α in the viscous term $\xi\dot{\alpha}$ in Equation (21) is computed using the backward Euler scheme as follows

$$\dot{\alpha} = \frac{\alpha_n - \alpha_{n-1}}{\Delta t}, \tag{22}$$

where α_n and α_{n-1} denote the values of the equivalent plastic strain at the current and previous time moments, respectively, and Δt is a time step.

The third component represents the influence of the DSA according to [13]

$$\sigma_B(t_a, \alpha) = \sigma_{B0}(\alpha)\left[1 - \exp\left(-\frac{t_a}{t_0}\right)^n\right]. \tag{23}$$

The formula particularly expresses the solute concentration at temporarily stopped mobile dislocations, which involves negative strain-rate sensitivity. It is driven by the strain aging time t_a. Moreover, t_0 is the characteristic time for the solute diffusion, which determines how fast the saturation of hardening component σ_B is reached. The saturation factor σ_{B0} (the maximum value of contribution σ_B) is assumed to depend linearly on the accumulated plastic strain measure α:

$$\sigma_{B0} = \sigma_{B00} + \sigma'_{B00}\alpha, \tag{24}$$

where σ_{B00} and σ'_{B00} are model parameters as well as exponent n in Equation (23).

The strain aging time t_a is related to a waiting time t_w (which a dislocation spends at an obstacle) by the differential equation:

$$\dot{t}_a = 1 - \frac{t_a}{t_w}, \tag{25}$$

where the waiting time is related to the plastic strain rate $\dot{\alpha}$

$$t_w = \frac{\Omega(\alpha)}{\dot{\alpha}}, \tag{26}$$

and the plastic strain increment Ω associated with the motion of dislocations between two obstacles (pinned configurations) is also assumed to depend linearly on α:

$$\Omega(\alpha) = \Omega_0 + \Omega_0' \alpha. \tag{27}$$

In the above equation Ω_0 and Ω_0' are model parameters.

Algorithmically, the evolution of t_a depends on the plastic strain increment $\Delta\alpha$ and can be computed for time increments as follows [13]:

$$t_a = \frac{t_a^n + \Delta t}{1 + \frac{\Delta\alpha}{\Omega(\alpha^n + \Delta\alpha)}}, \tag{28}$$

where the plastic strain rate $\dot{\alpha}$ has been approximated according to Equation (22).

Now, the model depends on temperature in a couple of ways: due to thermal expansion, plastic heating and thermal softening. It is assumed that only the basic mechanical parameters (Young modulus, initial and final yield strength) depend on temperature. Additionally, to examine the sensitivity of the McCormick model to temperature, the following dependence of parameter t_0 on temperature is assumed:

$$t_0(T) = t_{02} \exp(t_{01} T). \tag{29}$$

The parameters of this function t_{01} and t_{02} have been determined on the basis of experimental results presented in [25].

It is emphasized that, next to thermal softening assumed in Equation (20) and strain-rate softening present in Equation (23), geometrical softening due to large deformations is also present in the description; see, for instance, [58]. This version of the McCormick model incorporates two regularizing effects, i.e., rate dependence and heat conduction.

In more detailed material modeling, the first component of the yield strength can additionally include a damage-type reduction to represent an increasing porosity of the material related to large strains and leading to fracture. This extension of the model is here based on [51] where a reducing factor $\exp(-\beta z)$ decays from one to zero with increasing material degradation (β is a ductility parameter) and scales the hardening part of the yield strength. In the local version of the model, z would be taken equal to α; however, to control the influence of the degradation coefficient on the plastic strain localization process z is rather an averaged plastic strain measure, obtained from the following averaging equation [59]

$$z - l^2 \nabla_0^2 z = \alpha, \tag{30}$$

in which l is an internal length scale and, since so-called Lagrange averaging is employed according to [60], ∇_0 is the gradient operator in the material description. Homogeneous natural boundary conditions are assumed for Equation (30).

The yield function then reads

$$F_p(\boldsymbol{\tau}, \alpha, \dot{\alpha}, z, t_a, T) = f(\boldsymbol{\tau}) - \sqrt{2/3}\sigma_y(\alpha, \dot{\alpha}, z, t_a, T) \leq 0, \tag{31}$$

and the flow stress depends on equivalent plastic strain α, its rate $\dot{\alpha}$, (non-local) degradation parameter z, strain aging time t_a, and temperature T

$$\sigma_y(\alpha, \dot{\alpha}, z, t_a, T) = \sigma_H(\alpha, z, T) + \sigma_V(\dot{\alpha}) + \sigma_B(\alpha, t_a, T), \tag{32}$$

where

$$\sigma_H(\alpha) = \Big[(\sigma_{y0} + (\sigma_{yf} - \sigma_{y0})(1 - \exp(-\delta\alpha))\Big] \exp(-\beta z)[1 - H_T(T - T_0)], \tag{33}$$

represents saturation hardening scaled by the degradation coefficient $\exp(-\beta z)$ and by the linear thermal softening factor $1 - H_T(T - T_0)$. This last version of the model thus incorporates the rate and gradient dependence simultaneously; cf., for instance, [61,62].

3. Balance Equations

Due to the distinction between the reference and the current configurations in the large strain analysis, the governing equations can be formulated in the material or spatial description; see, for instance, [46,63], respectively. In the described model, spatial quantities are used, but they refer to the volume or surface in the reference configuration; see [64].

The first governing equation for the analyzed coupled problem imposes static equilibrium in the local form

$$J\mathrm{div}(\boldsymbol{\tau}/J) = \mathbf{0}. \tag{34}$$

In Equation (34) $\mathrm{div}(\cdot)$ is the divergence computed with respect to spatial coordinates and body forces have been neglected. The equilibrium Equation (34) is completed with the boundary conditions for displacement vector $\mathbf{u}$ and for traction vector $\mathbf{t}$:

$$\begin{array}{rcl} \mathbf{u} = \hat{\mathbf{u}} & \text{on} & \partial\mathcal{B}_u, \\ \mathbf{t} = \boldsymbol{\tau}\cdot\mathbf{n} = \hat{\mathbf{t}} & \text{on} & \boldsymbol{\varphi}(\partial\mathcal{B}_\tau), \end{array} \tag{35}$$

where $\mathbf{n}$ is the normal to the body surface.

The second governing equation represents the energy balance written in the temperature form for a non-stationary heat transport, as follows.

$$c\frac{\partial T}{\partial t} - J\mathrm{div}(-\mathbf{q}/\mathrm{J}) - \mathcal{R} = 0. \tag{36}$$

In Equation (36), $\mathcal{R}$ is a heat source density per unit of volume. It includes so-called plastic heating, i.e., the source density due to plastic dissipation written in the simple form [45]

$$\mathcal{R} = \chi\sigma_y\dot{\alpha}, \tag{37}$$

where χ denotes a heat dissipation factor [65], assumed to be constant. The energy balance Equation (36) is completed with appropriate boundary conditions:

$$\begin{array}{rcl} T = \hat{T} & \text{on} & \partial\mathcal{B}_T, \\ \mathbf{q}\cdot\mathbf{n} = \hat{q} & \text{on} & \boldsymbol{\varphi}(\partial\mathcal{B}_q), \end{array} \tag{38}$$

and an initial condition stating that for $t = 0$ we have $T = T_0$ in $\mathcal{B}$.

For the gradient-enhanced version of the model, the averaging Equation (30) is an additional balance equation. The averaged plastic strain z is an additional fundamental unknown, discretized in addition to displacements and temperature, leading to a three-field formulation of the coupled BVP.

The weak forms of the governing equations are the basis for the finite element implementation. Multiplication of Equation (34) by test function $\delta\mathbf{u}$, integration over the

volume of body $\mathcal{B}$ and application of the divergence theorem as well as Neumann boundary conditions lead to the weak form of the linear momentum balance

$$\int_{\mathcal{B}} (\nabla \delta \mathbf{u} : \boldsymbol{\tau}) \mathrm{d}V + \int_{\boldsymbol{\varphi}(\partial \mathcal{B}_\tau)} \delta \mathbf{u} \cdot \hat{\mathbf{t}} \mathrm{d}a = 0. \tag{39}$$

The weak form of Equation (36) is obtained using the standard procedure and the backward Euler scheme for time integration. As a result, the following integral equation is required to be valid for the current time

$$\int_{\mathcal{B}} \left[\delta T \frac{c}{\Delta t} (T - T_n) + k \nabla \delta T \cdot \nabla T - \delta T \mathcal{R} \right] \mathrm{d}V + \int_{\boldsymbol{\varphi}(\partial \mathcal{B}_q)} \delta T \hat{q} \mathrm{d}a = 0, \tag{40}$$

where T_n is the value of temperature at the previous time moment and Δt is the time increment. Finally, the weak form of Equation (30) is written as follows

$$\int_{\mathcal{B}} \left[\delta z (z - \alpha) + l^2 \nabla_0 \delta z \cdot \nabla_0 z \right] dV = 0. \tag{41}$$

Equations (39), (40), and optionally (41) are required to be valid for any admissible weighting functions $\delta \mathbf{u}$, δT and δz, respectively. After the introduction of finite element approximations of the two or three fundamental unknowns according to the Galerkin approach, a set of algebraic equations can be obtained for a monolithic solution algorithm.

4. Implementation and Computational Tool

The numerical implementation and testing of the coupled model is performed in Wolfram Mathematica packages AceGen and AceFEM, developed by Korelc [66]. The first package is used to program user-supplied procedures for the finite element method, in particular the tangent and residual subroutine for the Newton-Raphson algorithm and the postprocessing subroutine. The code is prepared in a special meta-language and automatically translated by AceGen. The routine can then be transferred to a chosen finite element environment (e.g., ABAQUS, FEAP), but an integrated FE engine AceFEM can also be used, and this is the case here. AceFEM is equipped with convenient pre- and post-processing tools and perfectly cooperates with AceGen in the computational process.

The main advantage of AceGen, from the researcher's point of view, is its ability to perform automatic differentiation of symbolic expressions. It is worth emphasising that the material model which is developed to simulate the PLC phenomenon results in a highly non-linear two- (or three-) field problem which is solved using the iterative Newton–Raphson algorithm which requires linearization of the governing equations. This part of the model preparation is very often the most challenging part of the implementation process. The application of automatic differentiation in the AceGen package significantly improves this step. If the residual (with all explicit and nested dependencies between variables) is properly defined, then the tangent matrix components are computed automatically as derivatives of the residual with respect to the unknowns. What is more, the finite element subroutine produced by AceGen is efficient and robust, since the code generator simplifies the symbolic expressions and has built-in optimization tools. A detailed description of AceGen features can be found e.g., in [66].

In fact, following the recommendation of Korelc [66], instead of introducing discretization into the residual Equations (39), (40) and optionally (41), pseudo-potentials are formulated for the equilibrium, energy balance and plastic strain averaging, minimization of which is equivalent to the residual equations. Specific forms of the potentials related to the governing equations considered in this model can be found in [42]. It should be mentioned that the model under consideration involves large strain plasticity and requires a solution of the non-linear set of equations at the level of Gauss points to calculate the values of internal variables. Thus, the relations between the internal variables and the global unknown fields are not given as explicit functions and the process of the automatic

differentiation has to be affected by the definition of appropriate exceptions. For more details, the reader is referred to [42,66,67].

Discretization is introduced into the pseudo-potentials following the classical Ritz approach, which yields a more robust solution procedure. An extensive description of the AceGen implementation of a large strain (gradient-enhanced) thermo-plasticity models can be found in [42,43]. The codes for thermo-visco-plasticity with the McCormick extension given in Equation (23) are developed based on the same approach.

The user subroutines in AceGen are prepared for three-dimensional finite elements, in particular hexahedral elements H8 with linear interpolation of all fields (displacement, temperature and, if relevant, averaged strain) and eight Gauss points. The linear interpolation is favorable in terms of computational effort, but it is known that plasticity simulations are affected by volumetric locking if full integration is used. Therefore, the so-called F-bar enhancement, see e.g., [68], is employed for the mechanical part of the formulation.

5. Simulation of PLC Effect

5.1. Test Description

In the numerical simulations of the PLC effect, two different samples are considered. First, an example computation for a simple tensile rod sample is made to show how the propagative instability is reproduced; see Figure 1, left. The rod dimensions are $10 \times 10 \times 500$ mm. One end of the rod is fixed and a longitudinal displacement increasing to 75 mm (15% of the sample length) is uniformly applied at the other end within 100 s (the strain rate is 1.5×10^{-3} s^{-1}). Fifty identical hexahedral elements with linear interpolation of all fields are used and one element is used in the cross section.

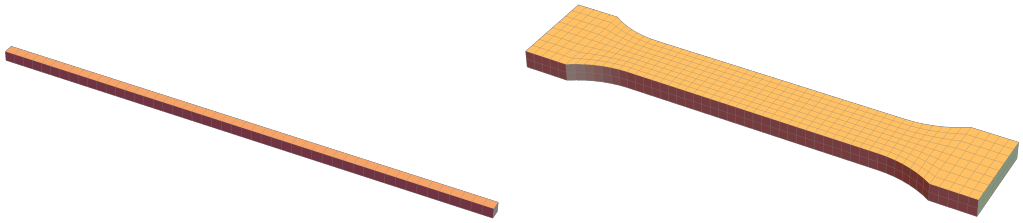

Figure 1. Geometry of samples and meshes, rod (**left**) and bone-shape sample (**right**).

Then, simulations are performed for a configuration based on the experimental bone-shape plate sample analyzed in [49]; see Figure 1, right. The dimensions of the computed configuration are as follows: total length 102 mm, length of the middle part 57 mm, thickness 4 mm, width of middle part 12.5 mm, radius of fillets 12.5 mm, width of broader parts 20 mm. The bone-shape sample is uniformly elongated by 14.25 mm in 285 s. The element size in the central part of the mesh is approximately 2 mm.

For both specimens, insulation thermal boundary conditions are applied. The basic set of material model parameters for our study are taken from [13,25,49] for room temperature 25 °C and listed in Table 1. The results of the simulations are compared with the experimental results from [49].

The two variants of the material model described in Section 2 are used: the thermo-visco-plastic model and the thermo-visco-plastic model with the gradient enhancement. For comparison with experiments, two options for the characteristic time of solute diffusion t_0 (called solute diffusion time in brief) are considered: either constant or depending on temperature. After the comparison with experiments the parametric study is performed. For the thermo-visco-plastic model, four sets of computations are made for different values of viscosity, heat conductivity, solute diffusion time, and maximum tension time. For the gradient-enhanced model, two sets of computations are carried out for different values of internal length and ductility parameter.

In Figure 2, the relations between the strain aging time t_a and the relative extension $\Delta L/L$ are plotted for the two analyzed tests and selected points in the configurations, showing abrupt jumps of t_a according to the McCormick model, representing the DSA

phenomenon. The left plot is obtained for the tensile rod, and the right one for the bone-shape sample.

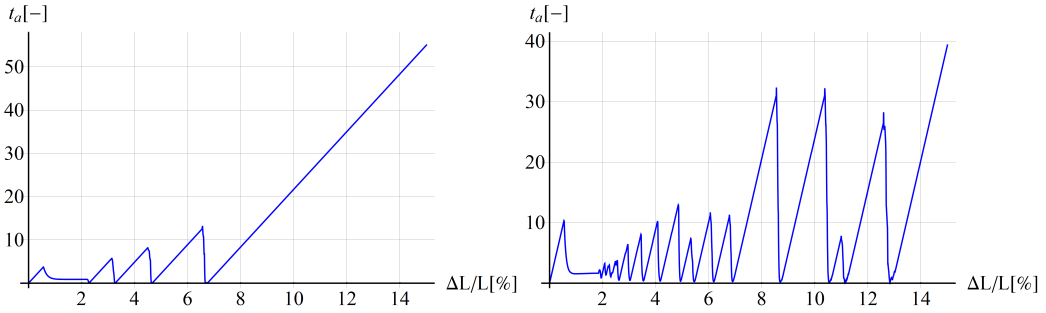

Figure 2. Strain ageing time vs. longitudinal displacement for rod benchmark at the right end of the sample (**left**) and for the bone-shape plate in tension at the centre of the sample (**right**).

To avoid convergence problems, the thermo-plastic model with the gradient enhancement is not used without the viscosity part. Since the McCormick part of the yield strength introduces recurring strain rate softening stages, the non-linear simulation algorithm fails without viscosity and it seems the gradient term is insufficient to prevent this.

Table 1. Basic set of mechanical, thermal and McCormick model parameters

Property	Symbol	Value	Unit
Young modulus	E	68.56	GPa
Poisson ratio	ν	0.3	-
Initial yield strength	σ_{y0}	367.5	MPa
Final yield strength	σ_{yf}	488.8	MPa
Saturation constant	δ	16	MPa
Viscosity	ξ	40	MPa · s
Conductivity	k	121	J/(s·K·m)
Heat capacity	c	2,423,750	J/(m^3·°C)
Thermal expansion coeff.	α_T	23.2×10^{-6}	1/°C
Thermal softening modulus	H_T	0.0016	1/°C
Heat dissipation factor	χ	0.9	-
Solute diffusion time	t_0	0.125	s
EMC model param.	Ω_0	13.62×10^{-4}	-
EMC model param.	Ω_0'	7.2×10^{-4}	-
EMC model param.	σ_{B00}	18.9	MPa
EMC model param.	σ_{B00}'	567.78	MPa
EMC model exponent	n	3^{-1}	-
EMC model param.	t_{01}	0.051355	1/°C
EMC model param.	t_{02}	0.03462	s

5.2. Tensile Rod Benchmark Test

To simulate the PLC effect in a one-dimensional tension benchmark a simple 3D rod test is performed, see Figure 1 left.

In Figure 3 stress vs. the rod extension is plotted for the whole process (left plot) and the magnification of a one serration (right plot). The place of the arbitrarily chosen serration is marked by the red box on the left plot. Small serrations are visible at the beginning of the process and they gradually grow. After the diagram peaks, the serrations grow extensively, when they actually should vanish. Obviously, the model needs some modification to prevent this kind of behavior at the final (failure) stage, but proper modeling of this stage is outside the focus of this work.

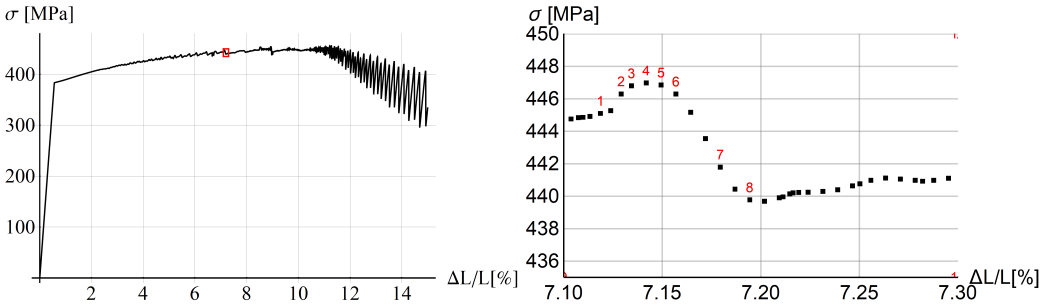

Figure 3. Stress vs. relative longitudinal displacement for rod benchmark: whole process (**left**) and one selected serration (**right**).

In the right diagram in Figure 3 selected states are numbered in red. In Figure 4 two columns of plots are presented for the serration and those states. Each plot shows the distribution of equivalent strain rate $\dot{\gamma}$ along the rod. For steps 2 and 3 before the peak, the band has a distributed form, while in the previous step 1, the band is localized. In the steps after the peak, $\dot{\gamma}$ localizes again at a different position.

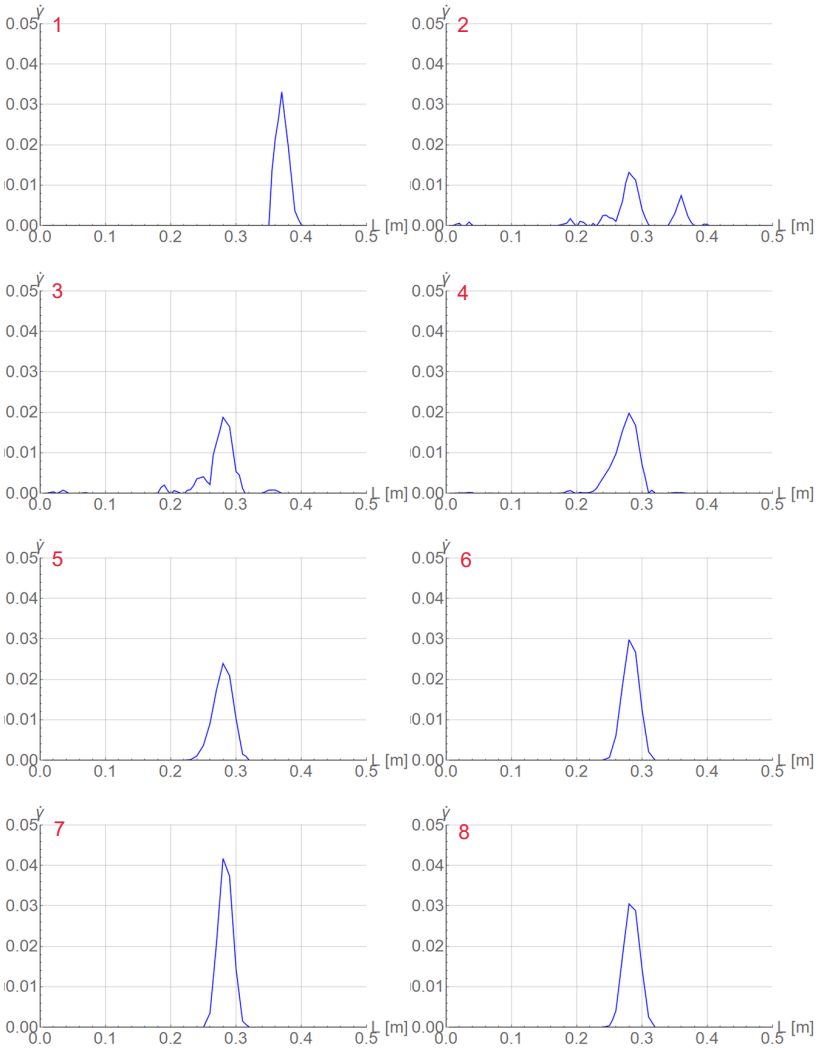

Figure 4. Distributions of $\dot{\gamma}$ at numbered states of selected serration for tensile rod test.

5.3. Comparison with Experiments for Bone-Shape Sample

The comparisons with experiments from [49] are made for the thermo-visco-plastic model and for its gradient-enhanced version, for three initial temperatures: 25 °C, 100 °C, and 200 °C. Table 2 contains the values of the Young modulus, initial and final yield strength for the three temperatures.

Table 2. Parameters for different temperatures

Property	Symbol	25 °C	100 °C	200 °C	Unit
Young modulus	E	68.56	65.56	46.62	GPa
Initial yield strength	σ_{y0}	367.5	360.3	312.9	MPa
Final yield strength	σ_{yf}	488.8	466.2	383.2	MPa

Figure 5 presents the results obtained for the former model and Figure 6 for the latter one. The EMC material model parameters are fitted for the case without the dependence of the solute diffusion time t_0 on temperature. The small differences in the elastic part of the response can be caused by neglecting the elongation of the broader sample parts in the computational experiment. Notice that the level of the yielding initiation is reduced with temperature, which is related to thermal softening, and the numerical model correctly reproduces the behaviour.

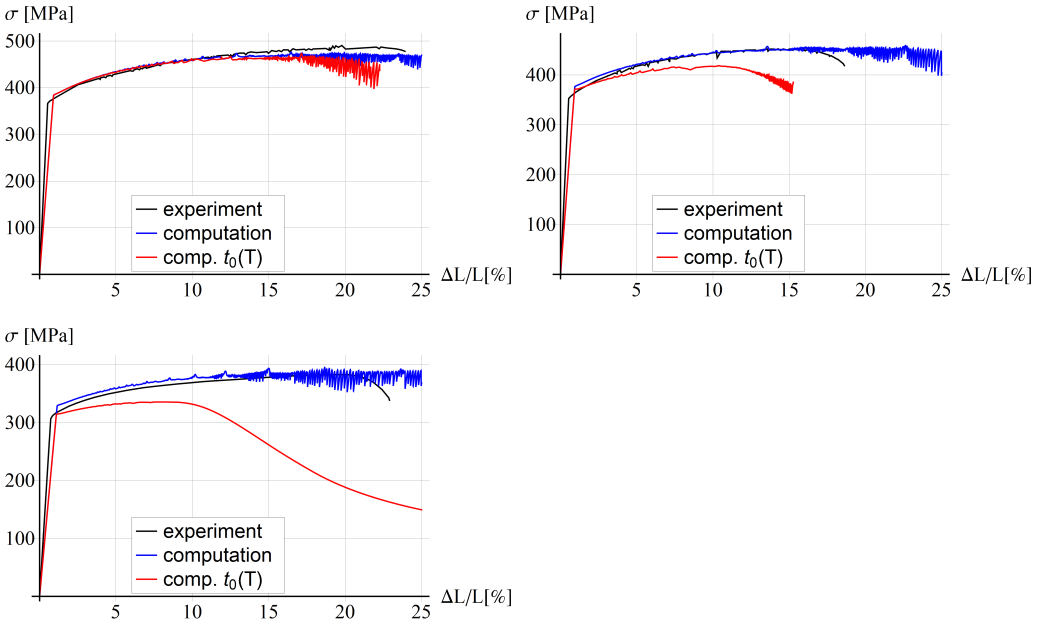

Figure 5. Stress vs. relative extension for thermo-visco plastic model for 25 °C (**left**, **top**), 100 °C (**right**, **top**), 200 °C (**left**, **bottom**).

When the constant value of $t_0 = 0.125$ s is assumed according to [13], we can observe in Figure 5 a good agreement in terms of global load–deformation response for the temperature equal to 25 °C and a partial agreement for higher temperatures. For 100 °C and 200 °C the blue lines are close to the experimental black lines at the beginning of the process, but they do not mimic the failure at the end for a similar extension as in the experiments. The red line for the model with the solute diffusion time depending on temperature enters softening a bit earlier for room temperature, but it shows a much softer response, far from the

experimental diagrams, for higher temperatures. For the temperature equal to 100 °C and 200 °C the softening stage is entered much earlier than in the experiment. In the latter case, all serrations have been smoothed, which is similar to the findings presented in [25]. The values of model parameters t_{01} and t_{02}, which control the dependence of t_0 on temperature, are based on [25], but obviously the exponential character of function $t_0(T)$ is not a suitable choice.

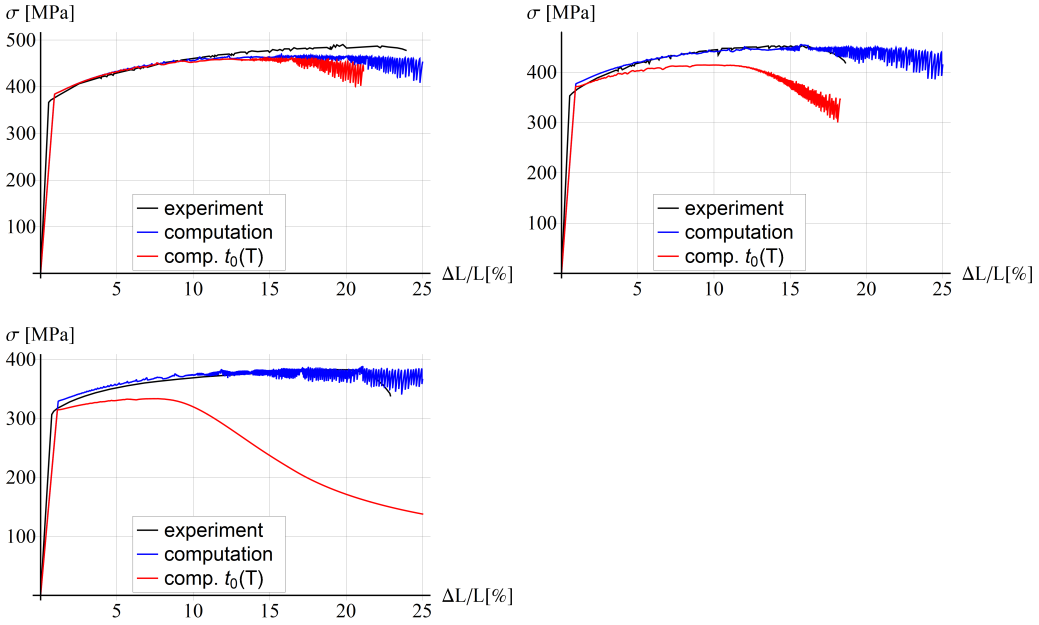

Figure 6. Stress vs. relative extension for thermo-visco plastic model with gradient enhacement for 25 °C (**left**, **top**), 100 °C (**right**, **top**), 200 °C (**left**, **bottom**).

A similar behaviour as for the thermo-visco-plastic model can be observed for the variant with the gradient enhancement for the internal length $l = 5$ mm and ductility parameter $\beta = 0.1$, see Figure 6. It seems that the gradient enhancement of the model with the assumed material parameters, related to an additional yield strength reduction, has a minor influence on the simulated stress-relative elongation diagrams. This aspect is further analyzed in the parametric study, as follows.

5.4. Parametric Study

Parametric studies for the two model variants, without and with the gradient enhancement, are performed. Six parameters are taken into account. For the thermo-visco-plastic model, the following parameters are varied: viscosity ξ (5, 40, 80 MPa·s), conductivity k (0, 50, 121, 200 J/(s·K·m)), solute diffusion time t_0 (0.01, 0.025, 0.125, 0.5, 5, 1000 s), and the duration of the elongation process t_{MAX} (28.5, 285, 2850 s).

For the gradient-enhanced model, the ductility β (0.1, 0.5, 1, 2 [-]) and the internal length l (0, 5, 10, 20 mm) are changed. The parametric studies are carried out for the reference temperature equal to 25 °C; thus, the mechanical material parameters (Young modulus, the initial and ultimate yield strengths) are appropriate for this assumption and are taken from [49]. As given in Table 1, the default values of varied parameters are: viscosity $\xi = 40$, conductivity $k = 121$, and solute diffusion time $t_0 = 0.125$. Moreover, the maximum tension time $t_{MAX} = 285$.

5.4.1. Thermo-Visco-Plastic Model

In Figure 7, stress–strain diagrams for different values of viscosity (left, top), conductivity (right, top), solute diffusion time (left, bottom) and maximum tension time (right,

bottom) are shown. The experimental diagram (black) for 25 °C is added for reference. There are no significant differences between the plots for different values of viscosity in the examined range of values; however, in the case when the viscosity ξ is equal to zero (not displayed here), the computation stops at the beginning of the process.

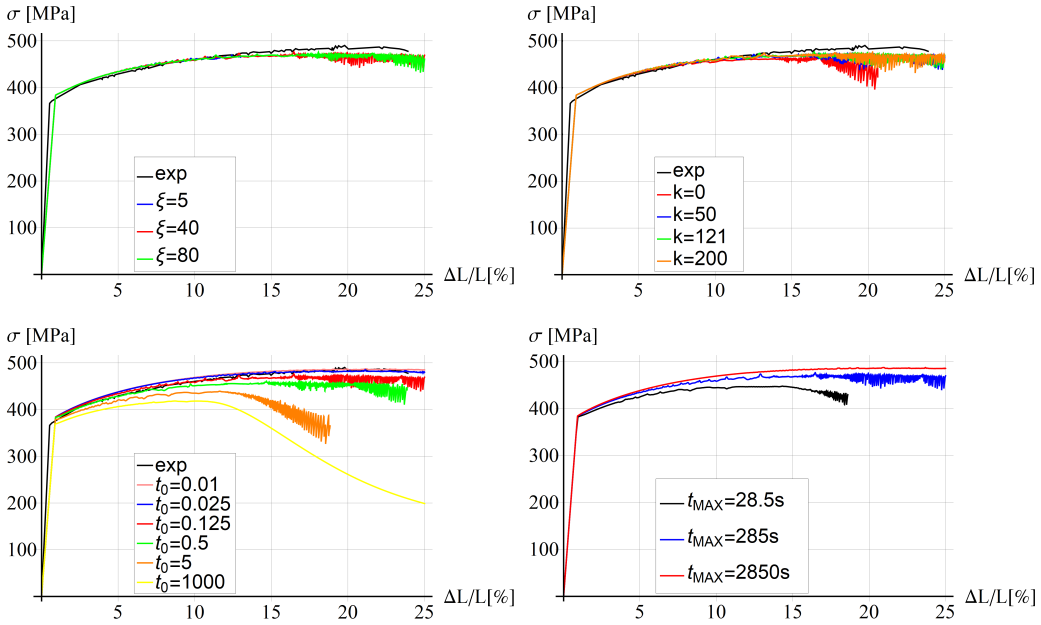

Figure 7. Stress vs. relative extension for different values of viscosity (**top**, **left**), conductivity (**top**, **right**), solute diffusion time (**bottom**, **left**) and maximum tension time (**bottom**, **right**).

In the second plot, it can be observed that the response is more brittle for smaller values of heat conductivity and no significant differences can be observed for higher values of k than 50 J/(s·K·m). The conductivity equal to 121 J/(s·K·m) is the value characteristic for the aluminium alloy used in the experiments described in [49].

The characteristic time of the solute diffusion affects the diagram smoothness and the load-carrying capacity. For high and low values of t_0, the diagrams are smoother and there are no excessive serrations at the end of the process. The diagrams are ordered from the largest value of t_0 (the most brittle response) to the smallest value (most ductile), which means the yield strength is lower for higher values of the solute diffusion time.

The last diagram in Figure 7 shows that the response is rate dependent and the higher the load rate (the smaller t_{max} is), the smaller the predicted load-carrying capacity. The diagram for the largest value of t_{max} is smooth and does not exhibit serrations at the end of the process contrary to the other diagrams.

The next Figures 8 and 9 are plotted for $\xi = 40$ MPa·s, $k = 121$ J/(s·K·m), $t_0 = 0.125$ s and $t_{max} = 285$ s. In Figure 9, two columns with distributions of $\dot{\gamma}$ along the central longitudinal axis of the dog-bone sample are shown for the numbered states in the load–displacement plot part for the selected serration shown in Figure 8. In Figure 10 the distributions of $\dot{\gamma}$ in the sample are shown corresponding to the results presented in Figure 9. Before the serration peak, a band is visible on the right-hand side of the sample; see Figure 9, first row left. Then, when the peak is approached, the band on the right starts to disappear and a band on the left-hand side appears. After the peak, see Figure 9 third row left, the traces of the right band vanish completely and only the left band is visible. The same sequence of states can be observed in Figure 10.

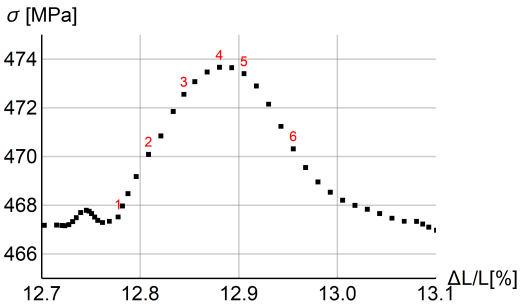

Figure 8. Stress vs. relative extension for one serration with step numeration ($\xi = 40$ MPa·s, $k = 121$ J/(s·K·m) and $t_0 = 0.125$ s).

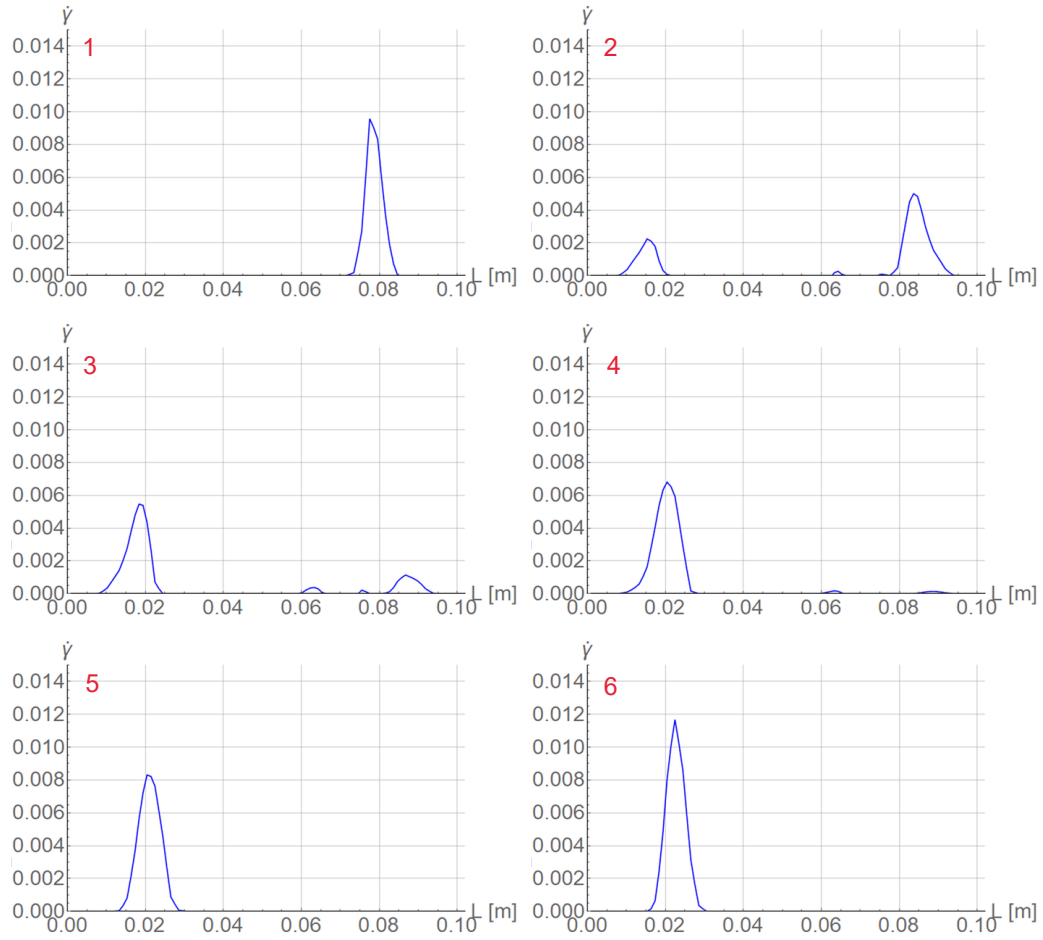

Figure 9. Distributions of $\dot{\gamma}$ along the specimen axis at numbered states for $\xi = 40$ MPa·s, $k = 121$ J/(s·K·m) and $t_0 = 0.125$ s.

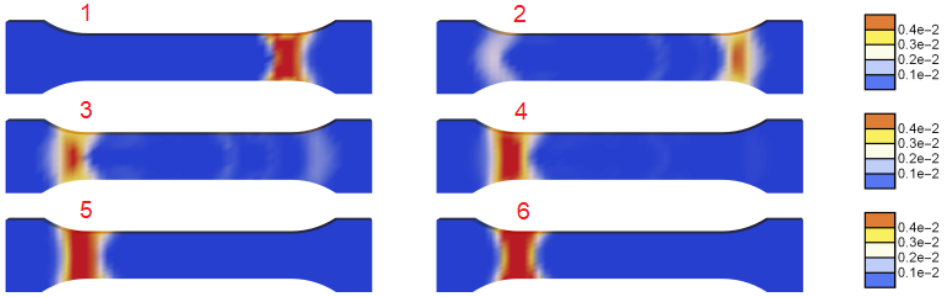

Figure 10. Distributions of $\dot{\gamma}$ at numbered states ($\xi = 40$ MPa·s, $k = 121$ J/(s·K·m) and $t_0 = 0.125$ s).

5.4.2. Thermo-Visco-Plastic Model with Gradient Enhancement

In Figure 11, diagrams for different values of the ductility parameter (left) and the internal length (right) are shown. For comparison, two additional diagrams are added; the black line is the experimental diagram for 25 °C, and the gray line is for the thermo-visco-plastic model with the following parameters: $\xi = 40$ MPa·s, $k = 121$ J/(s·K·m), $t_0 = 0.125$ s and $t_{max} = 285$ s.

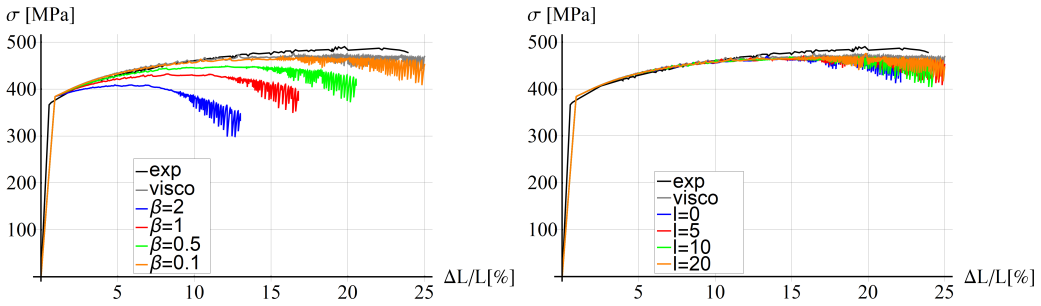

Figure 11. Stress vs. relative extension for different values of ductility and $l = 5$ mm (**left**) and for different internal lengths and $\beta = 0.1$ (**right**).

When the value of the ductility grows, the influence of the exponential reduction factor increases. It can be observed in Figure 11 (left) that for larger values of ductility, the load-carrying capacity is smaller and softening starts to dominate faster. The diagrams for different values of the internal length are presented in Figure 11 (right). There are no significant differences for the values of internal length larger than zero. The diagrams are close to the diagram obtained for the thermo-visco-plastic model. The diagram for $l = 0$ (blue line) is slightly more brittle and ends for $\Delta L/L \approx 22$ due to divergence of the simulation.

In Figure 12, the distributions of the plastic strain rate are compared for a series of states in the deformation history. The plots on the left are for $l = 0$ and the right ones for $l = 20$ mm. For small deformation, a uniform distribution of $\dot{\gamma}$ is observed, then a localized band is formed, which resembles a cross pattern of shear bands diffused by regularization and/or re-hardening. The reason can also be a too-coarse finite element mesh used for the simulation. The band travels through the process zone of the sample in a similar way irrespective of the assumed internal length. The plots do not show the expected influence of the length scale on the widths of the propagating localization zones. This is probably caused by the fact that the viscosity and heat conductivity provide sufficient regularization and the gradients active on the softening parts of the serrations merely counteract the additional softening source related to the yield stress degradation involved in the gradient-enhanced model.

Figure 13 presents parts of the stress-strain diagrams of one selected serration for two values of internal length $l = 0$ (left) and $l = 20$ mm (right). Further, Figure 14 shows the evolution of the distribution of the plastic strain rate $\dot{\gamma}$ for the two values of the internal length scale within one selected serration presented in Figure 13. The plots for $l = 0$ show disappearing and reappearing localization zones, while the plots for $l = 20$ mm present a moving band. However, also for one serration the maps show a negligible influence of the length scale on the widths of the propagating bands.

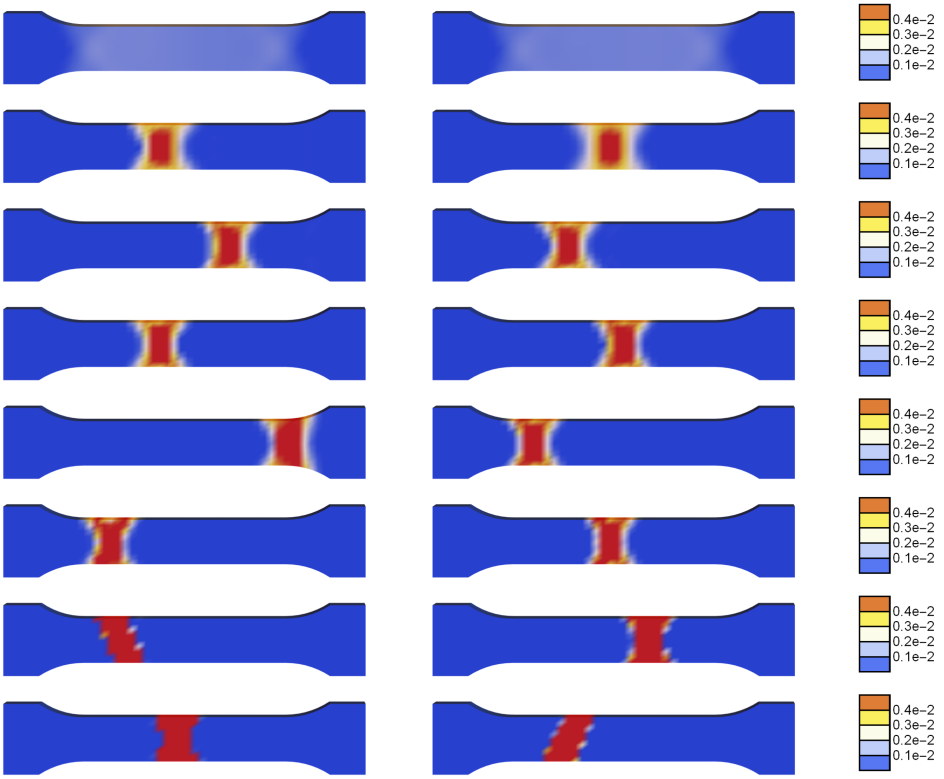

Figure 12. Distributions of $\dot{\gamma}$ at selected states in the deformation history for $l = 0$ (**left column**) and $l = 20$ mm (**right column**). For the rows of figures from top $\Delta L/L$ is equal to 3, 5, 7.5, 10, 12.5, 15, 17.5, 20.

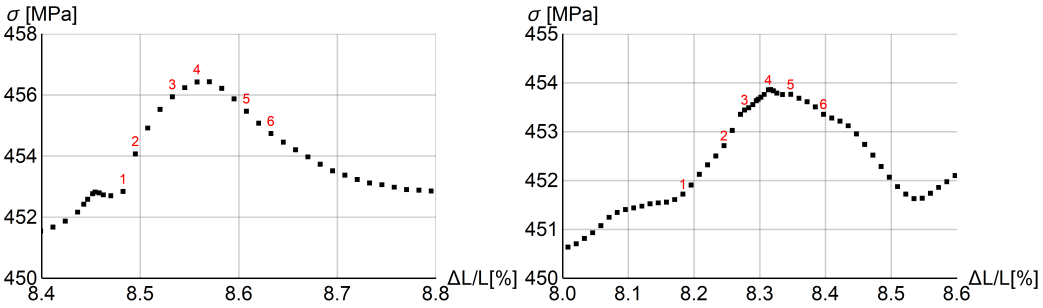

Figure 13. Stress vs. relative extension for selected serration and two values of internal length $l = 0$ (**left**) and $l = 20$ mm (**right**).

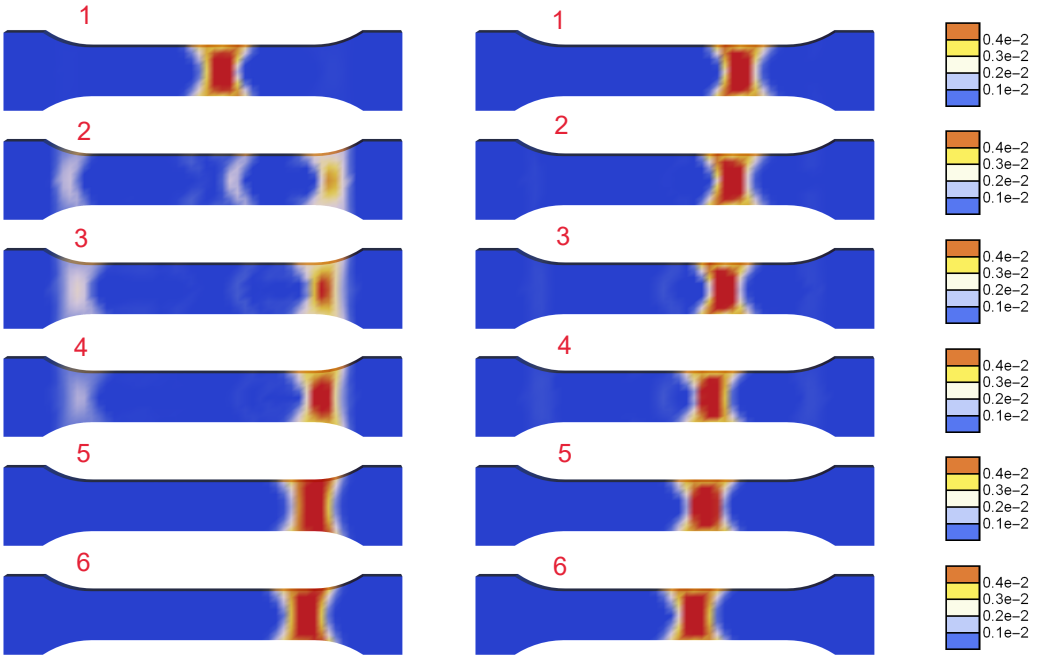

Figure 14. Distributions of $\dot{\gamma}$ at selected states in the deformation history, marked by numbers in Figure 13, for $l = 0$ (**left column**) and $l = 20$ mm (**right column**).

6. Conclusions

The Portevin–Le Chatelier (PLC) effect has been simulated using two versions of the large strain thermo-plastic Estrin–McCormick model. The model is capable of reproducing the results of the Dynamic Strain Aging (DSA) phenomenon: serrations in the load–displacement diagrams (repetitive changes of softening and hardening) and propagating localization zones. The model takes into account visco-plasticity and the second version also includes a gradient enhancement via an averaging equation for the equivalent plastic strain.

Two different configurations are used in simulations. A simple rod is considered first to show how the adopted constitutive model represents the PLC phenomenon. Then, tension of the experimental bone-shape sample from [49] is simulated, instability formation and propagation are studied, and a comparison with experimental results is performed. For both tests, detailed analyses of the evolution of the plastic strain rate for a selected serration have been presented. It seems that the localization band moves, but it rather gradually disappears and then reappears at a different position.

Further, a parametric study is performed. Different values of viscosity, conductivity, the time of solute diffusion in the DSA model, and the maximum tension time (loading rate) have been considered for the thermo-visco-plastic model. For the model with the gradient enhancement, the ductility parameter and the internal length have varied.

On one hand, the results of simulations are quite satisfactory: the simulated load–extension diagrams are quite close to the experimental results and the sensitivity to model parameters is in agreement with expectations. On the other hand, excessive post-peak serrations are visible for most of the computation, so a method to reduce them is needed. The adopted dependence of the parameters of the McCormick model on temperature led to results far from the experimental ones for higher temperatures, so this aspect requires further research and model improvement. Moreover, experimental studies are necessary to compare the shear band evolution in PLC simulations (and not only load–displacement plots) and to identify material model parameters in a similar way to [13,25].

Finally, the distributions of the equivalent plastic strain rate in the specimen for the gradient-enhanced model are examined for two values of the internal length scale $l = 0$ and $l = 20$ mm. They are compared for a series of states showing no significant differences in

the size of the localization bands. This can be caused by the relatively coarse discretization used, or by the fact that viscosity and heat conduction provide some regularization, which manifests itself in smoothing of the simulated bands and in a weak influence of gradients.

Author Contributions: All authors worked on the concepts of the research, formulation of the models and preparation of the manuscript. M.M. and B.W. programmed the models in AceGen, M.M. performed all computations and provided numerical results. The research outcomes were discussed by all authors. All authors have read and agreed to the published version of the manuscript.

Funding: The research was supported by the National Science Centre of Poland within grant number 2018/31/N/ST8/03573.

Institutional Review Board Statement: Not applicable.

Informed Consent Statement: Not applicable.

Data Availability Statement: The data presented in this study are available in the article.

Acknowledgments: The authors acknowledge valuable discussions on the research with A. Menzel from TU Dortmund, Germany/Lund University, Sweden.

Conflicts of Interest: The authors declare no conflict of interest.

Abbreviations

The following abbreviations are used in this manuscript:

EMC	Estrin–McCormick model.
PLC	Portevin–Le Chatelier.
DSA	Dynamic Strain Aging.
HMH	Huber–Mises–Hencky.
BVP	Boundary Value Problem.
FE	Finite Elements.

References

1. Cottrell, A.; Bilby, B. Dislocation theory of yielding and strain ageing of iron. *Proc. Phys. Soc. Sect. A* **1949**, *62*, 49–62. [CrossRef]
2. Bergstrom, Y.; Roberts, W. The application of dislocation model to dynamic strain ageing in α-iron containing interstitial atoms. *Acta Metall.* **1971**, *19*, 815–823. [CrossRef]
3. Portevin, A.; Le Chatelier, F. Sur un phénomène observé lors de l'essai de traction d'alliages en cours de transformation. *Comput. Rend. Acad. Sci. Paris* **1923**, *176*, 507–510.
4. Estrin, Y.; Kubin, L. Spatial coupling and propagative plastic instabilities. In *Continuum Models for Materials with Microstructure*; Mühlhaus, H.B., Ed.; John Wiley & Sons: Chichester, UK, 1995; pp. 395–450.
5. Wang, W.M. Stationary and Propagative Instabilities in Metals—A Computational Point of View. Ph.D. Thesis, Delft University of Technology, Delft, The Netherlands, 1997.
6. Wang, W.M.; Sluys, L.J.; de Borst, R. Viscoplasticity for instabilities due to strain softening and strain-rate softening. *Int. J. Numer. Meth. Eng.* **1997**, *40*, 3839–3864. [CrossRef]
7. Yilmaz, A. The Portevin–Le Chatelier effect: A review of experimental findings. *Sci. Technol. Adv. Mater.* **2011**, *12*, 063001. [CrossRef]
8. Jiang, H.; Zhang, Q.; Chen, X.; Chen, Z.; Jiang, Z.; Wu, X.; Fan, J. Three types of Portevin–Le Chatelier effects: Experiment and modelling. *Acta Mater.* **2007**, *55*, 2219–2228. [CrossRef]
9. Tamimi, S.; Andrade-Campos, A.; Pinho-da Cruz, J. Modelling the Portevin-Le Chatelier effects in aluminium alloys: A review. *J. Mech. Behav. Mater.* **2015**, *24*, 67–78. [CrossRef]
10. McCormick, P.G. Theory of flow localization due to dynamic strain aging. *Acta Metall.* **1988**, *36*, 3061–3067. 10.1016/ 0001-6160(88)90043-0. [CrossRef]
11. McCormick, P.G.; Ling, C. Numerical modelling of the Portevin–Le Chatelier effect. *Acta Metall. Mater.* **1995**, *43*, 1969–1977. [CrossRef]
12. Zhang, S.; McCormick, P.G.; Estrin, Y. The morphology of Portevin-Le Chatelier bands: Finite element simulation for Al-Mg-Si. *Acta Mater.* **2001**, *49*, 1087–1094. [CrossRef]
13. Böhlke, T.; Bondár, G.; Estrin, Y.; Lebyodkin, M. Geometrically non-linear modeling of the Portevin–Le Chatelier effect. *Computat. Mater. Sci.* **2009**, *44*, 1076–1088. [CrossRef]
14. Belotteau, J.; Berdin, C.; Forest, S.; Parrot, A.; Prioul, C. Mechanical behavior and crack tip plasticity of a strain aging sensitive steel. *Mater. Sci. Eng. A* **2009**, *526*, 156–165. [CrossRef]

15. Berdin, C.; Wang, H. Local approach to ductile fracture and dynamic strain aging. *Int. J. Fracture* **2013**, *182*, 39–51. [CrossRef]
16. Sarkar, A.; Maloy, S.A.; Murty, K.L. Investigation of Portevin-Le Chatelier effect in HT-9 steel. *Mater. Sci. Eng. A* **2015**, *631*, 120–125. [CrossRef]
17. Ren, S.; Morgeneyer, T.; Mazière, M.; Forest, S.; Rousselier, G. Effect of Lüders and Portevin-Le Chatelier localization bands on plasticity and fracture of notched steel specimens studied by DIC and FE simulations. *Int. J. Plasticity* **2021**, *136*, 102880. [CrossRef]
18. Kozłowska, A.; Grzegorczyk, B.; Morawiec, M.; Grajcar, A. Explanation of the PLC Effect in Advanced High-Strength Medium-Mn Steels—A Review. *Materials* **2019**, *12*, 1–14. [CrossRef]
19. Benallal, A.; Berstad, T.; Børvik, T.; Hopperstad, O.; Koutiri, I.; de Codes, R.N. An experimental and numerical investigation of the behaviour of AA5083 aluminium alloy in presence of the Portevin–Le Chatelier effect. *Int. J. Plasticity* **2008**, *24*, 1916–1945. [CrossRef]
20. Chen, J.; Zhen, L.; Fan, L.; Yang, S.; Dai, S.; Shao, W. Portevin-Le Chatelier effect in Al-Zn-Mg-Cu-Zr aluminum alloy. *Trans. Nonferr. Metals Soc. China* **2009**, *19*, 1071–1075. [CrossRef]
21. Coër, J.; Manach, P.; Laurent, H.; Oliveira, M.; Menezes, L. Piobert–Lüders plateau and Portevin–Le Chatelier effect in an Al–Mg alloy in simple shear. *Mech. Res. Commun.* **2013**, *48*, 1–7. [CrossRef]
22. Reyne, B.; Manach, P.Y.; Moës, N. Macroscopic consequences of Piobert–Lüders and Portevin–Le Chatelier bands during tensile deformation in Al-Mg alloys. *Mater. Sci. Eng. A* **2019**, *746*, 187–196. [CrossRef]
23. Mazière, M.; Besson, J.; Forest, S.; Tanguy, B.; Chalons, H.; Vogel, F. Numerical aspects in the finite element simulation of the Portevin–Le Chatelier effect. *Comput. Methods Appl. Mech. Engrg.* **2010**, *199*, 734–754. [CrossRef]
24. Manach, P.; Thuillier, S.; Yoon, J.; Coër, J.; Laurent, H. Kinematics of Portevin–Le Chatelier bands in simple shear. *Int. J. Plasticity* **2014**, *58*, 66–83. [CrossRef]
25. Mansouri, L.Z.; Thuillier, S.; Manach, P.Y. Thermo-mechanical modeling of Portevin–Le Châtelier instabilities under various loading paths. *Int. J. Mech. Sci.* **2016**, *115*, 676–688. [CrossRef]
26. Lebyodkin, M.; Dunin-Barakowskii, L.; Bréchet, Y.; Estrin, Y.; Kubin, L.P. Spatio-temporal dynamics of the Portevin–Le Chatelier effect: Experiment and modelling. *Acta Mater.* **2000**, *48*, 2529–2541. [CrossRef]
27. Rizzi, E.; Hähner, P. On the Portevin–Le Chatelier effect: Theoretical modeling and numerical results. *Int. J. Plasticity* **2004**, *20*, 121–165. [CrossRef]
28. Graff, S.; Forest, S.; Strudel, J.L.; Prioul, C.; Pilvin, P.; Béchade, J.L. Strain localization phenomena associated with static and dynamic strain ageing in notched specimens: Experiments and finite element simulations. *Mater. Sci. Eng. A* **2004**, *387–389*, 181–185. [CrossRef]
29. Darowicki, K.; Orlikowski, J.; Zieliński, A. Investigation of changes in the type B PLC effect of Al–Mg–Cu type alloy for various strain rates. *Mater. Sci. Eng. A* **2008**, *496*, 478–482. [CrossRef]
30. Mazière, M.; Forest, S. Strain gradient plasticity modeling and finite element simulation of Lüders band formation and propagation. *Continuum Mech. Thermodyn.* **2015**, *27*, 83–104. [CrossRef]
31. Xu, J.; Chen, G.; Fu, S. Complexity analysis of the Portevin-Le Chatelier in an Al alloy at different temperatures. *Theor. Appl. Mech. Lett.* **2021**, *11*, 100233. [CrossRef]
32. Skoczeń, B.; Bielski, J.; Tabin, J. Multiaxial constitutive model of discontinuous plastic flow at cryogenic temperatures. *Int. J. Plasticity* **2014**, *55*, 198–218. [CrossRef]
33. Tabin, J. Kinematic and thermal characteristic of discontinuous plastic flow in metastable austenitic stainless steels. *Mech. Mater.* **2021**, *163*, 104090. [CrossRef]
34. Bartels, A.; Bartel, T.; Canadija, M.; Mosler, J. On the thermomechanical coupling in dissipative materials: A variational approach for generalized standard materials. *J. Mech. Phys. Solids* **2015**, *82*, 218–234. [CrossRef]
35. Li, Z.; Ma, Q.; Cui, J. Second-order two-scale finite element algorithm for dynamic thermo–mechanical coupling problem in symmetric structure. *J. Comput. Phys.* **2016**, *314*, 712–748. [CrossRef]
36. Aldakheel, F.; Miehe, C. Coupled thermomechanical response of gradient plasticity. *Int. J. Plasticity* **2017**, *91*, 1–24. [CrossRef]
37. Moleiro, F.; Madeira, J.; Carrera, E.; Reddy, J. Design optimization of functionally graded plates under thermo-mechanical loadings to minimize stress, deformation and mass. *Compos. Struct.* **2020**, *245*, 112360. [CrossRef]
38. Ahmed, S.R.; Sarkar, P.R. Displacement-function modeling of thermo-mechanical behavior of fiber-reinforced composite structures. *Int. J. Mech. Sci.* **2021**, *211*, 106739. [CrossRef]
39. Rose, L.; Menzel, A. Identification of thermal material parameters for thermo-mechanically coupled material models. *Meccanica* **2021**, *56*, 393–416. [CrossRef]
40. Liu, Z.; Li, Z.; Ma, Q.; Jiang, X. Thermo-mechanical coupling behavior of plate structure under re-entry aerodynamic environment. *Int. J. Mech. Sci.* **2022**, *218*, 107066. [CrossRef]
41. Oppermann, P.; Denzer, R.; Menzel, A. A thermo-viscoplasticity model for metals over wide temperature ranges—Application to case hardening steel. *Computat. Mech.* **2022**, *69*, 541–563. [CrossRef]
42. Wcisło, B.; Pamin, J. Local and non-local thermomechanical modeling of elastic-plastic materials undergoing large strains. *Int. J. Numer. Meth. Eng.* **2017**, *109*, 102–124. [CrossRef]
43. Pamin, J.; Wcisło, B.; Kowalczyk-Gajewska, K. Gradient-enhanced large strain thermoplasticity with automatic linearization and localization simulations. *J. Mech. Mater. Struct.* **2017**, *12*, 123–146. [CrossRef]

44. Holzapfel, G.A. *Nonlinear Solid Mechanics. A Continuum Approach for Engineering*; John Wiley & Sons: Chichester, UK, 2000.
45. Wriggers, P.; Miehe, C.; Kleiber, M.; Simo, J. On the coupled thermomechnical treatment of necking problems via finite element methods. *Int. J. Numer. Meth. Eng.* **1992**, *33*, 869–883. [CrossRef]
46. Simo, J.C.; Miehe, C. Associative coupled thermoplasticity at finite strains: Formulation, numerical analysis and implementation. *Comput. Methods Appl. Mech. Eng.* **1992**, *98*, 41–104. [CrossRef]
47. Mucha, M.; Wcisło, B.; Pamin, J. Simulation of Lueders bands using regularized large strain elasto-plasticity. *Arch. Mech.* **2021**, *73*, 83–117. [CrossRef]
48. Korelc, J. Automation of the Finite Element Method. In *Nonlinear Finite Element Methods*; Wriggers, P., Ed.; Springer: Berlin/Heidelberg, Germany, 2008; pp. 483–508.
49. Lipski, A.; Mroziński, S. The effects of temperature on the strength properties of aluminium alloy 2024-T3. *Acta Mech. Autom.* **2012**, *6*, 62–66.
50. Simo, J.C. A framework for finite strain elastoplasticity based on maximum plastic dissipation and the multiplicative decomposition: Part 1. Continuum formulation. *Comput. Methods Appl. Mech. Eng.* **1988**, *66*, 199–219. [CrossRef]
51. Geers, M.G.D. Finite strain logarithmic hyperelasto-plasticity with softening: A strongly non-local implicit gradient framework. *Comput. Methods Appl. Mech. Eng.* **2004**, *193*, 3377–3401. [CrossRef]
52. Ristinmaa, M.; Wallin, M.; Ottosen, N.S. Thermodynamic format and heat generation of isotropic hardening plasticity. *Acta Mech.* **2007**, *194*, 103–121. [CrossRef]
53. Lee, E.H. Elastic plastic deformation at finite strain. *ASME Trans. J. Appl. Mech.* **1969**, *36*, 1–6. [CrossRef]
54. Lee, E.H.; Liu, D.T. Finite-strain elastic-plastic theory with application to plane-wave analysis. *J. Appl. Phys.* **1967**, *38*, 19–27. [CrossRef]
55. Lu, S.C.H.; Pister, K.S. Decomposition of deformation and representation of the free energy function for isotropic thermoelastic solids. *Int. J. Solids Struct.* **1975**, *11*, 927–934. [CrossRef]
56. Simo, J.C.; Hughes, T.J.R. *Computational Inelasticity. Interdisciplinary Applied Mathematics*; Springer: New York, NY, USA, 1998; Volume 7.
57. Wcisło, B. Simulations of thermal softening in large strain thermoplasticity with degradation. *Eng. Trans.* **2016**, *4*, 563–572.
58. Okazawa, S. Structural bifurcation for ductile necking localization. *Int. J. Non-Linear Mech.* **2009**, *45*, 35–41. [CrossRef]
59. Peerlings, R.H.J.; de Borst, R.; Brekelmans, W.A.M.; de Vree, J.H.P. Gradient-enhanced damage for quasi-brittle materials. *Int. J. Numer. Meth. Eng.* **1996**, *39*, 3391–3403. [CrossRef]
60. Wcisło, B.; Pamin, J.; Kowalczyk-Gajewska, K. Gradient-enhanced damage model for large deformations of elastic-plastic materials. *Arch. Mech.* **2013**, *65*, 407–428.
61. Oka, F.; Mühlhaus, H.B.; Yashima, A.; Sawada, K. Quasi-Static and Dynamic Characteristics of Strain Gradient Dependent Non-Local Constitutive Models. In *Material Instabilities in Solids*; de Borst, R., van der Giessen, E., Eds.; Wiley: Chichester, UK; pp. 387–404.
62. Sluys, L.J.; Wang, W.M. Macroscopic Modelling of Stationary and Propagative Instabilities. In *Material Instabilities in Solids*; de Borst, R., van der Giessen, E., Eds.; John Wiley & Sons: New York, NY, USA; pp. 489–505.
63. Simo, J. Numerical Analysis and Simulation of Plasticity. In *Handbook of Numerical Analysis. Numerical Methods for Solids (Part 3)*; Ciarlet, P., Lions, J., Eds.; Elsevier Science: Boca Raton, FL, USA, 1998; Volume VI, pp. 183–499.
64. Miehe, C. Entropic thermoelasticity at finite strains. Aspects of the formulation and numerical implementation. *Comput. Methods Appl. Mech. Eng.* **1995**, *120*, 243–269. [CrossRef]
65. Taylor, G.I.; Quinney, H. The latent energy remaining in a metal after cold working. *Proc. R. Soc. Lond. Ser. A* **1934**, *143*, 307–326. [CrossRef]
66. Korelc, J. Automation of primal and sensitivity analysis of transient coupled problems. *Computat. Mech.* **2009**, *44*, 631–649. [CrossRef]
67. Korelc, J.; Wriggers, P. *Automation of Finite Element Methods*; Springer International Publishing: Cham, Switzerland, 2016.
68. de Souza Neto, E.; Peric, D.; Owen, D. *Computational Methods for Plasticity. Theory and Applications*; John Wiley & Sons: Chichester, UK, 2008.

materials

MDPI

Article

Stress Field Evaluation in Orthotropic Microstructured Composites with Holes as Cosserat Continuum

Farui Shi [1,2,3], Nicholas Fantuzzi [3,*], Patrizia Trovalusci [4], Yong Li [1,2,*] and Zuoan Wei [1,2]

1 State Key Laboratory of Coal Mine Disaster Dynamics and Control, Chongqing University, No. 174 Shazhengjie, Shapingba, Chongqing 400044, China; farui.shi@unibo.it (F.S.); weiza@cqu.edu.cn (Z.W.)
2 School of Resources and Safety Engineering, Chongqing University, No. 174 Shazhengjie, Shapingba, Chongqing 400044, China
3 Department of Civil, Chemical, Environmental and Materials Engineering, University of Bologna, Viale del Risorgimento 2, 40136 Bologna, Italy
4 Department of Structural and Geotechnical Engineering, Sapienza University of Rome, Via A. Gramsci 53, 00197 Rome, Italy; patrizia.trovalusci@uniroma1.it
* Correspondence: nicholas.fantuzzi@unibo.it (N.F.); yong.li@cqu.edu.cn (Y.L.)

Abstract: It is known that the presence of microstructures in solids such as joints and interfaces has an essential influence on the studies of the development of advanced materials, rock mechanics, civil engineering, and so on. However, microstructures are often neglected in the classical local (Cauchy) continuum model, resulting in inaccurate descriptions of the behavior of microstructured materials. In this work, in order to show the impact of microstructures, an implicit 'non-local' model, i.e., micropolar continuum (Cosserat), is used to numerically investigate the effects of direction and scale of microstructures on the tension problem of a composite plate with a circular hole. The results show that distributions of field variables (such as displacements and stresses) have an obvious directionality with respect to the microstructures' direction. As the scale of microstructures increases, such a direction effect becomes more evident. Unlike the isotropic material where stress concentration occurs at the vertex of the hole and the stress concentration factor is close to 3, for the microstructured composite, the stress concentration can be observed at any location depending on the microstructures' directions, and the concentration factor can exceed 3 to a maximum close to 9 as the increasing scale of microstructures. In addition, differences in the mechanical behavior between Cosserat and Cauchy models can be also observed; such differences are more evident for the material showing a pronounced orthotropic nature.

Keywords: composite materials; microstructure direction; Cosserat continuum; stress concentration; scale effect

Citation: Shi, F.; Fantuzzi, N.; Trovalusci, P.; Li, Y.; Wei, Z. Stress Field Evaluation in Orthotropic Microstructured Composites with Holes as Cosserat Continuum. *Materials* **2022**, *15*, 6196. https://doi.org/10.3390/ma15186196

Academic Editor: Alexander Yu Churyumov

Received: 2 August 2022
Accepted: 4 September 2022
Published: 6 September 2022

1. Introduction

Microstructure is one of the most critical factors that involves many kinds of materials such as rock, ceramic, alloy, human cortical bone, etc. [1–4]. As an internal structure, microstructure can play a crucial role in determining the gross behavior and mechanical response of materials [5]. However, the microstructures in materials distribute randomly with different lengths and directions, which complicates the understanding of the material's response. In general, materials with microstructure have weaker strength than in intact materials [6,7]. Guo et al. [8] experimentally investigated the effect of bedding angle in phyllite under unloading confining pressures, where the rock bedding joints can be regarded as microstructures. They found that the rock shows different strengths as the bedding angle changes. Numerical research on the tunnel surrounding rocks with different inclination angles also shows a directional effect on the distributions of displacements and stress around the tunnel [9]. By reviewing indentation tests at the micron scale, Bauer et al. [10] demonstrate that an obvious length scale effect (i.e., non-locality) can be

found when the material's intrinsic length scales are comparable with the dimension of specimens. Therefore, it is of importance to describe the macroscopic response of these materials by considering the influences of the microstructures.

The existence of microstructure results in the heterogeneity characteristic of materials. There are various methods that can be used to model the behavior of microstructured materials. Discrete modeling with interactions of each constituent in materials is a good option because it can produce an accurate result; however, this approach is often computationally cumbersome [11–13]. Alternatively, homogenizing the heterogeneous material as an equivalent continuum could be an efficient approach because it is faster and takes less computational cost [14]. Nevertheless, the application of this approach depends on selections of the homogenization method and macroscopic continuum theory that need to reveal the presence of microstructures. As is known, the classical Cauchy continuum may have disadvantages in describing the gross behavior of microstructured materials since it lacks in internal length descriptions [15,16]. This calls for the application of the non-local continuum theory, as this approach can reveal the presence of internal lengths [17]. In the non-local theory, internal lengths can be represented by adding extra degrees of freedom or parameter as internal variables, corresponding to the so-called implicit and explicit non-local descriptions, respectively [18,19].

The Cosserat continuum theory is a widely used implicit non-local model to investigate the microstructured material's behavior. After the completed mathematical foundations of the micropolar continuum was achieved, this theory became very popular (since the 70s). The Cosserat model introduces to each material point an extra degree of freedom, termed microrotation, which is different from the local rigid rotation (i.e., macrorotation). As a result, the stress and strain fields become asymmetric in this model, which is different from the classical Cauchy model with symmetric measurements. Moraes et al. [1] found that the asymmetrical property in the Cosserat model can be helpful to improve the description of the mechanical behavior of the materials such as rocks. The asymmetric strains also correspond to the relative rotation between the microrotation and macrorotation. Pau and Trovalusci [20] found that the relative rotation is significant in anisotropic materials, whereas it can be negligible in orthotetragonal materials where the internal length trends to vanish. With the advantage of keeping the memory of the microstructure, the Cosserat continuum was used to study many kinds of materials such as layered materials [21,22], fiber-reinforced materials [23,24], granular materials [25], and composites [26–28]. Using a homogenization process for the Cosserat continuum, Trovalusci and Masiani [29] numerically and experimentally studied the mechanical behavior of an inclined masonry structure in which microstructures (interfaces) show a different direction from the ordinary masonry structure. However, the results of this literature only showed the micropolar effect resulted from the Cosserat continuum but the effect of microstructures direction was not further discussed.

In this work, the effects of the microstructure's direction and length scale in a composite are studied to extend the understanding of microstructured materials, such as advanced materials with various microstructured and layered rocks with inclined angles. The composite considered here is made of rectangular blocks interacting with each other through their elastic interfaces, and it is homogenized as a Cosserat continuum by an energetic-equivalence-based homogenization technique [30]. Thus, the characteristic of non-locality is involved in this study. Six directions and four length scales of the microstructure are investigated by the finite element method (FEM) for a tension problem of a composite plate with a circular hole. Therefore, this work also focuses on the stress concentration problem of microstructured materials. This problem has been widely reported in previous studies [31–34]. Holes in materials can induce stress concentration around it and hence reduce the mechanical properties [35]. However, a number of solutions have been carried out for holes in isotropic plates [36]. With the increasing research interests on materials, especially with microstructures, it is essential to gain a better understanding in modeling the mechanical behavior of these materials.

This paper is structured as follows. After the introduction section, Section 2 introduces the Cosserat theory and its FEM implementation. Section 3 presents the model, parameters, methods, etc. used in the simulations of the tension problem for a plate with a circular hole. In Section 4, numerical simulations are conducted and results of displacements, stresses, and relative rotation are shown. The stress distribution around the hole is discussed and the simulation results are analyzed in Section 5. In the end, conclusions and remarks are drawn in Section 6.

2. Cosserat Continuum and Its FEM Implementation

The Cosserat continuum is considered to be a multi-scale tool [37] that can be used to investigate the mechanical behavior of materials where the microstructures and, in particular, internal lengths, play a crucial role. As an implicit' non-local continuum, it is equipped with additional degrees of freedom revealing the presence of microstructures. That is, for two-dimensional (2D) Cosserat media, each material point has two translation degrees of freedom u_1, u_2 and an additional microrotation degree of freedom ω. The microrotation ω is an independent degree of freedom and it is different from the macro-rotation θ which is defined as the skew-symmetric part of the gradient of displacement. Thus, a peculiar measurement, the relative rotation $\theta - \omega$, can be defined in this continuum. A general displacement vector for the Cosserat material point can be expressed as:

$$\boldsymbol{d}^\top = \begin{bmatrix} u_1 & u_2 & \omega \end{bmatrix} = \begin{bmatrix} \boldsymbol{u}^\top & \omega \end{bmatrix} \tag{1}$$

where $\boldsymbol{u}^\top = \begin{bmatrix} u_1 & u_2 \end{bmatrix}$. Due to the introduction of ω, the tangential strains in the Cosserat model are not reciprocal, i.e., $\varepsilon_{12} \neq \varepsilon_{21}$, and the microcurvature component is introduced as an additional strain measure; therefore, the linear strain–displacement relation can be expressed as:

$$\begin{bmatrix} \boldsymbol{\varepsilon} \\ \boldsymbol{\chi} \end{bmatrix} = \begin{bmatrix} \boldsymbol{L} & \boldsymbol{M} \\ 0 & \nabla \end{bmatrix} \begin{bmatrix} \boldsymbol{u} \\ \omega \end{bmatrix} \tag{2}$$

where $\boldsymbol{\varepsilon}^\top = \begin{bmatrix} \varepsilon_{11} & \varepsilon_{22} & \varepsilon_{12} & \varepsilon_{21} \end{bmatrix}$ contains the normal and tangential strains and $\boldsymbol{\chi}^\top = \begin{bmatrix} \chi_1 & \chi_2 \end{bmatrix}$ contains the microcurvatures. ∇ is the gradient operator, and

$$\begin{aligned} \boldsymbol{L} &= \begin{bmatrix} \frac{\partial}{\partial x_1} & 0 & \frac{\partial}{\partial x_2} & 0 \\ 0 & \frac{\partial}{\partial x_2} & 0 & \frac{\partial}{\partial x_1} \end{bmatrix}^\top, \\ \boldsymbol{M} &= \begin{bmatrix} 0 & 0 & 1 & -1 \end{bmatrix}^\top \end{aligned} \tag{3}$$

With the strain measures, the stresses of the Cosserat continuum can be obtained by a linear elastic constitutive equation as:

$$\begin{bmatrix} \boldsymbol{\sigma} \\ \boldsymbol{\mu} \end{bmatrix} = \begin{bmatrix} \mathbb{A} & \mathbb{B} \\ \mathbb{B}^\top & \mathbb{D} \end{bmatrix} \begin{bmatrix} \boldsymbol{\varepsilon} \\ \boldsymbol{\chi} \end{bmatrix} \tag{4}$$

where $\boldsymbol{\sigma}^\top = \begin{bmatrix} \sigma_{11} & \sigma_{22} & \sigma_{12} & \sigma_{21} \end{bmatrix}$ contains the normal and tangential stresses and $\boldsymbol{\mu}^\top = \begin{bmatrix} \mu_1 & \mu_2 \end{bmatrix}$ contains the couple stresses. The tangential stress components are also not reciprocal ($\sigma_{12} \neq \sigma_{21}$). The constitutive sub-matrices $\mathbb{A}$, $\mathbb{B}$, and $\mathbb{D}$ collect the constitutive terms A_{ijhk}, B_{ijh}, and D_{ij}, where i, j, h and $k = 1, 2$.

A detailed three-dimensional finite element formulation for the Cosserat continuum can be found in [38]. For the sake of simplicity, the displacement-based finite element implementation for 2D Cosserat theory is presented here to model the behavior of microstructured material. Firstly, in the finite element procedure, displacement and microrotation fields should be approximated by the nodal values of an element. In this study, for avoiding

the element locking problem, a bi-quadratic ($\boldsymbol{N_u}$) and a bi-linear ($\boldsymbol{N_\omega}$) shape function are, respectively, used for the displacement and microrotation approximation:

$$\begin{array}{ll} \boldsymbol{u} & = \boldsymbol{N_u}\tilde{\boldsymbol{u}} \\ \boldsymbol{\omega} & = \boldsymbol{N_\omega}\tilde{\boldsymbol{\omega}} \end{array} \tag{5}$$

where $\tilde{\boldsymbol{u}}$ and $\tilde{\boldsymbol{\omega}}$ are nodal displacement and microrotation values. In the present paper, nine-node quadrangular elements are considered for an element. All nine node values are used to approximate the displacements, whereas values at four corner nodes are used for the microrotation. $\boldsymbol{N_u}$ and $\boldsymbol{N_\omega}$ can be expressed as:

$$\begin{array}{ll} \boldsymbol{N_u} & = \begin{bmatrix} {N_1}^u & 0 & \dots & {N_9}^u & 0 \\ 0 & {N_1}^u & 0 & \dots & {N_9}^u \end{bmatrix}, \\ \boldsymbol{N_\omega} & = \begin{bmatrix} {N_1}^\omega & \dots & {N_4}^\omega \end{bmatrix} \end{array} \tag{6}$$

Substituting Equation (5) into (2), the strain vectors become:

$$\begin{array}{ll} \boldsymbol{\varepsilon} & = \begin{bmatrix} \boldsymbol{L}\boldsymbol{N_u} & \boldsymbol{M}\boldsymbol{N_\omega} \end{bmatrix} \begin{Bmatrix} \tilde{\boldsymbol{u}} & \tilde{\boldsymbol{\omega}} \end{Bmatrix}^\top = \boldsymbol{B_\varepsilon}\tilde{\boldsymbol{d}}, \\ \boldsymbol{\chi} & = \begin{bmatrix} 0 & \nabla\boldsymbol{N_\omega} \end{bmatrix} \begin{Bmatrix} \tilde{\boldsymbol{u}} & \tilde{\boldsymbol{\omega}} \end{Bmatrix}^\top = \boldsymbol{B_\chi}\tilde{\boldsymbol{d}} \end{array} \tag{7}$$

where $\boldsymbol{B_\varepsilon}$ and $\boldsymbol{B_\chi}$ are the derivatives of the shape functions. $\tilde{\boldsymbol{d}}$ is the unknown nodal values collecting $\tilde{\boldsymbol{u}}$ and $\tilde{\boldsymbol{\omega}}$. Substituting Equation (7) into Equation (4), the constitutive relations become:

$$\begin{array}{ll} \boldsymbol{\sigma} & = \mathbb{A}\boldsymbol{B_\varepsilon}\tilde{\boldsymbol{d}} + \mathbb{B}\boldsymbol{B_\chi}\tilde{\boldsymbol{d}}, \\ \boldsymbol{\mu} & = \mathbb{B}^\top\boldsymbol{B_\varepsilon}\tilde{\boldsymbol{d}} + \mathbb{D}\boldsymbol{B_\chi}\tilde{\boldsymbol{d}} \end{array} \tag{8}$$

Now, the stress and couple stress measures can be obtained from the nodal values. Considering a domain $\mathcal{A}$ and boundary Γ, the principle of virtual work can be expressed as:

$$\int_{\mathcal{A}} \delta\boldsymbol{\varepsilon}^\top\boldsymbol{\sigma} + \delta\boldsymbol{\chi}^\top\boldsymbol{\mu}\, d\mathcal{A} = \int_{\mathcal{A}} \delta\boldsymbol{u}^\top\mathbf{b}\, d\mathcal{A} + \int_{\Gamma} \delta\boldsymbol{u}^\top\bar{\boldsymbol{t}} + \delta\boldsymbol{\omega}^\top\overline{\boldsymbol{m}}\, d\Gamma \qquad \forall\delta\boldsymbol{u}, \delta\boldsymbol{\omega} \tag{9}$$

where δ is the variational operator, $\boldsymbol{b}$ is the body force vector. $\bar{\boldsymbol{t}}$ and $\overline{\boldsymbol{m}}$ are the traction and couple-traction vectors applied on the boundary Γ. The components (t_i and m_i) of $\bar{\boldsymbol{t}}$ and $\overline{\boldsymbol{m}}$ should satisfy the equilibrium at external boundary as $t_i = \sigma_{ij}n_j$ and $m_i = \mu_j n_j$, where n_j is the components of the outward unit normal to the boundary. Substituting Equations (5), (7) and (8) into (9) and excluding body forces, we obtain:

$$\delta\tilde{\boldsymbol{d}}^\top \underbrace{\int_{\mathcal{A}^e} \left(\boldsymbol{B_\varepsilon}^\top\mathbb{A}\boldsymbol{B_\varepsilon} + \boldsymbol{B_\varepsilon}^\top\mathbb{B}\boldsymbol{B_\chi} + \boldsymbol{B_\chi}^\top\mathbb{B}^\top\boldsymbol{B_\varepsilon} + \boldsymbol{B_\chi}^\top\mathbb{D}\boldsymbol{B_\chi} \right) d\mathcal{A}^e}_{\boldsymbol{K}^e} \tilde{\boldsymbol{d}} = \delta\tilde{\boldsymbol{d}}^\top \underbrace{\int_{\Gamma^e} \begin{bmatrix} \boldsymbol{N_u}^\top\bar{\boldsymbol{t}} \\ \\ \boldsymbol{N_\omega}^\top\overline{\boldsymbol{m}} \end{bmatrix} d\Gamma^e}_{\boldsymbol{F}^e} \quad \forall\delta\tilde{\boldsymbol{d}} \tag{10}$$

where $\boldsymbol{K}^e$ and $\boldsymbol{F}^e$ are the element stiffness matrix and the element nodal force vector. They can be computed numerically by a Gauss–Legendre integration with 3×3 grid. If considering arbitrary $\delta\tilde{\boldsymbol{d}}$, we can obtain the standard finite element formulation as:

$$\boldsymbol{K}^e\tilde{\boldsymbol{d}} = \boldsymbol{F}^e \tag{11}$$

At the end, the unknown $\tilde{\boldsymbol{d}}$ can be obtained by solving this equation. With this solution, in the post-processing stresses and strains are firstly computed at Gauss points for each element and then an extrapolation technique is used to get stresses and strains at element nodal points.

The above implementations are achieved by an updated MATLAB code based on codes of a classical 2D Cauchy continuum as presented in [39].

3. Numerical Simulation

In this section, we intend to numerically investigate the effects of direction and scale of microstructures for a composite material that can be considered as an assembly made of rigid rectangular blocks in contact with elastic interfaces (Figure 1), where each rectangular block has the width of b and height of h. The assembly is arranged as an interlocking structure and the interfaces of blocks form the microstructures of this composite material. A homogenization procedure presented in [30] can be used to describe the assembly as an equivalent Cosserat continuum. In this work, 7-block representative volume element (RVE) that is highlighted with orange color in Figure 1 is used for the homogenization procedure to produce the Cosserat constitutive matrix in Equation (4). In the highlighted RVE, the blocks' centroids are represented by green crosses, and red lines mean the outward unit normal vectors of the central block's interfaces. The direction of microstructures can be changed by transforming the assembly of an angle β from $x - y$ coordinate system to $X - Y$ coordinate system as shown in Figure 1. In this study, we select 6 values of β $(0°, 30°, 60°, 90°, 120°, 150°)$. Furthermore, to obtain various scales of microstructures, 4 different block sizes are used by fixing the height of block $h = 0.1$ m and changing the aspect ratio $\rho = b/h = 1.5, 3, 7$, and 15, where a greater ρ corresponds to a longer rectangular block, as a consequence, showing more orthotropic nature.

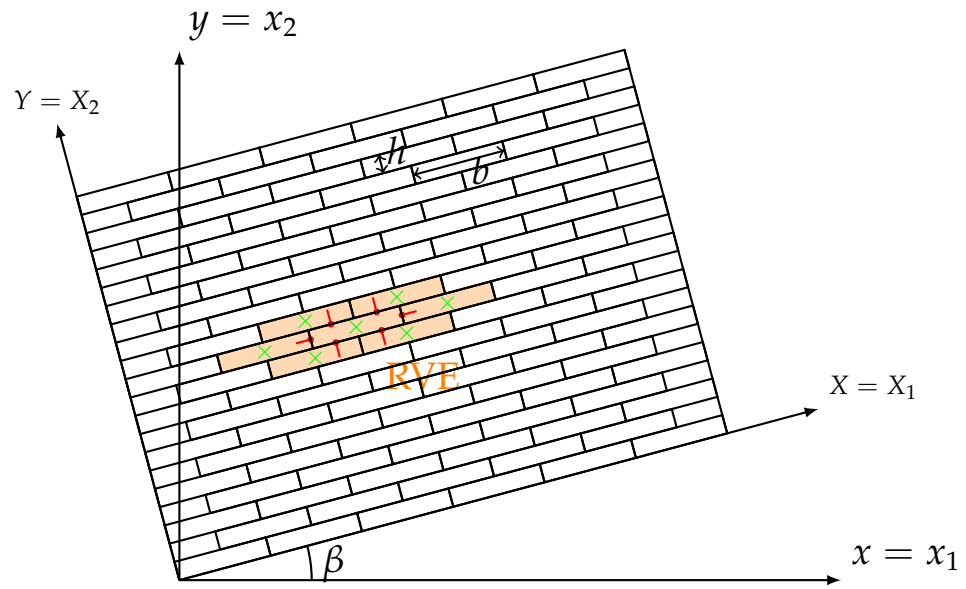

Figure 1. Schemes of the considered assembly and RVE.

The blocks interact among themselves through elastic common interfaces. The adopted spring stiffness at the interfaces is:

$$K = \begin{bmatrix} k_n & 0 \\ 0 & k_t \end{bmatrix} \tag{12}$$

where k_n and k_t are the normal and tangential stiffness per unit length, respectively. Here we have $k_n = 576.58$ MPa/m and $k_t = 288.29$ MPa/m. The rotation stiffness of interface is computed $k_r = k_n(d/2)^2$, where d is the length of interface. Therefore, the Cosserat constitutive matrices of the reference RVE when $\beta = 0°$ can be obtained by the homogenization technique that is based on an equivalence energy criterion between the material's discrete system of and the continuum model [30]. The constitutive matrix of transformed assembly can be obtained as follows:

$$\boldsymbol{C} = \boldsymbol{Q}^\top \boldsymbol{C_0} \boldsymbol{Q} \tag{13}$$

where $\boldsymbol{C_0}$ is the constitutive matrix when $\beta = 0°$, $\boldsymbol{Q}$ is the usual transformation matrix [40].

For comparison, the Cauchy continuum is also considered here to carry out the same simulations as performed by the Cosserat continuum. Because of the lack in microstructures, the constitutive relation of the Cauchy continuum has the form of: $\boldsymbol{\sigma} = \hat{\mathbb{A}}\boldsymbol{\varepsilon}$, where the matrix $\hat{\mathbb{A}}$ is obtained from $\mathbb{A}$ and their relationship can be found in the previous literature as [41]:

$$\begin{aligned}
\hat{A}_{1111} &= A_{1111} \\
\hat{A}_{1122} &= A_{1122} \\
\hat{A}_{2222} &= A_{2222} \\
\hat{A}_{1112} &= (A_{1112} + A_{1121})/2 \\
\hat{A}_{2212} &= (A_{2212} + A_{2221})/2 \\
\hat{A}_{1212} &= (A_{1212} + A_{2121} + 2A_{1221})/4
\end{aligned} \tag{14}$$

Tables 1–4 list the constitutive components of all configurations, where components keeping zero for all configurations are not reported. It can be seen that there are more zero components when $\beta = 0^\circ$ and 90°. Actually, only diagonal components of the constitutive matrix exist and an orthotropic nature of the material is observed for these two transformation angles. For other angles, all components of matrices $\mathbb{A}$ and $\mathbb{D}$ appear. Consequently, materials with these RVEs show a centrosymmetric nature [30]. $\mathbb{B} = 0$ for all configurations, meaning there is no coupling between stresses/microcurvatures and microcouples/strains. As the aspect ratio ρ increases, constitutive components change monotonously except for A_{2222}, A_{1212} of Cosserat continuum and $\hat{A}_{2222}$ of Cauchy continuum when $\beta = 0^\circ$. Because of the fixed height of blocks (h), these components stay the same with increasing ρ.

Table 1. Cosserat and Cauchy constitutive parameters for RVE with block parameter $\rho = 1.5$, A_{ijkl}, $\hat{A}_{ijkl}$ [MPa], D_{ij} [MPa·m^2].

	0°	**30°**	**60°**	**90°**	**120°**	**150°**
A_{1111}	102.70	80.97	58.45	57.66	58.45	80.97
A_{1122}	0	10.47	10.47	0	10.47	10.47
A_{1112}	0	25.94	13.85	0	−13.85	−25.94
A_{1121}	0	5.66	−6.44	0	6.44	−5.66
A_{2222}	57.66	58.45	80.97	102.70	80.97	58.45
A_{2212}	0	−6.44	5.66	0	−5.66	6.44
A_{2221}	0	13.85	25.94	0	−25.94	−13.85
A_{1212}	28.83	51.01	74.44	75.68	74.44	51.01
A_{1221}	0	10.47	10.47	0	10.47	10.47
A_{2121}	75.68	74.44	51.01	28.83	51.01	74.44
D_{11}	0.57	0.47	0.29	0.19	0.29	0.47
D_{12}	0	0.16	0.16	0	−0.16	−0.16
D_{22}	0.19	0.29	0.47	0.57	0.47	0.29
$\hat{A}_{1111}$	102.70	80.97	58.45	57.66	58.45	80.97
$\hat{A}_{1122}$	0	10.47	10.47	0	10.47	10.47
$\hat{A}_{1112}$	0	15.80	3.71	0	−3.71	−15.80
$\hat{A}_{2222}$	57.66	58.45	80.97	102.70	80.97	58.45
$\hat{A}_{2212}$	0	3.71	15.80	0	−15.80	−3.71
$\hat{A}_{1212}$	26.13	36.60	36.60	26.13	36.60	36.60

Table 2. Cosserat and Cauchy constitutive parameters for RVE with block parameter $\rho = 3$, A_{ijkl}, $\hat{A}_{ijkl}$ [MPa], D_{ij} [MPa·m^2].

	0°	**30°**	**60°**	**90°**	**120°**	**150°**
A_{1111}	237.84	183.34	93.24	57.66	93.24	183.34
A_{1122}	0	9.46	9.46	0	9.46	9.46
A_{1112}	0	85.04	74.12	0	−74.12	−85.04
A_{1121}	0	3.90	−7.02	0	7.02	−3.90
A_{2222}	57.66	93.24	183.34	237.84	183.34	93.24
A_{2212}	0	−7.02	3.90	0	−3.90	7.02
A_{2221}	0	74.12	85.04	0	−85.04	−74.12
A_{1212}	28.83	85.14	178.83	216.22	178.83	85.14
A_{1221}	0	9.46	9.46	0	9.46	9.46
A_{2121}	216.22	178.83	85.14	28.83	85.14	178.83
D_{11}	3.64	2.87	1.33	0.56	1.33	2.87
D_{12}	0	1.33	1.33	0	−1.33	−1.33
D_{22}	0.56	1.33	2.87	3.64	2.87	1.33
$\hat{A}_{1111}$	237.84	183.34	93.24	57.66	93.24	183.34
$\hat{A}_{1122}$	0	9.46	9.46	0	9.46	9.46
$\hat{A}_{1112}$	0	44.47	33.55	0	−33.55	−44.47
$\hat{A}_{2222}$	57.66	93.24	183.34	237.84	183.34	93.24
$\hat{A}_{2212}$	0	33.55	44.47	0	−44.47	−33.55
$\hat{A}_{1212}$	61.26	70.72	70.72	61.26	70.72	70.72

Table 3. Cosserat and Cauchy constitutive parameters for RVE with block parameter $\rho = 7$, A_{ijkl}, $\hat{A}_{ijkl}$ [MPa], D_{ij} [MPa·m^2].

	0°	**30°**	**60°**	**90°**	**120°**	**150°**
A_{1111}	756.76	604.96	255.41	57.66	255.41	604.96
A_{1122}	0	−22.97	−22.97	0	−22.97	−22.97
A_{1112}	0	328.47	354.99	0	−354.99	−328.47
A_{1121}	0	−52.27	−25.75	0	25.75	52.27
A_{2222}	57.66	255.41	604.96	756.76	604.96	255.41
A_{2212}	0	−25.75	−52.27	0	52.27	25.75
A_{2221}	0	354.99	328.47	0	−328.47	−354.99
A_{1212}	28.83	225.68	665.32	908.11	665.32	225.68
A_{1221}	0	−22.97	−22.97	0	−22.97	−22.97
A_{2121}	908.11	665.32	225.68	28.83	225.68	665.32
D_{11}	59.06	44.97	16.81	2.72	16.81	44.97
D_{12}	0	24.40	24.40	0	−24.40	−24.40
D_{22}	2.72	16.81	44.97	59.06	44.97	16.81
$\hat{A}_{1111}$	756.76	604.96	255.41	57.66	255.41	604.96
$\hat{A}_{1122}$	0	−22.97	−22.97	0	−22.97	−22.97
$\hat{A}_{1112}$	0	138.10	164.62	0	−164.62	−138.10
$\hat{A}_{2222}$	57.66	255.41	604.96	756.76	604.96	255.41
$\hat{A}_{2212}$	0	164.62	138.10	0	−138.10	−164.62
$\hat{A}_{1212}$	234.23	211.26	211.26	234.23	211.26	211.26

Table 4. Cosserat and Cauchy constitutive parameters for RVE with block parameter $\rho = 15$, A_{ijkl}, $\hat{A}_{ijkl}$ [MPa], D_{ij} [MPa·m^2].

	0°	**30°**	**60°**	**90°**	**120°**	**150°**
A_{1111}	2486.50	2096.86	882.44	57.66	882.44	2096.86
A_{1122}	0	−217.57	−217.57	0	−217.57	−217.57
A_{1112}	0	1189.82	1441.04	0	−1441.04	−1189.82
A_{1121}	0	−389.32	−138.10	0	138.10	389.32
A_{2222}	57.66	882.44	2096.86	2486.50	2096.86	882.44
A_{2212}	0	−138.10	−389.32	0	389.32	138.10
A_{2221}	0	1441.04	1189.82	0	−1189.82	−1441.04
A_{1212}	28.83	722.98	2546.41	3675.70	2546.41	722.98
A_{1221}	0	−217.57	−217.57	0	−217.57	−217.57
A_{2121}	3675.70	2546.41	722.98	28.83	722.98	2546.41
D_{11}	933.59	703.25	242.57	12.23	242.57	703.25
D_{12}	0	398.96	398.96	0	−398.96	−398.96
D_{22}	12.23	242.57	703.25	933.59	703.25	242.57
$\hat{A}_{1111}$	2486.50	2096.86	882.44	57.66	882.44	2096.86
$\hat{A}_{1122}$	0	−217.57	−217.57	0	−217.57	−217.57
$\hat{A}_{1112}$	0	400.25	651.47	0	−651.47	−400.25
$\hat{A}_{2222}$	57.66	882.44	2096.86	2486.50	2096.86	882.44
$\hat{A}_{2212}$	0	651.47	400.25	0	−400.25	−651.47
$\hat{A}_{1212}$	926.13	708.56	708.56	926.13	708.56	708.56

In the following, a classical tension problem of a square plate with a circular hole is studied for all above-mentioned configurations. Figure 2 shows the sketch of the problem and its finite element meshing. The plate has a side length of 10 m and the radius of the hole is 1.25 m. A total of 1440 elements is used for this model. Due to the singular nature resulting from the presence of the hole, stress concentration is more likely observed around the hole under tension force. To make sure the results are reliable, a finer mesh is applied near the hole. Uniform tensile stress $\sigma_0 = 1$ MPa is applied on the right side of the plate. The left side of the plate is fixed symmetrically in the x-direction and the bottom left point is additionally fixed in the y-direction. In the present paper, the direction and scale effect of microstructure is investigated by setting various β and ρ. The simulation results are shown below.

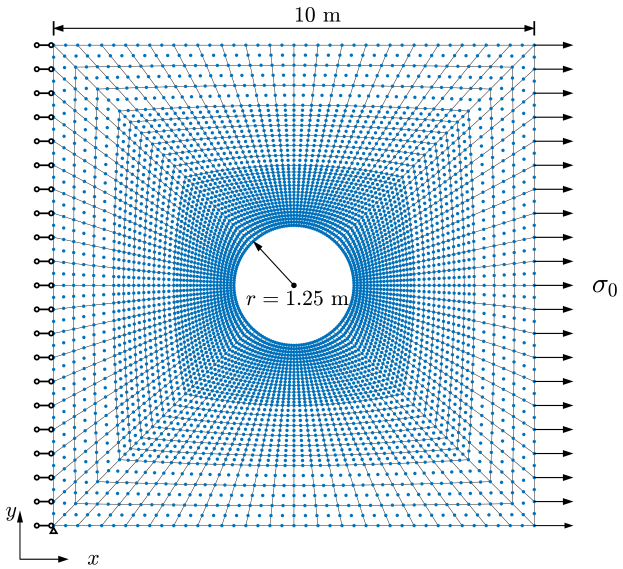

Figure 2. Sketch of the plate with hole problem and its finite element mesh.

4. Results

The results of displacements and stresses for the Cosserat and Cauchy models and relative rotation for the Cosserat model are presented in this section to show the effects of microstructure's direction and scale on the behavior of microstructured composite materials. Figure 3 depicts the horizontal displacement results u_1 of Cosserat and Cauchy models. It can be seen that change in direction of microstructure has a significant effect on u_1 for both two models. The smallest u_1 can be observed when $\beta = 0°$. As β changes from 0° to 150°, u_1 increases to the greatest at $\beta = 90°$ and then decreases but this is expected for the shortest block case $\rho = 1.5$. In the case of $\rho = 1.5$, the greatest u_1 occurs at $\beta = 60°$ and 120° but that is also close to u_1 at $\beta = 90°$. For all β representing the directions of microstructure, u_1 has a reduction as ρ increases. For the plate with the shortest blocks, displacement localization can be observed at the middle of the right side of the plate. However, as ρ increases, displacement localization reduces and uniform displacement distribution can be observed at the right side of the plate.

It can be seen from Figure 3 that the difference in u_1 between Cosserat and Cauchy models is not obvious for the orthotropic materials ($\beta = 0°$ and 90°). Here we take the difference in the maximum u_1 between the two models as Δu_1. For various ρ, Δu_1 is 3.02–8.63 mm when $\beta = 0°$ and 2.13–5.85 mm when $\beta = 90°$. However, the difference is more evident for the centrosymmetric materials. Δu_1 increases from 20 mm to 69 mm as ρ increases when $\beta = 30°, 60°, 120°$, and 150°.

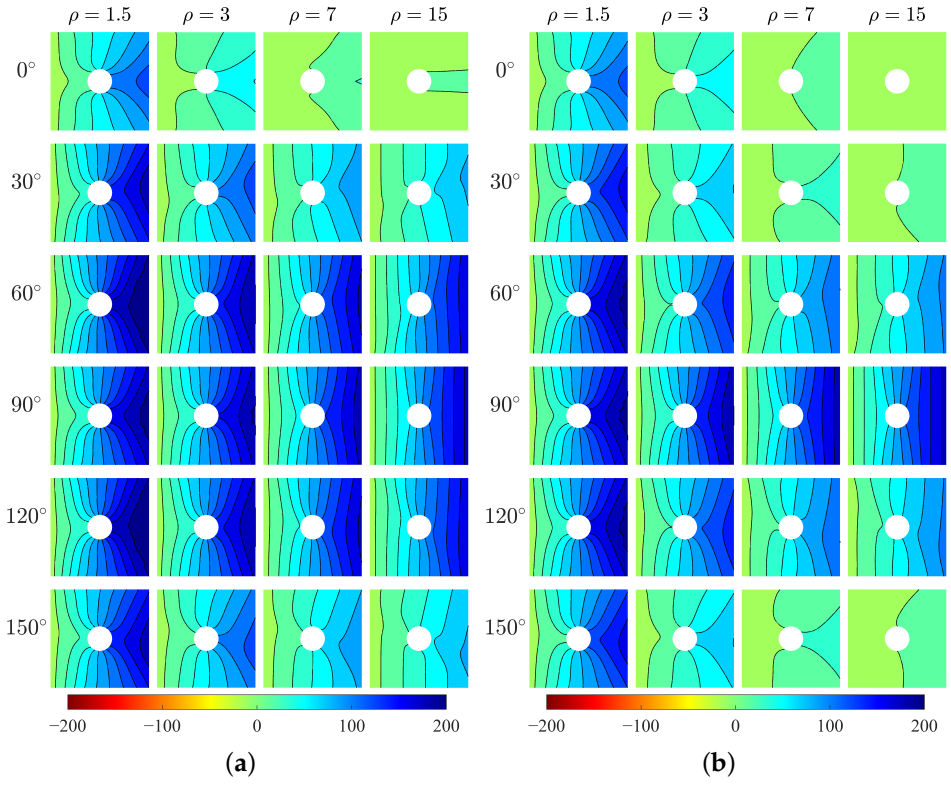

Figure 3. Horizontal displacement u_1, mm, (**a**) Cosserat, (**b**) Cauchy.

Figure 4 depicts the vertical displacement results u_2 for two models. The orthotropic materials ($\beta = 0°$ and 90°) show negligible u_2 under the horizontal tension stress for both models. However, the centrosymmetric materials with other transformation angles can produce clear u_2 with more or less directionality.

It should be noted that there is a big difference in u_2 between Cosserat and Cauchy models. u_2 of these two models has a similar distribution only when $\rho = 1.5$. As ρ increases, u_2 distributions of two models become different. When $\beta = 30°$ and 150°, the Cosserat

continuum shows high-intensity u_2 distribution on the right plate as ρ increases, e.g., the maximum u_2 is up to 117 mm when $\beta = 150°$; however, u_2 from the Cauchy continuum has no clear high-intensity distribution with ρ and the maximum u_2 is just 77 mm when $\beta = 150°$. An opposite difference between two models can be observed when $\beta = 60°$ and 120°, that is high-intensity u_2 distribution can be observed by the Cauchy but not the Cosserat model.

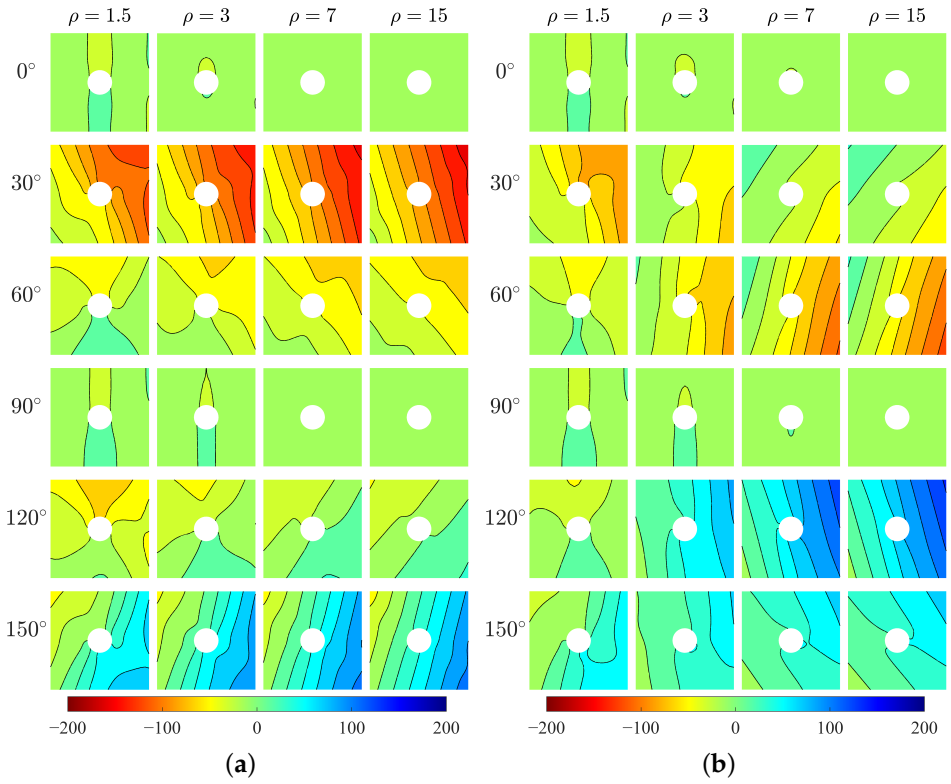

Figure 4. Vertical displacement u_2, mm, (**a**) Cosserat, (**b**) Cauchy.

The horizontal stresses σ_{11} of the two models are shown in Figure 5. The results show directionality of distribution of σ_{11} with respect to the direction β. For orthotropic materials, the high-stress area is parallel to the x-direction and the peak stress happens at the top and bottom points of the hole edge (i.e., $x = 0$). However, for centrosymmetric materials, the high-stress area is inclined with the x-direction by an angle that can be related to the direction of microstructure, and the location of peak stress changes. It can be seen the directionality of σ_{11} is more evident for greater ρ. As the increase of ρ, the high-stress area becomes wider. The exception happens at $\beta = 90°$ which shows the opposite behavior. The existence of the hole as a singularity can result in the concentration of stress around the hole edge. In the following, the stress concentration at the hole boundary will be discussed.

Vertical stress σ_{22} (Figure 6) also shows directionality of stress distribution with respect to β. There can be seen a difference in σ_{22} between two models for various ρ. For relative short blocks ($\rho = 1.5$ and 3), two models produce closed behavior of σ_{22}. However, for longer blocks ($\rho = 7$ and 15) especially at $\beta = 60°, 90°$ and 120°, σ_{22} from Cauchy model is significantly greater than that from Cosserat model.

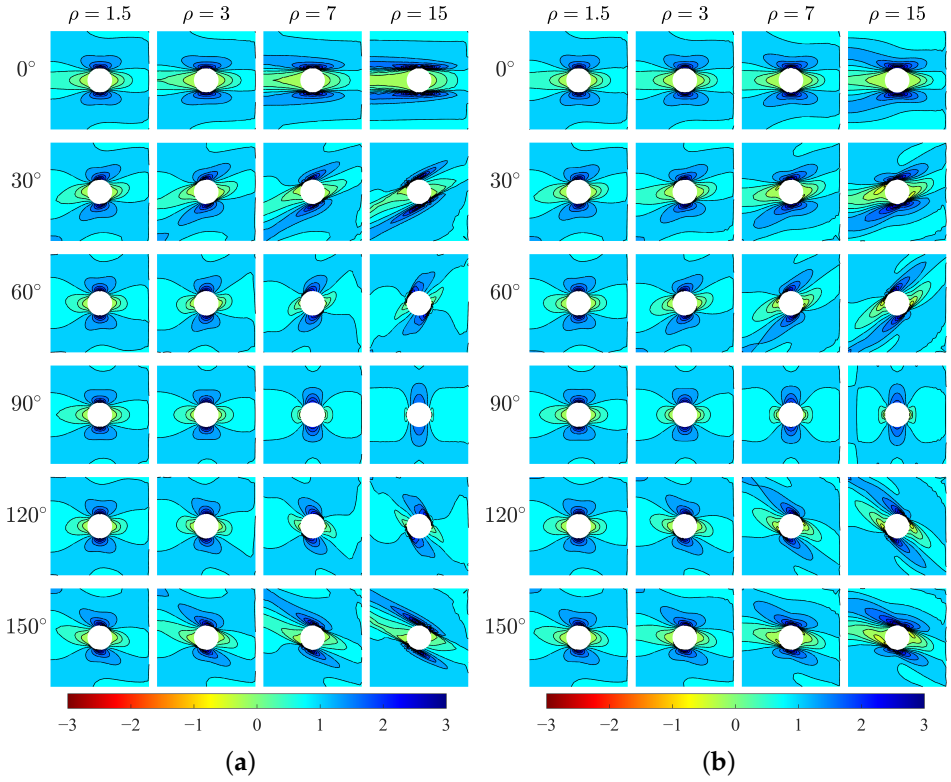

Figure 5. Horizontal stress σ_{11}, MPa, (**a**) Cosserat, (**b**) Cauchy.

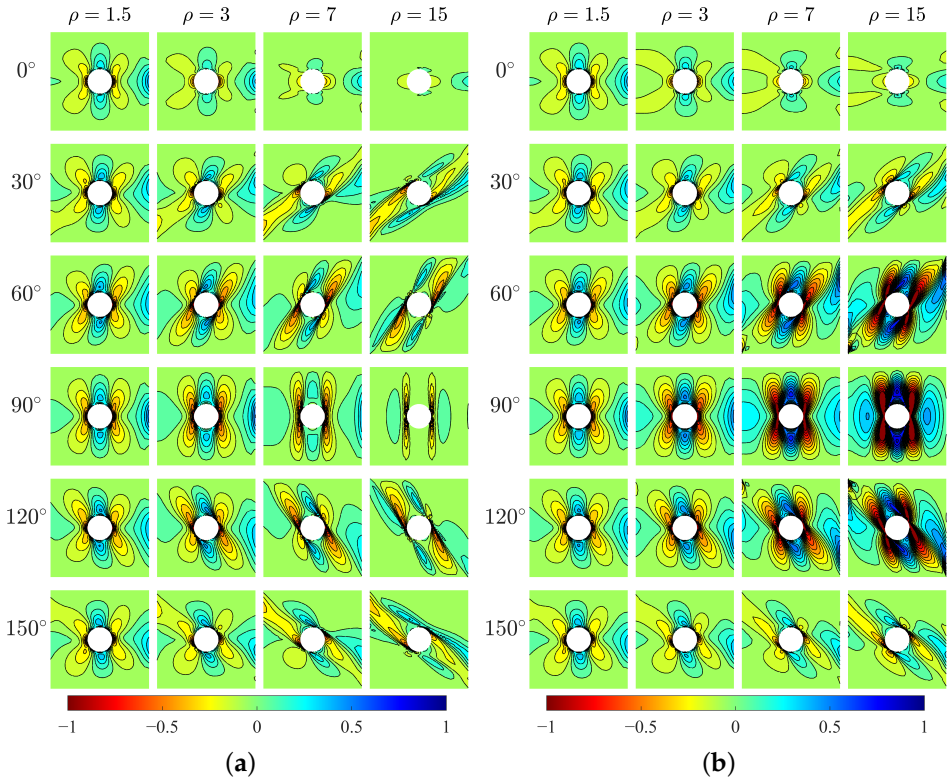

Figure 6. Vertical stress σ_{22}, MPa, (**a**) Cosserat, (**b**) Cauchy.

The relative rotation, defined as the difference between macrorotation (θ) and microrotation (ω), is a peculiar measurement in the Cosserat model. Figure 7 shows the relative rotation $\theta - \omega$ for the Cosserat model. The directionality of $\theta - \omega$ distribution can be also observed and that is more evident as ρ increases. For orthotropic materials, $\theta - \omega$ shows point symmetric behavior with respect to the hole center where positive and negative $\theta - \omega$ can be both observed, but the value of $\theta - \omega$ is close to 0. Thus, the Cosserat model is very close to the Cauchy one. For $\beta = 30^\circ$ and 60°, the plate domain mainly undergoes a positive relative rotation. Oppositely, for $\beta = 120^\circ$ and 150°, this domain mainly undergoes a negative $\theta - \omega$. The above-mentioned indicates that relative rotation can be affected by the direction of microstructure. There is less relative rotation when the microstructures are arranged along parallel and perpendicular to the direction of force, whereas the microstructures arranged along other directions would result in an obvious relative rotation acting at a certain orientation.

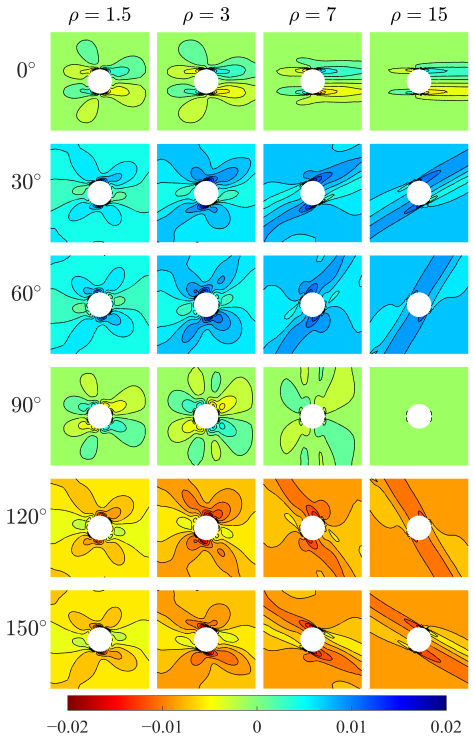

Figure 7. Relative rotation $\theta - \omega$ of Cosserat model.

5. Discussions

The problem of stress concentration has always been focused on due to the presence of singularity [32,42,43]. Under horizontal tension in this study, it can be seen that the stresses σ_{11} and σ_{22} in the plate (Figures 5 and 6) is mainly concentrated around the boundary of the hole. To better show the stress distribution, in the following, by transforming the stress state from Cartesian coordinate to polar coordinate, the hoop stress σ_h at the hole boundary is depicted for two models in the polar coordinate system as shown in Figure 8. In this way, σ_h represents σ_{22} when the polar angle equals to 0 or π, whereas the hoop stress denotes σ_{11} when the polar angle is $\pi/2$ or $3\pi/2$. Therefore, the location and magnitude of σ_h can be clearly observed. For both Cosserat and Cauchy models, it can be seen that the distribution of σ_h at the hole boundary is point symmetric to the center of hole and also shows directionality that depends on the aspect ration ρ and angle β.

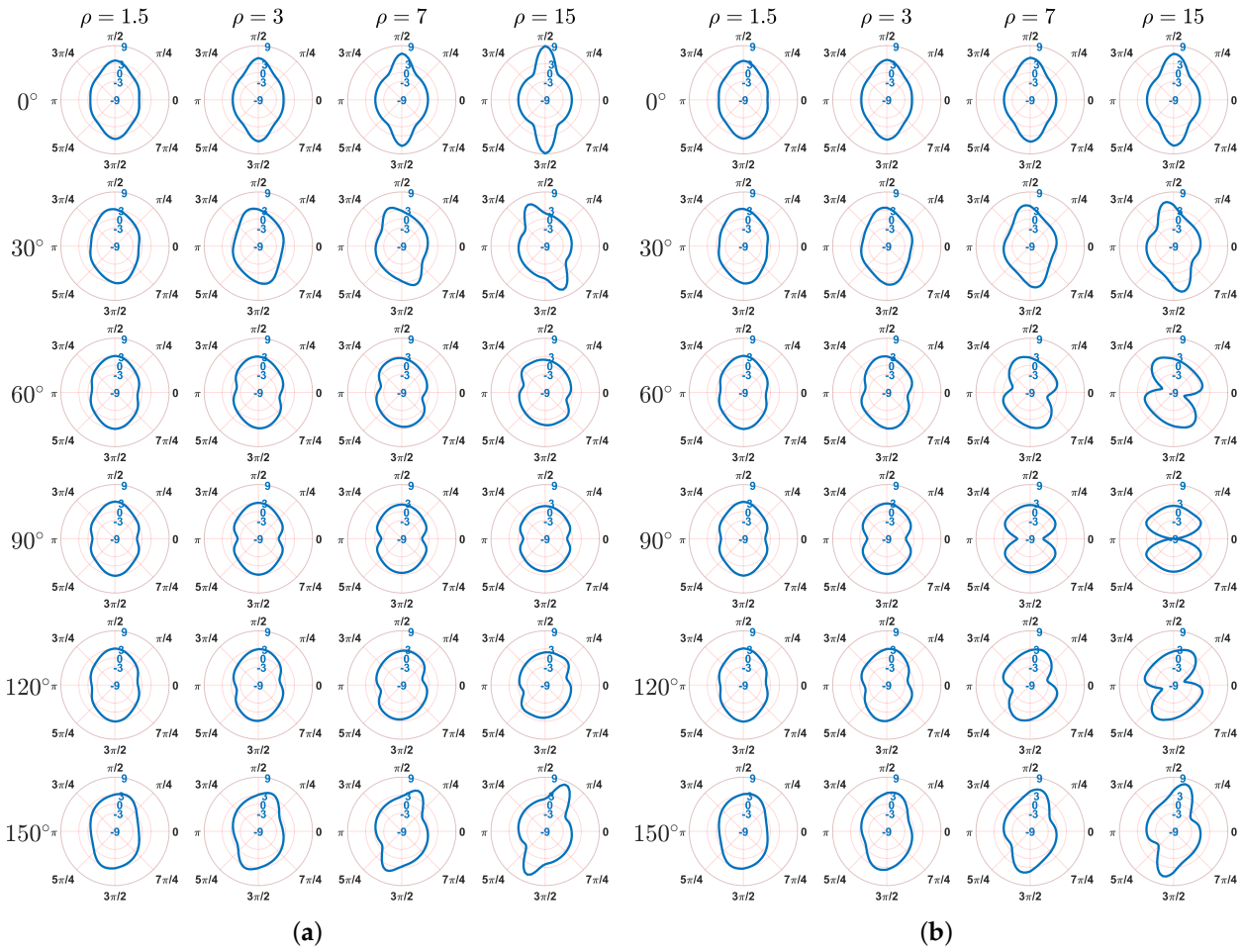

Figure 8. Distribution of the hoop stress σ_h at the hole boundary, MPa, (**a**) Cosserat, (**b**) Cauchy.

For the orthotropic materials, the distribution of σ_h is symmetrical along the vertical direction ($\pi/2 - 3\pi/2$) in the polar coordinate. The highest σ_h can be observed at the top and bottom points of the hole boundary (i.e., polar angle equals to $\pi/2$ and $3\pi/2$) for the Cosserat model and Cauchy model when $\beta = 0°$, indicating that the peak stress results from the horizontal stress σ_{11}. As for the Cauchy model when $\beta = 90°$, it is consistent with the above results for small ρ. As ρ increases, the highest σ_h trend to be occurred at the right and left points of the hole boundary (i.e., polar angle equals to 0 and π). Since we observed a significant σ_{22} concentration in the Cauchy model in Figure 6b, the vertical stress σ_{22} is able to result in the peak stress for these cases. For centrosymmetric materials, the distribution of σ_h is no longer symmetrical along the vertical direction but deviates from it to more or less of an extent because of the transformation angle of rectangular blocks. Thus, the highest σ_h does not occur at these special points, i.e., polar angle equals to 0, $\pi/2$, π, or $3\pi/2$. This is consistent with the results by early study [9], which investigates the stress distribution of the layered surrounding rock tunnel by considering different angles of rock joints (microstructures). It is also shown that the stress distribution is symmetrical when angle equals to 0° and 90°. When the angle is 45° the stress presents an asymmetric distribution and the tunnel even comes into being eccentric-pressed.

It should be noted that the effect of β is less for smaller ρ. When $\rho = 1.5$, the distribution of σ_h is close to each other, that is, the highest σ_h is located near to the top and bottom point of hole boundary and its value close to 3, whereas the lowest σ_h near to right and left points and its value is around 1. Such a result is close to the well-known analytical solution for an infinite isotropic plate with a circular hole [33,44]. However, as ρ increases, the directionality of σ_h distribution becomes more evident and the extreme values of σ_h

also vary. For example, when $\beta = 0^\circ$, as increase in ρ the highest value of σ_h can increase to 9. In addition, the difference between the Cosserat and Cauchy models gets bigger with increasing ρ. The smallest values of σ_h are not lower than -3 for the Cosserat continuum, whereas lower σ_h to -9 can be obtained from the Cauchy continuum, especially when $\beta = 60^\circ, 90^\circ$, and 120°.

By investigating measurements of displacements, stress, etc, and the stress distribution of the square plate with circular hole under horizontal tension stress, a direction effect of microstructures can be found for the present problem. With different transformation angle β, the plate can produce mechanical behavior showing obvious directionality. Such a direction effect of microstructures can be also found in previous studies on surrounding rock roadway and tunnels with different dip angles of surroundings [9,45], where the joints of surrounding rocks can represent the microstructure interfaces. In this present paper, similar behaviors are often observed when $\beta = 0^\circ$ and 90°. That is because the microstructures in these two cases are both parallel and perpendicular to the x-direction, showing an orthotropic nature. The difference between these two cases is actually due to the different values of ρ ($\rho < 1$ when $\beta = 90^\circ$ whereas $\rho > 1$ when $\beta = 0^\circ$); therefore, measurements of these two cases have similar behavior but different intensities under the horizontal tension stress. As for microstructures not parallel or perpendicular to the x-direction, i.e., $\beta = 30^\circ, 60^\circ, 120^\circ$ and 150°, it can be seen from the constitutive matrices (Tables 1–4) that more coupling in the constitutive components such as dilatancy components [46] appear for these cases, showing a centrosymmetric nature. The centrosymmetric material can show different behavior from the orthotropic material by coupling different stresses and strains as well as the couple stresses and curvatures. As the transformed constitutive matrix is related to β (Equation (13)), the behavior of the centrosymmetric material depends on β. Under horizontal tension stress, it is shown that u_1 first increases and then decreases with β. Oppositely, as β increases the maximum σ_h first decreases and then increases. Such an effect of β can be compared with the previous study [8] where a similar effect was found, that is, the strength of phyllite decreases first and then increases with the increase of bedding angle.

The direction effect of microstructures is more evident for higher ρ. When ρ is small (e.g., $\rho = 1.5$), the width of the rectangular block b is close to its height h. Thus, the assembly made of such blocks can show a nearly orthotetragonal behavior (close to isotropic) that is less sensitive to change in the microstructure direction. This could also account for the small differences between Cosserat and Cauchy results when ρ is small since it was known that orthotetragonal materials are very close to Cauchy continua [30,47].

With the increase in ρ, the assembly becomes more orthotropic and the measurements can show more obvious directionality with respect to β. As the length of microstructure (i.e., internal length) is introduced to the Cosserat continuum, asymmetries are generated for the shear stress and shear strain fields. Therefore, in the Cosserat model each stress is coupled with asymmetric shear strains through two constitutive components (A_{ij12} and A_{ij21}), and vice-versa. In the Cauchy model, there is just one component ($\hat{A}_{ij12}$). When ρ is small, the difference between A_{ij12} and A_{ij21} is not evident. As ρ increases, such difference increases rapidly, showing a higher degree of asymmetry. However, $\hat{A}_{ij12}$ of the Cauchy model is an arithmetic mean by A_{ij12} and A_{ij21} (Equation (14)), which cannot show the asymmetric behavior of continua. Thus, the difference between the results from Cosserat and Cauchy models may be induced, especially for higher ρ. Moreover, since the microstructures are considered in the Cosserat continuum, the additional sub-matrix $\mathbb{D}$ is involved in the Cosserat constitutive relation rather than the Cauchy one. The components of $\mathbb{D}$ are negligible for small ρ but become prominent as ρ increases. It has been found that the stress can be re-distributed within the Cosserat continuum [34]. For the smaller ρ, the Cosserat continuum behaves close to the Cauchy continuum as mentioned above. As a result, the re-distribution of stress can be neglected. However, as the scale of the microstructure increases, such a re-distribution can be more prominent for higher ρ. This can be used to

account for the difference in σ_{22} between the Cosserat and Cauchy continuum, especially for large ρ.

6. Conclusions

The present paper investigates the mechanical behavior of the microstructured composite treated as Cosserat continuum by considering various microstructure's directions (β) and scales (ρ). According to the constitutive parameters obtained from the Cosserat homogenization procedure, the composite studied here can be classified as orthotropic and centrosymmetric materials depending on the direction β. The simulations are conducted for a tension problem of a microstructured plate with a circular hole, so this paper also focuses on the stress distribution around the hole. The main conclusions are as follows:

(1) The mechanical behavior of microstructured composite changes as the microstructure's directions β, thereby showing a directionality of measurement distribution such as stresses. In general, orthotropic materials show similar behaviors but with different intensities, and the behavior of centrosymmetric is related to various β.
(2) The increasing microstructure's scale ρ can results in more evident effect of β and difference between the Cosserat and Cauchy models. Such an effect of ρ is clearer for the centrosymmetric materials than orthotropic materials.
(3) The Cosserat continuum is able to better describe the direction effect of microstructures due to the relative rotation that not only shows the directionality of distribution but also varies with the microstructure direction. The Cauchy continuum does not have such advantages because there is no relative rotation and tangential strains are symmetric.
(4) The extreme value and its location of the hoop stress σ_h around the hole depend on β. For smaller ρ, the highest and smallest σ_h are close to 3 and -1, which is similar with the classical result of the isotropic material. As ρ increases, a highest σ_h up to 9 can be observed.
(5) Difference in the hoop stress σ_h between the Cosserat and Cauchy model is mainly in the smallest σ_h, especially for greater ρ when $\beta = 60^\circ, 90^\circ$, and 120°. All the smallest σ_h of the Cosserat model are greater than -3, whereas the Cauchy model can have a σ_h as low as -9.

From this present study, the effect of the microstructure's directions on mechanical behavior of microstructured composite can be found, especially for the composite with large scale of the microstructure. The area applying the development of this research can be for microstructured materials with various dimensions (from micromaterials to macromaterials), where the scale of the microstructure should be comparable to the material's dimension. For example, the layered rock with joints has different dip angle due to the geological formation. The stress distribution can be also used for such composite with singularity, not only the circular shape used here, but alternative shapes. The rectangular microstructures with standard interlocking give a basic and important research aspect of the effect of the microstructure's direction and scale. As more and more advanced materials are developed nowadays, various microstructures formations are interesting to be studied in future research.

Author Contributions: Conceptualization, N.F. and P.T.; methodology, F.S., N.F. and P.T.; software, F.S., N.F. and P.T.; validation, F.S.; formal analysis, F.S.; investigation, F.S.; resources, N.F. and P.T.; data curation, F.S.; writing—original draft preparation, F.S., N.F. and P.T.; writing—review and editing, F.S., N.F., Y.L., P.T. and Z.W.; visualization, Y.L.; supervision, N.F., P.T. and Z.W.; project administration, N.F. and P.T.; funding acquisition, Y.L. All authors have read and agreed to the published version of the manuscript.

Funding: This study is supported by: Italian Ministry of University and Research PRIN 2017, project No. 2017HFPKZY (B88D19001130001); Sapienza Research Grants "Progetti Grandi" 2021 (B85F21008380001); Natural Science Foundation of Chongqing (cstc2020jcyj-msxmX0570); Fundamental Research Funds for the Central Universities (2020CDJ-LHZZ-004, 2020CDJQY-A046); State Key

Laboratory of Coal Mine Disaster Dynamics and Control (2011DA105287-MS201903). The first author thanks the funds from China Scholarship Council (CSC) (No. 202006050138).

Institutional Review Board Statement: Not applicable.

Informed Consent Statement: Not applicable.

Data Availability Statement: Some or all data, models, or code that support the findings of this study are available from the corresponding author upon reasonable request.

Conflicts of Interest: The authors declare no conflict of interest.

References

1. Moraes, A.; de Figueiredo, R.P.; Vargas, E.d.A., Jr. Mechanics of Cosserat Generalized Continuum and Modelling in Structural Geology. *Anuário Instituto Geociências* **2020**, *43*, 366–375. [CrossRef]
2. Cook, R.F.; Lawn, B.R.; Fairbanks, C.J. Microstructure-strength properties in ceramics: I, effect of crack size on toughness. *J. Am. Ceram. Soc.* **1985**, *68*, 604–615. [CrossRef]
3. Filip, R.; Kubiak, K.; Ziaja, W.; Sieniawski, J. The effect of microstructure on the mechanical properties of two-phase titanium alloys. *J. Mater. Process. Technol.* **2003**, *133*, 84–89. [CrossRef]
4. Hoc, T.; Henry, L.; Verdier, M.; Aubry, D.; Sedel, L.; Meunier, A. Effect of microstructure on the mechanical properties of Haversian cortical bone. *Bone* **2006**, *38*, 466–474. [CrossRef]
5. Liao, Z.; la Monaca, A.; Murray, J.; Speidel, A.; Ushmaev, D.; Clare, A.; Axinte, D.; M'Saoubi, R. Surface integrity in metal machining—Part I: Fundamentals of surface characteristics and formation mechanisms. *Int. J. Mach. Tools Manuf.* **2021**, *162*, 103687. [CrossRef]
6. Nassir, M.; Settari, A.; Wan, R. Joint stiffness and deformation behaviour of discontinuous rock. *J. Can. Pet. Technol.* **2010**, *49*, 78–86. [CrossRef]
7. Chen, Y.; Lin, H.; Ding, X.; Xie, S. Scale effect of shear mechanical properties of non-penetrating horizontal rock-like joints. *Environ. Earth Sci.* **2021**, *80*, 192. [CrossRef]
8. Guo, X.; Tan, Z.; Wang, X.; Li, A.; Ma, Z.; Wu, Y. Effect of Bedding Angle and Mineral Composition on Mechanical Properties and Fracture Behavior of Phyllite Under Unloading Confining Pressures. *Geotech. Geol. Eng.* **2020**, *38*, 3611–3621. [CrossRef]
9. Wang, J.; Deng, X.; Cao, W. Numerical Analysis on the Stability of Layered Surrounding Rock Tunnel Under the Conditions of Different Inclination Angle and Thickness. *Am. J. Traffic Transp. Eng.* **2019**, *4*, 67–74.
10. Bauer, S.; Schäfer, M.; Grammenoudis, P.; Tsakmakis, C. Three-dimensional finite elements for large deformation micropolar elasticity. *Comput. Methods Appl. Mech. Eng.* **2010**, *199*, 2643–2654. [CrossRef]
11. Baraldi, D.; Reccia, E.; Cecchi, A. In plane loaded masonry walls: DEM and FEM/DEM models. A critical review. *Meccanica* **2018**, *53*, 1613–1628. [CrossRef]
12. Yang, D.; Sheng, Y.; Ye, J.; Tan, Y. Discrete element modeling of the microbond test of fiber reinforced composite. *Comput. Mater. Sci.* **2010**, *49*, 253–259. [CrossRef]
13. Reccia, E.; Leonetti, L.; Trovalusci, P.; Cecchi, A. A multiscale/multidomain model for the failure analysis of masonry walls: A validation with a combined FEM/DEM approach. *Int. J. Multiscale Comput. Eng.* **2018**, *16*, 325–343. [CrossRef]
14. Tuna, M.; Kirca, M.; Trovalusci, P. Deformation of atomic models and their equivalent continuum counterparts using Eringen's two-phase local/nonlocal model. *Mech. Res. Commun.* **2019**, *97*, 26–32. [CrossRef]
15. Trovalusci, P. Molecular Approaches for Multifield Continua: Origins and current developments. In *Multiscale Modeling of Complex Materials: Phenomenological, Theoretical and Computational Aspects*; Sadowski, T., Trovalusci, P., Eds.; Springer: Vienna, Austria, 2014; pp. 211–278.
16. Altenbach, H.; Eremeyev, V.A. *Generalized Continua—From the Theory to Engineering Applications*; Springer: Berlin/Heidelberg, Germany, 2012; Volume 541.
17. Kunin, I.A. *Elastic Media with Microstructure I. One-Dimensional Models*; Springer: Berlin/Heidelberg, Germany, 1982.
18. Tuna, M.; Trovalusci, P. Scale dependent continuum approaches for discontinuous assemblies: 'Explicit' and 'implicit' non-local models. *Mech. Res. Commun.* **2020**, *103*, 103461. [CrossRef]
19. Eringen, C. *Microcontinuum Field Theories*; Springer: Berlin/Heidelberg, Germany, 1999.
20. Pau, A.; Trovalusci, P. Block masonry as equivalent micropolar continua: The role of relative rotations. *Acta Mech.* **2012**, *223*, 1455–1471. [CrossRef]
21. Bigoni, D.; Gourgiotis, P.A. Folding and faulting of an elastic continuum. *Proc. R. Soc. A Math. Phys. Eng. Sci.* **2016**, *472*, 20160018. [CrossRef] [PubMed]
22. Adhikary, D.; Dyskin, A. A Cosserat continuum model for layered materials. *Comput. Geotech.* **1997**, *20*, 15–45. [CrossRef]
23. Shirani, M.; Steigmann, D.J. A Cosserat Model of Elastic Solids Reinforced by a Family of Curved and Twisted Fibers. *Symmetry* **2020**, *12*, 1133. [CrossRef]
24. Krishnan, J. A Cosserat Theory for Solid Crystals—With Application to Fiber-Reinforced Plates. Ph.D. Thesis, UC Berkeley, Berkeley, CA, USA, 2016.

25. Chu, X.; Yu, C.; Xu, Y. The dilatancy and numerical simulation of failure behavior of granular materials based on Cosserat model. *Interact. Multiscale Mech.* **2012**, *5*, 157–168. [CrossRef]
26. Fantuzzi, N.; Trovalusci, P.; Luciano, R. Material Symmetries in Homogenized Hexagonal-Shaped Composites as Cosserat Continua. *Symmetry* **2020**, *12*, 441. [CrossRef]
27. Colatosti, M.; Fantuzzi, N.; Trovalusci, P. Time-history analysis of composite materials with rectangular microstructure under shear actions. *Materials* **2021**, *14*, 6439. [CrossRef]
28. Colatosti, M.; Shi, F.; Fantuzzi, N.; Trovalusci, P. Mechanical characterization of composite materials with rectangular microstructure and voids. *Arch. Appl. Mech.* **2022**, 1–16. [CrossRef]
29. Trovalusci, P.; Masiani, R. Non-linear micropolar and classical continua for anisotropic discontinuous materials. *Int. J. Solids Struct.* **2003**, *40*, 1281–1297. [CrossRef]
30. Trovalusci, P.; Masiani, R. Material symmetries of micropolar continua equivalent to lattices. *Int. J. Solids Struct.* **1999**, *36*, 2091–2108. [CrossRef]
31. Rezaeepazhand, J.; Jafari, M. Stress analysis of perforated composite plates. *Compos. Struct.* **2005**, *71*, 463–468; Fifth International Conference on Composite Science and Technology. [CrossRef]
32. Toubal, L.; Karama, M.; Lorrain, B. Stress concentration in a circular hole in composite plate. *Compos. Struct.* **2005**, *68*, 31–36. [CrossRef]
33. Dimitri, R.; Fantuzzi, N.; Tornabene, F.; Zavarise, G. Innovative numerical methods based on SFEM and IGA for computing stress concentrations in isotropic plates with discontinuities. *Int. J. Mech. Sci.* **2016**, *118*, 166–187. [CrossRef]
34. Fantuzzi, N.; Leonetti, L.; Trovalusci, P.; Tornabene, F. Some novel numerical applications of Cosserat continua. *Int. J. Comput. Methods* **2018**, *15*, 1850054. [CrossRef]
35. Pandita, S.D.; Nishiyabu, K.; Verpoest, I. Strain concentrations in woven fabric composites with holes. *Compos. Struct.* **2003**, *59*, 361–368. [CrossRef]
36. Savin; Nikolaevich, G. Stress Concentration around Holes. *Aeronaut. J.* **1961**, *65*, 772. [CrossRef]
37. Ramézani, H.; El-Hraiech, A.; Jeong, J.; Benhamou, C.L. Size effect method application for modeling of human cancellous bone using geometrically exact Cosserat elasticity. *Comput. Methods Appl. Mech. Eng.* **2012**, *237*, 227–243. [CrossRef]
38. Eremeyev, V.; Skrzat, A.; Stachowicz, F. On FEM evaluation of stress concentration in micropolar elastic materials. *Nanosci. Technol. Int. J.* **2016**, *7*, 297–304. [CrossRef]
39. Ferreira, A.J.; Fantuzzi, N. *MATLAB Codes for Finite Element Analysis: Solids and Structures*, 2nd ed.; Springer: Berlin/Heidelberg, Germany, 2020.
40. Mühlhaus, H.B. 8-Continuum Models for Layered and Blocky Rock. In *Analysis and Design Methods*; Fairhurst, C., Ed.; Pergamon: Oxford, UK, 1993; pp. 209–230.
41. Fantuzzi, N.; Shi, F.; Colatosti, M.; Luciano, R. Multiscale homogenization and analysis of anisotropic assemblies as Cosserat continua. *Int. J. Multiscale Comput. Eng.* **2022**, *20*, 87–103. [CrossRef]
42. Dal Corso, F.; Shahzad, S.; Bigoni, D. Isotoxal star-shaped polygonal voids and rigid inclusions in nonuniform antiplane shear fields. Part II: Singularities, annihilation and invisibility. *Int. J. Solids Struct.* **2016**, *85*, 76–88. [CrossRef]
43. Jafari, M.; Ardalani, E. Stress concentration in finite metallic plates with regular holes. *Int. J. Mech. Sci.* **2016**, *106*, 220–230. [CrossRef]
44. Sharma, D.S. Stress concentration around circular/elliptical/triangular cutouts in infinite composite plate. In Proceedings of the World Congress on Engineering, London, UK, 6–8 July 2011; Volume 3, p. 6.
45. Xu, Z. Study on the influence of angle of bedding plane on stability of roadway surrounding rock in layered mass. *IOP Conf. Ser. Earth Environ. Sci.* **2021**, *781*, 022014. [CrossRef]
46. Shi, F.; Fantuzzi, N.; Trovalusci, P.; Li, Y.; Wei, Z. The effects of dilatancy in composite assemblies as micropolar continua. *Compos. Struct.* **2021**, *276*, 114500. [CrossRef]
47. Fantuzzi, N.; Trovalusci, P.; Luciano, R. Multiscale analysis of anisotropic materials with hexagonal microstructure as micropolar continua. *Int. J. Multiscale Comput. Eng.* **2020**, *18*, 265–284. [CrossRef]

materials

MDPI

Article

Validation of Alternative Beam T-Junction Fem Models for Complex Tubular Structures

Francisco Badea [1], JoseLuis Olazagoitia [1,*] and JesusAngel Perez [2]

[1] Department of Industrial Engineering and Automotive, Nebrija University, Santa Cruz de Marcenado 27, 28015 Madrid, Spain
[2] Department of Construction and Manufacturing Engineering, Mechanical Engineering Area, University of Oviedo, 33203 Gijón, Spain
* Correspondence: jolazago@nebrija.es

Abstract: The finite element analysis of tubular structures is typically based on models constructed employing beam-type elements. This modeling technique provides a quick and computationally efficient option for calculation. Nevertheless, it shows a series of limitations related to the simplicity of this type of element, among which the inability of accounting for the stiffness behavior at the joint level is of notable importance when modeling complex tubular structures. Despite these limitations, the alternative of simulating complex tubular structures with shell- or volume-type elements is highly costly due to the complexity of the modeling process and the computational requirements. Previous research has proposed alternative beam models that improve the estimations when modeling these structures. These research validations were limited to simple models. This paper presents a validation process utilizing a previously developed beam T-junction model in a complex tubular structure, intended to be representative for buses' and coaches' upper structures. Results obtained reveal that the accuracy of beam element type models can be significantly improved with the adequate implementation of elastic elements to account for the real junction stiffness.

Keywords: finite element analysis; structural optimization; beam T-junctions; beam model validation

Citation: Badea, F.; Olazagoitia, J.; Perez, J. Validation of Alternative Beam T-Junction Fem Models for Complex Tubular Structures. *Materials* **2022**, *15*, 6468. https://doi.org/10.3390/ma15186468

Academic Editor: Roberto Citarella

Received: 5 August 2022
Accepted: 14 September 2022
Published: 17 September 2022

Publisher's Note: MDPI stays neutral with regard to jurisdictional claims in published maps and institutional affiliations.

1. Introduction

The study and analysis of structures using the finite element method (FEM) is key to the development of complex structural systems [1]. In fact, CAD design and FEM analysis allow for the quick evolution of a sketch from a design to a structure capable of withstanding the required stresses, and these methods are widely accepted in the industry.

In FEM programs, it is possible, depending on the model to be represented, to choose three main types of elements: beam, shell, and volume elements. Although there are certain rules, the selection of the best type of element for a particular application is a generally complicated process, in which several factors must be considered. For example, it is necessary to know the characteristics and complexity of the structures to be simulated, the limitations of existing computational resources, the type of simulation, and the expected accuracy of the computational results [2–4].

The analyst's experience is often key in determining the best path to take in each case. In the particular case of large tubular structures such as those that can be found in buses and coaches, it is very common, for example, to use beam-type elements, due to the flexibility, limited computational need, and speed that they allow in the analysis of complex structures [5–7]. Models based on beam elements are comparatively simpler than those based on shell or volume types.

Although beam elements are often the preferred choice for tubular profile structures, they have some fundamental limitations due to their simple formulation. One of the main limitations is the impossibility to faithfully reproduce the localized behavior at the

joint level. In these elements, the attachment with the environment is reduced to a single infinitely rigid node [8,9], which leads to estimation errors in the calculation [10].

The use of shell and volume elements in tubular element joints makes it possible to obtain more realistic joint models [1,11]. This is possible because the joint topology at the joint level can be captured by these element types with higher accuracy. In this way, it is possible to obtain accurate models that overcome the limitations of beam-type elements in this type of tubular structures. Previous research has shown that the differences in the calculation of stiffness of tubular structures modeled with beam elements versus models made with shell or volume models can vary between 5 and 45% [10,12]. The final error depends on various parameters of the tubular elements used, such as the shape of the tube cross-section and its thickness, as well as the complexity of the overall structure. The greater the complexity of the structure, the greater the difference in stiffness calculation between models made with different types of elements, since the error induced at each joint will have a deviating effect in the global response.

Tubular structural elements can be used in many applications, such as buses and coaches. The stiffness of the structure in buses uses large tubular elements and their configuration is often considerably complex. It is usual to use beam elements in their calculation since modeling with shell or volume elements is usually very time-consuming due to the complexity of the models [9]. In addition, they require a higher computational power that on many occasions does not compensate the accuracy of the obtained results.

For this reason, it would be desirable for the modeling of this type of structure to have a calculation methodology that takes advantage of the simplicity of beam-type tubular structures but improves the results through the altered modeling of the joints. There can be found several modelling proposals in the bibliography to improve ordinary beam elements accuracy. For example, B. Horton et al. [13] proposed models with modified stiffness characteristics at the adjacent elements of the joints. The same methodology was applied in [14] to account for the local stiffness modification due to crack development in beam-type structures. Additionally, hybrid models, where shell or volume element types are used for the joints, and beam elements for the rest of the beam sections, can be found with significant improvements reported [15,16]. This shell-beam or volume-beam hybrid modelling technique is still time-consuming since connection elements are to be configured at zones where the element type is modified, and thus not attractive for larger models with an important number of joints to be configured. Finally, several approaches can be found that focus on modifying the stiffness characteristics of the joint by introducing elastic elements [8,17].

This article presents a complete methodology for comparing different modelling techniques of beam-type structures. In the study, volume, ordinary beam, and alternate beam modelling techniques, presented in [8], are analyzed. The results are validated against a real structure with respect to which the results are compared and the best methodology to obtain a model based on beam-type joints with improved T-junctions is proposed.

To understand the methodology used, it is important to present the way of modeling the junctions between tubular elements. For simplicity, two possibilities of T-junctions between tubular elements are presented, which will be called T1 and T2. Figure 1 presents graphically the effective connections between these tubular elements.

It is important to note that the type of actual T-joint (either T1 or T2) has a direct influence on the final behavior of the structure, determining its behavior as a function of the type, size, and direction of the load applied to it. Regardless of this reality, the pure equivalent model based on beam elements will in all cases be composed of four nodes and three beam elements. Therefore, these results in the T1 or T2 junctions are blurred in the model, resulting in an infinitely stiff joint in all cases and a loss of the starting information.

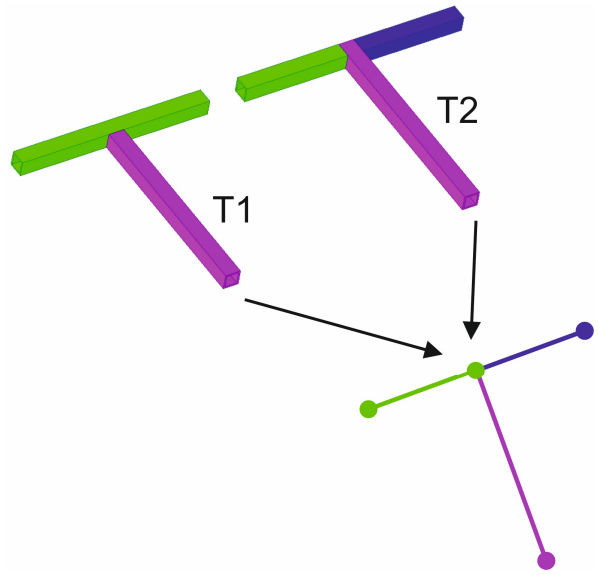

Figure 1. T-junctions equivalent beam-type element model. T1 junction with two elements (green and purple) and T2 with three elements (green, purple and dark blue).

To illustrate how the T-joint model of Figure 1 is modified in [8], Figure 2 presents two joint schemas, where the junction of both tubular elements is rigid in its left image (a) and is flexible in the right image (b). This flexibility is represented by the introduction of stiffness k1 to k6 at the intersection point of both tubular elements. These stiffness values are experimentally pre-determined to faithfully represent real T-joints. These stiffness values do not change the dimensions of the structure in any way. The direct effect of them into the joint causes the displacement $\delta 1 > \delta$ in all cases.

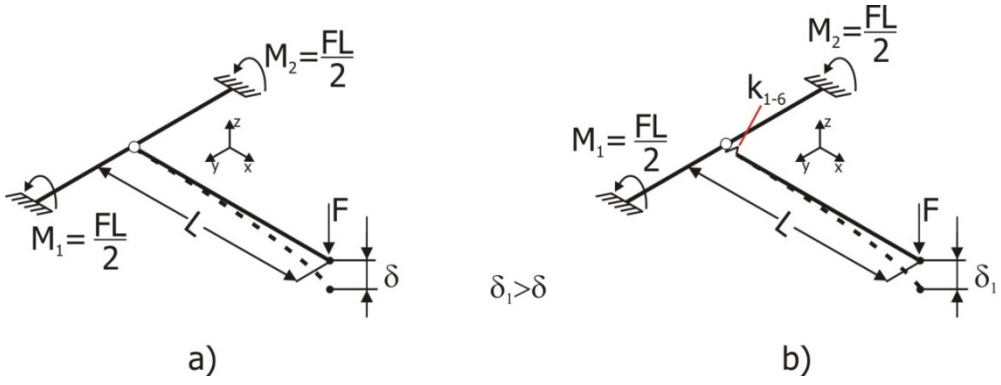

Figure 2. Diagrams comparing the behavior of a standard beam T-junction and the alternative beam T-junction model for the same load state. (**a**) Rigid junction (**b**) flexible junction.

The consequence of the implementation of the junction-specific stiffness is an improvement in the accuracy, as it was already shown and validated for simple structural components in [8]. Nevertheless, a more realistic validation against a complex structure was still pending. This paper covers this aspect, showing the capability of the proposed methodology to increase beam-based FEM models' accuracy and describing some key aspects to take into account when scaling from single-joint to complete complex structures. The application scope of this methodology is limited to the elastic deformation range of the structure, since the spring elements introduced are linear, i.e., k1 to k6 stiffnesses are constant. Equivalent methodology could be developed with nonlinear springs and damping elements to analyze structures responses beyond the elastic range.

In summary, the present work, applied together with the results supplied in [8], provides a complete methodology for improving beam-type element models accuracy

for complex structures typically used in buses and coaches, without incurring increased computational costs and model preparation times.

2. Methodology

The results of the alternative T-junction model were verified for the simple T-junctions analyzed [8]. In that work, the complete methodology to obtain the proper spring stiffness values for each type of junction is described. Nonetheless, extrapolating the results to more complex tubular structures require a specific experimental validation process to assess the improvement capability of the alternative beam model proposed when crossed influences take place among the joints of the structure.

As the research carried out was intended to be applied to buses' and coaches' upper structures, it was sought to use structures of these characteristics for the validation experiments. Since these structures are hard to come upon, a validation structure was designed and built having representative characteristics of buses' and coaches' upper structures (Figure 3).

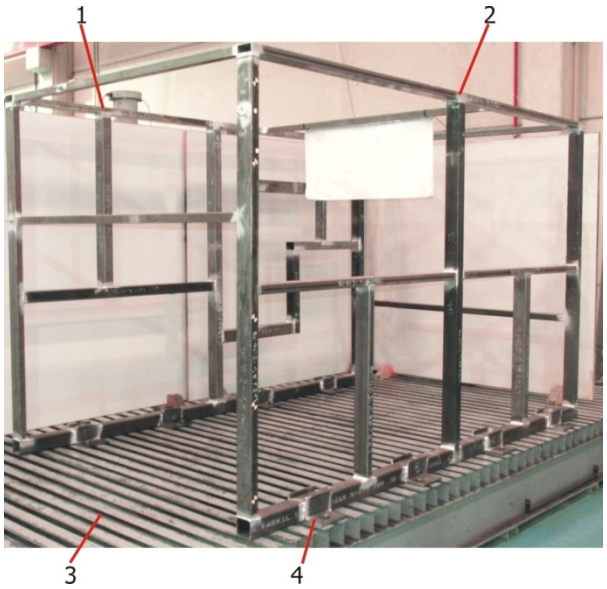

Figure 3. Tubular structure for the experimental validation.

The response of the validation structure under the prescribed load is captured by means of analog dials and later compared to the following finite element models:

- Model constructed with volume-type elements: The most complex and accurate modeling element type. Although unattractive for practical use in the industry, it was used as a comparison basis.
- Ordinary beam element type model: used to evaluate the improvement of the alternative beam models.
- Alternative beam element type: As will be shown in the next section, the assignment of the joint type (T1 or T2) might not be obvious in some specific cases. To analyze the influence of choosing between different criteria, three models are presented and evaluated in the paper.

A further description on the validation structure and the finite element models is given in the following section.

The measured displacements at the evaluation points are then compared to the predictions of the different models in order to assess the accuracy of the models with respect to reality and the improvements achieved with the alternative beam models. Results will be discussed in Section 4.

3. Experimental Validation

3.1. Validation Structure Description

The tubular validation structure was built with two significantly different sides from a geometric point of view. One of the sides was configured in a very similar way to what is commonly found in buses and coaches (Figure 3, number 2), whereas the opposite side had a significantly asymmetric configuration (Figure 3, number 1), so that a wide range of joint configurations is analyzed during the tests. Figure 4 shows a detail of the dimensions of both sides of the structure.

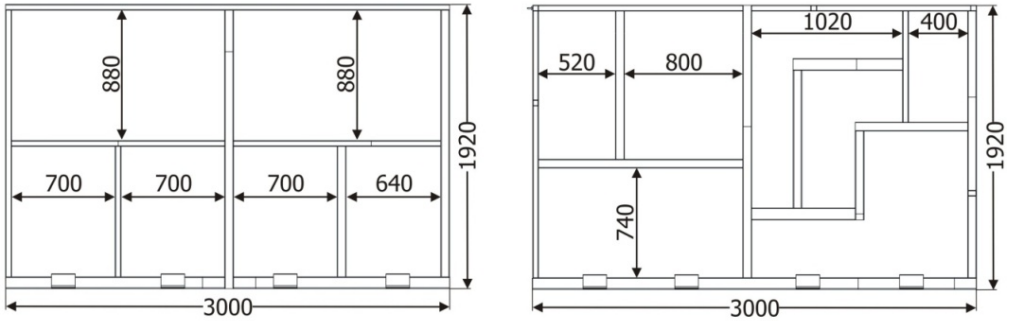

Figure 4. Geometric configuration of the sides of the tubular validation structure. Unit: mm.

The experiments with the tubular validation structure were done on a universal test bench (Figure 3, number 3). Additionally, a solution had to be found to properly constrain the structure during testing to avoid errors introduced by the displacement of the restriction points, since these displacements are not accounted for on virtual FEM models. To minimize these errors, 100 mm × 100 mm × 10 mm L-shaped profiles welded to the base profiles of the tubular structure (Figure 3, number 4) were used. In all, 8 restriction points were used. To ensure proper clamping at the restrictions' points, bolts were tightened to 70% of their yield strength limit. Figure 5 illustrates welds in one of the base profiles with the clamping devices and a rectangular profile.

Figure 5. Clamping weld details.

3.2. Experimental Setup

The following Figure 6 shows an overview of the experimental setup assembly of the validation structure over the test bench. The structure (Figure 6, number 8) was conceived to be tested on a universal test bench (Figure 6, number 5) for which clamping devices had to be used (Figure 6, number 9), which were first welded to the base profiles of the validation structure and then bolted to the universal test bench with M20 bolts and threaded metal blocks.

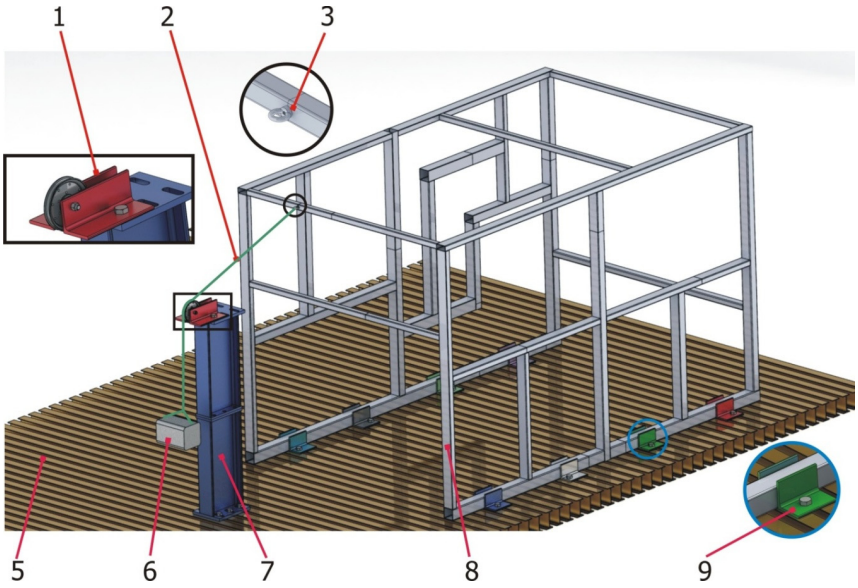

Figure 6. Three-dimensional CAD model with the characteristics of the experimental assembly corresponding to the testing of the validation structure.

In order to minimize uncertainties with respect to the force applied, a calibrated weight was used (Figure 6, number 6) as a load input.

With the objective of achieving a wide range characterization of loading, composed load states were input to the structure. The direction of the force was accurately selected by changing the orientation of the pulley (Figure 6, number 1) that conveys the force of the nylon cord. Additionally, by using H-shaped test bench supports, the height of the pulley could be changed to modify the vertical angle of the force applied (Figure 6, number 7). Finally, a deviation in the transverse direction was obtained by changing the position of the H-shaped test bench supports in that direction.

The load was transferred to the structure by means of a nylon thread (Figure 6, number 2) tied to the corresponding eyebolts (Figure 6, number 3).

To obtain a complete and representative characterization of the validation structure, a total of 14 measuring points were defined and distributed throughout its geometry so that representative information of the global response was obtained. It was also taken into consideration the necessity to define measuring sections at different distances from the joints themselves and/or the clamping devices, so that a clearer picture of the behavior of the beam-type elements could be studied. Figure 7 shows a 3D CAD model of the validation structure on which the defined measuring sections are indicated.

Two dial gauges were used to capture the displacement at the measuring sections, one to measure small displacements of 0–5 mm with a 0.001 mm resolution, and another for larger displacements of 0–25 mm with a 0.01 mm resolution.

Due to the number of sections and their different locations in the validation structure, specific supports were used to fix the dial gauges depending on the sections measured.

Of the 14 sections defined, in four of them (a3, a4, a8, and a9), only the displacements in the Y direction were characterized since these sections were in the base profiles of the structure in regions very close to the clamping devices, so the displacements in the other directions could be neglected. In the rest of the sections, displacements in the two most significant directions were characterized. For example, in section a1, the displacements were measured in directions X and Y, whereas in section a13, the displacements were measured in directions Z and Y.

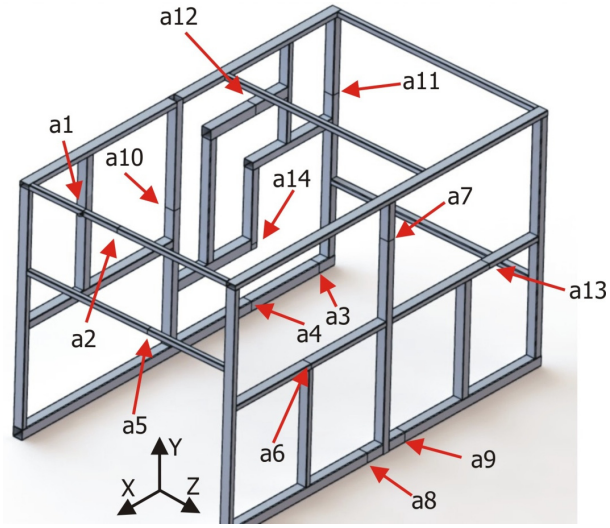

Figure 7. Sections used to characterize the validation structure, identified as a1 to a14.

As with the validation experiments for the simple junctions [8], the following set of criteria was adopted to minimize the sources of error and achieve better-quality results:

1. To attach the dial gauges, the back clamping system was used in order to avoid any differences in measurement due to friction between the sensor and the standardized clamping system. By way of example, Figure 8 presents the mounting of the dial gauge for the displacement measurement of the a2 section.
2. A semi-automatic system was used to read and acquire the data from the dial gauges by using a high-resolution photographic camera with an external trigger in order to avoid estimation errors between measurements.
3. The defined sections were cleaned and smoothed using solvents and scouring pads with rough polymer fibers so the surfaces would not show any defects. Adhesive strips were also attached to each of these sections. As an example, Figure 9 shows a detail of the region adjacent to the a13 measurement section.

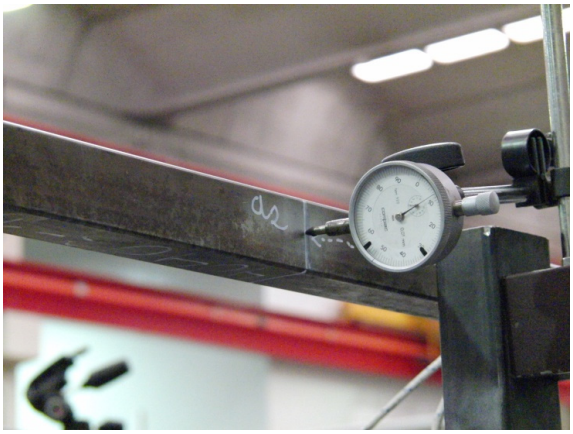

Figure 8. Mounting of the dial gauge for the displacement measurement of the a2 section.

The same preparation process was used for each of the sections defined in the validation structure. To accept the measurements, the same quality criteria were used as for the experimental analyses of the simple junctions [8]. In this way, the standard deviations for a set of measurements in the same section were less than 0.005 mm for the 0.001 mm resolution dial gauges, and less than 0.05 mm for the 0.01 mm resolution dial gauges. For each of the sections defined, load and unload cycles were carried out by means of a hydraulic actuator which gave and released support to the calibrated weights during each

cycle. A total of 15 measurements were taken for each section, which were found to be an optimal compromise for obtaining precise results with the least number of measurements per point.

Figure 9. Detail of the region adjacent to the a13 measurement section.

3.3. FEM Model of the Validation Structure Modeled with Beam-Type Elements

To model the validation structure with beam-type elements, the modeling principles set out in [8] were adopted. Following the methodology proposed in this sub-section, the principal axes for each of the tubular profiles of the structure were identified and extracted. The regions where there were separations between the beam elements were also identified and corrected. Figure 10 shows the validation structure model built with beam-type elements.

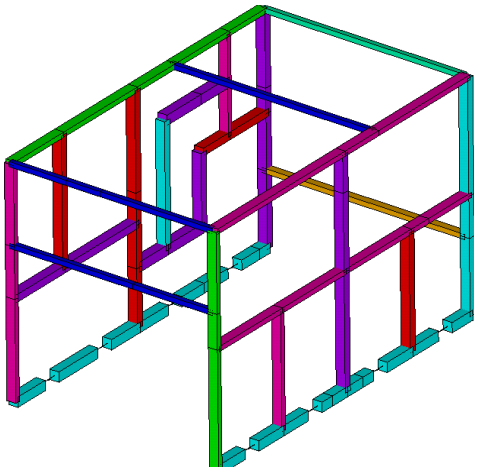

Figure 10. Validation structure modeled with beam-type elements. Beam colors refer to the following sections employed: Light blue: 80 mm × 80 mm × 3 mm, red: 80 mm × 60 mm × 3 mm, purple: 80 mm × 60 mm × 2 mm, green: 80 mm × 40 mm × 3 mm, lilac: 80 mm × 40 mm × 2 mm, dark blue: 40 mm × 40 mm × 3 mm.

This figure presents two superimposed representations of the validation structure. The original base model built with beam-type elements is represented with black dotted lines, to which the model generated by a graphic option of the program was superimposed to reveal the elements, based on the cross-section properties defined. Key points were defined at the locations of the measuring sections in order to ensure that a node would be present in these points and therefore nodal displacement results could be extracted.

The equivalent moments of inertia were calculated in the cross-section of the clamping devices and were assigned to the beam elements, as shown in Figure 11.

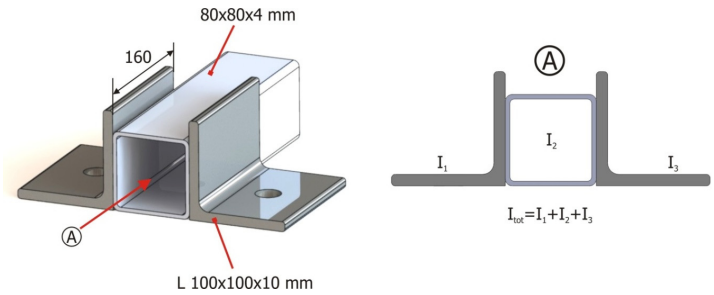

Figure 11. Characteristics of the structure and calculation of the moment of inertia equivalent to the cross-section in the regions of the clamping devices.

3.4. Characteristics of the Validation Structure Modeled with Alternative Beam T-Junctions

Implementing the alternative beam T-junction elements in accordance with the developed methodology requires determining the dimensional characteristics and the configuration of each of the joints (T1 or T2). A total of 38 joints were identified in the validation structure, as can be seen in the diagram presented in Figure 12. In this figure, each one of the junctions was identified with a circle and a number; for clarity purposes, one of the sides has red circles and the other side green circles.

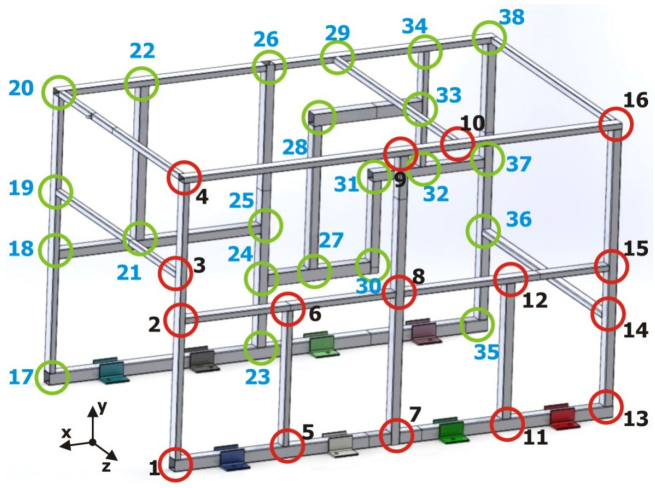

Figure 12. Diagram identifying the total number of joints in the validation structure.

Implementing the alternative junctions into a complex tubular structure requires identifying each of the junctions of the structure in accordance with the analyzed joint configurations (T1 or T2). As presented in Figure 13, most of the junctions can be easily assimilated with T1 or T2, as is the case with points 1 to 3, but some others cannot be easily determined or just have no clear equivalence. Over the 38 joints, 33 of them were easily assimilated to T1 or T2, whereas for 5 joints (4, 8, 16, 20, and 38), this similitude was not obvious.

To further analyze the junctions with no clear equivalence to T1 or T2 configurations, different models with various combinations were developed and evaluated. Although a complete description of all the combinations analyzed is out of the scope of the article, the best three configurations will be described in the following paragraphs (Figure 14).

For the first variant (a), joint 8 was modeled as a single type T2 joint, whereas for joints 4, 16, 20, and 38, the modeling characteristics were adhered to (a T1 and a T2) but changed the direction of application of the type T2 junction. For the second variant (b), it was decided to model all the type T1 and T2 joints that could be clearly identified in the structure and to keep all the joints showing uncertainties (8, 4, 16, 20, 38) as normal junctions. Finally, for the third variant (c), all the conflictive joints were assimilated as type T1 joints, keeping all the continuous profiles unmodified.

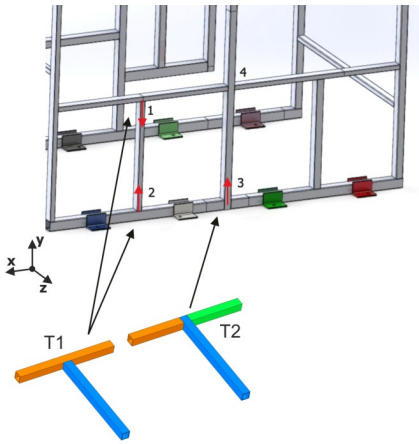

Figure 13. Equivalence of the complex structure joints to the T1 and T2 junctions.

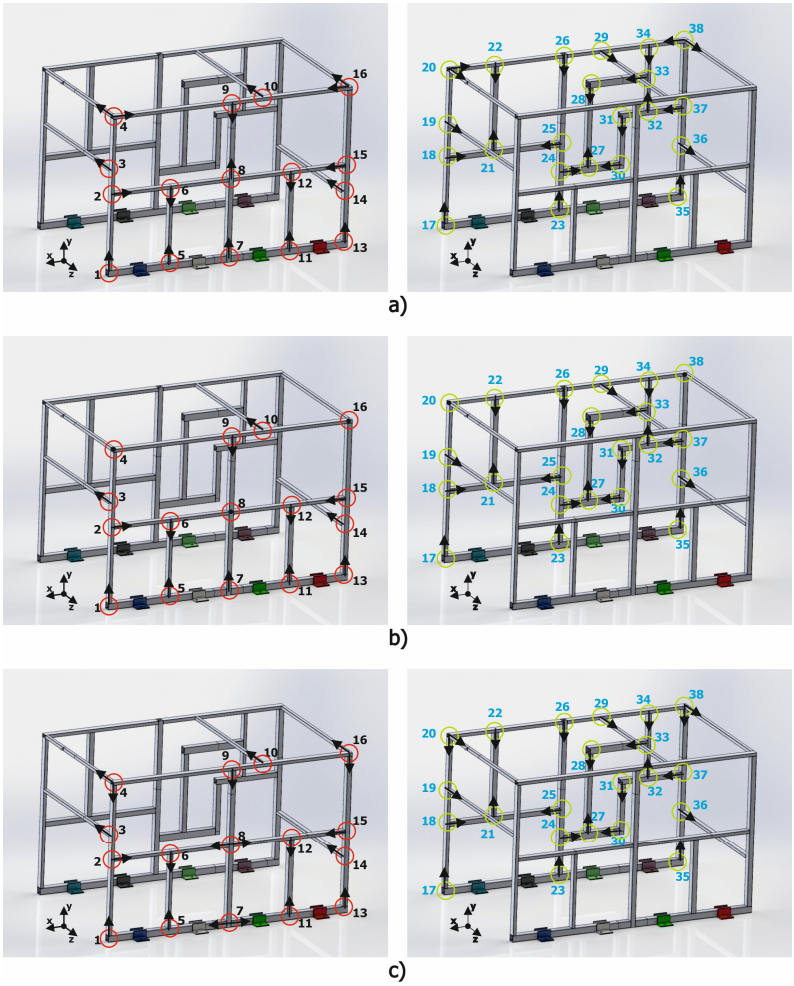

Figure 14. Joint configurations analyzed. Variant (**a**), Variant(**b**) and Variant (**c**).

The stiffness values of the elastic elements used for each of the analyzed joints were found through comparative simulations using joints modeled with volume-type elements as reference models, following the recommendations of [8].

It should be highlighted that the stiffness values at the joint levels obtained with the methodology of [8] are significantly high, ranging between 1×10^5–1×10^6 (N/m). These stiffnesses in some manner quantify the contribution of the joint to the deformation of the T-junctions in the linear domain. Ideally, it would be desired to improve each junction

with sets of elastic elements so that the complex beam structure provides the most accurate possible results. Despite that the assimilation to a joint type in 5 out of the 38 joints of the validation structure is not obvious, it was demonstrated in [8] that although between the T1 and T2 junctions there are significant differences, these differences were comparatively lower than the ones in comparison to the regular beam junction. In other words, assigning a junction as T1 when it is a T2 would induce fewer deviations than just having it as a regular beam.

3.5. Characteristics of the Validation Structure Modeled with Volume-Type Elements

An additional model of the validation structure was constructed using volume-type elements. Although modeling rectangular beam section structures with volume-type elements has been demonstrated to be an excessively costly approach, it was decided to configure this model to be used for comparison purposes, due to its intrinsic high accuracy.

The following Figure 15 illustrates the structure modelled with volume-type elements. It was modelled using linear hexahedral elements of size 3 mm, which corresponds to the minimum thickness of the rectangular beams employed in the validation structure. Tube joints were modeled by means of bonded-type contacts, without considering the weld seam geometry.

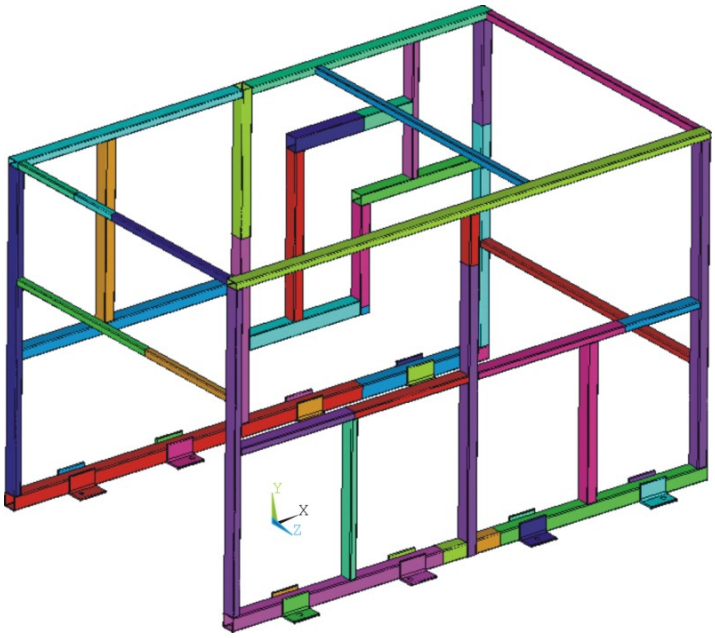

Figure 15. Detailed model of the validation structure, modeled with volume-type elements.

4. Results and Discussion

Comparative analyses were performed for the evaluation of the improvements between the validation structure and the different finite element models of the validation structure. Table 1 summarizes the displacement relative deviations for each of the finite element models evaluated with respect to the values measured in the experimentally analyzed validation structures.

From the observation of the results Table 1, the following aspects can be observed:

1. The best approximations obtained correspond to the detailed volume-type element model.
2. The beam and the alternative beam models show significant deviations for sections a3, a4, a8, and a9 (Figure 7). These sections are located at short distances from the clamps, for which local effects are influencing the results, which cannot be characterized using beam-type elements. It can also be seen that these sections do not undergo any significant changes in the alternative beam models.

3. Focusing on alternative beam models, variant (c) shows the best approximations to the experimental validation structure and to the detailed volume element model. The calculations are even better displacement estimations than those of the latter at a5 and a10 sections.

Table 1. Deflection relative differences of the FEM models with respect to the experimental results.

	Exp Volume Deviation	Exp Beam Deviation	Exp Alt Beam Var (a) Deviation	Exp Alt Beam Var (b) Deviation	Exp Alt Beam Var (c) Deviation
Characterized sections	[%]	[%]	[%]	[%]	[%]
a1	6.03	43.96	15.80	33.21	13.89
a2	5.93	43.39	15.91	33.87	15.57
a3	15.38	67.35	66.88	65.63	60.54
a4	8.43	97.35	97.34	97.21	97.29
a5	13.46	45.58	13.14	23.15	11.20
a6	6.01	88.95	69.83	64.87	23.54
a7	6.59	35.49	15.43	12.98	9.31
a8	44.64	71.09	81.14	82.46	82.24
a9	21.55	94.57	89.25	82.22	82.25
a10	6.22	40.25	1.16	3.30	2.87
a11	6.68	32.40	15.58	10.73	8.54
a12	12.37	49.23	14.25	13.16	14.21
a13	17.41	56.96	26.81	22.89	23.50
a14	14.46	53.30	48.95	27.48	21.28
Absolute average deviation	13.23	58.56	40.81	40.94	33.30
Absolute average deviation without clamps (discarding the a3, a4, a8, a9 values)	9.52	48.95	23.69	24.56	14.39

Since the ultimate objective of the implementation of alternative beam models is to improve the accuracy of tubular structures modeled in this manner, it was considered necessary to perform an additional evaluation of the capability of the models to predict stress distributions.

It was observed in [8] that the stress distributions resulting from analyzing the simple junctions modeled with beam or alternative beam type elements showed no significant differences. Nevertheless, it seems interesting to extend the analysis to complex structures, where the effect of the local stiffness modification at the joint level might show crossed influences.

Due to the inherent limitation of beam-type elements to account for local stress raisins at the joint level, the analysis is focused on the comparison of the general stress distribution maps. The volume element type model was used as a reference for the evaluation, since this type of model, although discarded for general use due to the high computational costs that it entails, can predict stress maps with high precision.

The resulting Von Mises stress distributions obtained for volume, ordinary beam, and the alternative beam with the best results (c) are showed in Figure 16. It is observed that both ordinary and alternative beam models show rather similar stress distributions, which are also similar to the reference volume model.

Although a detailed stress analysis of the models is not in the scope of the article, it is noted that the significant improvement in terms of deflection observed on the alternative beam model has limited influence on the general stress distribution for complex structures.

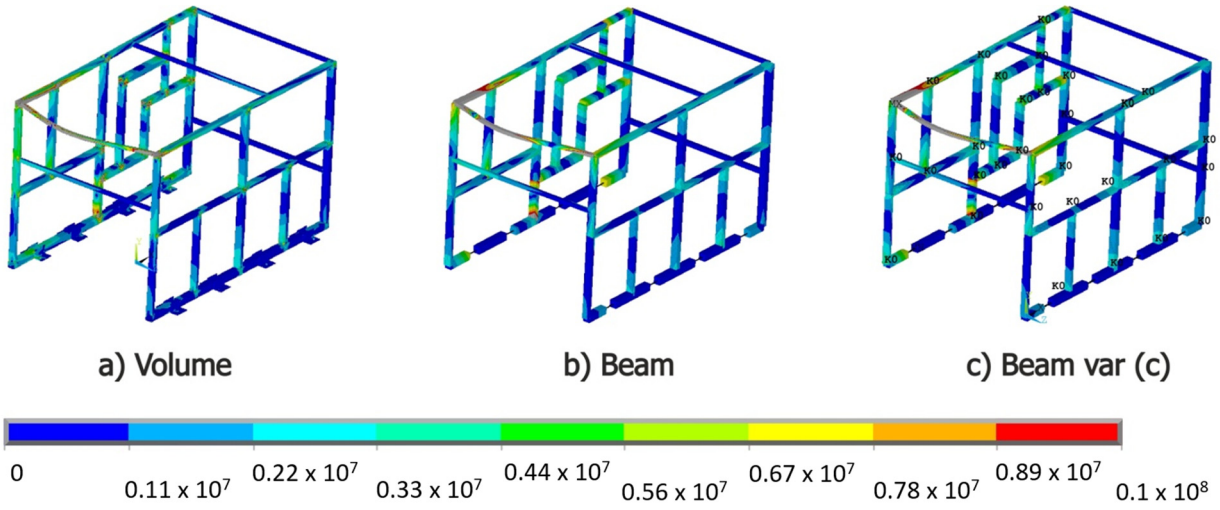

Figure 16. Von Mises stress maps for the validation structure modeled with volume, beam, and alternative beam type elements [MPa].

5. Conclusions

In the present paper, a test of specific complex structures was designed and built in order to conduct the validation of the alternative beam element type modeling technique presented in [8].

The structure was subjected to a controlled load, and displacements were captured at a total of 14 measuring sections for comparison purposes.

For such complex structures, the application of the stiffness accuracy improvement by means of elastic elements becomes less obvious, since the assignation of T1 or T2 joints' configuration is not evident anymore for some joints. In the case of the validation of the structure used in this work, a total of five junctions were identified in which the selection was not clear and so the optimization of those particular junctions implied a detailed specific analysis for which different configurations were modelled for these junctions and compared to the experimental data, together with an ordinary beam element type and a volume element type model.

For the ordinary-type elements, the deviations with respect to the validation structure were found to be notable, with the beam model being approximately 58% stiffer.

By using the developed alternative T-junctions, it was shown that the characteristics of beam models' behavior can be modified. Evaluating the differences between the experimental structure and the models built, and ignoring the measurements corresponding to the support beams of the structure (sections a3, a4, a8, and a9), a reduction in the average deviations from almost 49% to 14% was achieved. It was also noticed that these models are indeed affected by the proper choice of elastic element configuration, ranging from an average error of 27% to 14%. In any case, even the worst selection of the elastic elements for the junctions shows a significant accuracy improvement with respect to the ordinary beam model. Additionally, by analyzing the stress distributions in the different finite element models, it was found that the elastic elements inserted into the joints did not show significant influence on the stress distribution.

From the results presented in this work, it can be concluded that the utilization of the alternative beam T-junction model for the behavioral optimization of tubular structures represents a feasible methodology throughout which significant improvements of the analyzed model estimations can be obtained.

The authors would like to remark that, when performing studies throughout finite element analysis, it is necessary to take into consideration the fact that the beam-type elements represent a simplified element derived from the shell- and volume-type elements, which implies a series of intrinsic limitations determined by their own formulation.

Author Contributions: Conceptualization and methodology, F.B. and J.P.; software, F.B. and J.O.; validation, F.B.; formal analysis, F.B., J.P. and J.O.; investigation, F.B.; resources, F.B. and J.O.; writing—original draft preparation, F.B., J.P. and J.O.; writing—review and editing, F.B., J.P. and J.O.; visualization and supervision, J.O. and J.P.; project administration, F.B.; funding acquisition, J.O. and F.B. All authors have read and agreed to the published version of the manuscript.

Funding: This research was partially funded by the Cátedra Global Nebrija-Santander en Recuperación de Energía en el Transporte de Superficie.

Institutional Review Board Statement: Not applicable.

Informed Consent Statement: Not applicable.

Data Availability Statement: Not applicable.

Conflicts of Interest: The authors declare no conflict of interest.

References

1. Adams, V.; Askennazi, A. *Building Better Products with Finite Element Analysis*; OnWord Press: Jefferson, NY, USA, 1999.
2. Lee, K.; Nikolaidis, E. Identification of Flexible Joints in Vehicle Structures. *AIAA J.* **1992**, *30*, 482–489. [CrossRef]
3. Eriksson, P. Optimisation of a Bus Body Structure. *Heavy Veh. Syst.* **2001**, *8*, 1–16. [CrossRef]
4. Kim, H.S.; Hwang, Y.S.; Yoon, H.S. Dynamic Stress Analysis of a Bus Systems. In Proceedings of the 2nd MSC Worldwide Automotive Conference, Dearborn, MI, USA, 9–11 October 2000.
5. Gauchia, A.; Diaz, V.; Boada, M.J.L.; Boada, B.L. Torsional Stiffness and Weight Optimization of a Real Bus Structure. *Int. J. Automot. Technol.* **2010**, *11*, 41–47. [CrossRef]
6. Lan, F.; Chen, J.; Lin, J. Comparative Analysis for Bus Side Structures and Lightweight Optimization. *Proc. Inst. Mech. Eng. Part D J. Automob. Eng.* **2004**, *218*, 1067–1075. [CrossRef]
7. Gombor, B. Dynamic Analysis of a Bus Body Frame: Determination of the Loads and Stresses. *Veh. Syst. Dyn.* **2005**, *43*, 807–822. [CrossRef]
8. Alcalá, E.; Badea, F.; Martin, Á.; Aparicio, F. Methodology for the Accuracy Improvement of FEM Beam Type T-Junctions of Buses and Coaches Structures. *Int. J. Automot. Technol.* **2013**, *14*, 817–827. [CrossRef]
9. Garcia, A.; Vicente, T. Characterization and Influence of Semi-Rigid Joints in the Buses and Coaches Structural Behavior. In Proceedings of the Bus & Coach Experts Meeting, 33rd International Conference on Vehicle Safety, Keszthely, Hungary, 2–4 September 2002.
10. Arribas, D.; Badea, F.; Perez, J.Á. Análisis y Optimización Estructural de Autobuses Mediante Modelos Matemáticos. *X Congr. Ing. del Transp.* **2012**.
11. GMBH, R.B. *Bosch Automotive Handbook*; Robert Bosch GmbH: Gerlingen, Germany, 2011.
12. Badea, F.M.; Alcala, E.; Grimaldi, R.; Ogando, A.; Aparicio, F. Optimización de Uniones y Estructuras de Autobuses. In Proceedings of the XVII Congreso Nacional de Ingeniería Mecánica, Gijón, España, 24 November 2010; p. 8.
13. Horton, B.; Gurgenci, H.; Veidt, M.; Friswell, M.I. Finite Element Model Updating of a Welded Space Frame. *Proc. Int. Modal Anal. Conf.-IMAC* **2000**, *1*, 529–535.
14. Skrinar, M. Improved Beam Finite Element for the Stability Analysis of Slender Transversely Cracked Beam-Columns. *Comput. Mater. Sci.* **2009**, *45*, 663–668. [CrossRef]
15. Donders, S.; Takahashi, Y.; Hadjit, R.; Van Langenhove, T.; Brughmans, M.; Van Genechten, B.; Desmet, W. A Reduced Beam and Joint Concept Modeling Approach to Optimize Global Vehicle Body Dynamics. *Finite Elem. Anal. Des.* **2009**, *45*, 439–455. [CrossRef]
16. Moroncini, A.; Cremers, L.; Baldanzini, N. Car Body Concept Modeling for NVH Optimization in the Early Design Phase at BMW: A Critical Review and New Advanced Solutions. In Proceedings of the International Conference on Noise and Vibration Engineering 2012, ISMA 2012, including USD 2012: International Conference on Uncertainty in Structure Dynamics, Leuven, Belgium, 17–19 September 2012; Volume 5, pp. 3809–3823.
17. Liu, F.; Wang, L.; Jin, D.; Wen, H. Equivalent Continuum Modeling of Beam-like Truss Structures with Flexible Joints. *Acta Mech. Sin. Xuebao* **2019**, *35*, 1067–1078. [CrossRef]

materials

MDPI

Article

Stochastic Reliability-Based Design Optimization Framework for the Steel Plate Girder with Corrugated Web Subjected to Corrosion

Damian Sokołowski * and Marcin Kamiński

Chair of Structural Reliability, Faculty of Civil Engineering, Architecture and Environmental Engineering, Lodz University of Technology, Al. Politechniki 6, 90-924 Lodz, Poland
* Correspondence: damian.sokolowski@p.lodz.pl

Abstract: This paper proposes the framework for reliability-based design optimization (RBDO) of structural elements with an example based on the corrugated web I-girder. It tackles the problem of topological optimization of corroding structures with uncertainties. Engineering restrictions follow a concept of the limit states (LS) and extend it for stability and eigenfrequency assessment. The reliability constraints include all the LS; they are computed according to first- and second-order reliability methods. The RBDO example minimizes the bridge girder cross-section while satisfying the structural reliability level for the ultimate and the serviceability limit states, stability, and eigenfrequency. It takes into consideration two uncorrelated random effects, i.e., manufacturing imperfection and corrosion. They are both Gaussian; the first of them is applied at assembly time, while the second is applied according to the time series. The example confronts three independent FEM models with an increasing level of detailing, and compares RBDO results for three concurrent probabilistic methods, i.e., the iterative stochastic perturbation technique (ISPT), the semi-analytical method, and the Monte Carlo simulation. This study proves that the RBDO analysis is feasible even for computationally demanding structures, can support automation of structural design, and that the level of detailing in the FEM models influences its results. Finally, it exemplifies that reliability restrictions for LS are much more rigorous than for their deterministic counterparts, and that the fastest ISPT method is sufficiently accurate for probabilistic calculations in this RBDO.

Keywords: reliability-based design optimization; stochastic perturbation technique; Monte Carlo simulation; semi-analytical method; topological optimization; corrugated web; corrosion

Citation: Sokołowski, D.; Kamiński, M. Stochastic Reliability-Based Design Optimization Framework for the Steel Plate Girder with Corrugated Web Subjected to Corrosion. *Materials* **2022**, *15*, 7170. https://doi.org/10.3390/ma15207170

Academic Editors: Luigi Calabrese, Angelo Marcello Tarantino, Carmelo Majorana, Raimondo Luciano and Michele Bacciocchi

Received: 8 September 2022
Accepted: 10 October 2022
Published: 14 October 2022

1. Introduction

Contemporary structural designs require powerful tools for optimization purposes, which must be effective, fast, and easy to use. Together with an exponential increase in computational power, the traditional analytical approach to the optimization of Civil Engineering structures has become significantly outdated. In the majority of designs, this approach has already been replaced by more accurate deterministic methods, among which the finite element method plays a crucial role, and they are largely implemented in commercial software. Such an optimization strategy is applied for example in [1]; its goal is commonly focused on structural topology [2,3]. The traditional deterministic design appears to be suboptimal when significant uncertainties must be taken into account, such as climatic loads, material uncertainties, assembly errors, and corrosion or soil conditions, just to name a few. They cannot be avoided in structural and especially civil engineering designs. This is why a new concept called reliability-based design optimization (RBDO) arose, where the uncertainties are directly included in the design. An acceptable contrast between the efficiency of deterministic and reliability optimization is given in [4] and an exhaustive review of the concepts of RBDO is available [5] or in [6]. RBDO is well researched, especially for steel truss structures e.g., [7,8], and frames e.g., [9,10], where the computation effort of

each optimization loop is acceptable. They are not so common in more complex problems involving the plate, shell, or composite structures, where the computation is much more demanding and the amount of strength and serviceability checks much higher; such construction is considered in this study. This extreme computational intensiveness is well depicted in [11] and still constitutes a major issue. Computational intensiveness is caused not only by the number of limit states but also by the high number of deterministic and random design variables, whose impact on these states is not always known a priori to RBDO. This aspect is commonly tackled by an initial sensitivity analysis, which determines the susceptibility of structural response to a variation of design parameters. It has been used with success for many years e.g., in [12], and eliminates unnecessary variables from further computation. Application of the RBDO could also include corrosion effects [13], which constitute a major topic of this paper.

Although some new concepts are still being put forward [14,15], the RBDO methods are quite mature now and allow a very efficient (but computationally demanding) design. What they still lack is the ability to define a reliable life of structures, so that the optimization is not aimed purely at modifications of the pristine materials, but also takes into consideration the degradation of its work throughout the service life. This is what we propose in our concept of RBDO, which allows a service life optimization with a reliability-based design approach for the determination of the reliable service life of steel structures that are subject to corrosion. Corrosion affects the strength and serviceability of steel structures, including their capacity, stability, and durability. Its effects are depicted for example in [16,17]. It is also a major reason for the careful and costly maintenance of steel structures [18] and together with fire softening it constitutes the main weakness of this material. Corrosion affects steel already at erection time, which is quite different from reinforced concrete where the onset of corrosion is shifted from this initial time [19] and calculated for example according to Fick's second law. This is because steel structures are directly affected by chloride attack and are not covered by other materials. Of course, there exist a variety of covers such as special paints or chrome plating and various additives (see for instance weathering steel), but even such techniques do not prevent this phenomenon completely; they require repetitive application during the service life of steel constructions. Corrosion especially affects thin-walled structures, where small pitting corrosion placed in a susceptible place, or a small reduction in thickness may cause serious loss of capacity. A fine example of such structures are those with sinusoidally corrugated webs currently applied in girders (also arched ones [20]) and also composite structures, where the deck is made of concrete and the web of constructional steel [21].

The corrugated web considerably increases rigidity and shear capacity [22], and decreases sensitivity to a local stability loss in the web [23], thus reducing the occurrence of local buckling. It also allows for reduced self-weight [24], as compared to conventional flat web I-girders, and does not increase the complexity of execution, as trusses do. The usage of these assets has increased, especially in structural applications such as bridges, pedestrian walkways, hangars, and industrial buildings. Interestingly, corrugated webs also outperform flat webs in energy dissipation and could be used in anti-seismic structures [25]. The first studies of the SIN web girders were conducted in the late 1990s [26], yet they are still new in civil engineering applications and have several disadvantages for such applications. They offer a weaker contribution to bending [27] and cause an additional normal stress distribution in flanges coming from transverse bending [28] compared to the regular I-beams; they also have complex bending–shear interaction [29]. To make matters worse, there still is a lack of design standards or specifications dealing with the behavior of such webs and SIN web girders.

This is why in recent years there has been intensive research on their basic behavior connected with stress [30], elastic critical moment, buckling [31,32], and shear [33,34]; they are computed in this study within the concept of limit states. A very interesting problem is the capacity and serviceability of such constructions in fire conditions [35], which considerably reduce the bearing capacity of steel structures and also their reliability.

Reliability-based computations of structural elements with a corrugated web are also available [36,37] and even a weight optimization could be found [38], but RBDO has not yet been proposed for such structures; this is especially true when corrosion is the leading random effect. Consequently, there is a need to develop recommendations that properly address the reliability issues of such girders, which is also the reason for their choice as an example for the proposed framework.

The principal objective of this paper is to propose an RBDO framework with a special focus on structural elements and constructions that must satisfy complex restrictions of engineering standards. The secondary goal is to successfully apply this framework to a computationally challenging example of the sinusoidally corrugated web I-girder. The study assumes the possibility of optimizing the topology of civil engineering structures subjected to uncertain corrosion evolution and engineering restrictions for a specified reliable service life. Further, it assumes that FEM modeling accuracy and probabilistic solver play a crucial role in the accuracy and timing of RBDO results. Next, it assumes the importance of the steel and environment type as well as the choice of the WLSM weighing function for the solution.

Therefore, a design optimization framework and additional theoretical background for time-dependent reliability civil engineering analysis have been presented and applied for the case study of the steel plate girder with a sinusoidally corrugated I web. The results obtained in this paper would allow for more optimal designing of such structures and may be applied to other steel and concrete structures.

2. Theoretical Background

According to the current design codes, the structural elements' durability period adopted is 50 years, and this is usually ensured by repeated design trials with the goal of minimizing weight or cost, alternatively optimization of its capacity for different limit states. In such terms, a designer solves an optimization problem with a clearly defined set of restrictions, which are first of all (1) the minimum capacity of the element, secondly (2) geometrical constraints, (3) material restrictions, (4) maximum deformations, and (5) other physical constraints. The most tedious work is usually required in the first of these, i.e., in ensuring a minimum capacity of the element. This is because the element (and an entire structure) is subjected to multiple loads of different morphology and with different placement (wind, snow, traffic load, vibrations, self-weight, machinery, etc.), which may or may not occur at the same time. That is why an engineer must check the structural capacity for multiple combinations, which almost always require a different computational approach. This work proposes a framework, according to which such optimization could be utilized with a specified goal of optimization. It takes into consideration a classical approach of limit states proposed by the Eurocode 0 [39] and also a more refined, higher-order probabilistic design method directly using the reliability theory, where the judgment of service life is done based on the reliability indices β_g of the designed elements. Such refinement is advised in Appendices B and C of this design norm [39]. Within this framework, multiple structural elements may be assessed, and the entire structure could be optimized. The objective function may be purely topological, as in the below example, but it may also be cost-oriented, when the total cost of an element is optimized, or may minimize the difference of all the indices β_g. The method selected for optimization purposes is deterministic non-gradient regular search, in which the main loop encompasses the subsequent steps of (1) deterministic verification of restrictions, (2) verification of the given limit states, and finally, (3) checks of the reliability indices. This is shown in Figure 1, where the optimization problem depends on the design time t and input uncertainty ω; at each step, a new topology $W(\overline{\omega}; t)$ is proposed. A non-gradient approach is selected because in most civil engineering designs gradient cannot be explicitly computed. This is because each of the combinations defined in multiple limit states would be different and movement in any direction of the design domain may give converse results for multiple combinations. The main objective of this algorithm is structural optimization and the main

loop depicted in Figure 1 starts with an arbitrary point in the optimization domain (starting geometry of the element) that should be selected according to the engineering practice. At first, the most straightforward conditions are checked, i.e., geometrical, material, and physical constraints. Then, a cross-sectional class is determined, because its change demands different checks of the limit states and the reliability indices. Upon this, the finite element method is utilized to solve the mechanical problem and its results are used in the determination of both, the limit states and reliability indices. Verification of the physical restrictions and cross-sectional class is straightforward and depends strictly on the selected material, geometry, and static scheme of the specific element. The FEM must be carefully formulated for each part so that the parameters existent in the objective function could be easily (or preferably automatically) ameliorated and the subsequent model solved; this will be explained in detail for the specific context of the example.

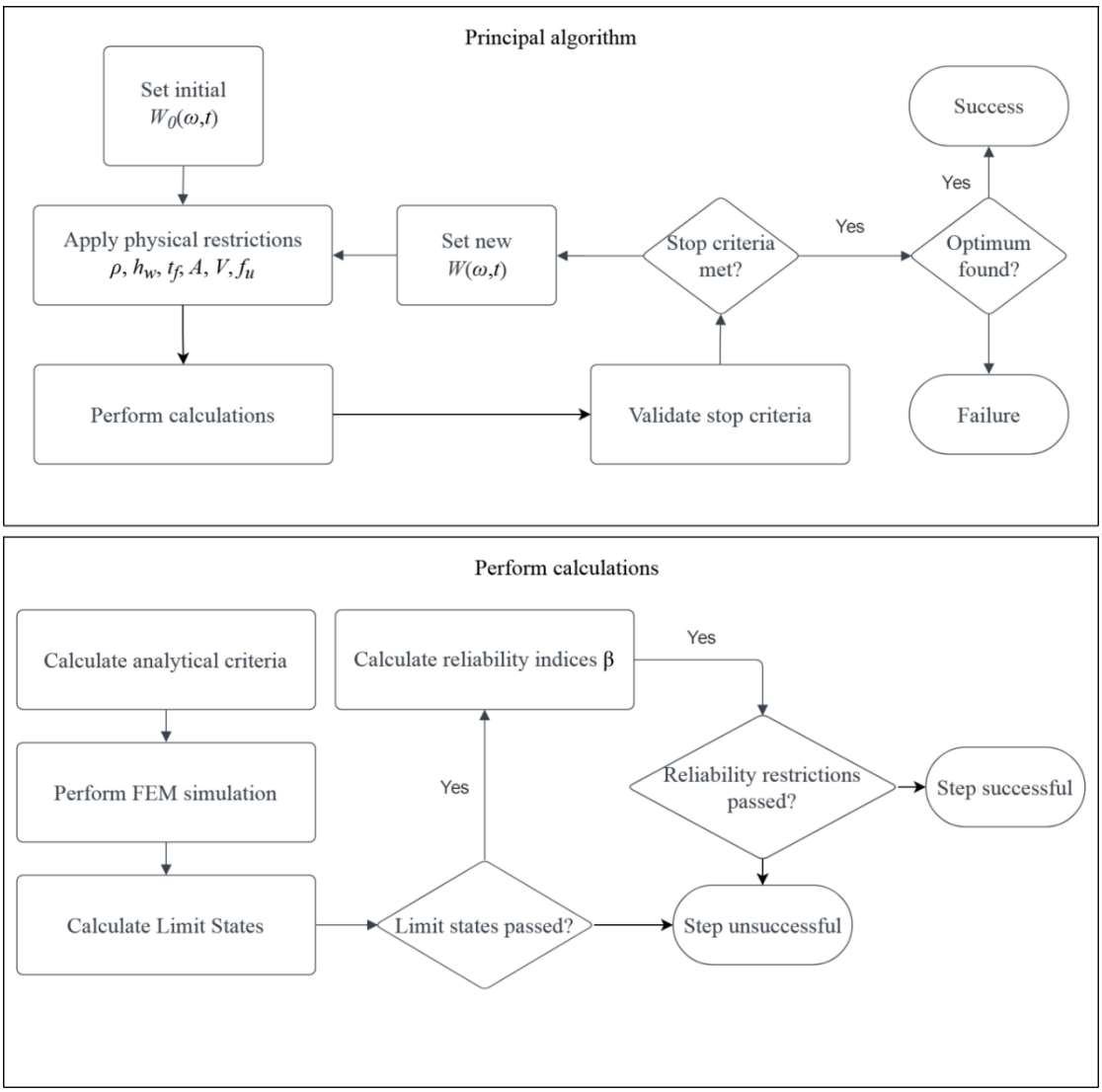

Figure 1. Principal algorithm of the method and calculation process.

Designing processes requiring a detailed explanation include the 'Calculate Limit States', 'Calculate Reliability indices' β_g, and 'Validate stop criteria'. According to a common definition, a limit state is a state in which the construction element or an entire structure will fail due to a specified external action. The design codes in their basic form define the ultimate limit state (ULS) and serviceability limit state (SLS), which describe either the conditions in which the construction will fail (ULS) or will stop working in an

acceptable way (SLS); the hierarchy of LS is shown on Figure 2. If the design is made based on the FEM, not the analytical approach, each element must meet five fundamental conditions for the linear regime of the structural materials. First, (1) the general stresses σ_{ij} and (2) the reduced (commonly Huber–Mises) stresses σ_{red} must be lower than the plastic limit. In the case of the linear civil engineering structures, these are limited to the longitudinal normal stresses σ_{11} and the shear stresses σ_{12} (or τ). Additionally, (3) the structure must be stable and buckle neither locally nor globally (but local buckling is sometimes permitted when additional structural elements are added to the designed part); this constraint is depicted in Figure 2 by $\xi\ (W,t)$. The last condition in the ULS encompasses (4) the first eigenfrequencies, which must be high enough not to be triggered by the wind or traffic; usually, the minimum is set to 5 Hz. In the SLS, (5) deformations of this element must be limited, which include the deflections $u\ (W,t)$ and also displacements at its ends (or borders) and connections to other parts $\delta_i\ (W,t)$.

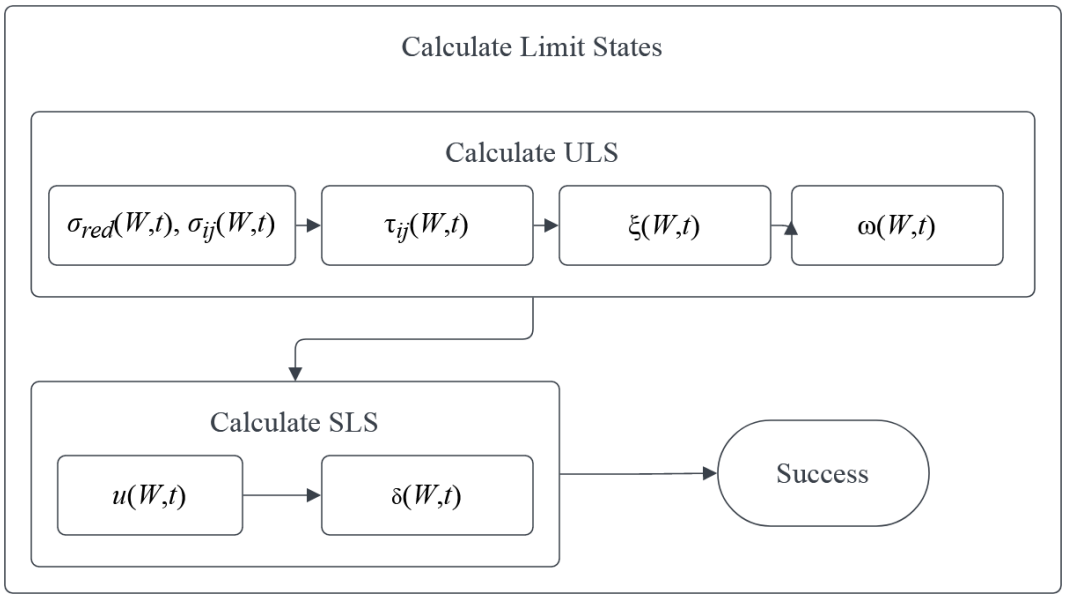

Figure 2. Procedure for the determination of the limit states.

One may also include requirements for exceptional states, such as collision, fire loads, or checks for fatigue, but they are out of the scope of this work; this is important because of their rare inclusion in design purposes in civil engineering practice. All the mentioned states could be checked implicitly using the results of the subsequent FEM analyses, which are static, eigenfrequency, and critical load tasks available in the most common programs such as ABAQUS, ANSYS, Catia, or DIANA. Please note, that some of the limit states may be checked globally for each part or an entire structure, such as $\xi\ (W,t)$ or $\varpi\ (W,t)$, while the others must be met for all the points of the structure (in FEM, for all the elements). These include the stresses, strains, deflections, deformations, and displacements, all of them depending strictly on the objective function—the topology of the element. If all restrictions in both limit states are met, the optimization could proceed to the next process—a check of the reliability indices β_g.

A process of the determination of reliability indices β_g serves for a final check of the restrictions and could be started only if all the previous ones are met. This is because the limit functions g are almost directly taken from the limit states and used in the numerator of the reliability indices β_g. This process is depicted in Figure 3, which defines the flow of computations at this stage of optimization. It starts with optimization of the response function, then it determines the probabilistic coefficients, and finally calculates the reliability indices serving as the final restrictions. These indices are computed first at time $t = 0$ with an initial uncertainty ω_0 and only then for $t\ \epsilon\ (0;t_d)$ and ω, where t_d is designed service

life. This is because the design may be already unacceptable when no aging (or corrosion) of the material is included. The checks of reliability are performed for all the restrictions from the limit states separately and each of them must be met so that the current topology can be accepted. In this process, neither the amount nor the probability density function (PDF) is strictly limited, and the total number of uncertainty sources depends upon the probabilistic methods applied, as does the PDF for each of these.

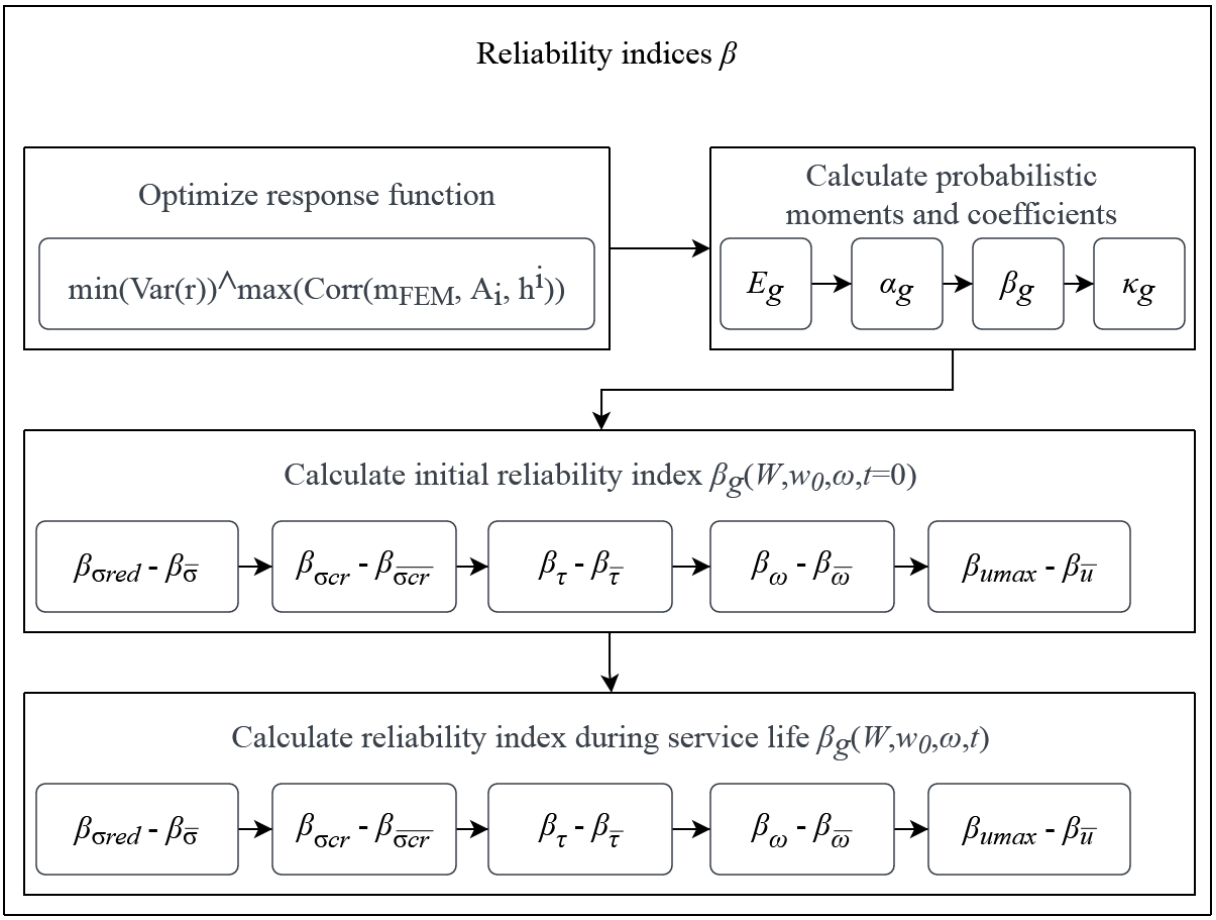

Figure 3. Procedure for the determination of reliability indices.

Checks for $t = 0$ are performed for both the first-order reliability method (FORM) and the second-order reliability method (SORM) in sequential order; this order of analysis is defined by O in Figure 3. The last computation of reliable service life is computed solely by the FORM (for $O = 1$) and plotted in the service time domain. Unlike the majority of papers that propose only one method of probabilistic calculus (see for example [40]), we propose three concurrent methods, the iterative stochastic perturbation technique, the semi-analytical method (AM), and the crude Monte Carlo simulation (MCS). Please note that the computation of reliability restrictions is not limited to the above methods.

Determination of the response function, the first task in reliability-focused computations, serves as an inner optimization problem. It is solved at each optimization step just before the determination of probabilistic characteristics. It is devoted to the determination of a continuous response function of the capacity of the girder $f_c(W)$ from its discrete representation solved via the FEM. This is required in computations of subsequent limit functions g defined as the difference of this capacity and the reaction to external action or an engineering limit $f_e(W)$.

$$g(W) = f_c(W) - f_e(W). \tag{1}$$

Please note that the analytical formula relating the objective function and the functions of girder capacity cannot be explicitly derived analytically, which is why the FEM is used for its retrieval. The inner optimization problem is solved by deterministic non-gradient search in the discrete domain of the order of the response polynomial and the number of terms in this polynomial. Restrictions include several terms $n_{Ai} > 0\ \epsilon$ N and the order of polynomial $P_O > 0\ \epsilon$ N. The optimization aim is twofold—minimization of the weighted least squares method (WLSM) variance and maximization of correlation of the polynomial and the FEM results.

$$\min(Var(\bar{r})) \wedge max\left(Corr\left(m_{FEM}, A_i h^i\right)\right) \tag{2}$$

where higher precedence is set to the correlation. The stop function is generally not required in this problem because of a finite number of allowable points in the discrete optimization domain. P_O is limited to $10 \div 30$, firstly because of no real correlation gain for higher order polynomials, and secondly because of difficulties with its behavior outside or neighboring to the probing range of the FEM. Such optimization is performed for each of the limit functions. In the exemplary problem, only u_{max} was taken into consideration, whose an explicit mathematical formulation is proposed as

$$\begin{gathered} u(\omega;t) = N \cdot q(\omega;t) = N \cdot A_i(t) \cdot h^i(\omega;t);\ r^2 = \left(m_{FEM} - A_i h^i\right)^2 :\ \min\left(\sum_{j=1}^{n} r_j^2\right) \rightarrow A_j; \\ \min(Var(r)) \wedge max\left(Corr\left(m_{FEM}, A_i h^i\right)\right) \end{gathered} \tag{3}$$

where $u(\omega;t)$ is the maximum deflection, N stands for shape function, A_i are defined as the coefficients of approximating polynomial, h^i define the subsequent powers of the design variable, and r is a residuum coming from a difference of the FEM result m_{FEM} and the result coming from the polynomial response function $A_i h^i$.

The weighted least squares method (WLSM) solved at each optimization step uses the following polynomial approximation:

$$u(b) \cong D^{(P_o)} b^{P_o} = f(\mathbf{D}, b) \quad P_o = 1, \ldots, s; s < n. \tag{4}$$

where the polynomial basis of the sth order P_O is used and solved around the web thickness of the current optimization step. This web thickness also serves as a mean value of the main random parameter included in the probabilistic calculus, indexed here by b. As a result n different pairs $\left(b^{(\alpha)}, \mathbf{u}^{(\alpha)}\right)$ for $\alpha = 1, \ldots, n$ are returned, whose arguments belong to the neighborhood of expectation of b itself. The residuals in each trial point are introduced to get an algebraic condition for these expansion coefficients. They are next minimized. After relevant modifications, the following regular matrix equations are obtained

$$\left((\mathbf{J})^T \mathbf{w}\, \mathbf{J}\right) \mathbf{D} = (\mathbf{J})^T\, \mathbf{w}\, \mathbf{u} \tag{5}$$

Such a system of equations (with the dimensions $n\ x\ s$) is solved symbolically in MAPLE [41].

The last process in the design loop is a stop condition and it is depicted in Figure 4. It evaluates if the optimized solution is found or not. Success occurs when at least one step finds a more optimal solution than W_0. Failure is identified when (1) one of the indices from restrictions is within the margin of β_T at design service time t_d and (2) n_s subsequent steps do not decrease the objective function (fail to optimize the W). An additional stop is defined for $i_{T,max} = 1000$ steps to ensure a cutoff of the optimization with weak correlation; its fulfillment may lead either to optimization success when at least one of the previous W fulfilled all restrictions or optimization failure. A more elaborate stop condition may also be applied, but its inclusion would increase the computation time, which proves critical for engineering purposes. Please note that the solution and optimization convergence

will depend on the starting structural configuration W_0 and it is recommended to repeat optimization with different W_0, using a different kind of initial cross-section for example.

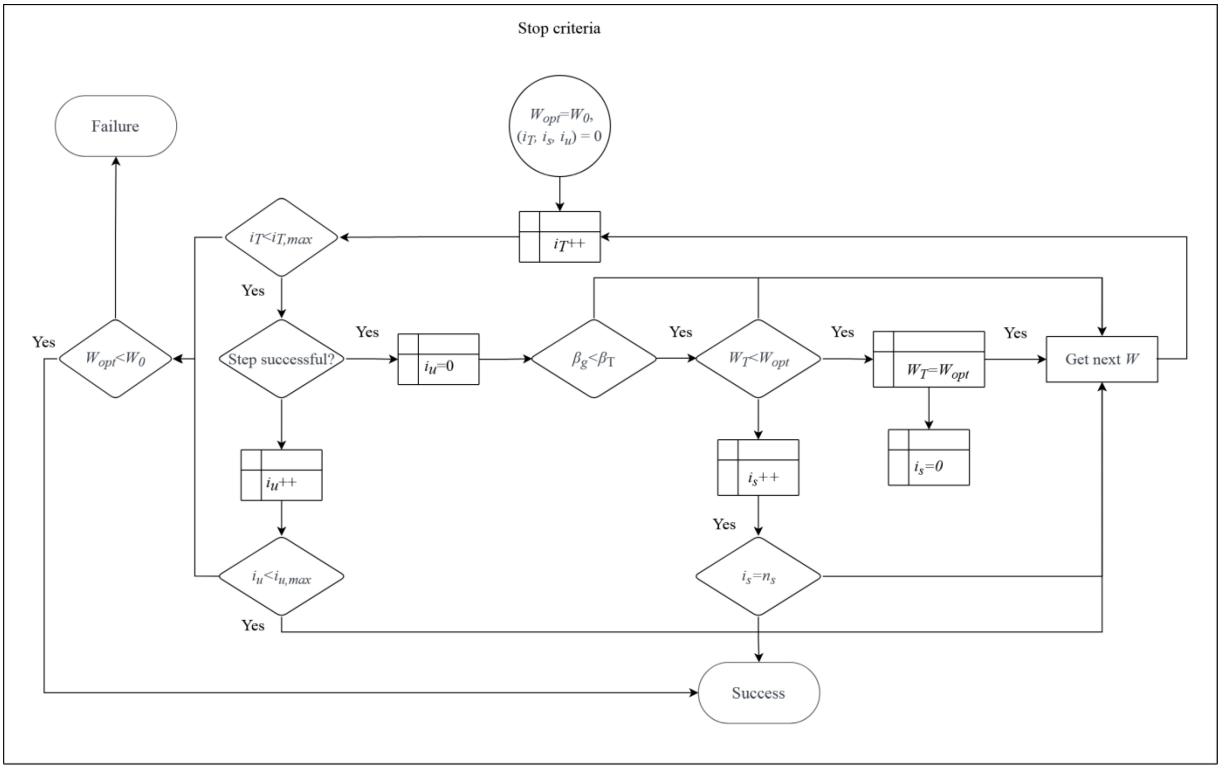

Figure 4. Definition of stop criteria.

The reliability calculus at the initial time is only according to initial imperfections. A formulation of such a problem could be found in [42]. The final reliable life check is performed according to two random variables, namely the corrosion penetration depth and fabrication imperfection. This is possible in the stochastic context with the introduction of the relevant resulting functions of corrosion penetration depth into both, the web thickness mean value and its initial variation. Expected value of random web thickness b can be computed as

$$E[b] = \int_{-\infty}^{+\infty} b\, p_b(x)dx \equiv \frac{1}{M}\sum_{i=1}^{M} b^{(i)} \tag{6}$$

while its variance as

$$\begin{aligned} Var(b) &= \int_{-\infty}^{+\infty} (b - E[b])^2 p_b(x)dx + Var(d) - 2Corr(b,d) \\ &\equiv \tfrac{1}{M-1}\sum_{i=1}^{M}\left(b^{(i)} - E[b]\right)^2 + Var(d) - 2Corr(b,d) \end{aligned} \tag{7}$$

where $E[d]$ is the expected value of corrosion penetration depth directly affecting the mean value of web thickness b; the correlation between these two stochastic variables $Corr(b,d)$ is set to 0.

The reliability indices β_{FORM} and β_{SORM} may serve for initial reliability as well as structural health monitoring. The first of these could be computed in the following way:

$$\beta_{g,\,\mathrm{FORM}} = \frac{E[g]}{\sigma[g]} \tag{8}$$

where β_g stands for the reliability index of a specific limit function, $E[g]$ is the expectation of this function g, and $\sigma[g]$ is its standard deviation. A reliability index $\beta_{g,FORM}$ assumes a normal probability distribution of a given random (response) function; $\beta_{g,SORM}$ is defined as [37]

$$\beta_{g,\,\mathrm{SORM}} = -\Phi^{-1}\left(P_{f2}\right) \tag{9}$$

where P_{f2} denotes the probability of failure for the chosen probability distribution of the function relative to $\beta_{g,\,\mathrm{FORM}}$ in the following manner:

$$P_{f2} = \frac{\Phi\left(\beta_{g,\,\mathrm{FORM}}\right)}{\sqrt{1+\beta_{g,\,\mathrm{FORM}}.\kappa}}, \tag{10}$$

where κ is the curvature approximating the primary surface defined by the following formula:

$$\kappa = \frac{\frac{\mathrm{du}^{(m)}}{\mathrm{db}_0^{k_2}}}{\left(1+\left(\frac{\mathrm{du}^{(m)}}{\mathrm{db}_0^{k}}\right)^2\right)^{\frac{3}{2}}}. \tag{11}$$

3. Numerical Illustration

Let us consider a corrugated web I-beam girder that is suspected of corrosion, as in Figure 5.

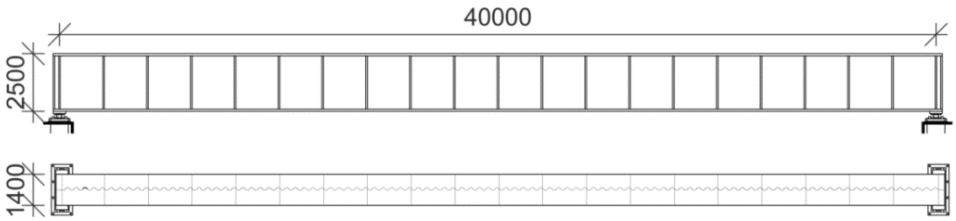

Figure 5. The layout of the girder in [mm].

In such girders, the web is predominantly affected by this phenomenon, which leads to loss of bearing capacity during its service life. This girder is subjected to topological optimization, whose goal is to optimize the cross-section that ensures reliability for 50 years of service according to Eurocode 0, Appendix B [39]. Optimization is performed within the framework proposed in Figure 1, where the limit states are checked based on three FEM models; the indices β_g are verified for stresses, deflections, eigenfrequencies, and stabilities, while the final constraints of reliability are based on displacement; the following objective function $W\left(\varpi;t\right)$ is proposed:

$$\begin{aligned} W(\omega;\omega_0;t) &= \left(A_w(\omega;\omega_0;t)+2A_f\right)\cdot L = \left(t_w(\omega;\omega_0;t)\cdot h_w+2A_f\right)\cdot L \\ &= \left(\left(t_{w_0}(\omega_0)-2\cdot\left(A(\omega)+t^{B(\omega)}\right)\right)\cdot h_w+2A_f\right)\cdot L \end{aligned} \tag{12}$$

As a function of ϖ_0—the coefficient of variation of the web thickness at time $t=0$, ϖ—coefficient of variation of corrosion as well as of time t; $t=0$ stands for an assembly time, in which exposure to the external environment begins. In this function, A_w and A_f are the cross-sectional areas of the web and the flange, h_w stands for the height of the web, and t_w denotes the thickness of the web. Let us note that in common civil engineering designs the flanges are much thicker than the web and are placed horizontally so that they are not so susceptible to corrosion. This is why the time dependence of this topology is generally based on the web, whose thickness decreases with corrosion. This thickness is uncertain already after its fabrication process, which is imposed by an initial coefficient of

variation ϖ_0 and is then subjected to stochastic corrosion of the form $A\ (\varpi)+t^{B(\varpi)}$. In this term $t_w = t_{w0}(\omega_0) - 2\cdot\left(A(\omega)+t^{B(\varpi)}\right)$, where the quotient 2 depicts the susceptibility of t_w to corrosion from both sides. The corrosion function strictly depends on the environment and steel type, to which it is subjected, and is taken from Melchers 2002. Its coefficients are shown in Table 1, which summarizes the corrosion parameters for rural, urban, and marine environments separately for the carbon and weathering steels. This table shows that the marine environment is specified by the highest CoV, and has expectations a little smaller than the urban environment, while the rural environment is the least invasive. The weathering steel is much less affected by corrosion, as both parameters, A and B, have smaller mean values and CVS than the carbon steel in a corresponding environment type. Nonetheless, the downside of this type of steel is its cost.

Table 1. Statistical parameters of corrosion for various steel types [43].

Parameters	Carbon Steel		Weathering Steel	
	A (10^{-3} mm)	**B**	**A (10^{-3} mm)**	**B**
Rural environment				
Expectation	34.0 (model 1)	0.65	33.3 (model 2)	0.498
CoV	0.009	0.10	0.34	0.09
Urban environment				
Expectation	80.2 (model 3)	0.539	50.7 (model 4)	0.567
CoV	0.42	0.40	0.30	0.37
Marine environment				
Expectation	70.6 (model 5)	0.789	40.2 (model 6)	0.557
CoV	0.66	0.49	0.22	0.10

A corrosion model applied in this work comes from the additional experiments reported in the literature and is applied with the parameters adjacent to the carbon steel in an urban environment. Its expected value reads

$$E[D(t)] = 3.52\cdot10^{-3}e^{2.81\cdot10^{-24}(1.05\cdot10^{12}\ +1.00\cdot10^{11}\ln(t))^2} \tag{13}$$

The variance is introduced as

$$\begin{gathered} Var(D(t)) = 7.57\cdot10^{-3}t^{1.19}e^{1.12\cdot10^{-1}\ln(t)^2} - 5.65\cdot10^{-4}t^{1.19}e^{5.63\cdot10^{-2}\ln(t)^2+3.13} \\ +1.24\cdot10^{-5}t^{1.19}e^{6.24+5.63\cdot10^{-2}\ln(t)^2}. \end{gathered} \tag{14}$$

They are both truncated by the third vital number for the reader's convenience.

The principal restrictions for this objective function come solely from the requirements of the bearing capacity, stability, eigenfrequency, and allowable deformation of the girder, which are a cross-section within its design service life. This, in turn, is defined in the current civil engineering design code, Eurocode 0 [39], which in its annexes proposes the limits of reliability index β_g for each of the limit states (LS). They are divided into the ultimate limit state (ULS), in which the girder must withstand the normal, reduced, and shear stresses, have high enough first eigenfrequency, as well as not be susceptible to buckling. The second LS is the serviceability limit state (SLS), in which the deflection of this girder must be limited by the value of $l/250$. In such terms, there exist six restrictions for its reliability:

$$\begin{gathered} \beta_\tau(t) - \beta_{\hat{\tau}}(t) \geq 0;\ \beta_{\sigma_{red}}(t) - \beta_{\hat{\sigma}}(t) \geq 0;\ \beta_\Omega(t) - \beta_{\hat{\Omega}}(t) \geq 0; \\ \beta_{\sigma_{cr}}(t) - \beta_{\hat{\sigma}_{cr}}(t) \geq 0;\ \beta_{u_{max}}(t) - \beta_{\hat{u}}(t) \geq 0;\ \beta_{\tilde{\xi}}(t) - \beta_{\hat{\xi}}(t) \geq 0; \end{gathered} \tag{15}$$

Further restrictions are connected to the geometry of the girder, its volume V, and cross-sectional area A, which must be all positive.

$$\varrho,\ h_w\ ,\ t_w,\ t_f,\ h_f,\ A,\ V\ >\ 0 \tag{16}$$

The geometry of this girder includes the height of the web h_w , its width t_w as well as the height h_f and width t_f of the flange. Let us note that the resulting checks of bearing capacity required by the Eurocode changes together with an increase of cross-sectional class and therefore its slenderness must be limited to keep the checks unified in terms of both, the flange and the web $0\ <\ h_w\ /t_w <\ 72$, $0\ <\left(\frac{h_f}{2} - t_w - a\right)/t_f <\ 9$. Otherwise, the procedure of determination of the limit states and the reliability indices would have to be changed substantially each time the section class changes.

The material selected for the design purposes is constructional steel. This choice determines all the material restrictions, including the density $\varrho\ \in\ 7.75$–$8.05\ [\mathrm{g/cm}^3]$ and the plastic limit of this steel f_u, which is here narrowed to the most common steels available on the international market, i.e., $f_u \in \{195, 235, 275, 355, 420, 460\}$ MPa with corresponding Young modulus $E = 210$ GPa and Poisson ratio of $\mu = 0.3$. The material model applied in all the computations for constructional steel is linear with plastic limit f_u.

Additional restrictions proceed directly from the external requirements or the investor and include static schemes and loads. These are the designed length of the girder $L = 40$ m, external load in form of a uniform pressure applied on the upper flange $q = 150$ kN/m, and degrees of freedom restricted at the ends of the girder as simple supports—although they are not directly included in the objective function but in the FEM model.

The inner optimization problem is solved here with the order of response polynomial in the range of $16\ >\ P_O >\ 0\,\epsilon\ N$. A maximum polynomial order is set, because previous optimization problems show that the solution starts to degrade already at $P_0 >\ 10$.

A shortened version of the results for one of these optimizations devoted to maximum deflection is given in Table 2. It shows that the accuracy of the WLSM approximation measured by its total error E_{WLSM}, variance α_{WLSM}, and correlation coefficient of the response function and the discrete FEM results C_{WLSM} does not necessarily increase with an increase of the polynomial order or number of terms included. Moreover, the optimum order is not possible to determine a priori to solving the optimization problem. Interestingly, the limitation of the terms with a constant P_O has a minor influence on C_{WLSM} but increases both E_{WLSM} and α_{WLSM}. It must be noted that together with an increase of the P_O and n_A the computation complexity and length are also increased. Generally, the optimum order is in the range of $P_O \in \{5; 10\}$ and full polynomials are preferred. An additional problem in this inner optimization is the type of weights in the WLSM W_S. The considered weighting schemes are equal W_{SE}, triangular W_{ST}, and Dirac W_{SD}; the last weighting scheme places greater importance on the realizations around the mean (or middle) of the uncertain parameter, and the equal weighting scheme puts the same weight on all the discrete data points but has problems when they are not the smooth and triangular type of weights, which decreases the importance of the data points with an increase of their distance from the mean. It is quite efficient for the low P_O but for this weighting scheme E_{WLSM} and α_{WLSM} increase very fast together with an increase in P_O. Dirac-type of weight puts the same importance on the mean as for all the other data points. It ensures the best C_{WLSM} at the highest order, keeps a very small error and low variance for a high span of P_O, and returns the smoothest approximation. This is why it was selected for further optimizations and the other weighting schemes were removed from the checks of a reliable life prediction. From Table 2, it could be also concluded that the optimum approximation was reached for a full polynomial of the ninth order and WLSM with a Dirac-type of weighting.

Table 2. Selected WLSM polynomial approximations of the extreme displacement versus random input.

Displacement WLSM Polynomial Choice for Different Weights										
No.	P_o	C_{WLSM}			E_{WLSM} [10^{-2}]			α_{WLSM} [10^{-5}]		
		W_{SD}	W_{ST}	W_{SE}	W_{SD}	W_{ST}	W_{SE}	W_{SD}	W_{ST}	W_{SE}
1	1st, f	0.994	0.9941	0.9941	2.105	2.166	2.124	6.216	6.414	6.554
2	3rd, f	0.9959	0.9959	0.9958	1.722	**1.720**	1.770	4.282	4.293	4.333
3	5th, f	0.9962	0.4008	0.0016	1.65	50.82	123.6	3.902	3063	18.530
4	6th, f	0.9966	0.0954	0.1556	**1.401**	202.1	58.01	3.492	66.200	446.5
5	9th, f	**0.9969**	0.3295	0.3789	1.427	67.29	57.93	**3.207**	6014	421.3
6	10th, f	0.9954	0.1112	0.3769	1.752	587.1	53.35	4.762	42.935	336.6
7	6th, p5	0.996	0.9958	0.9952	1.754	1.82	1.794	4.184	4.311	4.521
8	11th, p5	0.996	**0.996**	0.9958	1.748	1.739	1.758	4.111	**4.113**	4.388
9	15th, p5	0.9958	0.9958	0.9957	1.747	1.751	1.764	4.324	4.337	4.414
10	9th, p4	0.9958	0.9958	0.9958	1.739	1.743	**1.758**	4.319	4.333	4.389

Such an optimized third-order maximum deflection function valid for the SLS is given below:

$$E[R_{\mathrm{SLS}}] = 8.09 - 3.13{\cdot}10^{-2}(E[t_w]) + 2.91{\cdot}10^{-4}(E[t_w])^2 - 9.71{\cdot}10^{-7}(E[t_w])^3. \quad (17)$$

In this expression, the expectation of web thickness includes an influence of fabrication error $E[t_{w0}]$ existent at $t = 0$ and corrosion $E[D(t)]$ so that $E[t_w] = E[t_{w0}] - 2{\cdot}E[D(t)]$. Let us note that together with the total allowed deflection this maximum deflection function serves as a numerator in an expression of $\beta_{g,\,FORM}$ as $E[g_{\mathrm{SLS}}] = L/350 - E[R_{\mathrm{SLS}}]$.

A variance of each limit state is available simply as $\mathrm{diff}(E[g], t_w)^2{\cdot}\mathrm{Var}(t_w)$, where $E[g]$ represents the expected value of each limit state; for SLS it is $E[g_{\mathrm{SLS}}]$. The variance of web thickness could be obtained as $Var(t_w) = Var(t_{w0}) + 2{\cdot}Var(D(t))$; fabrication error and corrosion phenomenon are considered here as uncorrelated. An initial coefficient of variation of fabrication error is assumed as $\alpha(t_{w0}) = 0.05$.

The indices $\beta_{\hat{\sigma}}$, $\beta_{\hat{\sigma_{cr}}}$, $\beta_{\hat{u}}$, $\beta_{\hat{\tau}}$ and $\beta_{\hat{\Omega}}$ define the threshold for each of the reliability restrictions, while $\beta_{\sigma_{red}}$, $\beta_{u_{max}}$, β_{Ω}, β_{τ}, and $\beta_{\sigma_{cr}}$ denote the indices of reliability computed according to the first-order reliability method (FORM, see Equation (8)) or second-order reliability method (SORM, see Equation (9)). They strictly follow the types of checks made in the limit states of the framework but include the uncertainty disregarded in LS; a detailed formulation for a FORM and SORM is given in the theoretical background. Restrictions of β_g are always in the form of a difference between the threshold indices $\beta_{\hat{g}}$ and the resulting indices defining the girder β_g. The threshold indices are piecewise constant functions with required service time t_s, which by default is 50 years [39]. The minimum values corresponding to $t_s = 50$ for $\beta_{\hat{\sigma}}$, $\beta_{\hat{\sigma_{cr}}}$, $\beta_{\hat{\tau}} = 3.8$ and $\beta_{\hat{u}}$, $\beta_{\hat{\Omega}}$, $\beta_{\hat{\xi}} = 1.5$. This is basically because the former defines the ULS and the latter the SLS. In its first-order formulation, β_g is a simple quotient of the expected value of the limit function $g - E[g]$ and the standard deviation of $g - \sigma[g]$. In turn, the limit function is a difference between the capacity of the girder and its response to an external action or an engineering limit; there may exist multiple limit functions for a single engineering structure (such as for this girder). Owing to this, there exist also multiple formulations of the limiting indices, whose definition is very close to the limit states existent in the approach of Eurocode; for the context of this example, the following indices must be defined:

- β_{σ}—a reliability index for the maximum normal stress;
- $\beta_{\sigma_{red}}$—for the maximum stress according to the Huber–Mises criterion;

- β_τ—for the ultimate shear stress;
- $\beta_{u_{max}}$—for the ultimate deflection of this girder;
- β_Ω—for the eigenfrequency;
- $\beta_{\bar{\xi}}$—for the stability defined by the critical load (CL).

In this example $\beta_T = 0.3$, $i_s = 1$, $i_u = 5$, and $i_T = 100$. Additionally, the process of determination of β_g was postponed until the limit states were optimized, which allowed substantial optimization time savings.

3.1. Numerical Model Description

The FEM simulations are provided by the use of an FEM system ABAQUS [44] with the use of three 3D full-scale models reported below:

- Volumetric (model 1)—having the highest level of detailing including the ribs and welds, made with hexa—end tetrahedral elements;
- Shell model with ribs (model 2)—with a moderate level of detailing including inner and support ribs, based on the quad-dominated shell elements;
- Shell model without ribs (model 3)—with only the basic level of detailing including solely the web and flanges, based on the quad-dominated shell elements.

Their discretization has been shown in Figure 6. This is done to show the importance of the FEM models for optimization purposes and to contrast the results coming from different levels of detailing in the numerical model. The details available in these models are summarized in Table 3. This table firstly shows the type of elements used in the three models, their total number, and the total number of nodes. The highest number of nodes and elements are given in the first model, which is because of the FEM formulation based on the 3D elements. The third model has more than five times fewer elements and the second is a little less than the third. This is very close for the number of nodes, which are also the highest for the first model and the lowest for the second model; the highest level of detail is provided in the first model. They include the web flanges, ribs, and welds, the second model does not include welds, and the third postpones welds and ribs. This is strictly related to the number of parts and instances (provided in brackets of Table 3) created in these models—only 5 were required in the simplest third model and 563 in the first, mostly because of the very sophisticated welding required for the SIN web I-beams. This is also why the quantity of tied connections in the different models differs dramatically—only 6 for the third model and almost 1400 for the first. The latter part of Table 3. summarizes the constitutive models, analysis types, and the type and number of interactions between the modeled parts. The constitutive model applied, and the types of analyses performed for these models are the same, because of the optimization requirements. Static and static general analyses return stresses σ_{ij}, Huber–Mises stress σ_{red}, and ultimate deflection u_{max}.

Table 3. Details of the full-scale FEM models.

Model No.	Elements			Number of Parts in the Model	Details Modeled	Constitutive Model	Types of Analysis	Interaction Type, Quantity
	Type	Total Number of FEs	Total Number of Nodes					
1.	C3D8R	573,043	925,741	93 (563)	- Web - Flanges - Ribs - welds	Linear elastic with the plastic limit	- Static - Static, general - Buckling - Frequency	Tie, 1392 connections
	C3D10	152,460						
2.	S4R	77,422	85,777	10 (55)	- Web - Flanges - Ribs			Tie, 178 connections
	S3	1768						
3.	S4R	100,800	221,200	5 (5)	- Web - Flanges			Tie, 6 connections

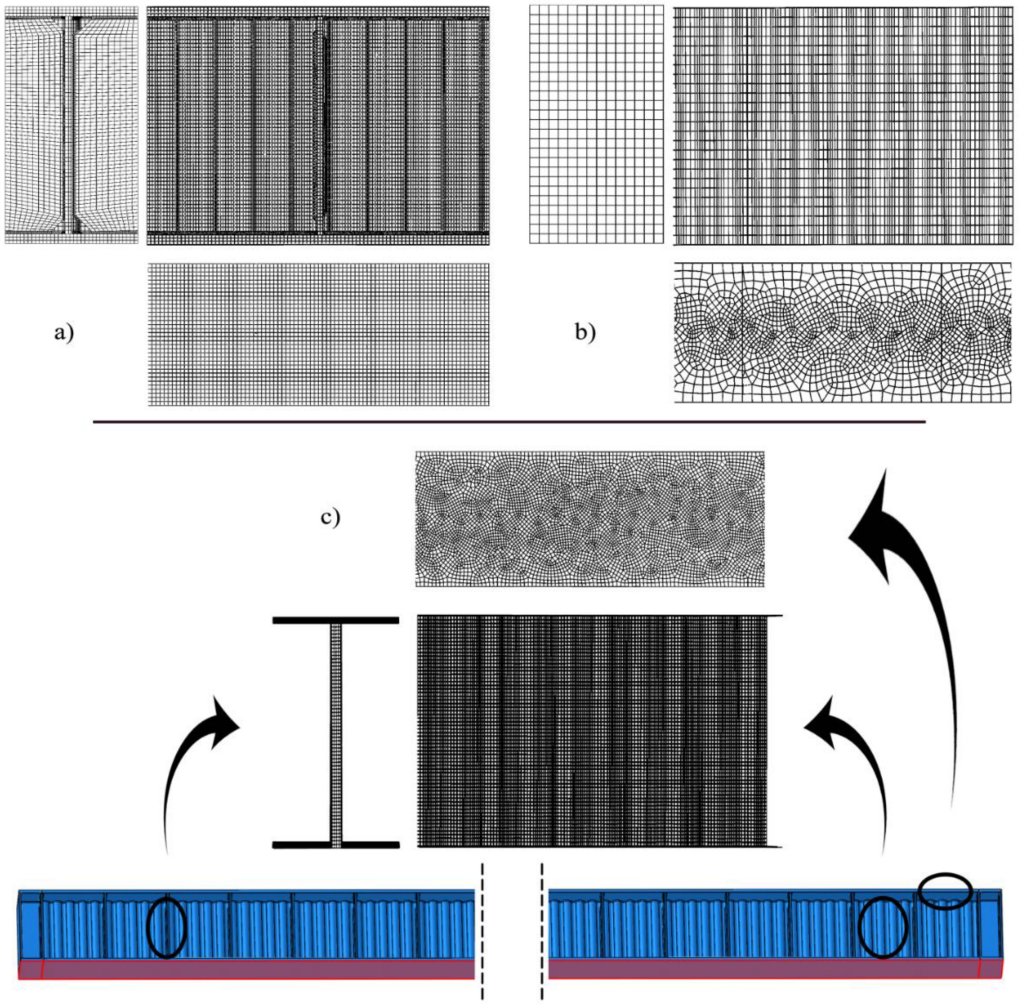

Figure 6. ABAQUS discretization of the girder, (**a**) with ribs and welds (volumetric, model 1), (**b**) with ribs (shell, model 2), (**c**) without ribs (shell, model 3).

The buckling analysis outputs the critical load ξ and the frequency analysis returns the eigenfrequency Ω. All of them are used in the checks of LS and β_g. The constitutive relation is set to linear with a plastic limit to conform to the standard approach of the Eurocode [39].

The topics that require further attention are the details of discretization and features included in different models. The details of discretization are shown in Figure 6, which brings us closer to the mesh used in all three studies. The first two shell models (models 2 and 3) have a quad-dominated mesh with a free meshing technique, allowing the best adaptivity of the elements to the geometry, while the volumetric model—a mixture of hexahedral and tetrahedral finite elements of both structured and unstructured meshes with different sizes. This variability is provided to optimize the time effort and computational accuracy. A structured hexahedral mesh is applied to the web and flanges, while the unstructured meshing technique is preserved in the welds; this is because of their complex geometry. The mesh of ribs and webs in the shell models is structured and composed of quad elements, while one of the flanges is a mixture of quadratic and triangular elements that adapt to the sinusoidal pattern of the web; this is visualized in Figure 6. Elements used in all computations are conventional stress-displacement-based FEs. The C3D8 is a linear brick, with eight nodes, reduced integration, and a single integration point. The C3D10 is a second-order 10-node tetrahedral element with four integration points at each tetrahedral vertex. S4R is a shell with four nodes, reduced integration, and a single central integration point. It has implemented hourglass control and finite membrane strains. S3 is a three-node triangular general-purpose shell with finite membrane strains. The simple

support was modeled with linear constraints. They were placed directly below the middle of the support rib (models 1 and 2) or at the outer edge of the bottom flange (model 3) along the bottom flange width. On the left side only rotational DOF (UR1) was allowed; on the right, UR1 and displacement along the length of the girder were allowed (U2). The load was applied as the equal surface load on the entire upper flange of the girder. Its magnitude was equal to 107.14 kN/m^2 (equivalent to 150 kN/m) including the dead load. The geometry of this girder was adopted exactly as given in Figure 5.

The latter detail—features modeled—illustrates a development of numerical research. Each consecutive model made in ABAQUS brings new additional details, namely the ribs and welds depicted in Figure 7 for the first model. It is also quite important that this first model consists of three-dimensional elements. This enables not only a more accurate stress analysis through the thickness of the modeled parts but also makes possible a check of interaction between the different elements of the girder and its utilization in terms of internal stress. They both are not available in the simplified models.

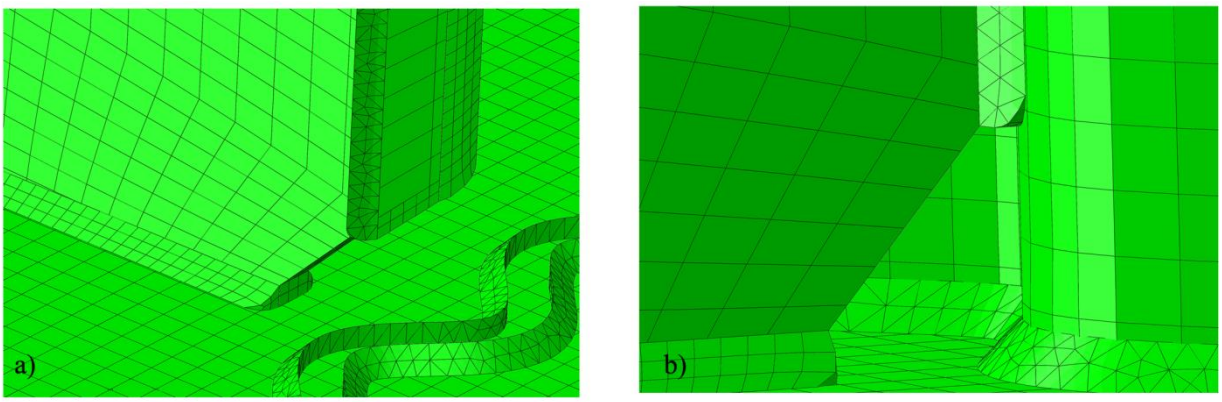

Figure 7. Additional views on the discretization for a volumetric model of the girder (model 1). (**a**) the details of the weld discretization; (**b**) welded connection of the ribs with the sinusoidal web.

3.2. Deterministic Limit States Analysis

Computation of the limit states is performed based on the results taken from the FEM simulations, which are summarized in Table 4, where σ_{cr}, τ, u_{max}, ω, and ξ are shown for the vicinity of the optimal web thickness t_w= 56 mm. This table firstly shows that the stresses and displacements increase together with an increase of t_w (an increase of W (t_w)), while the ω and ξ increase. All these effects are desirable, because the smaller the stresses and strains, the lower the usage of the material, and, secondly, the higher the critical loads and eigenfrequencies, the higher the margin between stability loss and the current state. Moreover, an addition of the welds has rather a marginal stiffening effect, because the displacements from the second and the third model are very close, at least in the considered loading scheme. A slightly higher u_{max} for the first model comes principally from the addition of the welds and the difference between volumetric and shell FEM formulation. This is not true for the ultimate stresses and stability, both of which are significantly affected by the ribs. They decrease the ultimate stresses in the FEM for σ_{cr} and τ that are returned for the models without ribs. Interestingly, the addition of ribs directly connected to the web does not essentially change the stress flow of shear in the web, yet causes its strong reduction. This happens especially in the first model, which additionally detects quite a high shear in the entire web-flange weld, even in the middle of the girder span.

Table 4. Comparison of the results from the three FEM models.

t_w	σ_{cr} [MPa]			τ [MPa]			u_{max} [cm]			ω [Hz]			ξ (CL)		
	Model No.			Model No.			Model No.			Model No.			Model No.		
	3	2	1	3	2	1	3	2	1	3	2	1	3	2	1
51	484.8	212.0	225.6	127.6	67.45	87.12	7.126	7.206	7.710	1.39	1.37	1.73	4.398	7.304	1.708
52	484.5	211.7	229.	127.2	67.0	89.95	7.117	7.198	7.702	1.39	1.37	1.73	4.409	7.317	1.716
53	484.2	211.4	232.7	126.9	66.69	92.92	7.108	7.191	7.698	1.4	1.36	1.72	4.420	7.329	1.725
54	483.9	211.1	234.2	126.5	66.35	81.78	7.100	7.183	7.686	1.4	1.36	1.72	4.431	7.342	1.737
55	483.7	210.8	236.0	126.1	66.02	82.00	7.091	7.175	7.681	1.4	1.36	1.72	4.442	7.356	1.753
56	483.3	210.6	234.5	125.7	65.70	83.51	7,084	7.168	7.673	1.4	1.36	1.71	4.453	7.369	1.778
57	482.4	210.3	231.6	125.2	65.39	84.06	7.076	7.161	7.669	1.4	1.35	1.71	4.464	7.383	1.776
58	481.7	210.0	235.4	124,8	65.10	84.05	7.069	7.153	7.656	1.39	1.35	1.71	4.475	7.399	1.784
59	481.0	209.7	227.6	124.4	64.78	85.71	7.061	7.145	7.653	1.39	1.35	1.71	4.487	7.414	1.802
60	480.3	209.5	238.9	123.9	64.51	85.22	7.054	7.138	7.651	1.39	1.34	1.70	4.498	7.430	1.810
61	479.6	209.2	229.0	123.5	64.24	84.57	7.048	7.131	7.642	1.39	1.34	1.70	4.510	7.445	1.812

The stresses induced in the middle of the span on the outer surface of flanges are comparable in all the models, but their placement is at the flange in the shell models and in the weld of the volumetric model. This placement is also the cause for a little oscillatory effect of the maximum stresses in the first model, where small changes in the thickness must also result in a change of the mesh; this effect is not observed in the shell models. A stress state is determined in the FEM at the post-processing stage, which is the major cause of its susceptibility to all discretization changes. Such problems are not observed in displacements, being the direct results of the FEM, nor in the global characteristics of $\overline{\omega}$ and ξ; the character of stresses and their pattern is considered in a separate study.

Further, it is seen that the critical loads (*CL*) returned from the three models differ significantly for the three models. This is first because of the stiffening effect of the ribs for different global modes of buckling, and secondly because of the volumetric FEM formulation of the first model. This is evidenced in Table 4, which defines the ratio of the load at stability loss q_{max} to the level of loading coming from external actions according to the Eurocode $q_{initial}$ with a subtracted initial load:

$$\frac{q_{max}}{q_{initial}} = CL + 1. \tag{18}$$

CL is much lower for the first model than for the others. It is because it was the only one that returned a local buckling of the support rib. Other models returned only the global losses of stability, the first of which was always rotation-torsional. They occur for quite a high magnitude of the *CL* (critical load ratio of over 4.45 or 7.37) for a girder, which is initially loaded to 88.4% of its ultimate bending capacity according to the assumptions of the Eurocode. The critical load in the volumetric model is much lower, but all the critical modes of behavior until the 25th one can be easily avoided by an increase in the thickness of the support or, preferably, a change in its geometry from plate to corrugated (insensitive to local buckling). Quite interestingly, the addition of the ribs increased the *CL* by about 50% for the shell model. No buckling is detected in the web itself, either by stiffened or unstiffened models. This proves the high contribution of the wavy web to the overall stability of the girder and the reasonable significance of its thickness, whose increase enlarges the critical load. This increase is consistent with an engineering intuition, but it does not stop the underneath mechanism leading to the buckling of the girder. Contrary to the results of the critical load, these for eigenfrequency show almost perfect agreement for models 1–2 and give a slightly lower quantity for the third one. This difference is increasing

for the higher eigenfrequency modes (see Table 4), which is caused by the change in the linear dead load of a girder due to the stiffening ribs and welds, yet does not significantly hinder the character of these modes.

It must be additionally mentioned that a choice of the proper ultimate stress or displacement for purposes of LS and reliability restrictions is not a trivial task, especially when a complex 3D structure is considered and modeled with the use of shell or volumetric FEM elements. The global ultimate stress does not necessarily give a proper condition for the ULS and may turn out to be inappropriate for restrictions. Even for such conceptually uncomplicated structural elements as a simply supported beam, the ultimate stress may lie in other places than those distinguished by the beam theory (as happens in this study). In such conditions, reliability shall be checked not only for the location of the ultimate stress but also for these other locations detected in the beam theory, because the material in these places may be susceptible to local instability (as in all plate structures). Because of this, the ultimate stress allowed in such locations may be highly reduced and conversely, the material can be locally stronger in a location of ultimate stress predicted by the FEM (e.g., when some confinement exists). Therefore, in all complex structures, one should always first determine its possible weak points and check the reliability for all of these, not only the one for the ultimate stress or displacement revealed by the FEM results.

3.3. Probabilistic Aspects

The determination of the reliability indices β_g and related optimization procedures have been both programmed and completed in the computer algebra system MAPLE. The WLSM is based on the discrete results of three FEM models (see Table 3) and for three types of weights, Dirac, equal, and triangular (see Table 2). The input random parameter is web thickness with a mean value taken from the objective function W and updated in each loop of the optimization. The probabilistic density function (PDF) of this thickness is Gaussian and we treat here two separate random problems. The first is at $t = 0$ and is connected with a fabrication error (manufacturing imperfection) of this thickness with coefficient of variation (COV) in the range of $\alpha(\omega_0) \in \{0; 0.15\}$, and a second, where in addition to ω_0, a second random variable is corrosion penetration depth, where time t is a design variable in a range of $t \in \langle 0; 50 \rangle$ years. This second check is also a final and most severe restriction in the optimization loop because it takes into consideration the degradation of the girder with time. The formulation of the probabilistic moments and coefficients is here threefold:

- First of all, the coefficients are computed by direct differentiation of the random variable computed from the response function together with its PDF; this is called the semi-analytical approach (AM);
- Secondly, the generalized iterative stochastic perturbation technique is applied with up to 10th order approximation of the response function by the Taylor expansion—including the first 10 terms of this expansion; this is called the SPT [42];
- Finally, the crude Monte Carlo simulation (MCS) is used to return these coefficients; this is called the MCS.

Such an approach is selected for purposes of comparison between these three methods and also for redundancy so that even if one method fails in a specific optimization step or for the specific g, the indices could still be calculated and compared. A crude MCS with $5 \cdot 10^5$ trials is chosen to dissolve all the doubts about the accuracy of a more refined Monte Carlo method. The spectrum of the web thickness used in each step is $t_{w,\,i} \pm 5$ mm with a difference of 1 mm for each computation, so that the response function is optimized based on 11 FEM results around the mean value defined at each optimization loop. The algorithm developed in MAPLE fully encompasses the process of reliability indices β (see Figures 1 and 3) and $\beta_{\sigma_{cr}}$, and for $t \in \langle 0; 50 \rangle$ only $\beta_{u_{max}}$ is restricted, which is done for the computation efficiency and simplicity of this example.

3.4. Reliability Restrictions β_g

The final reliability calculations are shown for the optimized W, for which t_w= 56 mm. The structure of the reliability assessment for this W is divided into three main sections:

- The first of these determines the influence of different types of weighting schemes and FORM vs. SORM formulations. It takes the manufacturing imperfection as an input variable, is based on the volumetric FEM model, and is calculated for $t = 0$.
- The second analysis uses a Dirac-type of weighting scheme and compares the results of stochastic equations with manufacturing imperfection as a random parameter for all three FEM models and deterministic results. This is done to highlight the impact of the FEM and model accuracy on the girder's output reliability. It is also performed at $t = 0$.
- The last study incorporates two random variables, including the fabrication imperfection ω_0 and corrosion penetration depth ω, and serves as the last restriction for the optimization purposes of this girder.

This is done firstly to show the results for the optimized W and secondly to emphasize the most important factors in the optimization, i.e., the FEM model, order of reliability assessment, and type of the weighting scheme in the optimization of the WLSM. Three independent methods of computation, AM, MCS, and SPT are used for simultaneous verification of the results. The probabilistic moments and coefficients are shown only for one, most restrictive limit function and solely relative to the weighting scheme, which is done to show their general outlook and present relation with an input uncertainty. The other ones return analogous results.

3.4.1. Initial Restriction of β_g—WLSM Weighting Scheme

Computations of reliability-induced restrictions for the girder at $t = 0$ include the determination of the first four probabilistic moments and coefficients of all the limit functions considered, i.e., $E_g(\alpha(\omega_0))$, $\alpha_g(\alpha(\omega_0))$, $\beta_g(\alpha(\omega_0))$, and $\kappa_g(\alpha(\omega_0))$, and its reliability index $\beta_g(\alpha(\omega_0))$. They are depicted in Figures 8–17 and are computed relative to the coefficient of variation of web thickness inflicted by an uncertain fabrication error $\alpha\ (\omega_0)$. This ensures an easy way of check of these restrictions for the chosen level of uncertainty and avoids the need for repetition of the entire optimization process in the case when its level is slightly increased. The full results are shown only for the most restrictive condition, which is a critical load (CL). The results of all other ones are limited solely to the index of reliability according to SORM; this is done for the brevity of the results.

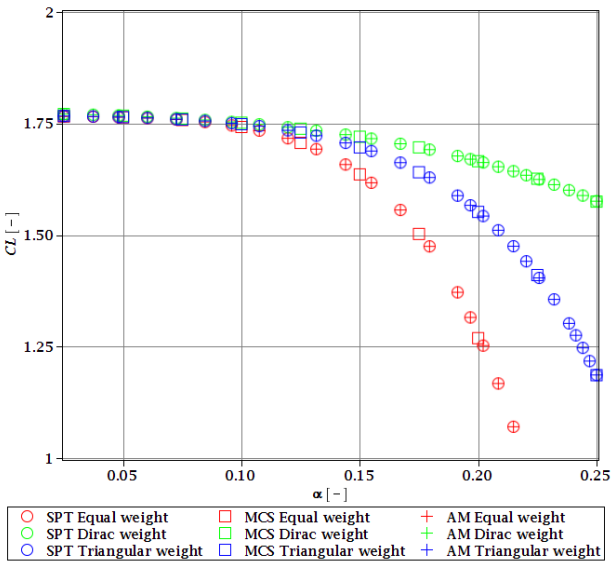

Figure 8. Expectations of the critical load for different types of weights.

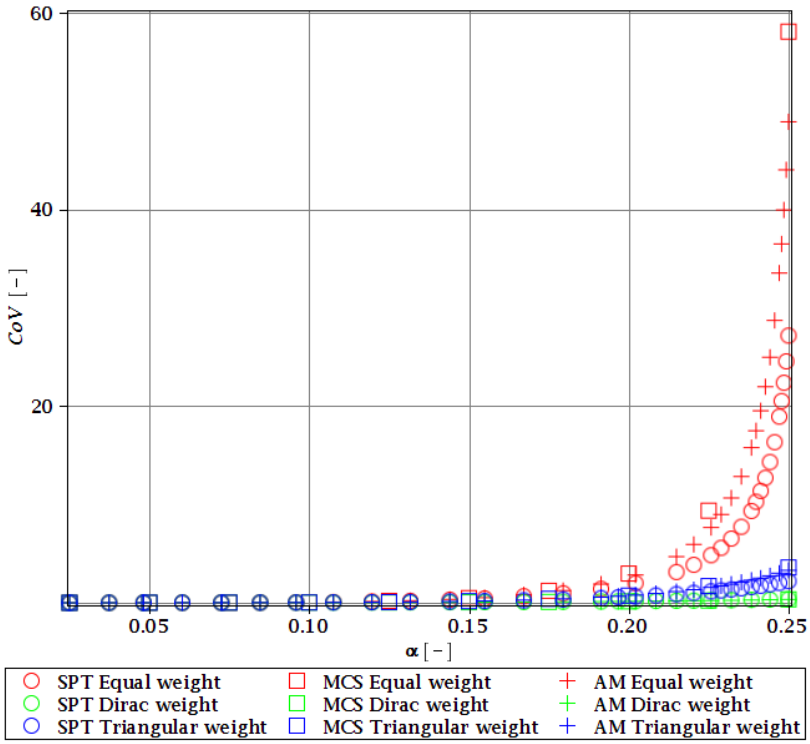

Figure 9. CoV of the critical load for different types of weights.

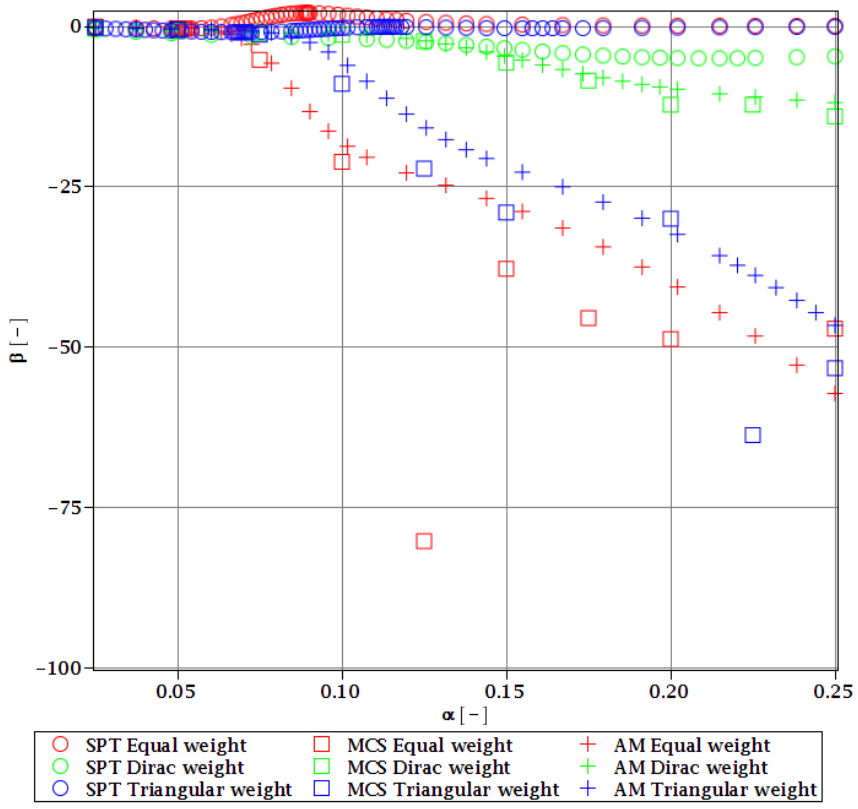

Figure 10. The skewness of the critical load for different types of weights.

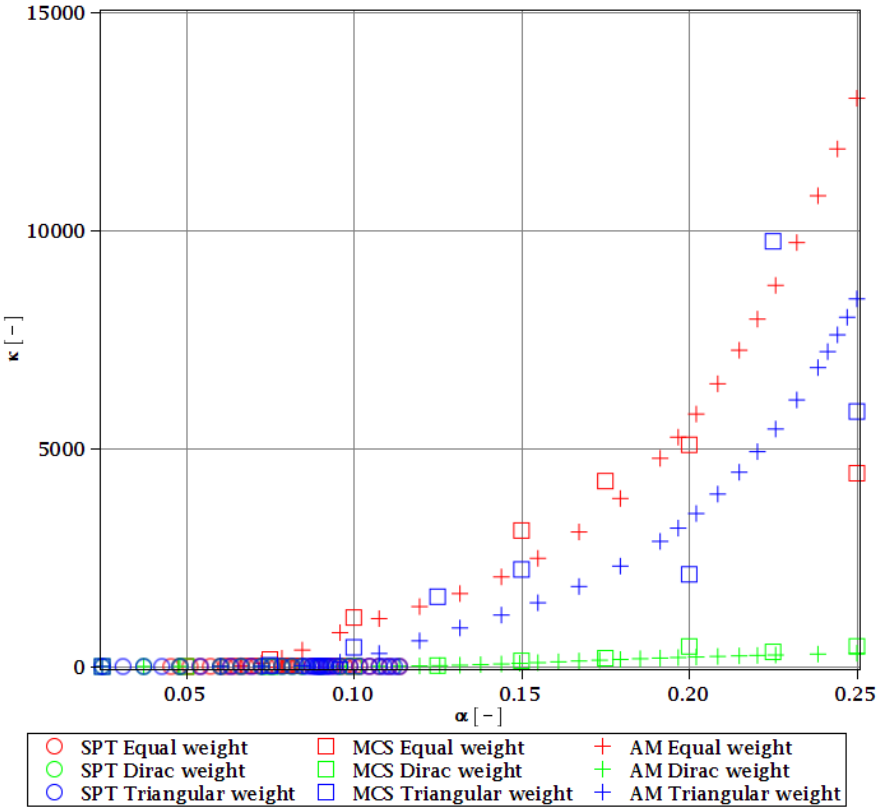

Figure 11. Kurtosis of the critical load for different types of weights.

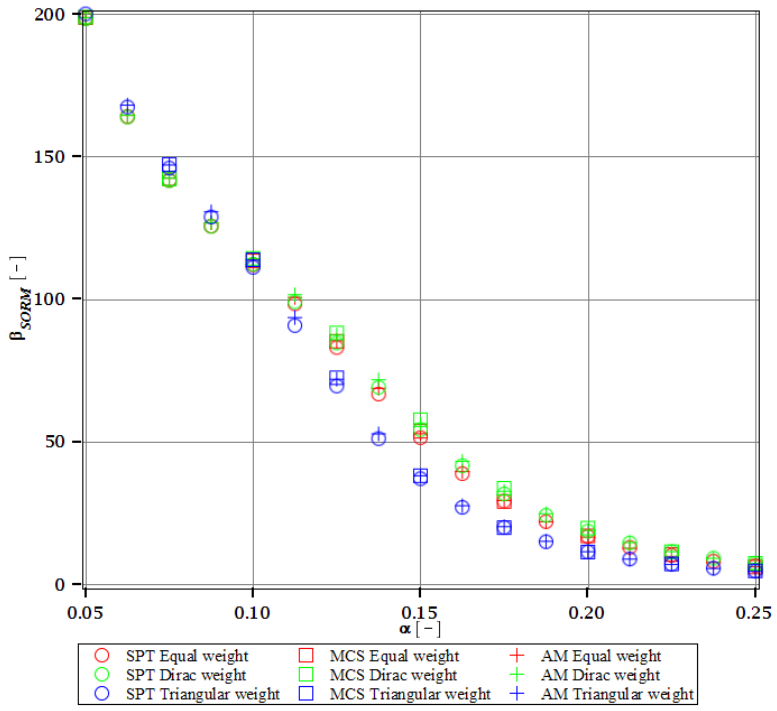

Figure 12. Reliability index of the corrugated I-beam for different types of weights according to the second-order reliability method (SORM)—displacement.

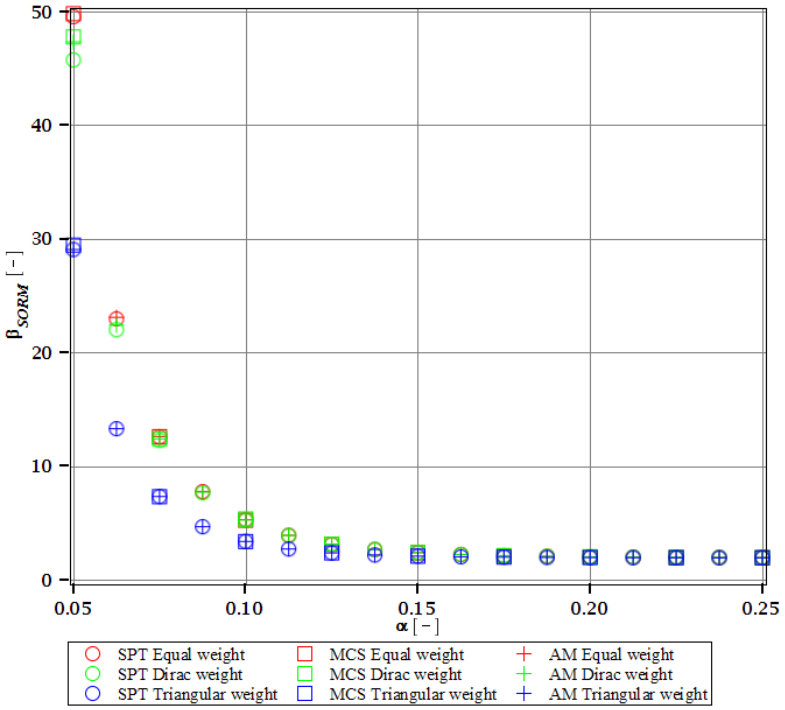

Figure 13. Reliability index of the corrugated I-beam for different types of weights according to the second-order reliability method (SORM)—normal stress.

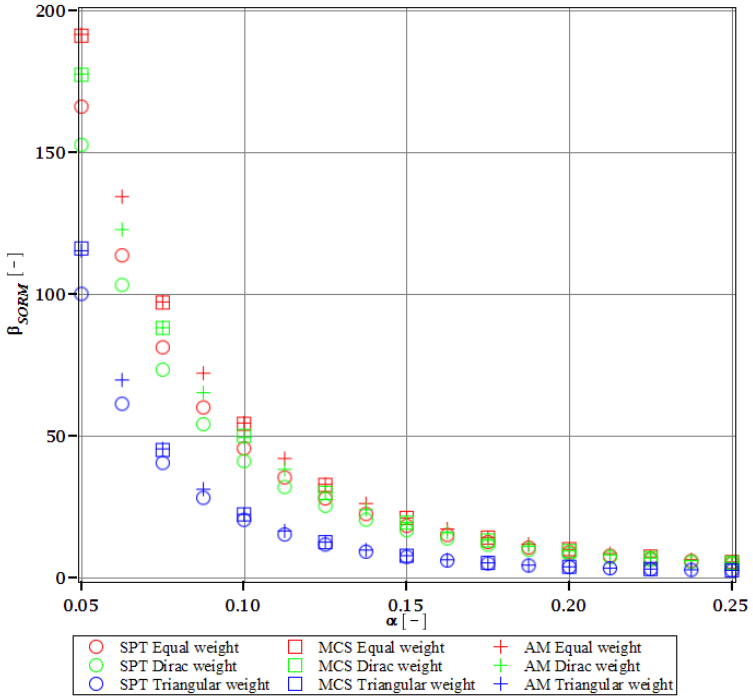

Figure 14. Reliability index of the corrugated I-beam for different types of weights according to the second-order reliability method (SORM)—shear.

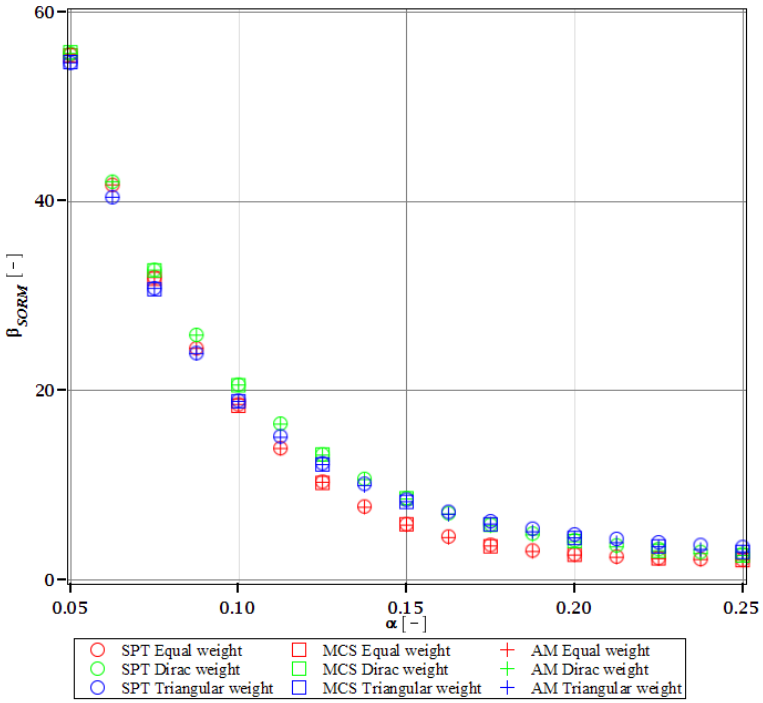

Figure 15. Reliability index of the corrugated I-beam for different types of weights according to the second-order reliability method (SORM)—eigenfrequency.

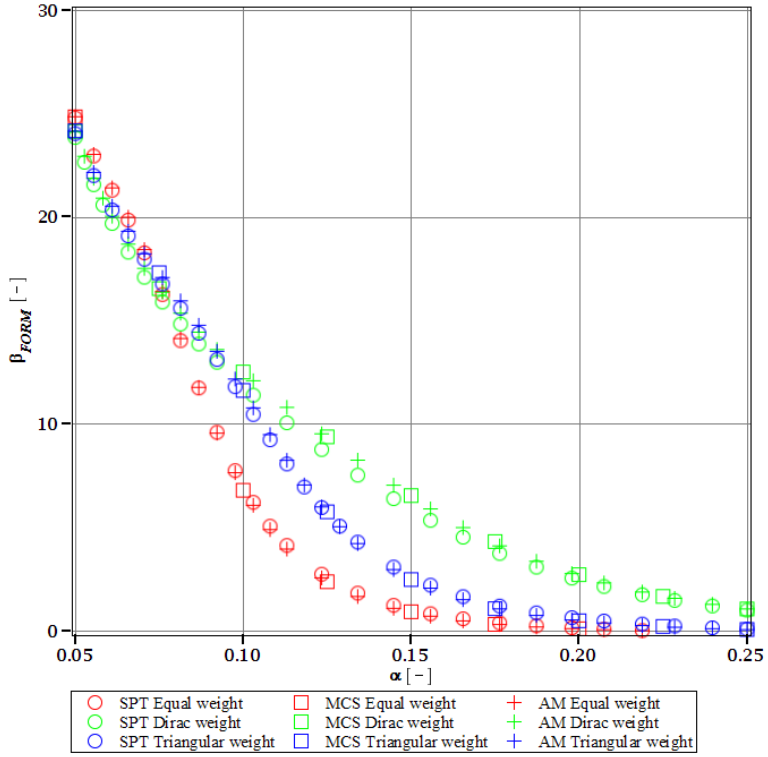

Figure 16. Reliability index of the corrugated I-beam for different types of weights according to the first-order reliability method (FORM)—critical load.

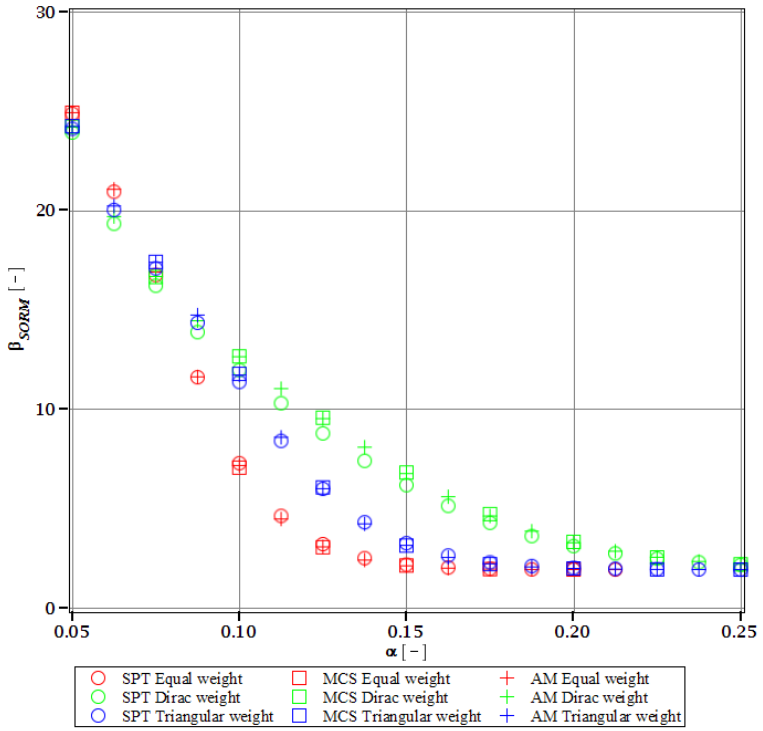

Figure 17. Reliability index of the corrugated I-beam for different types of weights according to the second-order reliability method (SORM)—critical load.

The lower probabilistic coefficients for the limit state based on stability criterion $E_{\tilde{\xi}}(\alpha(\omega_0))$ and $\alpha_{\tilde{\xi}}(\alpha(\omega_0))$ firstly show that they both are highly affected by the uncertainty caused by the manufacturing error. The expected values (Figure 8) decrease, and the coefficient of variation (Figure 9) increases together with an increase in this uncertainty and the rate of this change always increases. Interestingly, the changes in the $E_{\tilde{\xi}}$ are up to 50% and the coefficient of variation is multiple times higher than for the input. The three methods of computation show a perfect agreement.

The skewness $\beta_{\tilde{\xi}}(\alpha(\omega_0))$ and kurtosis $\kappa_{\tilde{\xi}}(\alpha(\omega_0))$ for the critical load depicted in Figures 10 and 11 represent a converse character. The skewness is predominantly negative, while the kurtosis is positive. They both have quite a strong relationship with the input uncertainty, and they reach very high magnitudes of up to 120 for $\beta_{\tilde{\xi}}$ and 13,000 for $\kappa_{\tilde{\xi}}$. A scatter of the three stochastic methods is quite high, but still, the AM and MCS demonstrate a quite comparable trend. The SPT is effective here only up to $\alpha = 0.1$, but it is the fastest.

The indices of reliability β_{σ}, $\beta_{\sigma_{red}}$, β_{τ}, $\beta_{u_{max}}$, β_{Ω}, and $\beta_{\tilde{\xi}}$ include all the relevant limit states and are all shown in Figures 12–17. They principally show a high converse dependence on the input uncertainty of manufacturing error and are also affected by the WLSM weighting scheme. The lowest initial reliability is reported for the critical load (see Figures 16 and 17). This is a direct effect of two main factors. The first of these is the fact that even the deterministic safety is quite small here (function close to one, which constitutes its lower limit, see Table 4). The second is connected with a magnitude of the CoV, which is very high for this state function (Figure 9) and has a strong exponential character relative to the input CoV. With an increasing input uncertainty, this smallest index rapidly decreases, but still from approx. $\alpha\ (\omega_0) = 0.07$ the lower bound of reliability is governed by the normal stress shown in Figure 13. The indexes also depend upon the type of weight of WLSM. This difference is the strongest for the two indices constituting the lower bound of the reliability, namely the normal stress and the critical load, and additionally for the shear (see Figures 13, 14 and 16). This is because their first two probabilistic moments show the highest dependence on the type of weight applied.

The character of a relationship between the reliability index and an input uncertainty is not always smooth and without local inflection points. The indices for the ultimate displacement, as well as critical load, show small fluctuations through their course, especially around $\alpha\ (\omega_0) = 0.10$. Such fluctuations are intriguing, but for now, their cause has not been determined.

The last comparison is the FORM vs. SORM index of reliability, which is given based on critical load, the most difficult reliability restriction at $t = 0$. It is based on Figures 16 and 17.

The graphs according to both orders have a very similar character. This is expected, because the applied SORM is based on the Gaussian input probability density and, therefore, these indices should be comparable. An important observation is that β_g according to SORM is less dependent on the type of weight and has a little higher magnitude for an extensive input uncertainty. Finally, the SORM approach corrects the errors coming from the FORM, i.e., the diverging or scattered character of β_g for some limit functions. An additional observation is concerned with the interchangeability of these three probabilistic methods applied in restrictions of the reliability index; all the methods show an almost perfect agreement for all the state functions. Due to this, when only one stochastic variable is taken into consideration, all the methods can be used alternatively. In such conditions, the most preferable one seems to be the stochastic perturbation method (SPT), which is not dependent on a direct derivation, does not require a considerable number of trials (as the MCS), and is also the swiftest.

The last, yet most important, observation is a total limit of input uncertainty coming from the fabrication imperfection that allows for fulfilling the restriction of reliability β_g. This limit differs for all the state parameters and ranges from $\alpha\ (\omega_0) = 0.09$ to around $\alpha\ (\omega_0) = 0.21$. The lowest one constitutes a total limit, and therefore the objective function with optimum $t_w = 56$ mm is $\alpha\ (\omega_0) = 0.09$. This limit corresponds to the limit function of critical load (ξ). This is a reasonable result because for most of the constructional elements the fabrication error causes uncertainty in t_w lower than $(\omega_0) = 0.05$. Nonetheless, reliability restrictions at $t = 0$ are not the most rigorous, which undoubtedly are the ones connected with a joint effect of corrosion and the considered fabrication error. Improving the resistance of the girder to stability loss would be enough to increase the overall reliability of this girder at $t = 0$, but it may not be sufficient to improve reliability in the corrosive environment.

3.4.2. Initial Restriction of β_g

The differences in initial reliability restriction fulfillment for the three models are shown in Figures 18–21. They depict the FORM indices for the four most important limit states, i.e., β_σ, $\beta_{u_{max}}$, β_Ω, and β_ξ in the function of the $\alpha\ (\omega_0)$ and for $t = 0$. These plots are principally presented to highlight the importance of the choice of the FEM model type and its accuracy in fulfillment of the reliability restrictions for the objective function. They are all computed with the use of the Dirac weighting scheme and with three alternative probabilistic methods, MCS, AM, and SPT. These indices perfectly justify the purpose, being vastly dependent on the model type and almost uniform for all the probabilistic methods. Therefore, it is highly recommended to put more effort during the modeling process of the FEM and into the collection of data coming from these simulations than into the choice and scrutiny of the probabilistic method. The probabilistic coefficients bring no more information for optimization purposes and therefore they are not included. One may refer to Figures 8–11 for the required information.

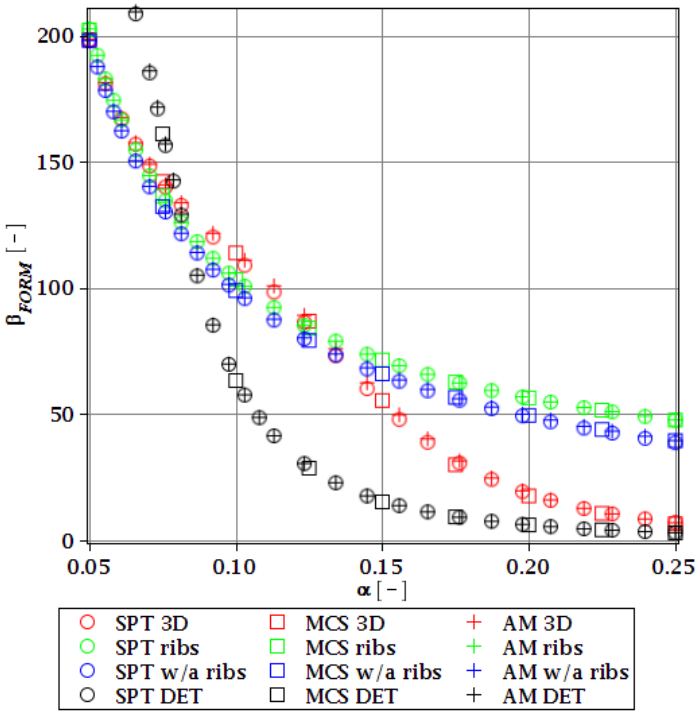

Figure 18. Reliability index of the corrugated I-beam for three ABAQUS models according to FORM and based on the deflection.

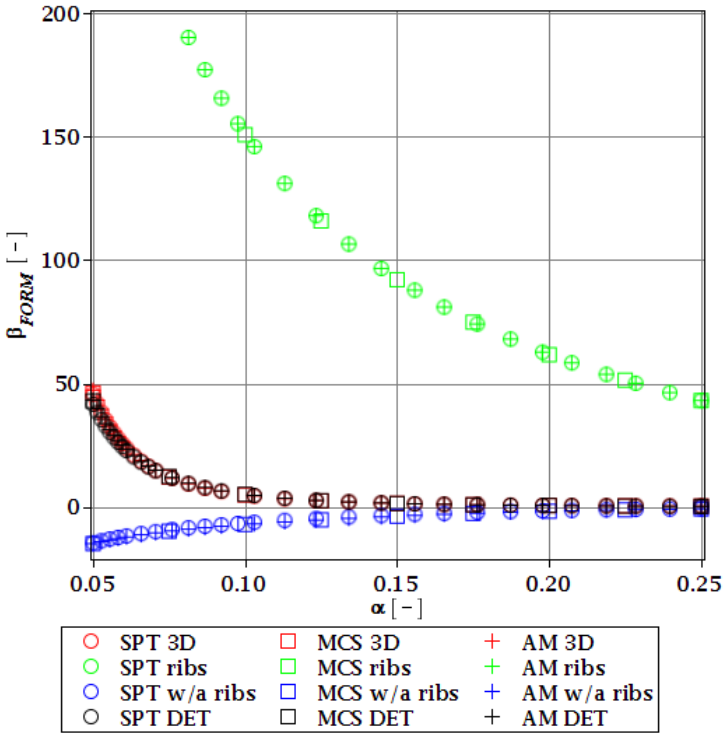

Figure 19. Reliability index of the corrugated I-beam for three ABAQUS models according to FORM and based on the ultimate normal stress.

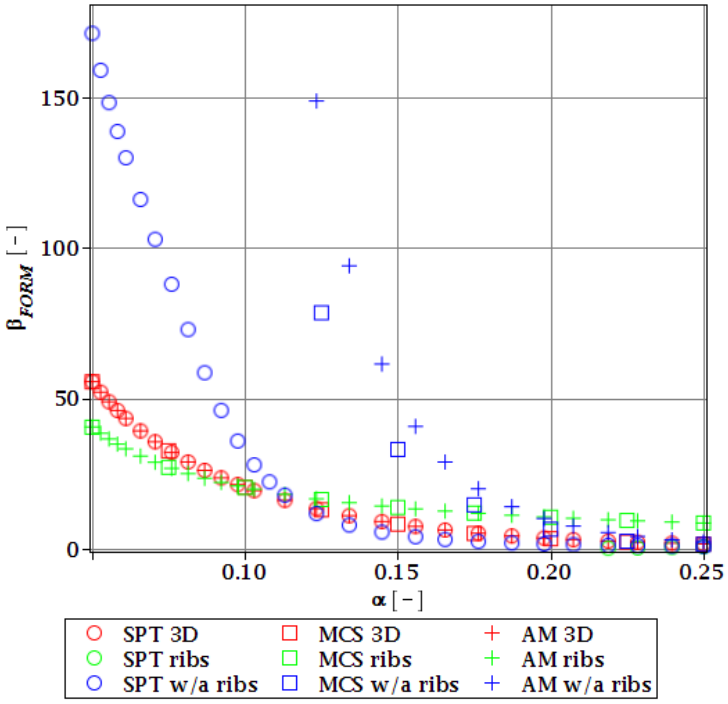

Figure 20. Reliability index of the corrugated I-beam for three ABAQUS models according to FORM and based on the eigenfrequencies.

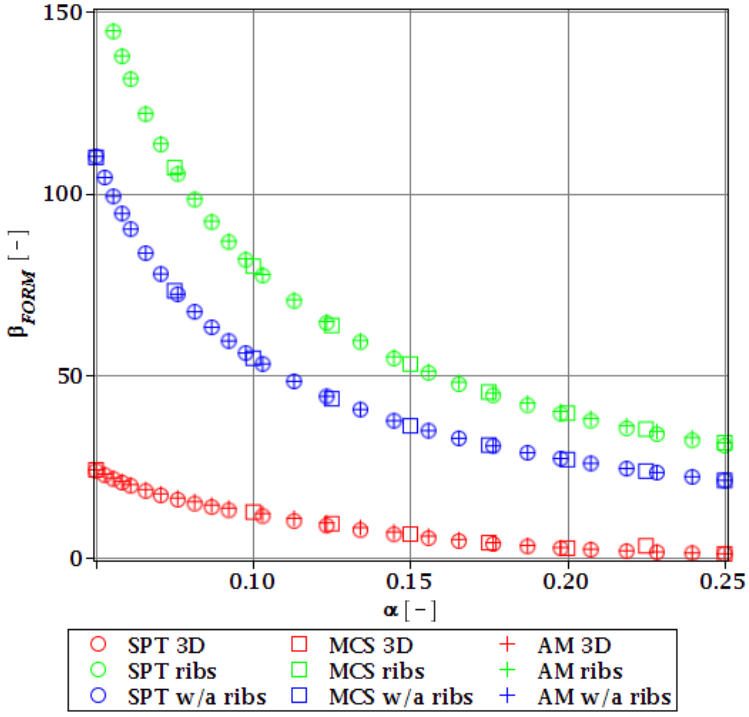

Figure 21. Reliability index of the corrugated I-beam for three ABAQUS models according to FORM and based on the critical load.

From Figures 18–21 it is first seen that the reliability margin decreases together with an increase of $\alpha\ (\omega_0)$. It is in the range of $50 \div 150$ for a small $\alpha\ (\omega_0) < 0.01$, but it rapidly decreases and reaches zero for $\alpha\ (\omega_0) \in (0.10; 0.14)$; this is still much higher than typical uncertainty caused by the fabrication imperfection. The second observation concerns the inexistence of a limit state setting the reliability restriction for the entire

$\alpha\ (\omega_0)$. For each level of uncertainty, this limit is set in different LS, and therefore the topological optimization is not trivial—each limit state depends on multiple parameters of the model. The highest restriction is decisive, which is not unique for the different models. On the other hand, the first model is also the most restrictive for a majority of the cases and because it is also the most detailed one, it should be the one taken for the final optimization. This is because it had the smallest margin in the LS. An alternative approach is the inclusion of results from all the models for optimization purposes, but this would cause almost threefold longer computations because the FEM solution is very computationally-intensive. The correspondence between the three methods is almost perfect for all the four considered reliability indices and for all the FEM models, with only one exception of Figure 20 for the third, most simplified model (shell without ribs), for which neither of the methods converges.

One of the observations which should undoubtedly be highlighted is the fact that for all the limit states the reliability indices according to different models diverge not only in their initial value but also in the strength of their relation to $\alpha\ (\omega_0)$. A very good example is an index based on the deflection (Figure 18), which starts very high for the deterministic model and just over $\alpha\ (\omega_0) = 0.07$ crosses all the other indices to become the lowest (to constitute a lower limit) for all higher $\alpha\ (\omega_0)$. One more interesting relation is unveiled by the reliability index based on the ultimate normal stress (Figure 19) and computed according to the shell model (third model) which shows a negative value of the index. This is a direct outcome of an existence of the unacceptably high stress exceeding the plastic limit of the construction steel already in the FEM results. The existence of the negative index is incorrect and should by all means be excluded from further analysis. Nevertheless, unlike in $\alpha\ (\omega_0)$, its negative value gives a piece of important information for optimization purposes—that the element is not fulfilling restrictions already in the process of the limit states, and before reliability checks, a new optimization loop with a new value of W should have been already started.

3.4.3. Durability Analysis with β_g

The last and final restriction of the optimization problem is the reliable service life of the constructional element, which is set as $t = 50$ years. This restriction is formulated with the use of the FROM index of β_g and presented for the limit state of u_{max}. It is computed for the joint impact of the corrosion penetration depth and the manufacturing imperfection, both being random and uncorrelated. Reliability is calculated with three probabilistic methods, i.e., AM, MCS, and SPT. Corrosion is modeled according to the third model from Table 1 with two random parameters A and B, while the uncertainty of initial imperfection is set within the following bounds of $\alpha\ (\omega_0) \in\ [0.05; 0.25]$ with a Gaussian PDF. This imperfection is introduced during the production of the beam and is considered time-independent, while the corrosion process is described by a time series. The response function utilized for probabilistic calculations is calculated with an inner optimization problem and WLSM is based on the Dirac weighting scheme. The result is presented for the optimized objective function $W(t_w = 56\ \text{mm})$ and based on the most refined first FEM model. This final reliability restriction is depicted in Figure 22 as a function of service time $t \in\ (0; 50)$ years. It firstly shows that the limit of 1.8 is reached at around 60 years, and the margin of the restriction is within the stop criterion defined for this example as $\beta_T = 0.3$. Secondly, the uncertainty of an initial manufacturing imperfection only marginally affects the final result, and this is why its sole impact was checked in the preceding step of the optimization loop. This index starts at$\beta_g = 60$, sharply decreases in a convex manner with a decreasing slope and has an apparent limit of $\beta_g \cong\ 0$. This index shows a very good coincidence of the two probabilistic methods, the SPT and MCS. The third, semi-analytical method (AM) diverges from the others, and this is why it is not reported in Figure 22. This exemplifies the usability of this triple redundant method, which allows a successful check of restriction even when one of the probabilistic methods turns out to be unavailable or divergent for a specific step.

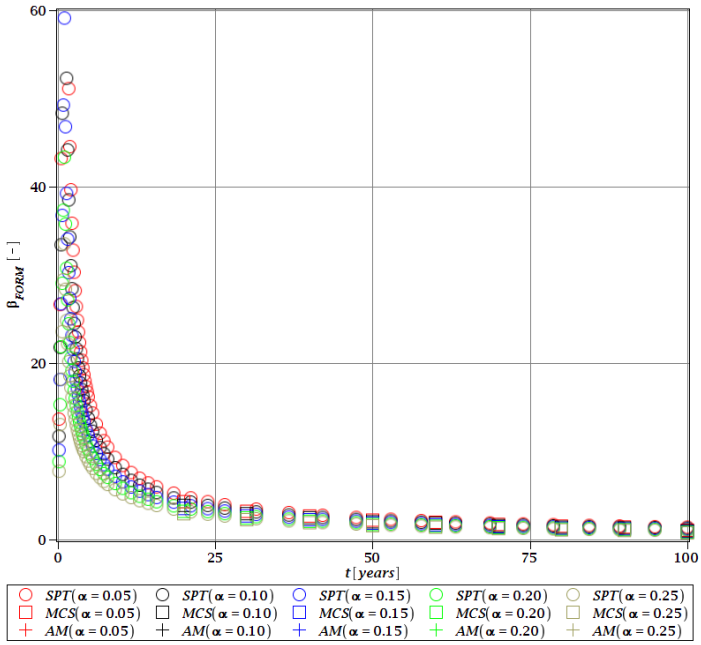

Figure 22. Reliability index of the corrugated I-beam for different types of weights according to FORM—deflection (SLS), the second-order polynomial.

4. Concluding Remarks

This paper presents an optimization framework for topological problems in the domain of civil engineering. It is exemplified by a successfully optimized simply supported SIN web I-girder. The main novelty in this paper is the concept of reliable service life prediction and its application to a computationally demanding structure. It allows automation of the reliability-based design of custom structural elements. The principal objective of the proposed RBDO algorithm is a determination of the best topology that satisfies all the design restrictions applicable to civil engineering structures during their service life. Restrictions include the limit states, i.e., the ultimate limit state and serviceability limit state, stability, and vibrations in the deterministic and reliability context. The limit functions are applied directly after the FEM results. The optimization loop consists of subsequent verification of physical and geometrical restrictions, FEM problem solution, verification of all deterministic design restrictions, and finally verification of reliability-based restrictions. This is done for a specified service life of construction. It could be applied to a wide variety of structural elements and entire structures; the limit functions could be obtained analytically, by BEM, FEM, neural networks, or with the use of any other algorithm that outputs the required state parameters.

The most critical points of this algorithm include the calculation of the representative limit functions for local state parameters, such as stresses and strains, FEM detailing, and interpretation of FEM results. For this reason, three concurrent models were proposed and shortly contrasted in the optimized solution; in current maturity, the algorithm uses a deterministic non-gradient search. It is intended for replacement in future works by a more effective method, such as neural networks.

The proposed algorithm is applied to a practical example of the SIN web I-girder. This provides additional insight into the reliability of such elements, as well as their susceptibility to loss of stability, vibrations, and deformability. It also adds some valuable remarks to the FEM modeling in RBDO problems. The results obtained in this work confirm that numerical modeling precision significantly affects the optimization outcome. This is because its choice has a direct effect on the stress state of the girder and its buckling. Different FEM models applied in this study return important dissimilarities in stress distribution, its maximum values, and placement of peaks. This is also true for buckling loads and their patterns. It is also exemplified here that the choice of the FEM formulation (volumetric vs. shell), as well

as the finite element type and order, significantly affects the optimization. Furthermore, it is difficult to set the required level of detail in the FEM model and the minimum amount of FEs before the RBDO. This is because the buckling load together with ultimate stresses and deflections have no clear correlation to the model accuracy. Therefore, a decrease in the level of geometric and computational precision may hide significant design problems. They include low buckling mode or high-stress peaks in the welds that are omitted by simplified models and lead to an overestimation of the overall reliability of this structure. Importantly, only the most detailed model revealed additional instabilities in the girder occurring at much smaller loads than the others and having a local, rather than global character.

The corrosion process affected the considered example in terms of both reliability and structural capacity. Its evolution increased the internal stresses and decreased critical loads. The influence of the initial fabrication error on the service life of the exemplary structure was marginal and may be omitted in future research. On the contrary, steel and environment type had a much more substantial effect on the service life of an exemplary structure. This is because of its direct effect on the evolution of corrosion depth and its uncertainty. Please note that maintenance, such as painting or plating, is not taken into consideration in the current algorithm. Performed regularly, it will increase the reliable life of the structure. Its inclusion is planned in future research.

The triple probabilistic calculations applied in this study provided a piece of important information on the convergence of probabilistic calculations that would be otherwise unavailable. On the other hand, their mutual application slowed down the optimization process. Computational time reduction could be achieved by limiting the RBDO to a single probabilistic method. The ISFEM is the most recommended in this case. It is the fastest and significantly accelerates the optimization process. Its accuracy is a little lower than that of the MCS, but the difference proved to be marginal for the considered example.

Author Contributions: Conceptualization, M.K.; methodology, D.S. and M.K.; data curation, D.S.; writing—original draft, D.S.; writing—review and editing, M.K.; software and methodology, D.S. and M.K. All authors have read and agreed to the published version of the manuscript.

Funding: This paper has been written in the framework of the research grant OPUS no. 2021/41/B/ST 8/02432 "Probabilistic entropy in engineering computations" sponsored by the National Science Center in Cracow, Poland.

Institutional Review Board Statement: Not applicable.

Informed Consent Statement: Not applicable.

Data Availability Statement: Not applicable.

Conflicts of Interest: The authors declare no conflict of interest.

References

1. Sophianopoulos, D.S.; Deri, A.E. Steel beam–to-column RBS connections with European profiles: I. Static optimization. *J. Constr. Steel Res.* **2017**, *139*, 101–109. [CrossRef]
2. Sigmund, O. On the design of compliant mechanisms using topology optimization. *Mech. Based Des. Struct. Mach.* **1997**, *25*, 493–524. [CrossRef]
3. Lewiński, T.; Czarnecki, S.; Dzierżanowski, G.; Sokół, T. Topology optimization in structural mechanics. *Bull. Pol. Acad. Sci.-Tech.* **2013**, *61*, 23–37. [CrossRef]
4. Lopez, C.; Baldomir, A.; Hernandez, S. The relevance of reliability-based topology optimization in early design stages of aircraft structures. *Struct. Multidisc. Optim.* **2018**, *57*, 417–439. [CrossRef]
5. Frangopol, D.M.; Maute, K. Life-cycle reliability-based optimization of civil and aerospace structures. *Comput. Struct.* **2003**, *7*, 397–410. [CrossRef]
6. Schuëller, G.I.; Jensen, H.A. Computational methods in optimization considering uncertainties—An overview. *Comput. Methods Appl. Mech. Eng.* **2008**, *198*, 2–13. [CrossRef]
7. Vo-Duy, T.; Duong-Gia, D.; Ho-Huu, V.; Nguyen-Thoi, T. An Effective Couple Method for Reliability-Based Multi-Objective Optimization of Truss Structures with Static and Dynamic Constraints. *Int. J. Comput. Methods* **2020**, *17*, 1950016. [CrossRef]
8. Kaveh, A.; Biabani Hamedani, K.; Kamalinejad, M. Set theoretical variants of optimization algorithms for system reliability-based design of truss structures. *Period. Polytech. Civ. Eng.* **2021**, *65*, 717–729. [CrossRef]

9. Ni, P.; Li, J.; Hao, H.; Yan, W.; Du, X.; Zhou, H. Reliability analysis and design optimization of nonlinear structures. *Reliab. Eng. Syst. Saf.* **2020**, *198*, 106860. [CrossRef]
10. Duan, Z.; Jung, Y.; Yan, J.; Lee, I. Reliability-based multi-scale design optimization of composite frames considering structural compliance and manufacturing constraints. *Struct. Multidiscipl. Optim.* **2020**, *61*, 2401–2421. [CrossRef]
11. Tsompanakis, Y.; Papadrakakis, M. Large-scale reliability based structural optimization. *Struct. Multidisc. Optim.* **2004**, *26*, 429–440. [CrossRef]
12. Mróz, Z.; Haftka, R.T. Design sensitivity analysis of non-linear structures in regular and critical states. *Int. J. Solids Struct.* **1994**, *31*, 2071–2098. [CrossRef]
13. Frangopol, D.M.; Hendawi, S. Incorporation of corrosion effects in reliability-based optimization of composite hybrid plate girders. *Struct. Saf.* **1994**, *16*, 145–169. [CrossRef]
14. Xiao, M.; Zhang, J.; Gao, L. A system active learning Kriging method for system reliability-based design optimization with a multiple response model. *Reliab. Eng. Syst. Saf.* **2020**, *199*, 106935. [CrossRef]
15. Meng, Z.; Li, G.; Wang, X.; Sait, S.M.; Yıldız, A.R. A Comparative Study of Metaheuristic Algorithms for Reliability-Based Design Optimization Problems. *Arch. Comput. Methods Eng.* **2021**, *28*, 1853–1869. [CrossRef]
16. Wang, Y.; Zhou, X.; Wang, H.; Kong, D.; Xu, S. Stochastic constitutive model of structural steel based on random field of corrosion depth. *Case Stud. Constr. Mater.* **2022**, *16*, e00972. [CrossRef]
17. Di Sarno, L.; Majidian, A.; Karagiannakis, G. The Effect of Atmospheric Corrosion on Steel Structures: A State-of-the-Art and Case-Study. *Bldgs* **2021**, *11*, 571. [CrossRef]
18. Han, X.; Yang, D.Y.; Frangopol, M. Optimum maintenance of deteriorated steel bridges using corrosion resistant steel based on system reliability and life-cycle cost. *Eng. Struct.* **2021**, *243*, 112633. [CrossRef]
19. García-Segura, T.; Penadés-Plà, V.; Yepes, V. Sustainable bridge design by metamodel-assisted multi-objective optimization and decision-making under uncertainty. *J. Clean. Prod.* **2018**, *202*, 904–915. [CrossRef]
20. Guo, Y.L.; Chen, H.; Pi, Y.L.; Bradford, M.A. In-plane strength of steel arches with a sinusoidal corrugated web under a full-span uniform vertical load: Experimental and numerical investigations. *Eng. Struct.* **2016**, *110*, 105–115. [CrossRef]
21. He, J.; Wang, S.; Liu, Y.; Dai, L.; Lyu, Z.; Li, C.; Xin, H.; Tan, C. The development of composite bridges with corrugated steel webs in China. *Proc. Inst. Civ. Eng. Bridge Eng.* **2021**, *174*, 28–44. [CrossRef]
22. Li, Y.; Zhang, W.; Zhou, Q.; Qi, X.; Widera, G.E. Buckling strength analysis of the web of a WCW H-beam: Part 2: Development and research on H-beams with Wholly Corrugated Webs (WCW). *J. Mater. Process. Technol.* **2000**, *101*, 115–118. [CrossRef]
23. Zirakian, T.; Lim, J.B.P.; Hajsadeghi, M.; Bahrebar, M. Structural performance of corrugated web steel coupling beams. *Proc. Inst. Civ. Eng. Struct. Build.* **2016**, *169*, 756–764. [CrossRef]
24. Pasternak, H.; Kubieniec, G. Plate girders with corrugated webs. *J. Civ. Eng.* **2010**, *16*, 166–171. [CrossRef]
25. Wang, S.; Liu, Y.; He, J.; Xin, H.; Yao, H. Experimental study on cyclic behavior of composite beam with corrugated steel web considering different shear-span ratio. *Eng. Struct.* **2019**, *180*, 669–684. [CrossRef]
26. Elgaaly, M.; Seshadri, A.; Hamilton, R.W. Bending strength of steel beams with corrugated webs. *J. Struct. Eng. ASCE* **1997**, *123*, 772–782. [CrossRef]
27. Sayed-Ahmed, E.Y. Plate girders with corrugated steel webs. *Eng. J.* **2005**, *42*, 1–13.
28. Kövesdi, B.; Jáger, B.; Dunai, L. Bending and shear interaction behavior of girders with trapezoidally corrugated webs. *J. Constr. Steel. Res.* **2016**, *121*, 383–397. [CrossRef]
29. Kövesdi, B.; Dunai, L.; Kuhlmann, U. Interacting stability behaviour of steel I-girders with corrugated webs. *Thin Wall. Struct.* **2012**, *61*, 132–144. [CrossRef]
30. Zhou, M.; Yang, D.; Zhang, J.; An, L. Stress analysis of linear elastic non-prismatic beams with corrugated steel webs. *Thin Wall. Struct.* **2017**, *119*, 653–661. [CrossRef]
31. Lopes, G.C.; Couto, C.; Real, P.V.; Lopes, N. Elastic critical moment of beams with sinusoidally corrugated webs. *J. Constr. Steel Res.* **2017**, *129*, 185–194. [CrossRef]
32. Elkawas, A.A.; Hassanein, M.F.; El Hadidy, A.M.; El-Boghdadi, M.H.; Elchalakani, M. Behaviour of corrugated web girders subjected to lateral-torsional buckling: Experimental tests and numerical modelling. *Structures* **2021**, *33*, 152–168. [CrossRef]
33. Hassanein, M.F.; Elkawas, A.A.; El Hadidy, A.M.; Elchalakani, M. Shear analysis and design of high-strength steel corrugated web girders for bridge design. *Eng. Struct.* **2017**, *146*, 18–33. [CrossRef]
34. Wang, P.Y.; Garlock, M.E.M.; Zoli, T.P.; Quiel, S.E. Low-frequency sinusoids for enhanced shear buckling performance of thin plates. *J. Constr. Steel Res.* **2021**, *177*, 106475. [CrossRef]
35. Sokołowski, D.; Kamiński, M. FEM Study of a Steel Corrugated Web Plate Girder Subjected to Fire. *Int. J. Appl. Mech. Eng.* **2021**, *26*, 201–218. [CrossRef]
36. Pimenta, R.J.; Queiroz, G.; Diniz, S.M.C. Reliability-based design recommendations for sinusoidal-web beams subjected to lateral-torsional buckling. *Eng. Struct.* **2015**, *84*, 195–206. [CrossRef]
37. Sokołowski, D.; Kamiński, M. Reliability analysis of the corrugated I-beam girder with ribs. *Eng. Comput. Mech.* **2015**, *168*, 49–58. [CrossRef]
38. Shon, S.; Yoo, M.; Kang, J.; Lee, S. Minimum Weight Design of Sinusoidal Corrugated Web Beam using Differential Evolution Algorithm. *Int. J. Steel Struct.* **2015**, *15*, 213–225. [CrossRef]
39. *PN-EN 1990:2004*; Basis of Structural Design. Polish Normalization Committee: Warsaw, Poland, 2004. (In Polish)

40. Papadrakakis, M.; Lagaros, N.D.; Plevris, V. Design optimization of steel structures considering uncertainties. *Eng. Struct.* **2005**, *27*, 1408–1418. [CrossRef]
41. Computer Algebra System MAPLE 2018 Documentation edn., 2019. Available online: https://fr.maplesoft.com/documentation_center/index.aspx (accessed on 17 February 2020).
42. Kamiński, M. *The Stochastic Perturbation Method for Computational Mechanics*; Wiley: Chichester, UK, 2013.
43. Melchers, R. *Structural Reliability Analysis and Prediction*; Wiley & Sons: Chichester, UK, 2002.
44. *Dassault Systèmes, version 2020x edn*; SIMULIA Abaqus Documentation, Dassault Systèmes Company: Velizy-Villacoublay, France, 2019.

materials

MDPI

Article

Cellular Automaton Mimicking Colliding Bodies for Topology Optimization

Bogdan Bochenek and Katarzyna Tajs-Zielińska *

Faculty of Mechanical Engineering, Cracow University of Technology, 31-155 Krakow, Poland
* Correspondence: katarzyna.tajs-zielinska@pk.edu.pl

Abstract: Needs and demands of contemporary engineering stimulate continuous and intensive development of design methods. Topology optimization is a modern approach which has been successfully implemented in a daily engineering design practice. Decades of progress resulted in numerous applications of topology optimization to many research and engineering fields. Since the design process starts already at the conceptual stage, innovative, efficient, and versatile topology algorithms play a crucial role. In the present study, the concept of the original heuristic topology generator is proposed. The main idea that stands behind this proposal is to take advantage of the colliding bodies phenomenon and to use the governing laws to derive original Cellular Automata rules which can efficiently perform the process of optimal topologies generation. The derived algorithm has been successfully combined with ANSYS, a commercial finite element software package, to illustrate its versatility and to make a step toward engineering applications. Based on the results of the tests performed, it can be concluded that the proposed concept of the automaton mimicking colliding bodies may be an alternative algorithm to other existing topology generators oriented toward engineering applications.

Keywords: topology optimization; cellular automaton; colliding bodies; heuristic update rules

Citation: Bochenek, B.; Tajs-Zielińska, K. Cellular Automaton Mimicking Colliding Bodies for Topology Optimization. *Materials* **2022**, *15*, 8057. https://doi.org/10.3390/ma15228057

Academic Editors: Michele Bacciocchi, Angelo Marcello Tarantino, Raimondo Luciano and Carmelo Majorana

Received: 12 October 2022
Accepted: 11 November 2022
Published: 15 November 2022

1. Introduction

As it has been observed over the years, topology optimization has been a dynamically developing research area with numerous applications to many research and engineering fields. The researchers community continuously works on innovative, efficient, and versatile topology optimization approaches, methods, and algorithms, whereas the spectrum of numerous solutions of topology optimization problems ranges from classic Michell structures to sophisticated contemporary engineering ones. The various approaches to the generation of optimal topologies have been presented along with emerging concepts which have been implemented in a broadly understood engineering area. The comprehensive discussion on various aspects of topology optimization has been provided by many survey papers: e.g., [1–4] recently complemented by Ribeiro et al. [5] and Logo and Ismail [6]. The long-lasting development of topology optimization confirms that it still remains one of the most important research fields within the area of structural and material design.

Along with the research issues of topology optimization, the practical aspects of engineering implementation of topology optimization techniques have become more and more important. As a result, the topology optimization tools are nowadays present in commercial engineering software. However, the black-box topology generators implemented into commercial software do not guarantee that the final results are the best available. Therefore, although remarkable achievements have been already made toward topology optimization application in engineering, there is still room for further investigations. Recently published papers [7–11] may serve here only as examples.

In the present study, the concept of the original heuristic topology generator is proposed. The main idea that stands behind this proposal is to take advantage of the colliding

bodies phenomenon, and use the governing laws to derive original Cellular Automata rules which can efficiently perform optimal topologies generation process. The inspiration for this proposal was the series of papers by Kaveh and co-workers [12–15] in which the concept of Colliding Bodies Optimization for a function minimization has been proposed. This paper proposes an original technique which is also inspired by the collision of bodies phenomenon but this time it is oriented toward optimization of structure topology. It is worth underlining that the rules are built so as to cope also with irregular finite element meshes. The derived algorithm has been combined with ANSYS 14.0, a commercial finite element software package, to illustrate its versatility.

As mentioned above, the applied approach is based on the concept of Cellular Automata (CA). Cellular Automata are built so as to mimic the behavior of complicated systems in a relatively easy way. From a computational point of view, the special local rules are implemented with a view to control the performance of a system under consideration. Hence, the local physical quantities are respectively updated, which allows us to describe the global behavior of the system. The concept of Cellular Automata has been known since the late 1940s when von Neumann and Ulam proposed this idea. Henceforth, this approach has been found interesting by researchers representing various fields but probably for the first time topology optimization has been discussed within the CA approach only in the paper by Inou et al. [16]. Many papers have been hereafter published on that subject, and the majority of them have appeared during the last two decades, see e.g., [17–20] or [21]. The efficient CA algorithm has been also proposed and then developed by Bochenek and Tajs-Zielińska [22,23] and recently [24,25].

The outline of the paper is as follows. In Section 2, the topology optimization problem is formulated, then the concept of Cellular Automata mimicking colliding bodies is introduced, and finally the algorithm built based on this idea is described. Its implementation in the topology generation process is illustrated by an introductory example. Original examples of topology generation of selected 2D structures are discussed in the first part of Section 3 presenting performance of the topology generator. Next in this section, utilizing results of the preliminary computations, the Cellular Automaton is combined with ANSYS as the efficient structural analysis tool and its application to selected, both plane and spatial, engineering tasks is presented. With a view to cover a broad area of implementations, the discussed tasks include also irregular cell lattice. Based on the results of performed tests, the paper ends with concluding remarks in Section 4.

2. Methods and Concepts

In this section, the topology optimization problem is formulated, the concept of Cellular Automata mimicking colliding bodies is introduced, and the algorithm built based on this idea is described. The introductory example illustrates the implementation of the proposed concept into the topology generation process.

2.1. Structural Topology Optimization

The most commonly formulated structural topology optimization problem is to generate material layout which within a design domain leads to a minimal value of the structure compliance c, Equation (1). Hence, one can follow the optimization problem formulated in a widely recognized paper by Sigmund [26]. The available material volume fraction κ is defined and treated in the optimization process as the constraint imposed on structure volume V, Equation (2). The finite element approach has been applied:

$$\text{minimize } c(\boldsymbol{d}) = \mathbf{u}^T \mathbf{k} \mathbf{u} = \sum_{i=1}^{N} d_i^p \mathbf{u}_i^T \mathbf{k}_i \mathbf{u}_i \tag{1}$$

$$\text{subject to } V(\mathbf{d}) = \kappa V_0 \tag{2}$$

$$\mathbf{k}\,\mathbf{u} = \mathbf{f} \tag{3}$$

$$0 < d_{min} \leq d_i \leq 1. \tag{4}$$

The quantity $\mathbf{u}_i$ denotes the displacement vector, $\mathbf{k}_i$ stands for the stiffness matrix, and both are defined for N elements. The design variable d_i, which represents the relative material density, is assigned to each element. In Equation (3), $\mathbf{k}$ represents the global stiffness matrix, $\mathbf{u}$ stands for the global displacement vector, and $\mathbf{f}$ is the vector of forces. Due to the simple bounds imposed in Equation (4) on the design variables with d_{min} (e.g., 10^{-9}) as a non-zero minimum value of relative density, singularity is avoided.

The SIMP (solid isotropic material with penalization) approach (e.g., [27]) in the form of power law is adapted as the material representation, see Equation (5). The modulus of elasticity E_i for each finite element is a function of the design variable d_i:

$$E_i = d_i^p E_0. \tag{5}$$

In Equation (5), the quantity E_0 stands for modulus of elasticity, defined for a solid material, whereas p (typically $p = 3$) is responsible for penalization of intermediate densities. This allows controlling the design process and leads to obtaining black-and-white resulting structures. During the topology generation process, a material is redistributed within the design domain, which results in removing parts unnecessary from design criteria viewpoint.

2.2. Concept of the Cellular Automaton Mimicking Colliding Bodies

The selection of a proper method of topology generation determines the effectiveness of the topology optimization process. Heuristic optimization techniques become popular among researchers because they are easy to implement numerically, gradient information is not required, and one can easily combine this type of algorithm with any finite element structural analysis code.

In this paper, the original heuristic topology generator built as Cellular Automaton which mimics Colliding Bodies (CAmCB) is proposed. The idea is that the design domain of the structure is decomposed into a lattice of cells which are usually equivalent to finite elements. For each cell, the surrounding cells form a neighborhood. The bodies are distributed within this lattice (Figure 1).

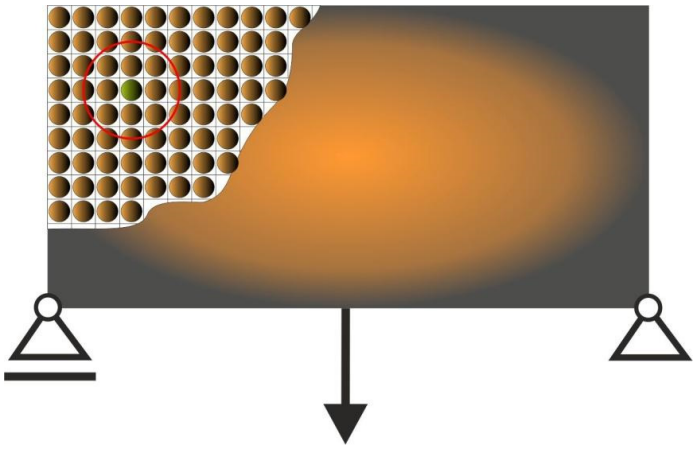

Figure 1. The cell lattice. A body is placed in each cell. The neighborhood, which is represented by the red circle, is identified around each body/cell.

Let us assume that the bodies have masses and velocities. Masses are proportional to cell areas whereas velocities are related to cell compliances. Furthermore, let us imagine that the neighboring bodies collide with the central one, which results in changing its status. In what follows, the central body can either be forced to remain in its position, or is pushed away (Figure 2).

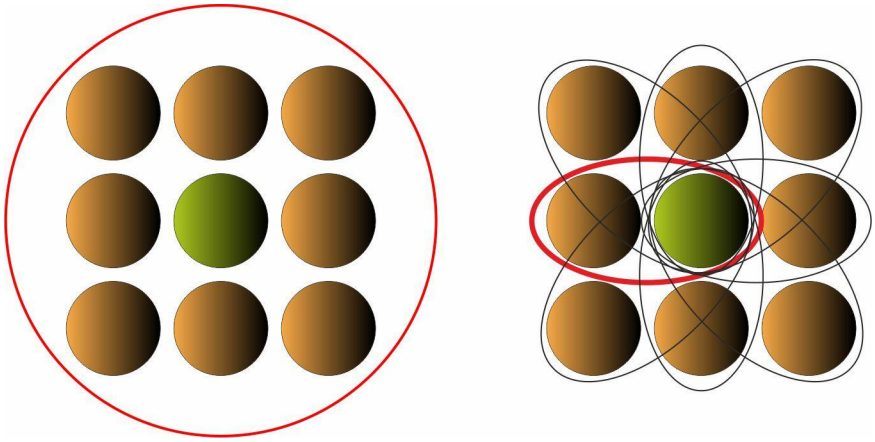

Figure 2. The cell neighborhood. The neighboring cells collide with the central one.

From a topology generation point of view, the interpretation is that the central cell remains solid, or is driven to become a void one (Figure 3).

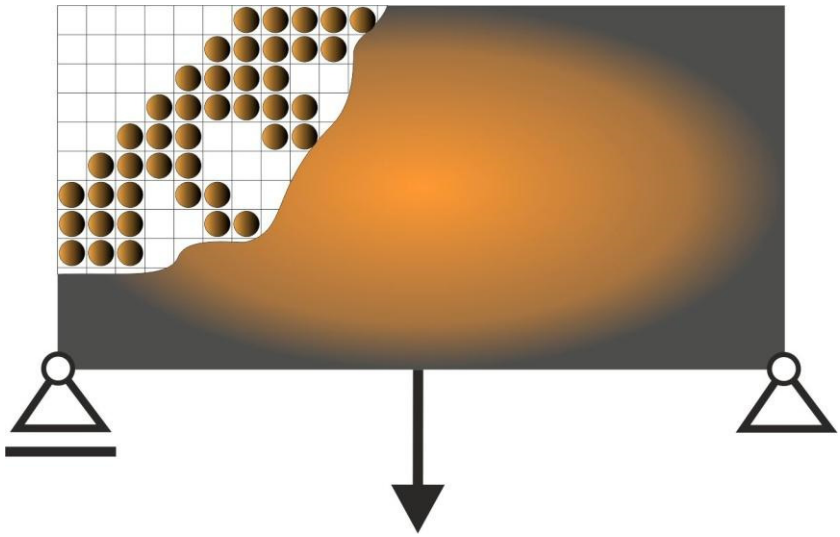

Figure 3. The topology generation. Some cells remain, some are eliminated.

2.3. Local Update Rules

While building Cellular Automaton, it is assumed that the interactions between bodies/cells take place only within the specified neighborhood, where they are governed by local rules which are identical for all cells, and are applied simultaneously to each of them. According to the concept of the paper, the local rules are derived so as to mimic collisions taking place between bodies/cells within each neighborhood. The governing equations based on the physics laws of momentum and energy are applied. Let us consider the central cell and a neighboring one colliding with it (Figures 4 and 5).

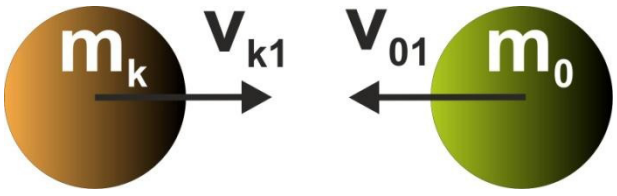

Figure 4. A neighboring body (k) collides with the central one (0). Before collision.

Figure 5. A neighboring body (k) collides with the central one (0). After collision.

The governing equations are as follows:

$$m_k v_{k1} - m_0 v_{01} = -m_k v_{k2} + m_0 v_{02} \tag{6}$$

$$\frac{1}{2} m_k v_{k1}^2 + \frac{1}{2} m_0 v_{01}^2 = \frac{1}{2} m_k v_{k2}^2 + \frac{1}{2} m_0 v_{02}^2. \tag{7}$$

Based on the above, the velocity of the central cell after collision equals:

$$v_{02} = \frac{(m_k - m_0) v_{01} + 2 m_k v_{k1}}{m_0 + m_k}. \tag{8}$$

As stated earlier, velocities are related to cell compliances and masses are proportional to cell areas. Equation (8) can be rewritten in the form of Equation (9):

$$F_{02} = \frac{(A_k - A_0) F_{01} + 2 A_k F_{k1}}{A_0 + A_k}, \tag{9}$$

where A represents the cell area and F is a function associated with local compliances. It is proposed to select the quantity F_{02} as the basis for building the update rule. Before that, the details regarding how to calculate F values are given.

Based on the results obtained from a structural analysis, the values of local compliances are calculated for all cells/elements. The compliances are sorted then in the ascending order, and those having the lowest and the highest values are identified. In the next step, N_1, N_2 are selected and values of F are assigned to cells $(i = 1, 2 \ldots n)$ according to Equation (10):

$$F_i = \begin{cases} -C & \text{if } i < N_1 \\ f_i & \text{if } N_1 \leq i \leq N_2 \\ C & \text{if } i > N_2 \end{cases}. \tag{10}$$

A monotonically increasing function representing cell compliances is selected for the intermediate interval $N_1 \leq i \leq N_2$ and then function values are assigned to the cells, respectively. Here, the linear function is selected to fulfill: $f_i(N_1) = -C$ and $f_i(N_2) = C$, thus:

$$f_i = 2C \frac{i}{N_2 - N_1} - C \frac{N_2 + N_1}{N_2 - N_1}. \tag{11}$$

The quantity C in Equation (11) is a user-specified parameter, usually equal to 1. The above described compliance mapping technique, represented by Equations (10) and (11), has been discussed also in [25].

Having finished with data preparation, the update rule can be built. Hence, repeating collisions for all neighboring cells, the average quantity F_{02} can be calculated based on Equation (12):

$$\overline{F}_{02} = \frac{1}{M} \sum_{k=1}^{M} F_{02(k)}. \tag{12}$$

Finally, the design variables can be updated according to Equation (13):

$$d_{new}^{(i)} = d^{(i)} + m \overline{F}_{02}, \tag{13}$$

where m denotes the move limit (e.g., $m = 0.2$).

2.4. Algorithm

In order to implement the above-proposed design rule, a numerical algorithm was built. The sequential approach was adapted for the optimization procedure, meaning that for each iteration, the structural analysis performed for the optimized element is followed by a local updating process. Simultaneously, for a specified volume fraction, a global volume constraint is applied. As a result, during the optimization process, the generated topologies preserve a specified volume fraction of a solid material.

The issue to discuss regards the form of Equation (9). In the case of a regular lattice of cells/elements, the first component of the numerator vanishes. In order to preserve the influence of the central cell compliance on the final result during the iteration process, it is proposed to modify the cells area representation:

$$A_i = A[1 + b(2r - 1)], \tag{14}$$

where

$$b = b_0\left(1 - \frac{t-1}{t_{max}-1}\right). \tag{15}$$

In Equations (14) and (15), b_0 is a small value, r is a random number taken from [0, 1] interval, t stands for the current iteration number, whereas t_{max} is a selected number of iterations. As a result, $A_i = A$ only for $t = t_{max}$.

In order to control the topology generation, the threshold values N_1 and N_2 can be modified so as to adjust the width of the interval [N_1, N_2] during the iteration process. It is proposed to start with a relatively wide interval, and then to reduce it successively. As a result, at the beginning of the topology generation process, the large design domain is searched by the Automaton, and the majority of void cells is eliminated. Then, during the iterative process while reducing the interval [N_1, N_2], the so-called gray cells of intermediate densities are eliminated, which finally results in obtaining distinct solid/void structures.

2.5. Introductory Example

The rectangular structure shown in Figure 6 has been chosen as the introductory example. The mesh of 3200 (80 × 40) square elements/cells has been generated to perform structural analysis and topology optimization for the data: $E_0 = 10$ GPa, $\nu = 0.3$, $P = 100$ N, $a = 40$ mm, $\kappa = 0.5$, $b_0 = 0.05$. As for the topology generation, the Moore type neighborhood, i.e., cells having common vertices with the central one, has been applied.

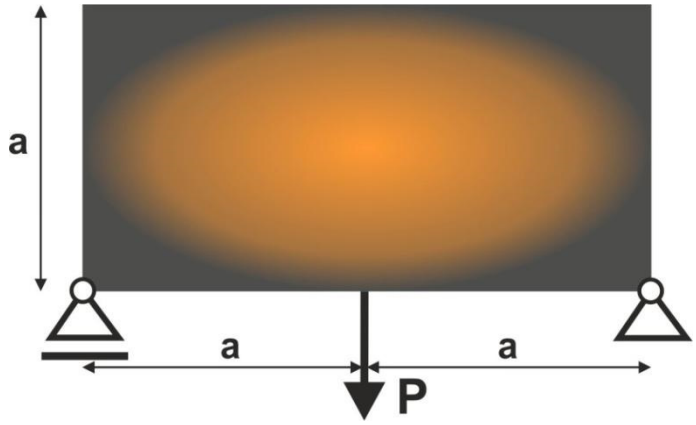

Figure 6. The rectangular structure with applied load and support.

The CAmCB algorithm found the final topology, which is shown in Figure 7, whereas the iteration history is given in Figure 8. The strategy of F_i, see Equation (10), implementation was as follows: one started with $N_1 = N{\cdot}0.02$, and then from iteration 25 $N_1 = N{\cdot}0.5$,

where N is the number of cells. Simultaneously, $N_2 = N \cdot 0.6$ has remained fixed for the entire iteration process.

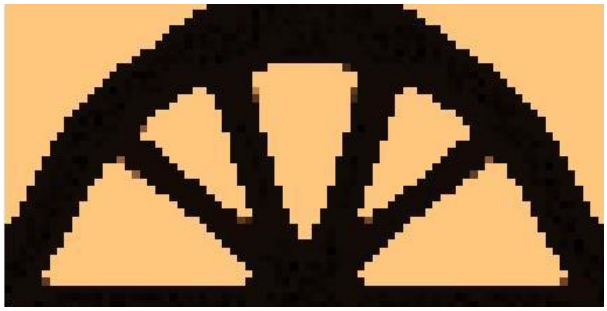

Figure 7. The final topology.

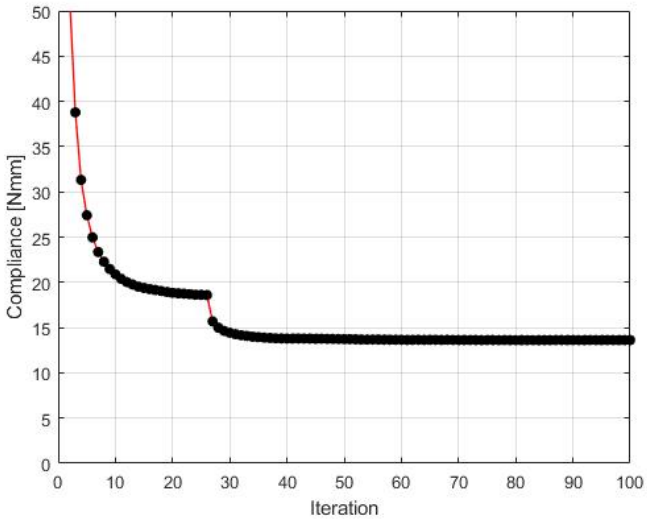

Figure 8. The compliance history. Minimal value: 13.62 Nmm. Black dots on the red line represent the compliance values for subsequent iterations.

The compliance value found for this structure is equal to 13.62 Nmm. This outperforms the solution reported in [25] where compliance of 14.02 Nmm has been obtained for the final topology.

3. Results and Discussion

The original examples of topology generation are discussed in this section, presenting the performance of the algorithm. With a view to cover a broad area of implementations, the discussed tasks regard plane and spatial structures. The case of irregular cell lattice is also considered.

In what follows, to illustrate more thoroughly how the proposed CAmCB algorithm works, some numerical examples have been selected. The algorithm performance is presented first for plane test structures, and then for plane and spatial engineering structures. For the test structures, a Matlab-based algorithm has been applied, whereas for engineering structures, the topology generator has been combined with the ANSYS system, which was responsible for performing the structural analysis.

3.1. Topology Generation for the Test Structures

The results of topology generation performed for four plane test structures are presented below.

3.1.1. Test Structure 1

To perform the first test, the structure shown in Figure 9 has been selected. The mesh of 60,000 (400 × 150) square elements/cells has been implemented, and structural analysis and topology optimization have been performed for the data: $E_0 = 10$ GPa, $\nu = 0.3$, $P = 100$ N, $a = 50$ mm, $\kappa = 0.25$, $b_0 = 0.05$. The Moore type neighborhood has been applied.

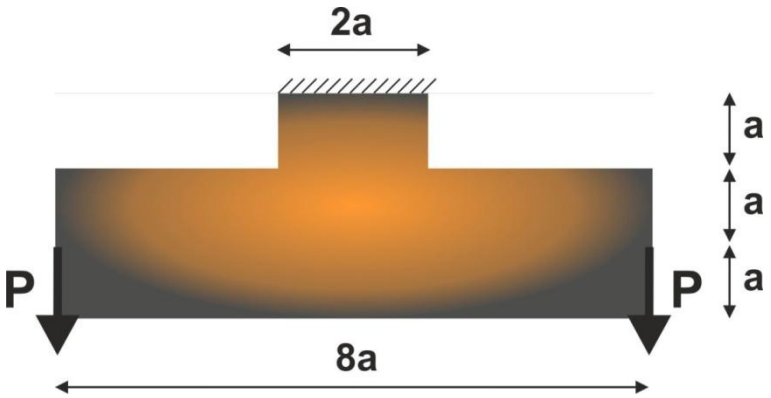

Figure 9. The test structure 1 with applied loads and support.

The algorithm found the final topology, which is shown in Figure 10, whereas the iteration history is given in Figure 11. The strategy of F_i implementation was as follows: one started with $N_1 = N \cdot 0.02$, and then from iteration 25 $N_1 = N \cdot 0.75$, and from iteration 75 $N_1 = N \cdot 0.9$. The quantity $N_2 = N \cdot 0.98$ has remained fixed for the whole iteration process.

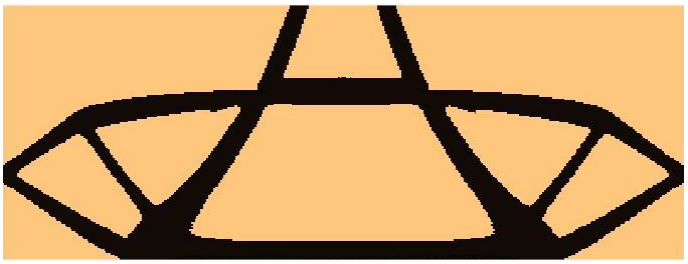

Figure 10. The final topology found for the test structure 1.

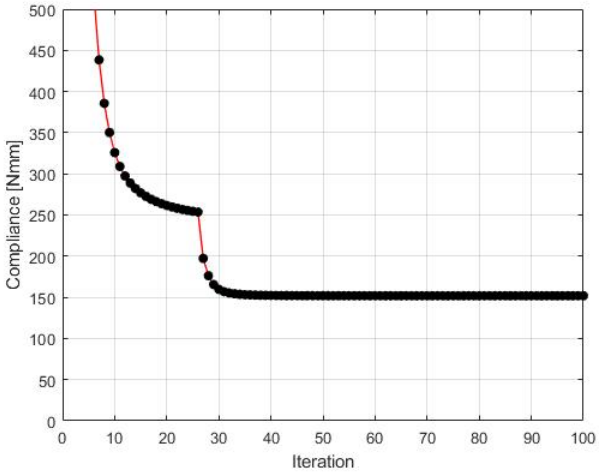

Figure 11. The compliance history for the test structure 1. Minimal value: 151.84 Nmm. Black dots on the red line represent the compliance values for subsequent iterations.

3.1.2. Test Structure 2

For the structure shown in Figure 12, the mesh of 80,000 (400×200) square elements/cells has been generated. The structural analysis and topology optimization have been performed for the data: $E_0 = 10$ GPa, $\nu = 0.3$, $P = 100$ N, $a = 100$ mm, $\kappa = 0.3$, $b_0 = 0.05$. The Moore type neighborhood has been applied.

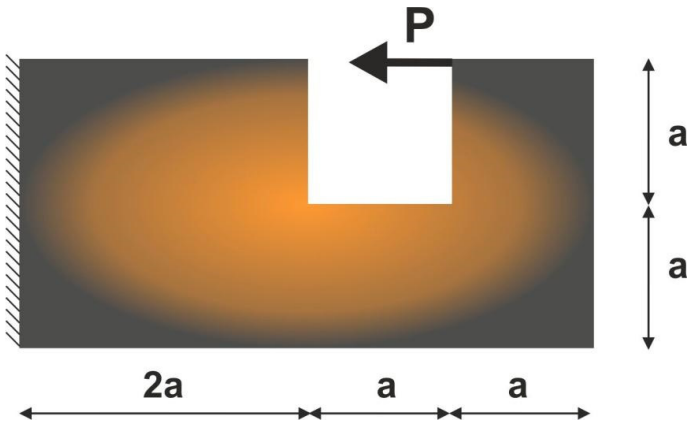

Figure 12. The test structure 2 with applied load and support.

The final structure topology found by the algorithm and the illustration of the compliance history are given in Figures 13 and 14, respectively. As for the strategy of implementation of F_i, one started with $N_1 = N \cdot 0.35$, and then from iteration 25 $N_1 = N \cdot 0.5$, from iteration 50 $N_1 = N \cdot 0.75$, and finally from iteration 75 $N_1 = N \cdot 0.9$. $N_2 = N \cdot 0.98$ has remained fixed for all iterations.

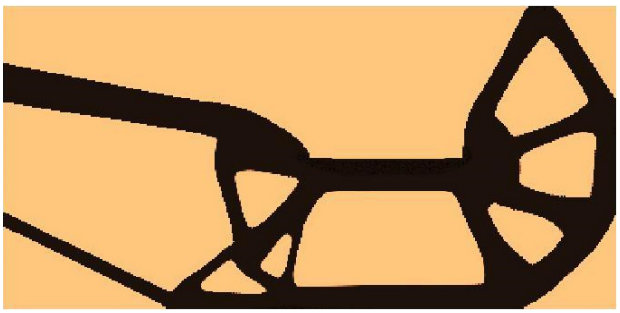

Figure 13. The final topology found for the test structure 2.

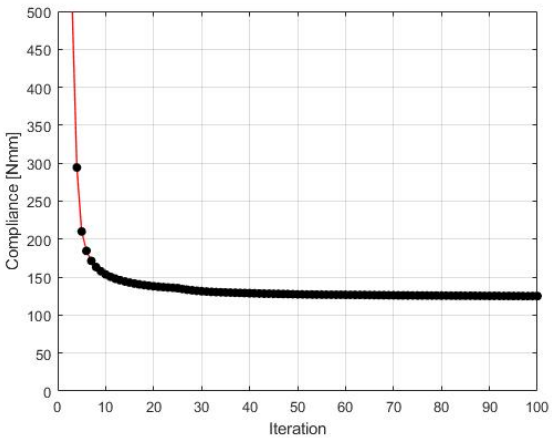

Figure 14. The compliance history for the test structure 2. Minimal value: 125.07 Nmm. Black dots on the red line represent the compliance values for subsequent iterations.

3.1.3. Test Structure 3

To perform the third test, the structure shown in Figure 15 has been proposed. The mesh of 80,000 (400 × 200) square elements/cells has been implemented and structural analysis and topology optimization have been performed for the data: $E_0 = 10$ GPa, $\nu = 0.3$, $P = 100$ N, $a = 10$ mm, $\kappa = 0.3$, $b_0 = 0.05$. The Moore type neighborhood has been applied.

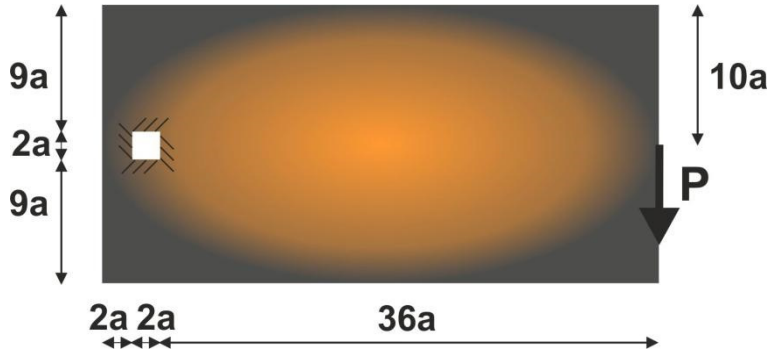

Figure 15. The test structure 3 with applied load and support.

The algorithm found the final topology, which is shown in Figure 16, whereas the iteration history is given in Figure 17. The strategy of F_i implementation was as follows: one started with $N_1 = N \cdot 0.02$, and then from iteration 25 $N_1 = N \cdot 0.75$, from iteration 50 $N_1 = N \cdot 0.75$, and finally from iteration 75 $N_1 = N \cdot 0.9$. The quantity $N_2 = N \cdot 0.98$ remained fixed for the whole iteration process.

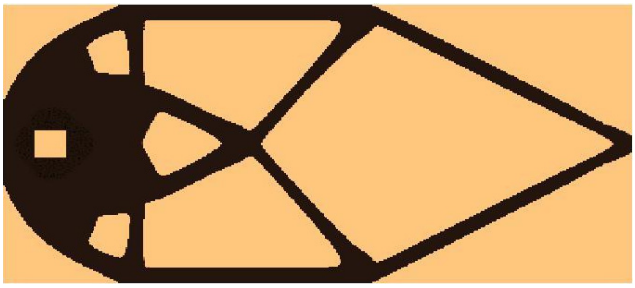

Figure 16. The final topology found for the test structure 3.

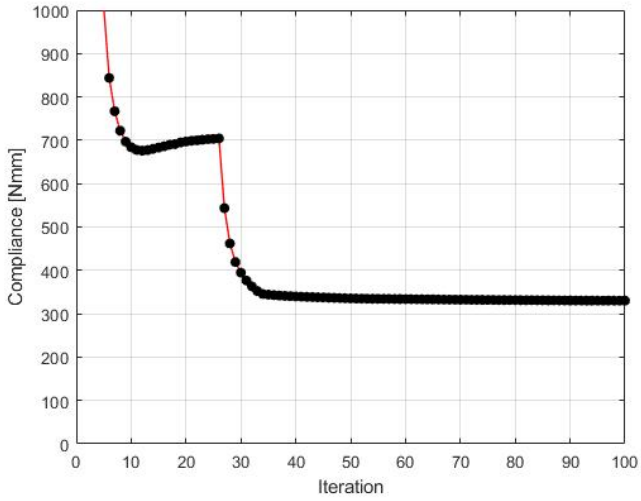

Figure 17. The compliance history for the test structure 3. Minimal value: 342.96 Nmm. Black dots on the red line represent the compliance values for subsequent iterations.

3.1.4. Test Structure 4

For the structure shown in Figure 18, the mesh of 137,500 (250 × 550) square elements/cells has been applied. The structural analysis and topology optimization have been performed for the data: $E_0 = 10$ GPa, $\nu = 0.3$, $P = 100$ N, $a = 50$ mm, $\kappa = 0.25$, $b_0 = 0.05$. The Moore type neighborhood has been applied.

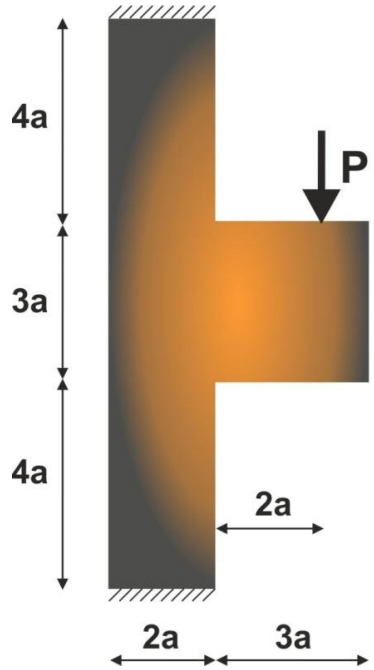

Figure 18. The test structure 4 with applied load and support.

The final structure topology found by the algorithm and the illustration of the compliance history are given in Figures 19 and 20, respectively. As for the strategy of F_i implementation: one started for $N_1 = N \cdot 0.02$, and then from iteration 25 $N_1 = N \cdot 0.5$, from iteration 50 $N_1 = N \cdot 0.75$, and finally from iteration 75 $N_1 = N \cdot 0.9$. $N_2 = N \cdot 0.98$ has remained fixed for all iterations.

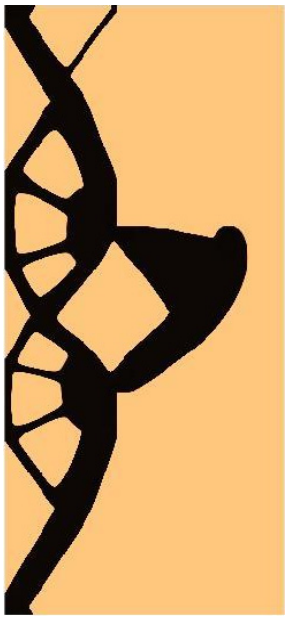

Figure 19. The final topology found for the test structure 4.

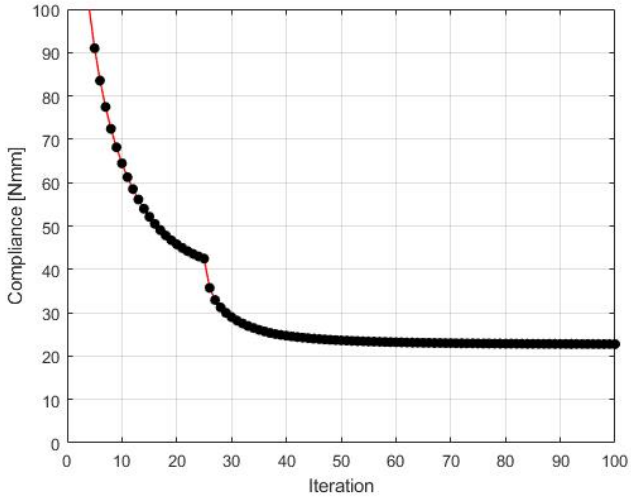

Figure 20. The compliance history for the test structure 4. Minimal value: 22.71 Nmm. Black dots on the red line represent the compliance values for subsequent iterations.

As can be seen from the above, the original CAmCB algorithm can effectively generate minimal compliance topologies. It is also worth comparing the obtained results with the ones which can be found for the considered structures when using other existing and popular approaches. The top88 algorithm [28] based on the optimality criterion and the PTOc one [29], utilizing the concept of proportional topology optimization have been selected for this purpose. The above papers provide Matlab codes of topology generators and these have been used to perform computations for the test structures defined earlier in this section. Table 1 gathers the results of these computations.

Table 1. Comparison of minimum compliance values [Nmm] found for the three algorithms.

Algorithm	Test Structure 1	Test Structure 2	Test Structure 3	Test Structure 4
CAmCB	151.84	125.07	342.96	22.71
top88 [28]	164.26	139.91	360.90	23.84
PTOc [29]	164.90	127.49	347.93	23.93

One can observe that the CAmCB algorithm proposed in this paper allows us to find results which can be better in terms of objective function values than the ones obtained with the use of other approaches selected for this comparison.

3.2. Engineering Applications

A series of illustrative engineering examples has been selected to examine the effectiveness of the introduced concept of the CAmCB topology generator. Both regular and irregular cell lattices are considered to show the algorithm performance and the versatility of the approach. As mentioned earlier, the proposed topology generator can be easily combined with any solver built on finite element methods. Hence, the optimization module has been linked to the professional system ANSYS to perform structural analyses. It is worth noting that the proposed algorithm does not require additional density filtering, the so-called gray elements are eliminated, and the checkerboard effect has not been observed for generated topologies.

3.2.1. Mechanical Part

The model of a control arm structure presented in Figure 21 has been chosen for this purpose. The mesh of 16,304 elements/cells has been generated to perform structural analysis and topology optimization for the data: $E_0 = 210$ GPa, $\nu = 0.28, \kappa = 0.4$, $b_0 = 0.01$. The structure consists of a non-optimized region presented in Figure 22 as a gray area whereas the design domain is presented as a red area. The structure is loaded

by two concentrated forces: a horizontal force equal to 7000 N and a vertical one equal to 2700 N. The horizontal displacement of nodes in the inner bound of the round hole A are equal to zero, while all nodes in area B are fixed.

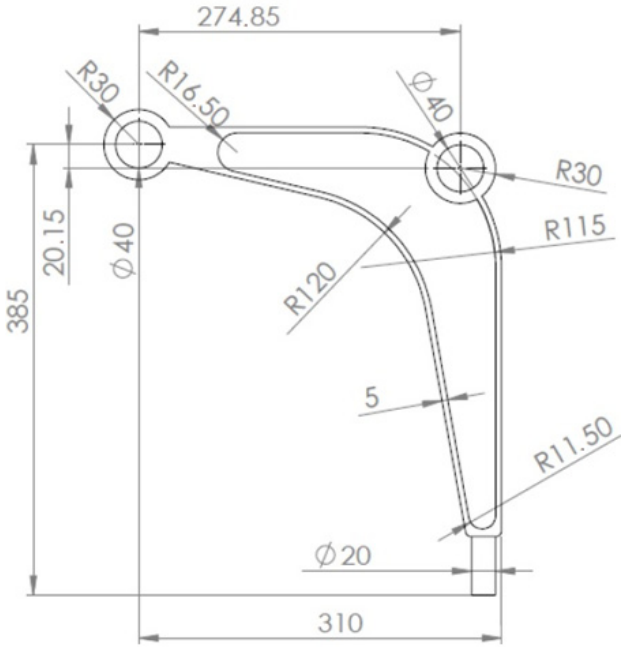

Figure 21. The control arm: dimensions in mm.

Figure 22. The design domain, loads, and supports of the control arm.

As for the strategy of F_i implementation: one starts with $N_1 = N \cdot 0.02$, and then from iteration 25 $N_1 = N \cdot 0.5$, and from iteration 50 $N_1 = N \cdot 0.75$, whereas $N_2 = N \cdot 0.98$ remains fixed for all iterations. This strategy has been applied for all presented engineering examples. It is worth pointing out that in order to complete the optimization process about 50 iterations are needed.

The algorithm found the final topology, which is shown in Figure 23. The resulting compliance equals 11,949 Nmm. Referring to the prior comparison of the results, the value of 12,372 Nmm was obtained when the algorithm [28] was utilized.

Figure 23. The final topology found for the control arm.

The CAmCB algorithm codes for the example considered in this section are provided in the Supplementary Files.

3.2.2. The Frame Structure-Generation of Topology for Irregular Cell Lattices

The aim of this example is to extend the presentation of the proposed algorithm toward an irregular grid of cells related to a non-regular mesh of finite elements. Resizing a traditional uniform grid of cells allows us to obtain flexible solutions, for e.g., extremely irregular design domains where it is difficult or impossible to cover them with uniform cells. Additionally, regions with stress concentrations, such as around holes or sharp edges, should be covered with a fine mesh, which is not necessary for the structure as a whole. The procedure of refining a mesh in selected regions can be used in order to achieve an accurate solution without an excessive increase of the number of elements caused by using a fine mesh implemented for the whole structure.

The example illustrating this case is the portal frame presented in Figure 24. The data is as follows: $E_0 = 200$ GPa, $\nu = 0.25$, $\kappa = 0.5$, $b_0 = 0.01$. The irregular lattice of cells is distributed according to Figure 25. For the irregular lattice of 14,024 cells (two-dimensional 6-node triangular elements—Plane82) ANSYS software was utilized for static analysis in the optimization process. The optimization has been performed and the obtained final topology is presented in Figure 26. Loads of 100 N each have been applied. The resulting compliance is equal to 5.03×10^{-3} Nmm.

The algorithm found the final topology, which is shown in Figure 26.

3.2.3. The Box Tube-Generation of Topology for Spatial Structure

The box tube shown in Figure 27 has been selected as the final example. The box tube cross section with 3 mm wall thickness is a square (100 mm $\times$ 100 mm), the tube is 250 mm long. Loads of 1000 N each have been applied as shown in Figure 28. The data is as follows: $E_0 = 200$ GPa, $\nu = 0.3$, $\kappa = 0.4$, $b_0 = 0.01$. A regular mesh of 11,088 three-dimensional 8-node elements (Solid45) has been applied for a static analysis made by ANSYS software (the length of the element edge is 3 mm). For the example of this section, the algorithm utilizes the von Neumann type of neighborhood. The resulting topology is presented in Figure 29, for which the final compliance equals 278.8 Nmm.

The algorithm found the final topology which is shown in Figure 29.

The algorithm performance was additionally tested based on the same example, repeating computations for low volume fraction $\kappa = 0.25$. The resulting topology for which the final compliance reaches the value equal to 586.3 Nmm is presented in Figure 30.

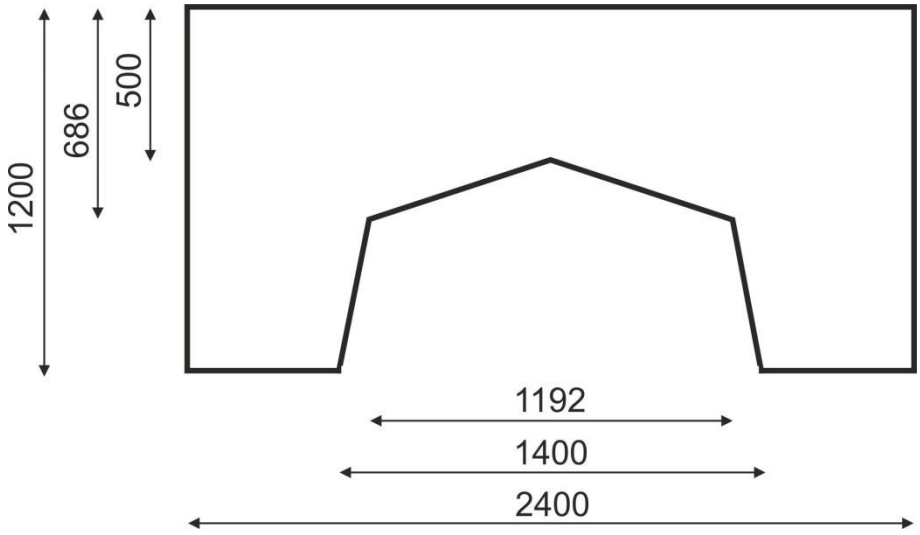

Figure 24. The portal frame: dimensions in mm.

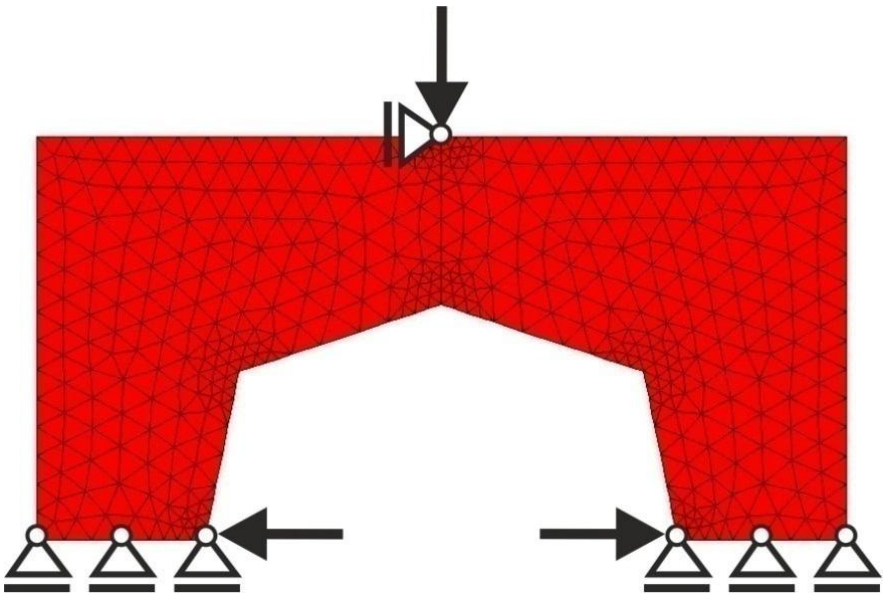

Figure 25. The design domain, loads, and supports of the portal frame.

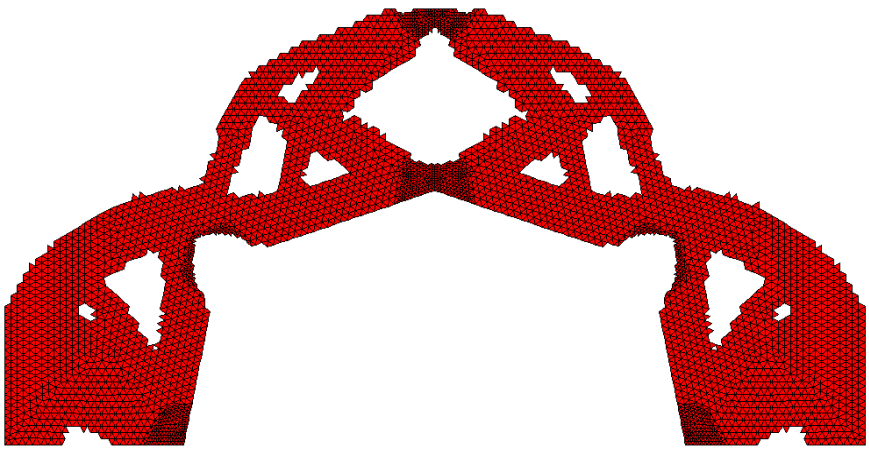

Figure 26. The final topology found for the portal frame.

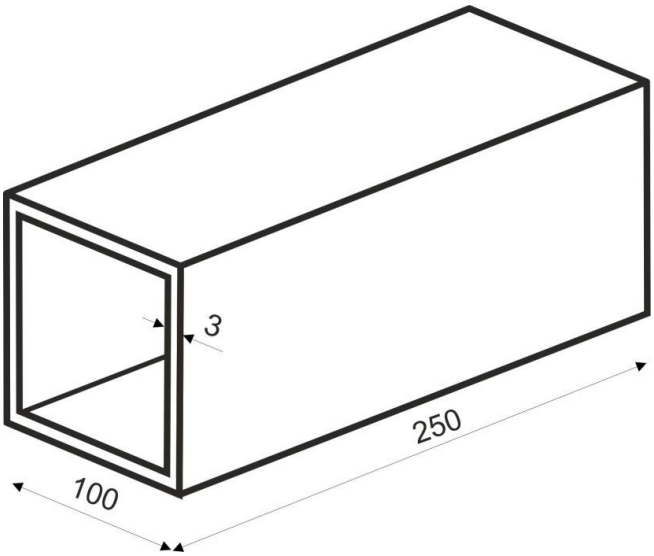

Figure 27. The box tube: dimensions in mm.

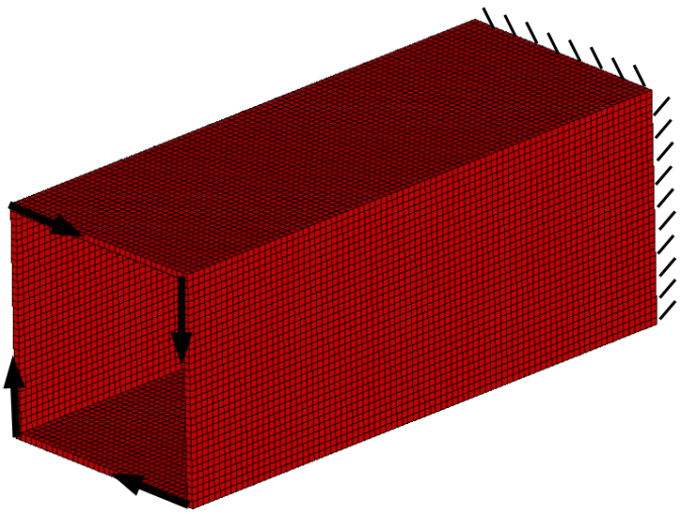

Figure 28. The design domain, loads, and supports of the box tube.

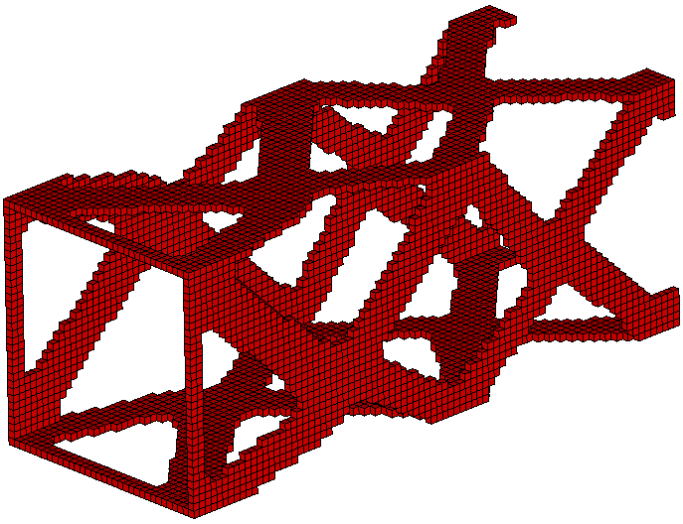

Figure 29. The final topology for the box tube for volume fraction $\kappa = 0.4$.

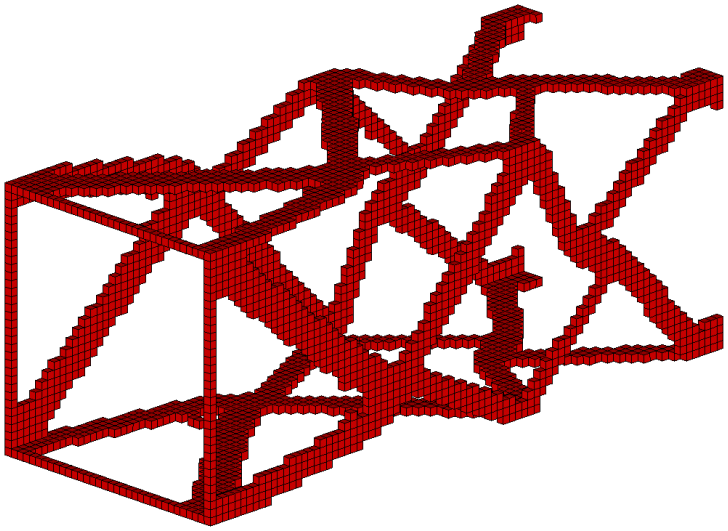

Figure 30. The final topology for the box tube for volume fraction $\kappa = 0.25$.

4. Concluding Remarks

The discussion regarding the proposed algorithm and its performance is summed up in this section. In the presented study, the original concept of Cellular Automaton mimicking Colliding Bodies (CAmCB) has been applied for topology optimization using the minimum compliance as the objective function. The CAmCB algorithm combines Cellular Automata heuristic with Colliding Bodies phenomenon to create a fast convergent technique which provides black-and-white topologies, without gray regions and the checkerboard effect. Moreover, additional density filtering is not necessary and there is no need to calculate gradients. In order to illustrate the effectiveness of the proposed CAmCB algorithm, selected numerical examples have been investigated. The algorithm performance is presented for plane test structures and for plane and spatial engineering structures. In the latter case, the proposed optimizer was combined with professional FEM analysis codes. The advantage of the developed algorithm is that it is a versatile technique which allows implementation of rectangular or triangular lattices, adaptation to highly non-uniform finite element lattices, as well as consideration of the total volume constraint with large and small volume fraction which is important especially for lightweight topology optimization. Preliminary studies reveal the possibility of applying CAmCB algorithm into uncommon but interesting issues such as the consideration of design-dependent loading (self-weight) or topology optimization of multi-material structures. The results of the tests performed so far are encouraging, which allows us to consider the proposed concept of the automaton mimicking colliding bodies phenomenon as an alternative algorithm to other existing topology generators suited for engineering applications.

Supplementary Materials: The following supporting information can be downloaded at: https://www.mdpi.com/article/10.3390/ma15228057/s1.

Author Contributions: As far as conceptualization, methodology, software, investigation, and writing the paper are concerned B.B. and K.T.-Z. contributed equally to this work. All authors have read and agreed to the published version of the manuscript.

Funding: The APC was funded by the Faculty of Mechanical Engineering Cracow University of Technology.

Data Availability Statement: The data presented in this study are available on request from the corresponding author.

Conflicts of Interest: The authors declare no conflict of interest.

References

1. Sigmund, O.; Maute, K. Topology optimization approaches. *Struct. Multidiscip. Optim.* **2013**, *48*, 1031–1055.
2. Deaton, J.D.; Grandhi, R.V. A survey of structural and multidisciplinary continuum topology optimization: Post 2000. *Struct. Multidiscip. Optim.* **2014**, *49*, 1–38. [CrossRef]
3. Liu, J.; Gaynor, A.T.; Chen, S.; Kang, Z.; Suresh, K.; Takezawa, A.; Li, L.; Kato, J.; Tang, J.; Wang, C.C.L.; et al. Current and future trends in topology optimization for additive manufacturing. *Struct. Multidiscip. Optim.* **2018**, *57*, 2457–2483.
4. Kentli, A. Topology optimization applications on engineering structures. In *Truss and Frames—Recent Advances and New Perspectives*; IntechOpen: London, UK, 2020. [CrossRef]
5. Ribeiro, T.P.; Bernardo, L.F.A.; Andrade, J.M.A. Topology optimisation in structural steel design for additive manufacturing. *Appl. Sci.* **2021**, *11*, 2112. [CrossRef]
6. Logo, J.; Ismail, H. Milestones in the 150-year history of topology optimization: A review. *Comput. Assist. Methods Eng. Sci.* **2020**, *27*, 97–132.
7. Azari Nejat, A.; Held, A.; Trekel, N.; Seifried, R. A modified level set method for topology optimization of sparsely-filled and slender structures. *Struct. Multidiscip. Optim.* **2022**, *65*, 85. [CrossRef]
8. Kazakis, G.; Lagaros, N.D. A simple Matlab code for material design optimization using reduced order models. *Materials* **2022**, *15*, 4972. [CrossRef]
9. Navez, T.; Schmidt, M.P.; Sigmund, O.; Pedersen, C.B.W. Topology optimization guided by a geometrical pattern library. *Struct. Multidiscip. Optim.* **2022**, *65*, 108. [CrossRef]
10. Fu, J.; Shu, Z.; Gao, L.; Zhou, X. A hybrid level set method for the topology optimization of functionally graded structures. *Materials* **2022**, *15*, 4483. [CrossRef]
11. Zhong, Y.; Yu, W.; Feng, H.; Wang, H.; Wang, R. Research on an effective bionic topology optimization method for engineering applications. *Eng. Opt.* **2022**. [CrossRef]
12. Kaveh, A.; Mahdavi, V.R. Colliding bodies optimization: A novel meta-heuristic method. *Comput. Struct.* **2014**, *139*, 18–27. [CrossRef]
13. Kaveh, A.; Ilchi Ghazaan, M. Enhanced colliding bodies optimization for design problems with continuous and discrete variables. *Adv. Eng. Softw.* **2014**, *77*, 66–75. [CrossRef]
14. Kaveh, A.; Ilchi Ghazaan, M. Computer codes for colliding bodies optimization and its enhanced version. *Int. J. Optim. Civ. Eng.* **2014**, *4*, 321–339.
15. Kaveh, A.; Mahdavi, V.R. *Colliding Bodies Optimization*; Springer: Cham, Switzerland, 2015.
16. Inou, N.; Shimotai, N.; Uesugi, T. A cellular automaton generating topological structures. In Proceedings of the 2nd European Conference on Smart Structures and Materials, Glasgow, Scotland, 12–14 October 1994; Volume 2361, pp. 47–50.
17. Tovar, A.; Patel, N.M.; Niebur, G.L.; Sen, M.; Renaud, J.E. Topology optimization using a hybrid cellular automaton method with local control rules. *J. Mech. Des.* **2006**, *128*, 1205–1216. [CrossRef]
18. Hassani, B.; Tavakkoli, M. A multi-objective structural optimization using optimality criteria and cellular automata. *Asian J. Civ. Eng.* **2007**, *8*, 77–88.
19. Penninger, C.L.; Tovar, A.; Watson, L.T.; Renaud, J.E. KKT conditions satisfied using adaptive neighboring in hybrid cellular automata for topology optimization. *Int. J. Pure Appl. Math.* **2011**, *66*, 245–262.
20. Afrousheh, M.; Marzbanrad, J.; Gohlich, D. Topology optimization of energy absorbers under crashworthiness using modified hybrid cellular automata (MHCA) algorithm. *Struct. Multidiscip. Optim.* **2019**, *60*, 1024–1034. [CrossRef]
21. Jia, J.; Da, D.; Loh, C.L.; Zhao, H.; Yin, S.; Xu, J. Multiscale topology optimization for nonuniform microstructures with hybrid cellular automata. *Struct. Multidiscip. Optim.* **2020**, *62*, 757–770. [CrossRef]
22. Bochenek, B.; Tajs-Zielińska, K. Minimal compliance topologies for maximal buckling load of columns. *Struct. Multidiscip. Optim.* **2015**, *51*, 1149–1157. [CrossRef]
23. Bochenek, B.; Tajs-Zielińska, K. GOTICA-generation of optimal topologies by irregular cellular automata. *Struct. Multidiscip. Optim.* **2017**, *55*, 1989–2001. [CrossRef]
24. Tajs-Zielińska, K.; Bochenek, B. Multi-domain and multi-material topology optimization in design and strengthening of innovative sustainable structures. *Sustainability* **2021**, *13*, 3435. [CrossRef]
25. Tajs-Zielińska, K.; Bochenek, B. Topology algorithm built as automaton with flexible rules. *Bull. Pol. Acad. Sci. Tech. Sci.* **2021**, *69*, e138813.
26. Sigmund, O. A 99 line topology optimization code written in MATLAB. *Struct. Multidiscip. Optim.* **2001**, *21*, 120–127. [CrossRef]
27. Bendsoe, M.P.; Sigmund, O. *Topology Optimization: Theory, Methods and Applications*; Springer: Berlin/Heidelberg, Germany, 2003.
28. Andreassen, E.; Clausen, A.; Schvenels, M.; Lazarov, B.S.; Sigmund, O. Efficient topology optimization in Matlab using 88 lines of code. *Struct. Multidiscip. Optim.* **2011**, *43*, 1–16. [CrossRef]
29. Biyikli, E.; To, A.C. Proportional topology optimization: A new non-sensitivity method for solving stress constrained and minimum compliance problems and its implementation in Matlab. *PLoS ONE* **2015**, *10*, e0145041. [CrossRef]

materials

MDPI

Article

Microscale Modeling of Frozen Particle Fluid Systems with a Bonded-Particle Model Method

Tsz Tung Chan [1,*], Stefan Heinrich [1], Jürgen Grabe [2] and Maksym Dosta [1]

[1] Institute of Solids Process Engineering and Particle Technology, Hamburg University of Technology (TUHH), 21073 Hamburg, Germany
[2] Institute of Geotechnical Engineering and Construction Management, Hamburg University of Technology (TUHH), 21073 Hamburg, Germany
* Correspondence: chan.tsz.tung@tuhh.de

Abstract: An inventive microscale simulation approach is applied to investigate the mechanics of frozen particle fluid systems (PFS). The simulation is based on the discrete element method (DEM) and bonded-particle model (BPM) approach. Discrete particles connected by solid bonds represent frozen agglomerates. Uniaxial compression experiments were performed to gather data for material modeling and further simulation model validation. Different typical mechanical behavior (brittle, ductile, dilatant) were reviewed regarding strain rates, saturation levels, and particle mechanical or surface properties. Among all these factors, strain rate significantly affects the mechanical behavior and properties of the agglomerates. A new solid bond model considering strain-dependent and time-dependent behavior is developed for describing the rheology of the frozen particle fluid systems. Without alternating Young's modulus and Poisson's ratio of the bond material, the developed solid model provides a suitable agreement with the experimental results regarding different strain rates.

Keywords: discrete element method; bonded-particle model; frozen particle fluid systems; material modeling; material micromechanics; creep

Citation: Chan, T.T.; Heinrich, S.; Grabe, J.; Dosta, M. Microscale Modeling of Frozen Particle Fluid Systems with a Bonded-Particle Model Method. *Materials* **2022**, *15*, 8505. https://doi.org/10.3390/ma15238505

Academic Editors: Michele Bacciocchi, Angelo Marcello Tarantino, Raimondo Luciano and Carmelo Majorana

Received: 13 October 2022
Accepted: 22 November 2022
Published: 29 November 2022

1. Introduction

Frozen particle fluid systems (PFS), such as frozen agglomerates or frozen soils (grounds), are classified as composite materials that have been vastly investigated in academic and industrial fields. Regarding natural science, frozen soils have been studied for centuries. Due to building projects being developed closer to the arctic region, artificial ground freezing (AGF) was introduced as a temporary stabilizing technique for mining and construction projects [1]. In the technical particle field, the exploration of the interplay of granular and liquid phases at freezing temperature, as well as the resulting micromechanical behavior of the final composite, plays an essential role in many processes, starting from the storing of humid materials at low temperatures in the silo, ending with cryogenic grinding of temperature-sensitive materials.

A considerable portion of frozen PFS is ice, which has been studied in the academic field for centuries. Mechanics of ice were well investigated throughout different scopes, such as the mechanical properties of polycrystalline ice and columnar-grained ice [2,3], viscoelastic properties [4], creep behavior [5], temperature effects on creep behavior [6], the influence of surface properties on bond interface performance [7], critical factor influence the formation of ice bond [8]. Recent research has attempted to develop an artificial neural network to establish a predictive database for ice mechanical behavior regarding ice type, temperature, and strain rate [9].

Nonetheless, simulation tools were applied to investigate the mechanical behavior of ice. For instance, the finite element model (FEM) was used for the high dynamic behavior of ice [10], the interaction between ship structure with broken ice by the elastic ice model [11],

or the discrete element method (DEM) used for interaction between a conical structure with sea ice in the arctic region [12].

Apart from the bond material alone, the composite of frozen PFS has been investigated for centuries due to different applications related to frozen soils. Available literature has investigated rheology on frozen soil and the application of AGF [13–15].

Similarly, numerous simulation works have been carried out on frozen soil and particle-reinforced composite failure progress with FEM and xFEM (extended finite element method) [15,16]. Resolving crack propagation with xFEM showed promising results. However, re-meshing was required after every consecutive step due to the changing geometry. FEM coupling with a thermo-hydro-mechanical model has been conducted to tackle the interaction between thermal, hydraulic, and mechanical loads [17]. Similar works using DEM to resolve the mechanical problems for frozen soils have been carried out [18,19], with creditable results revealed from the simulation.

The particle-based mesh-free discrete element method (DEM) is a numerical model for understanding particle dynamics introduced by Cundall and Strack [20]. The bonded-particle model (BPM) extends the soft-sphere formulation of DEM [21], in which solid bonds are created to connect primary particles and form the agglomerates. During the simulation, each bond is treated as a separate entity and can be removed or created to mimic fracture or even material sintering. Both BPM and DEM have been applied for tackling different mechanical problems, including damage progress of concrete or high-performance concrete [22,23], cemented sand [24], rock mechanics [25], or mechanics of biopolymer aerogel [26], and many other materials. The main advantages of BPM simulation are:

- Flexibility in agglomerate generation, in which all particles and bonds can have their unique material or geometrical properties;
- Capability in mimicking the breakage behavior of agglomerate, such as the crack initiation, propagation, failure plane, etc.;
- Diversity in functional model usage, with numerous choices of rheological models in the particle-particle, particle-wall relationship, and solid bond models.

The application of BPM demands high computational power due to the massive number of objects considered in the simulation and the small simulation time step. However, different parallelization techniques, especially focused on applying graphic process units (GPU), have efficiently compensated for such deficiencies [27].

In this contribution, a new solid bond model that combines strain-dependent linear elastic behavior with time-dependent creep behavior has been developed and integrated into the open-source DEM framework (MUSEN) [27]. The uniaxial compression experiment has proceeded for material parameter calibration and simulation model validation. Detail of the solid bond model and comparison between experimental and simulation results are discussed.

1.1. Ice Rheology

Ice rheology has been investigated for decades, with different literature analyzing the mechanical properties, viscoelastic properties, and creep behavior. Young's modulus of ice ranges between 9.7 and 11.2 GPa and Poisson's ratio from 0.29 to 0.32, obtained by the biaxial bending of ice plates at approximately -10 °C [28,29]. Ice tensile strength and compression strength react differently concerning temperature and strain rate. Ice's tensile strength ranges from 0.7 to 3.1 MPa, and compressive strength ranges from 5 to 25 MPa. The temperature-weakening effect on tensile strength is less than compressive strength [30].

Compared to temperature, strain rate has almost no effect on tensile strength but vastly alternates the compressive strength of ice. From 10^{-8} s^{-1} to 10^{-3} s^{-1}, the compressive strength increases with an increase in strain rate, surpassing 10^{-3} s^{-1} compressive strength decreases with an increase in strain rate [29].

Apart from mechanical properties, mechanical behavior is crucial to be identified. Ductile, dilatant, and brittle behavior can be identified in ice, mainly characterized by strain rate. In the case of high strain rates, brittle behavior prevails. Under tensile stress with a

high strain rate, the resistance to ice damage can be described by the nucleation and growth of cracks. The strength is limited by the grain size of the ice, which can vastly alternate the crack propagation. Under compressive strain, abrupt collapses occur at around 0.5% strain, in which the shear plane is located around 30° to the maximum principal stress plane [31].

Ductile behavior is mainly identified by strain-rate hardening and thermal softening, in which the activation energy almost doubled above −10 °C. The dislocation-based process dominates the primary behavior under low strain rate deformation. The deformation relationship is quantified by quasi-static creep [32], where the material experience permanent deformation under stress, which is well below the yield stress for a prolonged duration. Three different creep phases can be identified with decreasing, steady, and increasing strain rates [33]. The power law can be used to formulate a rheological model for the creep behavior of ice [5]. From this numerical relationship, the main dominance of ice under low strain rate loading depends on applied stress and temperature [31]. The power law for creep (Equation (1)) describes the creep strain rate $\dot{\varepsilon}_{n,cr}$, which depends on the applied stress σ and two model parameters A and m. These parameters should be adjusted to considered different material and temperatures:

$$\dot{\varepsilon}_{n,cr} = A \cdot \sigma^m \tag{1}$$

1.2. Rheology of Frozen Soil

Frozen soil shares remarkable similarities with ice in mechanical behavior, which is closely related to frozen PFS. Suitable insight into frozen PFS can be given by interpreting the characteristic of frozen soil. It has four typical mechanical behaviors: brittle failure, brittle behavior with failure just after the yield point, ductile behavior with strain hardening, and strain softening [34]. Literature regarding permafrost soil samples and artificially frozen soil has confirmed such behavior [35,36]. Apart from the strain rate, volumetric ice content plays a vital role in frozen soil's mechanical behavior. The ice content influences the frozen soil's ductility or brittleness [37]. Furthermore, the temperature, salinity, dynamic load, and refreezing slightly influence the mechanical strength and behavior of the frozen soil [38–42].

Regarding the unfrozen water in the frozen soil, various works of the literature showed a remarkable effect on the frozen soil's mechanical and creep behavior [43,44]. Due to the incompressible nature of water, unfrozen water in the frozen soil can transfer both negative and positive pressure. Still, water can be discharged with drainage, and the frozen soil's original form of stress state can be reestablished. However, due to its complexity, unfrozen water is not considered in both the experimental or simulation stages.

2. Materials and Methods

2.1. Uniaxial Compression Test

A universal texture measurement system, T.A. X.T. plus Texture Analyzer (Stable Micro System Ltd., Surrey, United Kingdom), was used to perform uniaxial compression tests. This setup was coupled with a self-constructed climate chamber, which aimed to maintain the ambient temperature of the inner cavity under the freezing point, thus preventing any thermal failure of specimens. It consisted of 3D-printed parts, coupled with radiators and radial fans, connected with a cryogenic unit (IKA Temperature Control, RC2 basic, lowest temperature: −20 °C). The chamber could maintain the ambient temperature at −10 °C, with less than 0.3 °C deviations. This experimental setup required a metal punch and base to protect the load cell and Texture Analyzer base, which were cooled down passively by the cool air in the climate chamber. Additionally, a 3D-printed fragment container is created to capture any fragment generated during the experiment, preventing the ice-particle pieces from being trapped in the radial fan. Three-dimensional CAD drawings of the climate chamber and coupled configuration are shown in Figure 1.

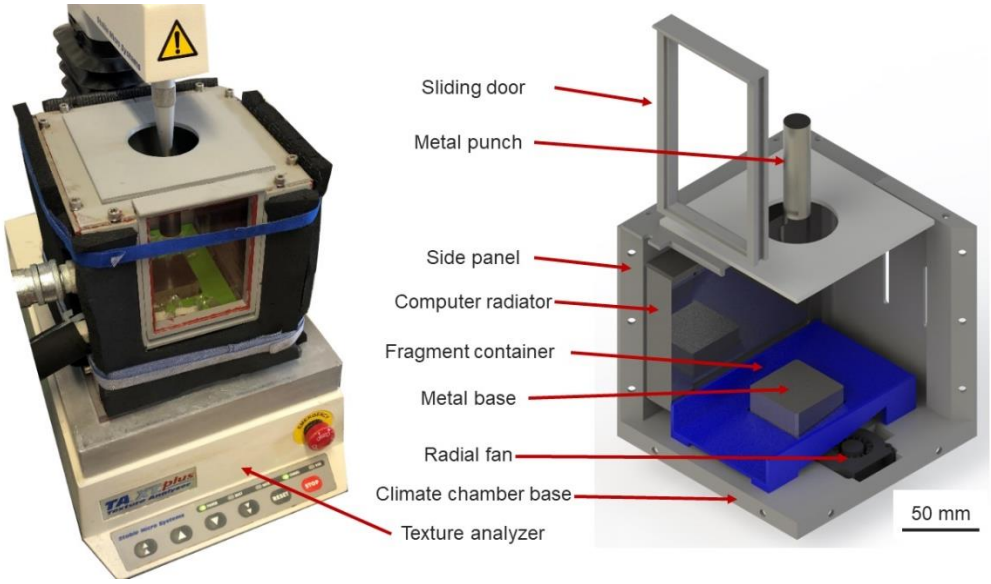

Figure 1. Texture Analyzer system equipped with a climate chamber: (**Left**) Climate chamber coupled with Texture Analyzer; (**Right**) CAD design.

2.2. Specimen Preparation

The experiments have been carried out for pure ice samples and afterward for the frozen PFS. Here, accurate specimen preparation has played a crucial role in the credibility of the experiment data since undesired defects influence the data's accuracy. For this purpose, special molds constructed with silicon have been used for the ice and PFS freezing process, as silicon is excellent for specimen extraction.

Nevertheless, different challenges have been faced during the preparation of samples. For example, freezing water in silicon mold was not acceptable. Defects, such as bulging, have been observed. Bulging was caused due to water expansion, as water decreases in density during the phase transition stage. The phase transition occurs from outside to inwards, forming a rigid shell of frozen water surrounding the inner unfrozen part. As the inner part expands during further freezing, such expansion breaks the outer shell in different directions. It creates different bulging or defects, leading to the sample's unpredictable geometry.

Hence, polycrystalline ice [6] was produced for the experiment based on the method proposed by [45], formed by the compression of snow in the initial stages. Firstly, crushed ice (1.12 mm–1.7 mm) formed after the freezing of distilled water was packed into the mold, and 0 °C distilled water was then injected from the bottom. Then, the specimen froze in the household refrigerator under −18 °C. The ice grain inside is randomly oriented to create a homogeneous structure. In addition, ice specimens produced by such a method were mainly formed from pre-frozen ice. The expansion rate of the specimen was kept under control, which allowed more delicate monitoring of stress and strain calculation.

Different particle types were considered for the frozen PFS specimen to cover the broadest range of interest. Samples of 10 ± 0.05 mm and 8 ± 0.05 mm in diameter were created, with a height-to-diameter ratio ranging around 1.6 ± 0.1. The 8 mm mold was designated to achieve higher stress, as the Texture Analyzer load cell can only withstand 500 N. The maximum compressive pressure achieved with the setup is 6.37 MPa (10 mm diameter) and 9.95 MPa (8 mm diameter), respectively.

An overview of primary particles utilized for sample preparations and their classification is provided in Table 1. Agglomerates are constructed by primary natural (obtained from nature without any shape or surface alternating processing) or technical (manufactured according to predefined geometry and surface properties) particles.

Table 1. Classification of primary particles used in experiments according to their properties.

	Stiffness		Shape		Surface Roughness		Particle Size (mm)
	Soft	**Hard**	**Spherical**	**Non-Spherical**	**Ra**	**Rz**	
Polyethene	X		X		12.808	50.723	1.8
Glass bead		X	X		1.767	11.462	1.65
Alpha-alumina		X	X		49.262	187.453	1.72
Quartz sand		X		X	13.416	49.623	0.5

The saturation level of investigated PFS was either 100% or 75%. The definition of saturation level is calculated according to the remaining volume, which is not occupied by particles. The number of particles in the specimen is the same across different saturation levels. The saturation level governed by what portion of the remaining volume was occupied by bond material is calculated as follows:

$$Saturation\ level = \frac{Volume_{bond}}{Volume_{specimen} - Volume_{particle}} \cdot 100\% \quad (2)$$

The samples with 100% saturation were prepared as follows. Firstly, primary particles were poured into the mold. Afterward, deionized water was injected from the mold's bottom and passed to the degassing chamber to avoid forming gas bubbles; hence no undesired defects existed in the agglomerates. For 75% saturation samples, a predefined amount of water was sprayed onto the particles, and then the particles were thoroughly mixed and filled into the mold.

Both types of PFS were then frozen overnight in a household refrigerator at −18 °C. PFS specimens were extracted from the silicon molds, and necessary adjustment with a utility knife blade was applied if the contact surface was not perpendicular to the sidewall. Two final samples with a diameter of 10 mm are shown in Figure 2.

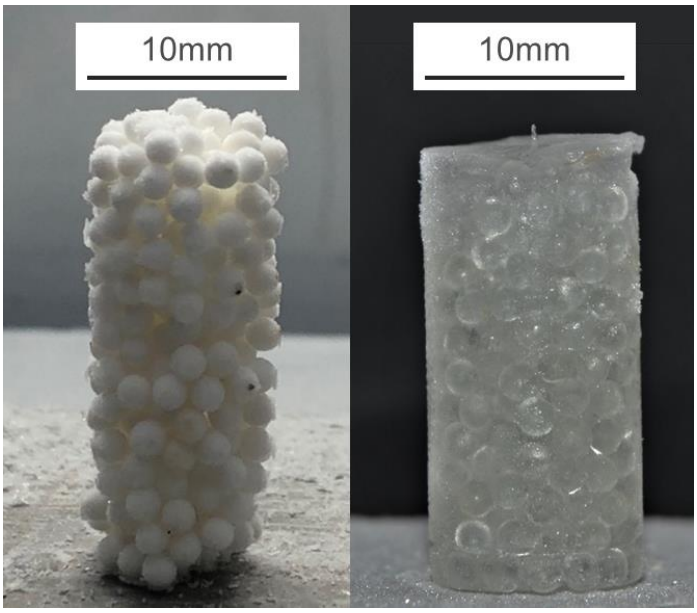

Figure 2. Two exemplary samples of frozen PFS: (**Left**) aggregate with alpha-alumina primary particles at 75% saturation level; (**Right**): glass bead PFS with 100% saturation.

2.3. Investigated Parameter Space

Since the strain rate has a decisive influence on the rheological behavior of ice and frozen soil [1,31], two different strain rates have been tested to review different PFS mechanical behavior. A total of 10^{-3} s^{-1} was applied for a low strain rate, and 10^{-2} s^{-1} was

used for a high strain rate. The strain rate is controlled by the compression speed, specified according to specimen height. The compression speed of 0.02 mm/s, which is two times larger than the minimal compression speed of the Texture Analyzer, was chosen as the low strain rate for all specimens. For high strain rate, compression speed is calculated by *specimen height* $\times$ 0.01. All experiments have been performed at a temperature of around -10 °C. The possibility of unfrozen water inside the agglomerate can be minimized with such a temperature.

2.4. Ice Creep Behavior

The polycrystalline ice specimen was loaded to a particular force, and the applied pressure was held for 240 s to review the creep behavior. Figure 3 shows the transition from the primary creep (decreasing in strain rate) to the secondary creep (steady in strain rate) in the experiment. However, an utterly constant strain rate was not yet achieved, which is crucial for calibrating the creep parameters for the simulation. In the literature, a steady strain rate was achieved after 100 min of force holding [32], which was impossible from the current experimental setup.

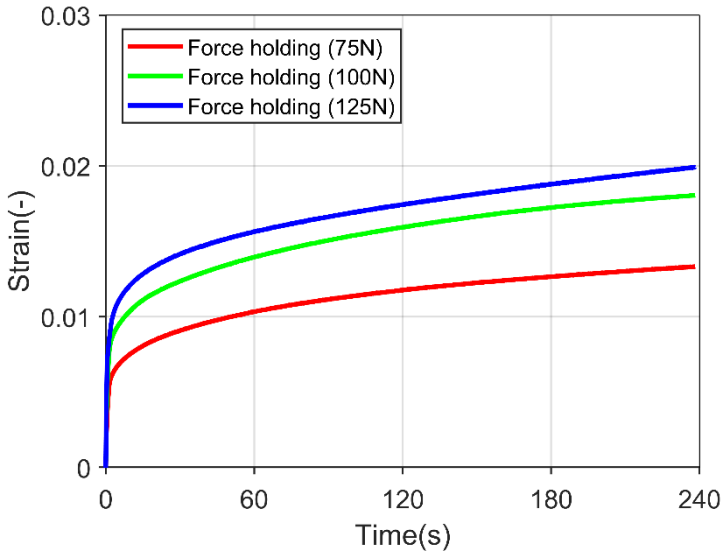

Figure 3. Polycrystalline ice specimen subjected to constant force load for 240 s under three different forces.

Compressive Young's modulus was estimated according to the primary loading part, in which a linear stress-strain relationship was observed. Several demonstration stress-strain curves are presented in Figure 4. Representative stress-strain curve of polycrystalline ice during creep experiment (primary loading phase) A linear relationship is fitted and the slope is obtained from the linear portion of the curve. The fitted curve is marked with a straight line on the figure. The compressive Young's modulus estimation does not consider the primary loading portion. As this portion usually has a lower stiffness. It is related to the surface of the ice column is not entirely in touch with the punch, and the punch was deforming the surface rather than compressing the complete column of ice. The compressive Young's modulus is 346.575 $\pm$ 48.2687 MPa.

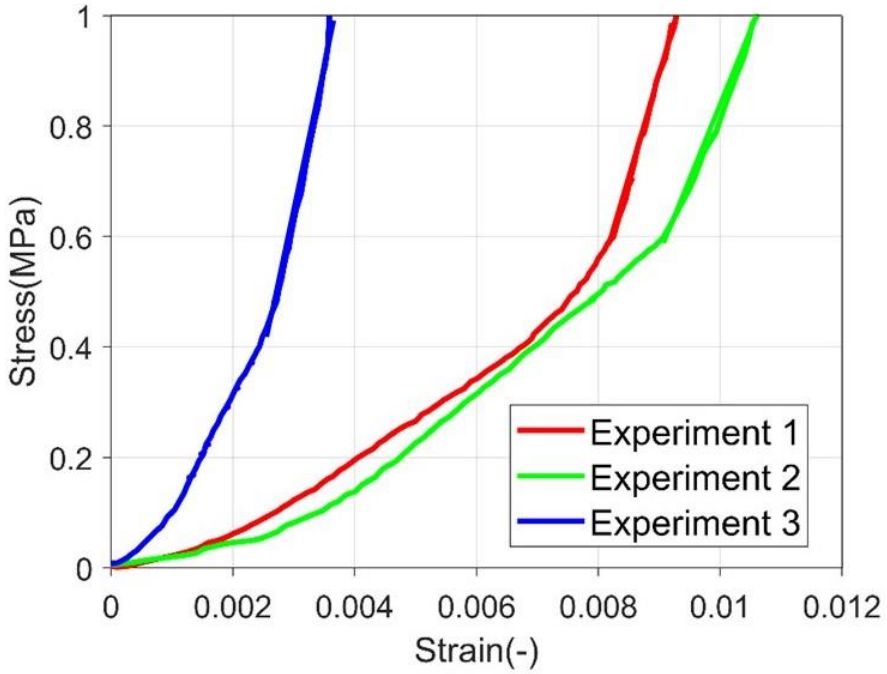

Figure 4. Representative stress-strain curve of polycrystalline ice during creep experiment (primary loading phase).

2.5. Fracture Patterns of Frozen PFS

Figure 5 shows the breakage pattern of the frozen PFS of different saturation levels during uniaxial compression under a high strain rate (10^{-2} s^{-1}). The fully saturated PFS samples can better transmit the pressure through the specimen. Thus, the cracks propagate from top to bottom, breaking the specimen into relatively large fragments containing numerous primary particles. In this case, the complete failure of the specimen occurred vigorously. In contrast, no large fragments were formed for PFS samples with 75% saturation. Only tiny pieces with several primary particles detached from the main structure during loading.

One additional phenomenon observed was the inhomogeneity of 75% saturation level PFS. The PFS is prepared by freezing particle water mixture. As the fridge temperature is kept at −18 °C, the water in the agglomerate cannot be frozen instantly. During the slow freezing process, part of the water around the particle performs a phase transition, and the remaining water is concentrated toward the lower portion of the agglomerate, forming an inhomogeneous specimen. Such a slow freezing process also imposes internal and bond structure differences concerning different primary particles. As the particle surface topography, particles' shape, separation distance, and liquid bridge size influence the successfulness of liquid bridge formation [46–48]. Thus, only the successfully formed liquid bridge forms a solid bond. This causes the differences in internal structure and bond structure to differ concerning different types of primary particles. However, it is impossible to gather the difference in the bond structure and internal structure in 75% saturation level PFS between different primary particles with the current experimental setup.

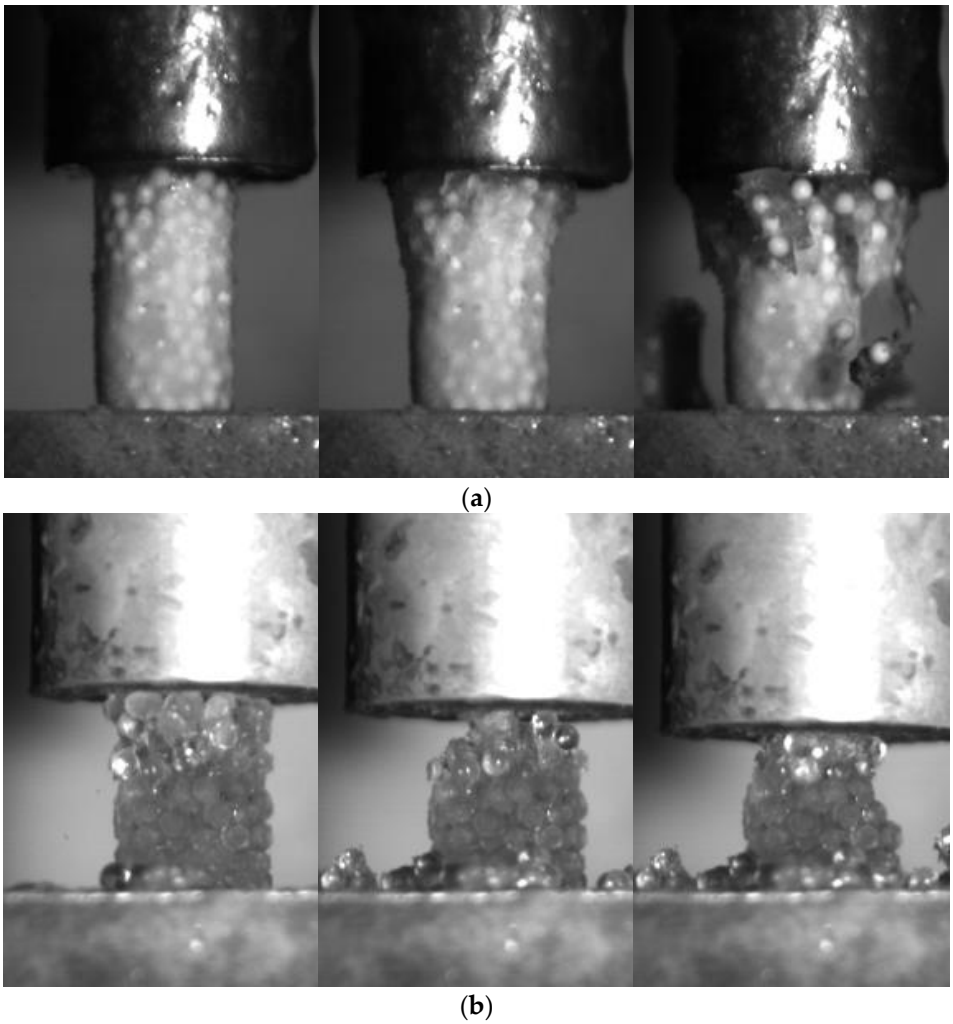

Figure 5. The fracture pattern for agglomerates at the strain rate is 10^{-2} s^{-1}: (**a**) 100% saturation, alpha-alumina PFS (Supplementary material: Video S1); (**b**) 75% saturation, glass PFS (Supplementary material: Video S2).

2.6. Mechanical Behavior of Frozen PFS

All possible mechanical behaviors can be observed in the experiments performed under different conditions, such as varied types of primary particles, strain rate, and saturation levels.

Figure 6 shows the stress-strain curve of some representative experiments for PFS with sand and alpha-alumina primary particles under high strain (HS) and low strain (LS) rates. The results show that the sand PFS under high strain rate loading reveals brittle failure. In the case of alpha-alumina and high strain rates, brittle behavior with failure is observed just after the yield point. Finally, ductile behavior with strain hardening is typical for sand PFS under low strain rate loading and strain softening for alpha-alumina PFS under low strain rates.

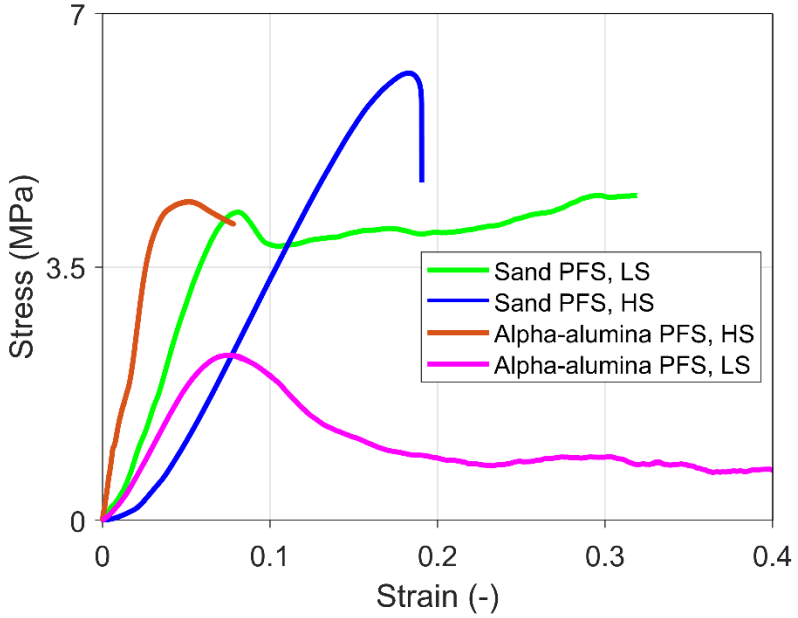

Figure 6. Representative stress-strain characteristics for different frozen PFS under a high strain (HS) rate of 10^{-2} s^{-1} and low strain (LS) rate of 10^{-3} s^{-1}.

2.7. Bonded-Particle Model Approach

Open-source GPU-accelerated DEM framework MUSEN was used to describe frozen PFS behavior. Among others, this system supports calculations with the bonded-particle model (BPM) [27]. In BPM, the spherical primary particles can be connected through solid bonds. Every single bond can have its unique dimensions and material properties. Bonds can be created or destroyed during simulation to mimic sintering or fracture behavior. The bond is modeled as a virtual cylindrical linkage between the particles. Bonds are treated as virtual objects with no volume or mass, and the internal force is calculated according to strain changes; in our case, time is also considered in the solid bond mathematical model.

Agglomerate is generated with two consecutive steps. The packing of primary particles is generated in a virtual volume according to the force-bias algorithm [26]. The virtual volume represents the geometry of the specimen. All particles are randomly generated in this pseudo space, which means no particles were generated outside the virtual volume. The number of particles is governed by the porosity preset in the particle generation progress. In each iteration, the overlaps between particles are detected, and force, which is proportional to the overlap, is calculated. Afterward, the primary particles are shifted according to this force. Generation completes if the maximum overlap is smaller than the target value. Finally, to build the agglomerate, particles are connected with solid bonds. The generation of bonds is governed by the minimum (L_{gen}^{min}) and maximum distance between the surface of spheres (L_{gen}^{max}). If the distance between the surfaces ranges between the preset value (L_{gen}^{min} and L_{gen}^{max}), bond is created. As mentioned, the bonds are treated as virtual objects; thus, overlapping between bonds is allowed. By alternating the limiting value L_{gen}^{max}, different amounts of bonds can be generated inside the same particle packing. In most cases, minimum distance (L_{gen}^{min}) is set to a negative value, as particle overlapping is allowed during package generation.

2.8. Solid Bond Model Considering Creep Behavior

The newly developed solid bond model aims to tackle the strain rate-dependent behavior of the bond material. Therefore, the component to consider the creep behavior has been included in the model. The particle-particle and particle-wall interactions are calculated according to the Hertz–Mindlin model, whereby the normal force is calculated

according to Hertzian theory [49], and the tangential force is calculated according to the model proposed by Mindlin et al. [50].

During simulation, the calculation of bond force is separated into the normal and tangential directions. The newly developed model coupled the strain-dependent elastic bond model with the time-dependent creep model. As schematically shown in Figure 6, the primary deformation stage of frozen PFS is in a linear elastic relationship [51]. The linear elastic strain-dependent relationship describes the primary loading phases of bonds. The total strain $\varepsilon_{n,to}$ in normal direction is calculated based on the initial L_I and current bond length L_c:

$$\varepsilon_{n,to} = \frac{L_c - L_I}{L_I} \tag{3}$$

Total strain in the normal direction can be decomposed into two parts:

$$\varepsilon_{n,to} = \varepsilon_{n,el} + \varepsilon_{n,cr} \tag{4}$$

where $\varepsilon_{n,el}$ is the elastic strain and $\varepsilon_{n,cr}$ is the irreversible deformation due to creep. The simulation automatically replaces plastic deformation with creep deformation [52]. Plastic deformation is regarded as an inelastic deformation, effectively the deformation due to creep under viscoelastic conditions. Normal bond stress σ_n is calculated by:

$$\sigma_n = \begin{cases} E \cdot \varepsilon_{n,el} & if\ \sigma_n < \sigma_{n,y} \\ \sigma_{n,y} & if\ \sigma_n \geq \sigma_{n,y} \end{cases} \tag{5}$$

where E is Young's modulus of the bond material and the $\sigma_{n,y}$ is the yield strength.

According to Norton [53], the power law describes the creep behavior of solid bonds (Equation (1)). The power law can provide approximately the same behavior concerning different applied stresses, which means the equation can provide an approximate same "shape" regardless of different applied stress [54]. Change of temperature during simulation is not considered for the model simplicity. The irreversible creep strain in the solid bonds is calculated iteratively in each time step as:

$$\varepsilon_{n,cr}(t + \Delta t) = \varepsilon_{n,cr}(t) + \Delta t \cdot A \cdot \left(\sigma_n(t)\right)^m \tag{6}$$

Δt denotes the simulation time step. The resulting bond force in the normal direction $F_{n,b}$ calculated by:

$$F_{n,b}\ (t + \Delta t) = E \cdot A_b \cdot (\varepsilon_{n,to} - \varepsilon_{n,cr}(t + \Delta t)) \tag{7}$$

where A_b is the bond's cross-cut area. With strain applied to the bond, normal stress response increased according to an approximately linear relationship. The calculation of bond normal stress during the loading part combines the linear strain-dependent relationship with the not linear time-dependent relationship. Bond normal stress increases until yield strength and holds. If strain remains unchanged after a specific time, force response decreases gradually, calculated according to the creep parameter and the previous time step's bond normal stress. A demonstration of the stress-time relationship for a single bond is shown in Figure 7.

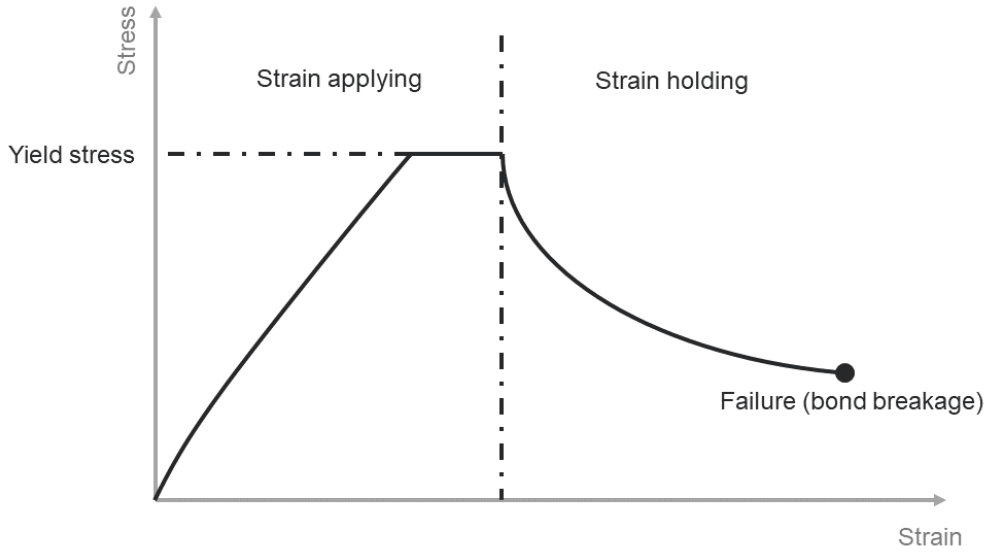

Figure 7. Schematic stress-strain diagram for solid bond under load in the normal direction.

Creep behavior is considered in both normal and tangential directions. The same power law of creep describes the creep behavior in the tangential direction. Unlike the calculation of strain in the normal direction, the bond deformation in the tangential direction $\vec{\delta}_t$ in every simulation step is updated according to the previous time step relative motion:

$$\vec{\delta}_t(t+\Delta t) = T\cdot\vec{\delta}_t(t) + \vec{v}_{t,rel}\cdot\Delta t \tag{8}$$

where T is the rotation matrix to consider the motion of connected particles between the current and previous time step [55], and $\vec{v}_{t,rel}$ is the relative velocity at the contact point in the tangential direction.

The tangential stress, which is crucial for the calculation of the tangential creep strain rate, is calculated according to the following:

$$\sigma_t = \frac{\left|\vec{\delta}_t\right|}{L_I}\cdot\frac{E}{2\cdot(1+v)} \tag{9}$$

where v is the Poisson's ratio of the bond material. The same power law with the same creep parameters A and m are used for the creep behavior in the tangential direction. Strain change due to creep in the tangential direction after every consecutive time step is calculated according to:

$$\vec{\varepsilon}_t(t+\Delta t) = \vec{\varepsilon}_t(t) + \varepsilon_{t,cr}(\Delta t)\cdot\vec{r}_t \tag{10}$$

where $\vec{r}_t$ is the unit vector of the bond in the tangential direction, which is defined by:

$$\vec{r}_t = \frac{\vec{\delta}_t(t)}{\left|\vec{\delta}_t(t)\right|} \tag{11}$$

The resulting tangential force can be calculated by:

$$\vec{F}_{t,b} = \frac{\vec{\delta}_t(t+\Delta t)}{L_I}\cdot\frac{E}{2\cdot(1+v)}\cdot A_b \tag{12}$$

Apart from the agglomerate mechanical behavior, the agglomerate fracture is considered in the model. This is accomplished by comparing the individual bond stresses under

loading with material properties such as normal σ_{max} and tangential strength τ_{max} as well as comparing the total strain and critical breakage strain $\varepsilon_{n,max}$ as:

$$\frac{\vec{F}_{n,b}}{A_b} + \frac{\vec{M}_{n,b} \cdot R_b}{I} \geq \sigma_{max} \tag{13}$$

$$\frac{\vec{F}_{t,b}}{A_b} + \frac{\vec{M}_{t,b} \cdot R_b}{J} \geq \tau_{max} \tag{14}$$

$$\varepsilon_{n,to} \geq \varepsilon_{n,max} \tag{15}$$

where R_b is the bond radius, $\vec{M}_{n,b}$ and $\vec{M}_{t,b}$ are the bending and torsional moments of the bond, respectively, I is the moment of inertia, and J is the polar (torsional) moment of inertia of the bond's cross-section.

Pressure melting and recreation of bonds are not considered in this solid bond model, as it vastly increases the complexity of the mathematical model, which has to consider the temperature, pressure, and factors governing the recreation of the bond.

The normal compressive strength alternated according to strain rate [29]. However, due to the nature of the model, implementing a relationship for calculating normal and tangential strength according to strain rate causes massive fluctuation in both values. The newly developed solid bond model has not considered the strain rate-dependent compressive strength relationship. Variance in bond normal strength due to strain rate or particle surface properties is compensated by alternating the bond normal and tangential strength concerning PFS constructed by different primary particles under different strain rates.

3. Result and Discussion

3.1. Experimental Result

The overview of Young's modulus and breakage stresses of frozen PFS under different saturation levels are presented in Figure 8. A reduction in the proportion of the bond material in the agglomerates vastly weakens the mechanical structure. This phenomenon can be observed from the value of the average Young's modulus and breakage stress, in which the reduction in saturation level decreases both values, incredibly massive in breakage stress. The reduction ratio in mechanical strength is significantly higher than the reduction ratio in the bond material volume fraction.

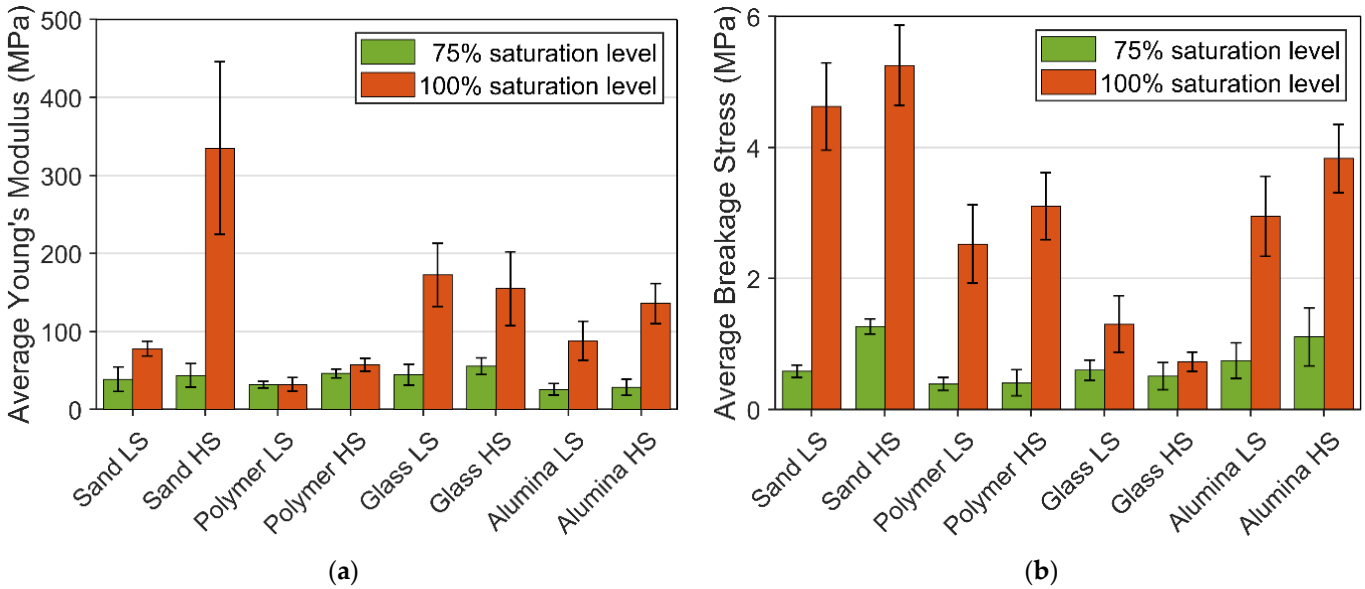

Figure 8. Average Young's modulus and breakage stress of different PFS: (**a**) Young's modulus; (**b**) Breakage stress.

For 100% saturation level PFS samples, Young's modulus increased with the increase in strain rate, except for the frozen PFS with glass particles. The strain rate of PFS with glass particles does not significantly influence Young's modulus. One of the possible reasons for that is the different creep behavior of ice in the contact zone between particle and bond. From Table 1, the glass bead has the lowest value in both Ra and Rz, which means the glass bead has the smoothest surface among all the primary particles. The smooth surface affects the contact zone behavior. This phenomenon can also be observed for the breakage stress of glass PFS with a 100% saturation level, where the aggregate reveals the lowest breakage strength under both strain rates. Overall, for all investigated materials, it can be observed that with an increased roughness, the strength increases, and the highest strength reveal aggregates containing non-spherical sand particles.

Young's modulus for sand PFS samples at different strain rates is also a vast difference. The surface properties of sand particles are similar to Polyethene particles. The much higher Young's modulus at a high strain rate is related to the primary particle's mechanical properties but is mainly associated with a lower porosity and, as a result, a more significant number of contacts for each particle. Consequently, a more compact and refined internal bond structure is formed inside such samples, which increases stiffness.

On the other hand, the lower value of Young's modulus at a low strain rate might be related to the pressure melting phenomenon, when the ice melts under pressure and then freezes again due to particle realignment. Due to the massive number of bonds in the sand PFS and the viscoelasticity of ice, this process can escalate, which causes a significant drop in Young's modulus at a low strain rate. However, the current experiment setup cannot prove such an assumption. The strain rate for saturation level 75% only slightly affects Young's modulus. However, for an unambiguous conclusion, it is necessary to conduct more experiments here, especially crucial data regarding the internal structure under pressure.

The average breakage stress of 100% and 75% saturation level PFS provided additional information about the mechanical behavior, presented in Figure 8. At 100% saturation level, an increase in strain rate leads to a higher fracture strength, except for the glass PFS, since the glass particle reveals a much smoother surface than other particles. The smooth surface leads to a weak interface between the bond material and the particle surface. At 75% saturation level, the high deviation within the experiment data does not allow for observing a clear trend except for the sand PFS, where it can be concluded that strain rate causes an increase in breakage stress. Apart from quantitative analysis of mechanical behavior, which is based on breakage stress, strain, and Young's modulus, the overall rheological behavior should be considered. Table 2 gives an insight into agglomerate behavior for different saturation levels, temperatures, strain rates, and particle properties.

Table 2. Mechanical behavior overview concerning saturation levels, temperatures, strain rates, and particle properties.

Saturation Level	Strain Rate	Smooth Particles (Polymer and Glass)	Rough Particles (Sand and Alpha-Alumina)
100%	Low	Mostly brittle with failure just after the yield point	Dilatant with slight strain softening or hardening
	High	Brittle failure	Brittle behavior with failure just after yield or brittle failure
75%	Low	Brittle failure	Dilatant with vast strain softening
	High	Brittle failure	Brittle failure

Particle surface properties and strain rate can influence mechanical behavior. Furthermore, the 75% saturation samples yielded more stepwise breakage under loading.

3.2. Simulation Setup

The agglomerates with 10 mm in diameter and 16 mm in height have been generated according to the section "Bonded-Particle Model Approach" procedure. The diameter of primary particles was tailored to the particles used in the experiment. Additionally, the driving velocity of the upper moving geometry (metal punch) was increased to 200 times (low strain rate: 4 mm/s, high strain rate: 32 mm/s) compared to the experiments to reduce the total computation time. The increase in moving geometry speed can lead to emerging of artificial elastic waves propagating through the material. The restitution coefficient for all particles and particle-wall interactions was reduced to 0.1 to prevent such a phenomenon. The restitution coefficient controls the amount of kinetic energy dissipated during simulation. In addition, the creep parameter has been adjusted accordingly.

For the spherical particles (polyethene, glass, alpha-alumina), spheres were used to represent the particles in the simulation. For non-spherical sand particles, the simulation has also used spheres to reproduce the particles due to contact detection occupying significant calculation power in DEM simulation. Computing the contact for spheres is less demanding, determined by the center distance being more or less than the distance of the combined radius. With non-spherical particles, not only is the distance considered, but also the relative rotation of particles needs to be taken into account. The simulation of non-spherical particles in DEM is tremendously more demanding than spherical particles [56].

The main model parameters and material properties of primary particles are listed in Table 3. The polymer particles, glass beads, and alpha-alumina Young's modulus were determined from self-performed experiments. Here the force-displacement characteristics obtained from uniaxial compression tests were used to adjust Young's modulus by fitting the Hertz model to experimental results [57]. Additionally, due to the non-spherical nature of sand particles, a uniaxial compression test for material modeling parameter calibration is impossible. In contrast, Young's modulus of sand particles was taken from the literature [58]. Both density and Poisson's ratio of different particles were taken from the literature [59–62].

Table 3. Main agglomerates properties used for simulation of different types of PFS with 100% saturation level.

Parameter	Polyethene/Glass/ Alpha-Alumina (Spherical)	Sand (Non-Spherical)
Particle diameter (mm)	1.8/1.7/1.65	0.5
Bond diameter (mm)	1.0	0.3
Particle density (kg/m^3)	960/2500/3960	2640
Particle Young's modulus (GPa)	0.8/72.3/150	72
Particle Poisson's ratio (-)	0.36/0.22/0.22	0.2
Maximal bond generation distance L_{gen}^{max} (mm)	0.7	0.2
Numbers of particles (-)	≈230	≈11,200
No. of bonds (-)	≈1100	≈66,000
Porosity (-)	0.44	0.42
Particle-wall sliding friction (-)	0.45/0.45/0.45	0.45
Particle-wall rolling friction (-)	0.05/0.05/0.05	0.5
Particle-particle sliding friction (-)	0.45/0.4/0.45	0.45
Particle-particle rolling friction (-)	0.05/0.05/0.05	0.5
Restitution coefficient (-)	0.1	0.1

The particle-particle, particle-wall sliding, and rolling friction were referenced from different literature, with further fine adjustment per trial-and-error procedure [62–64]. According to Gu et al. [65], the non-spherical PFS particle-particle and particle-wall sliding and rolling friction coefficients have been adjusted. In the DEM simulations, the shape of particles was neglected, and all investigated particles were modeled as spheres. Due to such a simplified representation, the value of rolling friction for non-spherical sand particles was much higher compared to spherical particles.

The material parameters for ice bonds have been adjusted according to experiments with 100% saturation. The simulation results are compared to averaged experiment stress-strain curve.

Young's modulus maintained the same for all different sets of experiments and was estimated at 350 MPa. The Poisson's ratio was taken from the literature as 0.31 [29]. Only the normal strength, tangential strength, and creep parameters A and m were tuned to individual experimental sets. The adjusted parameters for different sets of experiments are listed in Table 4. Particles investigated in this study have been selected due to their significant mechanical and surface properties differences. The creep parameters are adjusted by a trial-and-error procedure. It is related to two reasons. First, the creep parameter in the works of literature is calibrated concerning pure ice samples. The value cannot be applied to the simulation, as the contact zone influences the creep parameter concerning different primary particles. The second is the increased speed of moving geometry. Since the creep parameter is a time-dependent material parameter, any adjustment toward the simulation scene related to time influences the creep parameter setup.

Table 4. Material properties for ice bonds used for modeling different agglomerates at different loading rates.

	Primary Particles			
	Polyethene	**Glass**	**Alpha-Alumina**	**Natural Sand**
Normal and shear strengths				
- High strain rate (MPa)	3.5	4.2	20	20
- Low strain rate (MPa)	6	2.7	20	20
Creep parameter A (-)	0.1	0.1	0.3	0.1
Creep factor m (-)	0.1	0.1	0.16	0.1

Similar to the creep parameters, bond normal and tangential strength are tuned by the trial-and-error procedure. Consequently, the contact zone between ice bridges and particles was significantly varied. It is expected that the strength of the contact zone for smooth glass particles was much smaller than the similar strength for rough and highly porous alpha-alumina particles. Therefore, the bonds' normal and tangential strengths were varied to consider that effect. Primary sets of simulations were performed during the trial-and-error material parameter tuning procedure. Young's modulus and Poisson's ratio have kept unchanged throughout the process. Simulation results were transferred into the stress-strain curves, which were compared with the experimental result. The material parameters were then narrowed down to achieve accurate simulation results compared to the experiment result. Creep parameters concerning different primary particles are compared to validate the model capability. As shown in Table 4, only alpha-alumina PFS has a different creep parameter, which is correlated to its aggregated surface topography.

For modeling agglomerates with lower saturation degrees, the same material parameters for solid bonds were taken in Table 4. However, the bond generation parameters were alternated. New diameter and new maximal generation distance between particles L_{gen}^{max} were specified.

Compared to the 100% saturation degree, for the bond generation in the case of agglomerates with a low saturation degree of 75%, the maximal distance L_{gen}^{max} has been reduced to 0.01 mm. Such a value assumes that an ice bond is only formed when the particles are in contact or adjacent with a minimal distance. As mentioned, parameters constraining the successfulness of liquid bridge formation were related to the geometry, surface topography, separation distance, and size of the liquid bridge. As shown in Table 5, the total number of bonds for 75% saturation degree was almost halved compared to the 100% saturation level.

Table 5. Agglomerates bond generation set up for different types of PFS in 75% saturation level.

Parameter	Polyethylene/Glass/Alpha-Alumina (Spherical)	Sand (Non-Spherical)
Bond diameter (mm)	0.75	0.22
Maximal bond generation distance L_{gen}^{max} (mm)	0.01	0.01
Number of particles	≈230	≈11,200
Number of bonds	≈550	≈34,000

The cross-section area was also reduced to mimic the alternation in the internal bond structure. A quarter facilitates the bond diameter for agglomerates with spherical and non-spherical primary particles.

The assumption behind such a setup was the ice bridge formation deviation between particles in 100% and 75% saturation levels. At 100% saturation level, the cavity was occupied by water or particles, and both are incompressible substances. Solid bonds can completely enclose all primary particles inside the agglomerates. However, at a 75% saturation level, due to the volume reduction in bond substance, the individual geometry of the bonds between particles differs from the 100% saturation level agglomerate. The ice bridges are formed by the phase transition of the capillary liquid bridges. The starting geometry of ice bonds before phase transformation at 100% saturation level is entirely different from the 75% saturation level. Due to the difference in initial geometry, the deviation of the ice bond after phase transformation was accumulated. The ice bond of the 75% saturation is entirely different from the 100% saturation level. According to such an assumption, the reduction in bond diameter is applied to the simulation model.

In Figure 9, the agglomerates generated for different initial conditions are shown. The top part shows the agglomerates with spherical particles, and the lower part only shows the internal bond structure.

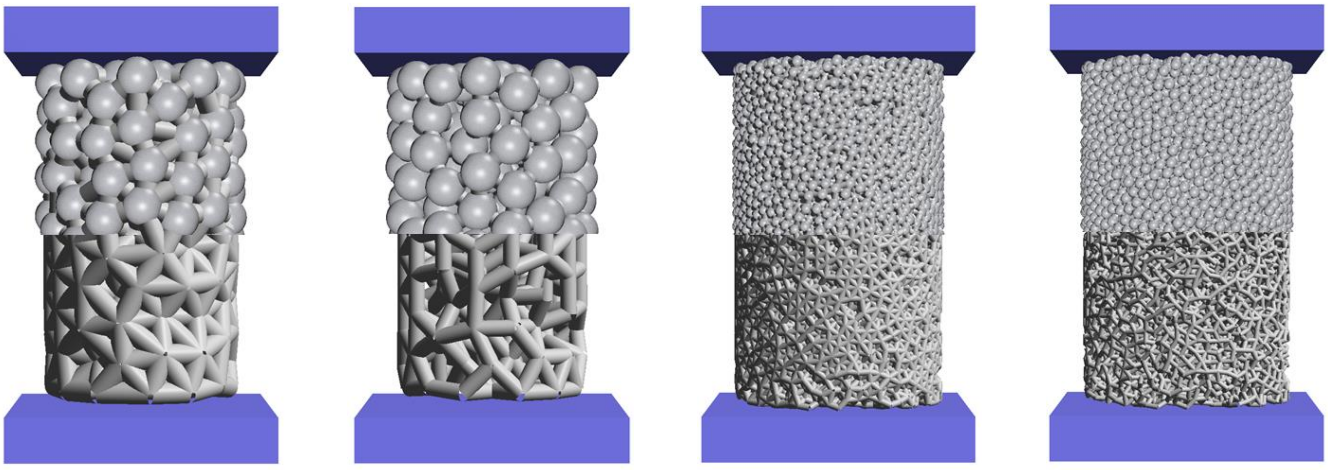

Frozen PFS with spherical particles at 100% saturation level

Frozen PFS with spherical particles at 75% saturation level

Frozen PFS with non-spherical particles at 100% saturation level

Frozen PFS with non-spherical particles at 75% saturation level

Figure 9. Representative agglomerate with diameter 10 mm, height 16 mm (**upper** part: agglomerates in complete form; **lower** part: agglomerates' internal structure).

3.3. Comparison of Simulation and Experimental Results

The simulation and experimental results for the uniaxial compression test for different agglomerates with varied strain rates are shown in Figure 10. It can be seen that simulation provides acceptable values in breakage stress, strain, and Young's modulus compared to experimental results. The proposed solid bond model can review different mechanical behavior regarding different strain rates.

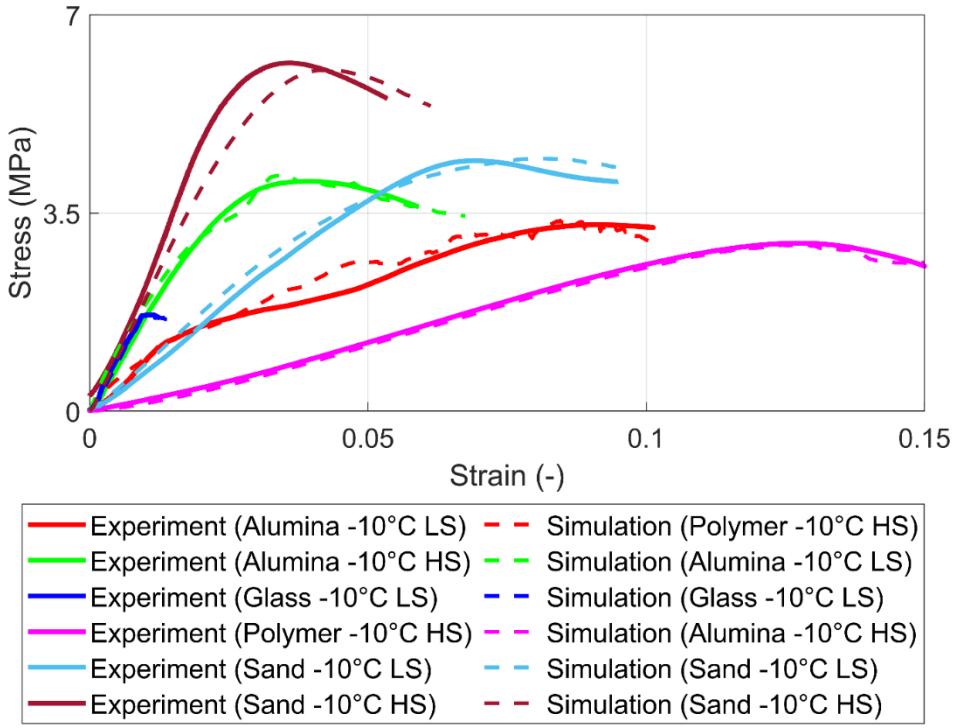

Figure 10. Experimental and simulation results for 100% saturation level for high strain (HS) rates (10^{-2} s^{-1}) and low strain (LS) rates (10^{-3} s^{-1}).

Without the variation of bonds' Young's modulus and Poisson's ratio, the proposed solid bond model can tackle the strain rate-dependent behavior with compensation of normal and tangential strength toward the particle surface properties. Last but not least, using alternated particle-particle and particle-wall friction coefficients to compensate for the shape deviation of simulation and experiment particles has proven feasible.

Apart from comparing the stress-strain data, the comparison between the experiment's average Young's modulus and breakage stress and simulation result is presented in Figure 11. All the simulation result lies within or very close to the average experiment value in both Young's modulus and breakage stress.

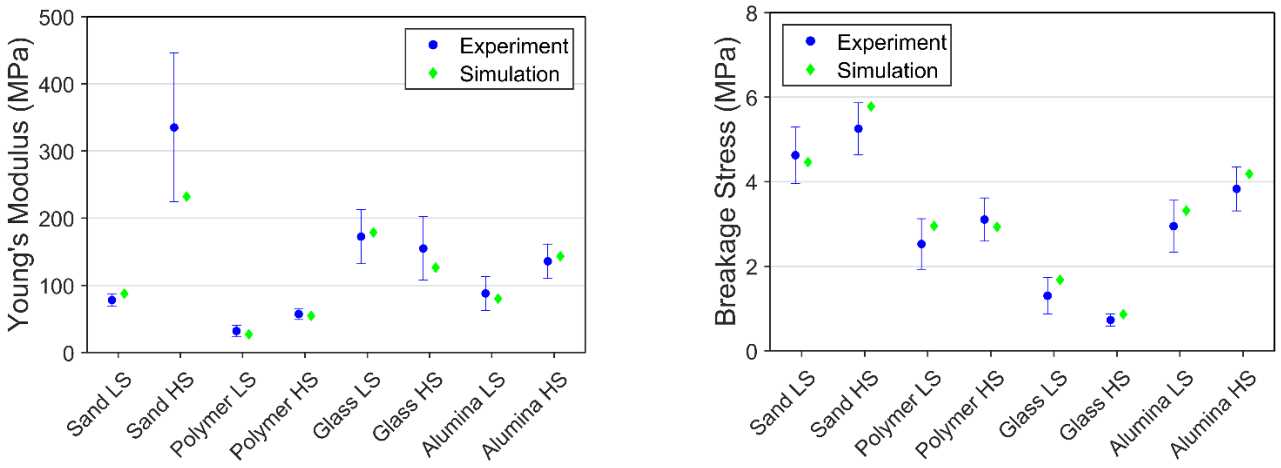

Figure 11. Comparison of experimental and simulation results for 100% saturation at −10 °C: (**a**) Young's modulus; (**b**) Breakage stress.

The deviation between every experimental data was enormous in lower saturation level PFS. The experimental data and data obtained by simulation were compared by comparing the values of breakage stress and Young's modulus.

The comparison of breakage stress and Young's modulus of agglomerates with lower saturation degrees is shown in Figure 12. Simulations were not aimed at achieving the exact value, as the material parameter of particles and bonds for different conditions were not alternated. Only the internal bond structure is adjusted to compensate for the deviation of saturation level. Breakage stress obtained from the simulation yielded acceptable agreement with the experiment, as most of the simulation result lies within or close to the standard deviation range, except for the alpha-alumina PFS. The internal structure of the lower saturation level is generated according to arbitrary values, leading to a big difference compared to the realistic structure. The simulation and experiment comparison shows that the weakening effect of reducing saturation level differs remarkably toward alpha-alumina particles.

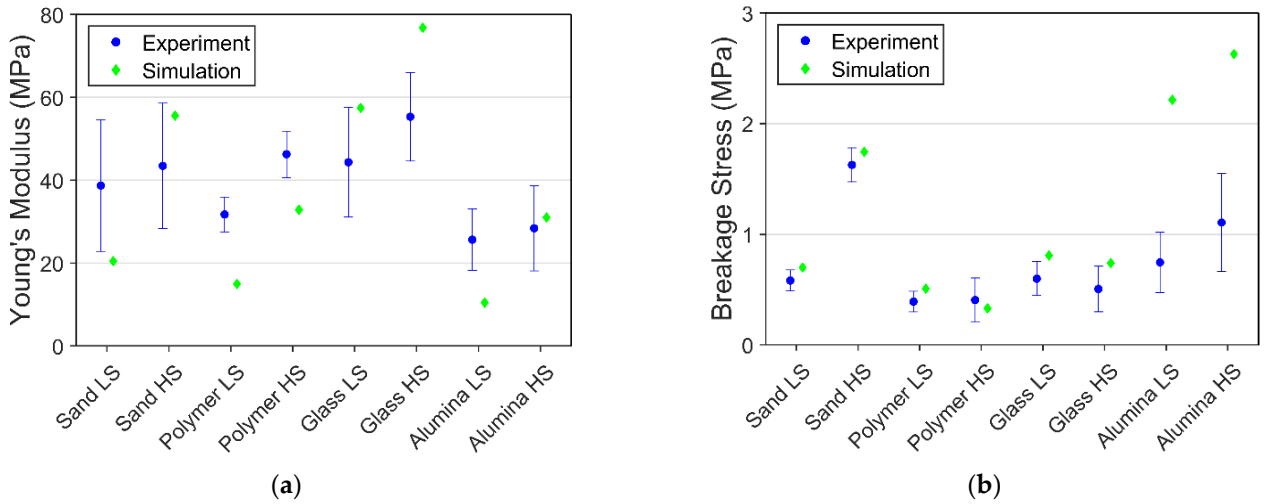

Figure 12. Comparison of experimental and simulation results for 75% saturation at −10 °C: (**a**) Young's modulus; (**b**) Breakage stress.

Young's modulus from simulation reveals more significant deviations to experimental data than breakage stress. The main reason is the lack of detailed information on the contact zone between the bond and the particle. Such information is particularly essential for the particle-bond interface creep behavior, thus alternating the elastic behavior of the agglomerate.

Contrary to the assumptions made in the model, the internal structures of glass bead PFS and alpha-alumina PFS might not be the same. The capillary properties of glass and alpha-alumina are different, leading to the formation of varying bond networks. Furthermore, another critical role may play in the particle size and shape variability for the sand PFS. Thus, using the same settings for the bond generation applied for spherical and non-spherical PFS imposes out-of-range discrepancies in simulation and experimental results for non-spherical PFS.

4. Conclusions

Both experiment and simulation studies for frozen PFS were performed in this contribution. The experiments presented results that are in suitable agreement with previous literature. Primary particles with different surface and mechanical properties were constructed to validate the influence on the agglomerate mechanical properties and behavior. The saturation level was alternated during the experiment phase, which reviews a vast weakening effect on the agglomerate.

The bonded-particle model, an extension of DEM, has been used to tackle the problem. A new solid bond model considering creep behavior has been developed and implemented into the MUSEN simulation framework. The developed model can simulate strain rate-dependent material, formulating the different mechanical responses under different strain rates. Nonetheless, particle composite material experiencing creep behavior or damage can also be simulated.

Throughout all different simulations, the bond Young's modulus and Poisson's ratio have kept the same, with creep parameters, normal and tangential strength tuned according to primary particles and strain rate. The simulation model has proven to be capable of considering the strain rate-dependent behavior of the frozen PFS. In the lower saturation levels of frozen PFS, the bond's material parameters were kept the same, and only the internal structure of the agglomerate in the simulation was changed. That shows a more considerable deviation in Young's modulus but acceptable values in breakage stress. Lack of data regarding the internal structure leads to a higher variation of simulation results under a lower saturation level in PFS experiments.

Supplementary Materials: The following supporting information can be downloaded at: https://www.mdpi.com/article/10.3390/ma15238505/s1, Video S1: 100% saturation, alpha-alumina PFS; Video S2: 75% saturation, glass PFS.

Author Contributions: Conceptualization, T.T.C. and M.D.; methodology, T.T.C. and M.D.; software, T.T.C. and M.D.; validation, T.T.C., S.H. and M.D.; investigation, T.T.C. and M.D.; data curation, T.T.C.; writing—original draft preparation, T.T.C. and M.D.; writing—review and editing, T.T.C., J.G., S.H. and M.D.; visualization, T.T.C.; supervision, S.H. and M.D.; project administration, S.H. and J.G.; funding acquisition, J.G. All authors have read and agreed to the published version of the manuscript.

Funding: The authors acknowledge the funding of this research by the German Research Foundation (Deutsche Forschungsgemeinschaft, DFG) in the framework of Research Training Group GRK2462: Processes in natural and technical Particle Fluid Systems (PintPFS) [DFG PintPFS, 2019] at Hamburg University of Technology (TUHH). Publishing fees funded by the Deutsche Forschungsgemeinschaft (DFG, German Research Foundation)—Projektnummer 491268466 and the Hamburg University of Technology (TUHH) in the funding programme *Open Access Publishing*.

Institutional Review Board Statement: Not applicable.

Informed Consent Statement: Not applicable.

Data Availability Statement: Data available on request.

Conflicts of Interest: Maksym Dosta has contributed to this work during his employment at TUHH. Other authors declare no conflict of interest.

References

1. Arenson, L.U.; Springman, S.M.; Sego, D.C. The Rheology of Frozen Soils. *Appl. Rheol.* **2007**, *17*, 12147–1. [CrossRef]
2. Goodman, D.J.; Frost, H.J.; Ashby, M.F. The plasticity of polycrystalline ice. *Philos. Mag. A* **1981**, *43*, 665–695. [CrossRef]
3. Gold, L.W. The process of failure of columnar-grained ice. *Philos. Mag.* **1972**, *26*, 311–328. [CrossRef]
4. Jellinek, H.H.G.; Brill, R. Viscoelastic Properties of Ice. *J. Appl. Phys.* **1956**, *27*, 1198–1209. [CrossRef]
5. Glen, J.W. The creep of polycrystalline ice. *Proc. R. Soc. Lond. Ser. A Math. Phys. Sci.* **1955**, *228*, 519–538. [CrossRef]
6. Mellor, M.; Testa, R. Effect of Temperature on the Creep of Ice. *J. Glaciol.* **1969**, *8*, 131–145. [CrossRef]
7. Hassan, M.F.; Lee, H.P.; Lim, S.P. The variation of ice adhesion strength with substrate surface roughness. *Meas. Sci. Technol.* **2010**, *21*, 075701. [CrossRef]
8. Nath, S.; Ahmadi, S.F.; Boreyko, J.B. How ice bridges the gap. *Soft Matter* **2019**, *16*, 1156–1161. [CrossRef]
9. Kellner, L.; Stender, M.; Polach, R.U.F.V.B.U.; Herrnring, H.; Ehlers, S.; Hoffmann, N.; Høyland, K.V. Establishing a common database of ice experiments and using machine learning to understand and predict ice behavior. *Cold Reg. Sci. Technol.* **2019**, *162*, 56–73. [CrossRef]
10. Pernas-Sánchez, J.; Pedroche, D.; Varas, D.; López-Puente, J.; Zaera, R. Numerical modeling of ice behavior under high velocity impacts. *Int. J. Solids Struct.* **2012**, *49*, 1919–1927. [CrossRef]
11. Wang, C.; Hu, X.; Tian, T.; Guo, C.; Wang, C. Numerical simulation of ice loads on a ship in broken ice fields using an elastic ice model. *Int. J. Nav. Arch. Ocean Eng.* **2020**, *12*, 414–427. [CrossRef]

12. Long, X.; Liu, S.; Ji, S. Breaking characteristics of ice cover and dynamic ice load on upward–downward conical structure based on DEM simulations. *Comput. Part. Mech.* **2020**, *8*, 297–313. [CrossRef]
13. Yershov, E.D. *General Geocryology*; Cambridge University Press: Cambridge, UK, 2004. [CrossRef]
14. Harris, J.S. *Ground Freezing in Practice*; Thomas Telford Limited: London, UK, 1995.
15. Wang, Y.; Chen, B.; Nie, C. Numerical Simulation of Nonlinear Fracture Failure Process of Frozen Soil. In Proceedings of the 2009 International Joint Conference on Computational Sciences and Optimization, Sanya, China, 24–26 April 2009; Volume 1, pp. 183–186. [CrossRef]
16. Wang, Z.; Ma, L.; Wu, L.; Yu, H. Numerical simulation of crack growth in brittle matrix of particle reinforced composites using the xfem technique. *Acta Mech. Solida Sin.* **2012**, *25*, 9–21. [CrossRef]
17. Nishimura, S.; Gens, A.; Olivella, S.; Jardine, R.J. THM-coupled finite element analysis of frozen soil: Formulation and application. *Géotechnique* **2009**, *59*, 159–171. [CrossRef]
18. Cuccurullo, A.; Gallipoli, D. *DEM Simulation of Frozen Granular Soils with High Ice Content. National Conference of the Researchers of Geotechnical Engineering*; Springer: Cham, Switzerland, 2020.
19. An, L.; Ling, X.; Geng, Y.; Li, Q.; Zhang, F. DEM Investigation of Particle-Scale Mechanical Properties of Frozen Soil Based on the Nonlinear Microcontact Model Incorporating Rolling Resistance. *Math. Probl. Eng.* **2018**, *2018*, 2685709. [CrossRef]
20. Cundall, P.A.; Strack, O.D.L. A discrete numerical model for granular assemblies. *Géotechnique* **1979**, *29*, 47–65. [CrossRef]
21. Dosta, M.; Dale, S.; Antonyuk, S.; Wassgren, C.; Heinrich, S.; Litster, J.D. Numerical and experimental analysis of influence of granule microstructure on its compression breakage. *Powder Technol.* **2016**, *299*, 87–97. [CrossRef]
22. Rybczyński, S.; Dosta, M.; Schaan, G.; Ritter, M.; Schmidt-Döhl, F. Numerical study on the mechanical behavior of ultrahigh performance concrete using a three-phase discrete element model. *Struct. Concr.* **2020**, *23*, 548–563. [CrossRef]
23. Beckmann, B.; Schicktanz, D.-I.K.; Reischl, D.-M.D.; Curbach, D.-I.E.M. DEM simulation of concrete fracture and crack evolution. *Struct. Concr.* **2012**, *13*, 213–220. [CrossRef]
24. Obermayr, M.; Dressler, K.; Vrettos, C.; Eberhard, P. A bonded-particle model for cemented sand. *Comput. Geotech.* **2012**, *49*, 299–313. [CrossRef]
25. Ouyang, Y.; Yang, Q.; Chen, X. Bonded-Particle Model with Nonlinear Elastic Tensile Stiffness for Rock-Like Materials. *Appl. Sci.* **2017**, *7*, 686. [CrossRef]
26. Dosta, M.; Jarolin, K.; Gurikov, P. Modelling of Mechanical Behavior of Biopolymer Alginate Aerogels Using the Bonded-Particle Model. *Molecules* **2019**, *24*, 2543. [CrossRef]
27. Dosta, M.; Skorych, V. MUSEN: An open-source framework for GPU-accelerated DEM simulations. *SoftwareX* **2020**, *12*, 100618. [CrossRef]
28. Gold, L.W. On the Elasticity of Ice Plates. *Can. J. Civ. Eng.* **1988**, *15*, 1080–1084. [CrossRef]
29. Petrovic, J.J. Review Mechanical properties of ice and snow. *J. Mater. Sci.* **2003**, *38*, 1–6. [CrossRef]
30. Haynes, F.D. *Effect of Temperature on the Strength of Snow-Ice*; U.S. Army Cold Regions Research and Engineering Laboratory: Hanover, NH, USA, 1978; Volume 78.
31. Schulson, E.M. The structure and mechanical behavior of ice. *JOM* **1999**, *51*, 21–27. [CrossRef]
32. Weertman, J. CREEP DEFORMATION OF ICE. *Annu. Rev. Earth Planet. Sci.* **1983**, *11*, 215–240. [CrossRef]
33. Naumenko, K.; Altenbach, H. *Modeling of Creep for Structural Analysis*; Springer Science & Business Media: Berlin/Heidelberg, Germany, 2007. [CrossRef]
34. Gold, L.W. Process of failure in ice. *Can. Geotech. J.* **1970**, *7*, 405–413. [CrossRef]
35. Arenson, L.U.; Johansen, M.M.; Springman, S.M. Effects of volumetric ice content and strain rate on shear strength under triaxial conditions for frozen soil samples. *Permafr. Periglac. Process* **2004**, *15*, 261–271. [CrossRef]
36. Arenson, L.U.; Almasi, N.; Springman, S.M. Shearing response of ice-rich rock glacier material. In Proceedings of the Eighth International Conference on Permafrost, Zurich, Switzerland, 21–25 July 2003; pp. 39–44.
37. Taylor, D.W. *Fundamentals of Soil Mechanics*; LWW: Philadelphia, PA, USA, 1948.
38. Arenson, L.U.; Springman, S.M. Triaxial constant stress and constant strain rate tests on ice-rich permafrost samples. *Can. Geotech. J.* **2005**, *42*, 412–430. [CrossRef]
39. Hooke, R.L.; Dahlin, B.B.; Kauper, M.T. Creep of Ice Containing Dispersed Fine Sand. *J. Glaciol.* **1972**, *11*, 327–336. [CrossRef]
40. Ting, J.M.; Martin, R.T.; Ladd, C.C. Mechanisms of Strength for Frozen Sand. *J. Geotech. Eng.* **1983**, *109*, 1286–1302. [CrossRef]
41. Arenson, L.U.; Sego, D.C. The effect of salinity on the freezing of coarse-grained sands. *Can. Geotech. J.* **2006**, *43*, 325–337. [CrossRef]
42. Zhao, S.P.; Zhu, Y.L.; He, P. Recent progress in research on the dynamic response of frozen soil. In Proceedings of the Eighth International Conference on Permafrost, Zurich, Switzerland, 21–25 July 2003; pp. 1301–1306.
43. Anderson, D.M.; Tice, A.R. Predicting Unfrozen Water Contents in Frozen Soils From Surface Area Measurements. *Highw. Res. Rec.* **1972**, *393*, 12–18.
44. Istomin, V.; Chuvilin, E.; Bukhanov, B. Fast estimation of unfrozen water content in frozen soils. *Earth's Cryosphere* **2017**, *21*, 116–120. [CrossRef]
45. Mellor, M.; Smith, J.S. Creep of Snow and Ice, Cold Regions Research and Engineering Laboratory, Vicksburg, U.S. Research Report. 1966. Available online: https://hdl.handle.net/11681/5879 (accessed on 20 November 2022).

46. Lian, G.; Thornton, C.; Adams, M.J. A Theoretical Study of the Liquid Bridge Forces between Two Rigid Spherical Bodies. *J. Colloid Interface Sci.* **1993**, *161*, 138–147. [CrossRef]
47. Willett, C.D.; Johnson, S.A.; Adams, M.J.; Seville, J.P. Chapter 28 Pendular capillary bridges. *Handb. Powder Technol.* **2007**, *11*, 1317–1351. [CrossRef]
48. Nguyen, H.N.G.; Zhao, C.-F.; Millet, O.; Selvadurai, A. Effects of surface roughness on liquid bridge capillarity and droplet wetting. *Powder Technol.* **2020**, *378*, 487–496. [CrossRef]
49. Mindlin, R.D.; Deresiewicz, H. Elastic Spheres in Contact Under Varying Oblique Forces. *J. Appl. Mech.* **1953**, *20*, 327–344. [CrossRef]
50. Tsuji, Y.; Tanaka, T.; Ishida, T. Lagrangian numerical simulation of plug flow of cohesionless particles in a horizontal pipe. *Powder Technol.* **1992**, *71*, 239–250. [CrossRef]
51. Dosta, M.; Antonyuk, S.; Heinrich, S. Multiscale Simulation of Agglomerate Breakage in Fluidized Beds. *Ind. Eng. Chem. Res.* **2013**, *52*, 11275–11281. [CrossRef]
52. Iwamoto, T.; Murakami, E.; Sawa, T. A finite element simulation on creep behavior in welded joint of chrome-molybdenum steel including interaction between void evolution and dislocation dynamics. *Technol. Mech. J. Eng. Mech.* **2010**, *30*, 157–168.
53. Norton, F.H. *The Creep of Steel at High Temperatures*; McGraw-Hill B. Company, Incorporated: Columbus, OH, USA, 1929.
54. Penny, R.K.; Marriott, D.L. *Design for Creep*; McGraw-Hill: New York, NY, USA; Columbus, OH, USA, 1971.
55. Dosta, M.; Bistreck, K.; Skorych, V.; Schneider, G.A. Mesh-free micromechanical modeling of inverse opal structures. *Int. J. Mech. Sci.* **2021**, *204*, 106577. [CrossRef]
56. Descantes, Y.; Tricoire, F.; Richard, P. Classical contact detection algorithms for 3D DEM simulations: Drawbacks and solutions. *Comput. Geotech.* **2019**, *114*, 103134. [CrossRef]
57. Leroy, B. Collision between two balls accompanied by deformation: A qualitative approach to Hertz's theory. *Am. J. Phys.* **1985**, *53*, 346–349. [CrossRef]
58. El Shamy, U.; Zamani, N. Discrete element method simulations of the seismic response of shallow foundations including soil-foundation-structure interaction. *Int. J. Numer. Anal. Methods Géoméch.* **2011**, *36*, 1303–1329. [CrossRef]
59. Wang, X.; Yang, J.; Xiong, W.; Wang, T. Evaluation of DEM and FEM/DEM in Modeling the Fracture Process of Glass Under Hard-Body Impact. *Int. Conf. Discret. Elem. Methods* **2017**, *188*, 377–388. [CrossRef]
60. Nitta, K.-H.; Yamana, M. *Poisson's Ratio and Mechanical Nonlinearity Under Tensile Deformation in Crystalline Polymers*; Intec: Rijeka, Croatia, 2012; pp. 113–132. [CrossRef]
61. Tan, Y.; Yang, D.; Sheng, Y. Study of polycrystalline Al2O3 machining cracks using discrete element method. *Int. J. Mach. Tools Manuf.* **2008**, *48*, 975–982. [CrossRef]
62. Lupo, M.; Sofia, D.; Barletta, D.; Poletto, M. Calibration of DEM simulation of cohesive particles. *Chem. Eng. Trans.* **2019**, *74*, 379–384. [CrossRef]
63. Cao, X.; Li, Z.; Li, H.; Wang, X.; Ma, X. Measurement and Calibration of the Parameters for Discrete Element Method Modeling of Rapeseed. *Processes* **2021**, *9*, 605. [CrossRef]
64. Daraio, D.; Villoria, J.; Ingram, A.; Alexiadis, A.; Stitt, E.H.; Munnoch, A.L.; Marigo, M. Using Discrete Element method (DEM) simulations to reveal the differences in the γ-Al2O3 to α-Al2O3 mechanically induced phase transformation between a planetary ball mill and an attritor mill. *Miner. Eng.* **2020**, *155*, 106374. [CrossRef]
65. Gu, X.; Zhang, J.; Huang, X. DEM analysis of monotonic and cyclic behaviors of sand based on critical state soil mechanics framework. *Comput. Geotech.* **2020**, *128*, 103787. [CrossRef]

materials

MDPI

Article

Modeling Cyclic Crack Propagation in Concrete Using the Scaled Boundary Finite Element Method Coupled with the Cumulative Damage-Plasticity Constitutive Law

Omar Alrayes [1], Carsten Könke [1], Ean Tat Ooi [2] and Khader M. Hamdia [3,*]

[1] Institute of Structural Mechanics, Bauhaus Weimar University, Marienstraße 15, 99423 Weimar, Germany
[2] School of Science, Engineering and Information Technology, Federation University, Ballarat, VIC 3350, Australia
[3] Institute of Continuum Mechanics, Leibniz Universität Hannover, 30167 Hannover, Germany
* Correspondence: hamdia@ikm.uni-hannover.de

Abstract: Many concrete structures, such as bridges and wind turbine towers, fail mostly due to the fatigue rapture and bending, where the cracks are initiated and propagate under cyclic loading. Modeling the fracture process zone (FPZ) is essential to understanding the cracking behavior of heterogeneous, quasi-brittle materials such as concrete under monotonic and cyclic actions. The paper aims to present a numerical modeling approach for simulating crack growth using a scaled boundary finite element model (SBFEM). The cohesive traction law is explored to model the stress field under monotonic and cyclic loading conditions. In doing so, a new constitutive law is applied within the cohesive response. The cyclic damage accumulation during loading and unloading is formulated within the thermodynamic framework of the constitutive concrete model. We consider two common problems of three-point bending of a single-edge-notched concrete beam subjected to different loading conditions to validate the developed method. The simulation results show good agreement with experimental test measurements from the literature. The presented analysis can provide a further understanding of crack growth and damage accumulation within the cohesive response, and the SBFEM makes it possible to identify the fracture behavior of cyclic crack propagation in concrete members.

Keywords: crack propagation; cohesive zone method; constitutive modelling; cyclic loading; scaled boundary finite element

Citation: Alrayes, O.; Könke, C.; Ooi, E.T.; Hamdia, K.M. Modeling Cyclic Crack Propagation in Concrete Using the Scaled Boundary Finite Element Method Coupled with the Cumulative Damage-Plasticity Constitutive Law. *Materials* **2023**, *16*, 863. https://doi.org/10.3390/ma16020863

Academic Editors: Angelo Marcello Tarantino, Carmelo Majorana, Raimondo Luciano and Michele Bacciocchi

Received: 22 November 2022
Revised: 29 December 2022
Accepted: 4 January 2023
Published: 16 January 2023

1. Introduction

Concrete structural elements very often fail due to fatigue fractures, in which repeated loading can lead to the growth of existing cracks [1–4]. To better understand the fatigue fracturing under cyclic loading, a detailed analysis of the fatigue behavior and the associated crack propagation is required for economical and reliable design of concrete structures.

The advanced studies on cyclic crack propagation are mostly empirical, wherein large number of data samples from experiments are used for fitting the relationship. The most commonly used approach to predict fatigue life and crack growth rate is the well-known Paris law [5,6]. This phenomenological law relates the amplitude of the stress state (defined by stress intensity factor K) and the crack growth rate da/dN, which can be considered a valuable tool for engineering fatigue analysis. However, it has been shown that Paris law loses much of its prediction ability when conditions are not ideal, such as with non-constant amplitude loading and short cracks [7,8]. Nevertheless, advanced numerical models have been developed widely to capture the phenomena behind the cyclic crack propagation under subcritical loading levels. Numerical simulations are more flexible in the sense

that they can predict fatigue life and crack growth under general loading conditions and geometries. They can be applied to study design variations in early design stages.

Several modeling approaches for crack propagation under cyclic and fatigue loading are well documented in the literature [9,10]. The cohesive zone model (CZM) has been implemented in classical fracture mechanics by [11,12] to reduce the mesh quality required for crack simulation. The CZM is based on elastic damage material for both monotonic and fatigue crack growth [13,14]. For concrete material, the softening damage, whose localization is governed numerically by finite element simulation, is aimed at simulating the propagation of the fatigue fracture in the cohesive process zone [15,16]. However, these types of models are used to accumulate damage only along the damaged locations of the loading/unloading paths.

The second type of crack simulation model is the phase field model (PFM). The concept of the PFM approach is to regularize free energy of degradation, which effectively reduces material fracture resistance under fatigue loading [17]. It was developed to predict quasi-static and dynamic fracturing in brittle and ductile regimes considering isotropic and anisotropic toughness [18]. This method introduces the degradation of the fracture energy as a function of a local energy-accumulation variable. As a result of repeated loading, the structural loading history is taken into consideration [19]. Similar approaches have been published recently in [20], which simulated fatigue crack growth. A nonlinear kinematic and isotropic hardening were considered. Differently, simulations of molecular dynamics can be used to evaluate the interfacial strength [21].

Additionally, discrete lattice models have many features of the discrete element method (DEM) to simulate the heterogeneous microstructure and crack propagation [22]. The formulation combines the damage mechanics and plasticity theory with a cyclic damage evolution law. The model characterizes the critical response of concrete material undergoing cyclic loading. The behavior obtained by the DEM simulations is a collective response constituted from all contacts and particles in the domain.

Many models in the literature [23–31] are dedicated to simulating the quasi-brittle behavior, including a set of constitutive equations for the monotonic, fatigue, and hysterical material responses. Furthermore, several calculation schemes also exist to predict tensile, flexural monotonic, and fatigue behavior [32,33]. The established damage law allows a damage accumulation process for random cycles. The damage model concludes the primary dissipative phenomenon, which is activated during unloading and reloading.

The scaled boundary finite element method (SBFEM) is a very attractive approach to modeling crack nucleation and propagation under general loading conditions [34–37]. The cohesive fracture and stress field can be determined using interface elements with zero thickness, which are inserted directly into the SBFEM [38–40]. The cohesive traction forces and the stress field close to the crack tip are accurately computed as they are defined analytically. This enables the onset of crack propagation to obtain the correct load-deflection response. Yang [41] developed the SBFEM to solve linear crack propagation in brittle materials under monotonic loading. He benefited from the salient feature of the high accuracy of the stress intensity factor (SIF) in SBFEM computed directly from singular stress solutions and flexible substructuring of each domain. The crack simulation of concrete slabs based on a cohesive zone model in an explicit SBFEM-FEM frame for seismic cyclic loading was reported in [42] to facilitate dynamic analysis. However, the calculation of coupled SBFEM-FEM analysis can be very computationally intensive. For cyclic loading, the crack evolution can also be simulated using quasi-static analysis. The accuracy of the method was validated by a cyclic damage test with a concrete beam. A fully automatic modeling methodology characterized by a simple remeshing algorithm was developed, and the mixed-mode crack propagation problem was efficiently solved. Yang and Deeks [43] further coupled the procedure of SBFEM with the FEM for quasi-brittle materials. An extended polygon scaled boundary finite element method [44] was developed to simulate nonlinear dynamic analysis. A direct remeshing algorithm for crack propagation was obtained for quasi-brittle materials. The study of dynamic fracture modeling by SBFEM

was developed in [45] to model the crack propagation of impact-test specimens. The stress intensity factor, displacement, and stresses were extracted from the dynamic solution.

In the present paper, we further extend the SBFEM for modeling cyclic-damage-induced cracks' behavior within the SBFEM framework. The model considers the cumulative crack opening/sliding measure to dominate the damage mechanism at the subcritical loading levels. Similar approaches have been proposed in [40] for the numerical simulation of concrete under monotonic loading. The novelty of our approach is to establish a link between the cyclic damage rate and the efficiency of the SBFEM in modeling crack propagation. By comparing the thermodynamic softening law of the constitutive model for fracture, several aspects have been provided, which include the loading–unloading path, the damage evolution during the load cycle, and the crack-opening traction behavior.

The paper is organized as follows. The theoretical formulation of the cohesive crack model inside SBFEM is represented in Section 2. The behavior of the constitutive material model is studied at the level of material point (Gauss point) in Section 3. The performance of the cohesive cyclic crack model within the thermodynamic framework is then reported, which was applied in [46]. In Section 4, we present the calibration and validation of the model based on the results of the cyclic flexural bending test of plain concrete published in the literature. We present numerical investigations focused on the effect of the loading sequence on the material behavior.

2. Scaled Boundary Finite Element (SBFEM)

2.1. Fundamentals

Figure 1 shows the basic concept of the cohesive crack model in the scaled boundary method for a typical bounded domain. The mesh is represented by a discretized collection of arbitrary-sided polygons, or (as in Figure 1a) quadtrees elements. Each element is maintained by a curve relative to a scaling center (x_0,y_0). This condition is satisfied by dividing the domain into many sub-domains, which can be made visible for each boundary. The boundary is discretized by one-dimensional finite elements with a local coordinate η in an interval of $-1 \leq \eta \leq 1$; see Figure 1b. Let (x_0,y_0) be the scaling center, and ξ is the radial coordinate with $\xi = 0$ at the center and $\xi = 1$ at the boundary. The coordinates on the boundary are interpolated by $x_b = [N(\eta)]\{x_{bn}\}$, and $y_b = [N(\eta)]\{y_{bn}\}$, where $[N(\eta)]$ is the vector of nodal shape functions, and $\{x_{bn}\}, \{y_{bn}\}$ are the nodal coordinates. The displacement field, $u(\xi, \eta)$, can be defined semi-analytically as

$$\{u(\xi, \eta)\} = [N_u(\eta)]\{u(\xi)\} \tag{1}$$

We calculate the nodal displacement functions $u(\xi)$ at the radial lines, ξ. Meanwhile, they are interpolated by the linear shape functions $[N_u(\eta)]$ in the direction of η, which are obtained by multiplying a suitable identity matrix with each element in $[N]$. Thus, the strain and the stress fields are formulated as:

$$\{\varepsilon(\xi, \eta)\} = [B_1(\eta)]\{u(\xi)\}_{,\xi} + (1/\xi)[B_2(\eta)]\{u(\xi)\} \tag{2}$$

$$\{\sigma(\xi, \eta)\} = [D]\{\varepsilon(\xi, \eta)\} = [D][B_1(\eta)]\{u(\xi)\}_{,\xi} + (1/\xi)[B_2(\eta)]\{u(\xi)\} \tag{3}$$

where $B_1(\eta)$ and $B_2(\eta)$ are the strain matrices, and D is the constitutive matrix [39]. The weak form of the elastic equilibrium of forces is obtained according to the principle of virtual work [47], or from the weighted residual technique; see ref. [34]. The governing equations can be written as follows:

$$[E_0]\xi^2\{u(\xi)\}_{,\xi\xi} + ([E_0] + [E_1] + [E_1^T])\xi\{u(\xi)\}_{,\xi} - [E_2]\{u(\xi)\} = 0 \tag{4}$$

$$\{P(\xi)\} = [E_0]\xi\{u(\xi)\}_{,\xi} + [E_1]^T\{u(\xi)\} \tag{5}$$

with $\{P\}$ being the load vector. Equation (4) includes second-order Cauchy–Euler equations, called the scaled boundary finite element equation in the displacement with the coefficient matrices $[E_0], [E_1], [E_2]$. Furthermore, Equation (4) is a homogeneous second-order differential Equation (in case there is no side face or body loads) with n unknowns.

By introducing a new variable $[\chi(\xi)]$ with Hamiltonian matrix Z, the system becomes a first-order ordinary differential equation [48] as

$$\xi[\chi(\xi)]_{,\xi} = -[Z][\chi(\xi)] \tag{6}$$

and

$$[\chi(\xi)] = [\{u(\xi)\}\{q(\xi)\}]^T \tag{7}$$

where $q(\xi)$ are analytical functions that represent the internal nodal forces vector:

$$\{q(\xi)\} = [E_0]\xi\{u(\xi)\}_{,\xi} + [E_1]^T\{u(\xi)\} \tag{8}$$

and the Hamitonian matrix is calculated as a function of $[E_0]$, $[E_1]$, $[E_2]$:

$$[Z] = \begin{bmatrix} [E_0]^{-1}[E_0]^T & -[E_0]^{-1} \\ -[E_2] + [E_1][E_0]^{-1}[E_1]^T & -[E_1][E_0]^{-1} \end{bmatrix} \tag{9}$$

An eigenvalue decomposition of [Z] follows [49]:

$$[Z]\begin{bmatrix} [\phi_u^{(n)}] & [\phi_u^{(p)}] \\ [\phi_q^{(n)}] & [\phi_q^{(p)}] \end{bmatrix} = \begin{bmatrix} [\phi_u^{(n)}] & [\phi_u^{(p)}] \\ [\phi_q^{(n)}] & [\phi_q^{(p)}] \end{bmatrix} \times \begin{bmatrix} [\lambda^{(n)}] & 0 \\ 0 & [\lambda^{(p)}] \end{bmatrix} \tag{10}$$

where $[\lambda]$ is the diagonal matrix of $\lambda^{(p)}$ and $\lambda^{(n)}$. The superscripts p and n refer to positive and negative. $[\phi_q^{(p)}]$, $[\phi_u^{(p)}]$, and $[\phi_u^{(n)}]$ are the eigenvectors corresponding to $\lambda^{(p)}$, $[\phi_q^{(n)}]$, and $[\lambda^{(n)}]$, respectively. The solution of Equation (6) yields:

$$\{q(\xi)\} = [\phi_q^{(n)}]\xi^{-[\lambda^{(n)}]}\{c^{(n)}\} + [\phi_q^{(p)}]\xi^{-[\lambda^{(p)}]}\{c^{(p)}\} \tag{11}$$

$$\{u(\xi)\} = [\phi_u^{(n)}]\xi^{-[\lambda^{(n)}]}\{c^{(n)}\} + [\phi_u^{(p)}]\xi^{-[\lambda^{(p)}]}\{c^{(p)}\} \tag{12}$$

$\{c^{(p)}\}$ and $\{c^{(n)}\}$ are the integration constants. For a bounded domain, the boundary condition at $\{\xi = 0\}$ produces $\{c^{(p)}\} = 0$. In this case, the modes of non-positive real components of eigenvalue $[\lambda]$ contribute to the solution of finite displacement at the scaling center.

The equivalent nodal forces on the boundary and the stiffness matrix of the domain are formulated, respectively, as

$$\{P\} = [\phi_q^{(n)}]\{c^{(n)}\} = [\phi_q^{(n)}][\phi_u^{(n)}]^{-1}\{u_b\} \tag{13}$$

$$[K] = [\phi_q^{(n)}][\phi_u^{(n)}]^{-1} \tag{14}$$

At the boundaries, the nodal displacements $\{u_b\}$ can be calculated from the global stiffness matrix K and load vector P.

Meanwhile, substituting Equation (11) into Equation (1) yields the displacement field in the bulk domain as

$$\{u(\xi,\eta)\} = [N_u(\eta)]\sum_{i=1}^{n} \xi^{-\lambda^{(n)}{}_i} c_i\{\phi_i\} \tag{15}$$

Hence, the stress field is formulated by

$$\{\sigma(\xi,\eta)\} = [D]\sum_{i=1}^{n} \xi^{-\lambda^{(n)}{}_i}([-\lambda^{(n)}][B_1(\eta)] + [B_2(\eta)])\{\phi_i\} \tag{16}$$

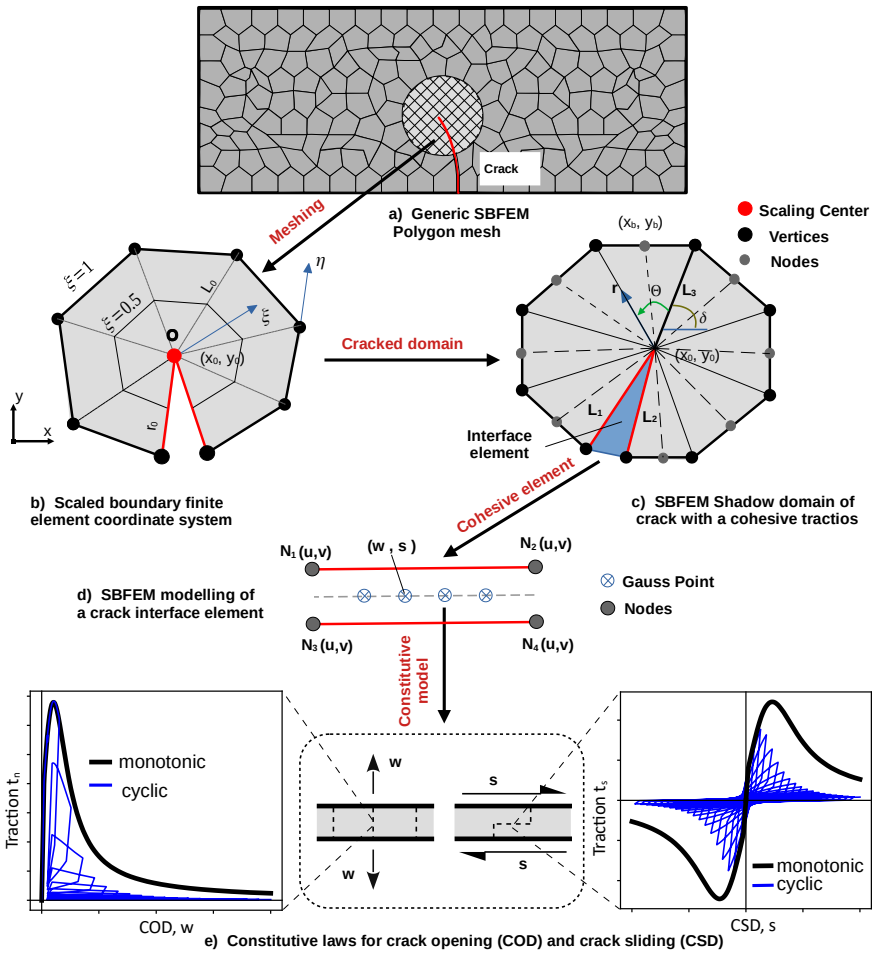

Figure 1. The concept of a cohesive crack model using the scaled boundary finite element method.

2.2. Stress Field at Crack Tip with Cohesive Tractions

The fracture process zone in a quasi-brittle material can transfer the cohesive forces between the crack faces. This is attributed to the interlocking of the aggregate, in addition to the surface friction. The cohesive traction representing the crack faces is applied as side-face forces. The equilibrium condition (Equation (4)) in a polygon containing a crack tip is augmented to include the load vector containing the side-face tractions, as in [43].

$$[E_0]\xi^2\{u(\xi)\}_{,\xi\xi} + ([E_0] + [E_1] + [E_1^T])\xi\{u(\xi)\}_{,\xi} - [E_2]\{u(\xi)\} - \{F_t(\xi)\} = 0 \qquad (17)$$

In this work, the cohesive force on the crack faces $\{F_t(\xi)\}$ will be computed based on the shadow domain procedure, which has been introduced by [40].

The concept of the cohesive cyclic crack model, as depicted in Figure 1, is shown in the following steps:

1. The mesh generation of the domain in Figure 1a and the cohesive zone in the surroundings of the crack polygon is defined. In this method, the generic mesh contains an arbitrarily many sided polygon in boundary regions, master cells far away from the boundaries, and the crack cells.
2. The crack cell is divided into two SBFEM cells to discretize the crack faces and to insert the interface elements into the SBFEM system. The local coordinates ξ, η of the SBFEM system are illustrated in Figure 1b.
3. The shadow domain is generated as shown in Figure 1c. It is implemented in order to calculate the cohesive tractions (side-face forces) and the nodal displacements throughout the crack subdomain. This method inserts a node at the crack tip with

three corresponding edges (two edges, L_1 and L_2, for each crack face, and one edge, L_3, to split the crack cell into two). Knowing the crack angle, θ, the orientation of L_3 is projected in a way that a straight line is extended from the crack tip with an angle θ. Then, the node closest to the intersection point at edge of the cracked cell is employed to split the polygon.

4. The SBFEM is directly coupled with zero-thickness, four node-interface elements along the crack path (Figure 1d) which are inserted along the lines of the mesh. The cohesive edges $(N_1,\ N_2,\ N_3,\ N_4)$ divide the subdomains into two divisions. The pair $(N_{1,u}\ N_{3,u})$ and $(N_{2,u}\ N_{4,u})$ form contact pairs with a set of crack opening (w). Additionally, the pair $(N_{1,v}\ N_{3,v})$ and $(N_{2,v}\ N_{4,v})$ form contact pairs with a set of crack sliding (s). As the crack propagates, the interface element domain is inserted into the mesh. This can satisfy the compatibility condition in the displacement between the SBFEM polygons and the interface elements.
5. Along the crack paths, the fracture process zone is characterized using softening laws of the thermodynamics; see Figure 1e. For concrete, the softening behavior for crack opening and sliding proposed model is based on [46] and defined in the next section. The model uses the cumulative measure of slip as a fundamental damage driving mechanism at the subcritical levels of loading.

In the fracture process zone, cohesive tractions t_n, t_s are expressed as a function of relative opening and sliding displacements d. In the local coordinate system, the stiffness matrix reads:

$$[k_{int}] = \frac{A}{2}\sum_{i=1}^{n_g} w_i {M_i}^T [k] M_i \tag{18}$$

where k is the stiffness of the softening laws, A is the crack surface area, w_i is the one-dimensional Gaussian weight, n_g is the number of integration points, and M_i is the linear shape function matrix [40]. The stiffness matrices of the interface element k_{int} can be assembled attractively. In this case, the local coordinates (ξ_p, η_p) in the shadow domain are defined first to obtain the coordinates (x, y) for a new node in the new crack cell. For this purpose, we use a search algorithm to determine the element in the shadow domain that includes the point (x, y). In doing so, the nodal displacements and the cohesive tractions are calculated along the crack. These are then mapped back to the crack cell to calculate the stress intensity factors required to determine if the crack propagates. The SIF considering the cohesive forces on the crack face is calculated by representing the cohesive forces as a power function in ξ following from the form of the side face traction vector $F_t(\xi)$, as in [43].

Linearly varying or constant distributed loads are approaches to representing a force over a particular distance. According to [47], when the side-face loads are distributed by a power function, then the modal displacement loads are

$$\{u_t(\xi)\} = \xi^{t+1}\{\phi_t\} \tag{19}$$

Substitution of Equation (19) into Equation (17) yields

$$[(t+1)^2[E_0] + (t+1)([{E_1}^T] - [E_1]) - [E_2]]^{-1}\{\phi_t\} + \{F_t\} = \{0\} \tag{20}$$

Rearranging will give the nodal displacements for the side-face load mode $\{\phi_t\}$ as

$$\{\phi_t\} = -[(t+1)^2[E_0] + (t+1)([{E_1}^T] - [E_1]) - [E_2]]^{-1}\{F_t\} = [B_1(t)]\{F_t\} \tag{21}$$

In order to express the cohesive tractions as a power of function, the normal traction distribution $\sigma(\xi)$ is assumed to be the summation of M raised to the power of function ξ:

$$\sigma(\xi) = f_t \sum_{i=1}^{M} e_i \xi^{ti} \tag{22}$$

where e_i is coefficient to be calculated. Considering a parameter μ, the exponents t_i are determined as $t_i = (i - 1 + \mu)$.

The tractions at the crack tip, the Gaussian points, and the crack mouth $\sigma_j (j = 1, M)$ are used to generate M number of equations as

$$\sigma_j = \sigma(\xi_j) = f_t \sum_{i=1}^{M} e_i \xi_j^{ti} \tag{23}$$

where $\xi_j = l_j / L$ is the distance from the jth point on the crack to the crack tip l_j and the length of the crack L. The coefficients $\{e\} = \{e_1 \ e_2 \ ... \ e_M\}^T$ are then calculated as

$$\{e\} = [S]^T {f_t}^{-1} \{\sigma\} \tag{24}$$

where $\{\sigma\} = \{\sigma_1 \ \sigma_2 \ ... \ \sigma_M\}^T$, and the matrix $[S]$ is

$$[S] = \begin{bmatrix} \xi_1^{t_1} & \xi_1^{t_2} & \cdots & \xi_1^{t_M} \\ \xi_2^{t_1} & \xi_2^{t_2} & \cdots & \xi_2^{t_M} \\ \vdots & \vdots & \ddots & \vdots \\ \xi_M^{t_1} & \xi_M^{t_2} & \cdots & \xi_M^{t_M} \end{bmatrix} \tag{25}$$

The nodal side-face load vector becomes

$$\{F_t(\xi)\} = \sum_{i=1}^{M} \xi^{t_i} \{F_{t_i}\} \tag{26}$$

with

$$\{F_t(\xi)\} = A f_t e_i \{R_1\} \tag{27}$$

and

$$\{R_1\} = \{-sin\delta \ \ cos\delta \ \ 0 \ \ \cdots \ \ 0 \ \ sin\delta \ \ -cos\delta\}^T \tag{28}$$

where $A =$ is the area of crack surface.

The displacement solution is thus expressed by two components: the modes of normal displacement due to external loading and the modes of side-face displacement due to cohesive tractions as

$$\{u(\xi, \eta)\} = [N(\eta)][\sum_{i=1}^{N} c_i \xi^{\lambda_i} \{\phi_i\} + \sum_{i=1}^{M} e_i \xi^{t_i+1} A f_t [B_1(t_i)] \{R_1\}] \tag{29}$$

On the subdomain boundary, the nodal displacement u_{bs} is calculated as

$$\{u_{bs}\} = [\phi]\{c\} + [\phi_t]\{e\} \tag{30}$$

where $[\phi]$ and $[\phi_i]$ are given in Equation (10), and the matrix $[\phi_t]$ is transformed as:

$$\{\phi_t\} = A f_t [B_1(t_1) \ \ B_1(t_2) \ \ \cdots \ \ B_1(t_M)] \{R_1\} \tag{31}$$

The nodal displacements u_{bs} in Figure 2 are gained by mapping the mesh from the shadow domain, as shown in Figure 2b. The constants $\{c\}$ are given by

$$\{c\} = [\phi]^{-1} (\{u_{bs}\} - [\phi_t]\{e\}) \tag{32}$$

Subsequently, Equation (29) is read as:

$$\{u(\xi, \eta)\} = [N(\eta)] \sum_{i=1}^{N+M} c_i \xi^{(\overline{\lambda_i} - 1)} \{\overline{\phi_i}\} \tag{33}$$

where

$$\begin{cases} \overline{\phi_i} = \phi_i, \ \overline{\lambda_i} = \lambda_i & \text{for } \ i = 1, \cdots, N \\ \overline{\phi_i} = \phi_t, \ \overline{\lambda_i} = t_i + 1 & \text{for } \ i = N+1 \cdots, N+M \end{cases}$$

The stress field can be calculated similarly to Equation (16) as

$$\{\sigma(\xi,\eta)\} = \sum_{i=1}^{N+M} c_i \xi^{(\overline{\lambda_i}-1)} \{\psi_i(\eta)\} \tag{34}$$

where each term in Equation (34) can be interpreted as a stress mode and

$$\{\psi_i(\eta)\} = [D](\overline{\lambda_i}[B_1(\eta)] + [B_2(\eta)])\{\overline{\phi_i}\} \tag{35}$$

Comparing Equation (15) and Equation (33), and Equation (16) and Equation (34) shows that when the cohesive traction is evaluated, an extra number (M) of displacement nodes and the same of stress modes are added to the displacement field and stress field, respectively.

The direction of crack propagation is then determined based on [43]. In order to consider a perfect crack path prediction, the SIFs of the semi-analytical SBFEM stress solutions are calculated.

2.3. Stress Intensity Factor (SIF) for Scaling Center at Crack Tip

The SBFEM has the advantage of accurately representing the crack zone's stress field without needing a more discretized mesh [38,50]. This tool enables the SIFs to be directly calculated from the semi-analytical solutions of the stresses. In this work, two SIFs are determined. The first is obtained from the linear elastic fracture mechanics solution at a generic load step and is used to determine the crack propagation direction. The side-face tractions are not considered in this case. The second concerns the crack cell considering the effect of the cohesive tractions obtained from the shadow domain. In both cases, the procedure to calculate the SIFs is the same. The only difference is the equation used to represent the stress field, i.e., Equation (16) in case 1 and Equation (34) in case 2. The procedure is outlined as follows:

Figure 1c shows the cracked domain modeled by the SBFEM. The location of the scaling center should be at the crack tip. There is no need to discretize the side faces connected to the scaling center. The SIF could be accurately computed from the semi-analytical solutions of the stresses [51]. The stress intensity factors solutions can be extracted from their definitions as follows.

$$\begin{Bmatrix} K_I \\ K_{II} \end{Bmatrix} = \lim_{r\to 0} \begin{Bmatrix} \sqrt{2\pi r}\sigma_{yy}|_{\theta=0} \\ \sqrt{2\pi r}\sigma_{xy}|_{\theta=0} \end{Bmatrix} \tag{36}$$

where r and θ represent the polar coordinates. As illustrated in Figure 1, r and θ originate at the crack tip and are correlated by

$$r = \xi L(\theta) \tag{37}$$

where $L(\theta)$ is the distance between any point A at the cracked domain and the crack tip ($L(\theta) = L_3$ in Figure 1c). Substituting Equation (37) in Equation (36) leads to

$$\begin{Bmatrix} K_I \\ K_{II} \end{Bmatrix} = \lim_{r\to 0} \begin{Bmatrix} \sqrt{2\pi L(\theta)} \sum_{i=0}^{n} c_i \xi^{-\lambda i-1}\sigma_{yy}|_{\theta=0} \\ \sqrt{2\pi L(\theta)} \sum_{i=0}^{n} c_i \xi^{-\lambda i-1}\sigma_{xy}|_{\theta=0} \end{Bmatrix} \tag{38}$$

From Equation (38), when $\xi \to 0$, all the corresponding stress modes that have $\lambda_i \geq 1$ will disappear. When $\lambda_i = 0.5$, singular stresses are obtained in mode I and mode II. An analytical solution of the limits in Equation (38) yields

$$\begin{Bmatrix} K_I \\ K_{II} \end{Bmatrix} = \sqrt{2\pi L_0} \sum_{i=I,II} \left(c_i \begin{Bmatrix} \xi^{-\lambda i-1}\sigma_{yy}|_{\theta=0} \\ \xi^{-\lambda i-1}\sigma_{xy}|_{\theta=0} \end{Bmatrix}_i \right) \tag{39}$$

2.4. Crack Growth Criterion

The zero-K condition based on [52] is used to determine crack propagation in the crack domain. Therefore, when the stress at the crack tip is finite, a cohesive crack propagates, and accordingly, no stress singularity exists. The crack will propagate in the condition

$$K_I(\theta) \geq 0 \tag{40}$$

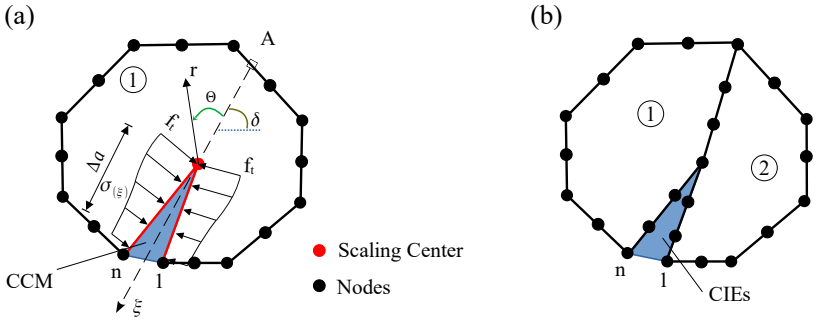

Figure 2. Calculation of k_I using shadow domain method: (**a**) cohesive crack model (CCM) in SBFEM; (**b**) subdomain discretization.

The crack length Δa and its angle θ are used to define the new location of the crack tip. Figure 2a displays the discretised SBFEM polygon and cracked subdomains of the cohesive crack model (CCM) after the first round of growth. In this shadow domain concept, the crack surfaces is discretized first, and then crack cell elements (CIEs) are inserted into the mesh. This will partition the crack subdomain S1 into two (S1 and S2 in Figure 2b). The CIEs are then used to calculate side-face traction along the crack, upon which the SIFs $K_I(\theta)$ can be defined to calculate the crack growth criterion. We apply the mesh mapping technique to calculate the nodal displacements of the cracked subdomain S1. The remeshing procedure during crack propagation is performed based on [40].

3. Cumulative Damage-Plasticity Based Constitutive Law

The constitutive behavior describing cyclic damage in the process zone is embedded in the definition of the interface elements. It has been defined using the thermodynamics-based uniaxial interface model proposed in [46,53,54]. The model assumes that the development of cyclic load is dominated by a cumulative level of the inelastic relative displacement within the interface. The uniaxial model can be applied for the normal behavior ($\sigma_N - w$) and for the shear behavior ($\tau - s$) of the interface as a unified constitutive model.

3.1. Brief Summary of the Model's Formulation

The regular formulation of the thermodynamically interface model is described briefly in this section. The Helmholtz free energy is defined as

$$\rho\psi(u, u^P, \omega, \alpha, z) = \frac{1}{2}(1-\omega)E(u-u^P)^2 + \frac{1}{2}\gamma\alpha^2 + \frac{1}{2}Kz^2 \tag{41}$$

where ρ is the density; E is the elastic stiffness; u represents the relative displacement at the interface (i.e., opening displacement $u = w$ in the normal direction and slip $u = s$ in the tangential/shear direction); K and γ represent the isotropic and kinematic hardening moduli, respectively. The state variables of the interface model are the inelastic displacement u^P, the damage variable ω, and the hardening variables z, α.

The thermodynamic forces, X and Z, and the related energy release rate, Y, can be calculated by differentiating Equation (41) with respect to each state variable as follows.

$$\sigma^P = \sigma = -\frac{\partial\rho\psi}{\partial u^P} = (1-\omega)E(u-u^P) \tag{42}$$

$$X = \frac{\partial \rho \psi}{\partial \alpha} = \gamma \alpha, \qquad Z = \frac{\partial \rho \psi}{\partial z} = Kz \tag{43}$$

$$Y = -\frac{\partial \rho \psi}{\partial \omega} = \frac{1}{2} E (u - u^P)^2 \tag{44}$$

where σ represents the stress components (i.e., normal stress σ_{N} in the case of opening displacement w, and shear stress τ in the case of slip displacement s). A yield function similar to plasticity theory, which defines the boundary between elastic and inelastic domains, is introduced into the effective stress space as follows.

$$f(\tilde{\sigma}, X, Z) = |\tilde{\sigma} - X| - Z - \sigma_0 \tag{45}$$

with $\tilde{\sigma}$ being the effective stress given as $\tilde{\sigma} = \sigma / (1 - \omega)$ and σ_0 being the elastic stress limit. The flow potential determining the damage evolution augments the threshold function (Equation (45)) with an extra term as

$$\phi = f(\tilde{\sigma}, X, Z) + \frac{S(1-\omega)^c}{(r+1)} \left(\frac{Y}{S} \right)^{r+1} \tag{46}$$

where S is the damage strength parameter, and c and r are exponential rate parameters. The evolution equations can be obtained by differentiating (Equation (46))

$$\dot{u}^P = \dot{\lambda} \frac{\partial \phi}{\partial \sigma^P} = \frac{\dot{\lambda}}{1 - \omega} \operatorname{sign}(\tilde{\sigma} - X) \tag{47}$$

$$\dot{\alpha} = -\dot{\lambda} \frac{\partial \phi}{\partial X} = \dot{\lambda} \operatorname{sign}(\tilde{\sigma} - X), \qquad \dot{z} = -\dot{\lambda} \frac{\partial \phi}{\partial Z} = \dot{\lambda} \tag{48}$$

$$\dot{\omega} = \dot{\lambda} \frac{\partial \phi}{\partial Y} = \dot{\lambda} \ (1 - \omega)^c \left(\frac{Y}{S} \right)^r \tag{49}$$

This model can be implemented as a time-stepping algorithm, as described in [46]. The damage accumulation under both monotonic and cyclic loading is described through the modified flow potential by [46,54].

3.2. Elementary Studies of the Cohesive Model

To illustrate the phenomenological behavior of the used constitutive model and its applicability for modeling cyclic and fatigue behavior, a material model of crack behavior at the point level (Gauss point) under opening and shear displacement is presented in this section.

The described parameters of monotonic and cyclic response material behavior are plotted in Figure 3. The exponential parameter c was used to control the dropped-down part of the crack opening (COD) and sliding (CSD) curve. The parameters c and r were applied for tuning the accumulation of the damage due to cyclic loading. The damage strength parameter S, however, could control the brittleness in the response. The model parameters for a common combination of concrete matrix C30/37 were identified using the parametric study reported in [46]. The setup of the study is provided in Figure 3 for monotonic loading and for cyclic loading, as the cohesive model parameters are summarized. The cohesive model stiffness (E) was set equal to Young's modulus of concrete. The parameters $\overline{\sigma}$, K, γ, S, r, and c were identified using a black line for the monotonic response and a blue line for the monotonic response.

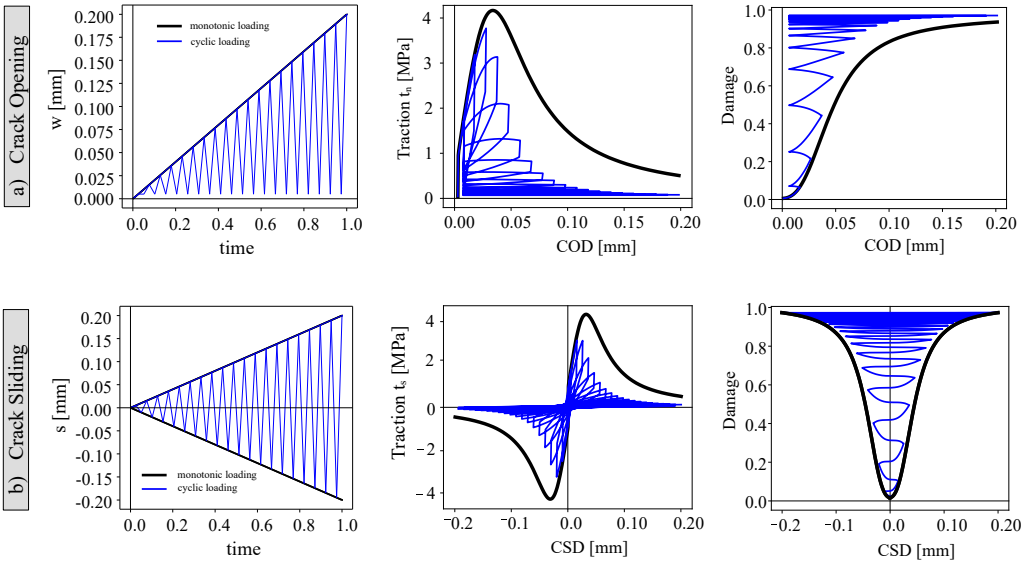

Figure 3. Characterization of the crack behavior under cyclic loading (blue lines) and monotonic loading (black lines) at the material-point level: (**a**) crack opening, (**b**) crack sliding.

The cyclic loading curves of the crack opening versus cyclic loading can be compared with the corresponding curves obtained numerically for monotonic loading. The described model was implemented using zero-thickness interface elements inside the SBFEM framework in Equation (18)). For the monotonic and the cyclic loading, the damage evolution for the loaded and unloaded responses is depicted in Figure 3 for crack opening and crack sliding. The accumulation of the damage parameter is nonlinear. The traction opening/sliding cohesive models for two loading scenarios are studied.

4. Numerical Validation

4.1. Test Setup

Three-point bending (TPB) tests were studied to validate the numerical method in this study. The contributions of both traction modes, k_n and k_s, in the cohesive zone model, were investigated. The investigations performed by [8] have shown that the inclusion of the normal energy dissipation dominated the response of post-peak crack mouth sliding displacement (CMOD). The nonlinear equilibrium equations were solved using Newton–Raphson iteration [55], which is characterized by strain softening in the process zone. The benchmark examples are TPB tests with a single-edge notch (Figure 4). Two sizes of the beam were considered in the tests: small beams with a cross-section height of $h = 200$ mm, and large beams with $h = 400$ mm. The beam width was $b = 100$ mm. The lengths of small and large beams were 600 and 1200 mm, respectively. For the notch depth, $h_0 = h/6$, whereas the maximum grain size (d_0) was 8 mm. The experimental measurements for the concrete beams were provided by Baktheer and Becks [8], and the material properties were adopted from [8], as listed in Table 1.

Table 1. Parameters of concrete [8].

Parameter	Denomination	Value	Unit
f_c	Compressive strength	63.61	[MPa]
f_{ct}	Tensile strength	4.28	[MPa]
E_c	Young's Modulus	34.468	[GPa]
ν	Poisson ratio	0.2	[-]

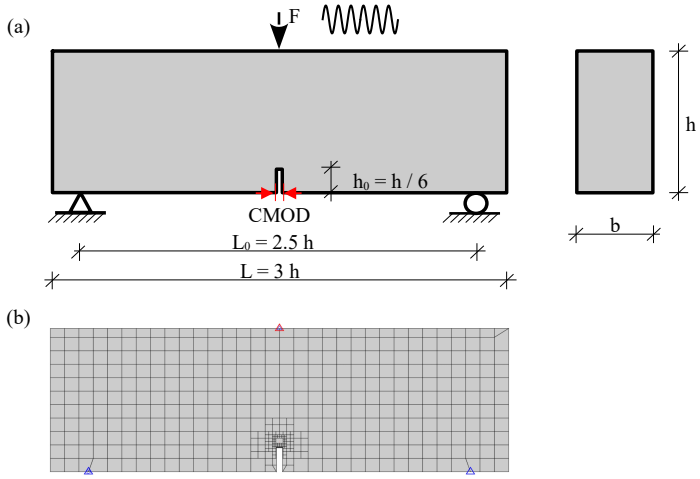

Figure 4. A single-notched concrete beam subjected to a three-point load. (**a**) Geometry, (**b**) initial mesh.

4.2. Loading Scenarios

Experimentally, the crack opening displacements and the mid span deflection of the tested beam were recorded, along with the applied force *F*. The TPB supported beam was tested symmetrically by displacement-controlled loading at the top edge. The typical two different loading scenarios are shown in Figure 5. In the SBFEM simulation, an incrementally increased monotonic load (Figure 5a) was applied with an increment size of 0.0005; there were 200 load steps. The load was controlled by the crack tip opening displacement (CMOD) until failure. In the second loading scenario, Figure 5b, a sequence of loading and unloading cycles was applied to define the CMOD. In this way, detailed characteristics of the post-peak loading and unloading of the load–CMOD curve were obtained. This can help to analyze the damage mechanism involved in the cyclic flexural behavior of concrete.

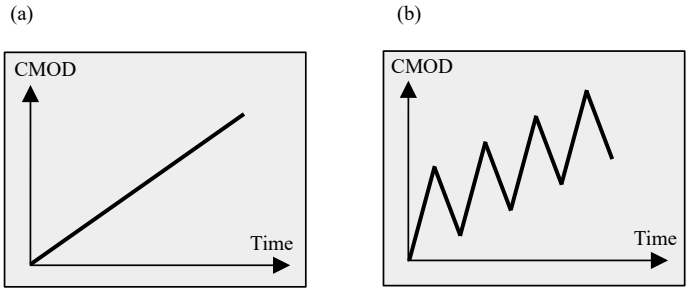

Figure 5. Typical loading scenarios of the studied tested beams: (**a**) monotonic behavior, (**b**) cyclic behavior.

4.3. Monotonic Loading

The softening curve parameters to model the fracture process zone are presented, and a range of values were applied based on the parametric study in Section 3. The material parameters were calibrated for two examples under monotonic loading. Then, the material model was validated using the size-effect calculations. The obtained numerical results for cyclic loading were obtained in additional to validating the method. For this investigation, the properties of the concrete and cohesive interface element are listed in Table 2.

Table 2. Model parameters for concrete cohesive interface element.

Parameter	Denomination	Value	Unit
E	Elastic cohesive modulus	2800.0	[MPa]
$\overline{\sigma}$	Reversibility limit	1.0	[MPa]
K	Isotropic hardening modulus	300.0	[MPa]
γ	Kinematic hardening modulus	200.0	[MPa]
S	Damage strength	2.5×10^{-4}	[MPa]
r	Damage accumulation parameter	1.0	[-]
c	Damage accumulation parameter	0.8	[-]

The tracked points for the notched pattern and the initial mesh were defined as shown in Figure 4b. For the small beam of cross-section height of $h = 200$ mm, the mesh consisted of 481 polygons and 584 nodes. Meanwhile, for the large beam ($h = 400$ mm), the initial mesh comprised 1483 polygons and 1628 nodes. Plane stress conditions were assumed.

Figure 6 compares the predicted load-crack mouth opening displacement (CMOD) of the TBP small beam with the experimental results reported by [8] under monotonic loading. The corresponding curve of the numerical predictions by SBFEM is depicted in Figure 6, plotted as a blue dashed line. The numerical results of the load–CMOD curve are in a good agreement with the experimental measurements. A maximum load of 18.75 kN was obtained at a CMOD of 0.017 mm. Interestingly, the load–CMOD curve of the numerical was not influenced by the length of crack propagation.

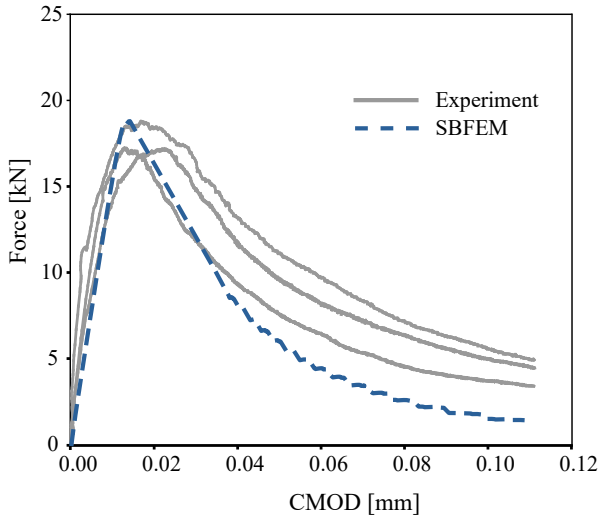

Figure 6. Numerical predictions of load–CMOD curves and the corresponding experimental curves for the single-notched three-point bending test under monotonic loading.

The crack propagation due to increasing load with initial Δ_a = 3.0 mm is shown in Figure 7. Our results show a straight crack path in the direction of the point of external load (F). Th fracture process zone extends up in the middle of the beam Figure 7b at peak load before cracking. At a load of 5.763 kN, the crack propagates in the post-peak region (Figure 7c). For this load level, the cohesive force vanishes. Finally, as the actual crack's length is increased, the fracture zone is shortened, as expected, by increasing the load level; see Figure 7d. The influence of the size of stiffness degradation is depicted for both small and large tests in Figure 8, which shows the numerical predictions, along with experimental measurements of monotonic tests based on [8]. The nominal strength (σ_N) of SBFEM numerical results were determined in the same way in [8] under monotonic behavior. It is calculated by [1,52]:

$$\sigma_N = \frac{c_n F_u}{bh}, \tag{50}$$

where F_u is the ultimate force and $c_n = 3L_0/(2h - h_0)$ is determined by the bending theory for notched beams. Figure 8 depicts a log–log plot of the the relative size of the beam (horizontal axis) and the nominal strength (vertical axis). The numerical results and the experiments of [8] indicate that the nominal strength is increased by decreasing beam size. The numerical results of nominal strength and the experimental data have a ratio of 1.01–1.04 for small beams, and a ratio of 0.98–1.02 for large beams. In addition, less scatter in the predictions of the large beams was obtained.

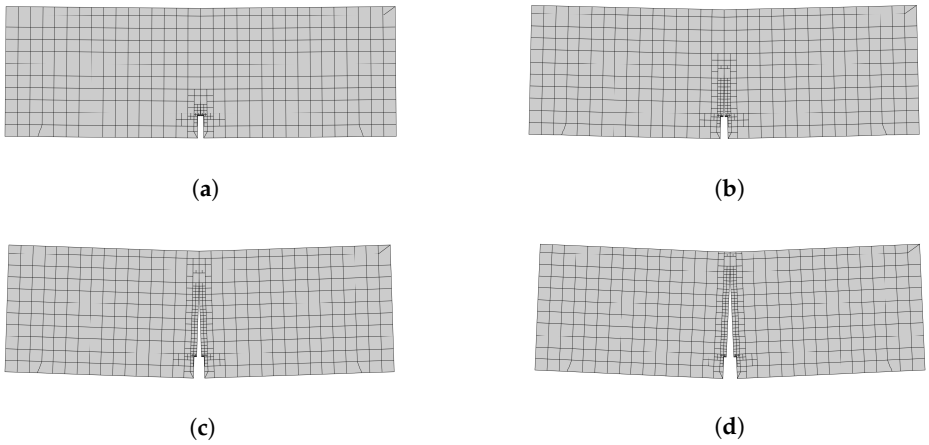

Figure 7. Crack propagation in SBEM subjected to three-point bending tests. (**a**) Load = 8.347 kN (pre-peak), (**b**) load = 18.75 kN (peak load), (**c**) load = 5.763 kN (post-peak), (**d**) load = 2.514 kN (post-peak).

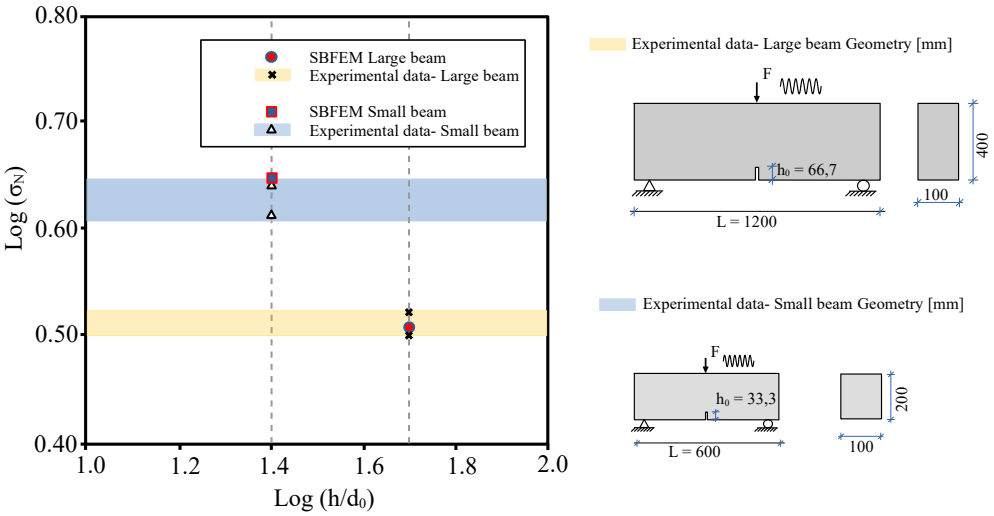

Figure 8. The effect of the size of the beam on the nominal strength under monotonic behavior.

4.4. Cyclic Loading

Figure 5 shows the numerical predictions and the experimental measurements for cyclically increasing loading. The loading was controlled by the CMOD for three unloading cycles and applied until failure. Good agreement of the numerical predictions (Figure 9b) with respect to the experiment tests (Figure 9a) is obvious.

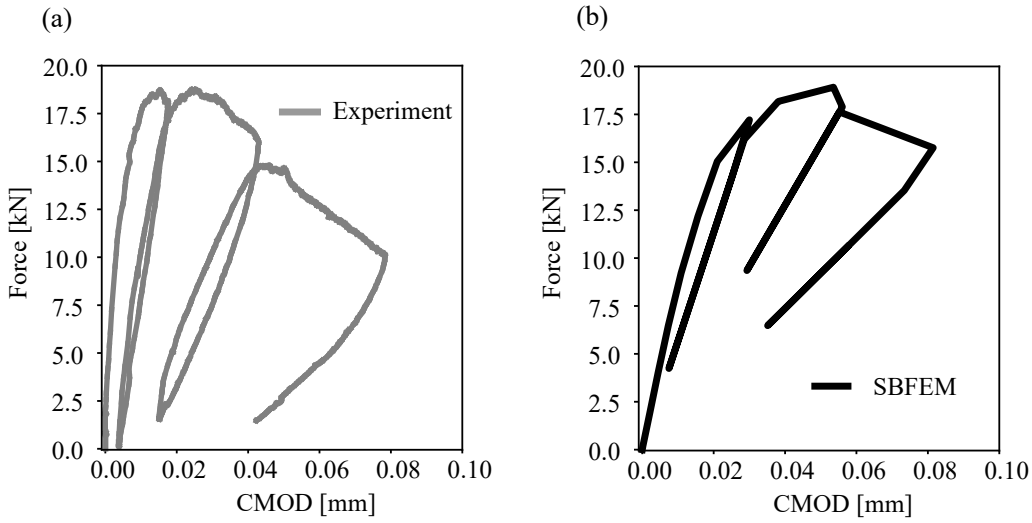

Figure 9. Comparison of numerical predictions (**a**) and experimental measurements (**b**) of Cyclic-CMOD curves for the single-notched three-point bending test.

Furthermore, in our analysis we explore the main dissipative mechanisms. For this purpose, the TPB beams were subjected to a few loading cycles with an incremental increase in the CMOD values. The obtained cyclic responses for both small and large beams are plotted in Figure 10a,b, respectively. One of the principal noticeable effects during the cyclic loading in the post-peak regime is the degradation of the unloading stiffness, which defines the value of the damage. From the damage evolution, it was observed that the damage parameter had a value larger than 0.5 at the first post-peak cyclic load for a small beam; the damage started to progress in the pre-peak subcritical load levels. Furthermore, the damage parameter ω has a value larger than 0.65 for a large beam.

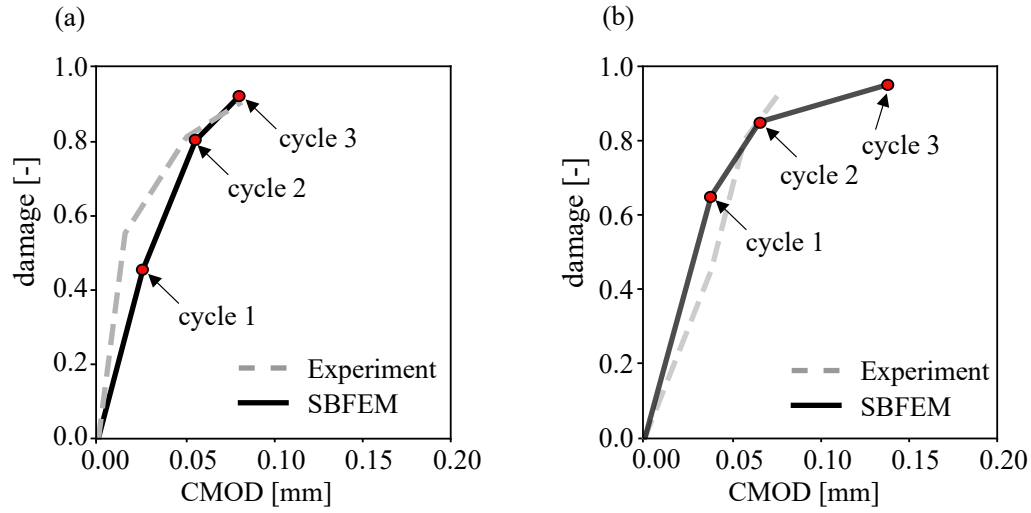

Figure 10. Post-peak cyclic behavior of SBFEM analysis and corresponding damage evolution for (**a**) a small beam and (**b**) a large beam.

This is explained by knowing that the developed crack showed a rough surface that is not fully closed during the unloading of the specimen. This was confirmed for the cyclic behavior in the simulation of SBFEM and experiment tests. Additionally, the stiffness degradation and the growth of unclosed crack openings were characterized for both sizes.

Plots of K_I-$CMOD$ are shown in Figure 11 for monotonic and cyclic applied loads. In Figure 11a, the points that represent the initial mesh of Figure 4 were calculated once $K_I \geq 0$. Then, the crack opened gradually based on a crack-propagation criterion. The

numerical calculation of K_I by SBFEM with a fewer degrees of freedom (DOFs) manifested good crack trajectory predictions.

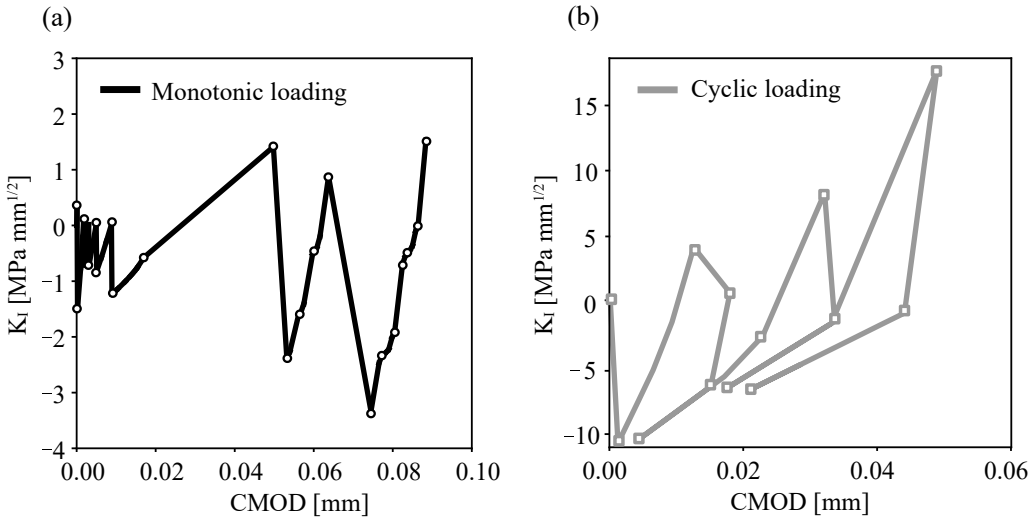

Figure 11. $K_I - CMOD$ and loading-point curves for mode-I bending beam for: monotonic loading (**a**) and cyclic loading (**b**).

Since the goal of the present study was to apply the constitutive law with a cumulative damage feature within SBFEM, we considered only mode-I cyclic crack propagation in our analysis. Further studies with applications to mixed modes loading are planned for future publications, where more advanced constitutive cohesive zone models could be used, e.g., [14,56].

5. Conclusions

Cracks in concrete can occur when the tensile stresses imposed by actions exceed the tensile strength of the material. Furthermore, the cracks can also be initiated under repeated loads with stress levels below the tensile strength. In this work, the cyclic cohesive crack procedure-based SBFEM was implemented to study the crack propagation in concrete. The proposed model showed the ability to simulate the monotonic and cyclic behavior of a cohesive crack interface element, e.g., a concrete interface. It provided a realistic prediction of cyclic damage behavior for up to several load cycles. The output for the numerical simulation of monotonic loading analysis showed full agreement with experimental data from the literature. The results differed 5% for the maximum peak force. Regarding the nominal strength, the ratio of the numerical results to the experimental data under monotonic loading varied between 1.01 and 1.04 for small beams. The ratio was 0.98–1.02 for large beams.

Additionally, the proposed procedure has been proved to be an efficient tool for estimating the damage level. The level of damage accumulation (ω) and material plasticity variables were calculated based on thermodynamics. The described damage model has been successfully implemented to describe the cyclic behavior of cohesive interface elements using SBFEM. The damage parameter ω has a value larger than 0.5 at the first post-peak cyclic load for a small beam, and has a value larger than 0.65 for a large beam. The cyclic responses obtained by SBFEM for both small and large beams presented good agreement with the experimental data.

The predicted load–CMOD responses in the validation examples were within the range measured in the cyclic and monotonic loading experiments. Testing results demonstrated that the most important factors for the overall simulation were the thermodynamic hardening modulus γ and the damage strength parameter S. The simulations executed to study the effect of the loading sequence offered successful results and demonstrated the effect of damage accumulation for realistic predictions for concrete structures.

Author Contributions: Methodology, O.A., C.K., E.T.O. and K.M.H.; Validation, O.A., C.K., E.T.O. and K.M.H.; Writing—original draft, Omar Alrayes, Carsten Könke, E.T.O. and K.M.H. All authors have read and agreed to the published version of the manuscript.

Funding: This research was funded by Deutsche Forschungsgemeinschaft (DFG, German Research Foundation)- Projektnummer 492535144.

Institutional Review Board Statement: Not applicable.

Informed Consent Statement: Not applicable.

Data Availability Statement: Not applicable.

Acknowledgments: Khader M. Hamdia thanks the support by Deutsche Forschungsgemeinschaft (DFG, German Research Foundation)—Projektnummer 492535144.

Conflicts of Interest: The authors declare no conflict of interest.

Nomenclature

η, ξ	Local coordinate system of SBFEM
$\{t\}$	Traction cohesive force vector
r, θ	Polar coordinate
Δ_a	Crack propagation length
L	Crack length
K_{int}	Stiffens matrix of interface element
$[J]$	Jacobian matrix on boundary
t	Crack thickness
$N(\eta)$	Nodal shape function
k	Stiffens matrix of the domain
u	Displacement field
d, w, s	Displacements on the crack faces
ε	Strain field
A	Crack surface area
D	Material constitutive matrix
w_i	Gaussian weight function
P	Equivalent nodal load vector
n	Number of integration points
$[E_0], [E_1], [E_2]$	Coefficient matrices of SBFEM system
F_n, F_s	Normal and shear cohesive traction forces
Z	Hamiltonian matrix
F_t	Nodal side face load
q	Internal nodal force vector
K_I, K_{II}	Crack mode I & mode II stress intensity factors
λ	Eigenvalue matrices
ϕ_t	Nodal displacement mode
e_i	Coefficent
ϕ	Eigenvector matrices
c	Integration constants of the SBFEM
$[B_1], [B_2]$	Strain-displacement matrices of SBFEM system
M	Number of displacement modes
σ	Stress field
$\{.\}$	Vector
$[.]$	Matrix
$[.]^T$	Transpose of Matrix
$[.]^{-1}$	Inverse of matrix
$\|\|.\|\|$	Norm of function, vector of matrix
δ	Crack angle
u_{bs}	Boundary nodal displacement

Thermodynamic Parameters	
ρ	Material density
E, ν	Elastic stiffness matrix, Possion's ratio
Y	Energy release rate
γ, K	Isotropic and kinematic hardening moduli
X, Z	Thermodynamic hardening forces
ω	Damage variable
α, z	Hardening material variables
c, r	Exponential damage parameters
S	Damage strength parameter
τ	Reversibility limit parameter

References

1. Bazant, Z.P.; Xu, K. Size effect in fatigue fracture of concrete. *ACI Mater. J.* **1991**, *88*, 390–399.
2. Bazant, Z.P.; Schell, W.F. Fatigue fracture of high-strength concrete and size effect. *ACI Mater. J.* **1993**, *90*, 472–472.
3. Gan, Y.; Zhang, H.; Zhang, Y.; Xu, Y.; Schlangen, E.; van Breugel, K.; Šavija, B. Experimental study of flexural fatigue behaviour of cement paste at the microscale. *Int. J. Fatigue* **2021**, *151*, 106378. [CrossRef]
4. Li, D.; Huang, P.; Chen, Z.; Yao, G.; Guo, X.; Zheng, X.; Yang, Y. Experimental study on fracture and fatigue crack propagation processes in concrete based on DIC technology. *Eng. Fract. Mech.* **2020**, *235*, 107166. [CrossRef]
5. Paris, P.C. A rational analytic theory of fatigue. *Trend Eng.* **1961**, *13*, 9.
6. Bhowmik, S.; Ray, S. An improved crack propagation model for plain concrete under fatigue loading. *Eng. Fract. Mech.* **2018**, *191*, 365–382. [CrossRef]
7. Nguyen, O.; Repetto, E.; Ortiz, M.; Radovitzky, R. A cohesive model of fatigue crack growth. *Int. J. Fract.* **2001**, *110*, 351–369. [CrossRef]
8. Baktheer, A.; Becks, H. Fracture mechanics based interpretation of the load sequence effect in the flexural fatigue behavior of concrete using digital image correlation. *Constr. Build. Mater.* **2021**, *307*, 124817. [CrossRef]
9. Sancho, J.M.; Planas, J.; Cendón, D.A.; Reyes, E.; Gálvez, J. An embedded crack model for finite element analysis of concrete fracture. *Eng. Fract. Mech.* **2007**, *74*, 75–86. [CrossRef]
10. Unger, J.F.; Eckardt, S.; Könke, C. Modelling of cohesive crack growth in concrete structures with the extended finite element method. *Comput. Methods Appl. Mech. Eng.* **2007**, *196*, 4087–4100.
11. Yang, B.; Mall, S.; Ravi-Chandar, K. A cohesive zone model for fatigue crack growth in quasibrittle materials. *Int. J. Solids Struct.* **2001**, *38*, 3927–3944. [CrossRef]
12. Dekker, R.; van der Meer, F.; Maljaars, J.; Sluys, L. A cohesive XFEM model for simulating fatigue crack growth under mixed-mode loading and overloading. *Int. J. Numer. Methods Eng.* **2019**, *118*, 561–577. [CrossRef]
13. Turon, A.; Costa, J.; Camanho, P.P.; Dávila, C.G. *Simulation of Delamination Propagation in Composites under High-Cycle Fatigue by Means of Cohesive-Zone Models*; Technical report; NASA Langley Research Center: Hampton, VA, USA, 2006. Available online: https://ntrs.nasa.gov/search.jsp?R=20070004889 (accessed on 24 August 2013).
14. Harper, P.W.; Hallett, S.R. A fatigue degradation law for cohesive interface elements—Development and application to composite materials. *Int. J. Fatigue* **2010**, *32*, 1774–1787. [CrossRef]
15. Kirane, K.; Bažant, Z.P. Microplane damage model for fatigue of quasibrittle materials: Sub-critical crack growth, lifetime and residual strength. *Int. J. Fatigue* **2015**, *70*, 93–105. [CrossRef]
16. Titscher, T.; Unger, J.F. Efficient higher-order cycle jump integration of a continuum fatigue damage model. *Int. J. Fatigue* **2020**, *141*, 105863. [CrossRef]
17. Carrara, P.; Ambati, M.; Alessi, R.; De Lorenzis, L. A framework to model the fatigue behavior of brittle materials based on a variational phase-field approach. *Comput. Methods Appl. Mech. Eng.* **2020**, *361*, 112731. [CrossRef]
18. Seleš, K.; Aldakheel, F.; Tonković, Z.; Sorić, J.; Wriggers, P. A general phase-field model for fatigue failure in brittle and ductile solids. *Comput. Mech.* **2021**, *67*, 1431–1452. [CrossRef]
19. Golahmar, A.; Kristensen, P.K.; Niordson, C.F.; Martínez-Pañeda, E. A phase field model for hydrogen-assisted fatigue. *Int. J. Fatigue* **2022**, *154*, 106521. [CrossRef]
20. Khalil, Z.; Elghazouli, A.Y.; Martínez-Pañeda, E. A generalised phase field model for fatigue crack growth in elastic–plastic solids with an efficient monolithic solver. *Comput. Methods Appl. Mech. Eng.* **2022**, *388*, 114286. [CrossRef]
21. Karimi, M.; Abrinia, K.; Hamdia, K.M.; Hashemianzadeh, S.M.; Baniassadi, M. Effects of functional group type and coverage on the interfacial strength and load transfer of graphene-polyethylene nanocomposites: A molecular dynamics simulation. *Appl. Phys. A* **2022**, *128*, 341. [CrossRef]
22. Nguyen, N.H.; Bui, H.H.; Kodikara, J.; Arooran, S.; Darve, F. A discrete element modelling approach for fatigue damage growth in cemented materials. *Int. J. Plast.* **2019**, *112*, 68–88. [CrossRef]
23. Baktheer, A.; Chudoba, R. Classification and evaluation of phenomenological numerical models for concrete fatigue behavior under compression. *Constr. Build. Mater.* **2019**, *221*, 661–677. [CrossRef]
24. Alliche, A. Damage model for fatigue loading of concrete. *Int. J. Fatigue* **2004**, *26*, 915–921. [CrossRef]

25. Kindrachuk, V.M.; Thiele, M.; Unger, J.F. Constitutive modeling of creep-fatigue interaction for normal strength concrete under compression. *Int. J. Fatigue* **2015**, *78*, 81–94. [CrossRef]
26. Desmorat, R.; Ragueneau, F.; Pham, H. Continuum damage mechanics for hysteresis and fatigue of quasi-brittle materials and structures. *Int. J. Numer. Anal. Methods Geomech.* **2007**, *31*, 307–329. [CrossRef]
27. Baktheer, A.; Aguilar, M.; Chudoba, R. Microplane fatigue model MS1 for plain concrete under compression with damage evolution driven by cumulative inelastic shear strain. *Int. J. Plast.* **2021**, *143*, 102950. [CrossRef]
28. Baktheer, A.; Aguilar, M.; Hegger, J.; Chudoba, R. Microplane damage plastic model for plain concrete subjected to compressive fatigue loading. In Proceedings of the 10th International Conference on Fracture Mechanics of Concrete and Concrete Structures, FraMCoS-X, Bayonne, France, 24–26 June 2019. [CrossRef]
29. Ueda, M.N.; Konishi, H.O. Quasi-Visco-Elasto-Plastic Constitutive Model of Concrete for Fatigue Simulation. In Proceedings of the International Conference on Fracture Mechanics of Concrete and Concrete Structures (FraMCoS-X), Bayonne, France, 24–26 June 2019. [CrossRef]
30. Baktheer, A.; Camps, B.; Hegger, J.; Chudoba, R. Numerical and experimental investigations of concrete fatigue behaviour exposed to varying loading ranges. In Proceedings of the Fib Congress, Melbourne, Australia, 7–11 October 2018; pp. 1110–1123, ISBN 978-1-877040-15-3.
31. Daneshvar, M.H.; Saffarian, M.; Jahangir, H.; Sarmadi, H. Damage identification of structural systems by modal strain energy and an optimization-based iterative regularization method. *Eng. Comput.* **2022**, 1–21. [CrossRef]
32. Heek, P.; Ahrens, M.A.; Mark, P. Incremental-iterative model for time-variant analysis of SFRC subjected to flexural fatigue. *Mater. Struct.* **2017**, *50*, 1–15. [CrossRef]
33. Krätzig, W.B.; Pölling, R. An elasto-plastic damage model for reinforced concrete with minimum number of material parameters. *Comput. Struct.* **2004**, *82*, 1201–1215. [CrossRef]
34. Song, C.; Wolf, J.P. The scaled boundary finite-element method—alias consistent infinitesimal finite-element cell method—For elastodynamics. *Comput. Methods Appl. Mech. Eng.* **1997**, *147*, 329–355. [CrossRef]
35. Ooi, E.; Yang, Z. Modelling multiple cohesive crack propagation using a finite element–scaled boundary finite element coupled method. *Eng. Anal. Bound. Elem.* **2009**, *33*, 915–929. [CrossRef]
36. Song, C.; Ooi, E.T.; Natarajan, S. A review of the scaled boundary finite element method for two-dimensional linear elastic fracture mechanics. *Eng. Fract. Mech.* **2018**, *187*, 45–73. [CrossRef]
37. Daneshyar, A.; Sotoudeh, P.; Ghaemian, M. The scaled boundary finite element method for dispersive wave propagation in higher-order continua. *Int. J. Numer. Methods Eng.* **2022**. [CrossRef]
38. Ooi, E.T.; Song, C.; Tin-Loi, F.; Yang, Z. Polygon scaled boundary finite elements for crack propagation modelling. *Int. J. Numer. Methods Eng.* **2012**, *91*, 319–342. [CrossRef]
39. Ooi, E.; Shi, M.; Song, C.; Tin-Loi, F.; Yang, Z. Dynamic crack propagation simulation with scaled boundary polygon elements and automatic remeshing technique. *Eng. Fract. Mech.* **2013**, *106*, 1–21. [CrossRef]
40. Ooi, E.; Natarajan, S.; Song, C.; Ooi, E. Crack propagation modelling in concrete using the scaled boundary finite element method with hybrid polygon–quadtree meshes. *Int. J. Fract.* **2017**, *203*, 135–157. [CrossRef]
41. Yang, Z. Fully automatic modelling of mixed-mode crack propagation using scaled boundary finite element method. *Eng. Fract. Mech.* **2006**, *73*, 1711–1731. [CrossRef]
42. Qu, Y.; Zou, D.; Kong, X.; Yu, X.; Chen, K. Seismic cracking evolution for anti-seepage face slabs in concrete faced rockfill dams based on cohesive zone model in explicit SBFEM-FEM frame. *Soil Dyn. Earthq. Eng.* **2020**, *133*, 106106. [CrossRef]
43. Yang, Z.; Deeks, A. Fully-automatic modelling of cohesive crack growth using a finite element–scaled boundary finite element coupled method. *Eng. Fract. Mech.* **2007**, *74*, 2547–2573. [CrossRef]
44. Rabczuk, T.; Zi, G. A meshfree method based on the local partition of unity for cohesive cracks. *Comput. Mech.* **2007**, *39*, 743–760. [CrossRef]
45. Jiang, X.; Zhong, H.; Li, D.; Chai, L. Dynamic Fracture Modeling of Impact Test Specimens by the Polygon Scaled Boundary Finite Element Method. *Int. J. Comput. Methods* **2022**, 2143010. [CrossRef]
46. Baktheer, A.; Chudoba, R. Pressure-sensitive bond fatigue model with damage evolution driven by cumulative slip: Thermodynamic formulation and applications to steel-and FRP-concrete bond. *Int. J. Fatigue* **2018**, *113*, 277–289. [CrossRef]
47. Deeks, A.J.; Wolf, J.P. A virtual work derivation of the scaled boundary finite-element method for elastostatics. *Comput. Mech.* **2002**, *28*, 489–504. [CrossRef]
48. Wolf, J.P.; Song, C. The scaled boundary finite-element method–a fundamental solution-less boundary-element method. *Comput. Methods Appl. Mech. Eng.* **2001**, *190*, 5551–5568. [CrossRef]
49. Man, H.; Song, C.; Natarajan, S.; Ooi, E.T.; Birk, C. Towards automatic stress analysis using scaled boundary finite element method with quadtree mesh of high-order elements. *arXiv* **2014**, arXiv:1402.5186.
50. Egger, A.W.; Triantafyllou, S.P.; Chatzi, E.N. The Scaled Boundary Finite Element Method for the Efficient Modeling of Linear Elastic Fracture. In Proceedings of the 9th International Conference on Fracture Mechanics of Concrete and Concrete Structures FraMCoS-9 V, Berkeley, CA, USA, 28 May–1 June 2016.
51. Song, C.; Wolf, J.P. Semi-analytical representation of stress singularities as occurring in cracks in anisotropic multi-materials with the scaled boundary finite-element method. *Comput. Struct.* **2002**, *80*, 183–197. [CrossRef]
52. Bazant, Z.P.; Li, Y.N. Stability of Cohesive Crack Model: Part I—Energy Principles. *J. Appl. Mech.* **1995**, *62*, 959–964. [CrossRef]

53. Baktheer, A.; Chudoba, R. Modeling of bond fatigue in reinforced concrete based on cumulative measure of slip. In Proceedings of the Computational Modelling of Concrete Structures, EURO-C 2018, Bad Hofgastein, Austria, 26 February–1 March 2018; CRC Press: Boca Raton, FL, USA, 2018, pp. 767–776. [CrossRef]
54. Baktheer, A.; Spartali, H.; Hegger, J.; Chudoba, R. High-cycle fatigue of bond in reinforced high-strength concrete under push-in loading characterized using the modified beam-end test. *Cem. Concr. Compos.* **2021**, *118*, 103978. [CrossRef]
55. Wunderlich, W.; Stein, E.; Bathe, K.J. *Nonlinear Finite Element Analysis in Structural Mechanics: Proceedings of the Europe-US Workshop Ruhr-Universität Bochum, Germany, 28–31 July 1980*; Springer Science & Business Media: Berlin/Heidelberg, Germany, 2013.
56. Chudoba, R.; Vořechovský, M.; Aguilar, M.; Baktheer, A. Coupled sliding–decohesion–compression model for a consistent description of monotonic and fatigue behavior of material interfaces. *Comput. Methods Appl. Mech. Eng.* **2022**, *398*, 115259. [CrossRef]

materials

MDPI

Article

Investigation on Performance of Hydraulically Expanded Joint of Titanium–Steel Clad Tubesheet

Jia Li [1], Juan Li [1], Yuyan Zhang [1] and Changyu Zhou [2,*]

[1] School of Mechanical and Electronic Engineering, Nanjing Forestry University, Nanjing 210037, China
[2] School of Mechanical and Power Engineering, Nanjing Tech University, Nanjing 211816, China
* Correspondence: changyu_zhou@163.com

Abstract: The performance of a hydraulically expanded joint between tubesheet and titanium tube was analyzed using a finite element numerical calculation. The connection strength of Q345R tubesheet and TA2-Q345R clad tubesheet was studied using a tight expansion method. The results proved that the residual contact pressure and pullout force of the tight expansion joint of TA2-Q345R clad tubesheet were greater than those of the Q345R tubesheet. However, the residual contact pressure of the expanded joint without a groove for the TA2-Q345R tubesheet and the pullout force failed to meet the requirement of connection strength. Hence, the groove was employed on the contact surface. The influences of groove position and groove width on the connection strength of the expanded joint with grooves in tubesheet hole were studied. The results show that the residual contact pressure of the clad tubesheet of grooving in the cladding layer was higher than that of grooving in the base layer. The effect of the position of groove in the cladding layer and base layer on the residual contact pressure could be neglected. A wider groove led to a higher residual contact pressure, which increased significantly when the groove width was 4 mm.

Keywords: TA2-Q345R clad tubesheet; expanded joint; residual contact pressure; groove width

Citation: Li, J.; Li, J.; Zhang, Y.; Zhou, C. Investigation on Performance of Hydraulically Expanded Joint of Titanium–Steel Clad Tubesheet. *Materials* **2023**, *16*, 1106. https://doi.org/10.3390/ma16031106

Academic Editors: Michele Bacciocchi, Angelo Marcello Tarantino, Raimondo Luciano and Carmelo Majorana

Received: 13 December 2022
Revised: 20 January 2023
Accepted: 22 January 2023
Published: 27 January 2023

1. Introduction

Titanium is an alloy with low density, high strength, and strong corrosion resistance, which is widely used in the chemical industry, marine ships, aviation, medical instruments, automotive industry, livelihood supplies, and other fields [1,2]. Because of its good economic and applicability, titanium-steel clad tubeplate structures are applied in titanium shells and tube heat exchangers.

The joint between the tube and tubesheet is the key part of the shell and tube heat exchanger, which is also prone to failure. Expansion is an important type of connection between the tube and tubesheet, which can be divided into hydraulic expansion, mechanical expansion, and explosion expansion. Among them, hydraulic expansion is a uniform flexible expansion method. The expansion pressure is easy to control and does not damage the inner wall surface of the expansion; thus, the joint is of good quality.

How to improve the sealing performance and tensile resistance of hydraulic expanded joints has always been the focus of research. Therefore, many research achievements have been made on the influence of material properties [3,4], machining accuracy [5,6], geometric parameters [7,8], manufacturing process [9,10], and other factors on the performance of joints. In order to improve the connection strength and sealing performance of the tube-to-tubesheet joints, tubesheet holes are grooved [11,12]. Material properties, especially plasticity, play a crucial role in obtaining accurate results close to true values [7]. Before finite element analysis, it is important to determine material properties such as yield stress [13]. Previous studies have shown that strain hardening is an important factor influencing the accuracy of joint numerical analysis results [14,15]. Previous studies mainly focused on the combination of a carbon steel tube and low-alloy steel tube sheet, or the

combination of a titanium tube and single-material tube sheet. For the combination of titanium tube and titanium–steel clad tubesheet, we can find reports on the stress analysis [16,17], creep of titanium [18], etc. However, there are few reports on the impact of the titanium–steel clad tubesheet cladding layer and grooving parameters on the performance of expanded joints. Jawad et al. [7] used experimental methods to study the expanded joint of titanium–steel clad tubesheet; the best result was obtained when the groove width was equal to $1.56\sqrt{r_o t}$, where r_o and t are the outside radius and thickness of the tube, respectively. The residual contact stress of titanium–steel clad tubesheet with a groove in the base layer was calculated by numerical simulation [19]. The above studies did not discuss the influence of groove form on titanium–steel clad tubesheet joint performance. By means of an experiment, Ma Qiulin [20] found that TA2 had the characteristic of elastic hysteresis after loading, and its residual contact pressure decreased with the increase in time after the completion of titanium tube expansion. Subsequently, the experimental results of the same research team [21] showed that, under 260 MPa hydraulic expansion pressure, after 96 h of unloading the expansion pressure, the pullout force of the joint decreased by 60% and 23%, corresponding to the expanded joint without grooves in the tubesheet hole and with two grooves in the tubesheet hole, respectively. Therefore, the residual contact pressure at the moment of expansion completion should not be used as the only basis for analyzing the performance of expanded joints, and the negative effect caused by elastic hysteresis should also be considered. Therefore, in this paper, the hydraulic expanded tube joint of a titanium–steel clad tubesheet is taken as the research object. Through numerical simulation, the sealing performance and connection strength of the tight expansion (joint without groove) are studied; furthermore, the joint with grooves is analyzed. The influence of the expansion method and structural parameters, including groove form, groove width, and groove location in the base, is investigated, which provides a basis for the optimization of the expansion structure of the clad tubesheet.

2. Finite Element Model Analysis

2.1. Material Performance

The tube was made of commercial pure titanium TA2, and the titanium–steel clad tubesheet material was TA2-Q345R, in which the base material was Q345R and the cladding material was TA2. The physical properties of the two materials are shown in Table 1. The true stress and strain of material were simulated using multilinear isotropic reinforcement material, and their mechanical property curves are shown in Figure 1.

Table 1. Material properties.

Material	Yield Strength, σ_s (MPa)	Elasticity Modulus, E ($\times 10^5$ MPa)	Poisson's Ratio, μ
TA2	380	1.1	0.41
Q345R	347	1.95	0.3

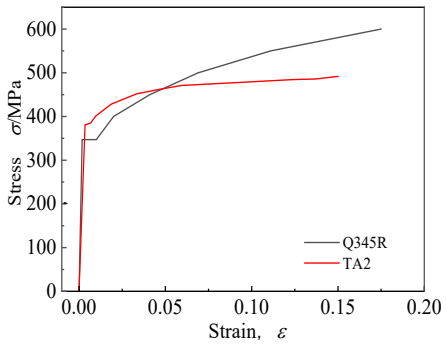

Figure 1. Tensile property curves of materials.

2.2. Finite Element Model

The tubes were arranged in regular triangles. Due to the periodicity of pipe drainage, a seven-hole model was adopted, and 1/12 of the circle, i.e., a 30° area, was taken as the research object, as shown in Figure 2a. The size of the tube was φ25 mm × 1.5 mm, and the length of the tube was 180 mm. The diameter of the tubesheet hole was 25.3 mm, the distance between the tube centers was 32 mm, the outer diameter of the tubesheet was 480 mm, and the total thickness of the tubesheet was 50 mm with a 38 mm base layer and a 12 mm cladding layer, conforming to the recommended scope of the standard [22].

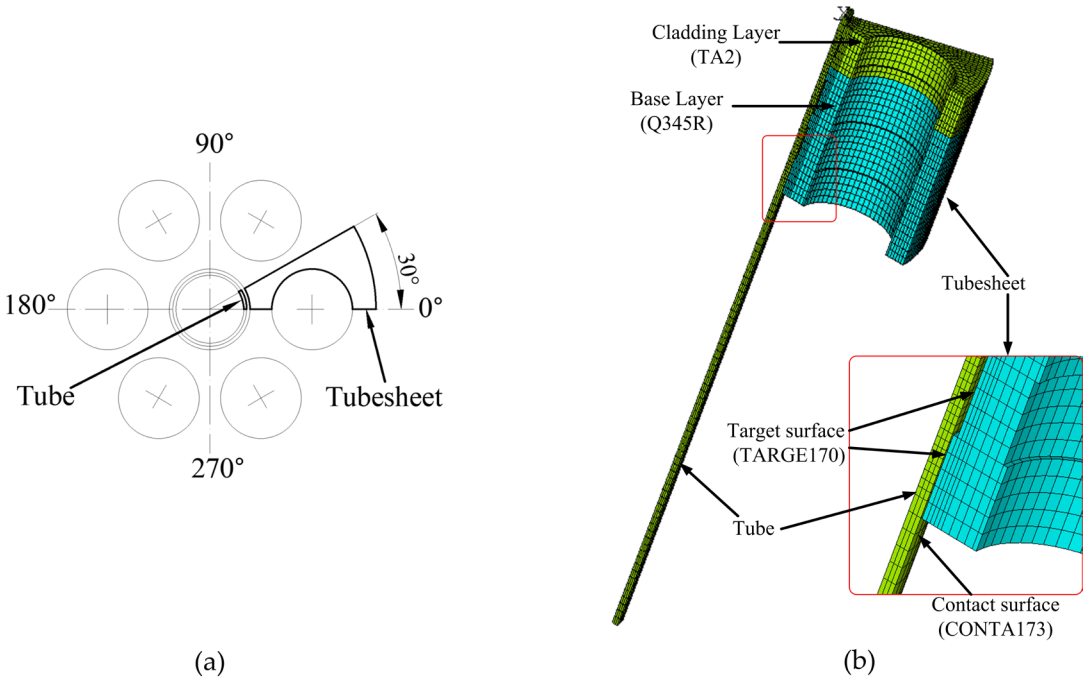

Figure 2. Finite element analysis: (**a**) analysis scope; (**b**) finite element mesh model.

Because the overall structure of all joints was similar, only the finite element model of the joint with grooved clad tubesheet holes is shown in this manuscript. The SOLID185 element was used to establish the finite element model of the expanded joint, as shown in Figure 2b. The mesh was finely divided near the expansion surface. The combination of the outer wall of the titanium tube and the inner wall of the tubesheet hole was a nonlinear contact problem. The outer wall of the titanium tube was the contact surface, and the CONTA173 contact surface element was selected. The inner wall of the tubesheet hole was the target surface, and the TARGE170 target surface element was selected. The contact algorithm adopted the Augmented Lagrange method, and the appropriate solution value was guaranteed by controlling the contact stiffness FKN and the maximum allowable penetration value FTOLN [23,24].

During expansion, expansion pressure was applied on the inner surface of tube; the tube end was subjected to axial and circumferential symmetric constraints, whereas the outer cylindrical surface of the tubesheet was axially constrained, and the remaining surfaces were free.

After expansion, the expansion pressure on the tube was removed. Under the pulling condition, the axial displacement constraint of the tube was removed, axial (Z-direction) displacement was applied, and the other boundary conditions remained unchanged. During calculation, an automatic step and large deformation were chosen, and a linear search to stabilize the calculation and the complete Newton–Rapson method were used.

3. Tight Expansion Analysis

3.1. Theoretical Calculation Method

Yan Huigeng's [25] theoretical calculation method of residual contact pressure based on the double-cylinder model is widely used for the calculation of residual contact pressure of the tight expansion, as shown in Equation (1).

$$p_c^* = (1-2c)p_i - \frac{2}{\sqrt{3}}\sigma_{st}\ln K_t, \tag{1}$$

Here,

$$c = 1/\left\{K_t^2(1-\mu_t) + 1 + \mu_t + \frac{E_t(K_t^2-1)}{E_s(K_s^2-1)}[1-\mu_s + K_s^2(1+\mu_s)]\right\},$$

where σ_{st} is the yield strength of the tube material (MPa), $K_t = r_o/r_i$ is the diameter ratio of the heat exchanger tube, r_o, r_i are respectively the inner and outer diameters of the heat exchanger tube, $K_s = R_o/R_i$ is the diameter ratio of the equivalent cylinder, R_o, R_i are respectively the inner and outer diameters of the equivalent cylinder, μ_t, μ_s are the Poisson's ratios of the tube and tubesheet material, respectively, and E_t, E_s are respectively the elastic moduli of the tube and tubesheet material (MPa).

However, Yan Huigeng's theoretical calculation method assumes that the tube material is an ideal elastic–plastic material, and σ_{st} in Equation (1) is the yield strength of the tube material without considering the strain strengthening of the material; thus, the theoretically calculated value of p_c^* is greater than the real value. Hao Junwen [13] proposed the concept of pipe equivalent yield strength σ_{seq} according to the research methods of predecessors [25], i.e., replacing σ_{st} in Equation (1) with σ_{seq}, as shown in Figure 3.

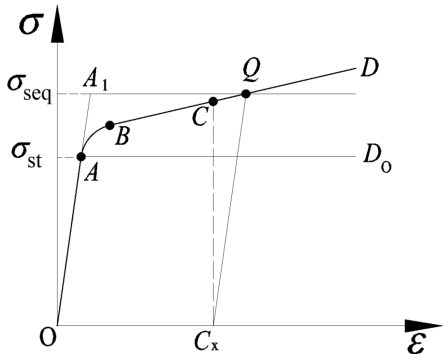

Figure 3. Schematic diagram for determining the equivalent yield strength.

As shown in Figure 3, the curve $\overline{OABCD}$ represents the true stress–strain curve of the titanium tube. The section $\overline{OA}$ is the elastic deformation stage, the section $\overset{\frown}{AB}$ is the partial plastic deformation stage, and the section $\overline{BD}$ is the full strain strengthening stage. Assuming that the tube contacts the tubesheet when the stress and strain develop to point C, and that the abscissa $C_x = g/r_o$ corresponding to point C is the strain value of the outer wall of the tube, g is the clearance between the outer wall of the tube and the inner wall of the hole. By making a straight line with a slope of E_t through the C_x point, the straight line intersects the curve at point Q. Then, the ordinate Q_y corresponding to point Q is the equivalent yield strength of the tube material σ_{seq}. According to the tensile curve of TA2 in Figure 1, σ_{seq} = 415 MPa, which is 35 MPa different from the original value of 380 MPa.

3.2. Comparison of Simulation Results and Theoretical Calculation Results

The experiment and numerical simulation results show that the friction coefficient f is related to many factors such as the accuracy of the machined surface and the properties of materials. According to the experimental data of the expansion connection between TA2

tube and Q345R tubesheet in the literature [20], the friction coefficient f was set to 0.28. The p_c^* with tube material TA2 and tubesheet material Q345R was simulated, and the results were respectively compared with the theoretical results of Yan [25] and Hao [13], as shown in Figure 4. It can be seen that the simulation value was much smaller than the value of Yan's theoretical method, and it was mainly consistent with the result of Hao's theoretical method, which is closer to the real situation. Therefore, the parameters of the simulation and the results were considered reasonable.

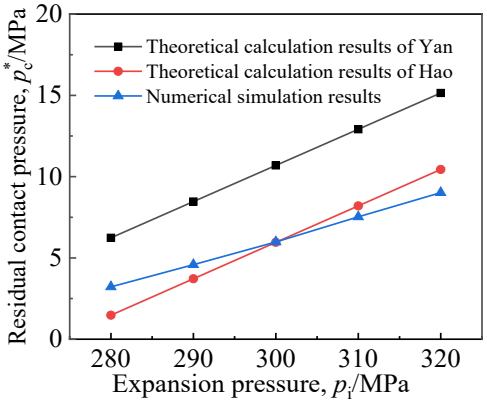

Figure 4. Comparison of calculation results [13,25].

3.3. Performance Analysis of Tight Expansion Joint

In order to investigate the influence of the cladding surface on the sealing performance of the expansion joint, the expansion and pulling processes of the joints between the TA2 tube and Q345R tubesheet, and between the TA2 tube and TA2-Q345R clad tubesheet under different expansion pressures were simulated. The average p_c^* on the contact surface and pullout force F were obtained, as shown in Figure 5.

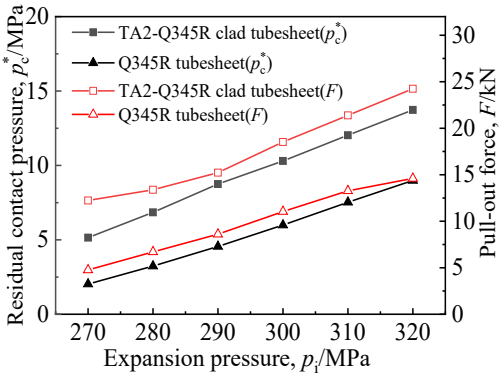

Figure 5. Tight expansion joints performance of two kinds of tubesheets.

It can be seen from Figure 5 that p_c^* and F of expanded joints of different materials increased with the increase in expansion pressure, and p_c^* and F of the TA2-Q345R clad tubesheet were both higher than those of the Q345R tubesheet under the same expansion pressure.

The pullout force provided by the expanded joint is expressed in Equation (2).

$$F > \pi dl[q]. \quad (2)$$

According to GB/T151-2014 "Heat Exchanger" [26], the allowable pullout force $[q]$ of the steel heat exchange tube of tight expansion is 2 MPa; thus, the pullout force should satisfy $F > 7.23$ kN according to Equation (2). For titanium expansion joints, the pullout force decreases with the time after the expansion due to the elastic hysteresis effect. A previous study [21] gave the relationship curve between the pullout force and time after the

expansion of the titanium tube and steel tubesheet. Considering that the pullout force of the joint decreases by about 75% during the period from the completion of manufacturing until service, the corresponding pullout force of the titanium tube should be greater than 28.92 kN at the moment of completion of the expansion. As can be seen from Figure 5, the pullout force of the joint still failed to meet this requirement even when the expansion pressure exceeded 320 MPa.

Figure 6 shows the contact pressure distribution on the contact surface of the TA2-Q345R clad tubesheet or Q345R tubesheet after loading and after unloading. According to Figure 6a,c, when the expansion pressure reached 320 MPa, there were two upper and lower sealing rings on the contact surface of the two tubesheet conditions, consistent with the simulation results in [4,27]. When the expansion pressure was unloaded, it can be seen from Figure 6b,d that there was a residual contact pressure ring on the contact surface of the tube side, but this was not obvious on the shell side. This is because the stiffness of the tube on the shell side was greater than that on the tube side; hence, it was not easy to expand and deform. It can also be found from Figure 6b,d that the residual contact pressure of the sealing ring of the TA2-Q345R clad tubesheet after unloading was greater than that of the Q345R tubesheet (57.9 MPa > 24.7 MPa) because the cladding layer of the clad tubesheet and the tube were the same material TA2. When the expansion pressure was removed, the tubesheet rebounded with the tube; thus, the contact pressure of the cladding part could maintain high values. Therefore, although the contact pressure of the base part decreased substantially because the elastic modulus of TA2 was less than that of Q345R, the average residual contact pressure in the whole contact range of the clad tubesheet was higher because the residual contact pressure of the cladding part was high, and the corresponding pullout force was also higher.

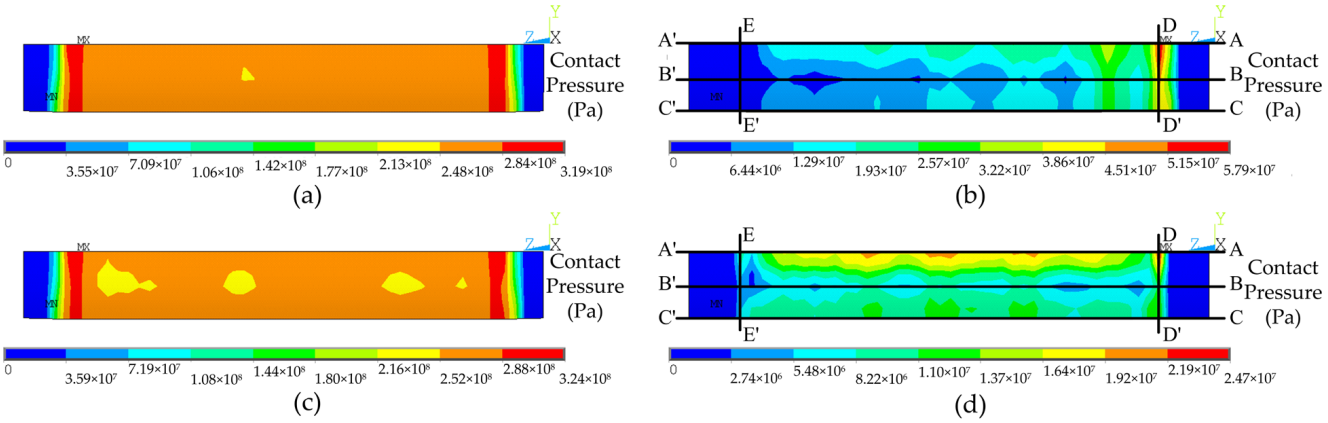

Figure 6. Contact pressure distribution on the contact surface of two kinds of tubesheets: (**a**) TA2-Q345R clad tubesheet after loading; (**b**) TA2-Q345R clad tubesheet after unloading; (**c**) Q345R tubesheet after loading; (**d**) Q345R tubesheet after unloading.

Three axial paths A–A′, B–B′, and C–C′ (in Figure 6) were taken at 0°, 15°, and 30° of the circular direction of the contact surface, and the residual contact pressure along the three paths was extracted as shown in Figure 7. It can be seen from Figure 7 that the highest contact pressure of the two tubeplates was at the same position in the axial direction (Z-direction). Compared with the Q345R tubesheet, the effective sealing range of the tube side of the clad tubesheet was closer to the expansion edge, the p_c^* value at the sealing ring was much higher than that of the Q345R tubesheet, and the p_c^* value of the middle and shell side of the two kinds of tubeplates was similar.

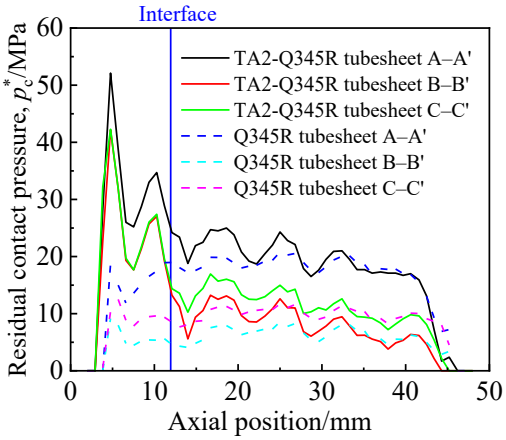

Figure 7. Axial distribution of residual contact pressure of the two kinds of tubesheets.

Figure 8 indicates the p_c^* on the circumferential paths D–D′ (tube side) and E–E′ (shell side) on two sealing rings. The results show that the p_c^* of the shell side of the two tubesheets was low, and the p_c^* at some point on the TA2-Q345R clad tubesheet was zero, indicating that, with the rebound of the TA2 tube after unloading, the sealing ring at some positions on the contact surface of the shell side gradually disappeared. When the heat exchanger is in service, the shell side medium would leak along the contact surface and extend to the pipe side, which would damage the contact surface and cause hidden dangers to the safe operation of the equipment. Therefore, the method of ungrooved hole tight expansion was not suitable for the titanium–steel clad tubesheet, and it was necessary to groove the tubesheet hole for strength expansion to improve the joint connection strength.

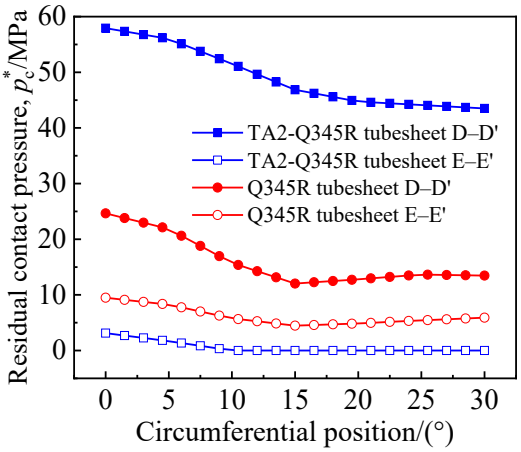

Figure 8. Circumferential distribution of residual contact pressure of Q345R tubesheet and TA2-Q345R clad tubesheet.

4. Expanded Joint with Grooved Clad Tubesheet Holes

In the standard GB/T 151-2014, the structure and dimension of the circumferential grooves in clad tubesheet holes are as shown in Figure 9. In order to study the effect of groove form on residual contact pressure and pullout force, four groove forms were designed, as depicted in Figure 10. Figure 10a–d feature one groove in the cladding layer only, one groove in the base layer only, one groove in the cladding layer and one groove in the base layer, and one groove in the cladding layer and two grooves in the base layer, respectively. The effects of groove width w, groove distance s, and groove spacing b on the connection strength and sealing performance are also investigated. The groove dimensions are listed in Table 2.

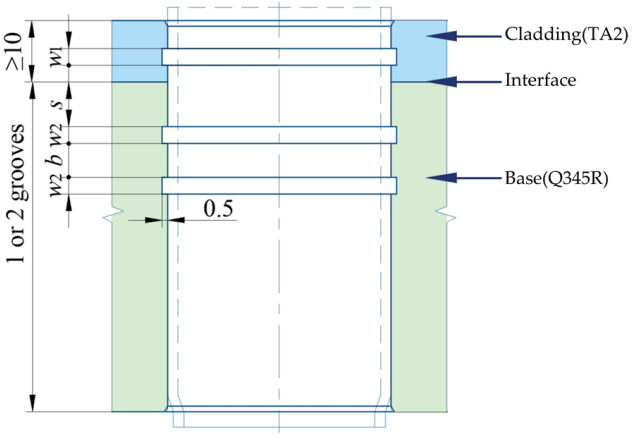

Figure 9. The structure and dimension of grooves.

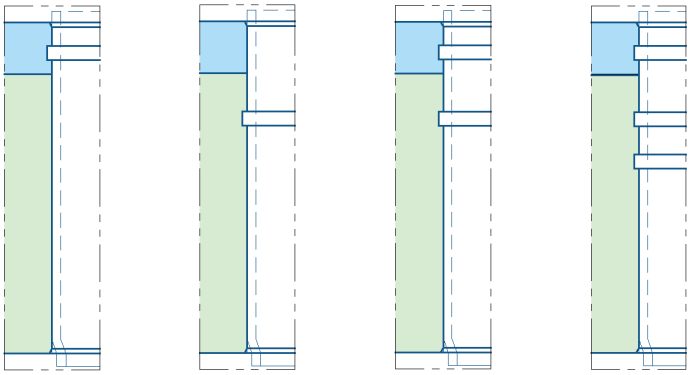

Figure 10. Four schemes for grooving: (**a**) one groove in the cladding layer only; (**b**) one groove in the base layer only; (**c**) one groove in the cladding layer and one groove in the base layer; (**d**) one groove in the cladding layer and two grooves in the base layer.

Table 2. Geometry of the grooves.

Parameter Level	Groove Width w_1 (mm)	Groove Width w_2 (mm)	Groove Distance S (mm)	Groove Spacing B (mm)
1	2	2	4	2
2	4	4	8	4
3	6	6	12	6
4	8	8	16	8
5		10	20	10
6		12		
7		14		

4.1. Effect of Groove Form

When a single groove was in the base layer or the cladding layer, the groove width w_1 or w_2 was 8 mm; when both the cladding layer and the base layer were grooved, the base layer groove width w_2 was 8 mm, and the cladding layer groove width w_1 was 6 mm. Figures 11 and 12 illustrate the residual contact pressure and pullout force at the moment of the expansion pressure being unloaded.

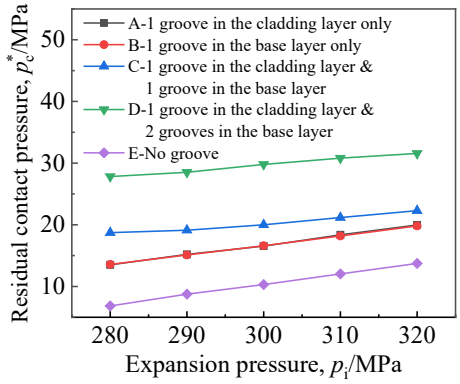

Figure 11. Effect of groove location on residual contact pressure.

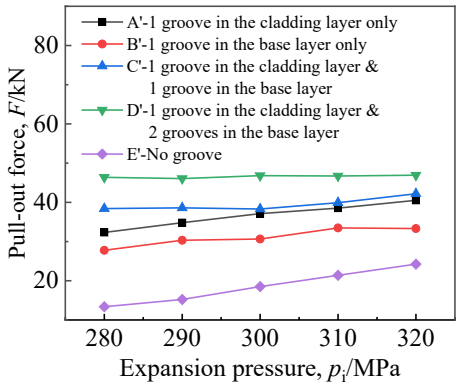

Figure 12. Effect of groove location on pullout force.

Figure 11 shows that joints with grooved holes had a higher residual contact pressure p_c^* than those without grooved holes, and p_c^* was positively correlated with expansion pressure. Lines A and B coincided, indicating that grooving in the base layer or the cladding layer had little effect on the average residual contact pressure. When there was a groove in the cladding layer, the grooving in the base layer significantly improved p_c^*, and the double grooving in the base layer was best.

As shown in Figure 12, the pullout force F almost increased with p_i, and p_i had a weak influence on F when the number of grooves was two or three. Under the same expansion pressure, the relationship of pullout force at different grooving locations was as follows: F for one groove in the cladding layer and two grooves in the base layer > F for one groove in the cladding layer and one groove in the base layer > F for one groove in the cladding layer only > F for one groove in the base layer only > F for no grooving. The pullout force of grooved joints was greater than 28.92 kN; therefore, when the strength expansion with a groove width of 8 mm was applied to titanium tubes, even when considering the decline in the pullout force caused by elastic hysteresis, it could still meet the requirements of the standard for the pullout force when the equipment is in service. In addition, during grooved expansion, the pullout force drop caused by elastic hysteresis is smaller than it is in the joint without groove [20]; thus, the pullout force value is more conservative. Although lines A and B coincided in Figure 11, the values of the pulling force in these two cases were quite different, indicating that the pullout force is related not only to the residual contact pressure but also to the deformation of the heat exchange tube near the groove.

Figure 13 depicts the distribution of residual contact pressure along the axial path at the position of circumfluence 0° when the expansion pressure was 280 MPa. Only two cases are considered in Figure 13: a single groove in the cladding and a single groove in the base. It can be seen from Figure 13 that, at the corner of each side of the groove, the residual contact pressure was high because deformed tubes sank into the groove during expansion. Both the tube and the cladding layer were titanium materials, and the rebound step was

consistent. Therefore, the maximum residual contact pressure between the titanium tube and the titanium cladding layer was greater than that between the titanium tube and the Q345R base layer. The titanium pipe sank more deeply in the cladding groove than in the base groove, and the pullout force was correspondingly greater.

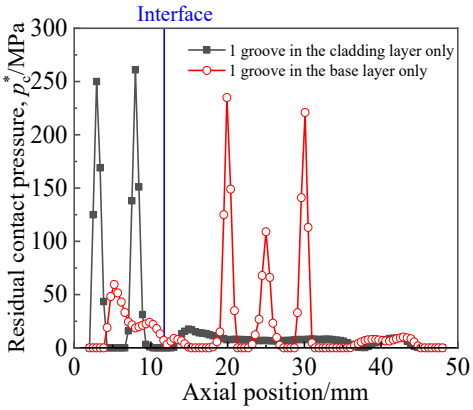

Figure 13. Axial distribution of residual contact pressure.

4.2. Effect of Groove Width

Figure 14 shows the influence of groove width on joint performance when the expansion pressure was 280 MPa, the groove depth was 0.5 mm, and four grooving locations were considered. If the expansion length allowed, the groove width was as large as possible. It can be seen from the results in Figure 14 that the groove width had a great influence on p_c^*. With the increase in groove width, p_c^* showed an overall upward trend. When the groove width was 10 mm, p_c^* approached the maximum, and the optimal groove width for uniform expansion was generally 8–10 mm [13]. It is worth noting that, when the groove width was 4 mm, p_c^* increased significantly and peaked earlier. In this paper, the expansion pressure of 290–320 MPa was also studied. The results show that a larger p_c^* was obtained when the groove width was 4 mm.

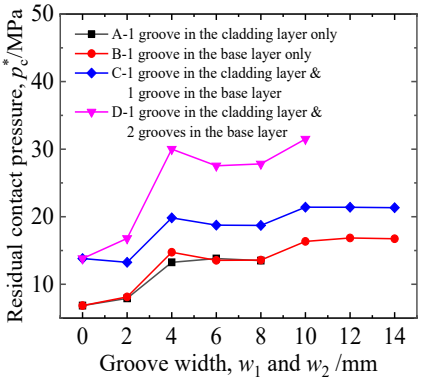

Figure 14. Effects of groove width on residual contact pressure.

The reasons were as follows: in the expansion process, the external surface of the tube and the grooved structure always contacted from the edge of the groove, followed by the bottom of the groove, and finally filled the side of the groove. When the groove width was 2 mm, a small part of the titanium tube "sank" into the groove, the concentrated line contact pressure was generated between the tube wall and the groove edge, and the residual contact pressure after unloading increased compared with that without grooving. When the width of the groove increased to 4 mm, the "sinking" effect was greater. However, because the slot width was smaller, the middle of the depression was not in contact with the bottom of the groove, and the titanium tube was close to the edge of the groove. At this time, the p_c^* of the outer wall of the tube at the corresponding groove corner increased

significantly. When the groove width was 6 mm and 8 mm, the titanium tube and the bottom of the groove contacted, and the corresponding position of the tube outer wall generated residual contact pressure. At the same time, "bottoming" led to a decrease in the titanium tube and groove edge line contact pressure, and the overall effect was a slight decrease in p_c^*. When the groove width was 10 mm, with the increase in contact area between the titanium tube and the groove bottom, the contact was more sufficient, and the p_c^* increased. When the groove width was greater than 10 mm, p_c^* showed a slight downward trend.

The elastic modulus of titanium was small, and the titanium tube could easily "sink" into the groove. Before contact with the bottom of the groove, the titanium tube contacted the edge line of the groove. The groove edge produced a high radial force on the outer surface of the titanium tube, which corresponded to a large p_c^*. Figure 15 shows the radial force of the outer surface of the titanium tube at the joint with a single groove in the base layer only, and groove widths of 2 mm, 4 mm, 6 mm, and 8 mm. It can be observed that, when the groove width was 4 mm, the radial force was the maximum.

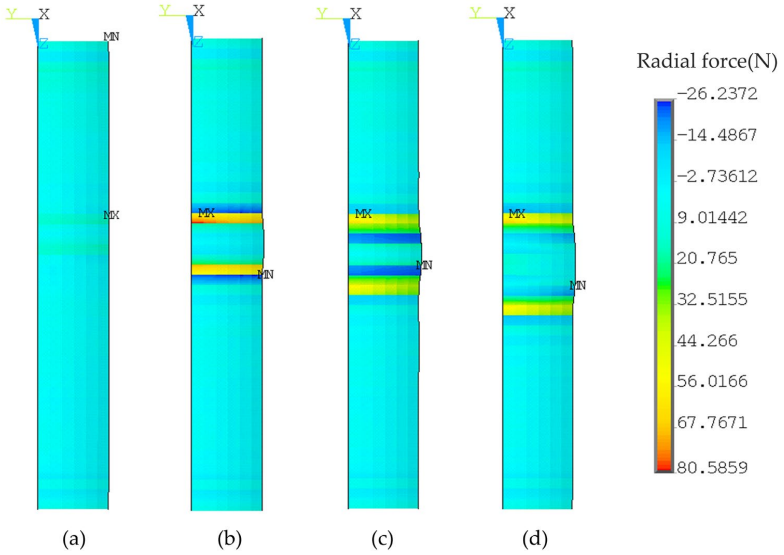

Figure 15. Effects of groove width on radial force at groove edge. (**a**) 2 mm; (**b**) 4 mm; (**c**) 6 mm; (**d**) 8 mm.

As shown in Figure 16, in general, the pullout force increased with the groove width. This is because, with the increase in groove width, the heat exchange tube "sank" into the groove more fully, and the shear force against the tube wall increased; hence, the pullout force increased. However, when the groove width continued to increase, equivalent to the increase in the initial expansion gap, the pullout force declined.

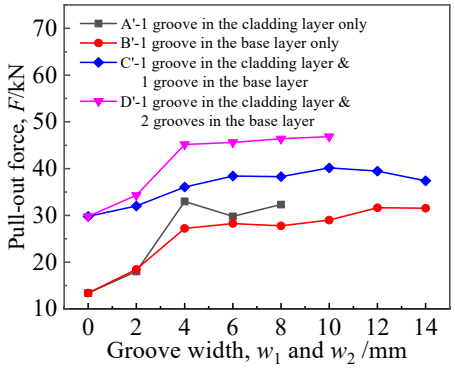

Figure 16. Effects of groove width on pullout force.

4.3. Effects of Groove Location in the Base

Figure 17 represents the influence of the distance from the single groove in the base layer to the clad interface on p_c^*, where w_1 was 6 mm and the width of the single groove in the base layer w_2 was 10 mm. As depicted in Figure 17, with the increase in distance from the single groove in the base layer to the interface, p_c^* showed an upward trend. In engineering practice, the distance from the single groove in the base layer to the interface can be appropriately increased to improve the performance of the expanded joint.

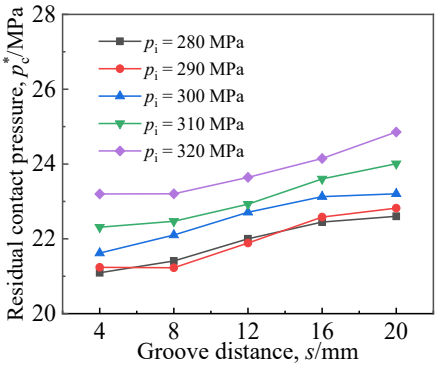

Figure 17. Effects of groove distance from the single groove in base to interface on residual contact pressure of joints.

Figure 18 shows the influence of double groove space b on p_c^*. Here, the width of the clad groove w_1 was 6 mm, the width of the double groove in the base layer w_2 was 10 mm, and the distance from the first groove in the base layer to the interface was 4 mm. As can be seen from the figure, the double groove space b had little influence on p_c^*. When the spacing was 6 mm, p_c^* exhibited the highest value.

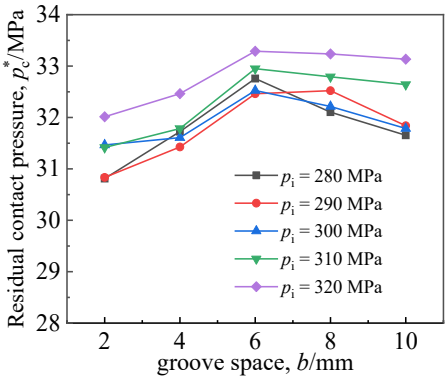

Figure 18. Effects of groove space on residual contact pressure of joints.

5. Conclusions

In this study, the finite element method was used to explore the influence of different expansion parameters on the performance of the expanded joint between a titanium–steel tubesheet and a titanium tube. The difference between a Q345R tubesheet and TA2-Q345R tubesheet in tight expansion was analyzed, and the effects of groove position and width on residual contact pressure p_c^* and pullout force F in the TA2-Q345R tubesheet expanded joint were analyzed. The following conclusions could be drawn:

(1) During tight expansion, the clad tubesheet and the tube were both made of titanium, the rebound after the expansion was consistent; thus, p_c^* and F in the cladding layer were higher than in the base layer. The connection strength of the TA2-Q345R clad tubesheet joint was better than that of the Q345R tubesheet joint.

(2) In the case of single groove, the residual contact pressure of grooving in the cladding layer was equivalent to that in the base layer, while the pullout force of grooving in

the cladding layer was higher than that in the base layer. When the number of grooves in the base layer was two, the optimal p_c^* and F could be obtained.

(3) The expansion performance of the joint was gradually enhanced with the increase in groove width within the range of 2–14 mm. When the groove width was 4 mm, the residual contact pressure increased significantly due to the higher radial force of the groove edge. The position of the groove had no obvious effect on the joint performance in the base layer or in the cladding layer.

Author Contributions: Conceptualization, J.L. (Jia Li) and C.Z.; data curation, J.L. (Jia Li) and J.L. (Juan Li); formal analysis, J.L. (Jia Li); funding acquisition, C.Z.; investigation, J.L. (Jia Li); methodology, J.L. (Jia Li) and C.Z.; project administration, C.Z.; resources, C.Z.; software, J.L. (Jia Li); supervision, C.Z.; validation, J.L. (Jia Li); visualization, J.L. (Jia Li), J.L. (Juan Li), and Y.Z.; writing—original draft, J.L. (Jia Li); writing—review and editing, J.L. (Jia Li), J.L. (Juan Li) and Y.Z. All authors have read and agreed to the published version of the manuscript.

Funding: This research was funded by the National Natural Science Foundation of China (grant numbers 51975271 and 51475223).

Institutional Review Board Statement: Not applicable.

Informed Consent Statement: Not applicable.

Data Availability Statement: Not applicable.

Conflicts of Interest: The authors declare no conflict of interest.

References

1. Qiu, G.Z.; Guo, Y.F. Current situation and development trend of titanium metal industry in China. *Int. J. Miner. Metall. Mater.* **2022**, *29*, 599–610. [CrossRef]
2. Wu, Z.W.; Li, S.; Zhou, F. Electrochemical and tribological properties of TiSiCN coatings in coolant. *Mater. Sci. Medzg.* **2019**, *25*, 159–165. [CrossRef]
3. Huang, X.P.; Xie, T. Modeling hydraulically expanded tube-to-tubesheet joint based on general stress-strain curves of tube and tubesheet materials. *J. Press. Vessel Technol.* **2011**, *133*, 031205. [CrossRef]
4. Ge, T.Z.; Li, J.; Zhou, C.Y.; He, X.H. Performance of hydraulic expanding-joint of titanium tube heat exchanger. *Rare Met. Mater. Eng.* **2018**, *47*, 3800–3805.
5. Sui, R.J.; Wang, W.Q.; Liu, Y.; Qu, Y.P. Effects of austenitic stainless steel tube and tubesheet hole dimensional deviations on the hydraulic expansion pressure. *Int. J. Press. Vessels Pip.* **2016**, *138*, 1–7. [CrossRef]
6. Yoganathan, R.; Shanmugam, N.S.; Ramanathan, A. Effects of thickness offset on the tube-to-tube sheet expansion joint strength: An experimental evaluation. *J. Mater. Eng. Perform.* **2022**, *31*, 2770–2782. [CrossRef]
7. Jawad, M.H.; Clarkin, E.J.; Schuessler, R.E. Evaluation of tube-to-tubesheet junctions. *J. Press. Vessel Technol.* **1987**, *109*, 19–26. [CrossRef]
8. Thekkuden, D.T.; Mourad, A.-H.I.; Bouzid, A.-H. Impact of Grooves in Hydraulically Expanded Tube-to-Tubesheet Joints. In Proceedings of the ASME 2020 Pressure Vessels & Piping Conference, Virtual, 3 August 2020.
9. Alaboodi, A.S. Finite element study of the hybrid expansion of tube-to-tubesheet joints. *Thin Wall Struct.* **2019**, *137*, 347–352. [CrossRef]
10. Bouzid, A.-H.; Zhu, L. A study of neighbouring tube expansion effect on the residual contact pressure of tube-to-tubesheet joints. *Int. J. Press. Vessels Pip.* **2018**, *165*, 185–192. [CrossRef]
11. Updike, D.P.; Kalnins, A.; Caldwell, S.M. Residual stresses in tube-tubesheet joints with grooves. *J. Press. Vessel Technol.* **1992**, *114*, 249–251. [CrossRef]
12. Wang, H.F.; Sang, Z.F. Effect of geometry of grooves on connection strength of hydraulically expanded tube-to-tubesheet joints. *J. Press. Vessel Technol.* **2005**, *127*, 430–435. [CrossRef]
13. Hao, J.W. Mechanical Analysis of Uniform-pressure Tube-expanding and Investigation of Rubber Tube-expanding Key Technology. Ph.D. Thesis, East China University of Science and Technology, Shanghai, China, 2006.
14. Allam, M.; Bazergui, A.; Chaaban, A. The Effect of Tube Strain Hardening Level on the Residual Contact Pressure and Residual Stresses of Hydraulically Expanded Tube-to-tubesheet Joint. In Proceedings of the ASME 1998 Pressure Vessels & Piping Conference, San Diago, CA, USA, 27–30 July 1998.
15. Laghzale, N.E.; Bouzid, A.-H. Theoretical analysis of hydraulically expanded tube-to-tubesheet joints with linear strain hardening material behavior. *J. Press. Vessel Technol.* **2009**, *131*, 061202. [CrossRef]

16. Wang, K.; Liu, Z.C.; Xu, W.F.; Tan, G.F.; Wang, Y.Q.; Ma, L. Stress Analysis and Optimization Research of Cladding Titanium-Steel Tube Sheets in Different Tube Patterns. In Proceedings of the ASME 2017 Pressure Vessels and Piping Conference, Waikoloa, HI, USA, 16–20 July 2017.
17. Wang, K.; Xu, W.F.; Liu, Z.C.; Liu, M.S. Stress Analysis and Optimization Research for Ti Clad Steel Tube Sheet. In Proceedings of the ASME 2015 Pressure Vessels and Piping Conference, Boston, MA, USA, 19–23 July 2015.
18. Yao, X.A.; Wang, H.F. Effect of creep on residual contact stress of hydraulically expanded tube-to-tubesheet joints. *Titanium Ind. Prog.* **2016**, *33*, 41–45.
19. Yao, X.A. Study on Connection Property of Titanium Expanded-and-Welded Tube-to-Tubesheet Joint. Master's Thesis, Nanjing Tech University, Nanjing, China, 2017.
20. MA, Q.L. Research on Time-Dependent Mechanical Behaviors of Commercially Pure Titanium and Its Tube-to-Tubesheet Joints. Ph.D. Thesis, East China University of Science and Technology, Shanghai, China, 2006.
21. Lin, J.F. Research on the Expanding-Joint of the Titanium Tube and the Tubesheet. Master's Thesis, East China University of Science and Technology, Shanghai, China, 2011.
22. *YS/T 749-2011*; Titanium-Steel Clad Tubesheet for Condenser and Heat Exchanger Used in Electric Power Station. National Technical Committee for Standardization of Non-ferrous Metals: Beijing, China, 2012.
23. Ni, X.Y.; Zhang, Y.H.; Zhao, H.X.; Pan, C.W. Numerical research on the biomechanical behaviour of braided stents with different end shapes and stent-oesophagus interaction. *Int. J. Numer. Meth. Biomed. Eng.* **2018**, *34*, e2971. [CrossRef] [PubMed]
24. Zhang, Y.H.; Ni, X.Y.; Pan, C.W. Finite element simulation and optimization of mechanical performance of the magnesium-alloy biliary stent. *Int. J. Numer. Meth. Biomed. Eng.* **2022**, *38*, e3592. [CrossRef] [PubMed]
25. Yan, H.G.; Zhang, B.S.; GE, L.T.; Li, P.N. Research on hydraulically expanding of heat exchangers(1)—Determination of the expanding pressure. *China Press. Vessel Technol.* **1996**, *36–40*, 3.
26. *GB/T 151-2014*; Heat Exchangers. National Boiler and Pressure Vessel Standardization Technical Committee: Beijing, China, 2015.
27. Wang, H.F.; Sang, Z.F.; Widera, G.E.O. Connection strength and tightness of hydraulically expanded tube-to-tubesheet joints. *J. Mater. Process. Technol.* **2007**, *194*, 93–99. [CrossRef]

materials

MDPI

Article

A Numerical Study of Crack Mixed Mode Model in Concrete Material Subjected to Cyclic Loading

Omar Alrayes [1], Carsten Könke [1] and Khader M. Hamdia [2,*]

[1] Institute of Structural Mechanics, Bauhaus Weimar University, Marienstraße 15, 99423 Weimar, Germany
[2] Institute of Continuum Mechanics, Leibniz Universität Hannover, 30167 Hannover, Germany
* Correspondence: hamdia@ikm.uni-hannover.de

Abstract: In quasi-brittle materials such as concrete, numerical methods are frequently used to simulate the crack propagation for monotonic loading. However, further research and action are required to better understand the fracture properties under cyclic loading. For this purpose, in this study, we present numerical simulations of mixed-mode crack propagation in concrete using the scaled boundary finite element method (SBFEM). The crack propagation is developed based on a cohesive crack approach combined with the thermodynamic framework of a constitutive concrete model. For validation, two benchmark crack-mode examples are modelled under monotonic and cyclic loading conditions. The numerical results are compared against the results from available publications. Our approach revealed good consistency compared to the test measurements from the literature. The damage accumulation parameter was the most influential variable on the load-displacement results. The proposed method can provide a further investigation of crack growth propagation and damage accumulation for cyclic loading within the SBFEM framework.

Keywords: mixed mode crack propagation; cohesive zone method; cyclic loading; SBFEM

Citation: Alrayes, O.; Könke, C.; Hamdia, K.M. A Numerical Study of Crack Mixed Mode Model in Concrete Material Subjected to Cyclic Loading. *Materials* **2023**, *16*, 1916. https://doi.org/10.3390/ma16051916

Academic Editors: Michele Bacciocchi, Angelo Marcello Tarantino, Raimondo Luciano and Carmelo Majorana

Received: 5 February 2023
Revised: 19 February 2023
Accepted: 22 February 2023
Published: 25 February 2023

1. Introduction

The application of fatigue fractures is essential in analysing the performance of concrete structures. In fracture mechanics, concrete discontinuities also have the most significant investigation in the field of engineering [1,2]. To better understand the rapid failure of concrete structures under cyclic loading, a detailed procedure of fatigue crack propagation is required. The prediction of the direction of crack propagation and orientation of quasi-brittle material as concrete is essential for the robust and reliable design of concrete structures.

In concrete material, modelling of crack propagation and the numerical simulation of crack growth remains an outstanding issue and a critical topic of ongoing research. Primarily, the finite element technique is mainly used to simulate the crack behaviour numerically. Still, discontinuities in material simulation cannot be fully demonstrated, since the finite element method (FEM) is based on a continuum approach.

The cracks are typically mapped by areas of high strain rates when using the smeared crack approach, as in Ref. [3]. The division of the crack opening into an equivalent element length of a finite element causes the effect of smeared crack formation. This method has a drawback in that it cannot accurately reflect the actual fracture pattern because the distortion and discontinuity in the displacement field are not mapped. Alternately, discontinuities are added at the element edges in the discrete crack approach [4]. This method is affiliated with a high numerical effort since each iteration step has a continuous re-meshing process.

Based on the extensions of the conventional FEM, cohesive numerical approaches in modelling crack propagation have been developed to avoid this disadvantage [5–8]. Particular crack tip components were created to reduce the mesh quality essential for crack

simulation by the FEM [9]. However, many difficulties have been reported by Ref. [10] for material modelling using the FEM framework. The nodal displacements for finite elements at the crack tip should be omitted when calculating the stress intensity factor (SIFs). To determine the crack propagation path, several theories have been put forward [11]. Since it has an approximate explicit solution for the crack growth direction (θ) as a function of the stress intensity factor under pure tension (K_I) and mixed-mode condition (K_{II}), the maximum tangential stress criterion is frequently used in FEM simulations of cyclic crack propagation. In this case, it should be noted that the procedure of mesh refinement is typically needed in the vicinity of the crack tip. The global or local re-meshing technique is the most standard method to describe monotonic and cyclic crack propagation under linear elastic fracture mechanics (LEFM) assumptions [11].

The cohesive zone model of Ref. [12] is most commonly used to model the process zone. The process zone is often modelled in FEM utilizing the zero-thickness interface elements. Interface elements are used in a variety of modelling techniques in the literature, such as placing them along the crack paths [13,14], inserting them along all element interfaces in the mesh [15–17], and placing them along the crack surfaces as the crack propagates [18–20]. While some methods are derived based on a priori information of the crack paths obtained from experiments [13,14,21], sophisticated re-meshing algorithms to propagate the crack with high mesh densities or particular finite elements were implemented to model the singular stress fields around crack tips [22,23]. High mesh densities are needed to achieve smooth and precise predicted crack paths, even though the methods developed in Refs. [15–17,24] do not. An additional nodal enrichment with special stress functions was included by using the extended finite element method (XFEM) to simulate singular stress zones around crack tip [25]. The same appealing property that does not require re-mesh to describe crack propagation is shared by XFEM and embedded crack models. The cohesive tractions at the crack edges are included in the governing equations to account for their work. Many research investigations have discussed cohesive crack propagation for statics and dynamics issues using XFEM [26,27].

Meanwhile, the scaled boundary finite element method (SBFEM) has been proposed recently to facilitate the dilemma of the computation burdens [28–31]. The SBFEM is a very efficient method in solving problems with unbounded media and singularities. The method's effectiveness in handling singularities and unbounded domain problems has prompted researchers to extend its applications to solve diverse problems in various engineering fields, such as fracture mechanics [32,33], dam reservoir interaction [34], electromagnetic [35] and image-based analysis [36]. In order to minimize computation costs, the SBFEM assigns no discretization of side-face boundaries [33]. Using polygon elements created by the SBFEM, Ref. [37] has developed an automatic LEFM-based crack propagation modelling technique. By utilizing SBFEM's appealing feature, the particular stress fields near crack tips were analytically represented [28]. The SBFEM has shown a considerable efficiency compared to the classical FEM in calculating the stress singularities [38]. Crack-tip mesh refinement, as in FEM, is avoided since the SBFEM calculates SIFs from the stress solutions at the edges of subdomains and the nodes on the domain boundary. Furthermore, a domain can be divided into subdomains in any required way, and the accuracy of the stress and SIFs solutions is specified based on the re-meshing procedure. Accordingly, this feature is more flexible in simulation crack propagation than in the FEM. In addition, the re-meshing procedure can be as simple as used in the boundary element method (BEM). Egger et al. [39] examined the computational efficiency of the SBFEM for solving linear elastic fracture mechanics problems. A comparison between the SBFEM, Extended finite element method (XFEM), and FEM was constructed by introducing different examples for calculating the SIFs. The output showed that the SBFEM reached the exact solution faster than XFEM. An extended finite element method by Ref. [40] was developed to simulate nonlinear dynamic analysis. A direct remeshing algorithm for crack propagation has been obtained in quasi-brittle materials. However, more investigations are required in modelling crack propagation for concrete under cyclic and fatigue loading. As the singularities of

cracks in the material interface are analytically calculated, the initial crack and the stress state can be easily defined.

In this study, the SBFEM framework developed in Ref. [32] is implemented to model cohesive crack propagation in quasi-brittle materials under cyclic loading. A new constitutive model based on Ref. [41] is implemented to model the propagating cracks that depend on the direction of applied loads. This model introduces an efficient simulation of concrete material under cyclic behaviour. At sub-critical loading levels, the model relies on the cumulative measure of propagation as a key damage-driving mechanism. The results of the proposed approach are validated against the methods in Refs. [42,43]. Concerning the concrete elements' fracture and material response, analyses are performed using the thermodynamic constitutive material law for concrete. The material model assumes a combination of plasticity and damage theory in Refs. [44–46]. Similarly, as in Ref. [47] the proposed method aims to simulate the crack propagation of concrete under cyclic loading. However, we further extend the SBFEM framework to simulate the mixed mode crack damage behaviour under various loading scenarios. As results, two mixed-mode crack propagation problems are modelled for monotonic and cyclic loading. The results are discussed and compared with the data available in publications.

The paper is structured as follows. In Section 2, the principle of the constitutive material model at the cohesive interface element is explained. In addition, the constitutive material model at the cohesive interface element for mixed-mode material response is investigated. Section 3 introduces the proposed mixed-mode crack procedure for concrete material using SBFEM. Additionally, the re-meshing procedure of crack propagation is introduced. Section 4 introduces a nonlinear crack model for cohesive interactions, and a flowchart for solving the SIFs is given. In Section 5, two numerical simulations are modelled to validate the nonlinear model. Based on the findings of the cyclic bending test of plain concrete that were published in the literature, we provide the calibration and validation of the proposed model. The effect of the loading sequence on the material's stiffness was the main focus of the numerical investigations.

2. Constitutive Relation under Cyclic Loading

The advanced material models define a direct relationship between the invariant of the strain and stress by linking the damage evolution with the strain, as in Refs. [10,48,49]. In order to reflect the opening/closure and growth of the micro-cracks and/or the frictional sliding along their length, the formulation of the dissipative mechanisms has been refined by introducing the internal sliding strain as a damage-driving variable within the framework of isotropic damage and internal sliding strain. This way, a unified model for monotonic and low cycle fatigue loads was proposed by Refs. [50,51].

Comparing the thermodynamic softening law of the constitutive model for the fracture, the proposed model has the ability to simulate the plastic deformation of the experimental results based on the plasticity and damage variables. Therefore, a numerical approach is introduced in this work to consider monotonic and cyclic behaviour. The proposed approach considers the cumulative measure of slip as an essential damage-driving mechanism at the subcritical loading levels, as illustrated in Figure 1. The constitutive behaviour of the embedded interface elements that represent the fracture process zone has been identified utilizing the thermodynamic-based interface model [1,47].

A cumulative measure of the inelastic displacement inside the interface governs the damaged evolution of concrete material. The evolution law in Equation (1) introduces the cumulative opening and/or sliding as the fundamental source of damage. The adopted failure criterion is identified based on the evolution law of the threshold function of the damage plasticty law, as described in Ref. [41]. In a manner similar to how Lemaitre's damage potential was presented in Ref. [52], this feature has been introduced through the modified flow potential in Refs. [50,53].

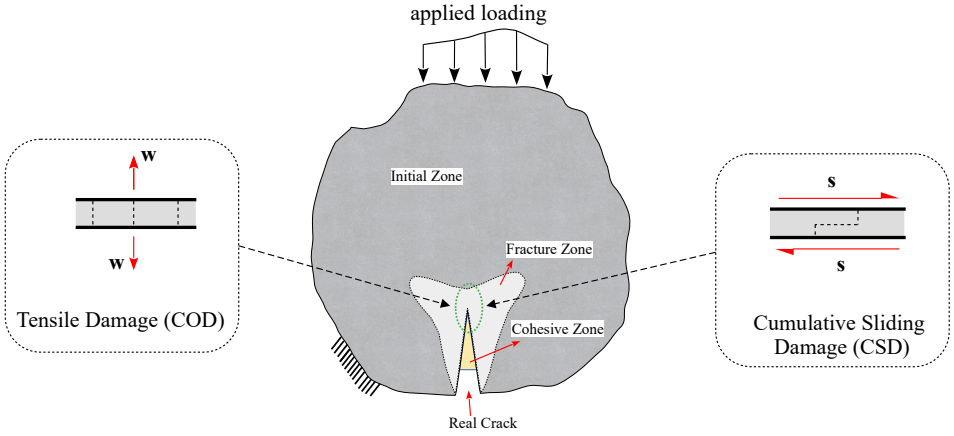

Figure 1. Modelling approach of the cohesive concrete zone for both crack opening and sliding.

$$\dot{\omega} = (1-\omega)^{c+1}\left(\frac{Y}{S}\right)^{r}\left(\frac{\sigma_n}{\tilde{\sigma_n} - m\sigma_0}\right)|\dot{u}^P| \tag{1}$$

with

$$\dot{u}^P = \frac{\dot{\lambda}}{1-\omega}\,\mathrm{sign}(\tilde{\sigma_n} - X) \tag{2}$$

where $\dot{u}^P$ is a representation of the relative displacement at the interface (i.e., opening displacement $w = COD$ in the normal direction and slip $s = CSD$ in the tangential/ shear direction, see Figure 1), Y is the energy release rate related to the damage mechanism, and X represent the thermodynamic force. The state variables of the damage variable ω, S are the damage strength parameter, and c, r are the exponential parameters controlling the accumulation rate of the damage. The $\tilde{\sigma_n}$, σ_0 and σ_n are the effective stress limits.

The introduced material model has been integrated as an implicit time-stepping method into the Scaled Boundary Finite Element Framework. The return mapping procedure is used to correct the internal variables after an elastic trial step, and the incremental multiplier at each time step is computed numerically from the consistency condition, $\dot{f}$. The exact process has been applied to the finite element framework by Ref. [41].

The incremental value $\Delta\lambda$ can be obtained by substituting the evolution equations into the consistency condition as in Refs. [47,51].

$$\Delta\lambda = \frac{f_{n+1}^{\text{trial}}}{E/(1-\omega_n) + \gamma + K} \tag{3}$$

where E is the elastic stiffness, K and γ represent the isotropic and kinematic hardening moduli, respectively. Due to the implicit form of the damage evolution Equation (1), the iterative Newton scheme is applied to identify an admissible state. For fatigue and cyclic simulations, this might be too expensive. As a result, we adopt the assumption of a damage quasi-constant over a time step in Refs. [41,54], which significantly speeds up the simulation without sacrificing accuracy. The proposed model needs a consistent algorithmic stiffness to ensure a reliable and effective numerical implementation. The algorithmic stiffness establishes a relationship between the rates of stress and displacement by

$$\dot{\sigma} = (E^{alg})\dot{u} \tag{4}$$

The stress rate then can be expressed as

$$\sigma = (1-\omega)E(\dot{u} - \dot{u}^P) - \dot{\omega}E(u - u^P) \tag{5}$$

The algorithmic stiffness is obtained by substituting the evolution equations for damage and displacement with the incremental multiplier in Equation (3) as

$$E^{alg} = (1-\omega)E - \frac{(1-\omega)E^2}{E+(\gamma+K)(1-\omega)} - \frac{(1-\omega)^c E^2 (u-u^p)(\frac{\overline{\sigma}}{\overline{\sigma}-m\sigma_0})(\frac{Y}{S})^r \text{sign}(\widetilde{\sigma}_{n+1}^{p,\text{trial}} - \gamma\alpha_n)}{(E/(1-\omega)+\gamma+K)} \quad (6)$$

Following the formulation of the equilibrium condition on a zero-thickness element of the interface, the described material model is embedded into the initial boundary value problem of the SBFEM in a usual manner.

3. Modelling Crack Propagation

3.1. Crack Tip Stress Field in the Presence of Cohesive Traction

Fracture in quasi-brittle materials such as concrete involves a process zone [55]. The numerical models and simulations consider the cracking phenomenon that can be detected physically. Due to surface friction and aggregate interlocking, normal and shear tractions can be transferred across crack surfaces. In this study, the interface elements are utilized to model the cohesive cracks that result from mixed-mode loading scenarios. Figure 2 illustrates a typical bounded domain of an interface element at the crack tip. The crack displacement in Figure 2b along the interface elements consists of crack opening displacement (*COD*) and crack sliding displacement (*CSD*). The nonlinear cohesive tractions for normal traction and tangential cohesion are σ and τ, respectively.

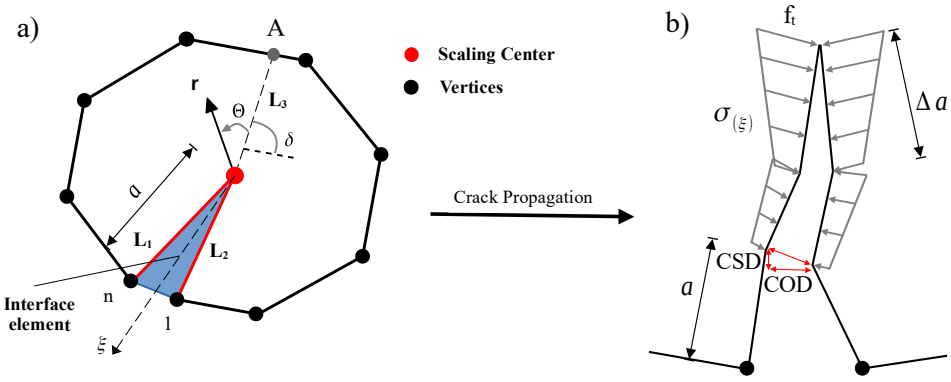

Figure 2. Crack propagation of interface SBFEM element: (**a**) interface cohesive model in SBFEM, (**b**) distribution of the cohesive forces.

The governing equations of SBFEM for an element containing a crack tip with side face tractions is motivated by the works in Ref. [38]. Along the radial lines, ξ nodal displacement functions $u(\xi)$ are used, while the displacement functions in the η direction are interpolated by the shape functions $[N(\eta)]$. The displacement field $u(\xi,\eta)$ is scaled as boundary coordinates and expressed including the normal displacement modes and the sideface displacement modes as

$$\{u(\xi,\eta)\} = [N(\eta)] \sum_{i=1}^{N+M} c_i \xi^{(\overline{\lambda_i}-1)} \{\overline{\phi_i}\} \quad (7)$$

where $\overline{\phi_i}$ is the side-face load mode, c_i is the integration constants, and $\overline{\lambda_i}$ is the eigenvalue matrix.

The stress field can be calculated in the presence of cohesive traction as

$$\{\sigma(\xi,\eta)\} = \sum_{i=1}^{N+M} c_i \xi^{(\overline{\lambda_i}-1)} \{\psi_i(\eta)\} \quad (8)$$

where each term in Equation (8) can be interpreted as a stress mode and

$$\{\psi_i(\eta)\} = [D](\overline{\lambda_i}[B_1(\eta)] + [B_2(\eta)])\{\overline{\phi_i}\} \tag{9}$$

where $[D]$ is the material constitutive matrix [43], $[B_1(\eta)]$ and $[B_2(\eta)]$ are the SBFEM strain-displacement matrices. In addition, it indicates that N is the number of displacement modes and stress modes, where an extra M are added to both fields when the cohesive traction is considered.

The stress intensity factors for the homogeneous material square root singular problem are defined as

$$\begin{Bmatrix} K_I \\ K_{II} \end{Bmatrix} = \sqrt{2\pi L_0} \sum_{i=I,II} \left(c_i \begin{Bmatrix} \xi^{-\lambda_i - 1}\sigma_{yy}|_{\theta=0} \\ \xi^{-\lambda_i - 1}\sigma_{xy}|_{\theta=0} \end{Bmatrix}_i \right) \tag{10}$$

where $L_0 = L_3$ is the distance between the crack tip and the point A at the crack surface direction on the boundary, see Figure 2a. c_i are integration constants. As $\xi \to 0$, two modes can yield singular stresses with $\lambda_i = 0.5$. These two stress modes will be considered as mode I and mode II.

3.2. Crack Propagation

The crack initiation in the SBFEM domain is determined according to the zero-K condition [56]. Once the stress at the crack tip is finite, a cohesive crack will propagate. Any crack that satisfies the zero-K condition at the end of each load step will be identified using the SBFEM-based algorithm created by Ref. [57]. This hypothesis assumes that a cohesive crack will propagate if there is no stress singularity and finite stress at the crack tip. The crack propagates under the following condition

$$K_I(\theta) \geq 0 \tag{11}$$

The procedure of crack propagation is illustrated in Figure 3 and is described as follows. In order to locate the new crack tip in each crack propagation step, it is necessary to first identify the crack propagation direction (Θ_c) and the specified crack propagation length (Δa). Once the stress intensity factors (SIFs) have been calculated from Equation (10), the Θ_c can be computed as in Ref. [58].

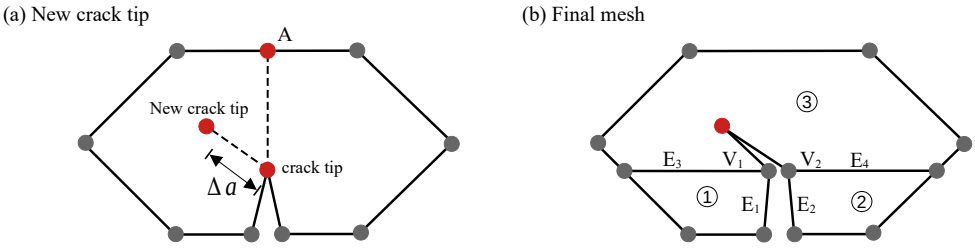

Figure 3. Crack propagation re-meshing procedure.

The re-meshing procedure is outlined in Figure 3a,b for one crack propagation step. Given Δa and Θ_c, the location of the new crack tip, shown in Figure 3a, is calculated and located in the cracked subdomain (point A is used to compute the SIFs). Two new vertices (V_1 and V_2 in Figure 3b) have been created from the former crack tip. Four new edges (E_1–E_4) are constructed along with the creation of two new subdomains (1 and 2). All edges of the newly cracked subdomain (3) must be visible from the new crack tip, and the new edges and subdomains are utilized to track the crack path.

The crack propagation criteria are examined when the external load increases. Once it is satisfied at a particular load, the crack length Δa and the crack angle θ are utilized to pinpoint the location of the new crack tip in the mesh as in Ref. [33].

The cohesive tractions along the crack are obtained based on the condition $K_I \geq 0$. The crack subdomain is split up into standard subdomains called cell interface elements

(CIEs). The new CIEs are then coupled with SBFEM normal cells. The system stiffness matrix can be created by assembling the stiffness matrices and equivalent nodal forces of the subdomains and CIEs. The SIFs can then be calculated once the nodal displacements and cohesive tractions along the crack are identified. The material softening is represented by the constitutive material model, explained in Section 2.

4. Implementation Procedure by SBFEM

The flow chart for the numerical process is shown in Figure 4. A further explanation of the numerical procedure is presented as follows:

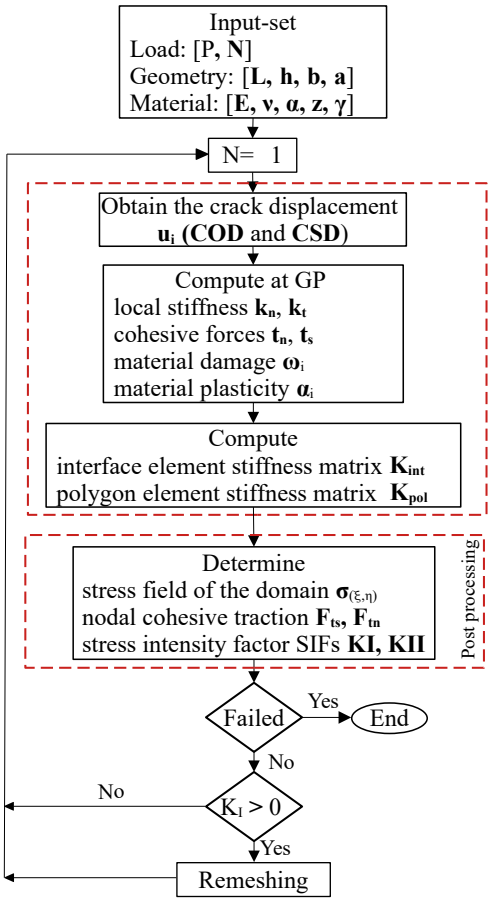

Figure 4. Key steps of the stress field domain and stress intensity factor SIFs.

1. Input the geometric dimensions of the specimen including; the span length L, height h, width b, and initial crack length a, along with the material parameters; the initial fracture toughness, Poisson's ratio ν, Young's modulus E, damage parameter ω, and the material plasticity α, γ and z under both static and cyclic loading P;
2. Establish the model (SBFEM) with the initial crack length a. Apply the external load P. Calculate the stress field of the domain, cohesive nodal traction, and the stress intensity factors (SIFs) K_I and K_{II}. Adjust the applied load until the initial cracking is reached;
3. Re-establish the SBFEM of the crack angle θ with crack length a. Δa is the increment of crack length. If $i = 1$, the number of cyclic loading $N_1 = 1$. Apply cyclic load P_{max} and the cohesive force according to Equation (13). Finally, the single and mixed mode K_I and K_{II} for monotonic and cyclic crack propagation process can be calculated according to Equation (10);

4. Repeat step 3 until the structure fails and the numerical simulation is terminated. Output the necessary parameters, such as the crack propagation path, the number of cyclic loads N, and $CMOD$ and $CMSD$ displacements.

The above modelling methodology has been implemented in a computer program using MATLAB software. Figure 4 shows a proposed flowchart of the program. The pre-processing step is to define the input set of the tested problem. The constitutive law is inserted into the SBFEM framework as an interface element at the crack tip. The nonlinear consistent interface model is solved using the displacement control algorithm to obtain the post-processing findings for monotonic and cyclic loading. The cyclic damage accumulation during loading and unloading is formulated within the constitutive model.

Based on the constitutive model at the material point level, the relative displacement of the crack surface u_i is calculated, including the opening displacement (COD) and the sliding displacement (CSD) of the crack surface. The key concept behind this method is the linear superposition of an iterative methodology applied to the relative displacement of the crack surface in order to solve and estimate the cohesive tractions on the crack surface.

The standard SBFEM solution of the stress intensity factor formula can calculate all three stress intensity factors.

$$K_I = K_I^P + K_I^C \tag{12}$$

where K_I is the total stress intensity factor and K_I^P and K_I^C are the components related to the external and cohesive forces, respectively. Thus, $K_I^P > 0$ when the crack expands due to the external force of the model, while $K_I^C < 0$ when the crack tends to close due to the cohesive force. When force balance is achieved as a result of the aspects covered by the external and cohesive forces, $K_I = 0$, equivalently. Therefore, $K_I \geq 0$ can be utilized as the criterion for considering whether the crack will continue to propagate or not as in Ref. [59]. The solution of the cohesive tractions is summarized with the following steps:

(a) As shown in Figure 4, the linear elastic assumptions of SBFEM can be used to determine the relative displacement u_i of the crack element when the structure is subject to the external force P. As a result, the corresponding cohesive traction t_i can be acquired;

(b) Both the external force and the cohesive force obtained in the previous step are applied to the structure, with the cohesive traction t_i being applied in the form of a side-face force and formulated in accordance with Equation (13). Along the fracture process region, cohesive tractions t_n, t_s are related to the relative opening and sliding displacements on the crack faces u

$$\{t\} = [k]\{u\} \tag{13}$$

where k is the stiffness of the softening laws.
The stiffness matrix of an interface element in the local coordinate system is:

$$[k_{int}] = \frac{A}{2}\sum_{i=1}^{n_g} w_i {M_i}^T [k] M_i \tag{14}$$

where A is the crack surface area, w_i is the one-dimensional Gaussian weight, n_g is the number of integration points, and M_i is the linear shape function matrix [33]. Based on Equation (14) the solution of the displacement and stress equations is calculated in Equations (7) and (8), respectively;

(c) Proceed until the variation depicted in Figure 4 is consistent with the relationship between t_i and u_{i+1}.

5. Numerical Simulation and Model Verification

5.1. Three-Point Bending Beam

The mixed mode I-II in the TPB beam under monotonic and cyclic loading was predicted based on the numerical procedure presented in Figure 4. The experimental test

results were done by Ref. [60] for concrete beams under mixed mode fracture. Table 1 summarizes the material parameters of the tested concrete specimens. The geometric dimensions of the specimen; TPB specimen with cross-section height of $h = 160$ mm. The beam height was scaled to the beam length and span, as shown in Figure 5. The beam width is kept constant with $b = 80$ mm. The notch depth was set to $h_0 = h/2$.

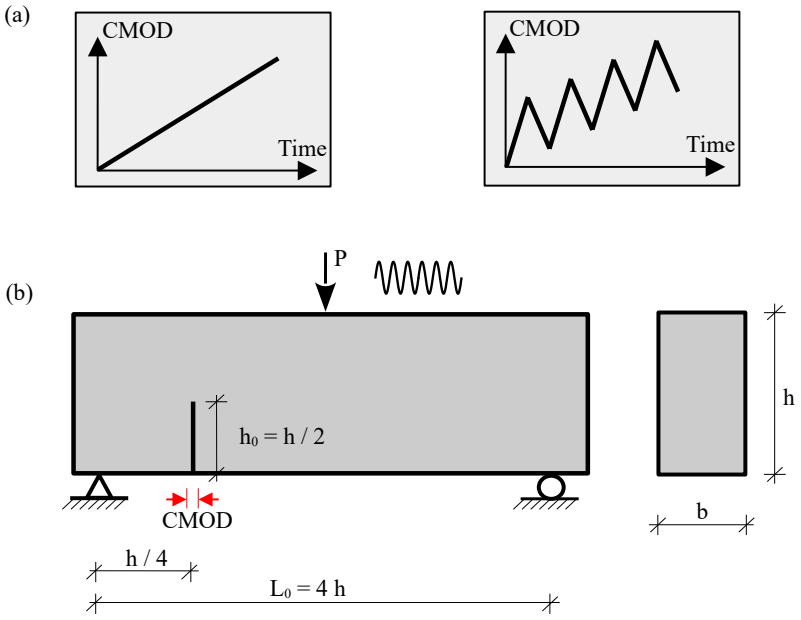

Figure 5. (**a**) Loading scenarios used in the simulation. Monotonic loading (**left**) and cyclic loading (**right**); (**b**) three-point bending beam for mixed mode crack propagation.

In the analyses, two systematic sets of loading scenarios are used. The first loading scenario introduces a typical monotonically increasing loading Figure 5a. In the second loading scenario, the sequence of unloading cycles are applied in Figure 5b.

Table 1. The parameters of the material of the experimental test in Ref. [60].

Parameter	Denomination	Value	Unit
f_c	Compressive strength	44.24	[MPa]
f_{ct}	Tensile strength	3.35	[MPa]
E_c	Young's Modulus	35.38	[GPa]
ν	Poisson ratio	0.21	[-]

The properties of the concrete and cohesive interface element for COD and CSD responses are listed in Table 2. The proposed constitutive model has a set of plastic parameters γ, K and the damage strength S, as reported in Ref. [47]. In this study, the nonidentical material response of the proposed model and the experimental data is caused by the unified parametric prediction of the calibrated material behaviour for both monotonic and cyclic loading scenarios. In this calibration, the unified parameters of monotonic and cyclic material response at the Gauss point are plotted in Figure 6. A comparison of the experimental [60] and numerical simulations is depicted in Figure 7 for the traction stress curve of the mixed-mode crack displacement under monotonic loading. It should be noted that more advanced cohesive constitutive laws with coupled normal and tangential damage evolution can be used, e.g., see Ref. [61].

Table 2. Model parameters for the concrete cohesive interface element.

Parameter	Denomination	Value	Unit
E	Elastic cohesive modulus	3000	[MPa]
$\overline{\sigma}$	Reversibility limit	2.0	[MPa]
K	Isotropic hardening modulus	400.0	[MPa]
γ	Kinematic hardening modulus	500.0	[MPa]
S	Damage strength	0.25×10^{-4}	[MPa]
r	Damage accumulation parameter	1.0	[-]
c	Damage accumulation parameter	2.0	[-]

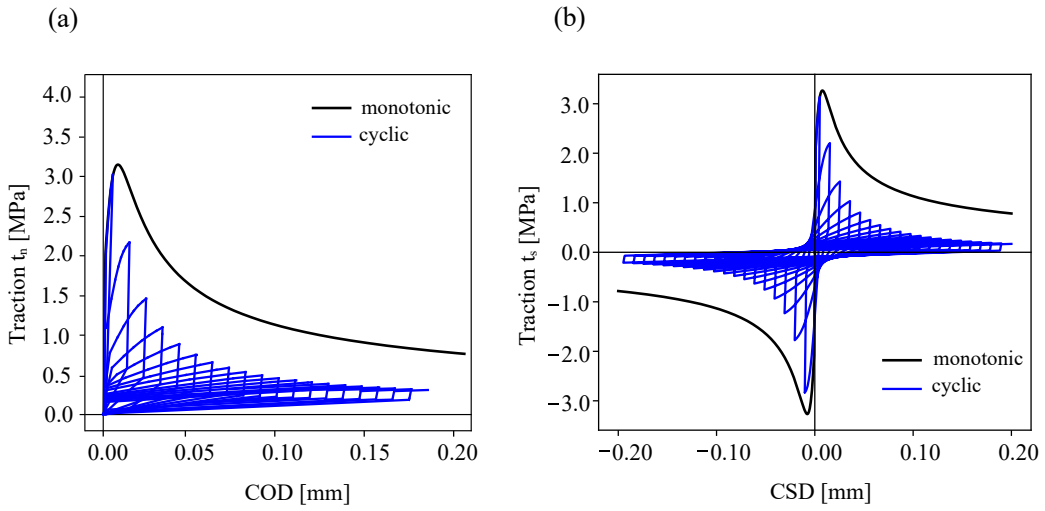

Figure 6. Cohesive traction response under cyclic loading (blue lines) and monotonic loading (gray lines) at the material point level: (**a**) traction-crack opening, (**b**) traction-crack sliding.

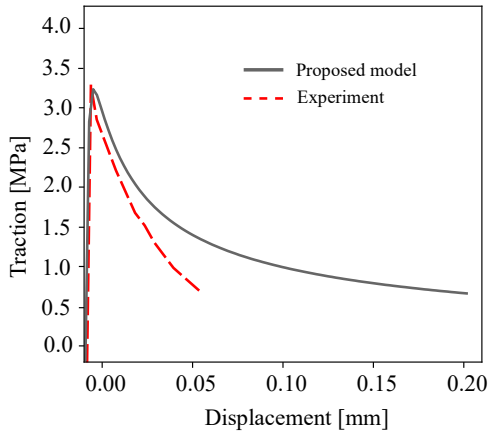

Figure 7. A comparison between the experimental measurements in Ref. [60] and the modelling results of the cohesive traction for mixed mode I-II fracture.

The two-dimensional SBFEM modelling was utilized to establish the mesh of the TPB beam. A total of 205 elements were used. The mesh refinement near the crack tip was refined, as depicted in Figure 8a. Based on COD and CSD derived from the SBFEM calculation, the SIFs were computed. Eventually, the complete mixed mode I-II cyclic and monotonic crack propagation in TPB beam was simulated, as illustrated in Figure 8b. The crack propagation due to the increasing load is shown in Figure 8b. The results showed a curved crack path in the direction of the point of the external load (F). The distribution of the traction forces is shown in Figure 8c.

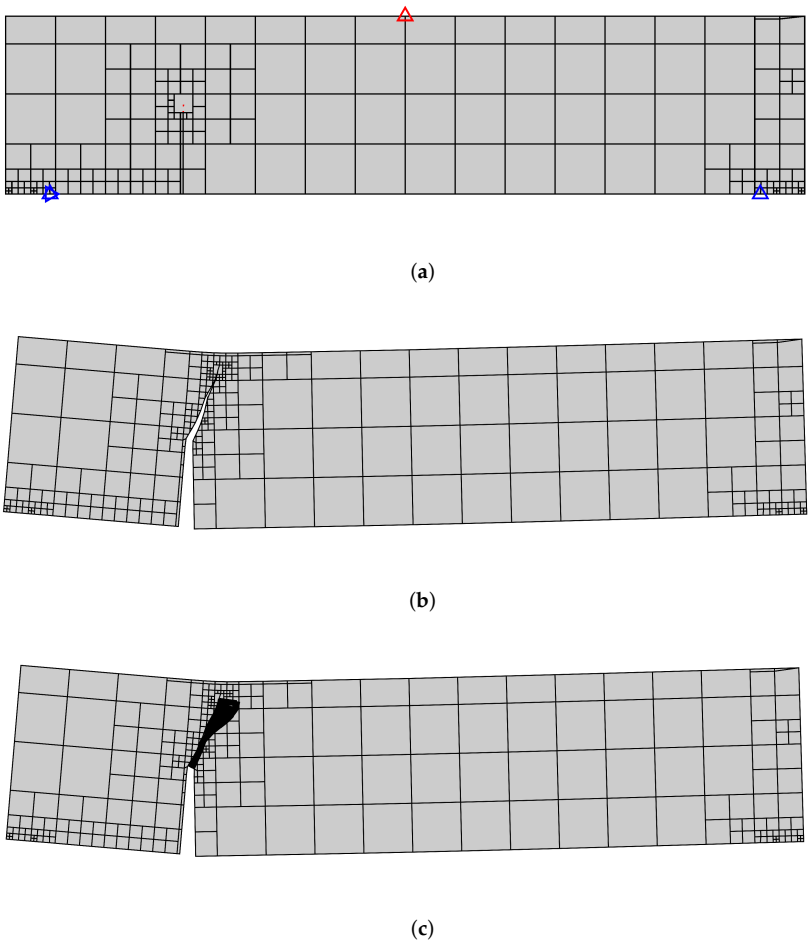

Figure 8. Predicted final crack paths of a TPB beam; (**a**) SBFEM mesh with 313 elements and boundary conditions, (**b**) predicted final crack path, (**c**) cohesive traction distribution.

To demonstrate the effectiveness of the numerical method, the SBFEM results of test simulation were compared with the experimental results in Ref. [60]. Figure 9 shows the comparison of the crack propagation paths for monotonic loading, where the shaded region contains the experimentally measured crack paths. As can be shown, there is a reasonable agreement between the numerically predicted paths in SBFEM and both numerical FEM, as well as the experimental results in Ref. [60].

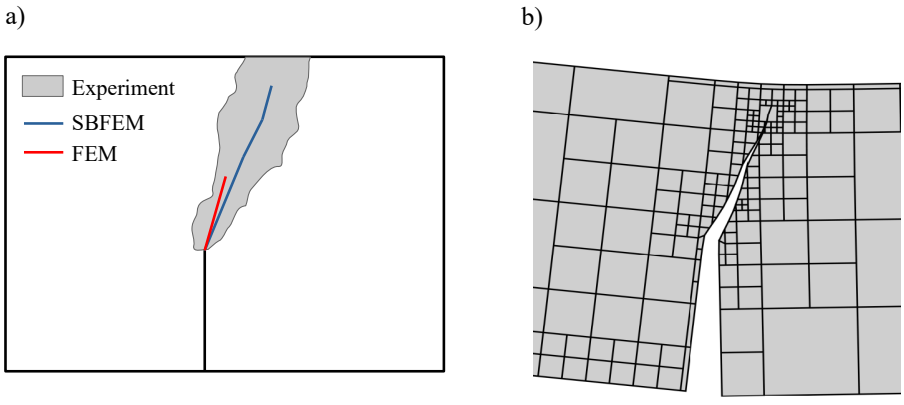

Figure 9. Predicted final crack paths of a TPB beam; (**a**) experimental shadow results in Ref. [60], (**b**) SBFEM simulation.

Figure 10 compares the predicted load-crack mixed-displacement of the TBP beam with the experimental results reported by Ref. [60] under monotonic loading. The SBFEM numerical predictions' related curve is shown in Figure 10, plotted in a black dashed line. The numerical results of the load-displacement curve are in good agreement with the experimental measurements. A maximum load of 53.1 kN is obtained at CMOD of 0.027 mm.

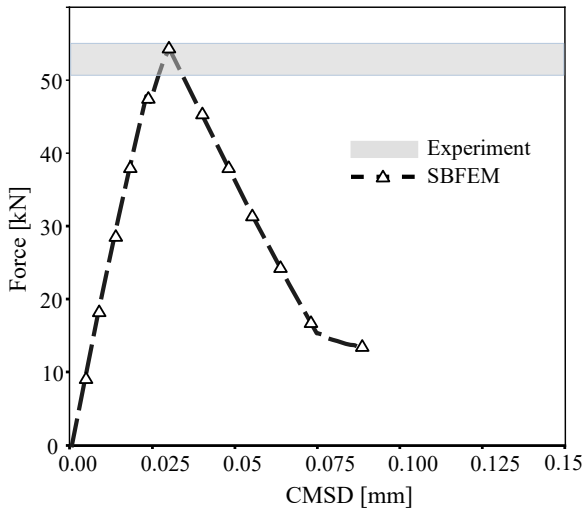

Figure 10. Numerical predictions of load-CMSD curves and the corresponding experimental data in Ref. [60] for the three-point bending test under monotonic loading.

Figure 11 shows the results of the monotonic SIFs for both mode I and mode II, where the numerically measured SIFs are plotted. In Figure 11a, the points representing the initial mesh of Figure 10 are calculated once $K_I \geq 0$. Then, the crack opens gradually based on a crack propagation criterion. The numerical calculation of K_I by SBFEM with a fewer number of degrees of freedom (DOFs) manifests good crack trajectory predictions.

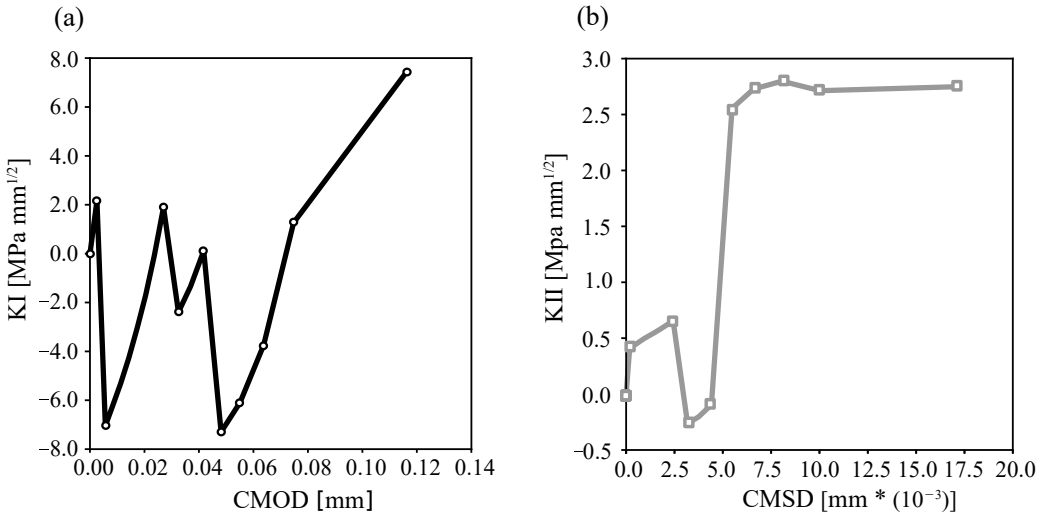

Figure 11. Mixedmode I–II crack displacement for monotonic loading: *KI*-CMOD (**a**) and *KII*-CMSD (**b**).

The experimental observations and numerical calculations for a cyclically mixed-mode loading are shown in Figure 12. The loading is controlled by the CMOD/CMSD, including eight unloading cycles. The results show that the numerical comparison of crack propagation CMSD is relatively stable while the CMOD increases as the N of the cycle

increases. As a result, there is a good agreement between the experiment results and the numerical predictions of CMSD in Figure 12.

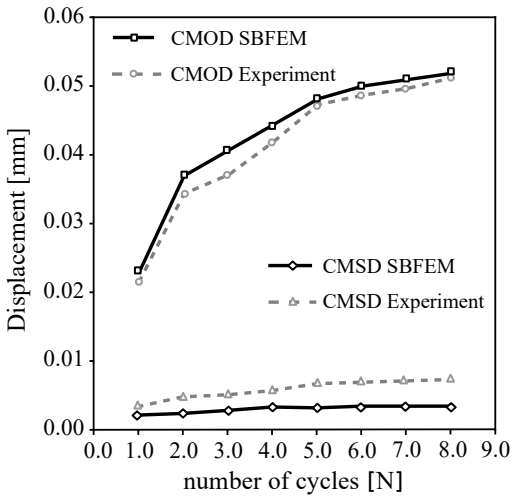

Figure 12. Crack displacement versus the number of cycles for experimental data in Ref. [60] and SBFEM; crack mouth opening *CMOD* and sliding *CMSD*.

5.2. Four-Point Bending Beam

The proposed method is next verified using the numerical results of the four-point bending concrete beam under mixed mode fracture [62]. The geometry, loads, and support conditions are illustrated in Figure 13. The width and height of the specimen are denoted by 100 × 100 [mm]. The material properties of the concrete beam are summarized in Table 3.

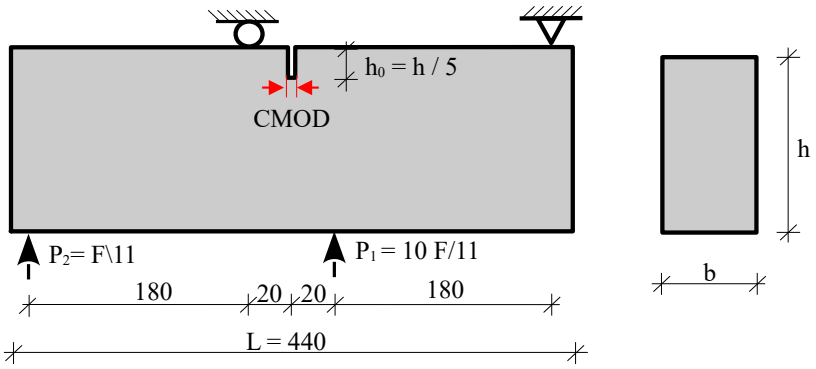

(**a**)

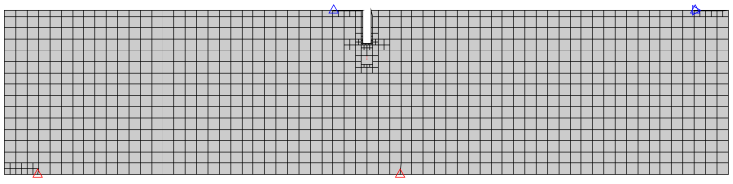

(**b**)

Figure 13. A single-notched concrete beam under monotonic mixed-mode loading. (**a**) Geometry, (**b**) initial mesh with boundary conditions.

Table 3. Parameters of the material in the experimental test by Ref. [63].

Parameter	Denomination	Value	Unit
f_{ct}	Tensile strength	3.44	[MPa]
G_f	fracture energy	0.126	[N/mm]
E_c	Young's Modulus	30.0	[GPa]
ν	Poisson ratio	0.20	[-]

A particular loading condition is implemented to generate mode II crack initiation for both monotonic and cyclic loading. The calculation is performed under displacement-controlled loading. For the analysis of the concrete beam, the following material properties are used, see Table 4 below.

Table 4. Model parameters for the concrete cohesive interface element.

Parameter	Denomination	Value	Unit
E	Elastic cohesive modulus	3500	[MPa]
$\overline{\sigma}$	Reversibility limit	2.0	[MPa]
K	Isotropic hardening modulus	400.0	[MPa]
γ	Kinematic hardening modulus	500.0	[MPa]
S	Damage strength	0.25×10^{-4}	[MPa]
r	Damage accumulation parameter	1.0	[-]
c	Damage accumulation parameter	2.0	[-]

The initial mesh of the tested beam is illustrated in Figure 13. The mesh consists of 1069 elements. The crack propagation length of $\Delta a = 22$ mm is adopted in the crack propagation simulation. Figure 14 compares the predicted traction point displacement response of the developed method with the numerical results of Ref. [62] in the literature. Overall, there is good agreement between the results of the developed method and the experimental measurements. The pre-peak response compares very well with the previously reported numerical results. The numerical SBFEM predicted a maximum load of 36.2 kN and is closest to both the experimental and FEM predictions of Ref. [62].

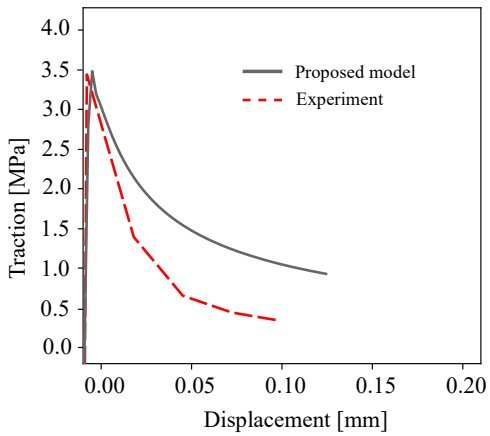

Figure 14. Comparison of the tested beam in Ref. [62] and the proposed cohesive traction for mixed modes I–II fracture.

Figure 15 represents the predicted crack propagation process. During the simulation, a crack propagates from the tip notch towards the loading point on the bottom surface of the four point bending beam. The paths of the crack in the experimental results and SBFEM are curved. In Figure 15, the predicted crack path of the FEM simulation in Ref. [62] seems to be more efficient, however, the mesh adaptive procedure of the SBFEM will produce more efficient results and reduce the computational time costs.

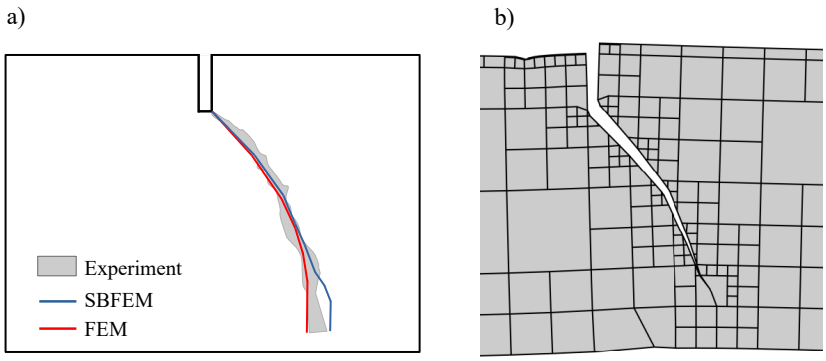

Figure 15. Predicted final crack paths of a tested beam; (**a**) the experimental shadow results in Ref. [62] and the numerical results and (**b**) SBFEM simulation.

Figure 16 compares the predicted load-crack displacement response of the developed method with the numerical FEM results of Ref. [62]. Overall, the results obtained from the developed method agree well with the numerical for the monotonic loading. The pre-peak response compares well with the previously published numerical results. All the numerical predictions below estimate the maximum load. The SBFEM predicted a maximum load of 34.8 kN and is closest to the FEM predictions.

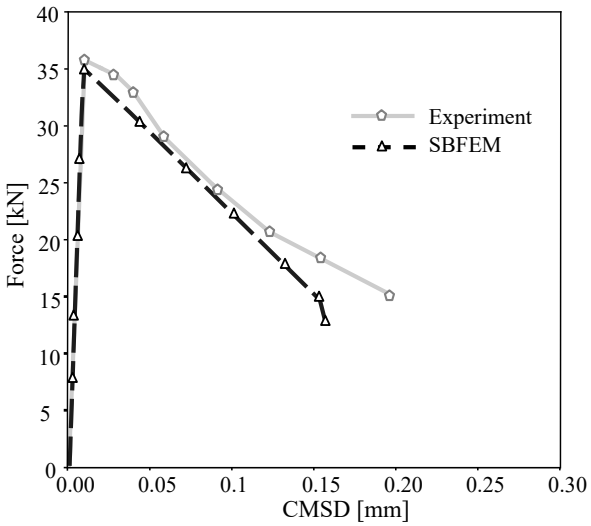

Figure 16. Numerical predictions of load-CMSD curves and the corresponding experimental data in Ref. [62] for the tested beam under monotonic loading.

Figure 17 shows SBFEM numerical predictions and FEM results for a cyclically mixed-mode loading. The loading is controlled by the CMSD, also including eight unloading cycles applied until failure. The results in Figure 17a show that the traction forces of SBFEM have a very good agreement with the numerical results in FEM. In Figure 17b, the crack displacement of the SBFEM simulation is more underestimated in comparison to the FEM measurements. The calculation of the mixed crack displacement at the material point, the number of load steps, and the democratization of the applied mesh have a significant effect on the SBFEM numerical results. However, more experimental data of cyclic mixed mode tests are required to validate the proposed numerical method.

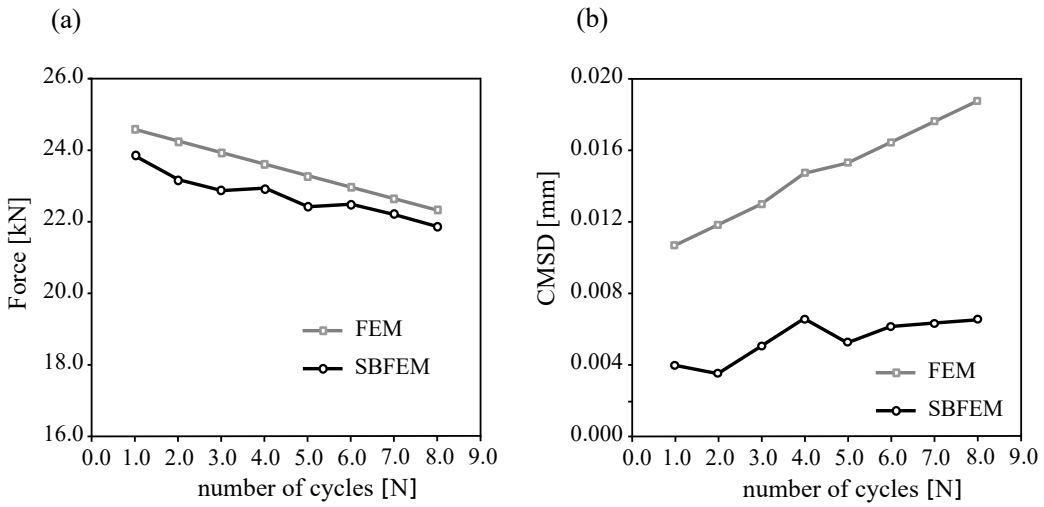

Figure 17. SBFEM numerical predictions of (**a**) load-CMSD curves and (**b**) crack displacement of the corresponding finite element data for tested beam under cyclic loading in Ref. [62].

6. Conclusions

In this paper, a newly developed SBFEM numerical method for mixed mode crack propagation in concrete under cyclic loading was proposed. The proposed procedure allowed accurate SIFs to be calculated directly from the SBFEM analytical framework without more discretization at crack-tip meshes or by using singular elements, as in FEM. Comparing the thermodynamic softening law of the constitutive model for fracture, several aspects have been provided, which incorporate the loading-unloading path, the damage evolution during the load cycle, and the crack traction displacement behaviour.

The cyclic behaviour of interfaces using SBFEM has been successfully described using the damage accumulation hypothesis. The proposed method showed the ability to simulate both monotonic and cyclic behaviour of a cohesive crack interface element, e.g., concrete interface, utilizing a consistent set of material parameters. The cyclic loading simulations' output agreed well with experimental data from the literature. The proposed method performed to study the effect of fatigue loading provides promising results and establishes a damage accumulation hypothesis for the simulation of multiple cohesive cracks under 1000 load cycles.

Author Contributions: Methodology, O.A., C.K. and K.M.H.; Validation, O.A., C.K. and K.M.H.; Writing—original draft, O.A., C.K. and K.M.H. All authors have read and agreed to the published version of the manuscript.

Funding: This research was funded by Deutsche Forschungsgemeinschaft (DFG, German Research Foundation)- Projektnummer 492535144.

Institutional Review Board Statement: Not applicable.

Informed Consent Statement: Not applicable.

Data Availability Statement: Not applicable.

Acknowledgments: Khader M. Hamdia thanks the support by Deutsche Forschungsgemeinschaft (DFG, German Research Foundation)—Projectnumber 492535144.

Conflicts of Interest: The authors declare no conflict of interest.

Nomenclature

$\dot{u}^P$	Relative displacement	ω	Damage variable
$w = COD$	Crack opening at material point	Y	Energy release rate
$s = CSD$	Crack sliding at material point	S	Damage strength parameter
c, r	Exponential damage parameters	$\sigma_n, \overline{\sigma}$	Effective stress limit
m	Material constant	E	Elastic stiffness
α	Hardening material variable	E	Elastic stiffness
$\sigma = t_n$	Cohesive normal stress	$\tau = t_s$	Cohesive tangential stress
E^{lag}	Element stiffness of the interface	γ, K	Isotropic and kinematic hardening moduli
η, ξ	Local coordinate system of SBFEM	$\overline{\lambda_i}$	Eigenvalue matrices
$\{u\}$	Displacement field	D	Material constitutive matrix
$N(\eta)$	Nodal shape function	K_{pol}	Stiffens matrix of the domain
$\overline{\phi_i}$	Eigenvector matrices	c_i	Integration constants of the SBFEM
$[B_1], [B_2]$	Strain-displacement matrices of SBFEM system	M	Number of displacement modes
P	External applied force	N	Number of load cycles
θ	Crack propagation angle	Δ_a	Crack propagation length
L_0	Crack length	K_{int}	Stiffens matrix of interface element
A	Crack surface area	w_i	Gaussian weight function
$CMSD$	Crack mouth sliding displacement	F_t	Nodal side face load
$CMOD$	Crack mouth opening displacement	K_I, K_{II}	Crack mode I & mode II stress intensity factors
$\{\sigma\}$	Stress field		

References

1. Baktheer, A.; Becks, H. Fracture mechanics based interpretation of the load sequence effect in the flexural fatigue behavior of concrete using digital image correlation. *Constr. Build. Mater.* **2021**, *307*, 124817. [CrossRef]
2. Rosso, M.M.; Asso, R.; Aloisio, A.; Di Benedetto, M.; Cucuzza, R.; Greco, R. Corrosion effects on the capacity and ductility of concrete half-joint bridges. *Constr. Build. Mater.* **2022**, *360*, 129555. [CrossRef]
3. Rots, J.G.; Nauta, P.; Kuster, G.; Blaauwendraad, J. Smeared crack approach and fracture localization in concrete. *HERON* **1985**, *1985*, 30.
4. Blanco, N.; Gamstedt, E.K.; Asp, L.; Costa, J. Mixed-mode delamination growth in carbon–fibre composite laminates under cyclic loading. *Int. J. Solids Struct.* **2004**, *41*, 4219–4235. [CrossRef]
5. Yang, B.; Mall, S.; Ravi-Chandar, K. A cohesive zone model for fatigue crack growth in quasibrittle materials. *Int. J. Solids Struct.* **2001**, *38*, 3927–3944. [CrossRef]
6. Dekker, R.; van der Meer, F.; Maljaars, J.; Sluys, L. A cohesive XFEM model for simulating fatigue crack growth under mixed-mode loading and overloading. *Int. J. Numer. Methods Eng.* **2019**, *118*, 561–577. .: 10.1002/nme.6026. [CrossRef]
7. Harper, P.W.; Hallett, S.R. A fatigue degradation law for cohesive interface elements – Development and application to composite materials. *Int. J. Fatigue* **2010**, *32*, 1774–1787. [CrossRef]
8. Turon, A.; Costa, J.; Camanho, P.P.; Dávila, C.G. *Simulation of Delamination Propagation in Composites under High-Cycle Fatigue by Means of Cohesive-Zone Models*; Technical Report; NASA Langley Research Center: Hampton, VA, USA, 2006. Available online: https://ntrs.nasa.gov/search.jsp?R=20070004889 (accessed on December 2006).
9. Tracey, D. Finite elements for three-dimensional elastic crack analysis. *Nucl. Eng. Des.* **1974**, *26*, 282–290. [CrossRef]
10. Pfister, T.; Petryna, Y.; Stangenberg, F. Damage modelling of reinforced concrete under multi-axial fatigue loading. In *Computational Modelling of Concrete Structures*; CRC Press: Boca Raton, FL, USA, 2006 ; pp. 421–429.
11. Bittencourt, T.N.; Wawrzynek, P.; Ingraffea, A.; Sousa, J. Quasi-automatic simulation of crack propagation for 2D LEFM problems. *Eng. Fract. Mech.* **1996**, *55*, 321–334. [CrossRef]
12. Hillerborg, A.; Modéer, M.; Petersson, P.E. Analysis of crack formation and crack growth in concrete by means of fracture mechanics and finite elements. *Cem. Concr. Res.* **1976**, *6*, 773–781. [CrossRef]
13. Sato, Y.; Tadokoro, T.; Ueda, T. Diagonal tensile failure mechanism of reinforced concrete beams. *J. Adv. Concr. Technol.* **2004**, *2*, 327–341. [CrossRef]
14. Segura, J.; Carol, I. Numerical modelling of pressurized fracture evolution in concrete using zero-thickness interface elements. *Eng. Fract. Mech.* **2010**, *77*, 1386–1399. [CrossRef]
15. Xu, X.P.; Needleman, A. Numerical simulations of fast crack growth in brittle solids. *J. Mech. Phys. Solids* **1994**, *42*, 1397–1434. [CrossRef]
16. Ruiz, G.; Pandolfi, A.; Ortiz, M. Three-dimensional cohesive modeling of dynamic mixed-mode fracture. *Int. J. Numer. Methods Eng.* **2001**, *52*, 97–120. [CrossRef]
17. Su, X.; Yang, Z.; Liu, G. Finite element modelling of complex 3D static and dynamic crack propagation by embedding cohesive elements in Abaqus. *Acta Mech. Solida Sin.* **2010**, *23*, 271–282. [CrossRef]

18. Xie, M.; Gerstle, W.H.; Rahulkumar, P. Energy-based automatic mixed-mode crack-propagation modeling. *J. Eng. Mech.* **1995**, *121*, 914–923. [CrossRef]
19. Ciancio, D.; Carol, I.; Cuomo, M. Crack opening conditions at 'corner nodes' in FE analysis with cracking along mesh lines. *Eng. Fract. Mech.* **2007**, *74*, 1963–1982. [CrossRef]
20. Khoei, A.; Barani, O.; Mofid, M. Modeling of dynamic cohesive fracture propagation in porous saturated media. *Int. J. Numer. Anal. Methods Geomech.* **2011**, *35*, 1160–1184. [CrossRef]
21. Qiao, P.; Chen, Y. Cohesive fracture simulation and failure modes of FRP–concrete bonded interfaces. *Theor. Appl. Fract. Mech.* **2008**, *49*, 213–225. [CrossRef]
22. Barsoum, R.S. Triangular quarter-point elements as elastic and perfectly-plastic crack tip elements. *Int. J. Numer. Methods Eng.* **1977**, *11*, 85–98. [CrossRef]
23. Karihaloo, B.L.; Xiao, Q. Accurate determination of the coefficients of elastic crack tip asymptotic field by a hybrid crack element with p-adaptivity. *Eng. Fract. Mech.* **2001**, *68*, 1609–1630. [CrossRef]
24. Prasad, M.; Krishnamoorthy, C. Computational model for discrete crack growth in plain and reinforced concrete. *Comput. Methods Appl. Mech. Eng.* **2002**, *191*, 2699–2725. [CrossRef]
25. Moës, N.; Dolbow, J.; Belytschko, T. A finite element method for crack growth without remeshing. *Int. J. Numer. Methods Eng.* **1999**, *46*, 131–150. [CrossRef]
26. Sancho, J.; Planas, J.; Gálvez, J.; Reyes, E.; Cendón, D. An embedded cohesive crack model for finite element analysis of mixed mode fracture of concrete. *Fatigue Fract. Eng. Mater. Struct.* **2006**, *29*, 1056–1065. [CrossRef]
27. Unger, J.F.; Eckardt, S.; Könke, C. Modelling of cohesive crack growth in concrete structures with the extended finite element method. *Comput. Methods Appl. Mech. Eng.* **2007**, *196*, 4087–4100. [CrossRef]
28. Song, C.; Wolf, J.P. The scaled boundary finite-element method—alias consistent infinitesimal finite-element cell method—for elastodynamics. *Comput. Methods Appl. Mech. Eng.* **1997**, *147*, 329–355. [CrossRef]
29. Ooi, E.; Yang, Z. Modelling multiple cohesive crack propagation using a finite element–scaled boundary finite element coupled method. *Eng. Anal. Bound. Elem.* **2009**, *33*, 915–929. [CrossRef]
30. Song, C.; Ooi, E.T.; Natarajan, S. A review of the scaled boundary finite element method for two-dimensional linear elastic fracture mechanics. *Eng. Fract. Mech.* **2018**, *187*, 45–73. [CrossRef]
31. Wolf, J.P.; Song, C. The scaled boundary finite-element method—A fundamental solution-less boundary-element method. *Comput. Methods Appl. Mech. Eng.* **2001**, *190*, 5551–5568. [CrossRef]
32. Ooi, E.; Song, C.; Tin-Loi, F.; Yang, Z. Automatic modelling of cohesive crack propagation in concrete using polygon scaled boundary finite elements. *Eng. Fract. Mech.* **2012**, *93*, 13–33. [CrossRef]
33. Ooi, E.; Natarajan, S.; Song, C.; Ooi, E. Crack propagation modelling in concrete using the scaled boundary finite element method with hybrid polygon–quadtree meshes. *Int. J. Fract.* **2017**, *203*, 135–157. [CrossRef]
34. Wang, Y.; Lin, G.; Hu, Z. A coupled FE and scaled boundary FE-approach for the earthquake response analysis of arch dam-reservoir-foundation system. In *Proceedings of the IOP Conference Series: Materials Science and Engineering*; IOP Publishing: Sydney, Australia, 2010; Volume 10, p. 012212.
35. Liu, J.; Lin, G.; Li, J.; Zhong, H. Analysis of quadruple corner-cut ridged square waveguide using a scaled boundary finite element method. *Appl. Math. Model.* **2012**, *36*, 4797–4809. [CrossRef]
36. Saputra, A.; Talebi, H.; Tran, D.; Birk, C.; Song, C. Automatic image-based stress analysis by the scaled boundary finite element method. *Int. J. Numer. Methods Eng.* **2017**, *109*, 697–738. [CrossRef]
37. Ooi, E.T.; Song, C.; Tin-Loi, F.; Yang, Z. Polygon scaled boundary finite elements for crack propagation modelling. *Int. J. Numer. Methods Eng.* **2012**, *91*, 319–342. [CrossRef]
38. Yang, Z.; Deeks, A. Fully-automatic modelling of cohesive crack growth using a finite element–scaled boundary finite element coupled method. *Eng. Fract. Mech.* **2007**, *74*, 2547–2573. [CrossRef]
39. Egger, A.W.; Triantafyllou, S.P.; Chatzi, E.N. The scaled boundary finite element method for the efficient modeling of linear elastic fracture. In Proceedings of the 9th International Conference on Fracture Mechanics of Concrete and Concrete Structures, Berkley, CA, USA, 9 June 2016.
40. Rabczuk, T.; Zi, G. A meshfree method based on the local partition of unity for cohesive cracks. *Comput. Mech.* **2007**, *39*, 743–760. [CrossRef]
41. Baktheer, A.; Chudoba, R. Pressure-sensitive bond fatigue model with damage evolution driven by cumulative slip: Thermodynamic formulation and applications to steel-and FRP-concrete bond. *Int. J. Fatigue* **2018**, *113*, 277–289. [CrossRef]
42. Becks, H.; Classen, M. Mode II Behavior of High-Strength Concrete under Monotonic, Cyclic and Fatigue Loading. *Materials* **2021**, *14*, 7675. [CrossRef]
43. Ooi, E.; Shi, M.; Song, C.; Tin-Loi, F.; Yang, Z. Dynamic crack propagation simulation with scaled boundary polygon elements and automatic remeshing technique. *Eng. Fract. Mech.* **2013**, *106*, 1–21. [CrossRef]
44. Baktheer, A.; Chudoba, R. Classification and evaluation of phenomenological numerical models for concrete fatigue behavior under compression. *Constr. Build. Mater.* **2019**, *221*, 661–677. [CrossRef]
45. Baktheer, A.; Aguilar, M.; Hegger, J.; Chudoba, R. Microplane damage plastic model for plain concrete subjected to compressive fatigue loading. In Proceedings of the 10th International Conference on Fracture Mechanics of Concrete and Concrete Structures, FraMCoS-X, ayonne, France, 23–26 June 2019. [CrossRef]

46. Aguilar, M.; Baktheer, A.; Chudoba, R. Numerical Investigation of Load Sequence Effect and Energy Dissipation in Concrete Due to Compressive Fatigue loading Using the New Microplane Fatigue Model MS1. In *Proceedings of the XVI International Conference on Computational Plasticity. Fundamentals and Applications COMPLAS 2021, Barcelona, Spain, 7–10 September 2021*; Onate, E., Peric, D., Chiumenti, M., de Souza Neto, E., Eds; February 2022. [CrossRef]
47. Alrayes, O.; Könke, C.; Ooi, E.T.; Hamdia, K.M. Modeling Cyclic Crack Propagation in Concrete Using the Scaled Boundary Finite Element Method Coupled with the Cumulative Damage-Plasticity Constitutive Law. *Materials* **2023**, *16*, 863. [CrossRef]
48. Alliche, A. Damage model for fatigue loading of concrete. *Int. J. Fatigue* **2004**, *26*, 915–921. [CrossRef]
49. Petracca, M.; Pelà, L.; Rossi, R.; Zaghi, S.; Camata, G.; Spacone, E. Micro-scale continuous and discrete numerical models for nonlinear analysis of masonry shear walls. *Constr. Build. Mater.* **2017**, *149*, 296–314. [CrossRef]
50. Desmorat, R.; Ragueneau, F.; Pham, H. Continuum damage mechanics for hysteresis and fatigue of quasi-brittle materials and structures. *Int. J. Numer. Anal. Methods Geomech.* **2007**, *31*, 307–329. [CrossRef]
51. Baktheer, A.; Chudoba, R. Modeling of bond fatigue in reinforced concrete based on cumulative measure of slip. In *Proceedings of the Computational Modelling of Concrete Structures, EURO-C 2018*; CRC Press: Bad Hofgastein, Austria, 2018; pp. 767–776. [CrossRef]
52. Baktheer, A.; Spartali, H.; Hegger, J.; Chudoba, R. High-cycle fatigue of bond in reinforced high-strength concrete under push-in loading characterized using the modified beam-end test. *Cem. Concr. Compos.* **2021**, *118*, 103978. [CrossRef]
53. Lemaitre, J.; Desmorat, R. *Engineering Damage Mechanics: Ductile, Creep, Fatigue and Brittle Failures*; Springer Science & Business Media: Berlin/Heidelberg, Germany, 2006.
54. Baktheer, A.; Aguilar, M.; Chudoba, R. Microplane fatigue model MS1 for plain concrete under compression with damage evolution driven by cumulative inelastic shear strain. *Int. J. Plast.* **2021**, *143*, 102950. [CrossRef]
55. Kobayashi, A.; Du, J. Fracture Process Zone Models for Concrete and Ceramics. In *Computational Mechanics' 86*; Springer: Tokyo, Japan, 1986; pp. 987–993.
56. Bazant, Z.P.; Li, Y.N. Stability of cohesive crack model: Part I—Energy principles. *J. Appl. Mech.* **1995**, *62*, 959–964. [CrossRef]
57. Ooi, E.; Man, H.; Natarajan, S.; Song, C. Adaptation of quadtree meshes in the scaled boundary finite element method for crack propagation modelling. *Eng. Fract. Mech.* **2015**, *144*, 101–117. [CrossRef]
58. Yang, Z. Fully automatic modelling of mixed-mode crack propagation using scaled boundary finite element method. *Eng. Fract. Mech.* **2006**, *73*, 1711–1731. [CrossRef]
59. Benkemoun, N.; Poullain, P.; Al Khazraji, H.; Choinska, M.; Khelidj, A. Meso-scale investigation of failure in the tensile splitting test: Size effect and fracture energy analysis. *Eng. Fract. Mech.* **2016**, *168*, 242–259. [CrossRef]
60. Jia, M.; Wu, Z.; Yu, R.C.; Zhang, X. Experimental and Numerical Study on Mixed Mode I–II Fatigue Crack Propagation in Concrete. *J. Eng. Mech.* **2022**, *148*, 04022044. [CrossRef]
61. Chudoba, R.; Vořechovský, M.; Aguilar, M.; Baktheer, A. Coupled sliding–decohesion–compression model for a consistent description of monotonic and fatigue behavior of material interfaces. *Comput. Methods Appl. Mech. Eng.* **2022**, *398*, 115259. [CrossRef]
62. Xu, Y.; Yuan, H. Computational analysis of mixed-mode fatigue crack growth in quasi-brittle materials using extended finite element methods. *Eng. Fract. Mech.* **2009**, *76*, 165–181. [CrossRef]
63. Van Mier, J.; Schlangen, E.; Visser, J.; Vervuurt, A. Experimental and numerical analysis of cracking in concrete and sandstone. In *Topics in Applied Mechanics*; Springer: Dordrecht, The Netherlands, 1993; pp. 65–72.

materials

MDPI

Article

Nonlinear Finite Element Model for Bending Analysis of Functionally-Graded Porous Circular/Annular Micro-Plates under Thermomechanical Loads Using Quasi-3D Reddy Third-Order Plate Theory

Jinseok Kim [1,*], Enrique Nava [1] and Semsi Rakici [2]

[1] Department of Mechanical and Aerospace Engineering, Western Michigan University, Kalamazoo, MI 49008, USA; enrique.navamunoz@wmich.edu
[2] School of Building Construction, Georgia Institute of Technology, Atlanta, GA 30332, USA
* Correspondence: jinseok.kim@wmich.edu

Abstract: A nonlinear finite element model for axisymmetric bending of micro circular/annular plates under thermal and mechanical loading was developed using quasi-3D Reddy third-order shear deformation theory. The developed finite element model accounts for a variation of material constituents utilizing a power-law distribution of a two-constituent material, three different porosity distributions through plate thickness, and geometrical nonlinearity. The modified couple stress theory was utilized to account for the strain gradient effects using a single material length scale parameter. Three different types of porosity distributions that have the same overall volume fraction but different enhanced areas were considered as a form of cosine functions. The effects of the material and porosity distribution, microstructure-dependency, the geometric nonlinearity, and various boundary conditions on the bending response of functionally-graded porous axisymmetric microplates under thermomechanical loads were studied using the developed nonlinear finite element model.

Keywords: nonlinear finite element analysis; axisymmetric plates; quasi-3D Reddy third-order theory; functionally-graded porous materials; modified couple stress theory

Citation: Kim, J.; Nava, E.; Rakici, S. Nonlinear Finite Element Model for Bending Analysis of Functionally-Graded Porous Circular/Annular Micro-Plates under Thermomechanical Loads Using Quasi-3D Reddy Third-Order Plate Theory. *Materials* **2023**, *16*, 3505. https://doi.org/10.3390/ma16093505

Academic Editors: Michele Bacciocchi, Angelo Marcello Tarantino, Raimondo Luciano and Carmelo Majorana

Received: 3 April 2023
Revised: 24 April 2023
Accepted: 28 April 2023
Published: 2 May 2023

1. Introduction

Functionally-graded materials (FGMs) are advanced engineering materials composed of two or more constituents with a continuous variation in their compositions. Unlike FGMs, laminated composites exhibit immediate changes in thermal and mechanical properties of the constituents, resulting in stress concentrations at the interfaces where two discrete materials bond together. This leads to delamination problems and the presence of residual stresses in conventional composites working under severe conditions. FGMs were developed by researchers in Japan in 1984 to overcome these issues encountered in a thermal coating material requirement of a hypersonic space plane project [1]. Since then, FGMs have been used in various fields such as aerospace, automobile, electronic, and medical industries due to their advantages over laminated composites and their flexibility to be designed according to the needs of the application field and working environment. The reader is referred to the following review articles [2–5] for details of the historical development of these materials, manufacturing techniques, and optimization of their functionality.

The FGMs have great potential for improving the performance of various components in engineering structures, especially circular and annular plates. Over the last few decades, researchers have extensively studied the behavior of functionally-graded (FG) circular and annular plates under thermal, mechanical, and combined thermomechanical loadings. Since FGMs were initially designed to withstand extreme thermal environments, most of the literature focuses on their thermal analysis. Typical FGMs used in these studies are

made from a mixture of ceramics for their low thermal conductivity and metals for their ductility and resistance to fracture caused by stresses likely to occur in high-temperature gradients. Additionally, the majority of studies on FG plates employ a power law or exponential distribution of materials through the thickness direction of the plates

In 1998, Reddy and Chin [6] conducted a numerical study to investigate thermomechanical responses of FG cylinders and plates under extreme thermal loading conditions using the first-order shear deformation plate theory (FSDT). In their study, the effects of thermomechanical coupling on the response of FGMs subjected to thermal shock were investigated. For the functionally-graded axisymmetric cylinder subjected to high thermal loading, the temperature distribution obtained from both coupled and uncoupled formulations did not show significant differences. However, it was observed that the radial stresses were more affected than the hoop stresses in the FG cylinder.

Using the FSDT, exact solutions of the static bending analysis of FG circular and annular plates having various boundary conditions were presented by Reddy et al. [7]. They derived the solutions of deflections, forces, and the moments of the FG plates based on FSDT in terms of the associated quantities for the isotropic plates based on the classical plate theory (CPT). Hence, the bending solutions of the FG circular plate became readily available whenever the CPT solution was known. Ma and Wang [8] studied the axisymmetric nonlinear bending and post buckling response of functionally-graded circular plates under thermal, mechanical and combined thermomechanical loading conditions. In this study, governing equations were derived using the von Kármán plate theory and the numerical solutions were obtained with the help of the shooting method. The results of this study showed that temperature distribution, deflection values, critical buckling temperature, and post buckling behavior of the functionally-graded circular plates were significantly affected by the volume fraction index.

Praveen and Reddy [9] introduced the finite element formulations that account for the transverse shear strains, rotary inertia, and von Kármán nonlinear strains to perform static and dynamic thermoelastic analysis of the functionally-graded ceramic-metal plates based on FSDT. In 2000, Reddy [10] presented the formulation and analytical solution of simply-supported rectangular FG plates using third order shear deformation plate theory (TSDT) including thermomechanical coupling, time dependency, and von Kármán geometric nonlinearity. From these two studies, it was concluded that the distribution of material constituents in the functionally-graded plates had a significant influence on the resulting thermoelastic response of FG plates. Najafizadeh and Heydari [11] investigated the thermal buckling analysis of functionally-graded circular plates under both uniform and non-uniform temperature changes by employing the TSDT.

Prakash and Ganapathi [12] employed the finite element method to carry out asymmetric-free vibration and thermoelastic stability analysis of functionally-graded circular plates. Nie and Zhong [13] studied the three-dimensional free and forced vibration analysis of functionally-graded circular plates and found that the lowest nondimensional frequency and circumferential wave number of the plate increased as the thickness-to-width ratio increased. They also observed that the magnitudes of the displacements and stresses became larger as the forcing frequency approached the natural frequency of the FG circular plate.

Efraim and Eisenberger [14] presented the free vibration analysis of variable thickness thick annular plates using the exact element method and the dynamic stiffness method. They used FSDT in their formulations and varied Poisson ratio according to the power law distribution in addition to elastic modulus and mass density. Golmakani and Kadkhodayan [15] presented another study that accounted for the gradation of Poisson ratio. They investigated the nonlinear bending analysis of annular FG plates based on both FSDT and TSDT. The same authors [16] later performed a large deflection analysis of circular and annular FG plates subjected to thermomechanical loading within the framework of FSDT, including von Kármán nonlinearity.

Saidi et al. [17] employed unconstrained third order shear deformation theory to analyze the axisymmetric bending and buckling behavior of thick FG circular plates.

Nosier and Fallah [18] reformulated governing equations of the FSDT into interior and edge-zone equations for functionally-graded circular plates. By introducing two sets of equations to define the edge-zone problem, they uncoupled the bending and extension equations, which made it possible to obtain analytical solutions for the asymmetric behavior of functionally-graded circular plates with various boundary conditions under mechanical and thermal loading. Later, they included the von Kármán nonlinear strains into their formulations and investigated the axisymmetric and asymmetric nonlinear bending of functionally-graded circular plates subject to linearly-varying transverse loading [19]. The axisymmetric bending analysis of FG circular plates under arbitrary transverse loads was studied by Yun et al. [20]. They obtained the analytical solutions for the FG circular plates with elastic simple and rigid slipping supports cases when the material property of the FG plate was varying with an exponential distribution. Another analytical study was conducted to solve for in-plane and out-of-plane free vibrations of thick FG circular and annular plates embedded in piezoelectric layers by Talabi and Saidi [21], employing TSDT. The effects of both electrical and mechanical boundary conditions, geometrical parameters of the plate, and in-plane displacements on the middle plane on the natural frequencies of FG circular and annular plates were discussed. Żur [22] applied the Neumann series method to investigate the free vibration behavior of discrete-continuous FG circular plates that may have several ring attachments such as masses, springs and damping elements.

The FG circular and annular plates can be further improved by adding porosity into their composition to decrease the weight of the structure and/or increase the insulation properties. Hence, it is important to examine the mechanical and thermal responses of FG porous plates under different loading and boundary conditions. A general solution of a porous FG circular plate that is supported by a non-uniform Kerr elastic foundation and subjected to non-axisymmetric, non-uniform shear and normal tractions, and a magnetic actuation was developed by Rad and Shariyat [23]. Their results showed that the radial displacement component was more prone to being affected by the induced magnetic actuation. Additionally, because of the presence of incompressible fluid in the pores in this study, as the porosity increased, the plates became stiffer. The buckling behavior of porous circular plate between piezoelectric layers under thermal loading was investigated by Jabbari et al. [24]. They showed that, as the porosity increased, the critical temperature decreased and the plate whose pores were saturated with fluid became unstable. On the other hand, the critical temperature of the plates can be decreased by increasing the thermal expansion coefficient of the fluid filling the pores and the piezoelectric layers. Zhao et al. [25] studied the free and forced vibration analysis of FG porous circular, annular, and sector plates with general elastic restraints using FSDT.

These extensive studies conducted on FG circular and annular plates show that these structures have an intrinsic advantage resulting from the non-homogeneity and smooth variations of the material properties. It is shown that the deflections and tensile stresses of FG circular and annular plates can be lower and critical buckling loads can be higher as compared to the homogeneous ones, depending on the predetermined variation of material properties of FG circular and annular plates. It is also possible to adjust the natural frequencies of these structures by changing the variation of the material distribution. Hence, all these conclusions make it attractive to examine the performance of the FGMs for the micro-scale structures. However, conventional continuum mechanics cannot capture the size dependency that is experimentally observed at the micro-scale [26–29]. Therefore, a higher order continuum theory is required for the accurate modeling and analysis of these structures. Couple stress theories [30–32], Erigen nonlocal elasticity theory [33] and the strain gradient elasticity theories [26,34,35] are some of the higher order continuum theories that take the size dependency into account. The modified couple stress theory is the most commonly employed theory because only a single length scale parameter is needed to include size effect.

Ke et al. [36] investigated the bending, buckling, and free vibration analyses of FG annular microplates with hinged–hinged and clamped–clamped boundary conditions. Their size-dependent annular microplate model was based on the Mindlin plate theory and the modified couple stress theory. This study showed that elastic buckling analysis was more sensitive to size effect than the free vibration analysis. Similar analyses were presented by Ansari et al. [37] for FG circular and annular microplates. They also employed Mindlin plate theory, but different to the previous study, size dependency was included using modified strain gradient elasticity theory. Both studies agreed that the smaller the dimensionless length scale parameter they had, the smaller the deflection but the higher the critical buckling load and natural frequencies that they obtained.

Reddy and Berry [38] presented the classical and the first order plate theories for axisymmetric bending of circular micro-plates including von Kármán nonlinear strains. Size dependency was captured with the modified couple stress theory. Later, Reddy et al. [39] used this theory to develop nonlinear finite element models for FG circular plates.

An analytical solution for the free vibration of FG circular and annular nanoplates was obtained by Hosseini-Hashemi et al. [40] based on Mindlin plate theory and Eringen nonlocal elasticity theory. Beni et al. [41] studied the same problem for FG cylindrical nanoshells using FSDT in conjunction with the modified couple stress theory. They presented the effects of the material length scale, distribution of the FGMs, nanotube thickness, and length on the fundamental frequencies. Eshraghi et al. [42] studied the bending and the free vibration analysis of FG annular and circular microplates subjected to thermal loading using the modified couple stress theory. They unified the displacement fields such that results for Kirchoff plate theory, Mindlin plate theory, and third order shear deformation plate theory can be generated. Additionally, not only the mechanical and thermal properties of the FG plates but also the material length scale parameter were not kept constant but were changed through the thickness direction, obeying a power law distribution. The transverse deflections, normalized circumferential and radial stresses, and the natural frequencies were presented for different thermal loading, material, and geometrical parameters. Ji et al. [43] developed a plate model capturing the size dependency for FG circular micro-plates based on the strain gradient theory of Zhou. They analyzed the bending and free vibration of a simply-supported circular micro-plate and the results were compared with those obtained by employing the strain gradient theory of Lam, the modified couple stress theory, and the CPT.

A free vibration and thermal buckling analysis of an FG porous circular micro-plate was conducted by Shojaeefard et al. [44] based on CPT and FSDT with modified couple stress theory. The effects of the temperature change, distribution of the material properties, size-dependency, and porosity on the fundamental frequencies and critical temperature were investigated. Kim et al. [45] presented the analytical solutions of bending, free vibration, and the buckling problem for FG porous micro-plates using CPT and FSDT in conjunction with the modified couple stress theory. Recently, Wang and Zhang [46] studied the thermal buckling and postbuckling responses of GPL-reinforced nanocomposite beams using the higher order shear deformation theory with temperature-dependent properties. Zhang et al. [47] carried out analytical studies on thermo-mechanical responses of porous functionally-graded, graphene-reinforced cylindrical panels based on a third order shear deformation theory. The acoustic characteristics of functionally-graded porous graphene reinforced nano composite plates (FG-PGRC) were studied by Xu et al. [48]. In their study, a higher order shear deformation theory was utilized to study the vibration and noise reduction of an FG-PGRC plate.

This study aimed to investigate the behavior of FG porous circular microplates under thermal and mechanical loadings, which has not been studied in the literature. To this end, a nonlinear finite element model was developed based on quasi-3D Reddy third-order shear deformation theory and the modified couple stress theory, taking into account von Kármán nonlinear strains to consider geometrical nonlinearity. The FGM was composed of two constituents based on a power law distribution through the thickness direction, and

three different porosity profiles were considered. Parametric analyses were conducted to investigate the effects of the distribution of material properties and porosity, size-dependency, geometric nonlinearity, and different boundary conditions on the static bending analysis of FG porous circular microplates.

2. Constitutive Models

2.1. Functionally-Graded Porous Materials

The model considers isotropic axisymmetric plates composed of two constituents with varying material properties and internal porosity through the thickness, modeled using a power-law distribution and cosine variation, respectively. The typical material properties of functionally-graded porous materials (FGPM) are thus captured in the model, as shown in Equation (1).

$$P(z) = [(P_t - P_b)f(z) + P_b](1 - \psi(z)), \qquad f(z) = \left(\frac{z}{h} + \frac{1}{2}\right)^n, \tag{1}$$

where P_t and P_b are material properties on the top and bottom surfaces of plates, n is power-index, $f(z)$ is a volume fraction function, and $\psi(z)$ is a porosity distribution function. Three different types of porosity distributions were considered in this study.

$$\begin{aligned} &\text{Type 1} : \psi(z) = \phi \cos\left[\pi\left(\frac{z}{h}\right)\right] \\ &\text{Type 2} : \psi(z) = \phi \cos\left[\frac{\pi}{2}\left(\frac{z}{h} + 0.5\right)\right] \\ &\text{Type 3} : \psi(z) = \phi \cos\left[\frac{\pi}{2}\left(\frac{z}{h} - 0.5\right)\right], \end{aligned} \tag{2}$$

where ϕ is the maximum porosity value along thickness direction. The distribution of porosity through the thickness of the plates was normalized to have the same porous volume, and it is important to investigate the effect of different porosity distributions [45]. Figure 1a displays the normalized porosity distribution throughout the thickness of the plate. Figure 1b–d show the effects of porosity distributions on the variation of typical materials properties. As an example, a porosity value was set to $\phi = 0.5$, three different power-law index values $n = 0, 0.5$, and 5.0 were set. The ratio of material properties on the top and bottom surfaces was assumed to be $\frac{E_t}{E_b} = 10$. The Type 1, Type 2, and Type 3 porosity distributions are a symmetric and center-enhanced, a bottom area enhanced, and a top area enhanced porosity distributions, respectively.

2.2. Modified Couple Stress Theory

The motion of the material particles in classical couple stress theory [30,49] is described to rotate the material particles in addition to forces in the classical continuum mechanics. The size-dependent effect was captured using two additional material constants in the classical couple stress theory. These two material constants are difficult to determine because of their indeterminacy. Eringen [33] proposed a micropolar theory and defined the motion of a particle using the location vector and inner product of a rigid vector. A modified couple stress theory using the concept of the representative volume elements and a higher order equilibrium condition was proposed by Yang et al. [32]. According to the modified couple stress theory, the deviatoric part of a couple stress tensor is only associated with the symmetric part of rotation gradient and it contributes to the total strain energy along with the classical strain energy. The strain energy potential of an axisymmetric plate based on the modified couple stress theory can be expressed as

$$\begin{aligned} U &= \frac{1}{2}\int_V (\boldsymbol{\sigma} : \boldsymbol{\varepsilon} + \boldsymbol{m} : \boldsymbol{\chi}) dV \\ &= \frac{1}{2}\int_{r_i}^{r_o} \left[\int_{-\frac{h}{2}}^{\frac{h}{2}} (\boldsymbol{\sigma} : \boldsymbol{\varepsilon} + \boldsymbol{m} : \boldsymbol{\chi}) dz\right] r dr, \end{aligned} \tag{3}$$

where r_i and r_o are the inner and outer radii of the plate, σ and ε are the Cauchy stress tensor and Von Kámán nonlinear strain tensor, $\boldsymbol{m}$ and $\boldsymbol{\chi}$ are the deviatoric part of the symmetric couple stress tensor and the symmetric curvature tensor. Note that the differential volume element dV can be written as $dV = rdrd\theta dz$ and 2π from the integration with respect to θ being omitted in Equation (3). The curvature tensor and the deviatoric part of the symmetric couple stress tensor are defined as [32]

$$\boldsymbol{\chi} = \frac{1}{2}\left[\boldsymbol{\nabla\omega} + (\boldsymbol{\nabla\omega})^{\mathrm{T}}\right] \tag{4}$$

$$\boldsymbol{m} = 2\mu\ell^2\boldsymbol{\chi}, \tag{5}$$

where $\boldsymbol{\omega}$ is the rotation vector, $\boldsymbol{\omega} = \frac{1}{2}\boldsymbol{\nabla} \times \boldsymbol{u}$, μ is the shear modulus, and ℓ is a length scale parameter.

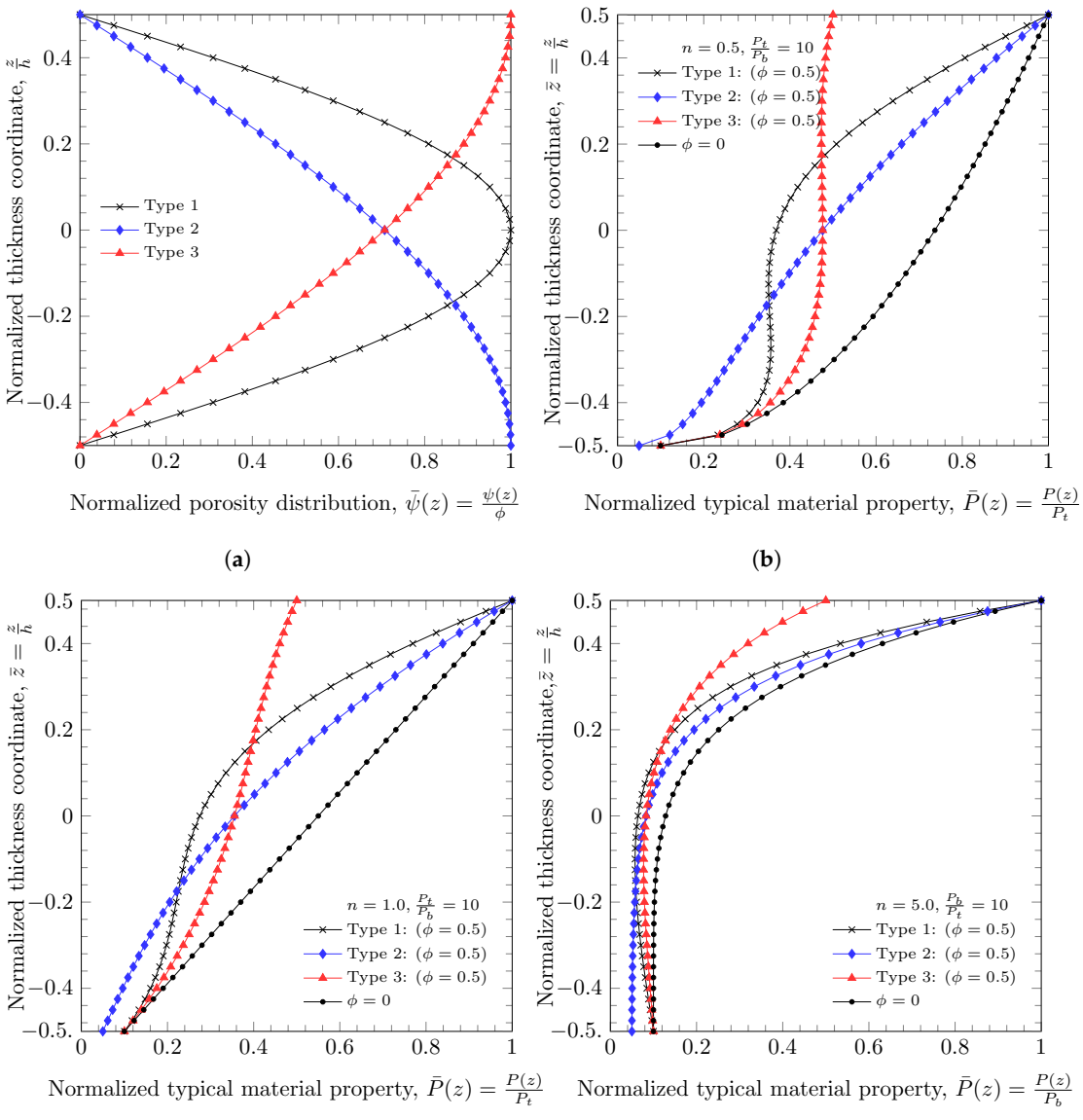

Figure 1. Distribution of porosity and a typical material property [45]. (**a**) Distribution of porosity through thickness. (**b**) Distribution of typical material property ($n = 0.5$). (**c**) Distribution of typical material property ($n = 1.0$). (**d**) Distribution of typical material property ($n = 5.0$).

In this study, an isotropic linear elastic material was assumed and the stress and strain relation [50] for an axisymmetric plate is

$$\begin{Bmatrix} \sigma_{rr} \\ \sigma_{\theta\theta} \\ \sigma_{zz} \\ \sigma_{rz} \end{Bmatrix} = \Lambda \begin{bmatrix} 1-\nu & \nu & \nu & 0 \\ \nu & 1-\nu & \nu & 0 \\ \nu & \nu & 1-\nu & 0 \\ 0 & 0 & 0 & \frac{1}{2}(1-2\nu) \end{bmatrix} \begin{Bmatrix} \varepsilon_{rr} - \alpha(T-T_0) \\ \varepsilon_{\theta\theta} - \alpha(T-T_0) \\ \varepsilon_{zz} - \alpha(T-T_0) \\ \varepsilon_{rz} \end{Bmatrix}, \tag{6}$$

where $\Lambda = E/[(1+\nu)(1-2\nu)]$, E is Young's modulus , which varies along the plate's thickness, ν is a constant Poisson's ratio in the elastic stiffness matrix. α is the thermal expansion coefficient, and T and T_0 are the temperature at a material point and the reference temperature of the undeformed body.

The nonzero curvatures and modified couple stresses are

$$\begin{Bmatrix} m_{r\theta} \\ m_{\theta z} \end{Bmatrix} = 2\ell^2\mu \begin{Bmatrix} \chi_{r\theta} \\ \chi_{\theta z} \end{Bmatrix}. \tag{7}$$

3. Quasi-3D Reddy Third-Order Plate Theory

3.1. Displacement and Strains

The displacement field of quasi-3D Reddy third-order plate theory can be derived from an assumption of a cubic variation of in-plane displacements and a quadratic variation of deflection (i.e., out-of-plane displacement) with zero tangential traction on top and bottom surfaces. The displacement field of cubic variation of in-plane displacement and a quadratic variation of deflection through thickness direction for axisymmetric plates takes the form of

$$\begin{aligned} u_r(r,z,t) &= u_0(r,t) + z\theta_r(r,t) + z^2\phi_r(r,t) + z^3\psi_r(r,t) \\ u_z(r,z,t) &= w_0(r,t) + z\theta_z(r,t) + z^2\phi_z(r,t). \end{aligned} \tag{8}$$

With the assumption of zero tangential traction on top and bottom surfaces, the displacement (8) can be written in the form of

$$\varepsilon_{rz}\left(r, \frac{h}{2}, t\right) = \varepsilon_{rz}\left(r, -\frac{h}{2}, t\right) = 0. \tag{9}$$

The form of quasi-3D Reddy third-order plate theory for axisymmetric plates takes

$$\begin{aligned} u_r(r,z,t) &= u_0(r,t) + z\theta_r(r,t) - \frac{z^2}{2}\frac{\partial\theta_z}{\partial r} - z^3c_1\left[\theta_r(r,t) + \frac{\partial\lambda(r,t)}{\partial r}\right] \\ u_z(r,z,t) &= w_0(r,t) + z\theta_z(r,t) + z^2\phi_z(r,t), \end{aligned} \tag{10}$$

where u_0 is the membrane displacement, θ_r is the rotation of a transverse normal about θ direction, w_0 is the deflection, θ_z and ϕ_z are the thickness stretch, $\lambda = w_0 + \frac{h^2}{4}\phi_z$ and $c_1 = \frac{4}{3h^2}$.

Based on the assumption of small strains and moderate rotations, nonzero von Kámán nonlinear strain for the axisymmetric plate is given by [39].

$$\begin{aligned} \varepsilon_{rr} &= \frac{\partial u_r}{\partial r} + \frac{1}{2}\left(\frac{\partial u_z}{\partial r}\right)^2 \\ \varepsilon_{\theta\theta} &= \frac{u_r}{r} \\ \varepsilon_{zz} &= \frac{\partial u_z}{\partial z} \\ \varepsilon_{rz} &= \frac{1}{2}\left(\frac{\partial u_r}{\partial z} + \frac{\partial u_z}{\partial r}\right). \end{aligned} \tag{11}$$

The non-zero strains with the displacement field (10) of quasi-3D Reddy third-order plate theory are defined as

$$\begin{Bmatrix} \varepsilon_{rr} \\ \varepsilon_{\theta\theta} \\ \varepsilon_{zz} \\ 2\varepsilon_{rz} \end{Bmatrix} = \begin{Bmatrix} \frac{\partial u_0}{\partial r} + \frac{1}{2}\left(\frac{\partial w_0}{\partial r}\right)^2 \\ \frac{u_0}{r} \\ \theta_z \\ \theta_r + \frac{\partial w_0}{\partial r} \end{Bmatrix} + z\begin{Bmatrix} \frac{\partial \theta_r}{\partial r} \\ \frac{\theta_r}{r} \\ 2\phi_z \\ 0 \end{Bmatrix} - z^2\begin{Bmatrix} \frac{1}{2}\frac{\partial^2 \theta_z}{\partial r^2} \\ \frac{1}{2r}\frac{\partial \theta_z}{\partial r} \\ 0 \\ -c_2\left(\theta_r + \frac{\partial \lambda}{\partial r}\right) + \frac{\partial \phi_z}{\partial r} \end{Bmatrix} - z^3\begin{Bmatrix} c_1\left(\frac{\partial \theta_r}{\partial r} + \frac{\partial^2 \lambda}{\partial r^2}\right) \\ \frac{c_1}{r}\left(\theta_r + \frac{\partial \lambda}{\partial r}\right) \\ 0 \\ 0 \end{Bmatrix}, \tag{12}$$

where $c_2 = \frac{4}{h^2}$. The symmetric part of the curvature tensor for axisymmetric plates is defined as

$$\begin{aligned} \chi_{r\theta} &= \frac{1}{2}\left(\frac{\partial \omega_\theta}{\partial r} - \frac{\omega_\theta}{r}\right) \\ \chi_{\theta z} &= \frac{1}{2}\frac{\partial \omega_\theta}{\partial z}, \end{aligned} \tag{13}$$

where $\omega_\theta = \frac{1}{2}\left(\frac{\partial u_r}{\partial z} - \frac{\partial u_z}{\partial r}\right)$. Thus, the $\chi_{r\theta}$ and $\chi_{\theta z}$ in terms of the displacements in Equation (10) take the form of

$$\begin{Bmatrix} \chi_{r\theta} \\ \chi_{\theta z} \end{Bmatrix} = \frac{1}{4}\begin{Bmatrix} \frac{\partial \theta_r}{\partial r} - \frac{\partial^2 w_0}{\partial r^2} - \frac{1}{r}\left(\theta_r - \frac{\partial w_0}{\partial r}\right) \\ -2\frac{\partial \theta_z}{\partial r} \end{Bmatrix} - \frac{z}{2}\begin{Bmatrix} \frac{\partial^2 \theta_z}{\partial r^2} - \frac{1}{r}\frac{\partial \theta_z}{\partial r} \\ c_2\left(\theta_r + \frac{\partial \lambda}{\partial r}\right) + \frac{\partial \phi_z}{\partial r} \end{Bmatrix} - \frac{z^2}{4}\begin{Bmatrix} c_2\left[\frac{\partial \theta_r}{\partial r} + \frac{\partial^2 \lambda}{\partial r^2} - \frac{1}{r}\left(\theta_r + \frac{\partial \lambda}{\partial r}\right)\right] + \frac{\partial^2 \phi_z}{\partial r^2} - \frac{1}{r}\frac{\partial \phi_z}{\partial r} \\ 0. \end{Bmatrix}. \tag{14}$$

3.2. Governing Equations

In this study, the soft-coupled thermoelastical behavior of functionally-graded porous materials was analyzed using the finite element method. The equations of equilibrium and the weak form finite element model for static bending problems of axisymmetric plate were obtained using the principle of virtual displacement.

$$\begin{aligned} 0 = &- \int_V (\sigma_{rr}\delta\varepsilon_{rr} + \sigma_{\theta\theta}\delta\varepsilon_{\theta\theta} + \sigma_{zz}\delta\varepsilon_{zz} + 2\sigma_{rz}\delta\varepsilon_{rz} + 2m_{r\theta}\delta\chi_{r\theta} + 2m_{\theta z}\delta\chi_{\theta z})dV \\ &+ \int_V (\bar{f}_i\delta u_i + \bar{c}_i\delta\omega_i)dV + \int_S (\bar{t}_i\delta u_i + \bar{s}_i\delta\omega_i)dS \\ &+ \int_{\Omega^t} (q_i^t\delta u_i + p_i^t\delta\omega_i)d\Omega^t + \int_{\Omega^b} \left(q_i^b\delta u_i + p_i^b\delta\omega_i\right)d\Omega^b, \end{aligned} \tag{15}$$

where σ_{ij} and m_{ij} are the symmetric part of the stress tensor and the deviatoric part of the couple stress tensor. $\bar{f}_i$ and $\bar{c}_i$ are the body forces and couples. $\bar{t}_i$, $\bar{s}_i$, and $\bar{d}$ are the surface forces and couples on the side surfaces. q_i^α and p_i^α are the surface forces and couples on top $(\alpha = t)$ and bottom $(\alpha = b)$ surfaces.

The governing equations of quasi-3D Reddy third order theory are

$$0 = \frac{1}{r}\left[\frac{\partial}{\partial r}\left(rN_{rr}^{(0)}\right) - N_{\theta\theta}^{(0)}\right] + F_r^{(0)} \tag{16}$$

$$\begin{aligned} 0 = \frac{1}{r}\Bigg\{ & \frac{\partial}{\partial r}\left(rN_{rr}^{(1)}\right) - N_{\theta\theta}^{(1)} - c_1\left(\frac{\partial}{\partial r}\left(rN_{rr}^{(3)}\right) - N_{\theta\theta}^{(3)}\right) - r\left(N_{rz}^{(0)} - c_2 N_{rz}^{(2)}\right) \\ & + \frac{1}{2}\left[\frac{\partial}{\partial r}\left(rM_{r\theta}^{(0)}\right) + M_{r\theta}^{(0)} - c_2\left(\frac{\partial}{\partial r}\left(rM_{r\theta}^{(2)}\right) + M_{r\theta}^{(2)} - 2rM_{\theta z}^{(1)}\right)\right]\Bigg\} \\ & + F_r^{(1)} - c_1 F_r^{(3)} \end{aligned} \tag{17}$$

$$\begin{aligned} 0 = \frac{1}{r}\Bigg\{ & \frac{\partial}{\partial r}\left[rN_{rr}^{(0)}\left(\frac{\partial w}{\partial r}\right)\right] + c_1\frac{\partial}{\partial r}\left[\frac{\partial}{\partial r}\left(rN_{rr}^{(3)}\right) - rN_{\theta\theta}^{(3)}\right] + \frac{\partial}{\partial r}\left(rN_{rz}^{(0)}\right) - c_2\frac{\partial}{\partial r}\left(rN_{rz}^{(2)}\right) \\ & + \frac{1}{2}\left[\frac{\partial}{\partial r}\left(\frac{\partial}{\partial r}\left(rM_{r\theta}^{(0)}\right) + M_{r\theta}^{(0)}\right) + c_2\frac{\partial}{\partial r}\left(\frac{\partial}{\partial r}\left(rM_{r\theta}^{(2)}\right) + M_{r\theta}^{(2)}\right) - 2c_2\frac{\partial}{\partial r}\left(rM_{\theta z}^{(1)}\right)\right]\Bigg\} \\ & + F_z^{(0)} + \frac{c_1}{r}\frac{\partial}{\partial r}\left(rF_r^{(3)}\right) \end{aligned} \tag{18}$$

$$\begin{aligned} 0 = \frac{1}{r}\Bigg\{ & \frac{1}{2}\frac{\partial}{\partial r}\left[\frac{\partial}{\partial r}\left(rN_{rr}^{(2)}\right) - N_{\theta\theta}^{(2)}\right] - N_{zz}^{(0)} \\ & + \left[\frac{\partial}{\partial r}\left(\frac{\partial}{\partial r}\left(rM_{r\theta}^{(1)}\right) + M_{r\theta}^{(1)} - rM_{\theta z}^{(0)}\right)\right]\Bigg\} + F_z^{(1)} + \frac{1}{2}\frac{\partial}{\partial r}\left(rF_r^{(2)}\right) \end{aligned} \tag{19}$$

$$\begin{aligned} 0 = \frac{1}{r}\Bigg\{ & \frac{1}{3}\frac{\partial}{\partial r}\left[\frac{\partial}{\partial r}\left(rN_{rr}^{(3)}\right) - N_{\theta\theta}^{(3)}\right] - 2rN_{zz}^{(1)} \\ & + \frac{\partial}{\partial r}\left[\frac{\partial}{\partial r}\left(rM_{r\theta}^{(2)}\right) + M_{r\theta}^{(2)} - 2rM_{\theta z}^{(1)}\right]\Bigg\} + F_z^{(2)} + \frac{1}{3}\frac{\partial}{\partial r}\left(rF_r^{(3)}\right), \end{aligned} \tag{20}$$

where $\left\{N_{ij}^{(k)}, M_{ij}^{(k)}\right\} = \int_{-\frac{h}{2}}^{\frac{h}{2}} z^k\{\sigma_{ij}, m_{ij}\}dz$ and $F_i^{(k)} = \int_{-\frac{h}{2}}^{\frac{h}{2}} z^k\left\{f_i + \left[q_i^t - 1^k q_i^b\right]\right\}dz$. Note that the body couple $\bar{c}_\theta$ is omitted in the governing equation.

The temperature distribution through thickness direction can be determined by solving the steady state energy equation,

$$-\frac{d}{dz}\left(k(z)\frac{dT}{dz}\right) = 0, \tag{21}$$

where $k(z)$ is heat conductivity and T is the temperature. The effective thermal conductivity is defined using the Maxwell–Eucken model described by Deng et al. [51]:

$$k(z) = k_s(z)\left[\frac{k_f + 2k_s(z) + 2\Phi\left(k_f - k_s(z)\right)}{k_f + 2k_s(z) - \Phi\left(k_f - k_s(z)\right)}\right], \tag{22}$$

where $k_s(z)$ and k_f are the thermal conductivity of the solid and fluid phases, respectively, and Φ is the porosity. In this study, the thermal conductivity of the solid is obtained using a power-law distribution described in previous section.

4. Finite Element Model

A weak from Galerkin finite element model for the circular plate bending is developed using the principle of virtual displacement (15) and a weak form is directly developed from the energy Equation (21) for steady state heat conduction problem. The details of weak form Galerkin finite element model can be found in Reddy [52].

The temperature T and generalized displacements $(u_0, \theta_r, w_0, \theta_z, \phi_z)$ are approximated in following form:

$$T(z) = \sum_{j=1}^{n} T_j \hat{\psi}_j(z) \tag{23}$$

$$u_0(r) = \sum_{j=1}^{n} u_j \psi_j(r) \tag{24}$$

$$\theta_r(r) = \sum_{j=1}^{n} \theta_j \psi_j(r) \tag{25}$$

$$w_0(r) = \sum_{J=1}^{2n} \Delta_J^{(1)} \phi_J(r) \tag{26}$$

$$\theta_z(r) = \sum_{J=1}^{2n} \Delta_J^{(2)} \phi_J(r) \tag{27}$$

$$\phi_z(r) = \sum_{J=1}^{2n} \Delta_J^{(3)} \phi_J(r), \tag{28}$$

where T_j are nodal temperatures through thickness direction; u_j, θ_j, and w_j are nodal displacements in the radial direction; $\hat{\psi}_j$ and ψ_j are the Lagrange interpolation functions; ϕ_J are the Hermite interpolation functions; $\Delta_J^{(i)}$ are generalized deflections and $i = 1, 2, 3$ correspond to w_0, θ_z, ϕ_z, respectively; n is the number of nodes in an element.

The finite element model of the steady state heat conduction problem is given by

$$\left[\hat{K}\right]^e \left\{T^e\right\} = \left\{\hat{F}\right\}^e, \tag{29}$$

where the stiffness matrix and external heat flux are

$$\hat{K}_{ij} = \int_{-\frac{h}{2}}^{\frac{h}{2}} k(z) \left(\frac{d\hat{\psi}_i}{dz} \frac{d\hat{\psi}_i}{dz} \right) dz \tag{30}$$

$$\hat{F}_i = q_i. \tag{31}$$

The finite element model of an axisymmetric plate static bending is given by

$$\begin{bmatrix} K^{11} & K^{12} & K^{13} & K^{14} & K^{15} \\ K^{21} & K^{22} & K^{23} & K^{24} & K^{25} \\ K^{31} & K^{32} & K^{33} & K^{34} & K^{35} \\ K^{41} & K^{42} & K^{43} & K^{44} & K^{45} \\ K^{51} & K^{52} & K^{53} & K^{54} & K^{55} \end{bmatrix}^e \begin{Bmatrix} \{u_0\} \\ \{\theta_r\} \\ \{w_0\} \\ \{\theta_z\} \\ \{\phi_z\} \end{Bmatrix}^e = \begin{Bmatrix} \{F^1\} \\ \{F^2\} \\ \{F^3\} \\ \{F^4\} \\ \{F^5\} \end{Bmatrix}^e. \tag{32}$$

The elements of the stiffness matrix, K^{lm}, and the elements of force vector, F^l, are defined in Appendix A.

The solution of the nonlinear finite element model (32) is obtained using Newton's iteration procedure. The linearized element equations take the form of

$$\mathbf{T}^e \left(\boldsymbol{\Delta}^{(i-1)} \right) \delta \boldsymbol{\Delta}^{(i)} = -\mathbf{R}^e \left(\boldsymbol{\Delta}^{(i-1)} \right), \tag{33}$$

where $\mathbf{T}^e$ is the tangent stiffness matrix, $\delta \boldsymbol{\Delta}^{(i)}$ is incremental displacements at the ith iteration, and $\mathbf{R}^e$ is the residual vector. The tangent matrix and residual are defined as [52]

$$\mathbf{T}^e = \frac{\partial \mathbf{R}^e}{\partial \boldsymbol{\Delta}^e}, \qquad \mathbf{R}^e = \left(\mathbf{K}^e \boldsymbol{\Delta}^e - \mathbf{F}^e \right)^{(i-1)}. \tag{34}$$

By solving the assembled global system equation, the global incremental displacement vector at ith iteration, $\delta\mathbf{U}^{(i)}$ is obtained.

$$\delta\mathbf{U}^{(i)} = -\left[\mathbf{T}\left(\mathbf{U}^{(i-1)}\right)\right]^{-1}\mathbf{R}^{(i-1)}. \tag{35}$$

The total displacement at the ith iteration is obtained by adding the incremental solution at the ith iteration to the previous solution at the $(i-1)$th iteration [39].

$$\mathbf{U}^{(i)} = \mathbf{U}^{(i-1)} + \delta\mathbf{U}^{(i)}. \tag{36}$$

In this study, we considered geometrical nonlinearity with elastic material behavior. For this purpose, the Newton's iteration is sufficient to obtain the converged solutions. However, when limit load, softening branches, or snap-through behavior are considered, another solution procedure, such as the arc length method, should be considered. These solution procedures can be used in conjunction with various numerical methods such as isogeometric techniques [53,54] or the Rayleigh Ritz method [55] in addition to the finite element method.

5. Numerical Results

In the numerical examples, we considered several examples of annular circular plates with various boundary conditions such as simply-supported and clamped boundary conditions. To validate the developed finite element model, we compared our results with available studies in the literature. We also conducted convergence studies to obtain optimal mesh size and different quadrature rules to make sure we avoided any locking phenomena. In this study, we used 16 elements and full quadrature rules for linear parts of the stiffness matrix and reduced quadrature rules for shear, nonlinear, and couple stress parts of the stiffness matrix.

Figure 2 shows the annular plate we studied. The numerical parameters for the validation study were adapted from the study of Reddy et al. [39]: h = 0.1, $r_o = 10h$, $r_i = 0.25r_0$, $E_1 = 10^6$, and $E_2 = 10^5$.

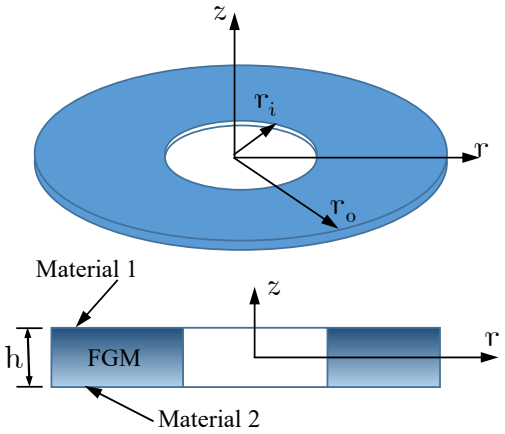

Figure 2. An axisymmetric FGM annular plate [39].

Figures 3–5 show that maximum deflection versus the load parameter $P = \frac{q_0 h^4}{E_c r_o^4}$ at the free edges, where q_0 is a distributed load on the top surface, h is the plate thickness, E_c is the Young's modulus of ceramic materials on the top surface, and r_o is the outer radius of the annular plate. The developed finite element model shows a good agreement with the study of Reddy et al. [39]. In this figure, the effects of the material variations based on the change of the power-law index, and the effect of length scale parameter are presented with various boundary conditions.

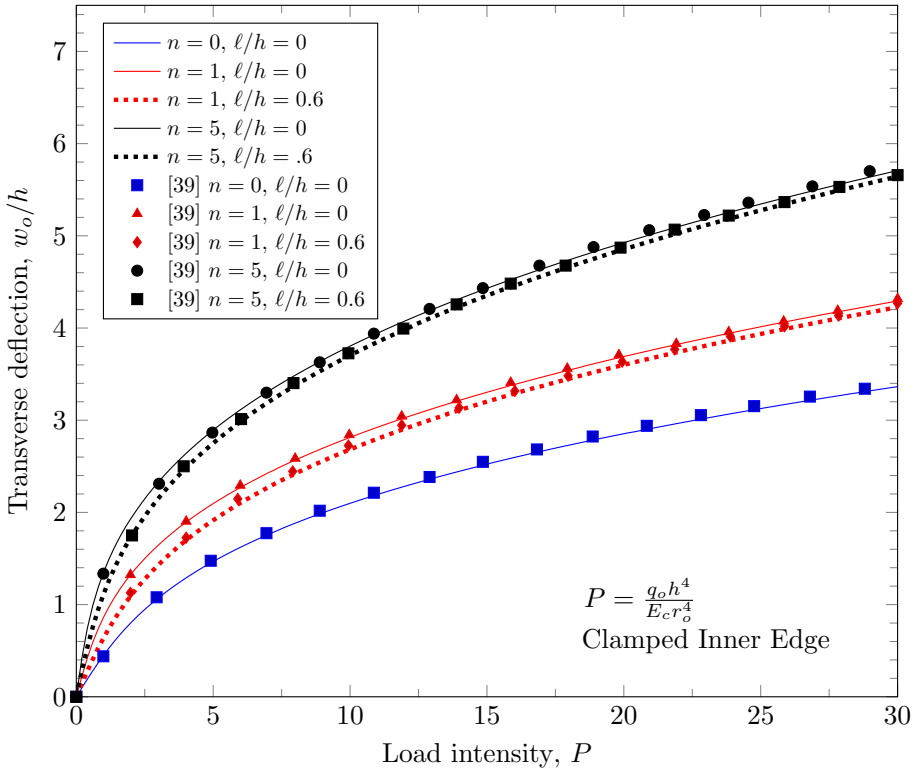

Figure 3. Maximum deflection at outer edge with clamped inner edge.

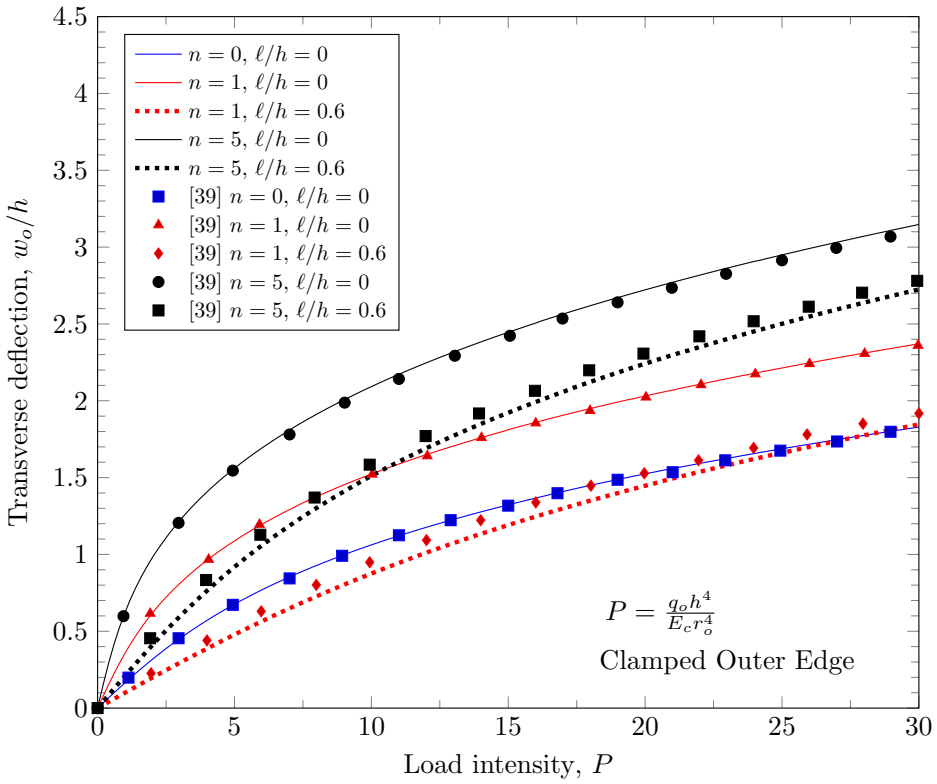

Figure 4. Maximum deflection at inner edge with clamped outer edge.

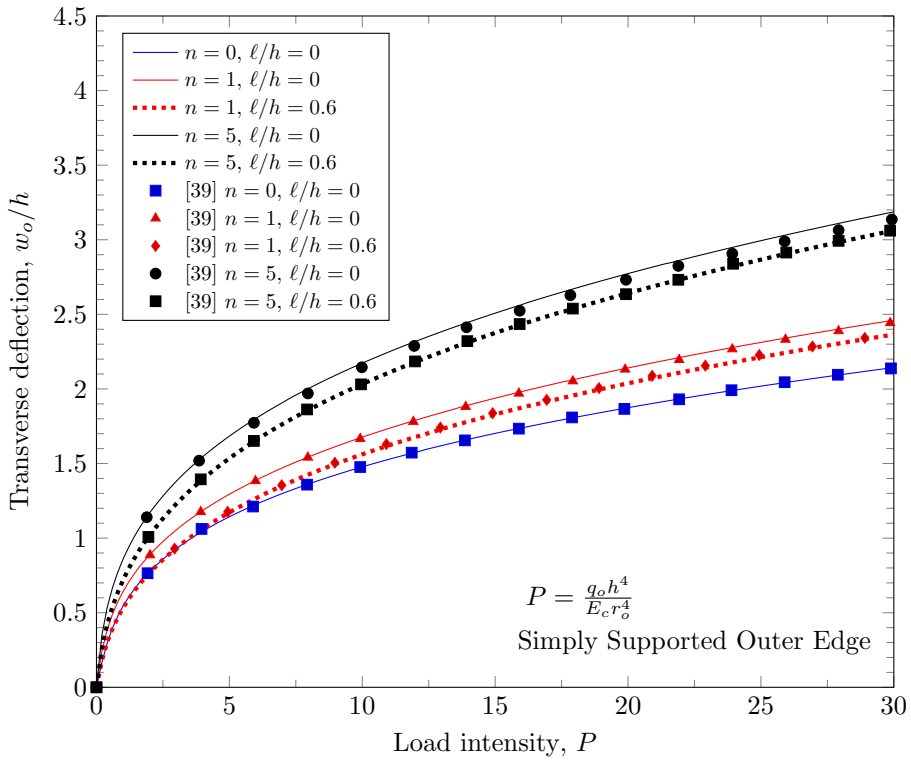

Figure 5. Maximum deflection at inner edge with simply-supported outer edge.

With the validated finite element model, we evaluated the effects of various parameters such as the length scale parameters, the shape of porosity distribution, power law index, and boundary conditions. In this study, we considered a porous functionally-graded material with Monel and zirconia and the material properties of them follow [56]:

$$K_m = 227.24\ \text{GPa}, \quad \mu_m = 65.55\ \text{GPa}, \quad \alpha_m = 15 \times 10^{-6}\ /\text{K}, \quad k_m = 25\ \text{W/mK} \quad \text{for Monel}$$
$$K_c = 125.83\ \text{GPa}, \quad \mu_c = 58.077\ \text{GPa}, \quad \alpha_c = 10 \times 10^{-6}\ /\text{K}, \quad k_c = 2.09\ \text{W/mK} \quad \text{for zirconia,}$$

where K_i is the bulk modulus, μ_i is the shear modulus, α_i is the thermal expansion coefficient, k_i is the thermal conductivity, and the subscription m and c indicate metal and ceramic, respectively. We assumed that the porous is filled with the air and the thermal conductivity of the air is assumed to be $k_a = 0.025572$ W/mK.

To induce thermal load, two different temperatures were applied on the top and bottom surfaces; 500 K was applied on the top surface and 300 K was applied on the bottom surface. Figure 6 shows the temperature distribution through plate thickness depending on the variation of material constituents and porosity distribution. The temperature distribution was obtained by solving the energy Equation (21). Three different types of porosity distributions and the variation of material constituents were considered. In the area where the volume fraction for porosity is larger, the thermal resistance becomes larger and the temperature change through the thickness is less than the area where the volume fraction of porosity is lesser. With a larger power-law index, the effective thermal conductivity is increased and thermal resistance becomes smaller because the volume fraction of metal is increased.

For illustration purposes, the same plate geometry as Reddy et al. [39] was used, and the effects of various parameters with clamped and simply-supported boundary conditions were considered.

Figures 7 and 8 show effects of the length scale parameter on the maximum deflection of FGM plates. When the power-law index is larger, the volume fraction of Monel is larger and the FGM plate becomes stiffer. The length scale parameter can capture the stiffening

behavior in micro scale structures. The deflections of FGM plates with various length scale parameters are shown in Figures 9 and 10.

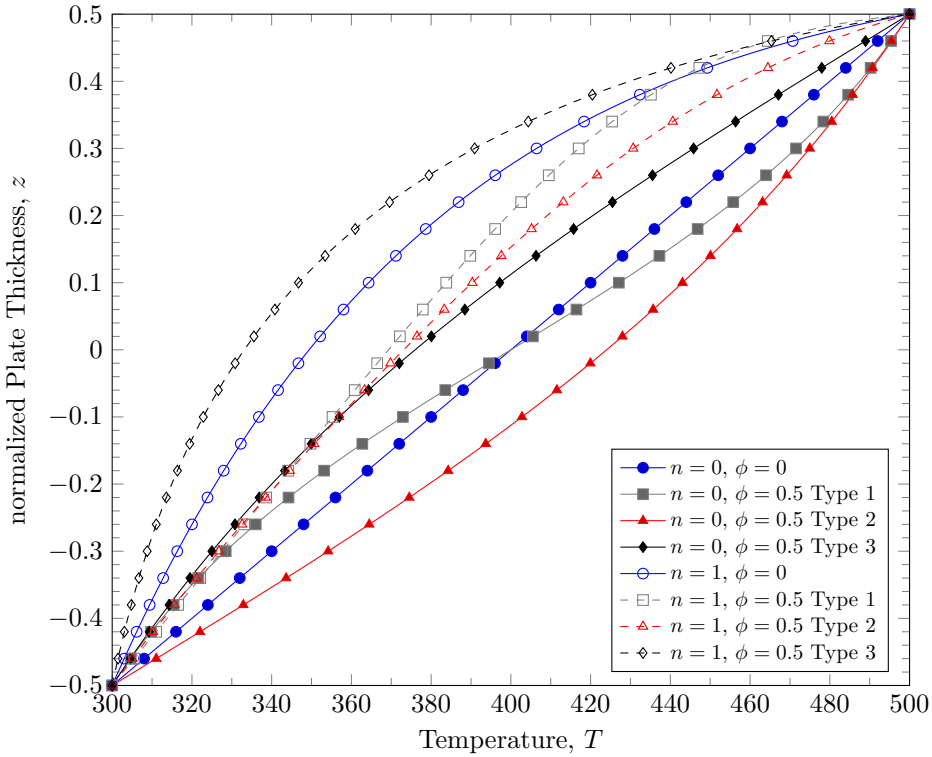

Figure 6. Temperature distribution of porous FGM.

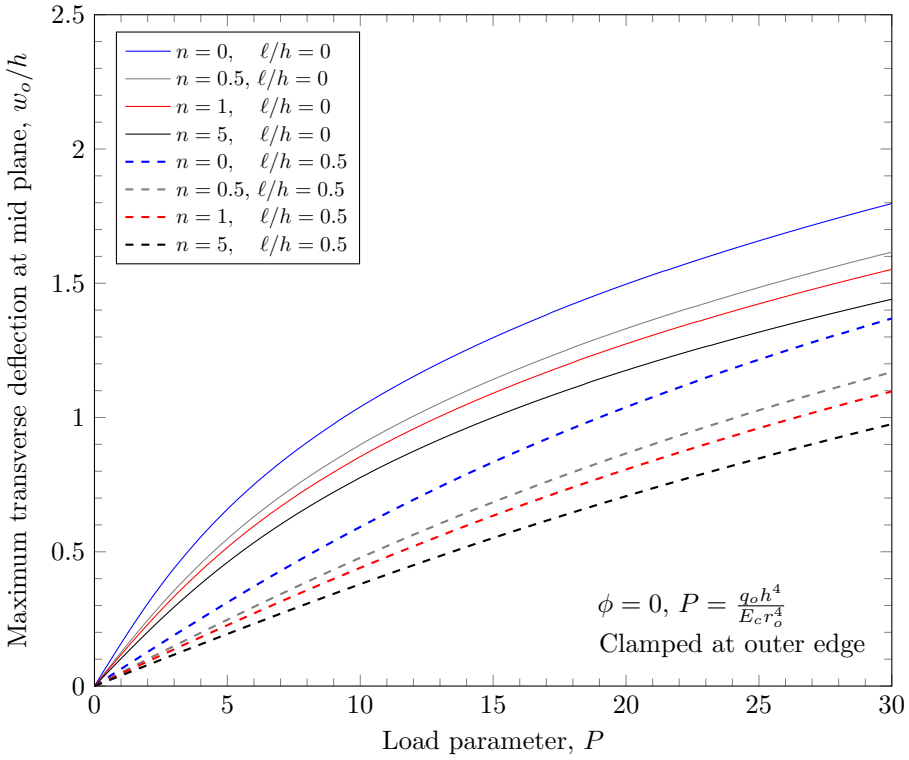

Figure 7. Maximum deflection of FGM with clamped outer edge with nonzero length scale parameters.

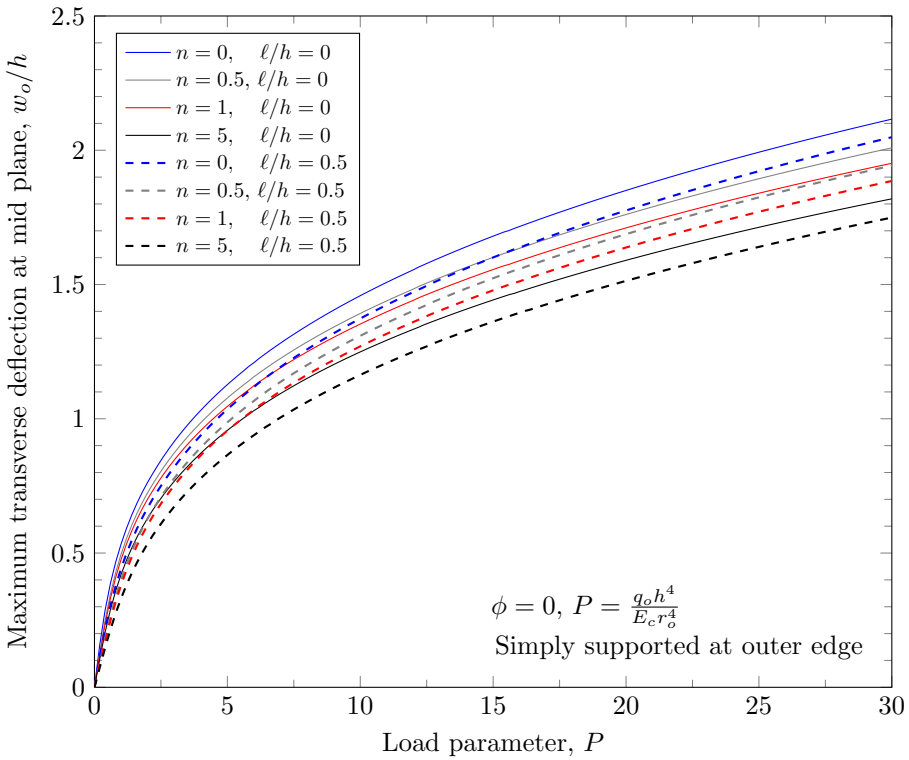

Figure 8. Maximum deflection of FGM with simply-supported outer edge with nonzero length scale parameters.

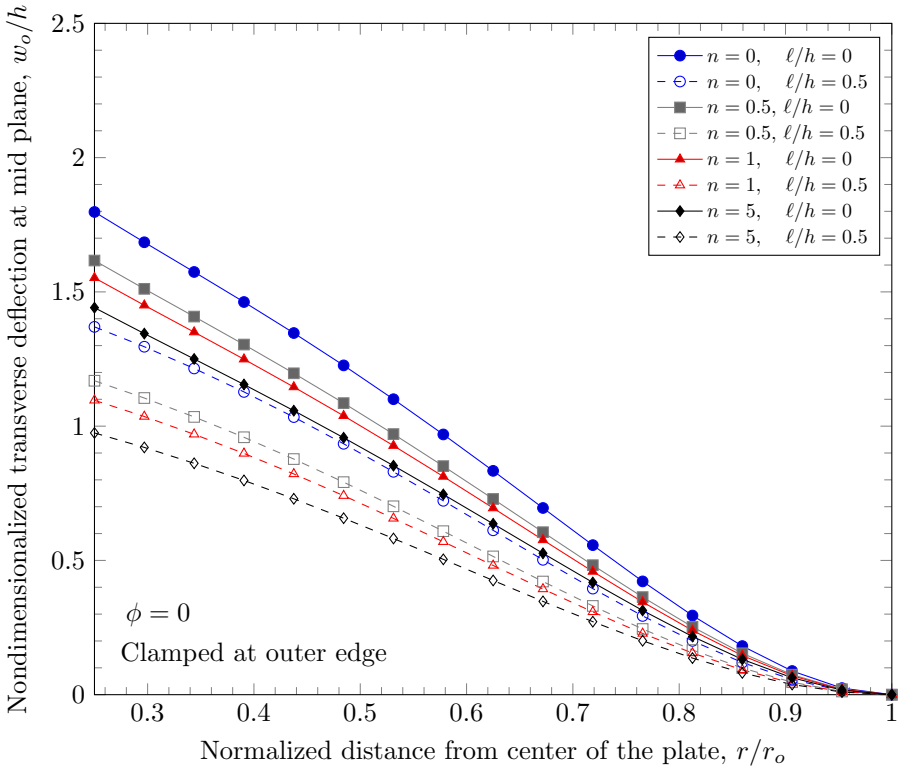

Figure 9. Deflection of FGM with clamped outer edge with nonzero length scale parameters.

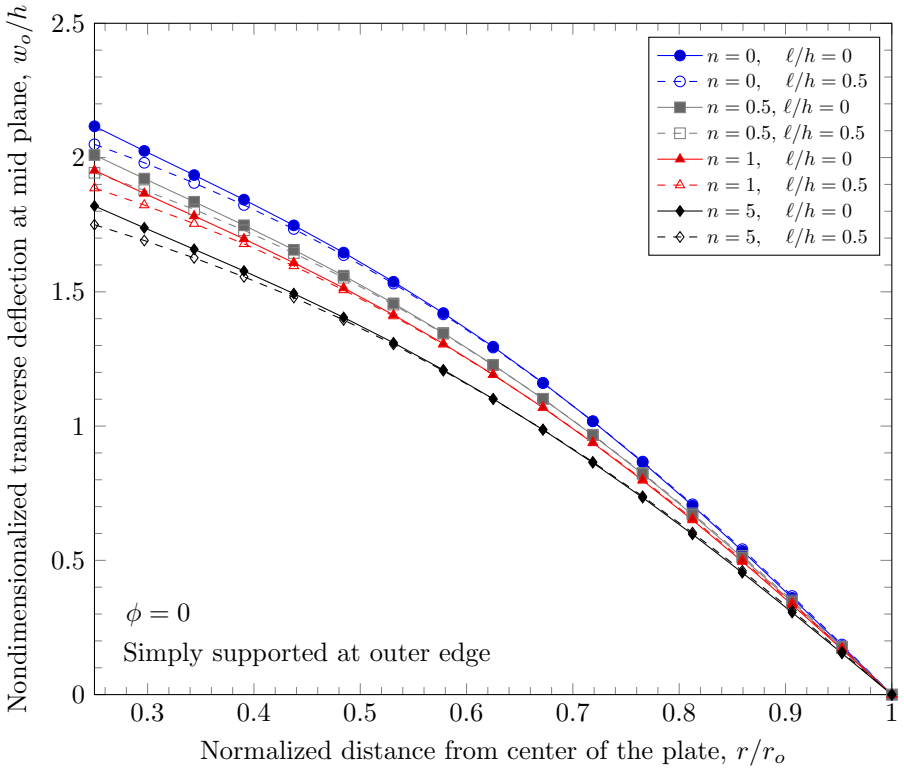

Figure 10. Deflection of FGM with simply-supported outer edge with nonzero length scale parameters.

The overall volume fraction of porosity in three porosity distributions is the same, but the enhanced porous areas are mid, bottom, and top surfaces with Type 1, Type 2, and Type 2 porosity distributions. The porous FGM is softer than non-porous FGM, and Type 1 results in the stiffest plates because the materials on the top and bottom surfaces remain. There are no differences in the plate bending stiffness between Type 1 and Type 2 distribution when a homogeneous material is assumed. When the power-law index is larger than zero, the volume fraction of stiffer material becomes larger in the FGMs. In the case of Type 2 distribution, the volume fraction of the stiffer material is decreased, and in the case of Type 3, the volume fraction of the softer material is decreased. Therefore, Type 2 will be softer than Type 3 in the case of FGMs. Figures 11 and 12 show the effects of three different porosity distributions and material variations on the maximum deflections with clamped and simply-supported outer edges, respectively. The deflections along the radial direction are shown in Figures 13 and 14.

Figures 15–18 show a normal stress distribution through the plate thickness. In the case of the clamped outer edge, the normal stress in the area where the volume fraction of porosity is larger is smaller than the area where the volume fraction of porosity is smaller because the area with larger porosity is softer than the other areas. It is clearly shown that the normal stress at the bottom surface ($z = -h/2$) with porosity distribution Type 3 is larger than porosity distribution Type 2, which enhances the porosity distribution in the lower area of the plates. In the case of the simply-supported outer edge, the normal stress distribution is a parabolic shape unlike the case of the clamped outer edge. This is because the thickness stretch is not constrained in the case of simply-supported boundary conditions. Only the mid plane deflection, w_0, is constrained. The nonzero length scale parameters make the FGM plate stiffer, but there are no material property changes, which results in smaller stresses.

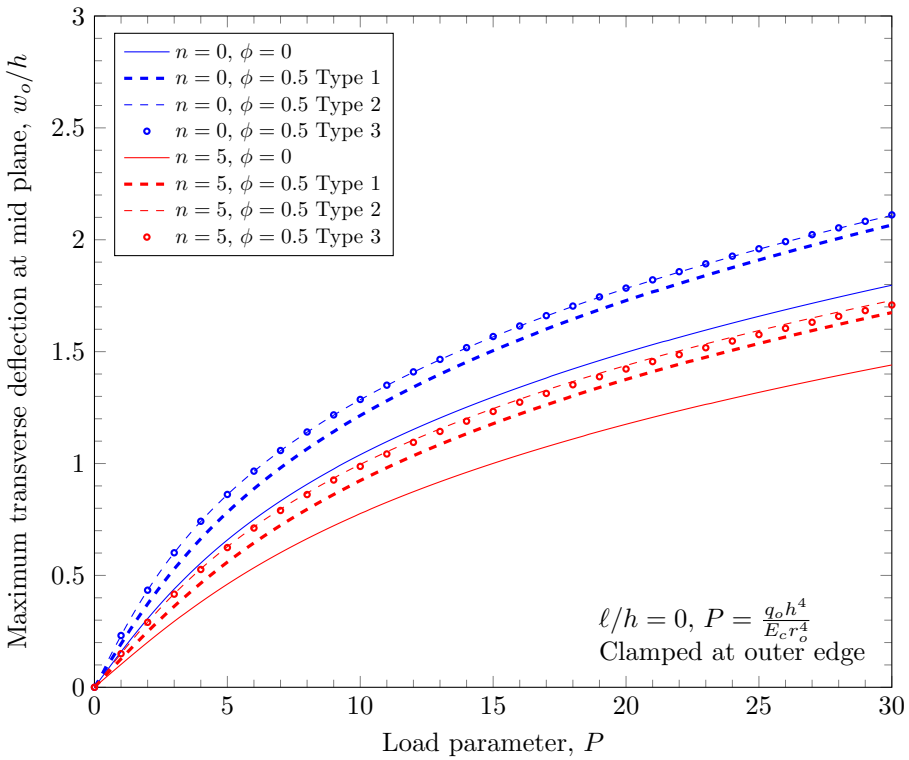

Figure 11. Maximum deflection of FGM with clamped outer edge with nonzero porosity.

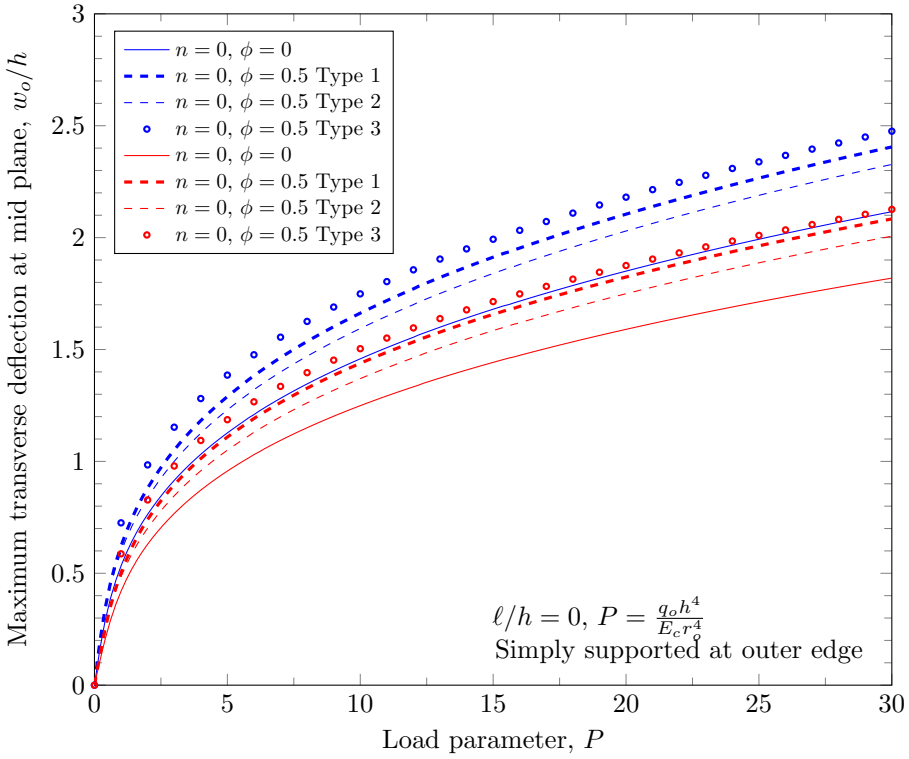

Figure 12. Maximum deflection of FGM with simply-supported outer edge with nonzero porosity.

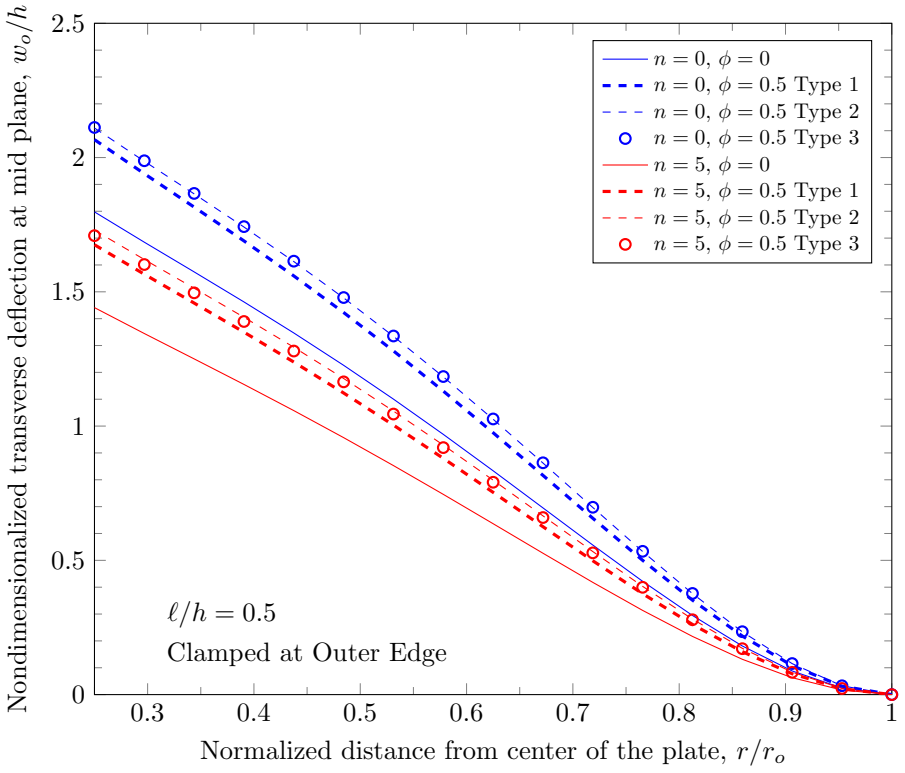

Figure 13. Deflection of FGM with clamped outer edge with nonzero porosity.

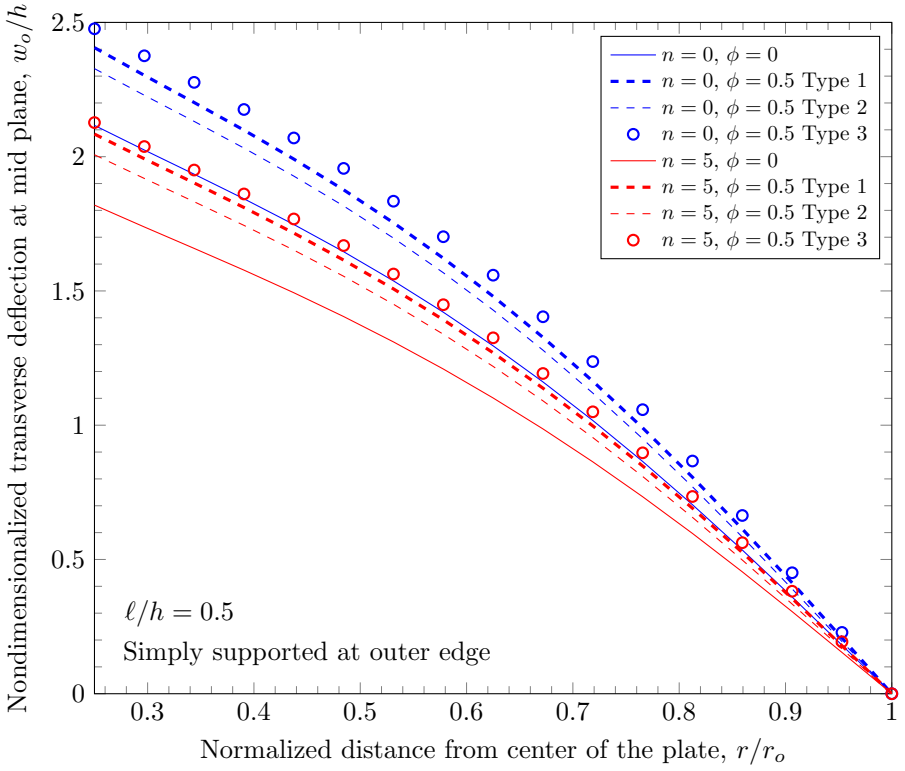

Figure 14. Deflection of FGM with simply-supported outer edge with nonzero porosity.

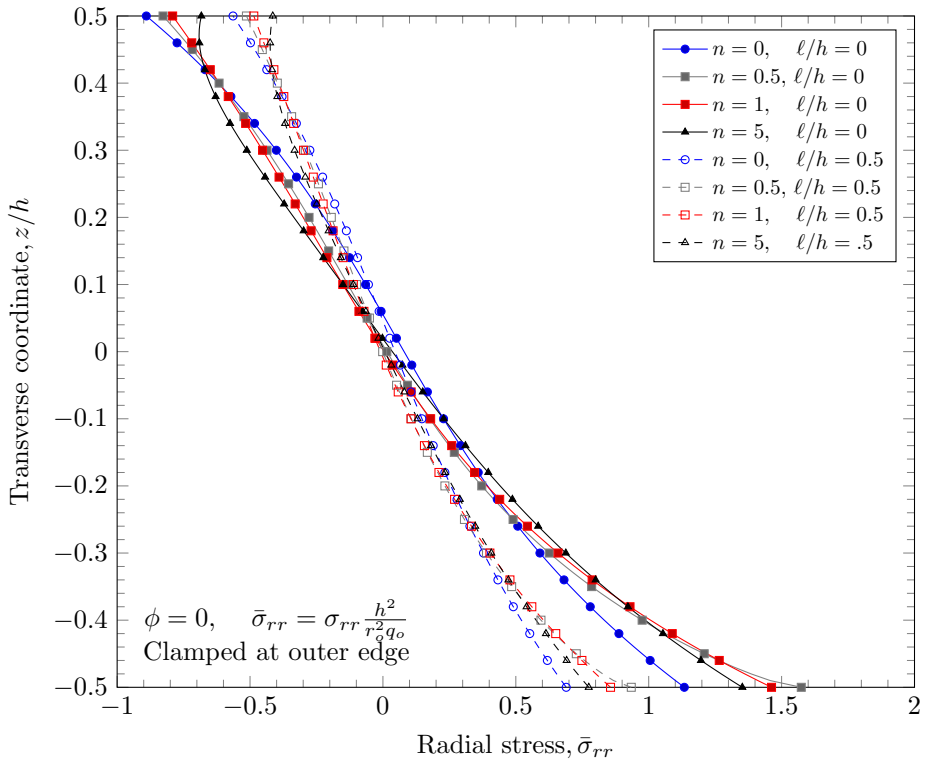

Figure 15. Normal stress variation through the thickness of plate with clamped outer edge with nonzero length scale parameters.

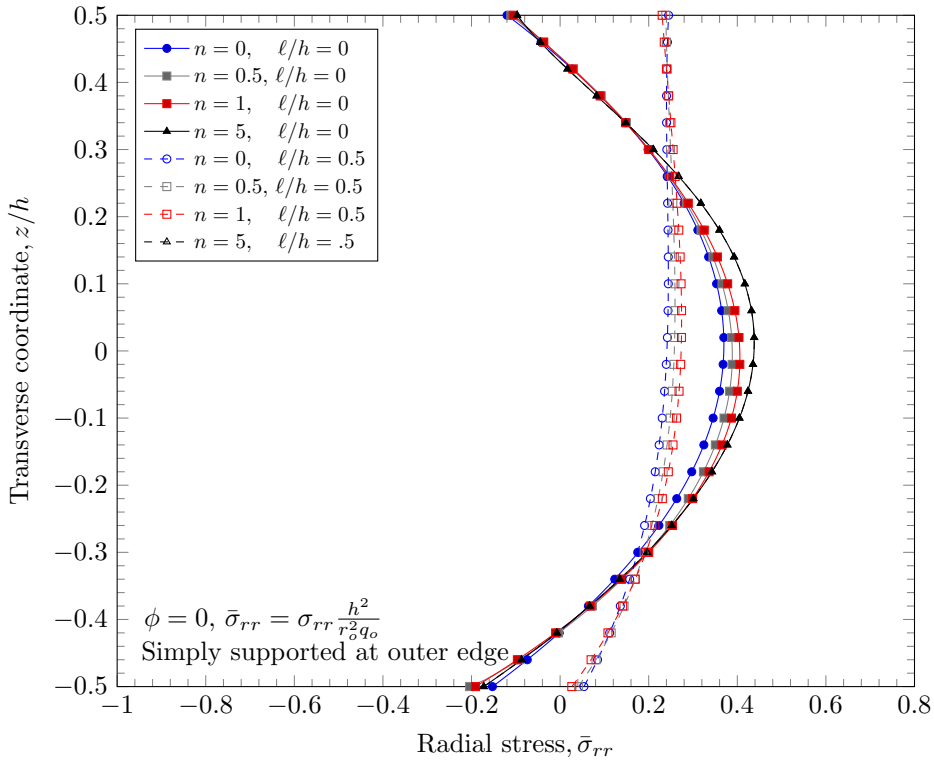

Figure 16. Normal stress variation through the thickness of plate with simply-supported outer edge with nonzero length scale parameters.

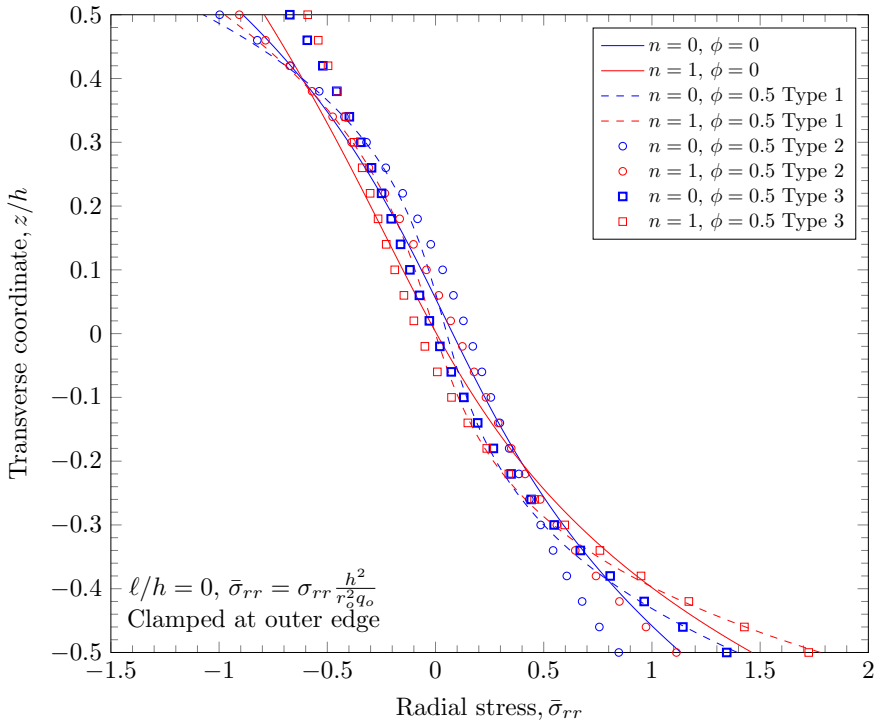

Figure 17. Normal stress variation through the thickness of plate with clamped outer edge with nonzero porosity.

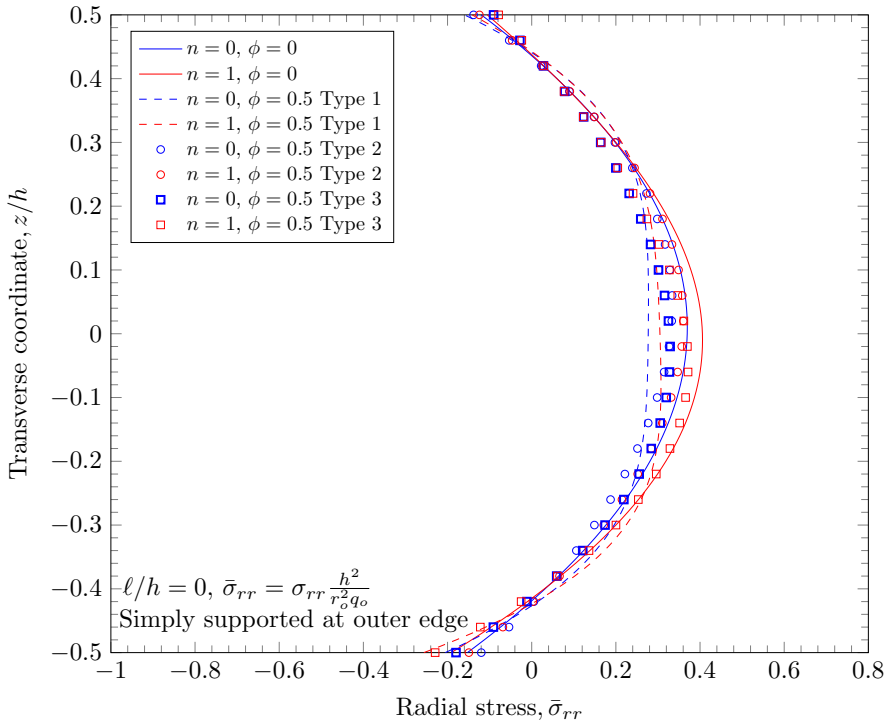

Figure 18. Normal stress variation through the thickness of plate with simply-supported outer edge porosity.

Figures 19–22 show transverse shear stress distributions through the plate thickness. Similar effects of porosity distribution and length scale parameter on the transverse shear stresses are observed. The length scale parameter makes the FGM plate stiffer and smaller stress values are obtained. However, the porosity distribution affects the material prop-

erties and larger stress values are present in stiffer areas. The proposed quasi-3D Reddy third-order plate theory can capture a parabolic variation of the transverse shear stresses, and it does not require a shear correction factor that is present in low order shear deformation theories.

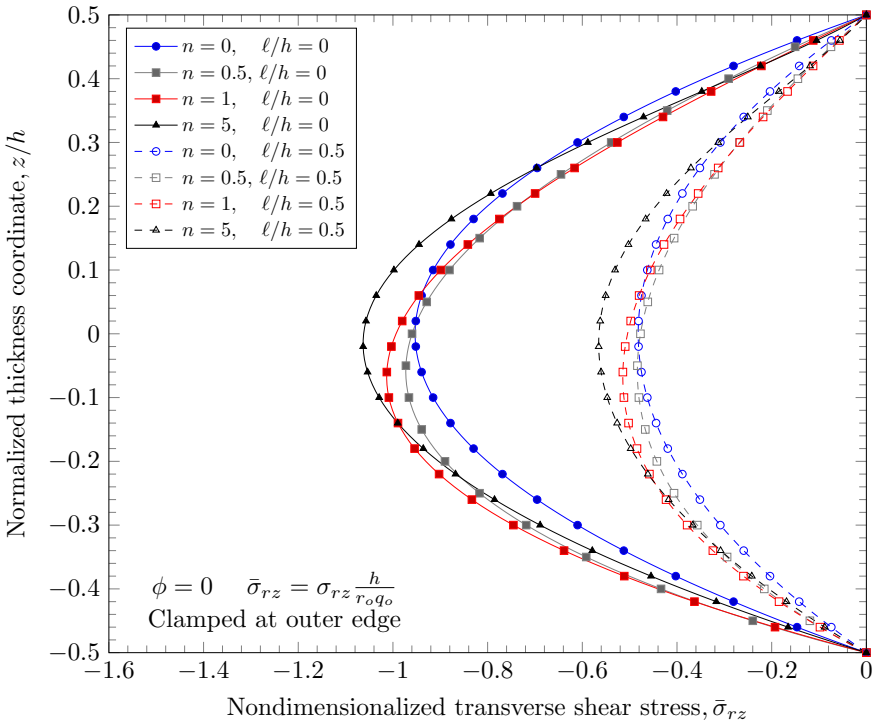

Figure 19. Transverse stress variation through the thickness of plate with clamped outer edge with nonzero length scale parameters.

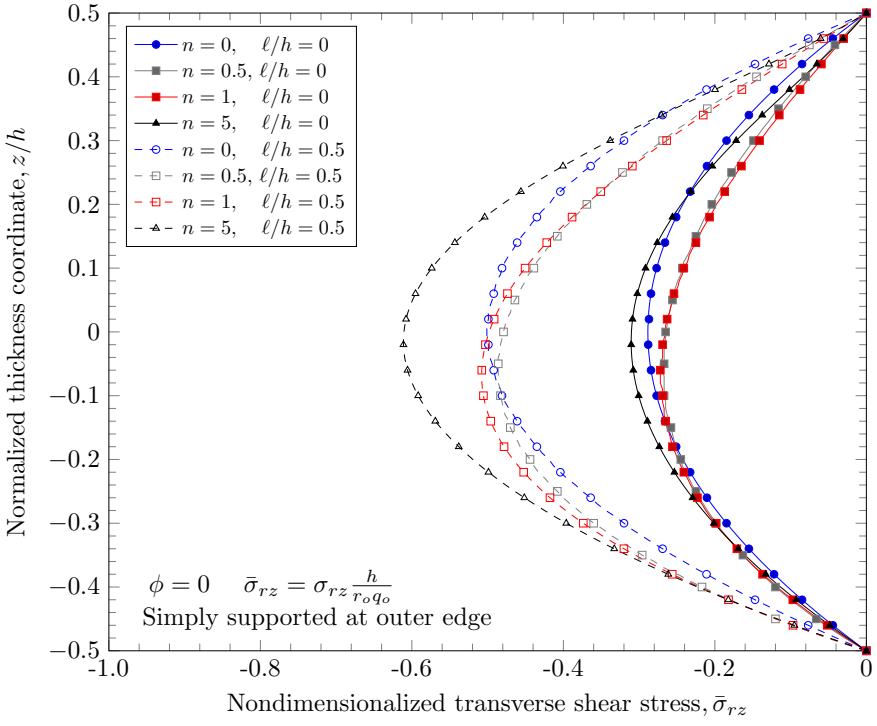

Figure 20. Transverse stress variation through the thickness of plate with simply-supported outer edge with nonzero length scale parameters.

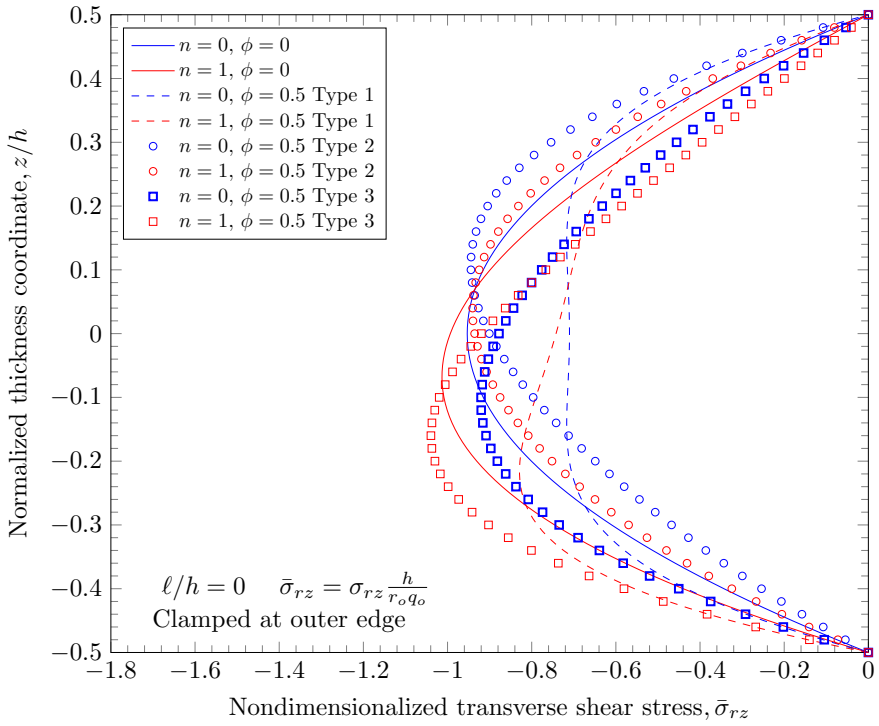

Figure 21. Transverse stress variation through the thickness of plate with clamped outer edge with nonzero porosity.

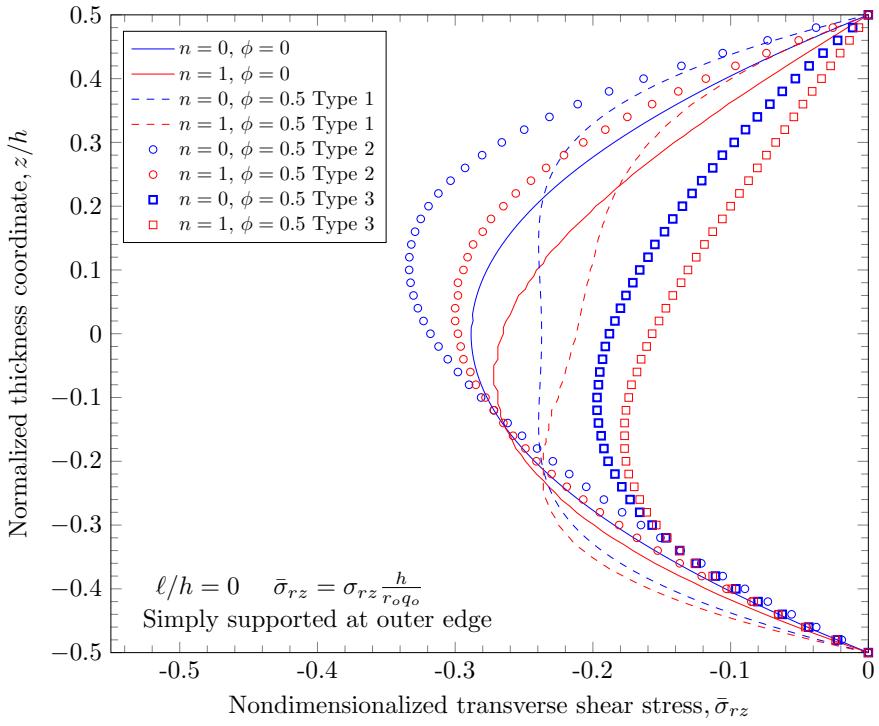

Figure 22. Transverse stress variation through the thickness of plate with simply-supported outer edge porosity.

Figures 23–26 show the effect of thermal load. The thermal load is induced by temperature boundary conditions; 500 K is applied on top surface and 300 K is applied on bottom surfaces. In the case of the clamped outer edge, the deflection is due to thermal load in the negative direction because the plate bends down due to the thermal load. This is clearly

shown in Figure 25. In the case of the simply-supported outer edge, the plate bends down due to the thermal load at the same place; the plate rotates about the outer edge which results in the positive deflection due to the thermal load.

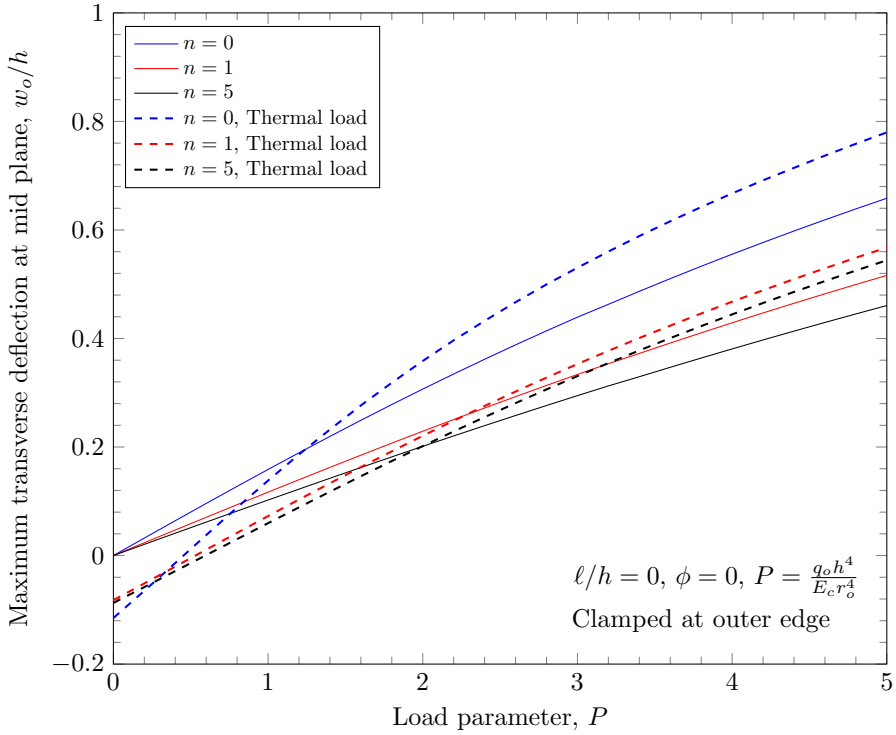

Figure 23. Maximum deflection of FGM under thermal load with clamped outer edge.

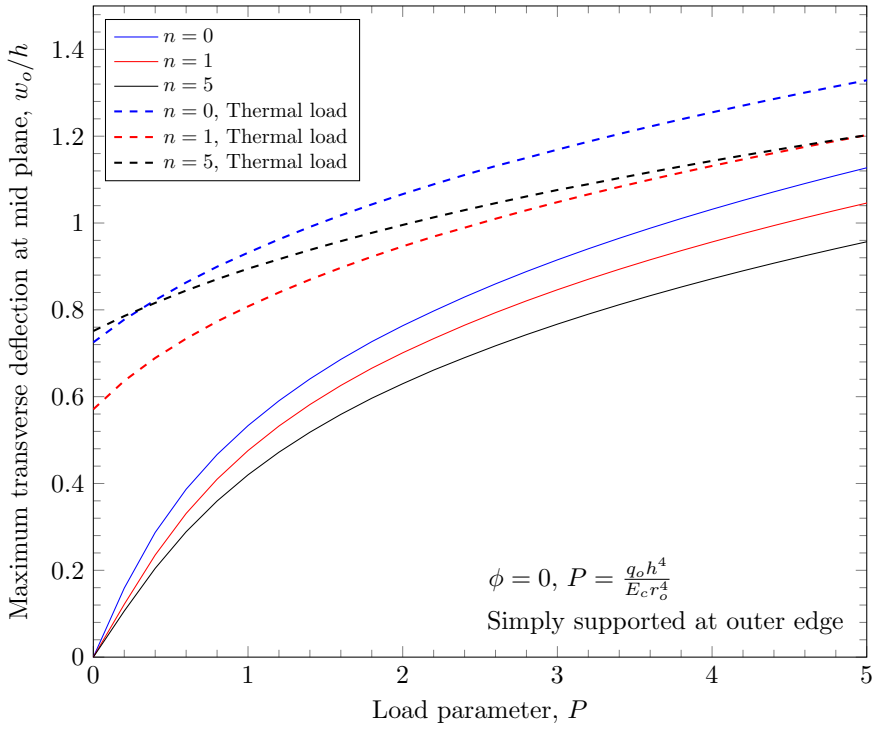

Figure 24. Maximum deflection of FGM under thermal load with simply-supported outer edge.

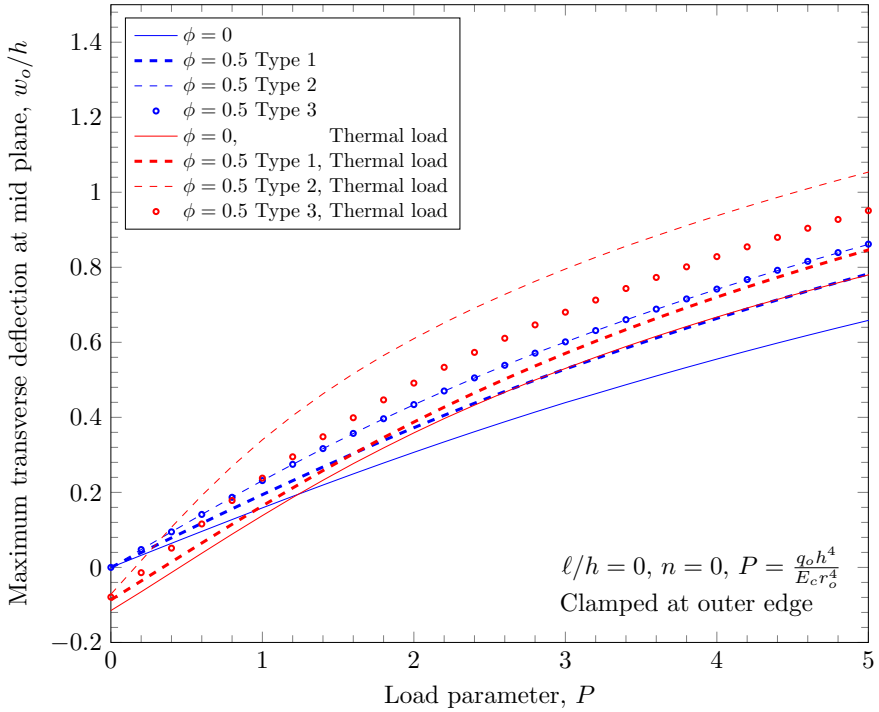

Figure 25. Maximum deflection of porous FGM under thermal load with clamped outer edge.

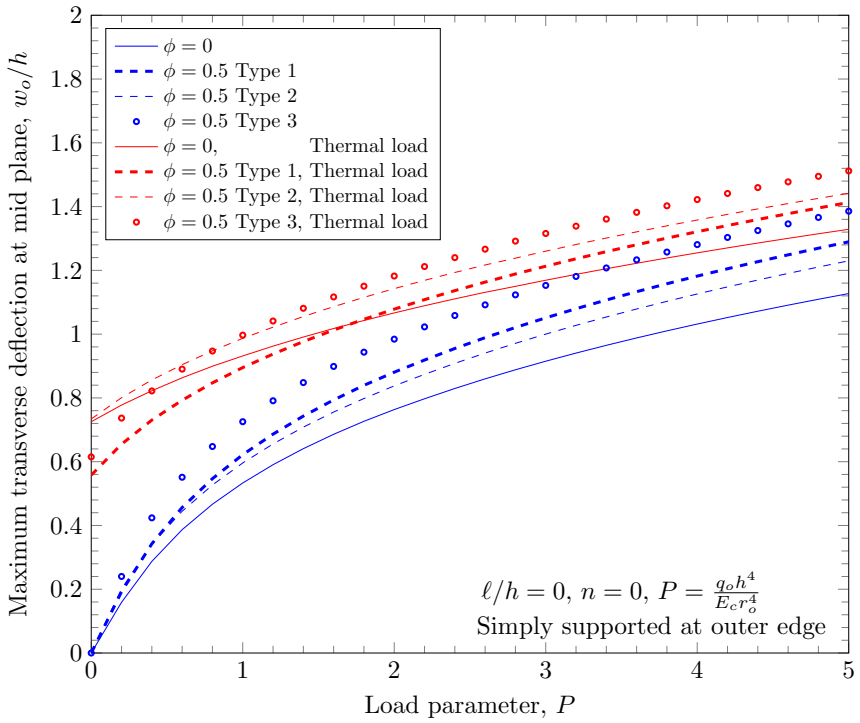

Figure 26. Maximum deflection of porous FGM under thermal load with simply-supported outer edge.

6. Conclusions

In this study, a nonlinear finite element (FE) model for axisymmetric circular/annular plates was presented. The developed finite element model accounts for geometric nonlinearity, variation of material constituents, microstructure size effects, and effects of porosity distributions. Using the developed FE model, the bending behavior of functionally-graded axisymmetric annular plates under thermomechanical loads was analyzed.

Numerical analysis results for an axisymmetric annular plate with various boundary conditions were presented. A parametric study was conducted to understand the effects of porosity distributions, the variation of material properties, and microstructure size on the bending behavior of axisymmetric annular plates. In summary, the following results were observed:

- The presence of pores results in higher thermal resistance and reduces the temperature variation;
- With a larger power law index, the plate becomes stiffer because the stiffer material is placed on the bottom surface;
- The length scale parameter can capture stiffening effects in microstructures. The stiffening effect does not change the material properties, so stress values are decreased with nonzero length scale parameters;
- The thermal and mechanical behavior of FGM plates highly depends on the porosity distribution type. The presence of pores makes the plate softer by reducing the moduli, resulting in smaller stress values;
- Depending on the boundary conditions, thermal loads can result in opposite deflections due to constrained rotational degrees of freedom.

The presented finite element model can be extended to an asymmetric circular/annular plate.

Author Contributions: Conceptualization, J.K.; Data curation, E.N.; Formal analysis, J.K.; Methodology, J.K.; Project administration, J.K.; Software, J.K. and E.N.; Validation, J.K. and E.N.; Writing—original draft, J.K. and S.R.; Writing—review & editing, J.K. All authors have read and agreed to the published version of the manuscript.

Funding: This research was funded by Western Michigan University Research Start-Up.

Institutional Review Board Statement: Not applicable.

Informed Consent Statement: Not applicable.

Data Availability Statement: The data presented in this study are available on request from the corresponding author.

Conflicts of Interest: The authors declare no conflict of interest.

Appendix A

$$K_{ij}^{11} = \int_{r_1}^{r_2} \left[A_{11}^{(0)} \left(\frac{\partial \psi_i}{\partial r} \frac{\partial \psi_j}{\partial r} + \frac{1}{r^2} \psi_i \psi_j \right) + \frac{A_{12}^{(0)}}{r} \left(\frac{\partial \psi_i}{\partial r} \psi_j + \psi_i \frac{\partial \psi_j}{\partial r} \right) \right] r dr \tag{A1}$$

$$K_{ij}^{12} = \int_{r_1}^{r_2} \left[\left(A_{11}^{(1)} - c_1 A_{11}^{(3)} \right) \left(\frac{\partial \psi_i}{\partial r} \frac{\partial \psi_j}{\partial r} + \frac{1}{r^2} \psi_i \psi_j \right) + \frac{1}{r} \left(A_{12}^{(1)} - c_1 A_{12}^{(3)} \right) \left(\frac{\partial \psi_i}{\partial r} \psi_j + \psi_i \frac{\partial \psi_j}{\partial r} \right) \right] r dr \tag{A2}$$

$$K_{iJ}^{13} = \int_{r_1}^{r_2} \left[\frac{A_{11}^{(0)}}{2} \left(\frac{\partial w_0}{\partial r} \right) \frac{\partial \psi_i}{\partial r} \frac{\partial \phi_J}{\partial r} - c_1 A_{11}^{(3)} \left(\frac{\partial \psi_i}{\partial r} \frac{\partial^2 \phi_J}{\partial r^2} + \frac{1}{r^2} \psi_i \frac{\partial \phi_J}{\partial r} \right) + \frac{A_{12}^{(0)}}{2r} \left(\frac{\partial w_0}{\partial r} \right) \psi_i \frac{\partial \phi_J}{\partial r} - c_1 \frac{A_{12}^{(3)}}{r} \left(\frac{\partial \psi_i}{\partial r} \frac{\partial \phi_J}{\partial r} + \psi_i \frac{\partial^2 \phi_J}{\partial r^2} \right) \right] r dr \tag{A3}$$

$$K_{iJ}^{14} = \int_{r_1}^{r_2} \left[-\frac{A_{11}^{(2)}}{2} \left(\frac{\partial \psi_i}{\partial r} \frac{\partial^2 \phi_J}{\partial r^2} + \frac{1}{r^2} \psi_i \frac{\partial \phi_J}{\partial r} \right) + A_{12}^{(0)} \left(\frac{\partial \psi_i}{\partial r} \phi_J + \frac{1}{r} \psi_i \phi_J \right) - \frac{A_{12}^{(2)}}{2r} \left(\frac{\partial \psi_i}{\partial r} \frac{\partial \phi_J}{\partial r} + \psi_i \frac{\partial^2 \phi_J}{\partial r^2} \right) \right] r dr \tag{A4}$$

$$K_{ij}^{15} = \int_{r_1}^{r_2} \left[-\frac{A_{11}^{(3)}}{3} \left(\frac{\partial \psi_i}{\partial r} \frac{\partial^2 \phi_J}{\partial r^2} + \frac{1}{r^2} \psi_i \frac{\partial \phi_J}{\partial r} \right) + 2A_{12}^{(1)} c_2 \left(\frac{\partial \psi_i}{\partial r} \phi_J + \frac{1}{r} \psi_i \phi_J \right) \right.$$
$$\left. - \frac{A_{12}^{(3)}}{3r} \left(\frac{\partial \psi_i}{\partial r} \frac{\partial \phi_J}{\partial r} + \psi_i \frac{\partial^2 \phi_J}{\partial r^2} \right) \right] r dr \tag{A5}$$

$$K_{ij}^{21} = \left[\left(A_{11}^{(1)} - c_1 A_{11}^{(3)} \right) \left(\frac{\partial \psi_i}{\partial r} \frac{\partial \psi_j}{\partial r} + \frac{1}{r^2} \psi_i \psi_j \right) \right.$$
$$\left. + \frac{1}{r} \left(A_{12}^{(1)} - c_1 A_{12}^{(3)} \right) \left(\frac{\partial \psi_i}{\partial r} \psi_j + \psi_i \frac{\partial \psi_j}{\partial r} \right) \right] r dr \tag{A6}$$

$$K_{ij}^{22} = \int_{r_1}^{r_2} \left\{ \left(A_{11}^{(2)} - 2c_1 A_{11}^{(4)} + c_1^2 A_{11}^{(6)} \right) \left(\frac{\partial \psi_i}{\partial r} \frac{\partial \psi_j}{\partial r} + \frac{1}{r^2} \psi_i \psi_j \right) \right.$$
$$+ \frac{1}{r} \left(A_{12}^{(2)} - 2c_1 A_{12}^{(4)} + c_1^2 A_{12}^{(6)} \right) \left(\frac{\partial \psi_i}{\partial r} \psi_j + \psi_i \frac{\partial \psi_j}{\partial r} \right)$$
$$+ \left(A_{55}^{(0)} - 2c_2 A_{55}^{(2)} + c_2^2 A_{55}^{(4)} \right) \psi_i \psi_j$$
$$+ \frac{1}{4} \left[\frac{1}{r^2} \left(B^{(0)} - 2c_2 B^{(2)} + c_2^2 B^{(4)} \right) \left(r^2 \frac{\partial \psi_i}{\partial r} \frac{\partial \psi_j}{\partial r} + \psi_i \psi_j \right) + 4c_2^2 B^{(2)} \psi_i \psi_j \right.$$
$$\left. \left. - \frac{1}{r} \left(B^{(0)} - 2c_2 B^{(2)} + c_2^2 B^{(4)} \right) \left(\psi_i \frac{\partial \psi_j}{\partial r} + \frac{\partial \psi_i}{\partial r} \psi_j \right) \right] \right\} r dr \tag{A7}$$

$$K_{ij}^{23} = \int_{r_1}^{r_2} \left\{ \frac{1}{2} \frac{\partial w_0}{\partial r} \left(A_{11}^{(1)} - c_1 A_{11}^{(3)} \right) \frac{\partial \psi_i}{\partial r} \frac{\partial \phi_J}{\partial r} - c_1 \left(A_{11}^{(4)} - c_1 A_{11}^{(6)} \right) \left(\frac{\partial \psi_i}{\partial r} \frac{\partial^2 \phi_J}{\partial r^2} + \frac{1}{r^2} \psi_i \frac{\partial \phi_J}{\partial r} \right) \right.$$
$$+ \frac{1}{2r} \frac{\partial w_0}{\partial r} \left(A_{12}^{(1)} - c_1 A_{12}^{(3)} \right) \psi_i \frac{\partial \phi_J}{\partial r} - \frac{c_1}{r} \left(A_{12}^{(4)} - c_1 A_{12}^{(6)} \right) \frac{\partial \psi_i}{\partial r} \frac{\partial \phi_J}{\partial r}$$
$$- \frac{c_1}{r} \left(A_{12}^{(4)} - c_1 A_{12}^{(6)} \right) \psi_i \frac{\partial^2 \phi_J}{\partial r^2} + \left(A_{55}^{(0)} - 3c_2 A_{55}^{(2)} + c_1^2 A_{55}^{(4)} \right) \psi_i \frac{\partial \phi_J}{\partial r}$$
$$- \frac{1}{4} \left[\left(B^{(0)} - c_2^2 B^{(4)} \right) \left(\frac{\partial \psi_i}{\partial r} \frac{\partial^2 \phi_J}{\partial r^2} - \frac{1}{r} \frac{\partial \psi_i}{\partial r} \frac{\partial \phi_J}{\partial r} \right) - 4c_2^2 B^{(2)} \psi_i \frac{\partial \phi_J}{\partial r} \right.$$
$$\left. \left. - \frac{1}{r} \left(B^{(0)} - c_2^2 B^{(4)} \right) \left(\psi_i \frac{\partial^2 \phi_J}{\partial r^2} - \frac{1}{r} \psi_i \frac{\partial \phi_J}{\partial r} \right) \right] \right\} r dr \tag{A8}$$

$$K_{ij}^{24} = \int_{r_1}^{r_2} \left\{ -\frac{1}{2} \left(A_{11}^{(3)} - c_1 A_{11}^{(5)} \right) \left(\frac{\partial \psi_i}{\partial r} \frac{\partial^2 \phi_J}{\partial r^2} + \frac{1}{r^2} \psi_i \frac{\partial \phi_J}{\partial r} \right) + \frac{1}{r} \left(A_{12}^{(1)} - c_1 A_{12}^{(3)} \right) \psi_i \phi_J \right.$$
$$+ \left(A_{12}^{(1)} - c_1 A_{12}^{(3)} \right) \frac{\partial \psi_i}{\partial r} \phi_J - \frac{1}{2r} \left(A_{12}^{(3)} - c_1 A_{12}^{(5)} \right) \left(\frac{\partial \psi_i}{\partial r} \frac{\partial \phi_J}{\partial r} + \psi_i \frac{\partial^2 \phi_J}{\partial r^2} \right)$$
$$+ \frac{1}{2} \left[\frac{1}{r} \left(B^{(1)} - c_2 B^{(3)} \right) \left(\frac{\partial \psi_i}{\partial r} \frac{\partial \phi_J}{\partial r} + \psi_i \frac{\partial^2 \phi_J}{\partial r^2} - r \frac{\partial \psi_i}{\partial r} \frac{\partial^2 \phi_J}{\partial r^2} \right) \right.$$
$$\left. \left. - \frac{1}{r^2} \left(B^{(1)} - c_2 B^{(3)} \right) \psi_i \frac{\partial \phi_J}{\partial r} + 2c_2 B^{(1)} \psi_i \frac{\partial \phi_J}{\partial r} \right] \right\} r dr \tag{A9}$$

$$K_{ij}^{25} = \int_{r_1}^{r_2} \left\{ -\frac{1}{3} \left(A_{11}^{(4)} - c_1 A_{11}^{(6)} \right) \left(\frac{\partial \psi_i}{\partial r} \frac{\partial^2 \phi_J}{\partial r^2} + \frac{1}{r^2} \psi_i \frac{\partial \phi_J}{\partial r} \right) + \frac{2}{r} \left(A_{12}^{(2)} - c_1 A_{12}^{(4)} \right) \psi_i \phi_J \right.$$
$$+ 2 \left(A_{12}^{(2)} - c_1 A_{12}^{(4)} \right) \frac{\partial \psi_i}{\partial r} \phi_J - \frac{1}{3r} \left(A_{12}^{(4)} - c_1 A_{12}^{(6)} \right) \left(\frac{\partial \psi_i}{\partial r} \frac{\partial \phi_J}{\partial r} + \psi_i \frac{\partial^2 \phi_J}{\partial r^2} \right)$$
$$+ \frac{1}{2} \left[\frac{1}{r} \left(B^{(2)} - c_2 B^{(4)} \right) \left(\frac{\partial \psi_i}{\partial r} \frac{\partial \phi_J}{\partial r} + \psi_i \frac{\partial^2 \phi_J}{\partial r^2} - r \frac{\partial \psi_i}{\partial r} \frac{\partial^2 \phi_J}{\partial r^2} \right) \right.$$
$$\left. \left. - \frac{1}{r^2} \left(B^{(2)} - c_2 B^{(4)} \right) \psi_i \frac{\partial \phi_J}{\partial r} + 4c_2 B^{(2)} \psi_i \frac{\partial \phi_J}{\partial r} \right] \right\} r dr \tag{A10}$$

$$K_{Ij}^{31} = \left[A_{11}^{(0)} \left(\frac{\partial w_0}{\partial r} \right) \frac{\partial \phi_I}{\partial r} \frac{\partial \psi_j}{\partial r} - c_1 A_{11}^{(3)} \left(\frac{\partial^2 \phi_I}{\partial r^2} \frac{\partial \psi_j}{\partial r} + \frac{1}{r^2} \frac{\partial \phi_I}{\partial r} \psi_j \right) \right.$$
$$\left. + \frac{A_{12}^{(0)}}{r} \left(\frac{\partial w_0}{\partial r} \right) \frac{\partial \phi_I}{\partial r} \psi_j - c_1 \frac{A_{12}^{(3)}}{r} \left(\frac{\partial \phi_I}{\partial r} \frac{\partial \psi_j}{\partial r} + \frac{\partial^2 \phi_I}{\partial r^2} \psi_j \right) \right] r dr \tag{A11}$$

$$K_{Ij}^{32} = \int_{r_1}^{r_2} \left\{ \frac{\partial w_0}{\partial r} \left(A_{11}^{(1)} - c_1 A_{11}^{(3)} \right) \frac{\partial \phi_I}{\partial r} \frac{\partial \psi_j}{\partial r} - c_1 \left(A_{11}^{(4)} - c_1 A_{11}^{(6)} \right) \left(\frac{\partial^2 \phi_I}{\partial r^2} \frac{\partial \psi_j}{\partial r} + \frac{1}{r^2} \frac{\partial \phi_I}{\partial r} \psi_j \right) \right.$$
$$+ \frac{1}{r} \frac{\partial w_0}{\partial r} \left(A_{12}^{(1)} - c_1 A_{12}^{(3)} \right) \frac{\partial \phi_I}{\partial r} \psi_i - \frac{c_1}{r} \left(A_{12}^{(4)} - c_1 A_{12}^{(6)} \right) \frac{\partial \phi_I}{\partial r} \frac{\partial \psi_j}{\partial r}$$
$$- \frac{c_1}{r} \left(A_{12}^{(4)} - c_1 A_{12}^{(6)} \right) \frac{\partial^2 \phi_I}{\partial r^2} \psi_j + \left(A_{55}^{(0)} - 3 c_2 A_{55}^{(2)} + c_1^2 A_{55}^{(4)} \right) \frac{\partial \phi_I}{\partial r} \psi_i$$
$$- \frac{1}{4} \left[\left(B^{(0)} - c_2^2 B^{(4)} \right) \left(\frac{\partial^2 \phi_I}{\partial r^2} \frac{\partial \psi_j}{\partial r} - \frac{1}{r} \frac{\partial \phi_I}{\partial r} \frac{\partial \psi_j}{\partial r} \right) - 4 c_2^2 B^{(2)} \frac{\partial \phi_I}{\partial r} \psi_j \right.$$
$$\left. \left. - \frac{1}{r} \left(B^{(0)} - c_2^2 B^{(4)} \right) \left(\frac{\partial^2 \phi_I}{\partial r^2} \psi_j - \frac{1}{r} \frac{\partial \phi_I}{\partial r} \psi_j \right) \right] \right\} r dr \tag{A12}$$

$$K_{IJ}^{33} = \int_{r_1}^{r^2} \left\{ \frac{1}{2} \left(\frac{\partial w_0}{\partial r} \right) \left(\frac{\partial w_0}{\partial r} A_{11}^{(0)} - \frac{c_2}{r} A_{12}^{(3)} \right) \frac{\partial \phi_I}{\partial r} \frac{\partial \phi_J}{\partial r} + \frac{c_1^2}{r} A_{12}^{(6)} \left(\frac{\partial^2 \phi_I}{\partial r^2} \frac{\partial \phi_J}{\partial r} + \frac{\partial \phi_I}{\partial r} \frac{\partial^2 \phi_J}{\partial r^2} \right) \right.$$
$$- c_1 A_{11}^{(3)} \left(\frac{\partial w_0}{\partial r} \right) \left(\frac{\partial \phi_I}{\partial r} \frac{\partial^2 \phi_J}{\partial r^2} + \frac{1}{2} \frac{\partial^2 \phi_I}{\partial r^2} \frac{\partial \phi_J}{\partial r} \right) + c_1^2 A_{11}^{(6)} \left(\frac{\partial^2 \phi_I}{\partial r^2} \frac{\partial^2 \phi_J}{\partial r^2} + \frac{1}{r^2} \frac{\partial \phi_I}{\partial r} \frac{\partial \phi_J}{\partial r} \right)$$
$$+ \left(A_{55}^{(0)} - 3 c_2 A_{55}^{(2)} + c_2^2 A_{55}^{(4)} \right) \frac{\partial \phi_I}{\partial r} \frac{\partial \phi_J}{\partial r} + \frac{1}{4} \left[c 2^2 B^{(4)} \left(\frac{\partial^2 \phi_I}{\partial r^2} \frac{\partial^2 \phi_J}{\partial r^2} + \frac{1}{r^2} \frac{\partial \phi_I}{\partial r} \frac{\partial \phi_J}{\partial r} \right) \right.$$
$$+ \left(B^{(0)} + 2 c_2 B^{(2)} \right) \left(\frac{\partial^2 \phi_I}{\partial r^2} \frac{\partial^2 \phi_J}{\partial r^2} + \frac{1}{r} \frac{\partial \phi_I}{\partial r} \frac{\partial \phi_J}{\partial r} \right)$$
$$\left. \left. - \frac{1}{r} \left(B^{(0)} + 2 c_2 B^{(2)} + c_2^2 \right) \left(\frac{\partial^2 \phi_I}{\partial r^2} \frac{\partial \phi_J}{\partial r} + \frac{\partial \phi_I}{\partial r} \frac{\partial^2 \phi_J}{\partial r^2} \right) \right] \right\} r dr \tag{A13}$$

$$K_{IJ}^{34} = \int_{r_1}^{r^2} \left\{ - \frac{1}{2} \left(\frac{\partial w_0}{\partial r} \right) \left(A_{11}^{(2)} \frac{\partial \phi_I}{\partial r} \frac{\partial^2 \phi_J}{\partial r^2} + \frac{A_{12}^{(2)}}{r} \frac{\partial \phi_I}{\partial r} \frac{\partial \phi_J}{\partial r} - 2 A_{12}^{(0)} \frac{\partial \phi_I}{\partial r} \phi_J \right) \right.$$
$$+ \frac{c_1}{2} A_{11}^{(5)} \left(\frac{\partial^2 \phi_I}{\partial r^2} \frac{\partial^2 \phi_J}{\partial r^2} + \frac{1}{r^2} \frac{\partial \phi_I}{\partial r} \frac{\partial \phi_J}{\partial r} \right) - c_1 A_{12}^{(3)} \left(\frac{1}{r} \frac{\partial \phi_I}{\partial r} \phi_J + \frac{\partial^2 \phi_I}{\partial r^2} \phi_J \right)$$
$$+ \frac{c_1}{2r} A_{12}^{(5)} \left(\frac{\partial \phi_I}{\partial r} \frac{\partial^2 \phi_J}{\partial r^2} + \frac{\partial^2 \phi_I}{\partial r^2} \frac{\partial \phi_J}{\partial r} \right) + \frac{1}{2} \left[2 c_2 B^{(1)} \frac{\partial \phi_I}{\partial r} \frac{\partial \phi_J}{\partial r} \right.$$
$$\left. \left. + \left(B^{(1)} + c_2 B^{(3)} \right) \left(\frac{\partial^2 \phi_I}{\partial r^2} \frac{\partial^2 \phi_J}{\partial r^2} - \frac{1}{r} \frac{\partial^2 \phi_I}{\partial r^2} \frac{\partial \phi_J}{\partial r} - \frac{1}{r} \frac{\partial \phi_I}{\partial r} \frac{\partial^2 \phi_J}{\partial r^2} + \frac{1}{r^2} \frac{\partial \phi_I}{\partial r} \frac{\partial \phi_J}{\partial r} \right) \right] \right\} r dr \tag{A14}$$

$$K_{IJ}^{35} = \int_{r_1}^{r^2} \left\{ - \frac{1}{3} \left(\frac{\partial w_0}{\partial r} \right) \left(A_{11}^{(3)} \frac{\partial \phi_I}{\partial r} \frac{\partial^2 \phi_J}{\partial r^2} + \frac{A_{12}^{(3)}}{r} \frac{\partial \phi_I}{\partial r} \frac{\partial \phi_J}{\partial r} - 6 A_{12}^{(1)} \frac{\partial \phi_I}{\partial r} \phi_J \right) \right.$$
$$+ \frac{c_1}{3} A_{11}^{(6)} \left(\frac{\partial^2 \phi_I}{\partial r^2} \frac{\partial^2 \phi_J}{\partial r^2} + \frac{1}{r^2} \frac{\partial \phi_I}{\partial r} \frac{\partial \phi_J}{\partial r} \right) - 2 c_1 A_{12}^{(4)} \left(\frac{1}{r} \frac{\partial \phi_I}{\partial r} \phi_J + \frac{\partial^2 \phi_I}{\partial r^2} \phi_J \right)$$
$$- \frac{c_1}{3r} A_{12}^{(6)} \left(\frac{\partial \phi_I}{\partial r} \frac{\partial^2 \phi_J}{\partial r^2} + \frac{\partial^2 \phi_I}{\partial r^2} \frac{\partial \phi_J}{\partial r} \right) + \frac{1}{2} \left[4 c_2 B^{(2)} \frac{\partial \phi_I}{\partial r} \frac{\partial \phi_J}{\partial r} \right.$$
$$\left. \left. + \left(B^{(2)} + c_2 B^{(4)} \right) \left(\frac{\partial^2 \phi_I}{\partial r^2} \frac{\partial^2 \phi_J}{\partial r^2} - \frac{1}{r} \frac{\partial^2 \phi_I}{\partial r^2} \frac{\partial \phi_J}{\partial r} - \frac{1}{r} \frac{\partial \phi_I}{\partial r} \frac{\partial^2 \phi_J}{\partial r^2} + \frac{1}{r^2} \frac{\partial \phi_I}{\partial r} \frac{\partial \phi_J}{\partial r} \right) \right] \right\} r dr \tag{A15}$$

$$K_{Ij}^{41} = \int_{r_1}^{r_2} \left[- \frac{A_{11}^{(2)}}{2} \left(\frac{\partial^2 \phi_i}{\partial r^2} \frac{\partial \psi_j}{\partial r} + \frac{1}{r^2} \frac{\partial \phi_I}{\partial r} \psi_j \right) + A_{12}^{(0)} \left(\phi_I \frac{\partial \psi_j}{\partial r} + \frac{1}{r} \phi_I \psi_j \right) \right.$$

$$-\frac{A_{12}^{(2)}}{2r}\left(\frac{\partial\phi_I}{\partial r}\frac{\partial\psi_j}{\partial r}+\frac{\partial^2\phi_I}{\partial r^2}\psi_i\right)\Bigg]rdr \tag{A16}$$

$$\begin{aligned}K_{IJ}^{42}=\int_{r_1}^{r_2}\Bigg\{&-\frac{1}{2}\Big(A_{11}^{(3)}-c_1A_{11}^{(5)}\Big)\left(\frac{\partial^2\phi_I}{\partial r^2}\frac{\partial\psi_j}{\partial r}+\frac{1}{r^2}\frac{\partial\phi_I}{\partial r}\psi_j\right)+\frac{1}{r}\Big(A_{12}^{(1)}-c_1A_{12}^{(3)}\Big)\phi_I\psi_i\\&+\Big(A_{12}^{(1)}-c_1A_{12}^{(3)}\Big)\frac{\phi_I\partial\psi_j}{\partial r}-\frac{1}{2r}\Big(A_{12}^{(3)}-c_1A_{12}^{(5)}\Big)\left(\frac{\partial\psi_i}{\partial r}\frac{\partial\phi_J}{\partial r}+\frac{\partial^2\phi_I}{\partial r^2}\psi_j\right)\\&+\frac{1}{2}\Bigg[\frac{1}{r}\Big(B^{(1)}-c_2B^{(3)}\Big)\left(\frac{\partial\phi_I}{\partial r}\frac{\partial\psi_j}{\partial r}+\frac{\partial^2\phi_I}{\partial r^2}\psi_j-r\frac{\partial^2\phi_I}{\partial r^2}\frac{\partial\psi_j}{\partial r}\right)\\&-\frac{1}{r^2}\Big(B^{(1)}-c_2B^{(3)}\Big)\frac{\partial\phi_I}{\partial r}\psi_j+2c_2B^{(1)}\frac{\partial\phi_I}{\partial r}\psi_j\Bigg]\Bigg\}rdr\end{aligned} \tag{A17}$$

$$\begin{aligned}K_{IJ}^{43}=\int_{r_1}^{r^2}\Bigg\{&-\frac{1}{4}\left(\frac{\partial w_0}{\partial r}\right)\left(A_{11}^{(2)}\frac{\partial\phi_I}{\partial r}\frac{\partial^2\phi_J}{\partial r^2}+\frac{A_{12}^{(2)}}{r}\frac{\partial\phi_I}{\partial r}\frac{\partial\phi_J}{\partial r}-2A_{12}^{(0)}\frac{\partial\phi_I}{\partial r}\phi_J\right)\\&+\frac{c_1}{2}A_{11}^{(5)}\left(\frac{\partial^2\phi_I}{\partial r^2}\frac{\partial^2\phi_J}{\partial r^2}+\frac{1}{r^2}\frac{\partial\phi_I}{\partial r}\frac{\partial\phi_J}{\partial r}\right)-c_1A_{12}^{(3)}\left(\frac{1}{r}\phi_I\frac{\partial\phi_J}{\partial r}+\phi_I\frac{\partial^2\phi_J}{\partial r^2}\right)\\&+\frac{c_1}{2r}A_{12}^{(5)}\left(\frac{\partial^2\phi_I}{\partial r^2}\frac{\partial\phi_J}{\partial r}+\frac{\partial\phi_I}{\partial r}\frac{\partial^2\phi_J}{\partial r^2}\right)+\frac{1}{2}\Bigg[2c_2B^{(1)}\frac{\partial\phi_I}{\partial r}\frac{\partial\phi_J}{\partial r}\\&+\Big(B^{(1)}+c_2B^{(3)}\Big)\left(\frac{\partial^2\phi_I}{\partial r^2}\frac{\partial^2\phi_J}{\partial r^2}-\frac{1}{r}\frac{\partial\phi_I}{\partial r}\frac{\partial^2\phi_J}{\partial r^2}-\frac{1}{r}\frac{\partial^2\phi_I}{\partial r^2}\frac{\partial\phi_J}{\partial r}+\frac{1}{r^2}\frac{\partial\phi_I}{\partial r}\frac{\partial\phi_J}{\partial r}\right)\Bigg]\Bigg\}rdr\end{aligned} \tag{A18}$$

$$\begin{aligned}K_{IJ}^{44}=\int_{r_1}^{r^2}\Bigg\{&A_{11}^{(0)}\phi_I\phi_J+\frac{A_{11}^{(4)}}{4}\left(\frac{\partial^2\phi_I}{\partial r^2}\frac{\partial^2\phi_J}{\partial r^2}+\frac{1}{r^2}\frac{\partial\phi_I}{\partial r}\frac{\partial\phi_J}{\partial r}\right)-\frac{A_{12}^{(2)}}{2}\left(\frac{\partial^2\phi_I}{\partial r^2}\phi_J+\phi_I\frac{\partial^2\phi_J}{\partial r^2}\right)\\&-\frac{A_{12}^{(2)}}{2r}\left(\frac{\partial\phi_I}{\partial r}\phi_J+\phi_I\frac{\partial\phi_J}{\partial r}\right)+\frac{A_{12}^{(4)}}{4r}\left(\frac{\partial^2\phi_I}{\partial r^2}\frac{\partial\phi_J}{\partial r}+\frac{\partial\phi_I}{\partial r}\frac{\partial^2\phi_J}{\partial r^2}\right)+B^{(0)}\frac{\partial\phi_I}{\partial r}\frac{\partial\phi_J}{\partial r}\\&+B^{(2)}\left[\frac{\partial^2\phi_I}{\partial r^2}\frac{\partial^2\phi_J}{\partial r^2}-\frac{1}{r}\left(\frac{\partial^2\phi_I}{\partial r^2}\frac{\partial\phi_J}{\partial r}+\frac{\partial\phi_I}{\partial r}\frac{\partial^2\phi_J}{\partial r^2}\right)+\frac{1}{r^2}\frac{\partial\phi_I}{\partial r}\frac{\partial\phi_J}{\partial r}\right]\Bigg\}rdr\end{aligned} \tag{A19}$$

$$\begin{aligned}K_{IJ}^{45}=\int_{r_1}^{r^2}\Bigg\{&A_{11}^{(1)}\phi_I\phi_J+\frac{A_{11}^{(5)}}{6}\left(\frac{\partial^2\phi_I}{\partial r^2}\frac{\partial^2\phi_J}{\partial r^2}+\frac{1}{r^2}\frac{\partial\phi_I}{\partial r}\frac{\partial\phi_J}{\partial r}\right)-\frac{A_{12}^{(3)}}{3}\left(3\frac{\partial^2\phi_I}{\partial r^2}\phi_J+\phi_I\frac{\partial^2\phi_J}{\partial r^2}\right)\\&-\frac{A_{12}^{(3)}}{3r}\left(3\frac{\partial\phi_I}{\partial r}\phi_J+\phi_I\frac{\partial\phi_J}{\partial r}\right)+\frac{A_{12}^{(5)}}{6r}\left(\frac{\partial^2\phi_I}{\partial r^2}\frac{\partial\phi_J}{\partial r}+\frac{\partial\phi_I}{\partial r}\frac{\partial^2\phi_J}{\partial r^2}\right)+2B^{(1)}\frac{\partial\phi_I}{\partial r}\frac{\partial\phi_J}{\partial r}\\&+B^{(3)}\left[\frac{\partial^2\phi_I}{\partial r^2}\frac{\partial^2\phi_J}{\partial r^2}-\frac{1}{r}\left(\frac{\partial^2\phi_I}{\partial r^2}\frac{\partial\phi_J}{\partial r}+\frac{\partial\phi_I}{\partial r}\frac{\partial^2\phi_J}{\partial r^2}\right)+\frac{1}{r^2}\frac{\partial\phi_I}{\partial r}\frac{\partial\phi_J}{\partial r}\right]\Bigg\}rdr\end{aligned} \tag{A20}$$

$$\begin{aligned}K_{Ij}^{51}=\int_{r_1}^{r_2}\Bigg[&-\frac{A_{11}^{(3)}}{3}\left(\frac{\partial^2\phi_I}{\partial r^2}\frac{\partial\psi_j}{\partial r}+\frac{1}{r^2}\frac{\partial\phi_I}{\partial r}\psi_j\right)+2A_{12}^{(1)}c_2\left(\phi_I\frac{\partial\psi_j}{\partial r}+\frac{1}{r}\phi_I\psi_j\right)\\&-\frac{A_{12}^{(3)}}{3r}\left(\frac{\partial\phi_I}{\partial r}\frac{\partial\psi_j}{\partial r}+\frac{\partial^2\phi_I}{\partial r^2}\psi_j\right)\Bigg]rdr\end{aligned} \tag{A21}$$

$$\begin{aligned}K_{Ij}^{52}=\int_{r_1}^{r_2}\Bigg\{&-\frac{1}{3}\Big(A_{11}^{(4)}-c_1A_{11}^{(6)}\Big)\left(\frac{\partial^2\phi_I}{\partial r^2}\frac{\partial\psi_j}{\partial r}+\frac{1}{r^2}\frac{\partial\phi_I}{\partial r}\psi_i\right)+\frac{2}{r}\Big(A_{12}^{(2)}-c_1A_{12}^{(4)}\Big)\phi_I\psi_j\\&+2\Big(A_{12}^{(2)}-c_1A_{12}^{(4)}\Big)\phi_I\frac{\partial\psi_j}{\partial r}-\frac{1}{3r}\Big(A_{12}^{(4)}-c_1A_{12}^{(6)}\Big)\left(\frac{\partial\phi_I}{\partial r}\frac{\partial\psi_j}{\partial r}+\frac{\partial^2\phi_I}{\partial r^2}\psi_j\right)\\&+\frac{1}{2}\Bigg[\frac{1}{r}\Big(B^{(2)}-c_2B^{(4)}\Big)\left(\frac{\partial\phi_I}{\partial r}\frac{\partial\psi_j}{\partial r}+\frac{\partial^2\phi_I}{\partial r^2}\psi_j-r\frac{\partial^2\phi_I}{\partial r^2}\frac{\partial\psi_j}{\partial r}\right)\\&-\frac{1}{r^2}\Big(B^{(2)}-c_2B^{(4)}\Big)\frac{\partial\phi_I}{\partial r}\psi_j+4c_2B^{(2)}\frac{\partial\phi_I}{\partial r}\psi_j\Bigg]\Bigg\}rdr\end{aligned} \tag{A22}$$

$$K_{IJ}^{53} = \int_{r_1}^{r^2} \left\{ -\frac{1}{6}\left(\frac{\partial w_0}{\partial r}\right)\left(A_{11}^{(3)}\frac{\partial^2\phi_I}{\partial r^2}\frac{\partial\phi_J}{\partial r} + \frac{A_{12}^{(3)}}{r}\frac{\partial\phi_I}{\partial r}\frac{\partial\phi_J}{\partial r} - 6A_{12}^{(1)}\phi_I\frac{\partial\phi_J}{\partial r}\right) + \frac{c_1}{3}A_{11}^{(6)}\left(\frac{\partial^2\phi_I}{\partial r^2}\frac{\partial^2\phi_J}{\partial r^2} + \frac{1}{r^2}\frac{\partial\phi_I}{\partial r}\frac{\partial\phi_J}{\partial r}\right) - 2c_1A_{12}^{(4)}\left(\frac{1}{r}\phi_I\frac{\partial\phi_J}{\partial r} + \phi_I\frac{\partial^2\phi_J}{\partial r^2}\right) - \frac{c_1}{3r}A_{12}^{(6)}\left(\frac{\partial^2\phi_I}{\partial r^2}\frac{\partial\phi_J}{\partial r} + \frac{\partial\phi_I}{\partial r}\frac{\partial^2\phi_J}{\partial r^2}\right) + \frac{1}{2}\Bigg[4c_2B^{(2)}\frac{\partial\phi_I}{\partial r}\frac{\partial\phi_J}{\partial r} + \left(B^{(2)} + c_2B^{(4)}\right)\left(\frac{\partial^2\phi_I}{\partial r^2}\frac{\partial^2\phi_J}{\partial r^2} - \frac{1}{r}\frac{\partial\phi_I}{\partial r}\frac{\partial^2\phi_J}{\partial r^2} - \frac{1}{r}\frac{\partial^2\phi_I}{\partial r^2}\frac{\partial\phi_J}{\partial r} + \frac{1}{r^2}\frac{\partial\phi_I}{\partial r}\frac{\partial\phi_J}{\partial r}\right)\Bigg]\right\} rdr \tag{A23}$$

$$K_{IJ}^{54} = \int_{r_1}^{r^2} \left\{ A_{11}^{(1)}\phi_I\phi_J + \frac{A_{11}^{(5)}}{6}\left(\frac{\partial^2\phi_I}{\partial r^2}\frac{\partial^2\phi_J}{\partial r^2} + \frac{1}{r^2}\frac{\partial\phi_I}{\partial r}\frac{\partial\phi_J}{\partial r}\right) - \frac{A_{12}^{(3)}}{3}\left(3\phi_I\frac{\partial^2\phi_J}{\partial r^2} + \frac{\partial^2\phi_I}{\partial r^2}\phi_J\right) - \frac{A_{12}^{(3)}}{3r}\left(3\phi_I\frac{\partial\phi_J}{\partial r} + \frac{\partial\phi_I}{\partial r}\phi_J\right) + \frac{A_{12}^{(5)}}{6r}\left(\frac{\partial\phi_I}{\partial r}\frac{\partial^2\phi_J}{\partial r^2} + \frac{\partial^2\phi_I}{\partial r^2}\frac{\partial\phi_J}{\partial r}\right) + 2B^{(1)}\frac{\partial\phi_I}{\partial r}\frac{\partial\phi_J}{\partial r} + B^{(3)}\left[\frac{\partial^2\phi_I}{\partial r^2}\frac{\partial^2\phi_J}{\partial r^2} - \frac{1}{r}\left(\frac{\partial\phi_I}{\partial r}\frac{\partial^2\phi_J}{\partial r^2} + \frac{\partial^2\phi_I}{\partial r^2}\frac{\partial\phi_J}{\partial r}\right) + \frac{1}{r^2}\frac{\partial\phi_I}{\partial r}\frac{\partial\phi_J}{\partial r}\right]\right\} rdr \tag{A24}$$

$$K_{IJ}^{55} = \int_{r_1}^{r^2} \left\{ 4A_{11}^{(2)}\phi_I\phi_J + \frac{A_{11}^{(6)}}{9}\left(\frac{\partial^2\phi_I}{\partial r^2}\frac{\partial^2\phi_J}{\partial r^2} + \frac{1}{r^2}\frac{\partial\phi_I}{\partial r}\frac{\partial\phi_J}{\partial r}\right) - \frac{2A_{12}^{(4)}}{3}\left(\frac{\partial^2\phi_I}{\partial r^2}\phi_J + \phi_I\frac{\partial^2\phi_J}{\partial r^2}\right) - \frac{2A_{12}^{(4)}}{3r}\left(\frac{\partial\phi_I}{\partial r}\phi_J + \phi_I\frac{\partial\phi_J}{\partial r}\right) + \frac{A_{12}^{(6)}}{9r}\left(\frac{\partial^2\phi_I}{\partial r^2}\frac{\partial\phi_J}{\partial r} + \frac{\partial\phi_I}{\partial r}\frac{\partial^2\phi_J}{\partial r^2}\right) + 4B^{(2)}\frac{\partial\phi_I}{\partial r}\frac{\partial\phi_J}{\partial r} + B^{(4)}\left[\frac{\partial^2\phi_I}{\partial r^2}\frac{\partial^2\phi_J}{\partial r^2} - \frac{1}{r}\left(\frac{\partial^2\phi_I}{\partial r^2}\frac{\partial\phi_J}{\partial r} + \frac{\partial\phi_I}{\partial r}\frac{\partial^2\phi_J}{\partial r^2}\right) + \frac{1}{r^2}\frac{\partial\phi_I}{\partial r}\frac{\partial\phi_J}{\partial r}\right]\right\} rdr \tag{A25}$$

$$F_i^1 = \int_{r_1}^{r^2} \left\{ \left(f_r^{(0)} + q_r^{(0)}\right)\psi_i + T_r^{(0)}\frac{\partial\psi_i}{\partial r} + \frac{1}{r}T_\theta^{(0)}\psi_i \right\} rdr \tag{A26}$$

$$F_i^2 = \int_{r_1}^{r^2} \left\{ \left[\left(f_r^{(1)} + q_r^{(1)}\right) - c_1\left(f_r^{(3)} + q_r^{(3)}\right) + \left(c_\theta^{(0)} + p_\theta^{(0)}\right) - c_2\left(c_\theta^{(2)} + p_\theta^{(2)}\right)\right]\psi_i + \left(T_r^{(1)} - c_1T_r^{(3)}\right)\frac{\partial\psi_i}{\partial r} + \frac{1}{r}\left(T_\theta^{(1)} - c_1T_\theta^{(3)}\right)\psi_i \right\} rdr \tag{A27}$$

$$F_I^3 = \int_{r_1}^{r^2} \left\{ \left(f_z^{(0)} + q_z^{(0)}\right)\phi_I - \left[c_1\left(f_r^{(3)} + q_r^{(3)}\right) + \left(c_\theta^{(0)} + p_\theta^{(0)}\right) + c_2\left(c_\theta^{(2)} + p_\theta^{(2)}\right)\right]\frac{\partial\phi_I}{\partial r} + \left(\frac{\partial w_0}{\partial r}\right)T_r^{(0)}\frac{\partial\phi_I}{\partial r} - c_1T_r^{(3)}\frac{\partial^2\phi_I}{\partial r^2} + \frac{1}{r}T_\theta^{(3)}\frac{\partial\phi_I}{\partial r} \right\} rdr \tag{A28}$$

$$F_I^4 = \int_{r_1}^{r^2} \left\{ \left(f_z^{(1)} + q_z^{(1)}\right)\phi_I - \left[\frac{1}{2}\left(f_r^{(2)} + q_r^{(2)}\right) + 2\left(c_\theta^{(1)} + p_\theta^{(1)}\right)\right]\frac{\partial\phi_I}{\partial r} + T_z^{(0)}\phi_I - \frac{1}{2}T_r^{(2)}\frac{\partial^2\phi_I}{\partial r^2} - \frac{1}{2r}T_\theta^{(2)}\frac{\partial\phi_I}{\partial r} \right\} rdr \tag{A29}$$

$$F_I^5 = \int_{r_1}^{r^2} \left\{ \left(f_z^{(2)} + q_z^{(2)}\right)\phi_I - \left[\frac{1}{3}\left(f_r^{(3)} + q_r^{(3)}\right) + 3\left(c_\theta^{(2)} + p_\theta^{(2)}\right)\right]\frac{\partial\phi_I}{\partial r} + 2T_z^{(1)}\phi_I - \frac{1}{3}T_r^{(3)}\frac{\partial^2\phi_I}{\partial r^2} - \frac{1}{3r}T_\theta^{(3)}\frac{\partial\phi_I}{\partial r} \right\} rdr \tag{A30}$$

where

$$A_{11}^{(k)} = \int_{-\frac{h}{2}}^{\frac{h}{2}} (z)^k\,(1-\nu)\Lambda(z)\,dz, \qquad A_{12}^{(k)} = \int_{-\frac{h}{2}}^{\frac{h}{2}} (z)^k\,\nu\Lambda(z)\,dz,$$

$$A_{55}^{(k)} = \int_{-\frac{h}{2}}^{\frac{h}{2}} (z)^k \frac{(1-2\nu)}{2} \Lambda(z)\, dz, \qquad B^{(k)} = \int_{-\frac{h}{2}}^{\frac{h}{2}} (z)^k \ell^2 (1-2\nu)\Lambda(z)\, dz,$$

$$f_{\xi}^{(k)} = \int_{-\frac{h}{2}}^{\frac{h}{2}} (z)^i \bar{f}_{\xi}\, dz, \qquad q_{\xi}^{(k)} = \left(\frac{h}{2}\right)^{(k)} \left[q_{\xi}^{t} + (-1)^{(k)} q_{\xi}^{b}\right],$$

$$\hat{c}_{\theta}^{(k)} = \int_{-\frac{h}{2}}^{\frac{h}{2}} (z)^k \bar{c}_{\theta}\, dz, \qquad p_{\theta}^{(k)} = \left(\frac{h}{2}\right)^{(k)} \left[p_{\theta}^{t} + (-1)^{(k)} p_{\theta}^{b}\right],$$

$$T_{\xi}^{(k)} = \int_{-\frac{h}{2}}^{\frac{h}{2}} (z)^k \sigma_{ij}^{T}\, dz \tag{A31}$$

for $k = 0, 1, 2, 3, 4, 6$, $\xi = r, \theta, z$, and σ_{ij}^{T} is the thermal stress due to the temperature difference $(T - T_0)$.

References

1. Koizumi, M. FGM activities in Japan. *Compos. Part B Eng.* **1997**, *28*, 1–4. [CrossRef]
2. Birman, V.; Byrd, L.W. Modeling and analysis of functionally graded materials and structures. *Appl. Mech. Rev.* **2007**, *60*, 195–216. [CrossRef]
3. Mahamood, R.M.; Akinlabi, E.T.; Shukla, M.; Pityana, S.L. Functionally graded material: An overview. In Proceedings of the World Congress on Engineering, London, UK, 4–6 July 2012.
4. Jha, D.K.; Kant, T.; Singh, R.K. A critical review of recent research on functionally graded plates. *Compos. Struct.* **2013**, *96*, 833–849. [CrossRef]
5. Swaminathan, K.; Sangeetha, D.M. Thermal analysis of FGM plates—A critical review of various modeling techniques and solution methods. *Compos. Struct.* **2017**, *160*, 43–60. [CrossRef]
6. Reddy, J.N.; Chin, C.D. Thermomechanical analysis of functionally graded cylinders and plates. *J. Therm. Stress.* **1998**, *21*, 593–626. [CrossRef]
7. Reddy, J.N.; Wang, C.M.; Kitipornchai, S. Axisymmetric bending of functionally graded circular and annular plates. *Eur. J. Mech. A/Solids* **1999**, *18*, 185–199. [CrossRef]
8. Ma, L.S.; Wang, T.J. Nonlinear bending and post-buckling of a functionally graded circular plate under mechanical and thermal loadings. *Int. J. Solids Struct.* **2003**, *40*, 3311–3330. [CrossRef]
9. Praveen, G.N.; Reddy, J.N. Nonlinear transient thermoelastic analysis of functionally graded ceramic-metal plates. *Int. J. Solids Struct.* **1998**, *35*, 4457–4476. [CrossRef]
10. Reddy, J.N. Analysis of functionally graded plates. *Int. J. Numer. Methods Eng.* **2000**, *47*, 663–684. [CrossRef]
11. Najafizadeh, M.M.; Heydari, H.R. Thermal buckling of functionally graded circular plates based on higher order shear deformation plate theory. *Eur. J. Mech. A/Solids* **2004**, *23*, 1085–1100. [CrossRef]
12. Prakash, T.; Ganapathi, M. Asymmetric flexural vibration and thermoelastic stability of FGM circular plates using finite element method. *Compos. Part B Eng.* **2006**, *37*, 642–649. [CrossRef]
13. Nie, G.J.; Zhong, Z. Semi-analytical solution for three-dimensional vibration of functionally graded circular plates. *Comput. Methods Appl. Mech. Eng.* **2007**, *196*, 4901–4910. [CrossRef]
14. Efraim, E.; Eisenberger, M. Exact vibration analysis of variable thickness thick annular isotropic and FGM plates. *J. Sound Vib.* **2007**, *299*, 720–738. [CrossRef]
15. Golmakani, M.E.; Kadkhodayan, M. Nonlinear bending analysis of annular FGM plates using higher-order shear deformation plate theories. *Compos. Struct.* **2011**, *93*, 973–982. [CrossRef]
16. Golmakani, M.E.; Kadkhodayan, M. Large deflection analysis of circular and annular FGM plates under thermo-mechanical loadings with temperature-dependent properties. *Compos. Part B Eng.* **2011**, *42*, 614–625. [CrossRef]
17. Saidi, A.R.; Rasouli, A.; Sahraee, S. Axisymmetric bending and buckling analysis of thick functionally graded circular plates using unconstrained third-order shear deformation plate theory. *Compos. Struct.* **2009**, *89*, 110–119. [CrossRef]
18. Nosier, A.; Fallah, F. Reformulation of Mindlin-Reissner governing equations of functionally graded circular plates. *Acta Mech.* **2008**, *198*, 209–233. [CrossRef]
19. Nosier, A.; Fallah, F. Non-linear analysis of functionally graded circular plates under asymmetric transverse loading. *Int. J. Non-Linear Mech.* **2009**, *44*, 928–942. [CrossRef]
20. Yun, W.; Rongqiao, X.; Haojiang, D. Three-dimensional solution of axisymmetric bending of functionally graded circular plates. *Compos. Struct.* **2010**, *92*, 1683–1693. [CrossRef]
21. Talabi, M.R.; Saidi, A.R. An explicit exact analytical approach for free vibration of circular/annular functionally graded plates bonded to piezoelectric actuator/sensor layers based on Reddy's plate theory. *Appl. Math. Model.* **2013**, *37*, 7664–7684. [CrossRef]
22. Żur, K.K. Free vibration analysis of discrete-continuous functionally graded circular plate via the Neumann series method. *Appl. Math. Model.* **2019**, *73*, 166–189. [CrossRef]

23. Rad, A.B.; Shariyat, M. Three-dimensional magneto-elastic analysis of asymmetric variable thickness porous FGM circular plates with non-uniform tractions and Kerr elastic foundations. *Compos. Struct.* **2015**, *125*, 558–574.
24. Jabbari, M.; Joubaneh, E.F.; Mojahedin, A. Thermal buckling analysis of porous circular plate with piezoelectric actuators based on first order shear deformation theory. *Int. J. Mech. Sci.* **2014**, *83*, 57–64. [CrossRef]
25. Zhao, X.J.; Wang, F.; Shuai, A.; Tang, C.J.; Wang, Q. Dynamics analysis of functionally graded porous (FGP) circular, annular and sector plates with general elastic restraints. *Compos. Part B Eng.* **2019**, *159*, 20–43. [CrossRef]
26. Fleck, N.A.; Muller, G.M.; Ashby, M.F.; Hutchinson, J.W. Strain gradient plasticity: Theory and experiment. *Acta Metall. Mater.* **1994**, *42*, 475–487. [CrossRef]
27. Ma, Q.; Clarke, D.R. Size dependent hardness of silver single crystals. *J. Mater. Res.* **1995**, *10*, 853–863. [CrossRef]
28. Stölken, J.S.; Evans, A.G. A microbend test method for measuring the plasticity length scale. *Acta Mater.* **1998**, *46*, 5109–5115. [CrossRef]
29. Chong, A.C.M.; Lam, D.C.C. Strain gradient plasticity effect in indentation hardness of polymers. *J. Mater. Res.* **1999**, *14*, 4103–4110. [CrossRef]
30. Toupin, R.A. Elastic materials with couple-stresses. *Arch. Ration. Mech. Anal.* **1962**, *11*, 385–414. [CrossRef]
31. Mindlin, R.D.; Tiersten, H.F. Effects of couple-stresses in linear elasticity. *Arch. Ration. Mech. Anal.* **1962**, *11*, 415–448. [CrossRef]
32. Yang, F.; Chong, A.C.M.; Lam, D.C.C.; Tong, P. Couple stress based strain gradient theory for elasticity. *Int. J. Solids Struct.* **2002**, *39*, 2731–2743. [CrossRef]
33. Eringen, A.C. Nonlocal polar elastic continua. *Int. J. Eng. Sci.* **1972**, *10*, 1–16. [CrossRef]
34. Fleck, N.A.; Hutchinson, J.W. A reformulation of strain gradient plasticity. *J. Mech. Phys. Solids* **2001**, *49*, 2245–2271. [CrossRef]
35. Lam, D.C.C.; Yang, F.; Chong, A.C.M.; Wang, J.; Tong, P. Experiments and theory in strain gradient elasticity. *J. Mech. Phys. Solids* **2003**, *51*, 1477–1508. [CrossRef]
36. Ke, L.L.; Yang, J.; Kitipornchai, S.; Bradford, M.A. Bending, buckling and vibration of size-dependent functionally graded annular microplates. *Compos. Struct.* **2012**, *94*, 3250–3257. [CrossRef]
37. Ansari, R.; Gholami, R.; Shojaei, M.F.; Mohammadi, V.; Sahmani, S. Bending, buckling and free vibration analysis of size-dependent functionally graded circular/annular microplates based on the modified strain gradient elasticity theory. *Eur. J. Mech. A/Solids* **2015**, *49*, 251–267. [CrossRef]
38. Reddy, J.N.; Berry, J. Nonlinear theories of axisymmetric bending of functionally graded circular plates with modified couple stress. *Compos. Struct.* **2012**, *94*, 3664–3668. [CrossRef]
39. Reddy, J.N.; Romanoff, J.; Loya, J.A. Nonlinear finite element analysis of functionally graded circular plates with modified couple stress theory. *Eur. J. Mech. A/Solids* **2016**, *56*, 92–104. [CrossRef]
40. Hosseini-Hashemi, S.; Bedroud, M.; Nazemnezhad, R. An exact analytical solution for free vibration of functionally graded circular/annular Mindlin nanoplates via nonlocal elasticity. *Compos. Struct.* **2013**, *103*, 108–118. [CrossRef]
41. Beni, Y.T.; Mehralian, F.; Razavi, H. Free vibration analysis of size-dependent shear deformable functionally graded cylindrical shell on the basis of modified couple stress theory. *Compos. Struct.* **2015**, *120*, 65–78. [CrossRef]
42. Eshraghi, I.; Dag, S.; Soltani, N. Bending and free vibrations of functionally graded annular and circular micro-plates under thermal loading. *Compos. Struct.* **2016**, *137*, 196–207. [CrossRef]
43. Ji, X.; Li, A.; Zhou, S. A comparison of strain gradient theories with applications to the functionally graded circular micro-plate. *Appl. Math. Model.* **2017**, *49*, 124–143. [CrossRef]
44. Shojaeefard, M.H.; Googarchin, H.S.; Ghadiri, M.; Mahinzare, M. Micro temperature-dependent FG porous plate: Free vibration and thermal buckling analysis using modified couple stress theory with CPT and FSDT. *Appl. Math. Model.* **2017**, *50*, 633–655. [CrossRef]
45. Kim, J.; Żur, K.K.; Reddy, J.N. Bending, free vibration, and buckling of modified couples stress-based functionally graded porous micro-plates. *Compos. Struct.* **2019**, *209*, 879–888. [CrossRef]
46. Wang, Y.; Zhang, W. On the thermal buckling and postbuckling responses of temperature-dependent graphene platelets reinforced porous nanocomposite beams. *Compos. Struct.* **2022** *296*, 115880. [CrossRef]
47. Zhang, W.; Wang, C.; Wang, Y. Thermo-mechanical analysis of porous functionally graded graphene reinforced cylindrical panels using an improved third order shear deformable model. *Appl. Math. Model.* **2023** *118*, 453–473. [CrossRef]
48. Xu, Z.; Zhang, Z.; Wang, J.; Chen, X.; Huang, Q. Acoustic analysis of functionally graded porous graphene reinforced nanocomposite plates based on a simple quasi-3D HSDT. *Thin-Walled Struct.* **2020**, *157*, 107151. [CrossRef]
49. Koiter, W.T. Couple stresses in the theory of elasticity. *Proc. K. Ned. Acad. Van Wet. Ser. B Phys. Sci.* **1964**, *67*, 17–44.
50. Reddy, J.N.; Kim, J. A nonlinear modified couple stress-based third-order theory of functionally graded plates. *Compos. Struct.* **2012**, *94*, 1128–1143. [CrossRef]
51. Deng, Z.; Liu, X.; Huang, Y.; Zhang, C.; Chen, Y. Heat Conduction in Porous Media Characterized by Fractal Geometry. *Energies* **2017**, *10*, 1230. [CrossRef]
52. Reddy, J.N. *An Introduction to Nonlinear Finite Element Analysis, with Applications to Heat Transfer, Fluid Mechanics, and Solid Mechanics*, 2nd ed.; Oxford University Press: Oxford, UK, 2014.
53. Garzon, J.; Gupta, V.; Simone, A.; Duarte, C.A. Bridging Scales with a Generalized Finite Element Method. *Procedia IUTAM* **2012**, *3*, 172–191. [CrossRef]

54. Liguori, F.S.; Magisano, D.; Leonetti, L.; Garcea, G. Nonlinear thermoelastic analysis of shell structures: Solid-shell modelling and high-performing continuation method. *Compos. Struct.* **2021**, *266*, 113734. [CrossRef]
55. Oliveri, V.; Milazzo, A.; Weaver, P.M. Thermo-mechanical post-buckling analysis of variable angle tow composite plate assemblies. *Compos. Struct.* **2018**, *183*, 620–635. [CrossRef]
56. Reddy, J.N.; Cheng, Z.Q. Three-dimensional thermomechanical deformations of functionally graded rectangular plates. *Eur. J. Mech. A/Solids* **2001**, *20*, 841–855. [CrossRef]

materials

MDPI

Article

Research on the Spring Creep Based on the Load Simulator of the Double Torsion Spring Steering Gear

Bo Zhang, Peijie Ren *, Zhuo Wang and Hongwen Ma

College of Mechanical and Electrical Engineering, Harbin Engineering University, Harbin 150001, China; zhangbo_heu@hrbeu.edu.cn (B.Z.); wangzhuo_heu@hrbeu.edu.cn (Z.W.); mahongwen@hrbeu.edu.cn (H.M.)
* Correspondence: rpj@hrbeu.edu.cn

Abstract: In this paper, creep at room temperature is studied using a mechanical double−spring steering−gear load table, and the results are used to determine the accuracy of theoretical and simulated data. A creep equation at room temperature, based on the parameters obtained by a new macroscopic tensile experiment method, is used to analyze the creep strain and creep angle of a spring under force. The correctness of the theoretical analysis is verified by a finite−element method. Finally, a creep strain experiment of a torsion spring is carried out. The experimental results are 4.3% lower than the theoretical calculation results, which demonstrates the accuracy of the measurement, with an error of <5% achieved. The results shows that the equation used for the theoretical calculation is highly accurate and can meet the requirements of engineering measurement.

Keywords: load simulator; double spring; pre-compression; creep effect; prototype experiment

Citation: Zhang, B.; Ren, P.; Wang, Z.; Ma, H. Research on the Spring Creep Based on the Load Simulator of the Double Torsion Spring Steering Gear. *Materials* **2023**, *16*, 3763. https://doi.org/10.3390/ma16103763

Academic Editors: Angelo Marcello Tarantino, Carmelo Majorana, Raimondo Luciano and Michele Bacciocchi

Received: 12 April 2023
Revised: 12 May 2023
Accepted: 14 May 2023
Published: 16 May 2023

1. Introduction

During flight, a missile control system gives instructions to control the wing of the steering gear to rotate at a certain Angle, which changes the direction and magnitude of the gas force acting on the missile, thus changing the missile's flight trajectory [1]. Therefore, the performance of its steering gear greatly influences the performance of a missile [2]. As steering gear is an integral component of an aircraft system, it is impossible to carry out a steering gear test after the design and manufacture of the system [3]. Therefore, it is necessary to test the performance of steering gear during its manufacture. A simulation load table is mainly used to simulate the force of steering gear during actual use in the environment [4].

At present, large-scale servos are mainly tested using electric and electro-hydraulic servo load simulators [1], while mechanical load simulators are widely used in small servo testing because of their high loading accuracy, small residual torque [5,6], small size, low manufacturing cost, simple structure, and easy maintenance.

For a mechanical load table, a spring torsion bar is generally used as the core component to provide load force. A spring torsion bar has the advantages of small error and high reliability [7]. In order to eliminate the non-linearity of spring reverse loading and the change of stiffness, and to reduce the zero balance range of a spring due to residual stress, friction, zero hysteresis, and other factors, Zhang [8] has proposed a mechanical load table with a structure of a double-spring coaxial reverse arrangement and pre-compression, which can effectively reduce the zero balance range. Because of the moment produced by the pre-compression of a spring, the spring will creep.

Zhu [9] studied the creep process of a precision helical tensile spring, which provided a method for measuring the creep of a tensile spring at room temperature. T. H. Alden [10] studied the strain hardening of 304 stainless steel during low temperature creep and proposed a theory that can be used to predict the creep curve and the hardening effect caused by creep. A. Oehlert [11] studied the room-temperature creep of high strength steel and found that creep can occur at lower stresses and that creep strain increases with creep

time and stress, but decreases with an increase of number of cycles. B. Alfredsson [12] conducted low-temperature creep experiments on martensite and bainite microstructures of high-strength rolling bearing steel, and found that the two exhibited different primary creep behaviors. The research results have certain guiding significance for the design and application of high-strength steel. Paul R. Barrett [13] developed a modified Coble creep model to describe the experimental low-stress creep rates in alloys with thermally stable precipitate structures. Brian K. Milligan [14] has studied the creep behavior of Al-Cu alloys at certain temperatures, and found that increasing the thermal stability of the precipitates in Al-Cu alloys can significantly improve their creep properties. Hu [15] explained how the evolution of microstructure affects the creep properties of a material physically, and evaluated several secondary phenomena in the curve of creep rate versus time of 316H stainless steel, which is vital to the realistic life assessment of critical engineering components. Wu [16] established the creep constitutive equation of a stainless steel spring to study the creep of a spring, and found that the higher the ambient temperature, the greater the creep strain of a stainless steel spring. When the service temperature increases from 25 °C to 320 °C, the 24h creep strain increases by five times.

At present, the research on creep mainly focuses on the creep behavior of materials, or the establishment of creep models under high temperature, but the research on creep at room temperature is relatively scarce. Most of the research on the creep behavior of springs has been carried out at high temperature and mainly focus on the stress relaxation of a spring [17–22]. In this paper, the influence of creep effect of a spring due to pre-compression is studied. The specific research contents are as follows: Through deconstruction and reorganization, using the original room-temperature creep constitutive equation as a basis, a room-temperature creep constitutive equation of a torsion spring with relevant parameters is obtained based on a macro-tensile test, which is then compared and verified by a finite-element simulation. The stress and strain of a spring are analyzed, and an accurate stress expression of the spring is obtained. Experiments are designed to verify the creep performance of a spring, and the error between the theoretical calculation results of spring creep strain and experimental data is obtained.

2. Creep Equation and Experimental Method of a Spring at Room Temperature

2.1. Creep Equation of a Spring at Room Temperature

In room-temperature creep, the creep deformation increases logarithmically with time, which is consistent with the first stage of typical creep. Strain hardening and fatigue models are usually used in creep theory at room temperature. The fatigue model is more accurate in fast loading, while the strain hardening model can be used in room-temperature creep under arbitrary loading [23].

According to the microscopic situation of room-temperature creep, Schoeck [24] proposed the constitutive equation of room-temperature creep:

$$\dot{\varepsilon}_{\mathrm{c}} = NAV\nu \exp\left(-\frac{U}{KT}\right), \tag{1}$$

where: $\dot{\varepsilon_c}$—room-temperature creep rate; N—dislocation density; A—the area of dislocations swept after passing an obstacle; V—activation volume; ν—vibration frequency of the dislocation line; U—thermal activation energy required to pass obstacles; K—Boltzmann constant; T—experimental temperature.

U can be expressed as the product of the thermal activation energy, U_0, minus the effective stress, σ_{eff}, acting on the dislocation line and the activation volume, V, namely:

$$U = U_0 - \sigma_{\mathrm{eff}} V. \tag{2}$$

In the strain hardening model, the external stress, σ, is constant, but due to the hardening effect, the effective stress, σ_{eff}, decreases with the increase of creep value, ε_c, namely:

$$\sigma_{\text{eff}} = \sigma - \theta\varepsilon_{\text{c}}, \tag{3}$$

where: θ—hardening coefficient at room-temperature creep; ε_c—creep value.

The relationship between room-temperature creep and creep time can be obtained by introducing Equations (2) and (3) into Equation (1), namely:

$$\varepsilon_{\text{c}} = \alpha \ln\left(\frac{t_{\text{c}}}{\tau} + 1\right), \tag{4}$$

where:

$$\alpha = \frac{KT}{\theta V}, \tau = \frac{KT}{\theta V}\frac{1}{NAB\nu}\exp\frac{U_0 - \sigma V}{KT}, \tag{5}$$

where: B—Burgers vector; θ—strain hardening coefficient.

Derived from Equation (4), the relationship between creep rate, $\dot{\varepsilon_c}$, and creep time, t_c, at room temperature can be obtained as follows:

$$\dot{\varepsilon}_{\text{c}} = \frac{\alpha}{t_c + \tau}. \tag{6}$$

After the end of loading, creep just appears. At this time, $t_c = 0$ and $\dot{\varepsilon_c} = \alpha/\tau = \dot{\varepsilon_{c0}}$, which can be substituted into Equation (6) to obtain the following relationship:

$$\dot{\varepsilon}_{\text{c}} = \left(\frac{t_c}{\alpha} + \frac{1}{\dot{\varepsilon}_{\text{c0}}}\right)^{-1}. \tag{7}$$

It can be seen from Equation (7) that the main influencing factors of creep rate are α and $\dot{\varepsilon_{c0}}$, which can be directly obtained by experiment. By fitting the experimental data with Equation (7), the creep rate equation can be obtained.

According to Equation (6), the room-temperature creep rate, $\dot{\varepsilon_c}$, can be obtained only after obtaining the influencing factors α and τ. However, these two factors are a measure of micro performance, which are difficult to obtain and not suitable for the situation of large individual differences. Therefore, Xiao [24] adopted a method to calculate room-temperature creep only with macro parameters, and the relevant parameters can be obtained through routine experiments, which is a more simple and convenient method in engineering applications.

The initial creep rate, $\dot{\varepsilon_c} = \alpha/\tau = \dot{\varepsilon_{c0}}$, at the beginning of creep can be combined with Equation (4) to obtain Equation (8):

$$\varepsilon_{\text{c}} = \alpha \ln\left(\frac{t}{\alpha}\dot{\varepsilon}_{\text{c0}} + 1\right). \tag{8}$$

Therefore, the parameter τ is transformed into the initial creep rate, $\dot{\varepsilon_{c0}}$. There is no difference between creep loading at room temperature and tensile-test loading. Therefore, the strain rate at the moment when the room-temperature creep loading is completed is equal to the rate when the creep is just carried out, and the creep stress is equal to the stress at the end of the loading.

The Ramberg–Osgood model [25] is usually used to describe the stress–strain curve of steel. This model was put forward in 1943. The main idea is that the strain of a material is composed of elastic deformation and plastic deformation. The nominal flow limit, $\sigma_{0.2}$, of a material is selected by the classical method, and the corresponding deformation $\varepsilon_{0.2}$ = 0.002, then the equation for the Ramberg–Osgood model is:

$$\varepsilon = \frac{\sigma}{E} + 0.002\left(\frac{\sigma}{\sigma_{0.2}}\right)^n, \tag{9}$$

where: $\sigma_{0.2}$—nominal flow limit; n—strain hardening coefficient.

The strain hardening coefficient can be selected by the classical method. If $\sigma = \sigma_{0.1}$ is used [26], the strain hardening coefficient is:

$$n = \frac{\ln(\varepsilon_{0.2}/\varepsilon_{0.1})}{\ln(\sigma_{0.2}/\sigma_{0.1})} \tag{10}$$

The above equation is accurate when the stress is less than the nominal flow limit, $\sigma_{0.2}$, but when the stress exceeds the nominal flow limit the calculated result of this model is larger than the actual result.

On the basis of the Ramberg–Osgood model [25], Kim J. R. Rasmussen [27] put forward the method of subsection fitting through experimental research. The boundary point is the nominal flow limit, $\sigma_{0.2}$. When the stress is less than the nominal flow limit, the Ramberg–Osgood model is used. After $\sigma_{0.2}$ is exceeded, the Ramberg–Osgood model is calculated in the translation coordinate system. Through a large number of experimental calculations and statistical analysis, an improved Ramberg–Osgood model is obtained:

$$\varepsilon = \begin{cases} \frac{\sigma}{E} + 0.002\left(\frac{\sigma}{\sigma_{0.2}}\right)^n, \sigma \le \sigma_{0.2} \\ \frac{\sigma-\sigma_{0.2}}{E_{0.2}} + \varepsilon_u\left(\frac{\sigma-\sigma_{0.2}}{\sigma_u-\sigma_{0.2}}\right)^m + \varepsilon_{0.2}, \sigma \ge \sigma_{0.2} \end{cases}. \tag{11}$$

(1) When $\sigma \le \sigma_{0.2}$, n is the strain hardening coefficient, which can be calculated by Equation (10).
(2) When $\sigma \ge \sigma_{0.2}$, $E_{0.2}$ is the initial Young's modulus at this stage, that is, the tangent modulus at 0.2% yield strength. Its value can be calculated by Equation (12):

$$E_{0.2} = \frac{E}{1 + 0.002n/e}, \tag{12}$$

where: e—parameter, $e = \sigma_{0.2}/E$; ε_u—total strain at final fracture; σ_u—stress at final fracture, i.e., tensile strength; m—index, m = 1 + 3.5$\sigma_{0.2}/\sigma_u$; $\varepsilon_{0.2}$—$\sigma_{0.2}$ corresponding total engineering strain, $\varepsilon_{0.2} = \sigma_{0.2}/E + 0.002$.

The strain rate at the loading stage can be obtained by deriving the time t from both sides of Equation (11) at the same time.

$$\frac{\mathrm{d}\varepsilon}{\mathrm{d}t} = \begin{cases} [\frac{1}{E} + 0.002n(\frac{\sigma}{\sigma_{0.2}})^{n-1}]\frac{\mathrm{d}\sigma}{\mathrm{d}t}, \sigma \le \sigma_{0.2} \\ [\frac{1}{E_{0.2}} + \varepsilon_{\mathrm{u}} m(\frac{\sigma-\sigma_{0.2}}{\sigma_{\mathrm{u}}-\sigma_{0.2}})^{m-1}\frac{1}{\sigma-\sigma_{0.2}}]\frac{\mathrm{d}\sigma}{\mathrm{d}t}, \sigma \ge \sigma_{0.2} \end{cases}. \tag{13}$$

It is known that the state at the end of loading is the initial state at the beginning of creep, that is, $\dot{\varepsilon_{c0-}} = \dot{\varepsilon_{c0+}} = \dot{\varepsilon}(\dot{T_1})$, and $\dot{\varepsilon_{c0}} = \alpha/\tau$. By substituting Equation (8), Equation (14) can be obtained:

$$\varepsilon_{\mathrm{c}} = \alpha(\sigma_{\mathrm{c}}) \ln[1 + \frac{t}{\alpha(\sigma_{\mathrm{c}})}\dot{\varepsilon}_1(\sigma_{\mathrm{c}})], \tag{14}$$

where σ_c is the constant stress in the creep stage of the material and its value is equal to the material stress at the completion of loading. Therefore, $\dot{\varepsilon}(\dot{\sigma_c}) = \dot{\varepsilon}(\dot{T_1})$. By using Equations (12) and (13), the creep value increases with the increase of creep time.

2.2. Spring Material and Size Parameters

The spring material is 65 Mn, and its specific performance parameters are shown in Table 1.

Table 1. Mechanical properties of 65 Mn Steel.

Elastic modulus/(MPa)	211,000
Poisson's ratio	0.288
Density/(t/mm^3)	7.83×10^{-9}
Tensile strength σ_b/(MPa)	1420
Yield strength σ_s/(MPa)	1136
Fatigue limit σ_{-1}/(MPa)	639

The spring calculation process has been mentioned in another article [8], and the spring size parameters are shown in Table 2 below.

Table 2. Main parameters of a torsion spring bearing the torque of 300 N·mm.

Torsion spring wire diameter/(mm)	1.8
Mean diameter of coil/(mm)	11
Total number of coils	4
Free angle/(°)	120
Torsion spring force arm/(mm)	15
Torsion spring pitch/(mm)	2.5
Torsion spring helix angle/(°)	4.14

2.3. Calculation of Temperature Creep in Spring Chamber

According to article [28], the maximum stress of a cylindrical helical torsional spring when it only withstands external torque T is:

$$\sigma_{\mathrm{bb}} = -\frac{\cos^3 a}{z_m C} T[0.154 + (0.246\cos^2 a - 0.096\sin^2 a)\frac{1}{C}], \tag{15}$$

$$\sigma_{\mathrm{tt}} = -\frac{\cos \alpha}{z_m} T[1 + 0.871\frac{\cos^2 \alpha}{C} + (0.032\sin^2 \alpha + 0.642\cos^2 \alpha)\frac{\cos^2 \alpha}{C}], \tag{16}$$

and

$$\tau_{\mathrm{tb}} = \tau_{\mathrm{bt}} = \frac{\sin \alpha}{z_t} T[1 + 0.635\frac{\cos^2 \alpha}{C} + 0.163\frac{\cos^4 \alpha}{C^2}], \tag{17}$$

where: a—torsion spring mounting Angle; z_m—flexural section coefficient; C—spring index; z_t—torsion section coefficient; α—helical angle.

According to Mohr's strength theory, the equivalent stress at the danger point of the spring is:

$$\sigma^* = \frac{1-m}{2}(\sigma_{\mathrm{tt}} + \sigma_{\mathrm{bb}}) + \frac{1+m}{2}\sqrt{(\sigma_{\mathrm{tt}} - \sigma_{\mathrm{bb}})^2 + 4\tau_{\mathrm{t}}^2} \tag{18}$$

and

$$m = \frac{\sigma_{\mathrm{st}}}{\sigma_{\mathrm{sc}}} \leq 1 \tag{19}$$

where: σ_{st}—tensile yield point; σ_{sc}—compressive yield point.

When the spring is compressed by 30°, the moment of a single spring is 300 N·mm. By substituting the relevant values in Table 2 into Equations (15)–(17), σ_{bb} = 16.869 MPa, σ_{tt} = 539.33 MPa, and τ_{bt} = 20.99 MPa can be obtained. By substituting these three values into Equation (18) (where m = 0.9231), the equivalent stress, σ^* = 525.38 MPa, of the spring danger point can be obtained.

Since the equivalent stress σ^* = 525.38 MPa is $\leq \sigma_{0.2}$ at the spring danger point, the strain rate at the spring danger point under constant external load can be obtained by substituting the parameter into Equation (13).

$$\frac{\mathrm{d}\varepsilon}{\mathrm{d}t} = [\frac{1}{E_0} + \frac{0.002n}{\sigma_{0.2}}(\frac{\sigma}{\sigma_{0.2}})^{n-1}]\frac{\mathrm{d}\sigma}{\mathrm{d}t} \tag{20}$$

When the equivalent stress $\sigma \leq \sigma_{0.2}$, in the loading stage, the relationship between stress and strain rate is given by Equation (20). Assuming that the loading rate is 1, the relationship between them is shown in Figure 1.

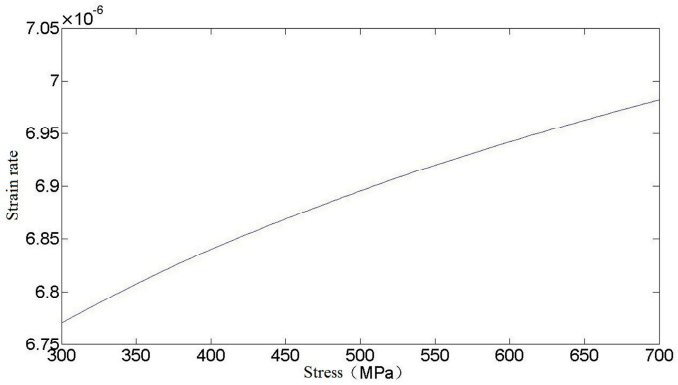

Figure 1. Relationship between stress and strain rate.

Upon substitution of the equivalent stress of the spring danger point into Equation (20), and applying the result to Equation (14), the calculation formula for creep strain under external load T = 300 N·mm is:

$$\varepsilon_c = \alpha(\sigma_c) \ln[1 + \frac{t}{\alpha(\sigma_c)}(\frac{1}{E_0} + \frac{0.002n}{\sigma_{0.2}}(\frac{\sigma}{\sigma_{0.2}})^{n-1})\frac{d\sigma}{dt}]. \quad (21)$$

In Equation (21), n and $\alpha(\sigma_c)$ can be obtained by fitting the data obtained from tensile and creep tests, where n = 1.113 and $\alpha(\sigma_c)$ is:

$$\alpha(\sigma_c) = 8.1427 \times 10^{-9}\sigma_c. \quad (22)$$

According to the relevant experiment experience of loading rate, in the tensile test, the value of loading rate is generally set at 5~40 MPa/min. According to relevant literature [29], the magnitude of strain in the first stage of the material obtained from loading rates within the range of 5~40 MPa/min remains basically unchanged, with slight differences in subsequent stages, but the difference is not significant. Therefore, to simplify the calculation, the loading rate is selected as 20 MPa/min, that is, $d\sigma/dt = 0.333$ MPa/s.

By integrating Equations (14), (20) and (22), and taking the loading rate as 0.333 MPa/s, the expression formula of creep stress can be obtained as follows:

$$\varepsilon_c = \alpha(\sigma_c) \ln[1 + \frac{t}{\alpha(\sigma_c)}(\frac{1}{3E} + \frac{0.002n}{3\sigma_{0.2}}(\frac{\sigma_c}{\sigma_{0.2}})^{n-1})]. \quad (23)$$

It can be seen from the above formula that creep strain is mainly related to time and stress, and the relationship between the three is shown in Figure 2.

As can be seen in Figure 2, the room-temperature creep of a cylindrical helical torsion spring shows a typical creep curve trend when the stress is determined. In the case of low stress, the creep of the torsion spring enters the second stage of stable creep in a short time. In the stable creep stage, the creep strain rate is small, and there is little increase in creep strain with time. In the condition of high stress, the first stage of creep of a torsion spring ends after a longer time, and the creep of the torsion spring enters the second stage of stable creep after a longer time. It can be seen that, in the same case, the greater the stress produced by a torsion spring, the longer the time it experiences in the first creep stage. In the stable creep stage, compared with the lower stress condition, the creep strain rate is larger, and the increase of creep strain is larger for a long time.

After derivation of time t on both sides of Equation (23), the relationship between creep rate of a cylindrical helical torsional spring, stress, and time can be obtained, as

shown in Figure 3. As can be seen from Figure 3, the creep rate decreases significantly with the increase of time. Compared with a state of low stress, the time of torsional spring creep in the first stage of creep increases obviously in a state of high stress, and the creep rate in the second stage of creep also increases obviously.

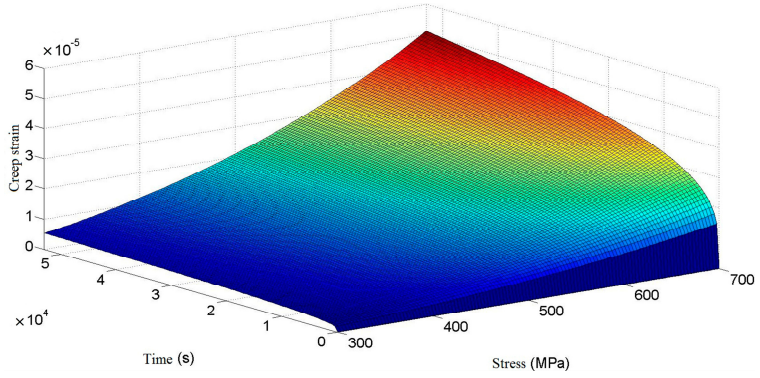

Figure 2. Relation of creep strain to stress and time.

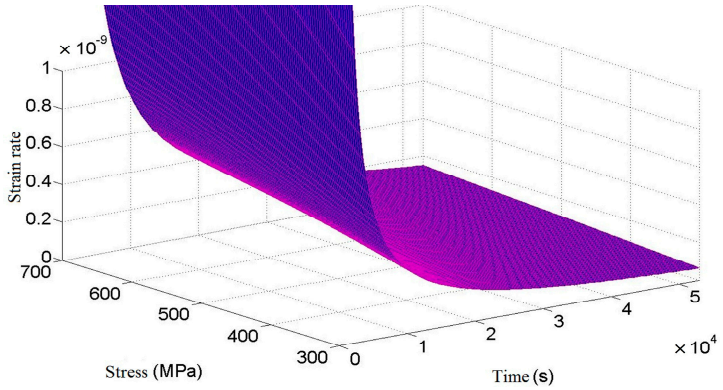

Figure 3. Relation of creep rate to stress and time.

Since the stress values in each part of the spring are not equal and cannot be calculated in detail, it is not practical to calculate the creep strain. In order to simplify the calculation and improve the safety margin, the creep strain values at the spring danger points are chosen to replace the creep strain values at each part of the spring. It can be seen from the above that the equivalent stress of the spring danger point is σ^* = 525.38 MPa, and the relationship between creep strain value and time can be obtained by substituting it into Equation (23), as shown in Figure 4.

It can be seen from Figure 4 that the creep strain curve after the torsional spring loading is in line with the first and second stages of the theoretical creep curve. With the increase of time, the creep strain continues to increase and the rate decreases to a fixed value. The creep strain of the torsional spring will not enter the third stage because it is at room temperature and the loading stress is not large.

In the elastic deformation stage, according to data [30], the stress–strain relationship in pure bending can be written as:

$$\varepsilon_e = \frac{(\rho + y)d\theta - \rho d\theta}{\rho d\theta} = \frac{y}{\rho}, \tag{24}$$

where: y is the distance between the linear strain on the section and the neutral axis, and assuming that each fiber is only subject to axial tension and compression, it can be obtained according to Hooke's law:

$$\sigma = E\varepsilon = E\frac{y}{\rho} \tag{25}$$

and

$$\frac{1}{\rho} = \frac{M}{EI_z}. \tag{26}$$

Therefore, the stress–strain relationship at the lower boundary of the section in the elastic stage of a torsion spring is:

$$\varepsilon_e = \frac{yM}{EI_z}. \tag{27}$$

According to the relationship between creep strain and elastic strain of a torsion spring, the change of rotation angle during creep of a torsion spring can be obtained, as shown in Figure 5.

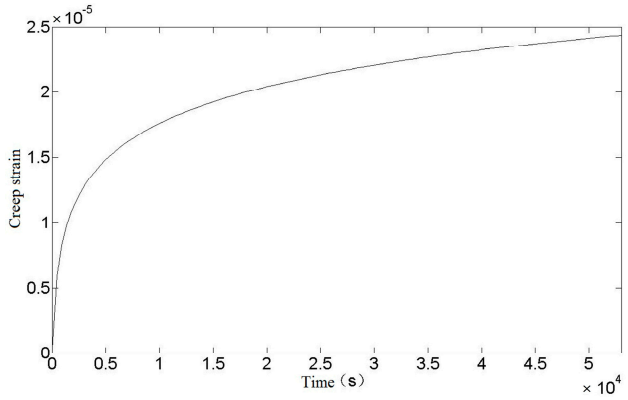

Figure 4. Relationship between creep strain and time of torsion spring.

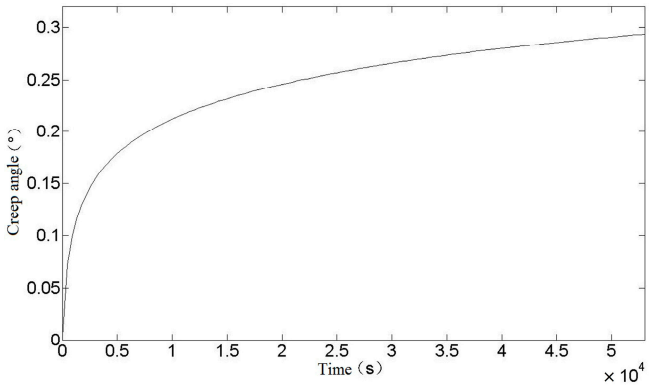

Figure 5. Relationship between creep angle and time of torsion spring.

In this paper, the creep process of a torsion spring is calculated theoretically, and the creep strain of a torsion spring at room temperature, and the relationship between creep angle and time, are obtained. The following uses the finite-element method to simulate the creep process of a torsion spring.

The simulation was carried out by using Abaqus. One end of the torsion spring was fixed, and a torque of 300 N·mm was applied to the other end. In the first analysis step, a torque of 300 N·mm was applied to make the spring undergo elastic deformation, and the time was 1 s. The second analysis step was creep analysis, which lasted for 54,000 s. The displacement results obtained are shown in Figure 6.

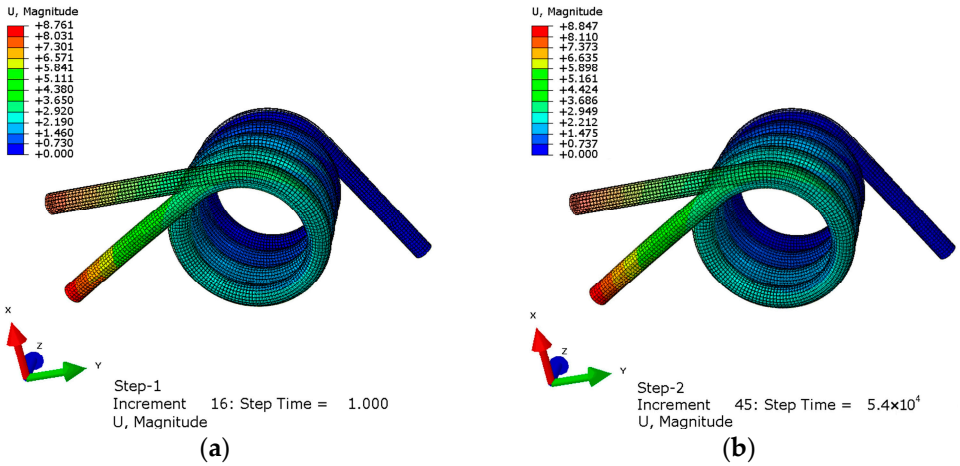

Figure 6. Torsion spring deformation diagram: (**a**) elastic deformation diagram (**b**) creep deformation diagram.

The shadow in Figure 6 is the image before the torsion spring is deformed. It can be seen from the figure that the displacement at the elastic deformation stage is 8.761 mm from the farthest point of the central axis of the spring. After 54,000 s, its deformation increases to 8.847 mm. Compared with the elastic stage, the creep deformation is 0.98% of the elastic deformation and the creep strain is 2.45×10^{-5}. In order to display the creep curve more clearly, the curve at the elastic deformation stage is ignored and only the curve within a period of time at the beginning of creep is truncated. The point is selected as the lower endpoint of the torsional spring applying force, and the creep curve is shown in Figure 7.

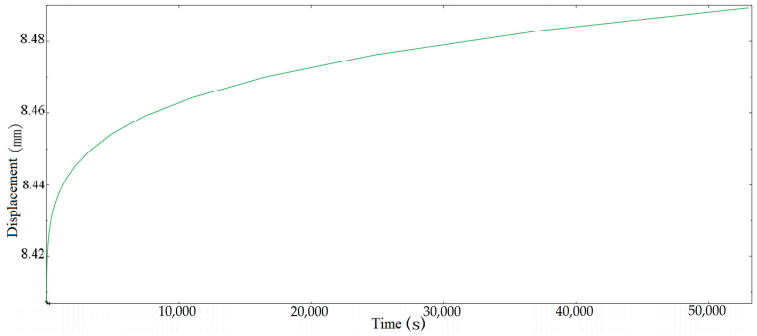

Figure 7. Creep simulation displacement of torsion spring.

It can be seen from Figure 7 that the creep simulation curve of a torsion spring is similar to the theoretical calculation curve, and a comparison between the simulation curve and the theoretical curve is shown in Figure 8.

It can be seen from Figure 8 that the theoretical calculation value of torsion spring creep is slightly less than the simulation value in the early stage, and the theoretical calculation value is slightly greater than the simulation result as time goes on. In the later period, the theoretical calculation is smaller than the simulation result. At 54,000 s, the theoretical calculation value of torsion spring creep is 0.2935°, while the simulation result is 0.3105°, which is 5.79% larger than the theoretical calculation, proving that the theoretical calculation formula is more accurate. Regarding the error between the theoretical calculation and simulation results: on the one hand, it may be because the software adopts traditional age-hardening creep theory in the finite-element simulation process, without considering the influence of some material properties, such as interaction and microstructure. In addition, when using this theory, parameters such as creep strain rate, creep activation energy, and initial hardness of materials need to be determined. If the actual material parameters are different from those used in the theoretical calculation, the calculation results will be biased.

On the other hand, it may be because some small quantities are omitted in the derivation of theoretical formulas, which leads to the change of calculation accuracy. However, on the whole, the error between the theoretical calculation results and the finite-element simulation results is within an acceptable error range, which shows that the theoretical calculation results are more accurate and can accurately predict and estimate the performance and life of a spring in use, which is of great significance for designing high-performance and reliable spring components.

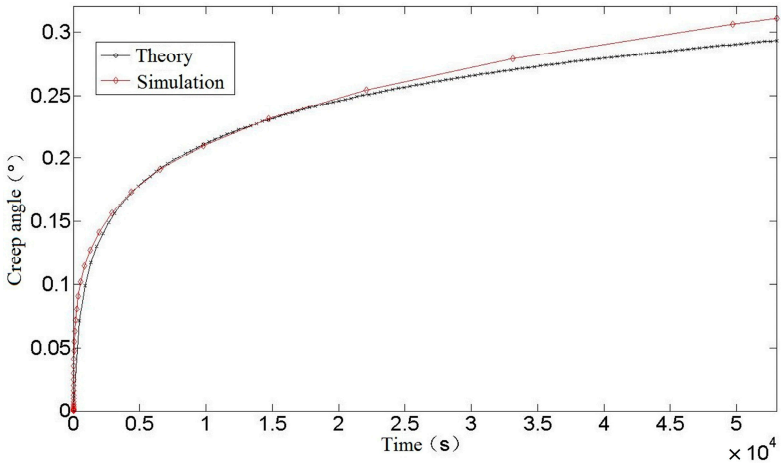

Figure 8. Comparison between theory and Simulation of torsion spring.

2.4. Experimental Method of Spring Chamber Temperature Creep

The structure of the cylindrical helical torsional spring loading table is shown in Figure 9, and is mainly composed of two identical unilateral loading mechanisms, a bottom plate, and a steering gear fixed seat. The unilateral loading mechanisms are fixed onto the bottom plate through support legs, and the rudder wing is locked by a bolt onto the gripper. The steering gear is installed on the steering gear seat and is locked by bolts. The deflection of the rudder wing is driven by the clamping claw to rotate the rotating shaft of the two unilateral loading mechanisms, and the torque is provided by the torsion springs in the unilateral loading mechanisms.

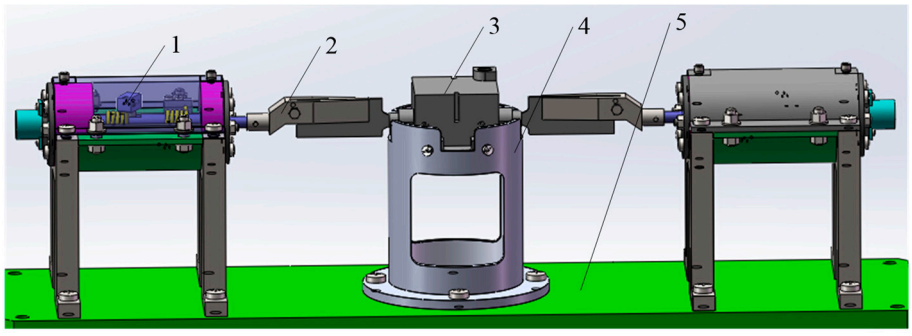

Figure 9. Torsion spring load table overall structure (1—unilateral loading mechanism; 2—gripper; 3—steering gear; 4—steering gear fixed seat; 5—bottom plate).

The internal structure of a unilateral loading mechanism is shown in Figure 10. The torsional spring loading platform mainly realizes the change of loading torque by replacing the unilateral loading mechanism. Different torsional springs correspond to different torque.

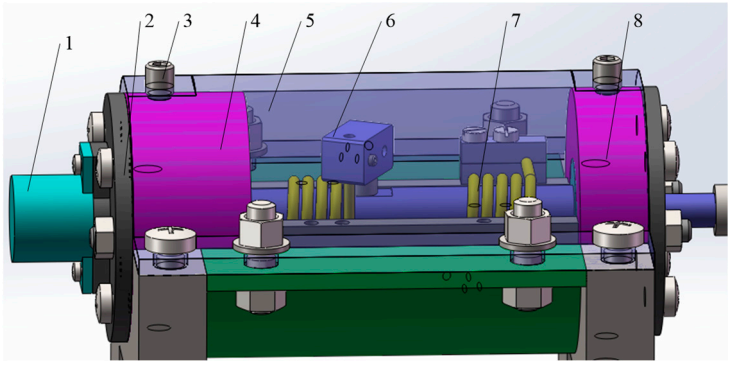

Figure 10. Unilateral loading structure internal structure (1—Angle sensor; 2—sensor seat; 3—fastening screws; 4—tail bearing seat; 5—stop cover; 6—torsional spring loading block; 7—torsional spring; 8—front bearing seat).

Each unilateral loading mechanism contains two torsion springs that are arranged in a coaxial reverse direction, and the rotating ends of the two torsion springs wind in opposite directions. The installation diagram is shown in Figure 11. Both torsion springs are pre-compressed by 30°. When the axial rotation is on one side, the force of one torsion spring increases and the compression Angle increases, while the compression Angle of the other torsion spring decreases.

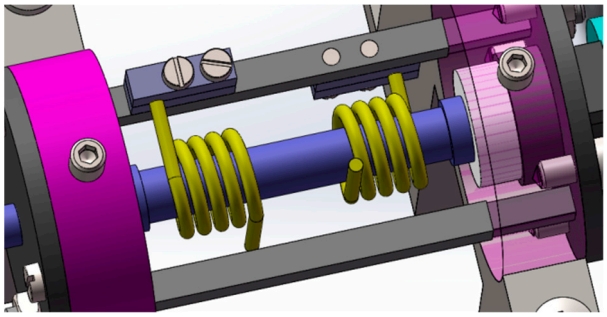

Figure 11. Double torsion spring installation diagram.

The rotation of the steering gear is transmitted to the torsion springs through the clamping claw, which provides the corresponding torque. The change of the output voltage of the rotary potentiometer is measured by a multimeter, and the rotation angle can be obtained by a certain conversion formula.

The specific experimental process is shown in Figure 12.

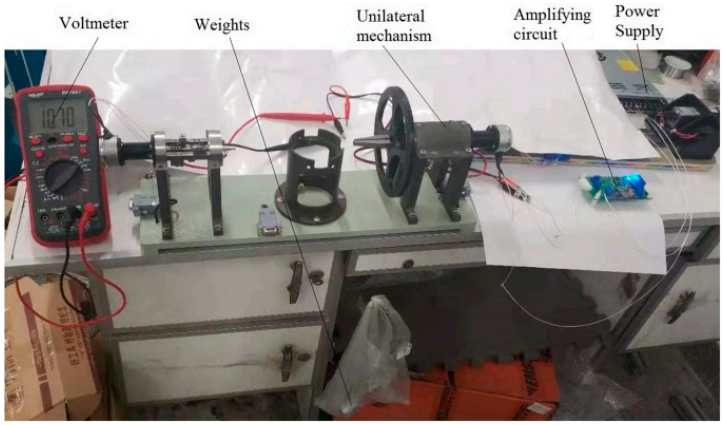

Figure 12. Creep test of spring on load table.

After loading the weight, the output voltage value of the Angle sensor can be measured by keeping the weight unchanged. After converting the voltage value into Angle, the relationship of the spring shape variable with time and the spring creep curve can be obtained.

3. Experimental Data and Analysis

After loading the weight, the angle change value can be obtained through the voltage change value of the voltmeter, and the experimental data are show in Table 3:

Table 3. Creep strain data sheet of torsion spring.

Time (s)	Angle (°)	Time (s)	Angle (°)
0	0	7500	0.174726
60	0.011457	8400	0.177591
210	0.054423	9600	0.180455
780	0.105982	12,420	0.211963
960	0.108846	12,600	0.214828
1080	0.11171	14,700	0.218987
1800	0.114575	18,700	0.226679
2100	0.126032	21,800	0.233096
2220	0.128897	24,900	0.245713
2280	0.131761	28,000	0.245677
3300	0.134625	32,100	0.2519
3600	0.13749	36,120	0.264493
3900	0.140354	40,120	0.265124
5200	0.15754	44,120	0.271456
5300	0.163269	49,000	0.277328
5340	0.166133	50,800	0.279596
5520	0.171862	54,000	0.281319

In order to facilitate direct observation, the data in the table were fitted and plotted, as shown in Figure 13.

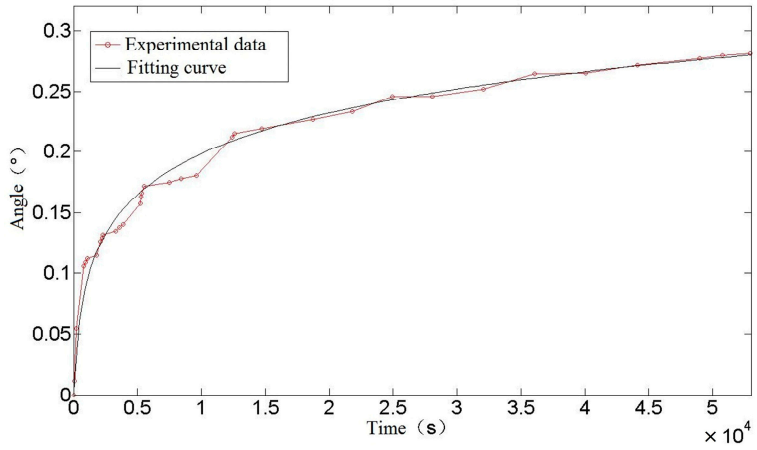

Figure 13. Creep curve of torsion spring.

It can be seen from Figure 13 that the creep test data and its fitting to a curve of a torsion spring conform to a typical creep curve. In the early stage of creep, the data fluctuate greatly, but in the later stage, the data tend to be stable. It is possible that, in the process of spring creep, after the sliding dislocation moves to barriers such as the grain boundary or second phase particles, the movement of dislocation stops gradually under the obstruction, and the phenomenon of accumulation appears. At this time, the number of moving dislocations decreases, which is reflected in the decrease of creep rate, or even

stagnation. As more and more accretion occurs, the dislocation will climb and slide over the barrier, which may be the reason for the step phenomenon in the creep experiment.

Figure 8, in the previous section, shows a comparison between a theoretical and simulated curve of torsion spring creep Angle. A comparison between theory, simulation, and experimental results is shown in Figure 14.

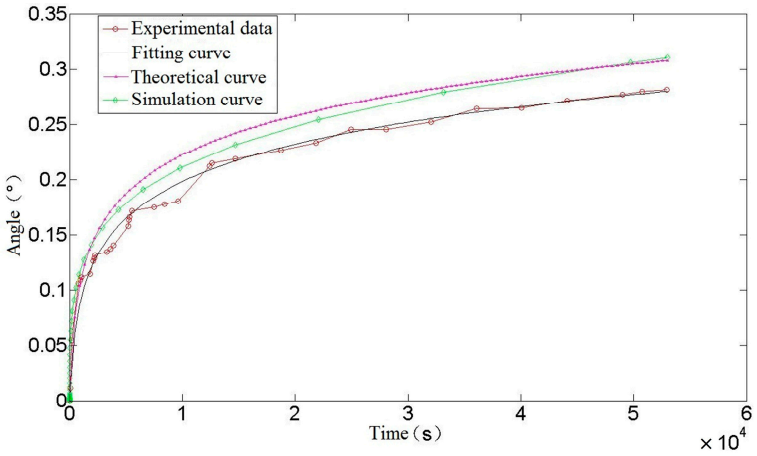

Figure 14. Comparison of creep angle curve of torsion spring.

As can be seen from Figure 14, the trend in creep strain for the theoretical calculation and finite-element simulation is the same as that of the experiment, and they all enter the stable creep stage at about 15,000 s. The theoretical calculation curve is highly consistent with the experimental fitting curve. At the initial stage of creep, the theoretical calculation curve basically coincides with the experimental data, and at the later stage of creep, the theoretical calculation creep rate is not much different from the experimental fitting curve. On the one hand, the source of error is the loss of precision caused by omitting some tiny quantities in the derivation of the theoretical calculation formula, on the other hand, it may be due to the slightly different properties of spring materials and materials in the data. At 54,000 s, the theoretical calculation is 4.3% larger than the experimental data creep value, and the error is acceptable in practical engineering application, which shows the accuracy of the theoretical calculation of torsion spring creep. As such it can be used to predict and estimate the performance and life of a spring in use, so as to avoid creep failure under high stress or long-term load conditions, thus ensuring the reliability and safety of mechanical components.

4. Conclusions

In this paper, the creep effect of a cylindrical helical torsion spring under pre-compression is studied. Firstly, through deconstruction and reorganization, using the original room-temperature creep constitutive equation as a basis, a room-temperature creep constitutive equation of a torsion spring can be obtained based on macroscopic tensile tests. Through the stress–strain analysis of a spring, the relationship between creep strain and time and stress of a cylindrical helical torsion spring is obtained, and the correctness of the theoretical calculation is verified by finite-element simulation.

Finally, in order to determine the influence of spring creep effect, a creep strain experiment of a torsion spring is carried out. Through experiments, it can be concluded that the cylindrical helical torsion spring enters a stable creep stage after about 15,000 s, and the creep strain angle is 0.28° after 54,000 s. By comparing the theoretical calculation results with the experimental results, it can be concluded that the error between the theoretical formula calculation results and the experimental results of a torsion spring is 4.3%, which is less than the engineering error range of 5%, which meets the requirements of engineering measurement and is of great significance for more accurately predicting and estimating

the performance and life of a spring in use, and designing high-performance and reliable spring elements.

Author Contributions: Methodology, P.R.; Validation, B.Z. and H.M.; Writing—review & editing, Z.W. All authors have read and agreed to the published version of the manuscript.

Funding: This research was funded by NNSFC (National Natural Science Foundation of China), grant number 51879063.

Institutional Review Board Statement: Not applicable.

Informed Consent Statement: Not applicable.

Data Availability Statement: Not applicable.

Conflicts of Interest: The authors declare no conflict of interest.

References

1. Fu, W.; Sun, L.; Yu, Y.; Zhu, S.; Yan, J. Design and Model-building of Motor-driven Load Simulator with Large Torque Outputs. *J. Syst. Simul.* **2009**, *21*, 3596–3598.
2. Xin, F.; Zhou, X.; Lei, Y.; Zhu, M.; Zhang, Z.; Yang, G. Design and performance analysis of torsion bar-load simulator. *J. Proj. Rocket Miss. Guid.* **2013**, *33*, 45–48.
3. Fan, D.; Guo, Z.; Yang, Z. Design of a Type of Load Simulator. *J. Mech. Eng.* **2013**, *12*, 152–154.
4. Liu, X.; Yuan, K. Controller Design and Simulation for High Load Servo Loading System. *Control Eng. China* **2014**, *21*, 210–218.
5. Shuck, L.Z.; Fogle, J.L. Dynamic micro-torque transducer. *Exp. Mech.* **1971**, *11*, 276–279. [CrossRef]
6. Yao, J.; Jiao, Z.; Shang, Y. Adaptive nonlinear optimal compensation control for electro-hydraulic load simulator. *Chin. J. Aeronaut.* **2010**, *23*, 720–733.
7. Cao, T.; Sun, X.; Ouyang, Q.; Zheng, S. Design of loading stand for reverse operation of navigating machine. *J. Beijing Univ. Aeronaut. Astronaut.* **2003**, *03*, 252–254.
8. Bo, Z.; Cheng, L.; Zhuo, W. Design and experimental study of zero-compensation steering gear load simulator with double torsion springs. *Measurement* **2019**, *148*, 106930.
9. Zhu, Z. Precision elastic element—Study on creep of spiral tension spring at room temperature. *Instrum. Manuf.* **1979**, *02*, 33–37.
10. Alden, T.H. Strain hardening during low temperature creep of 304 stainless steel. *Acta Metall.* **1987**, *35*, 2621–2626. [CrossRef]
11. Oehlert, A.; Atrens, A. Room temperature creep of high strength steels. *Acta Metall. Mater.* **1994**, *42*, 1493–1508. [CrossRef]
12. Alfredsson, B.; Arregui, I.; Lai, J. Low temperature creep in a high strength roller bearing steel. *Mech. Mater.* **2016**, *100*, 109–125. [CrossRef]
13. Barrett, P.; Hassan, T. A unified constitutive model in simulating creep strains in addition to fatigue responses of Haynes 230. *Int. J. Solids Struct.* **2020**, *185*, 394–409. [CrossRef]
14. Milligan, B.; Roy, S. Impact of microstructural stability on the creep behavior of cast Al–Cu alloys. *Mater. Sci. Eng.* **2020**, *772*, 138697. [CrossRef]
15. Hu, J.; Graham, G.; Hogg, S.; Higginson, R.; Cocks, A. Effect of microstructure evolution on the creep properties of a polycrystalline 316H austenitic stainless steel. *Mater. Sci. Eng.* **2020**, *772*, 138787. [CrossRef]
16. Wu, M.; Xiao, Y.; Wang, J.; Yang, W. Study on Creep and Stress Relaxation Behavior of Stainless Steel Springs. *Machinery* **2023**, *61*, 50–55.
17. DelLlano-Vizcaya, L.; Rubio-Gonzalez, C.; Mesmacque, G.; Banderas-Hernandez, A. Stress relief effect on fatigue and relaxation of compression springs. *Mater. Des.* **2007**, *28*, 1130–1134. [CrossRef]
18. Simon, P.A.; Gordon, M.; Andrew, S. Stress relaxation of nickel-based superalloy helical springs at high temperatures. *Mater. Sci. Eng.* **2014**, *613*, 117–129.
19. Salah, R.; Michael, K.; Christian, D. Stress Relaxation Behaviour in IN718 Nickel Based Superalloy during Ageing Heat Treatments. *Mater. Sci. Eng.* **2017**, *708*, 563–573.
20. Zhou, Y.; Wan, M. Investigation on the Degradation of Stress Relaxation of Hyperbolic Wire Spring Connectors. In Proceedings of the 2018 12th International Conference on Reliability, Maintainability, and Safety (ICRMS), Shanghai, China, 17–19 October 2018.
21. Yuan, M.; Yuan, H.; Xu, R.; Wang, Q. Reliability Assessment of Spring Based on Two Degradation Modeling Methods. In Proceedings of the 2018 12th International Conference on Reliability, Maintainability, and Safety (ICRMS), Shanghai, China, 17–19 October 2018.
22. Li, J.; Wang, Y.; Chen, X.; Yan, X.; Lu, X. Microstructure evolution in stress relaxation behavior of austenite AISI 304 stainless steel spring. *Mater. Charact.* **2019**, *148*, 266–271. [CrossRef]
23. Nabarro, F. The time constant of logarithmic creep and relaxation. *Mater. Sci. Eng. A* **2001**, *309*, 227–228. [CrossRef]
24. Xiao, F.; Wu, Y.; Zheng, J.; Miao, C.; Zhu, X. A load-holding time prediction method based on creep strain relaxation for the cold-stretching process of S30408 cryogenic pressure vessels. *J. Zhejiang Univ. Sci. A.* **2017**, *18*, 871–881. [CrossRef]
25. Ramberg, W. *Description of Stress-Strain Curves by Three Parameters*; NACA Technical Notes; NASA: Washington, DC, USA, 1943.

26. Yue, T.; Yuren, C. Ramberg-Osgood model fitting of tensile stress-strain curve of U71Mn rail steel. *Phys. Exam. Test.* **1991**, *5*, 36–41.
27. Rasmussen, K.J.R. Full-range stress-strain curves for stainless steel alloys. *J. Constr. Steel. Res.* **2003**, *59*, 47–61. [CrossRef]
28. Cheng, L. Research and Creep Mechanism Analysis of Dual Spring Zero Position Compensation Load Table. Master's Thesis, Harbin Engineering University, Harbin, China, 2020.
29. Xiao, F. Prediction Method for Room Temperature Creep of Austenitic Stainless Steel and Its Application in Strain Strengthening of Cryogenic Vessels. Ph.D. Thesis, Zhejiang University, Hangzhou, China, 2017.
30. Yang, Z. *Engineering Mechanics*; Harbin Engineering University Press: Harbin, China, 2010.

materials

MDPI

Article

Ballistic Impacts with Bullet Splash—Load History Estimation for .308 Bullets vs. Hard Steel Targets

Riccardo Andreotti [1,2,*], Andrea Casaroli [1], Ivan Colamartino [1], Mauro Quercia [2], Marco Virginio Boniardi [1] and Filippo Berto [3]

[1] Department of Mechanical Engineering, Politecnico di Milano, Via La Masa 1, 20156 Milano, Italy; andrea.casaroli@polimi.it (A.C.); ivan.colamartino@polimi.it (I.C.); marco.boniardi@polimi.it (M.V.B.)
[2] Callens®AREA3, Via Merini 37, 21100 Varese, Italy; mauro.quercia@area3.it
[3] Department of Chemical Engineering, Materials and Environment, La Sapienza University of Rome, Via Eudossiana 18, 00184 Roma, Italy; filippo.berto@uniroma1.it
* Correspondence: riccardo.andreotti@callensglobal.com; Tel.: +39-3485263334

Abstract: The study focuses on testing a simplified way of estimating the resultant force due to ballistic impacts resulting in a full fragmentation of the impactor with no penetration of the target. The method is intended to be useful for the parsimonious structural assessment of military aircrafts with integrated ballistic protection systems by means of large scale explicit finite element simulations. The research investigates the effectiveness of the method in allowing the prediction of the fields of plastic deformation collected by hard steel plates impacted by a wide range of semi-jacketed, monolithic, and full metal jacket .308 Winchester rifle bullets. The outcomes show the effectiveness of the method being strictly related to the full compliance of the considered cases with the bullet-splash hypotheses. The study therefore suggests the application of the load history approach only after careful experimental investigations on the specific impactor–target interactions.

Keywords: bullet splash; bullet-splash; ballistic impact; terminal ballistics; finite element method; ballistic protection; explicit solver; impact simulation; Creusabro®; Durostat®

Citation: Andreotti, R.; Casaroli, A.; Colamartino, I.; Quercia, M.; Boniardi, M.V.; Berto, F. Ballistic Impacts with Bullet Splash—Load History Estimation for .308 Bullets vs. Hard Steel Targets. *Materials* **2023**, *16*, 3990. https://doi.org/10.3390/ma16113990

Academic Editors: Angelo Marcello Tarantino, Carmelo Majorana, Raimondo Luciano and Michele Bacciocchi

Received: 19 March 2023
Revised: 19 May 2023
Accepted: 23 May 2023
Published: 26 May 2023

1. Introduction

For two decades, transient finite element simulation has represented a fundamental tool for the crashworthiness assessment and structural optimization of vehicles [1–3]. In the aerospace industry, airframe development passes through many steps of optimization against potential threats for the survivability of the vehicle such as bird impacts, hail impacts, emergency landing, ditching, and wire strike. All of these potential threats are faced by means of dedicated simulations involving extended parts or even the entire airframe, modelled in finite elements to verify the survivability of every layer of material and every single rivet connecting the structures. In this technological scenario, the development of a modern military aircraft follows the same methodological approach with the obvious complications due to the main aim of a military vehicle: to maximize the probability of surviving a real combat scenario. This implies that the critical components of the vehicle must be protected against the typical threat of warfare: ballistic impacts [4,5]. To do this, critical areas of the vehicle, such as the cockpit and the transmission, are surrounded by ballistic protection panels, which are experimentally verified to be able to withstand specific ballistic impacts without allowing any penetration of the bullets. In this field the aim of the simulations is therefore not to verify the ability of the protective panels to withstand the impact of the bullets but instead to verify the strength of the support structures to which the panels are attached against the impulsive loads due to several impact positions along the entire airframe, representing the random incidence of the shots during fire fights. In this scenario it is therefore fundamental to be able to model the stress propagation through the structure to verify the strength of every connection and part of the support system. This

involves many different load cases involving significant parts of the airframe modelled in full detail.

Protective panels typically consist of an external layer of hard ceramic tiles intended to fragment the hitting bullets during the first phase of the impact, and an internal layer made of composite fabric to withstand the local impact forces and absorb the residual energy without allowing the bullet fragments to penetrate the protection panel [6]. Therefore, the typical scenario of a perfectly working protection panel consists of a total fragmentation of the bullet with no penetration of the target. This phenomenon is called bullet splash, due to the fact that the fragmentation of the bullet makes its kinematics similar to the flow of a mass of a fluid being deflected by the target surface [7,8]. In this scenario Andreotti et al. (2021) first proposed a simplified approach to reduce the computational cost needed to simulate the forces acting on the target due to bullet splash, by considering the phenomenon as a fluid-structure interaction where a mass of fluid represents the behavior of the bullet fragments. The approach proved to be effective in predicting the local and global effects of bullet splashes due to 9 × 21 mm full metal jacket bullets hitting 4 mm AISI 304 plates [9]. Based on that experience, Andreotti et al. (2022) [10] proposed and validated a further simplified method to make the finite elements simulations more efficient and equally effective by avoiding the hydrodynamic part of the calculation, by introducing an estimated load history approach that consists in decoupling the bullet fragmentation phenomenon and the target reaction to avoid the costs of modelling the bullet, and introducing an equivalent impact force as a load curve *F(t)* to be directly applied to the impact point on the structure; the intensity vs. time curve is calculated based on the initial impact velocity and the density distribution of the specific bullets. The approach proved to be effective and extremely efficient for 9 × 21 mm full metal jacket bullets hitting 4 mm AISI 304 plates as well as for monolithic copper .308 rifle bullets hitting high hardness steel plates. The validation confirmed the equivalence between the fluid structure interaction and the load history approach in terms of stress waves propagating from the epicenter of the target, resultant forces at the constraint, and residual deformation fields of the plates [11,12].

In this paper we propose the application and experimental validation of the estimated load history approach to cover a wide range of rifle bullet typologies, from monolithic to partially jacketed and full metal jacket bullets. The validation has been performed by comparing the residual deformation field measured on steel plates impacted by the bullets and the residual deformation field predicted by finite element simulations where the applied load history was estimated based on experimental measurements of the impact velocity and density distribution of the tested bullets. The work gives the reader a reference for the effective applicability of the load history method for finite element simulations intended to simulate the stress propagation from ballistic protection panels to the support structures to assess, without the need to model the bullets, their fragmentation, and the interactions with the targets, therefore allowing a more parsimonious approach to the problem. This method is based on the hypothesis that the protective panel is able to withstand the ballistic impacts of the considered bullets at a certain velocity, resulting in a complete fragmentation of the bullet with no penetration or fragmentation of the target. Within these hypotheses the method consists in estimating the force history due to the impacts based only on the bullet sections and their impact velocity, and applying the estimated load history directly to the elements of the structure to simulate the structural phenomenon. Section 2 provides the reader with all the information to reproduce the conducted tests. In Section 3 we provide all the main analytical, numerical, and experimental results involved in the validation process. In Section 4 the results are discussed. In Section 5 we summarize the conclusions and further developments of the research.

2. Materials and Methods

To validate the load-history approach on a wide range of bullet typologies, we took into consideration four different .308 rifle bullets hitting dual-layered steel plates made of two different steels. Both steels have high strength and significant ductility so that they

can withstand the impacts without allowing the penetration of the bullets, and, at the same time, are able to collect residual deformations so that the field of residual displacements could be used as experimental evidence to compare with the numerical results for the validation of the approach.

2.1. Ballistic Test Procedures

The bullets were shot using a Remington 700 cal. 0.308 Winchester. The initial bullet velocity was measured using a Magnetospeed® V3 ballistic chronograph assembled at the rifle muzzle. Four different caliber .308 Winchester types of bullet were used: Soft Point (SP), Hollow Point (HP), Full Metal Jacket (FMJ) and Monolithic (MONO) bullets. Their main characteristics are summarised in Table 1. The external geometry and longitudinal section of the bullets was documented through a LEICA® M165 stereo microscope at 3.5× magnification. The bullets were sectioned using 120 grit abrasive paper, lubricated using water (Figure 1).

Table 1. Main data of the bullets used for experimentation as provided by the manufacturers. The nominal muzzle velocity is the expected velocity at the exit of the firearm. The nominal energy is the expected kinetic energy of the bullets at the exit of the firearm.

Bullet Type	Cal.	Bullet Mass [g]	Nominal Muzzle Velocity [m/s]	Nominal Energy [J]
Soft Point (SP)	308 Win	11.7	870	4428
Hollow Point (HP)	308 Win	10.9	800	3485
Full Metal Jacket (FMJ)	308 Win	9.5	865	3570
Monolithic (MONO)	308 Win	9.6	860	3550

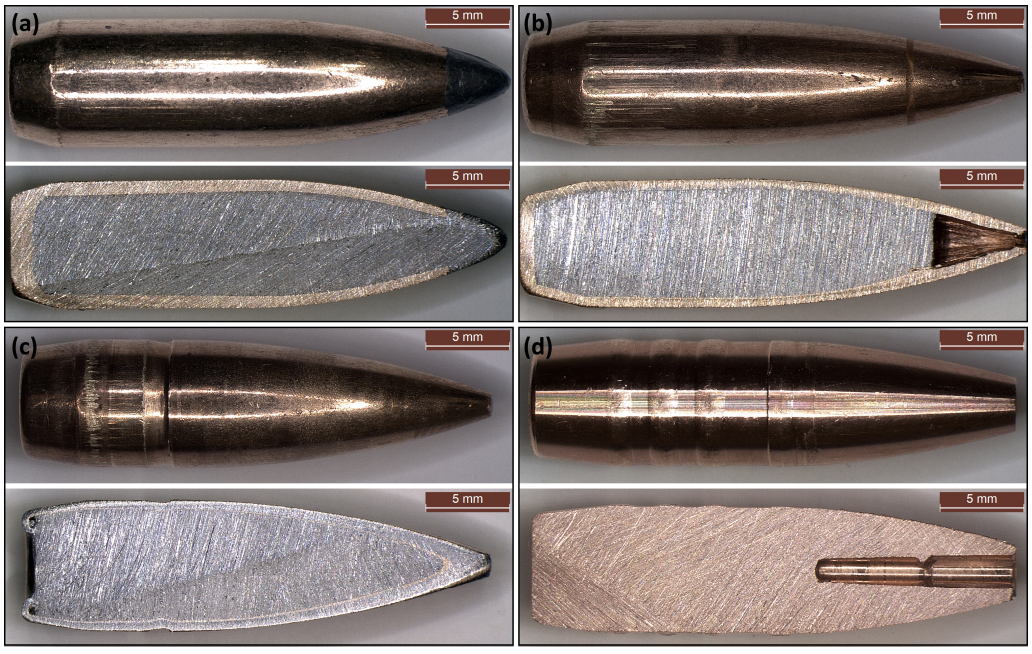

Figure 1. External geometry and longitudinal section of the bullets used for experimentation; (**a**) Soft Point, (**b**) Hollow Point, (**c**) Full Metal Jacket and (**d**) Monolithic.

The targets were obtained by joining two 4 × 500 × 500 mm plates. Two different high-strength structural steels were tested; their mechanical and metallurgical properties are detailed in Section 2.2. Four tests were carried out on each metal plate using the bullets detailed in Figure 1 and in Table 1. The nominal impact positions are detailed in Section 2.3.

The targets were positioned at 100 m from the rifle muzzle, oriented normally to the bullet trajectory. The metal plates were bolted to a steel and wood support frame

specially fabricated to carry out the tests. The support frame was designed to guarantee full visibility of the metal plate side from the cameras used to film the impacts. A panel with a chessboard pattern composed of black and white squares with a 20 mm side was installed on the opposite side. This solution was adopted to guarantee a dimensional reference for the high frequency camera shootings.

Upon completion of the tests, the bullet impact areas were accurately photographed both on the front and rear sides of the metal plates; the pictures are provided in Section 3.1. The dome-shaped bulges created by the bullets in the rear surface of the metal plates were also measured using a Borletti dial gauge with a sensitivity of 10 μm. The measurement procedure included tracing four reference lines slanted by 45° relative to each other. All the lines cross the apex of the bulges which was adopted as zero point. 14 measures of metal plate deformation were taken for each of the four lines, at a distance of ±5 mm, ±10 mm, ±15 mm, ±25 mm, ±35 mm, ±45 mm, and ±55 mm from the bulge apex. The values so obtained were plotted in diagrams (Section 3.4), each showing the minimum and maximum deformation of the metal plate measured at increasing distance from the bulge apex.

2.2. Mechanical and Metallurgical Characterisation of the Metal Plates

The targets were fabricated using high-yield stress structural steel plates. The two steel grades selected for the experimentation go under the trade names of Creusabro® 8000 [13–15] and Durostat® 400 [16]. They are characterised by a combination of very high tensile strength and optimum wear resistance. Their typical applications are ballistic shields and barriers, buckets for heavy equipment, dump truck beds, conveyor components, and rollers and rotors for grain mills and oil mills. The high level of hardness and tensile strength is obtained through controlled cooling after hot rolling. Their limited carbon content, together with a considerable manganese content (or manganese-nickel content in the case of Creusabro® 8000), allows them to have acceptable toughness and weldability characteristics, notwithstanding very high values of hardness and tensile strength. The significant amount of chromium and molybdenum guarantees the hardenability necessary to form a mixed martensite and bainite structure. Both steel grades are characterised by micrometric carbides finely dispersed in the metal and further improving abrasive wear resistance [14].

In comparison with Durostat® 400 steel, which is composed exclusively of martensite, bainite and carbides, Creusabro® 8000 steel also exhibits a small amount of residual austenite that turns into martensite when it is subjected to cold deformation. This property, known under the acronym TRIP (Transformation Induced by Plasticity), further improves the wear resistance and impact strength of Creusabro® 8000 steel compared to Durostat® 400 steel. The TRIP effect enhances steel hardness and its ability to absorb energy as the cold deformation increases [17,18].

The chemical composition of both steels was assessed by means of optical emission spectroscopy (OES). Tables 2 and 3 provide an overview of the results. Both steels meet the requirements of the applicable steel mill specifications. Comparing the two steels, it is clearly apparent that Creusabro® 8000 is much richer in alloying elements than Durostat® 400. Durostat® 400 does not contain molybdenum, and its carbon, chromium, and silicon content is less than half of the values measured in Creusabro® 8000. On the other hand, Durostat® 400 contains twice the amount of manganese, but it does not contain nickel which is present in a good quantity in Creusabro® 8000. The chemical composition clearly shows that Creusabro® 8000 is by far more hardenable but less weldable than Durostat® 400, compared to which it exhibits an equivalent carbon content that is higher by approximately 25% (CECreusabro®8000 = 0.63; CEDurostat®400 = 0.50). Having received the same heat treatment, Creusabro® 8000 is also harder and mechanically stronger thanks to its carbon content that is more than twice that of Durostat® 400.

Table 2. Chemical analyses of Creusabro® 8000 steel (wt%).

	C	S	P	Si	Mn	Ni	Cr	Mo
Metal Plate	0.21	0.002	0.009	0.74	1.18	0.49	0.70	0.26
Steel Mill Specs	0.28 Max	0.005 Max	0.018 Max	Unspecified	1.60 Max	1.00 Max	1.60 Max	0.40 Max

Table 3. Chemical analyses Durostat® 400 steel (wt%).

	C	S	P	Si	Mn	Al	Cr	Mo	B	Ti
Metal Plate	0.10	0.002	0.008	0.16	2.08	0.03	0.26	<0.01	0.001	0.021
Steel Mill Specs	0.18 Max	0.010 Max	0.025 Max	0.60 Max	2.10 Max	0.02 Min	1.00 Max	0.50 Max	0.005 Max	0.050 Max

Both metal plates were subjected to metallographic analyses and Vickers HV1 hardness tests. The samples were mirror polished using progressively finer abrasive paper (120 grit, 180 grit, 320 grit, 400 grit, 600 grit, and 1200 grit) and polishing cloths with diamond-based synthetic abrasive (grain size 3 µm and 1 µm). Lubrication was guaranteed using water with abrasive paper and the suspension containing the abrasive matter with the cloths. Metallographic etching was obtained using the reagent "Nital 2", a 2% nitric acid/ethanol solution. The pictures were captured using a LEICA® DM4000M optical microscope at 500× magnification. The same samples were also used to evaluate core hardness in the metal plates. The tests were conducted using a Vickers LEITZ®-WETZLAR® (Leica Camera AG, Wetzlar, Germany) micro-durometer fitted with a digital camera and set at the HV1 hardness scale (1 kgf, 30 s).

The tests confirm what was previously suggested by the chemical composition, i.e., both steel grades form martensite and bainite with carbides finely dispersed in the metal (Figure 2) [19]. This type of investigation could not reveal the small amount of residual austenite prescribed for Creusabro® 8000 steel that, in any case, exhibits an average hardness higher than Durostat® 400 (540 HV1 compared to 420 HV1).

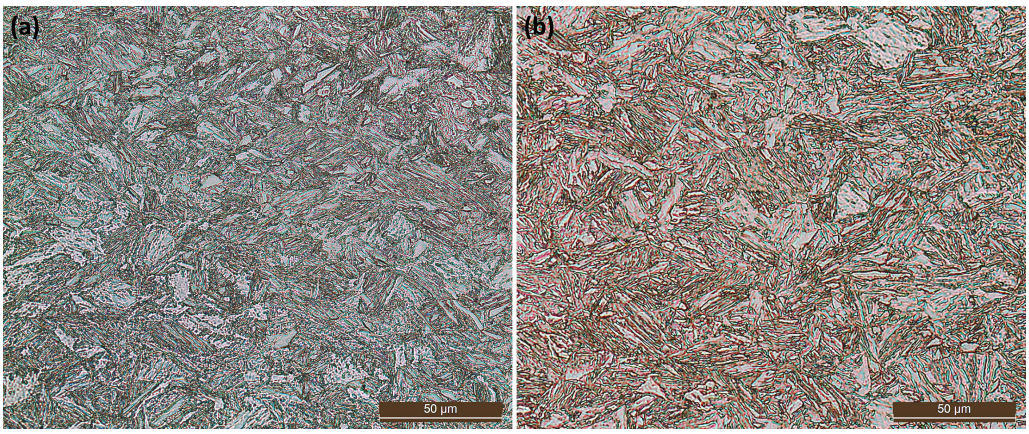

Figure 2. Metallographic images of the metal plates used for experimentation, made of (**a**) Creusabro® 8000 steel and (**b**) Durostat® 400 steel. Both steel grades form martensite and bainite with carbides finely dispersed in the metal (etching agent: Nital2—Magnification: 500×). This type of investigation could not reveal the small amount of residual austenite prescribed for Creusabro® 8000 steel.

The characterisation of the two steels was completed by conducting tensile tests at room temperature. Proportional specimens, obtained in compliance with the UNI EN ISO 6892-1:2020 standard, were used [20,21] (Figure 3). Results are summarised in Table 4, while the engineering stress/strain curves are shown in Figure 4.

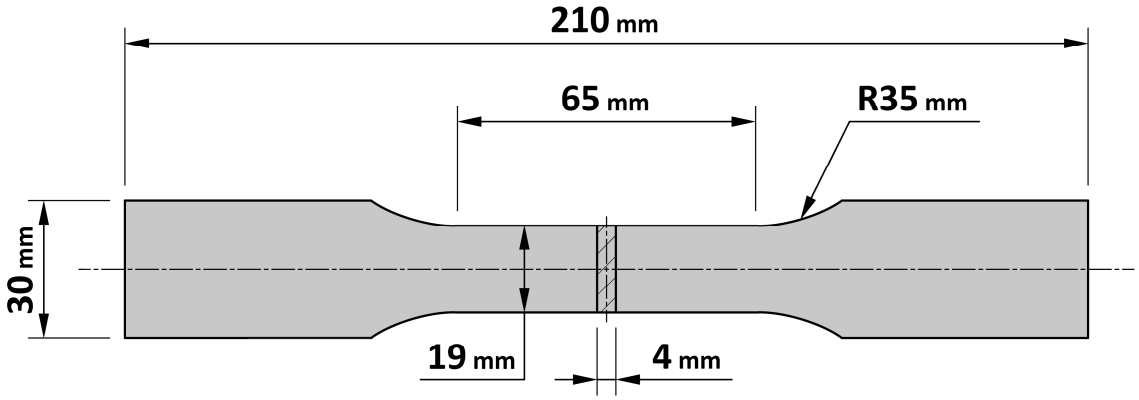

Figure 3. Geometry of the specimens used for the tensile tests. Proportional specimens obtained in compliance with the UNI EN ISO 6892-1:2020 standard were used [20].

Table 4. Summary of tensile tests results for the Creusabro® 8000 steel and Durostat® 400 plates used for experimentation.

	E [Gpa]	YS [Mpa]	UTS [Mpa]	YS/UTS	Ag%	A%
Creusabro® 8000	210	1190	1735	0.68	5	11
Durostat® 400	210	1100	1290	0.85	3	11

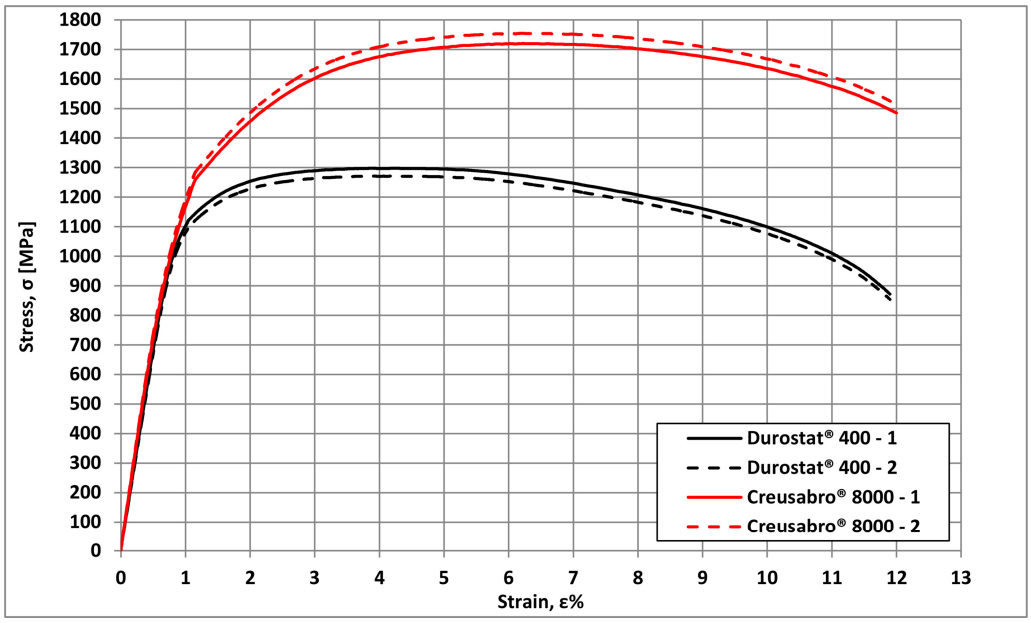

Figure 4. Engineering stress/strain curves for Creusabro® 8000 steel (red lines) and Durostat® 400 steel (black lines) plates used for experimentation.

The tensile tests confirm what had been anticipated by the hardness tests. The ultimate tensile strength and yield strength of Creusabro® 8000 exceed those of Durostat® 400 steel ($UTS_{Creusabro®\,8000}$ = 1735 Mpa; $YS_{Creusabro®\,8000}$ = 1190 Mpa; $UTS_{Durostat®\,400}$ = 1290 Mpa; $YS_{Durostat®\,400}$ = 1100 Mpa). The YS/UTS ratio and percentage elongation under maximum load, Ag%, are, respectively, equal to 0.85 and 3% in Durostat® 400 and 0.68 and 5% in Creusabro® 8000. Both steels exhibit analogous values of percentage elongation after fracture ($A\%_{Creusabro®\,8000}$ = $A\%_{Durostat®\,400}$ = 11%). These values confirm another important aspect revealed by chemical analyses: Creusabro® 8000 steel's strain hardening ability is higher than that of Durostat® 400 steel. Creusabro® 8000 is also superior to Durostat® 400

in terms of plastic deformation ability before reaching the necking point. Therefore, the Creusabro® 8000 steel exhibits superior performance compared to the Durostat® 400 steel in terms of tensile strength, hardness, and energy absorption capability. On the other hand, its weldability is poorer than in Durostat® 400.

2.3. Testing Setup and Impact Speed Computation

Two Phantom VEO 710 high speed cameras were used to capture the bullets' speed and trajectory. In particular, the first was positioned orthogonally with respect to the trajectory at a distance variable between 2250 and 2550 mm from the trajectory plane; the second one, instead, was positioned at the same orthogonal distance with an angle of 20° to obtain a perspective view of the shots. Data were acquired via two ethernet cables with a synchronized digital trigger. Further details for each shot are shown in Tables 5 and 6, while schemes of the data acquisition setup are shown in Figures 5 and 6.

Table 5. Data acquisition: camera 1.

Shot	Resolution [px]	Sampling Frequency [fps]
1	256 × 256	39,000
2	320 × 128	50,000
3	320 × 128	50,000
4	320 × 128	50,000
5	320 × 128	50,000
6	320 × 128	50,000
7	320 × 128	40,000
8	320 × 128	40,000

Table 6. Data acquisition: camera 2.

Shot	Resolution [px]	Sampling Frequency [fps]
1	320 × 256	33,000
2	320 × 152	48,000
3	320 × 152	48,000
4	320 × 152	48,000
5	320 × 152	48,000
6	320 × 152	48,000
7	320 × 152	48,000
8	320 × 152	48,000

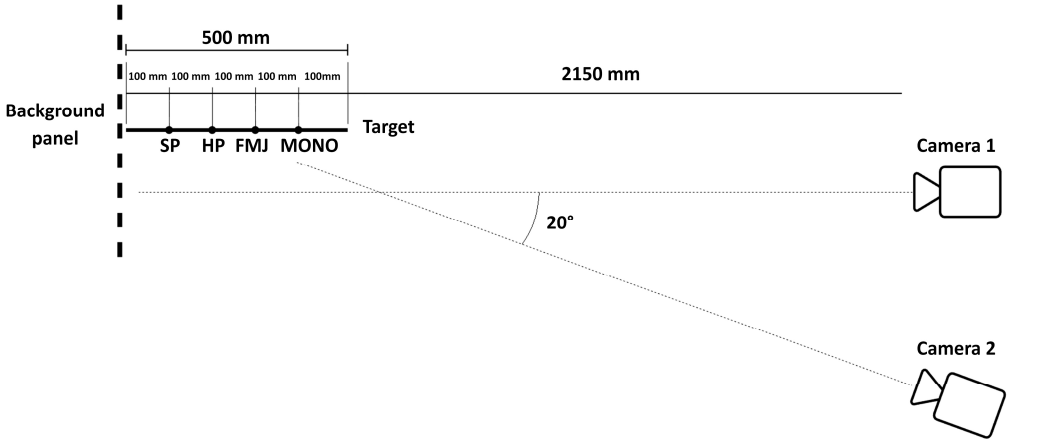

Figure 5. Scheme of the camera settings (top view).

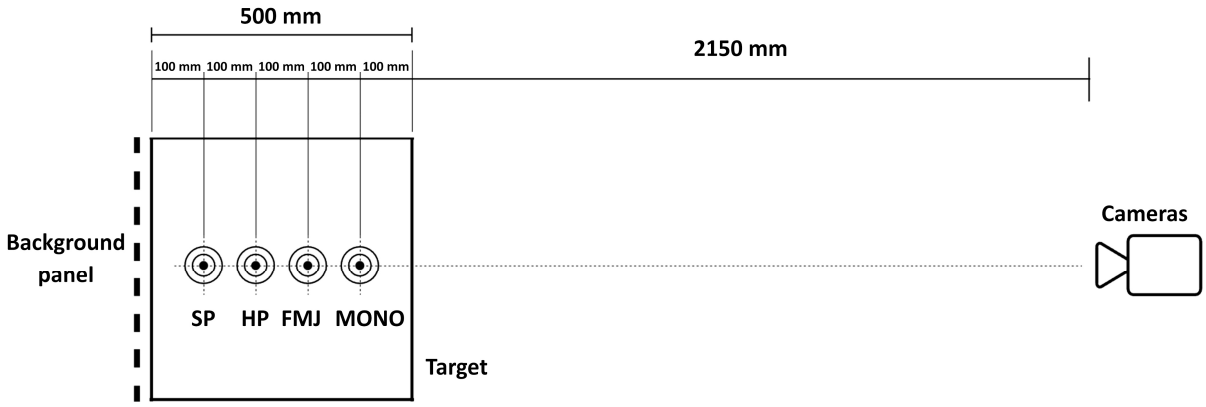

Figure 6. Scheme of the camera settings (front view).

While the perspective view was meant to capture the three-dimensional fragmentation dynamics of the projectile, the orthogonal videos were recorded to compute the projectile impact and exit speeds, via the well-known time-of-flight principle: knowing a priori the dimensions of a reference object, the video's resolution, and time history, the projectile trajectory is easily transformed into impact velocity. Such a method is one of the most used in ballistics to effectively evaluate the trajectory of bullets [22], with multiple applications in 2D and 3D analyses [23]. In the present work, even if the bullet itself could have been in principle used as reference for calibration, its small dimensions would have introduced a potentially high error; consequently, the reference object was a background reference plane, a chessboard panel attached perpendicularly to the frame. As described in Section 2.1, the chessboard was characterized by regular squares of 20 × 20 mm each, while the nominal trajectories were driven by four equally spaced targets in correspondence of the vertical midline of the plates. To minimize the error, the calibration procedure was performed on the highest possible number of squares, resulting in 0.8 mm/px. Once the calibration is performed, the bullet speed is computed by evaluating the distance travelled by the bullet and dividing it by the correspondent time interval. However, the fact that the reference plane used for calibration and the projectile trajectory plane were not coincident introduced a distortion factor between the measured and real speeds. The issue is easily solved if the position of the camera is fixed with respect to the reference plane: in that case the distortion factor is linear as a function of the distance of the bullet from that plane (Figure 7) and consequently the correction is straightforward.

Naming this distance d_1 and the observer-reference plane distance d_2, a correction factor C can be defined as follows:

$$C = 1 - \frac{d_1}{d_2} \tag{1}$$

Consequently:

$$v = Cv_{meas} \tag{2}$$

Considering the relatively low resolution and number of available frames capturing the bullet during the pre-impact phases, multiple measurements were carried out mapping the position of three sections of the bullet (frustum, beginning of the ogive, and tip) for multiple combinations of frames. This redundant procedure allowed us to average out the human error introduced by manual recognition of the projectile shape. A minimum of six measures per shot were collected and averaged to obtain the resulting impact velocities.

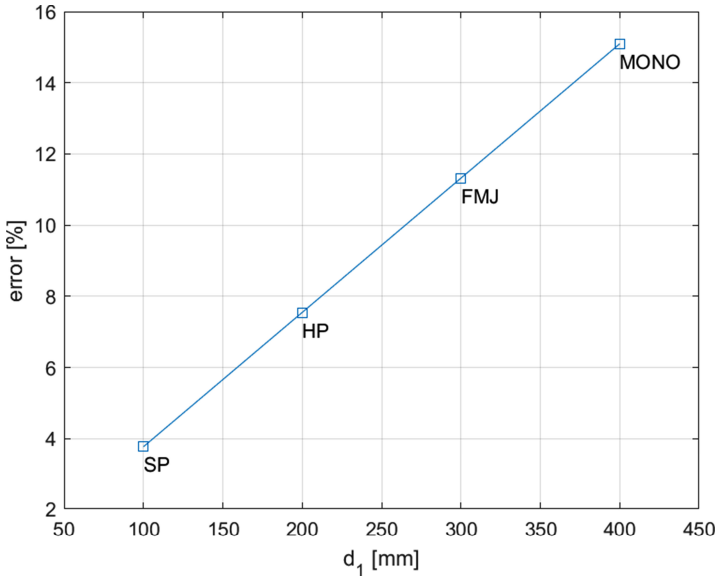

Figure 7. Error on position vs. observer-reference distance. The worst-case scenario is identified for the Monolithic bullets, for which the distance from the trajectory and the reference plane is 400 mm: the apparent speed in such cases is 15.1% higher than the real speed.

2.4. Bullet-Splash Load History Estimation

The load history estimation is based on two main hypotheses that must be verified experimentally:

- The bullet encounters complete fragmentation during the interaction with the target;
- The target can withstand the interaction without being penetrated, causing the deflection of the debris.

The load histories were calculated according to the progressive fragmentation theory introduced by Andreotti et al. in 2022 [10–12] for 90 degree bullet splashes. The load history formula allows us to reconstruct the $F(t)$ depending on the density distribution characterizing each section of the bullet and its impact speed. The interaction between the impactor and the target is treated as the interaction of a fluid flow, representing the flow of bullet debris, and a rigid, fixed plane normal to the axis of the bullet. The force at a generic time t is calculated as the time derivative of the elementary portion of the bullet ideally intersecting the target surface at that time. Considering the 90-degree deflection, the elementary variation in momentum can be expressed as:

$$dq = dmv \tag{3}$$

where v is the impact velocity of the bullet and m is its mass. Considering a homogeneous bullet with density ρ, assuming that the velocity variation only happens to the material ideally intersecting the impact surface, the elementary mass that is deflected in the elementary time dt is:

$$dm = \rho A(t) v dt \tag{4}$$

where $A(t)$ represents the intersection between the bullet volume and the impact surface plane, and $vdt = ds$ is the elementary translation of the bullet in dt. By substituting Equation (4) into Equation (3), and dividing both terms by dt, we obtain the expression of the impact force for a homogeneous bullet:

$$F(t) = \frac{dq(t)}{dt} = \rho A(t) v^2 \tag{5}$$

which integration in time correctly equals the initial momentum of the impactor:

$$q = \int F(t)dt = v\rho \int A(t)vdt = v\rho \int A(s)ds = v\rho V = vm \tag{6}$$

where V is the volume of the homogeneous bullet.

For a generic impactor, composed by M materials, the load history due to the bullet splash can therefore be expressed as the sum of M terms:

$$F(t) = \sum_{i=1}^{M} F_i(t) \tag{7}$$

Therefore, the generic expression of the estimated load history due to bullet splash is:

$$F(t) = v^2 \sum_{i=1}^{M} \rho_i A_i(t) \tag{8}$$

where ρ_i is the density of the i-th material, and $A_i(t)$ is the section of that material ideally intersecting the surface of the target at the interaction time t.

To estimate the load-history due to bullet-splash of the tested impactors the formula (Equation (8)) was applied to the bullets section (Figure 1) by imposing an impact speed equal to those experimentally measured for the tested impacts.

To acquire the $A_i(t)$ of the bullets, the first step consisted in mapping its sections normally to the axis of the bullet x. At N discrete axial coordinates x_j (30 to 50 points along the entire axis of the bullets, depending on their geometrical complexity) the radial coordinates of every material boundary were measured, so that, in general, the area of the i-th material at axial coordinate x_j could be calculated as the area of a hollow circle:

$$A_i(x_j) = \pi(Re_{ij}{}^2 - Ri_{ij}{}^2) \tag{9}$$

where Re_{ij} and Ri_{ij} are the external and internal radiuses of the i-th material at the j-th axial coordinate x_j.

Once the materials sections $A_i(x)$ were mapped, the $A_i(t)$ of the specific shot was calculated by converting the spatial coordinate into time coordinates, by dividing the x_j by the initial impact velocity v:

$$A_i(t_j) = A_i(\frac{x_j}{v}) \tag{10}$$

The resulting load history is therefore a discretized curve to be automatically interpolated by the finite element solver at every time-integration step:

$$F(t_j) = v^2 \sum_{i=1}^{m} \rho_i A_i(t_j) \tag{11}$$

2.5. Finite Element Simulation Setup

To verify the representativeness of estimated impulses, the considered impacts were simulated by applying the load histories to the plates by means of the explicit finite element solver LS-DYNA [24]. The plates were uniformly discretized with 2.5 mm fully integrated 4-node shell elements with 16 integration points in the thickness. The load was applied normally to the plates. Each shot was simulated by applying the corresponding load history as uniformly distributed on arbitrary areas, centered at the epicenter of the impacts, and with extensions comparable with the extension of the interaction marks visible on the impacted plates. The actual space distribution of the pressure fields acting during the impacts is in fact unknown. Therefore, to verify the sensitivity of the simulation results to the local pressure distribution, the same load history was applied on different arbitrarily defined distribution areas. The shots were simulated three times, by varying the extension

of the loaded surface according to the experimental observations (Figures 12 and 13). The different tested areas had 100 mm^2, 200 mm^2, and 400 mm^2 extensions (see Figure 8), representing, respectively, the minimum and maximum extension of the compression area, and the extension of the sliding area as experimentally observed on the impacted plates (Figures 12 and 13). The plates were constrained in the load direction x by zero translation of the boundary nodes, and with double orthogonal symmetry planes intersecting at the epicenter of the impacts. The constraint between the two plates was assured by setting a penalty contact with a static and dynamic friction coefficient of 0.65, typical for clean dry steel-on-steel interactions [25].

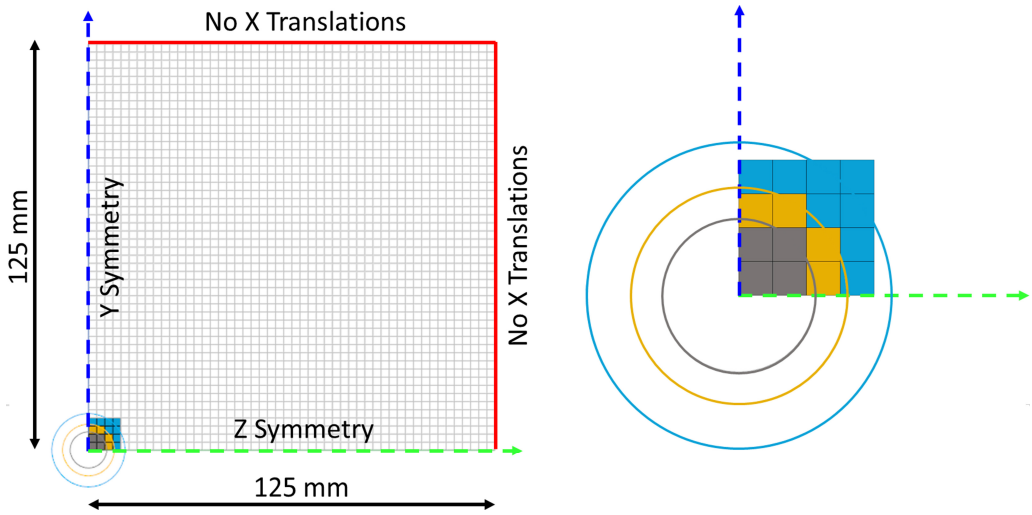

Figure 8. Overview (**left**) and detail (**right**) of the finite element model of the plate highlighting the choice and progressive increase in the loaded elements characterizing the three arbitrary load distributions: 100 mm^2 distribution (grey), 200 mm^2 distribution (yellow), and 400 mm^2 distribution (light blue); the three circles represent the area-equivalent circular extensions corresponding to the minimum and maximum limit of the compression area, and the external limit of the sliding area as experimentally observed on the impacted plates, respectively (Figures 12 and 13). Only a quarter of the plate was modeled, with orthogonal symmetry conditions.

2.5.1. Development of the Finite Element Model

The development of the finite element model here proposed was the result of three main steps, aiming at finding the most efficient discretization strategy to eventually allow engineers to correctly simulate the propagation of the stress waves caused by bullet splashes on generic, extended, ballistic protection panels. The development started from a highly detailed simulation of the local effects of the impacts, and progressively evolved towards more parsimonious models guaranteeing the same effectiveness in terms of predicting the residual deformation fields and the stress waves generated by the impacts.

The first step (Andreotti et al., 2021 [9]) consisted in simulating the bullet-splash phenomenon as a fluid structure interaction (FSI) to reproduce the progressive deflection of the bullet fragments interacting with the target. The model used for the FSI simulation was a 3D solid mesh composed of 0.3 mm hexahedral elements. The experimental validation of this model was based on the measurements of the micro-hardness and deformation fields across the impact surface of 4 mm AISI 304L steel plates impacted by 9 × 21 mm FMJ bullets. The validation demonstrated extreme accuracy in predicting the field of plastic strain as well as the overall residual deformation field.

The second step introduced the load history estimation method discussed in this paper. The method was first tested on the same experimental dataset analyzed by Andreotti et al. (2021) [9]. The simulation applied the estimated load history as a uniformly distributed load on arbitrary concentric circular areas, with the plate being discretized with the same 0.3 mm hexahedral elements mesh used for the validation of the FSI approach. The

comparison between the overall residual deformation field, the stress waves, and the resultant reaction forces validated the load history approach as an equally accurate way to simulate bullet-splash for macroscopic structural assessment purposes, allowing a reduction of the computational cost of 60% compared to FSI.

In the third step, to improve the efficiency of the method and its parsimony and suitability to real-world engineering applications, a progressive simplification of the structural model was introduced, leading to the full shell model here proposed. The validation of the 2.5 mm shell model was performed again on the 4 mm AISI 304L steel plates impacted by 9 × 21 mm FMJ bullets; the residual deformation field, the stress waves, and the resultant reaction forces predicted by the simulation were confirmed to be accurate in comparison with the experimental evidence and with the results of the most accurate simulation based on the 0.3 mm size solid finite element model (Andreotti et al., 2022 [10]).

Compared to the FSI simulation model, the 2.5 mm shell discretization allowed a reduction of the calculation cost of more than 99%, also guaranteeing accurate prediction of the structural effects of the impacts, thanks to a maximum stable integration time step of 0.46 μs, that guarantees an accurate reproduction of the considered impulses, whose duration is less than 50 μs, and is compatible with reasonable computational costs for real-world applications. The analyses discussed in the present paper were conducted with an initial time integration step equal to 90% of the maximum, i.e., 0.414 μs. It is important to notice that the 2.5 mm size was also identified as the maximum element size compatible with reasonable load application detail to distinguish the load distributions considered in the study. The optimization of the computational cost of the finite element model also considered the symmetries and the extension of the discretized plate. Preliminary tests were conducted on the entire model to verify the influence of the boundary effects on the different shot positions, concluding that no boundary effects were significant on the results; therefore, the overall dimensions of the finite element models of the plates were reduced to 125 × 125 mm, with two orthogonal symmetry planes, to represent a 250 × 250 mm plate impacted at the center. In fact, the dimensions of the plates are such that the local effects of the impacts cannot be influenced by the boundary constraints because the maximum duration of the considered load history is less than 50 μs while the time for the stress waves to travel back and forth from the epicenter to the constraints is around 100 μs (considering the sound speed in steel is equal to 5000 m/s).

2.5.2. Constitutive Model Associated with the Plates

The constitutive model associated with the plates is a kinematic elastic-plastic model with damage (*MAT_81*MAT_PLASTICITY_WITH_DAMAGE in Ls-Dyna kewords [26]). For Creusabro® 8000 the post-yield hardening is regulated by a constant modulus ETAN = 11,891.7 MPa; the initial necking strain is EPPF = 0.05827. For Durostat® 400 the hardening modulus is ETAN = 5759.59 MPa; the initial necking strain is 0.04402. The rate effect was implemented as a scale factor for the yield stress as a function of the strain rate according to Cowper–Symonds model (Equation (12)) [26] which parameters C = 396,500/s and p = 3.0745 were obtained from Boyce et al. (2007) [27]:

$$\sigma = \sigma_0 \left[1 + \left(\frac{\dot{\varepsilon}}{C} \right)^{1/p} \right] \tag{12}$$

where σ_0 is the quasi-static value of the yield stress, and σ is its generic dynamic value at strain rate $\dot{\varepsilon}$. Table 7 summerizes the parameters of the constitutive models.

Table 7. Table of the constitutive parameters associated with the Creusabro® 8000 and Durostat® 400 models associated with the plates: RO = density; E = Young Modulus; PR = Poisson Ratio; SIGY = Yield Stress; ETAN = linear hardening modulus; EPPF = initial necking strain; C, p = rate effect parameters according to the Cowper–Symonds model; EPPFR = ultimate failure strain.

	RO [kg/m^3]	E [GPa]	PR	SIGY [MPa]	ETAN [MPa]	EPPF	C [s^{-1}]	p	EPPFR
Creusabro® 8000	7800	210	0.33	1190	11,891.7	0.058	396,500	3.0745	0.11
Durostat® 400	7800	210	0.33	1100	5759.6	0.044	396,500	3.0745	0.11

2.5.3. Validation of the Finite Element Discretization

To verify the consistency of the results in terms of stress waves and deformation fields, sensitivity tests were conducted on models with different mesh sizes. In this subsection we compare the results of a single Creusabro® 8000 steel plate impacted by a monolithic .308 bullet at 735 m/s, simulated by applying the corresponding estimated load history to the sharpest distribution (100 mm^{2,} Figure 8). The results of the 2.5 mm shell model were compared with the results of an analogous model with 1.25 mm mesh size, therefore four times the nodal density. The comparisons show almost perfect adherence of the stress fields (Figure 9), stress waves (Figure 10), and residual displacement fields (Figure 11), validating the 2.5 mm shell discretization as an effective compromise between detailed load description, consistency of the results, and maximization of the time integration step for the containment of the computational cost in real-world industrial applications requiring the modelling of large structural systems.

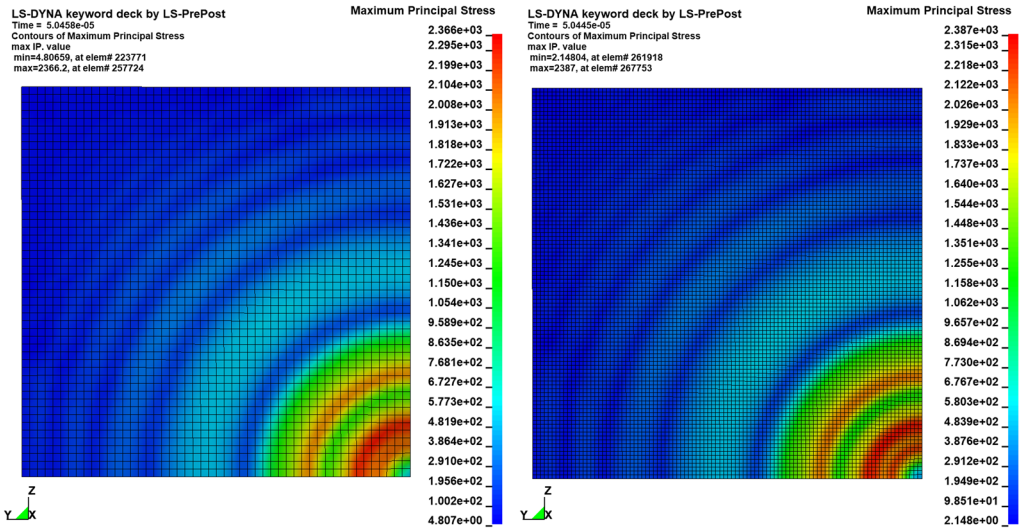

Figure 9. Stress field convergence. Comparison between the maximum principal stress field at 0.05 ms as predicted by the 2.5 mm model (**left**) and the 1.25 mm model (**right**). The difference in peak stress is less than 1%. No significant differences are visible. The stress wave is axially symmetric despite the squared shape of the arbitrary loaded surface.

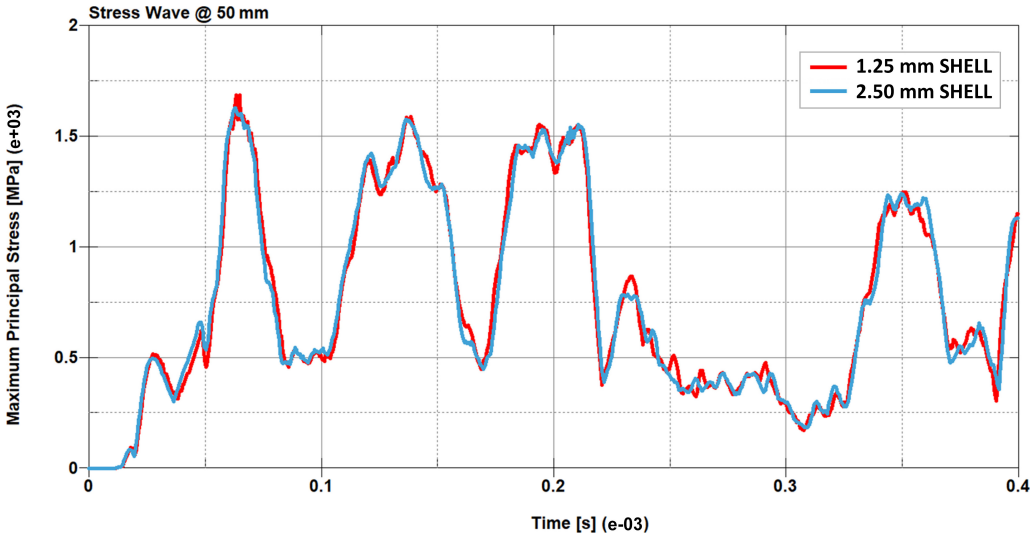

Figure 10. Maximum principal stress waves comparison at 50 mm from the origin. The predictions obtained by the higher nodal density model (red) and by the lower nodal density model (blue) are almost impossible to distinguish, even after 0.4 ms, which corresponds to around ten times the load application time. The maximum difference in peak stress is 10% after 0.23 ms, therefore 0.19 mm after the end of the loading time. This demonstrates that the stress prediction is consistent.

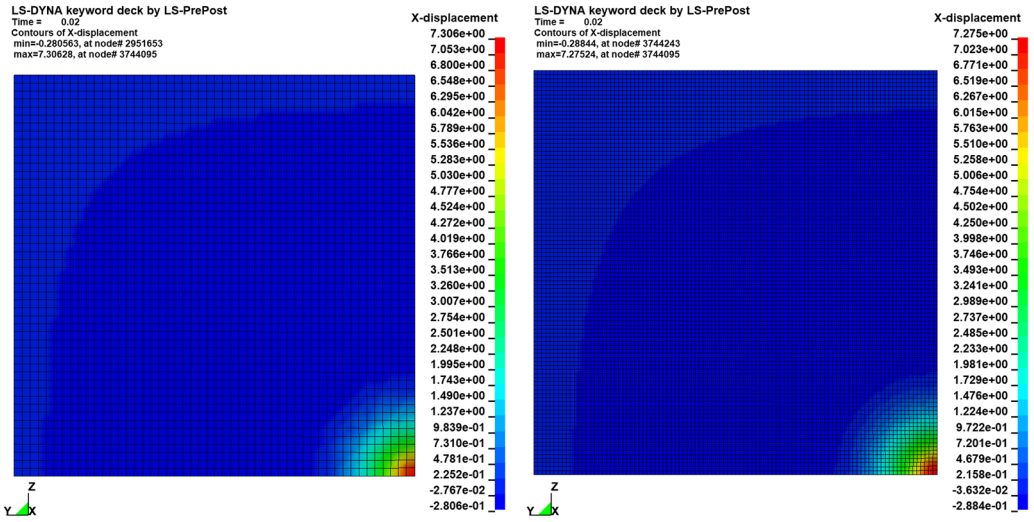

Figure 11. Residual deformation fields at 20 ms after the impacts [mm]. Comparison between the 2.5 mm shell model (**left**) and the 1.25 mm shell model (**right**). The predictions are equivalent; the maximum difference is less than 0.5% at the peak: 0.03 mm over 7.3 mm of maximum deformation.

3. Results

This section provides the experimental, analytical, and numerical results of the study. In Section 3.1 the pictures of the impacted plates and the frames capturing the evolution of the impacts are investigated to verify which of the considered impacts are compliant with the theoretical hypotheses of the bullet-splash. Section 3.2 summarizes the results of the measurements and estimations of the impact velocities. In Section 3.3 the load histories due to bullet-splash are plotted, having been calculated according to the theory from the measured impact velocities and the sections of the bullets. In Section 3.4, to verify the representativeness of the estimated load histories, the experimental fields of residual displacement are compared with the corresponding predictions obtained by means of explicit finite element simulations, where the discretized plates are loaded by direct application of the corresponding load curves.

3.1. Verification of the Bullet Splash Hypotheses

The verification of the hypotheses was performed by means of analyses of the experimental evidence. The inspection of the back plates allowed the verification of the non-penetration hypothesis. The inspection of the front plates allowed the verification of partial penetrations, here defined as the penetration of bullet material only through the front plate. The inspection of the full fragmentation of the bullets was performed by observation of the frames collected by means of the two high-frame-rate cameras in order to verify the gradual fragmentation of the bullet during the impact, the overall axial symmetry of the deflection kinematics, and the absence of major fragments rebounding from the plate and/or showing dimensions comparable with the bullets. A fragment was considered major if showing dimensions comparable with the calibre of the bullet. The presence of major fragments adhering to the impact surface was also verified by inspecting the plates.

3.1.1. Non-Penetration

The targets were able to withstand the ballistic impacts without allowing any part of the bullets to penetrate through the 8 mm thickness. Figures 12 and 13 show the effects of the impacts on the front and rear surfaces of the plates: the front views show the impact epicenter and the surrounding traces due to the radial debris deflection; the rear views show the bulges due to the residual plastic strain of the plates with no marks of penetration. It is worth noting that the Full Metal Jacket (FMJ) bullet caused the partial penetration of the first Durostat® 400 plate (Figure 14).

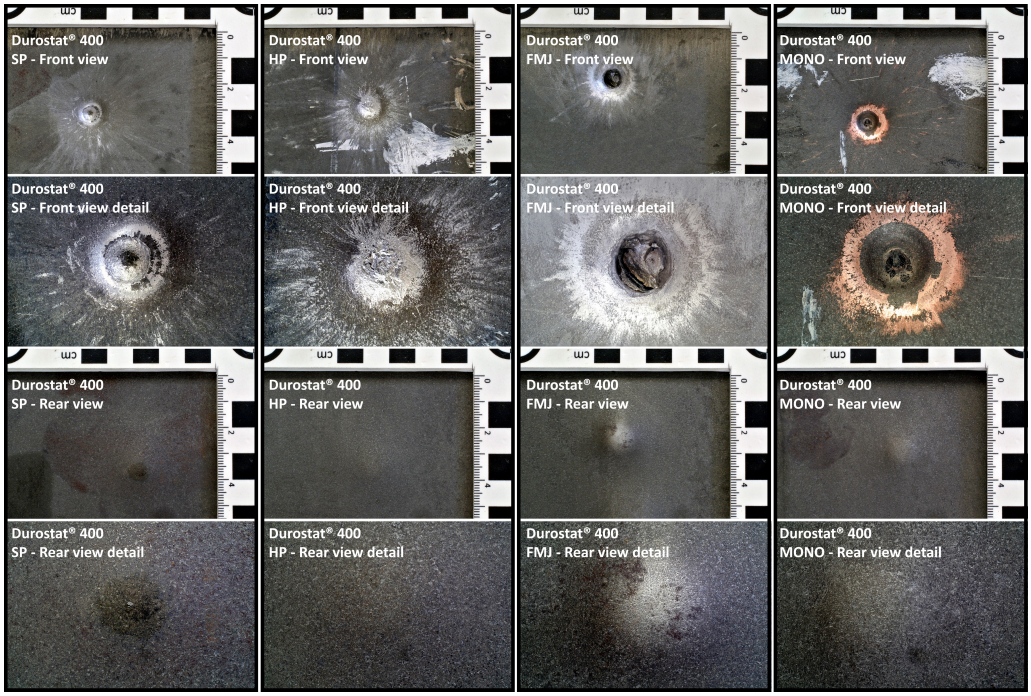

Figure 12. Front and rear surfaces of the Durostat® 400 plates impacted by the bullets. The impacted areas show the marks of the interaction with the bullets, which can be distinguished in a central area where the interaction appears to be more compressive, and a peripheral area where the radial marks show the effects of the sliding of the bullet debris. The sliding marks are evident from a diameter of approximately 11 to 16 mm (roughly 100 mm^2 to 200 mm^2), to a diameter of 20 to 25 mm around the epicenter (around 400 mm^2). The detailed front view of the FMJ effects shows the melted filler mixed with parts of the jacket, still blocked inside the crater.

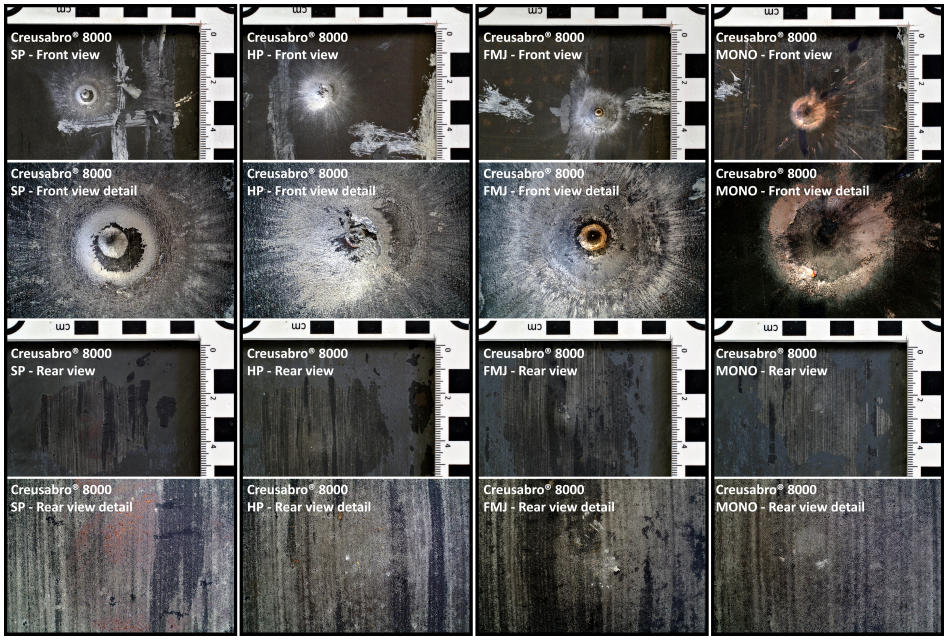

Figure 13. Front and rear surfaces of the Creusabro® 8000 plates impacted by the bullets. The impacted areas show the marks of the interaction with the bullets, that can be distinguished in a central area where the interaction appears to be more compressive, and a peripheral area where the radial marks show the effects of the sliding of the bullet debris. The sliding marks are evident from a diameter of approximately 11 to 16 mm (roughly 100 mm^2 to 200 mm^2), to a diameter of 20 to 25 mm around the epicenter (around 400 mm^2).

Figure 14. Partial penetration of FMJ bullet material through the first plate of Durostat® 400. Back of the first plate showing the penetration of some melted filler material.

3.1.2. Full Fragmentation

The analysis of the captured frames allowed to assess that all the bullets encountered full fragmentation and deflection, except for the FMJs. In fact, the FMJ impacting on Durostat® 400 partially penetrated the first plate, while part of the FMJ impacting on Creusabro® 8000 (Figure 15) was observed to slowly rebound after the impact, as a

solid volume (Figure 16). These cases are therefore not compliant with the proposed bullet-splash definition.

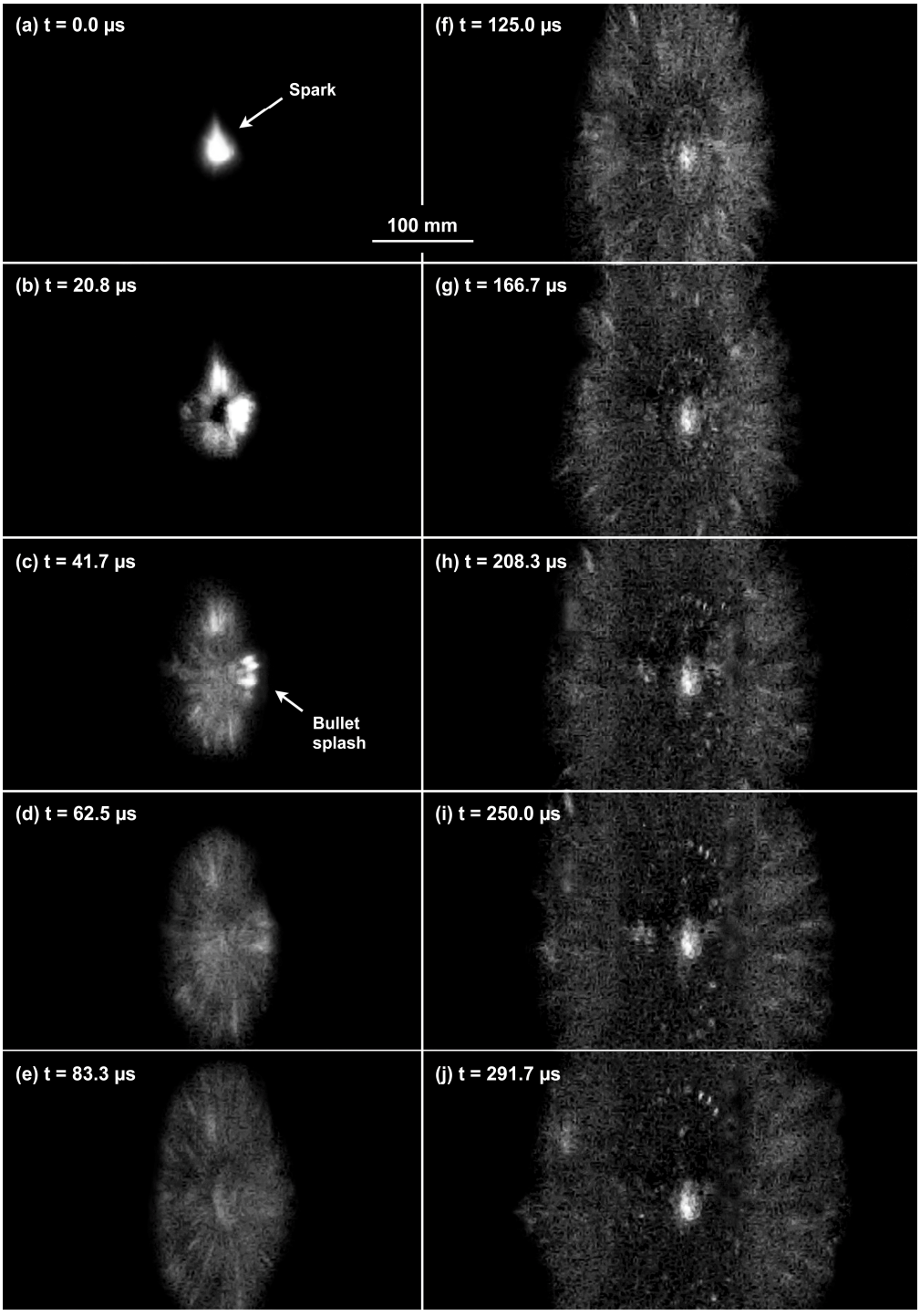

Figure 15. The figure shows ten frames of the first 0.3 ms after the impact for the combination FMJ-Creusabro® 8000, taken from the footage recorded by the perspective camera (Camera 2). The first frames (**a**–**c**) show the crushing of the bullet at its first contact with the target, allowing the appreciation of a spark caused by the high hardness of the plate. Fragments are then projected radially from the impact point starting from small particles (**c**–**f**), with slightly bigger fragments later ricocheting in annular patterns (**f**–**j**). Frames shown here are processed to show the parts of interest, filtering out the noise otherwise preventing the appreciation of the bullet fragmentation.

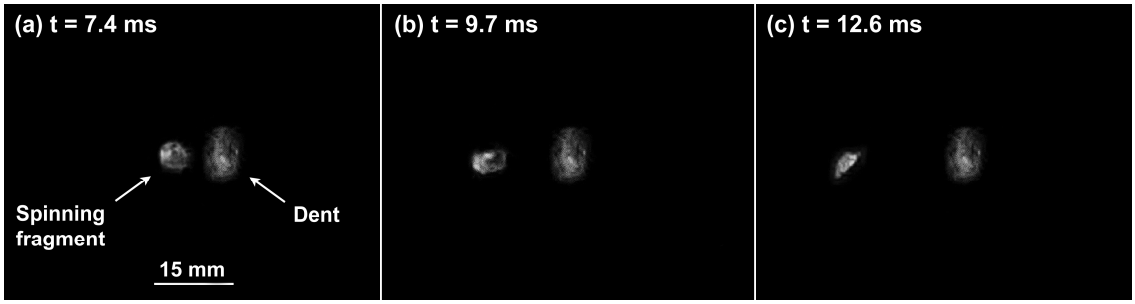

Figure 16. The figure shows a large fragment of the Full Metal Jacket bouncing back from the impact area of the Creusabro® 8000 plate. The shot is therefore non-compliant with the bullet-splash definition. The fragment translates with perpendicular speed measured at 4.4 ± 2% m/s. Mild spinning can be appreciated. The three frames shown here (**a**–**c**), extracted from the second camera footage, were processed to isolate the fragment from the dust created after the impact: for each frame, only the fragment and the dent on the plate are visible; an approximate dimensional reference for the dent and the fragment is reported in frame (**a**). The fragment has a diameter of around 7.5 mm and thickness of about 4 mm, with the shape similar to the bulge created on the plate.

3.2. Impact Velocity Estimation

The frame-by-frame analysis of the bullet kinematics before the impacts allowed identification of the impact velocity with a maximum error of ±5.7% (Table 8), except for shot 2 where the lack of light made the approach too uncertain. In this case the impact velocity was therefore estimated based on the muzzle velocity and the average percentage of speed loss calculated on four other Hollow Point bullets shot the same day in the same conditions (Table 9). The maximum error for shot 2 was therefore calculated as the sum of the maximum error due to muzzle velocity measurement (±2.8%) and the maximum error due to frame-by-frame approach on hollow point bullets (±5.7%). The maximum error associated with impact velocity of Shot 2 is therefore ±8.5%.

Table 8. Estimated impact velocities.

Shot	Bullet	Material	Impact Speed [m/s]	Maximum Error [%]
1	Soft Point (SP)	Durostat® 400	642	1.1
2	Hollow Point (HP)	Durostat® 400	645	8.5 *
3	Full Metal Jacket (FMJ)	Durostat® 400	769	1.2
4	Monolithic (MONO)	Durostat® 400	738	3.5
5	Soft Point (SP)	Creusabro® 8000	607	1.2
6	Hollow Point (HP)	Creusabro® 8000	702	5.7
7	Full Metal Jacket (FMJ)	Creusabro® 8000	736	2.9
8	Monolithic (MONO)	Creusabro® 8000	749	2.8

* Estimated based on the average velocity loss of four Hollow Point bullets shot in the same conditions.

Table 9. Average velocities at muzzle and at 100 m and relative losses for each bullet type. Averages are computed over a total of four shots per bullet type.

Bullet	v_{muzzle} [m/s]	v_{100m} [m/s]	Loss [%]
Soft Point (SP)	763	620	18.7
Hollow Point (HP)	814	727	10.7
Full Metal Jacket (FMJ)	843	731	13.3
Monolithic (MONO)	837	741	11.5

3.3. Estimated Load Histories

According to the proposed load history approach, eight load histories (Figures 17 and 18) were calculated, based on the bullets' section (Figure 1) and the mea-

sured impact velocities (Table 8). The mass distribution was reconstructed based on the scaled sections associated with the density values summarized in Table 10, so that the volume integration of the mapped density fields exactly equals the nominal masses of the bullets, and therefore the time integration of the load histories correctly corresponds to the momentum of the impacting bullets.

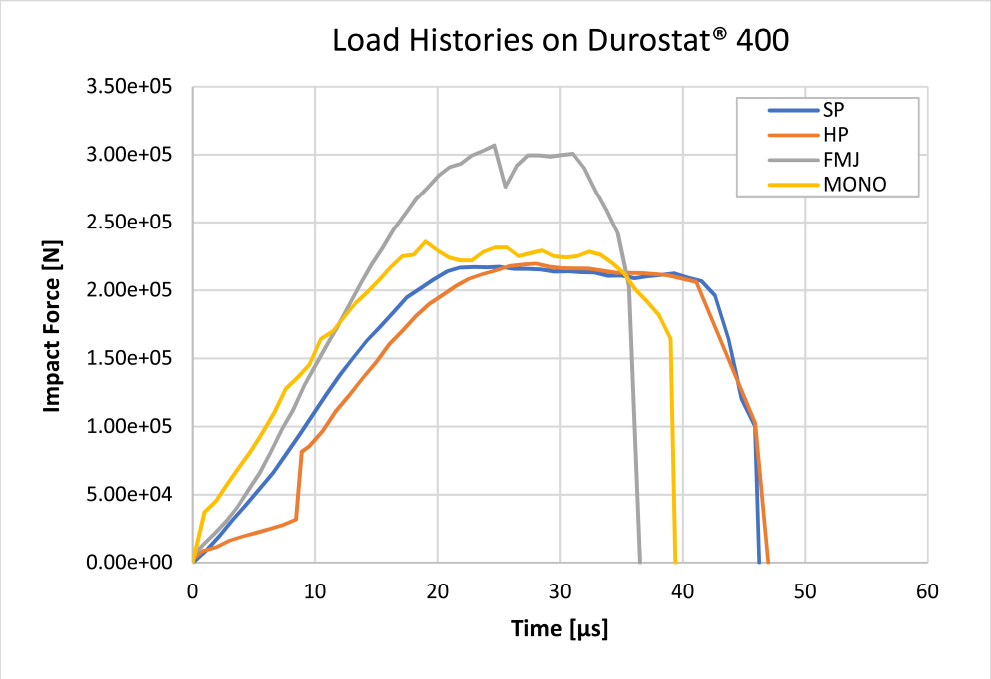

Figure 17. Load histories estimated according to Equation (8), applied to the impacts on Durostat® 400. The SP, HP and MONO bullets have similar force peaks around 220–230 kN. The FMJ reaches instead 307 kN force. The duration of the impulses ranges from 36 to 47 µs.

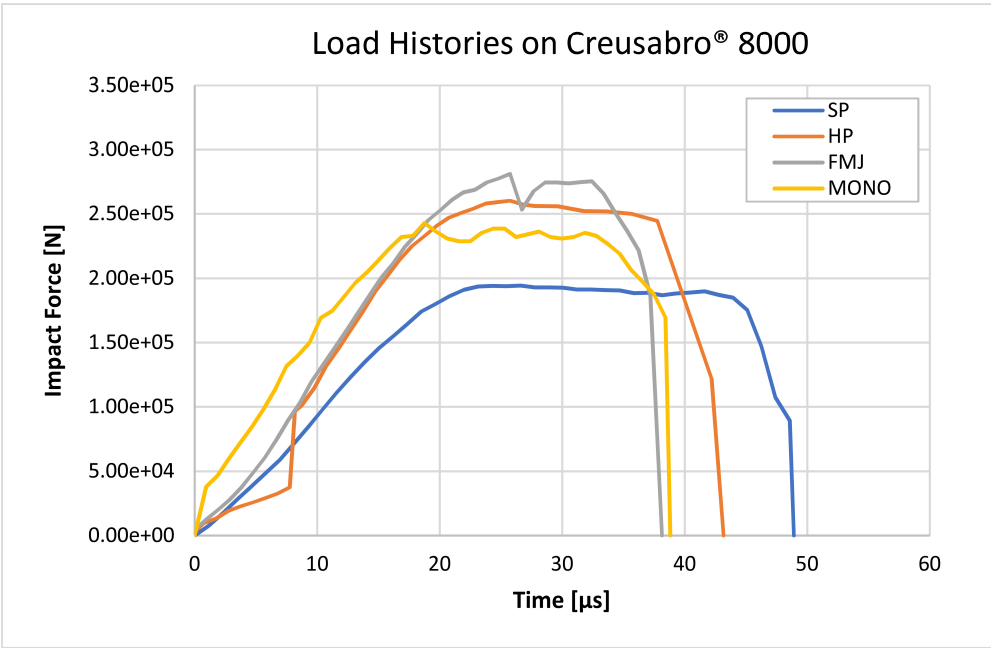

Figure 18. Load histories estimated according to Equation (8), applied to the impacts on Creusabro® 8000. The SP reaches 194 kN peak force, MONO reaches 243 kN, HP reaches 260 kN, and FMJ reaches 281 kN. The durations of the impulses range from 39 µs for FMJ to 49 µs for SP.

Table 10. Density values associated with the bullet materials for the four bullet types so that the volume integration of the density fields correspond to the nominal bullets' masses.

Bullet	ρ_{jacket} [kg/m^3]	ρ_{filler} [kg/m^3]	Bullet Mass [g]
Soft Point (SP)	8730	12,640	11.66
Hollow Point (HP)	8730	12,280	10.89
Full Metal Jacket (FMJ)	8730	11,325	9.53
Monolithic (MONO)	9425	-	9.59

3.4. Field of Residual Displacements

In Figures 19–34 we provide the comparison between numerical and experimental results in terms of residual displacements of the plates. The fields of residual displacements have been represented as a function of the radial distance from the apex of the bulges (Figures 19, 21, 23, 25, 27, 29, 31 and 33). The experimental measurements (represented with their variability due to a $\pm$0.5 mm error in positioning the instrument at the bulge apex) are compared with the simulation results obtained with the three arbitrary load distributions, where the same load history was distributed on 100, 200, and 400 mm^2 as described in Section 2.5.1. Based on the mapping of the residual displacements, three validation indexes have been considered: the apex displacement, the overall volume of the residual bulge, and the radial slope at 50 mm from the apex (the boundary of the measured range). The validation was conducted by dividing the indexes calculated on the simulation results by the indexes calculated on the experimental results. The validation results are presented as percentages, so that a validation higher than 100% means that the simulation overestimated the corresponding experimental index. To enhance the effects of the load distribution on the validation indexes, the three indexes were plotted as a function of the loaded area (Figures 20, 22, 24, 26, 28, 30, 32 and 34).

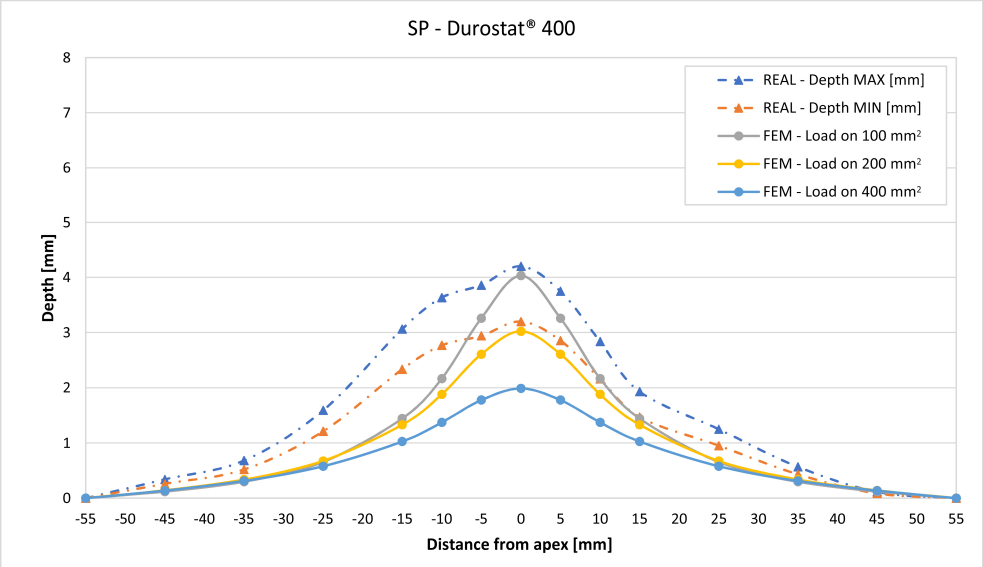

Figure 19. Residual displacements caused by the Soft Point bullet on Durostat® 400 plates. The predicted apex displacement for the 100 mm^2 distribution (grey line) is near the maximum experimental value (blue dotted line), around 4 mm. The predicted apex displacement for the 200 mm^2 distribution (yellow line) is near the minimum experimental value, around 3 mm. The predicted apex displacement for the 400 mm^2 distribution (light blue line) is around 1 mm lower than the minimum experimental value. The radial extension of the bulge is underestimated. Over 35 mm radial distance from the apex the three load distributions are impossible to distinguish.

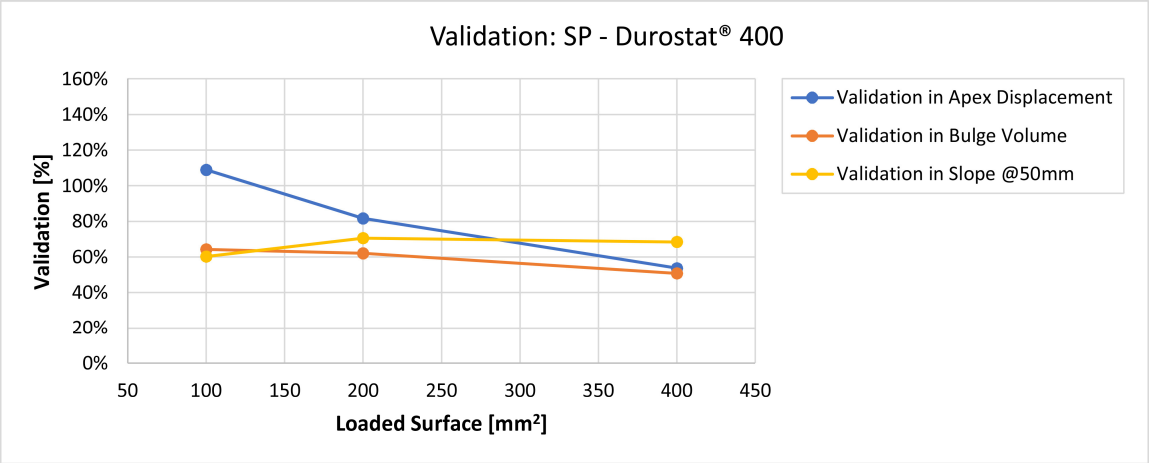

Figure 20. Soft Point bullet on Durostat® 400 plates: validation of the calculated residual displacement fields in terms of apex displacement (blue), total bulge volume (red), and slope at 50 mm (yellow). In abscissa the loaded area of the three arbitrary distributions. In terms of apex displacement, the 100 mm^2 distribution gives the best estimation (109%), while the 200 mm^2 and 400 mm^2 give 82% and 55%. The three distributions provide more consistent predictions in terms of bulge volume and slope, all between 51 and 68%.

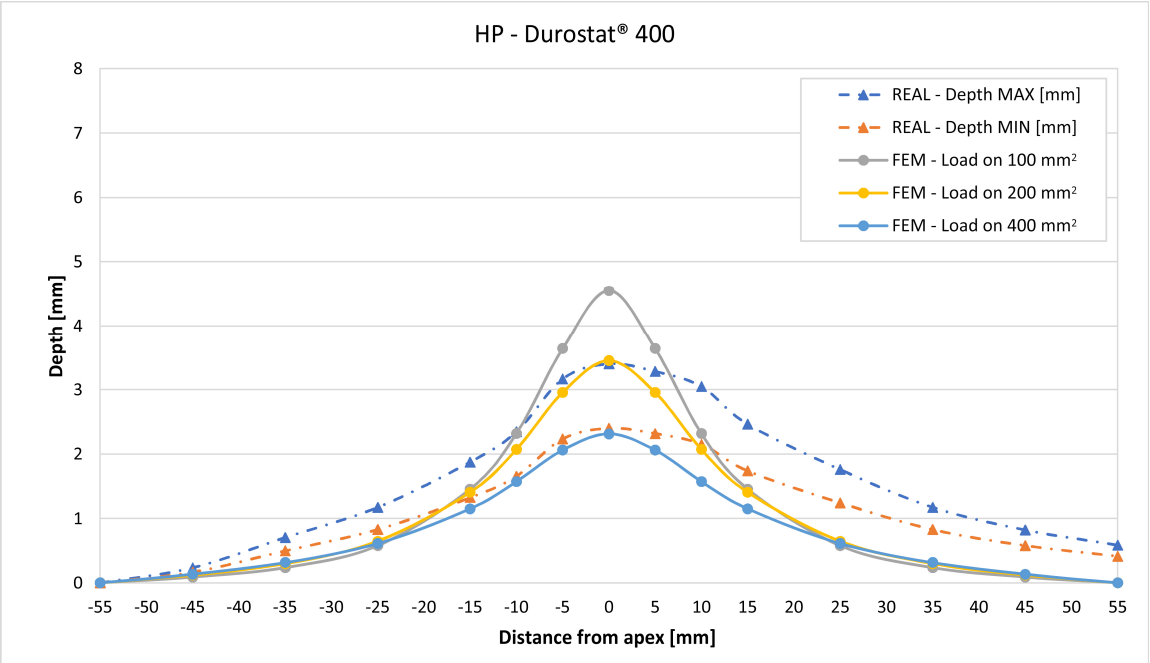

Figure 21. Residual displacements caused by the Hollow Point bullet on Durostat® 400 plates. The predicted apex displacement for the 100 mm^2 distribution (grey line) exceeds the maximum experimental value (blue dotted line) of about 1 mm. The predicted apex displacement for the 200 mm^2 distribution (yellow line) coincides with the maximum experimental value, around 3.4 mm. The predicted apex displacement for the 400 mm^2 distribution (light blue line) is almost coincident with the minimum experimental value. The radial extension of the bulge is slightly underestimated. Over 25 mm radial distance from the apex the three load distributions are almost impossible to distinguish.

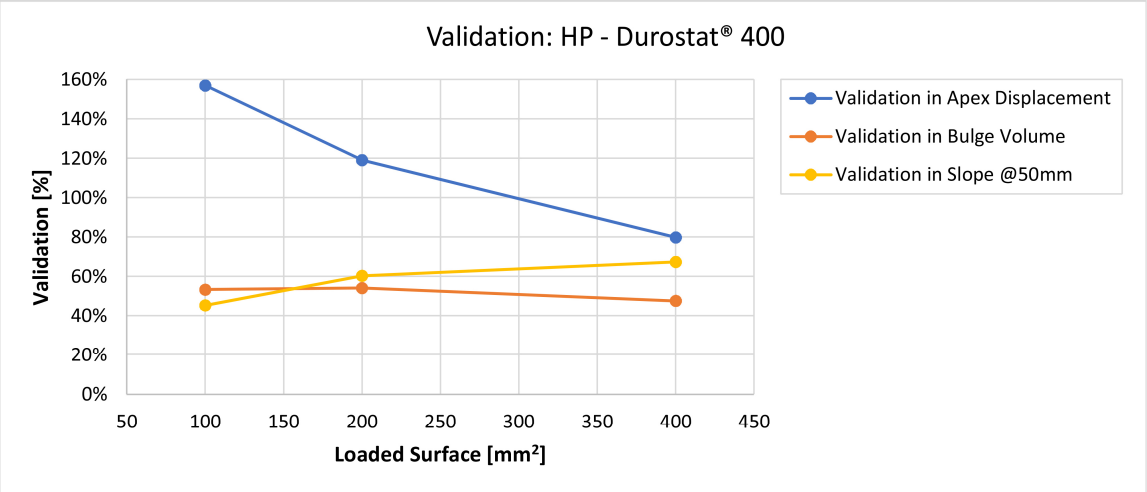

Figure 22. Validation for HP on Durostat® 400: validation of the calculated residual displacement fields in terms of apex displacement (blue), total bulge volume (red), and slope at 50 mm (yellow). In abscissa the loaded area of the three arbitrary distributions. In terms of apex displacement, the 200 mm^2 distribution gives the best estimation (119%), while the 100 mm^2 and 400 mm^2 give 157% and 80%. The three distributions provide more consistent predictions in terms of bulge volume and slope, all between 45% and 67%.

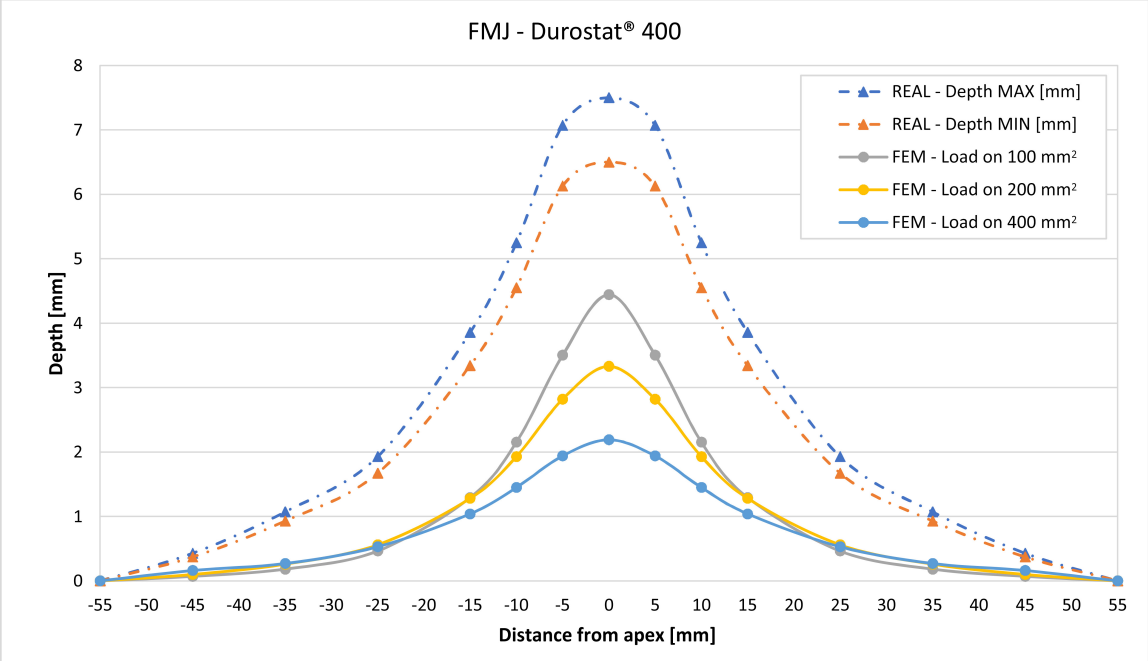

Figure 23. Residual displacements caused by the Full Metal Jacket bullet on Durostat® 400 plates. The predicted apex displacement for the 100 mm^2 distribution (grey line) underestimates the experimental range (blue and red dotted lines) of about 2.5 mm. The overall bulge extension is significantly underestimated. For radial distance over 25 mm from the apex, the three load distributions are almost impossible to distinguish.

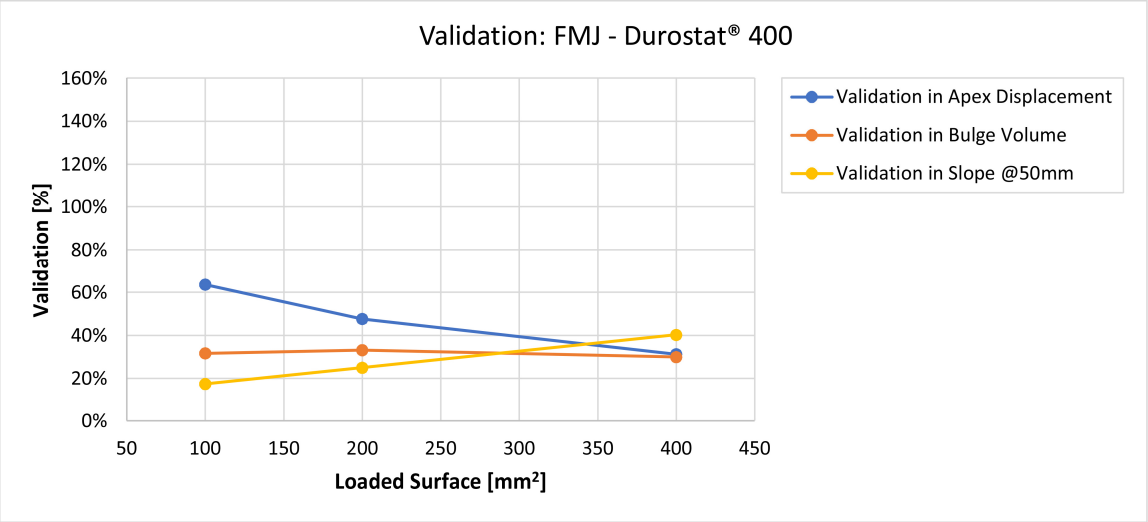

Figure 24. Validation for FMJ on Durostat® 400: validation of the calculated residual displacement fields in terms of apex displacement (blue), total bulge volume (red), and slope at 50 mm (yellow). In abscissa the loaded area of the three arbitrary distributions. In terms of apex displacement, the 100 mm^2 distribution gives the best estimation (63%), while the 200 mm^2 and 400 mm^2 give 48% and 30%. The three distributions provide consistent predictions in terms of bulge volume around 30–33%. In slope, the estimate increases as the distribution area, from 17.5% to 40%.

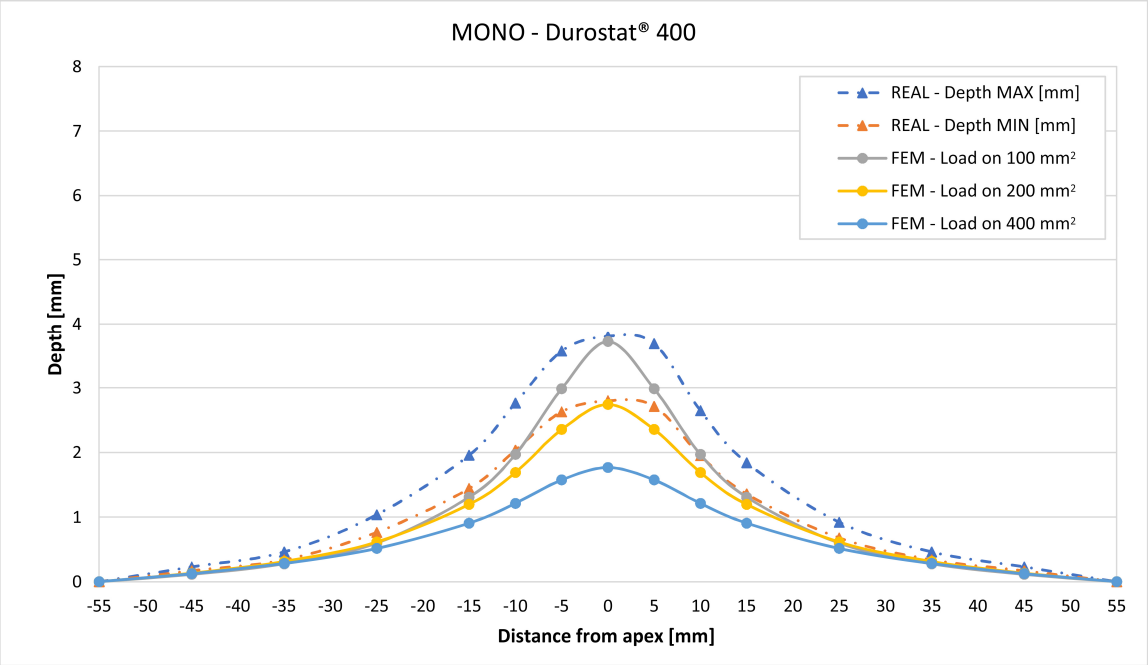

Figure 25. Residual displacements caused by the Monolithic bullet on Durostat® 400 plates. The predicted apex displacement for the 100 mm^2 distribution (grey line) is almost coincident with the maximum experimental value (blue dotted line). The predicted apex displacement for the 200 mm^2 distribution (yellow line) coincides with the minimum experimental value. The radial extension of the bulge is slightly underestimated. For radial distances over 35 mm from the apex, the three load distributions are impossible to distinguish.

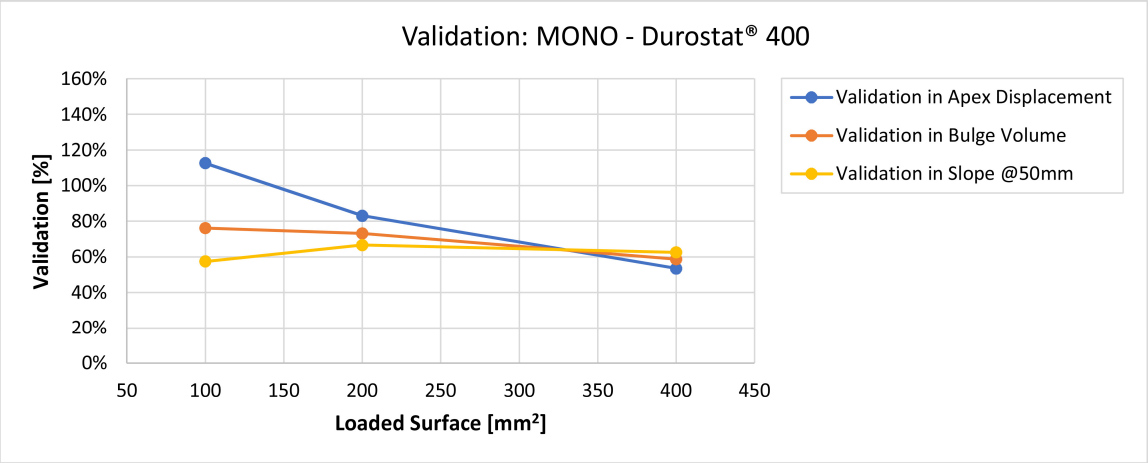

Figure 26. Validation for MONO on Durostat® 400: validation of the calculated residual displacement fields in terms of apex displacement (blue), total bulge volume (red), and slope at 50 mm (yellow). In abscissa the loaded area of the three arbitrary distributions. In terms of apex displacement, the 100 mm^2 distribution gives the best estimation (113%), while the 200 mm^2 and 400 mm^2 give 83% and 54%. The bulge volume predictions decrease from 76% to 63% as the area increases. The slope predictions are more consistent, between 57% and 67%.

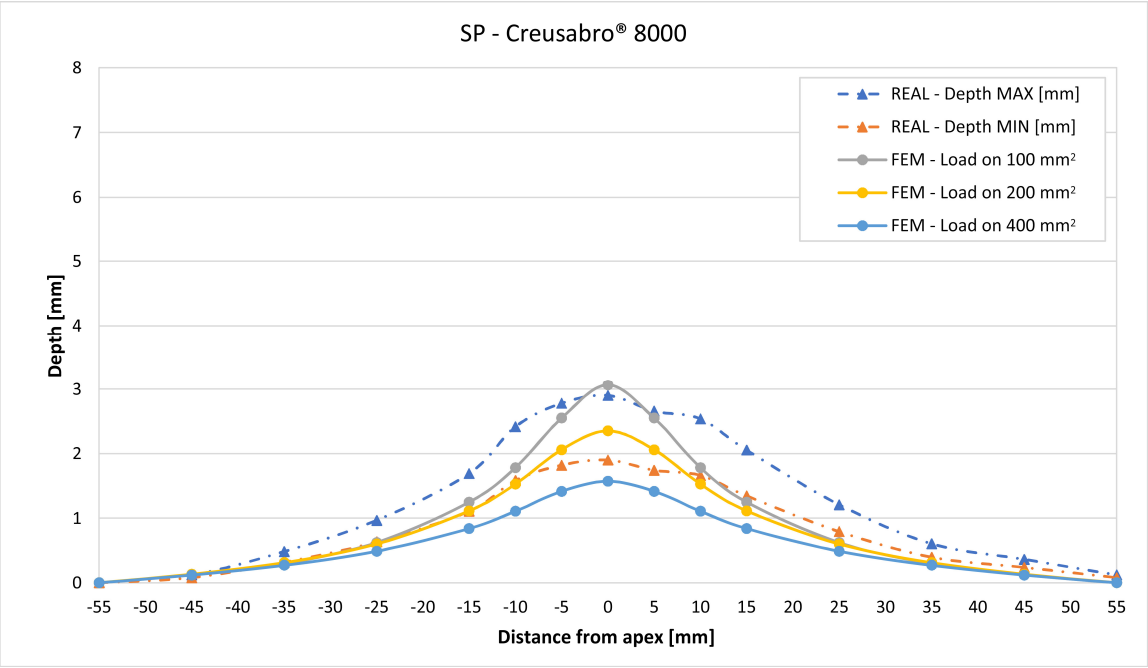

Figure 27. Residual displacements caused by the Soft Point bullet on Creusabro® 8000 plates. The predicted apex displacement for the 100 mm^2 distribution (grey line) slightly exceeds the maximum experimental value (blue dotted line). The predicted apex displacement for the 200 mm^2 distribution (yellow line) is in the middle of the experimental range. The predicted apex displacement for the 400 mm^2 distribution (light blue line) underestimates the minimum experimental value of about 0.5 mm. The radial extension of the bulge is slightly underestimated. Over 35 mm radial distance from the apex the three load distributions are impossible to distinguish.

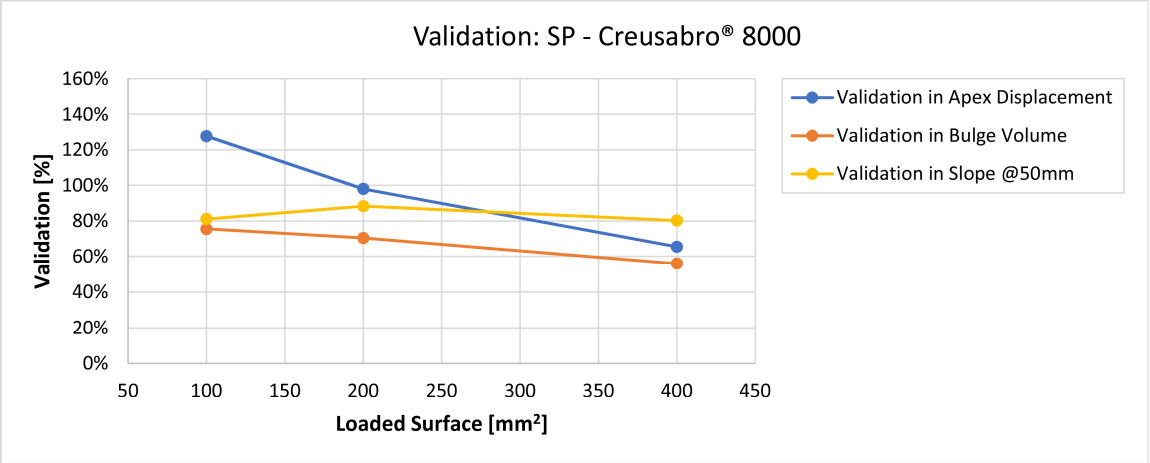

Figure 28. Validation for SP on Creusabro® 8000. Validation of the calculated residual displacement fields in terms of apex displacement (blue), total bulge volume (red), and slope at 50 mm (yellow). In abscissa the loaded area of the three arbitrary distributions. In terms of apex displacement, the 200 mm^2 distribution gives the best estimation (98%), while the 100 mm^2 and 400 mm^2 give 128% and 66%. The bulge volume predictions decrease from 81% to 56% as the area increases. The slope predictions are more consistent, between 80% and 88%.

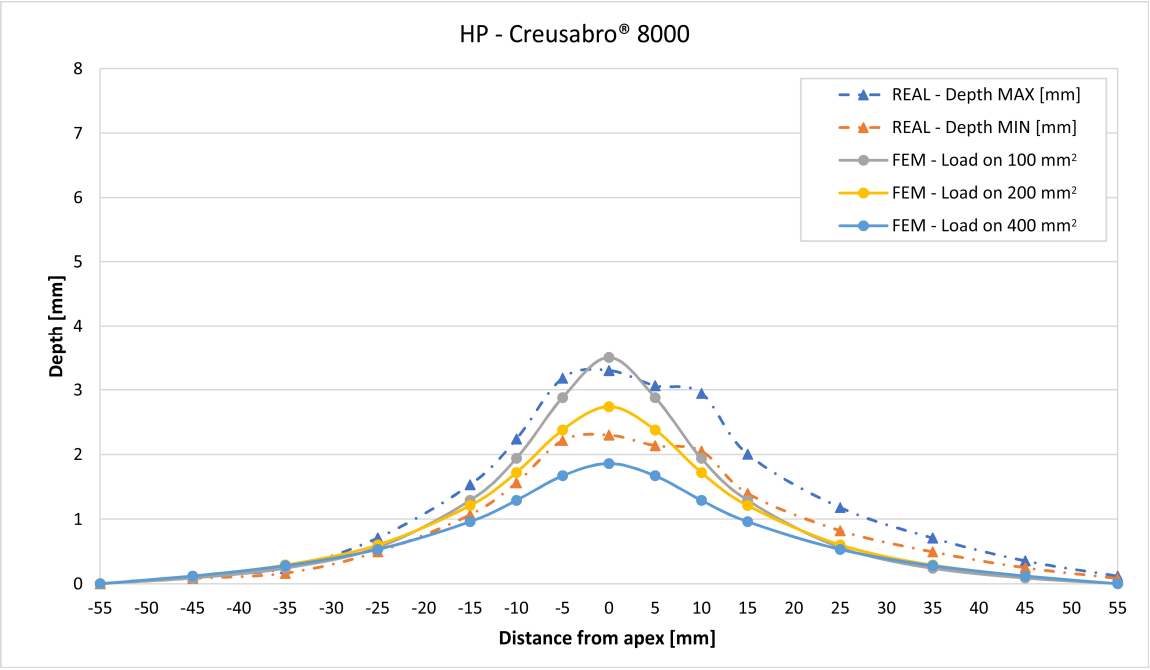

Figure 29. Residual displacements caused by the Hollow Point bullet on Creusabro® 8000 plates. The predicted apex displacement for the 100 mm^2 distribution (grey line) exceeds the maximum experimental value (blue dotted line) of about 0.2 mm. The predicted apex displacement for the 200 mm^2 distribution (yellow line) is in the middle of the experimental range. The predicted apex displacement for the 400 mm^2 distribution (light blue line) is 0.5 lower than the minimum experimental value. The radial extension of the bulge is slightly underestimated. For radial distances over 25 mm from the apex, the three load distributions are impossible to distinguish.

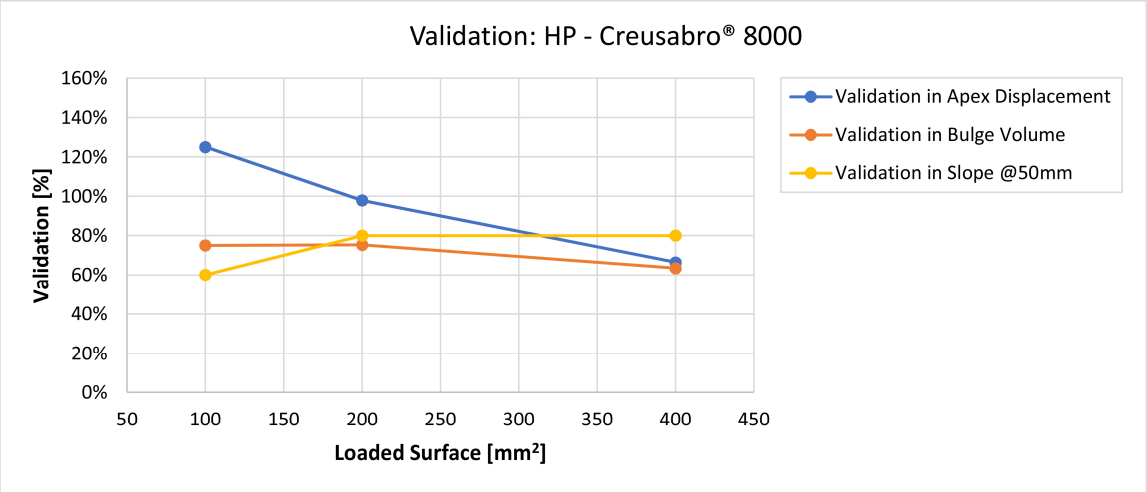

Figure 30. Validation for HP on Creusabro® 8000. Validation of the calculated residual displacement fields in terms of apex displacement (blue), total bulge volume (red), and slope at 50 mm (yellow). In abscissa the loaded area of the three arbitrary distributions. In terms of apex displacement, the 200 mm^2 distribution gives the best estimation (98%), while the 100 mm^2 and 400 mm^2 give 125% and 63%. The bulge volume predictions decrease from 75% to 63% as the area increases. The slope predictions increase from 60% (100 mm^2) to 80% (200 and 400 mm^2).

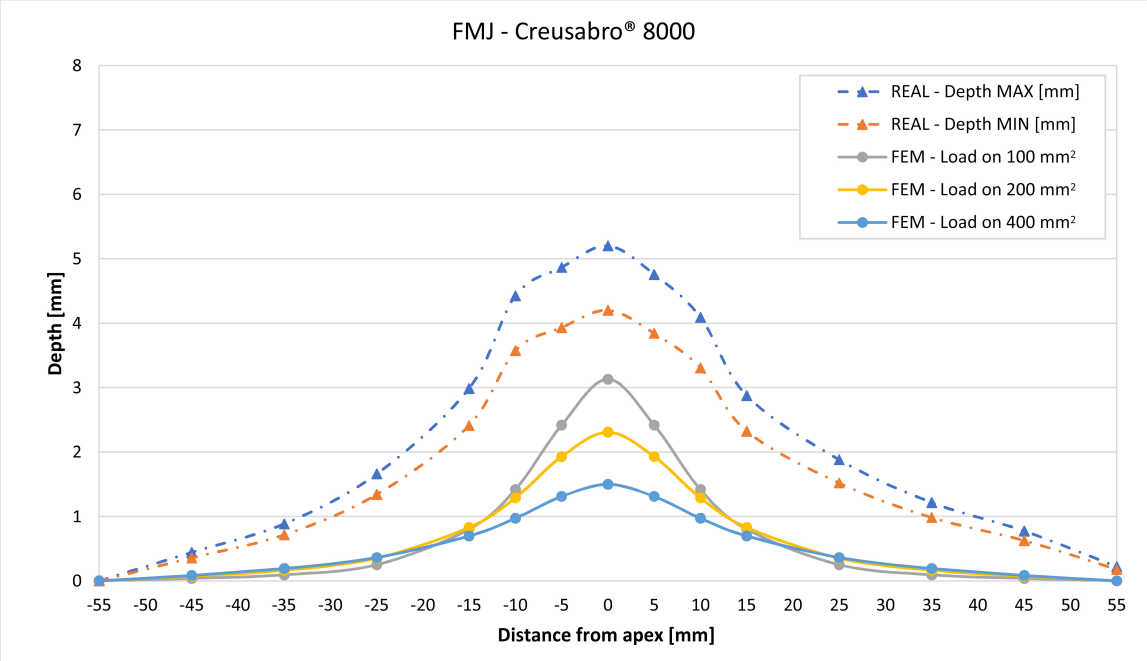

Figure 31. Residual displacements caused by the Full Metal Jacket bullet on Creusabro® 8000 plates. The predicted apex displacement for the 100 mm^2 distribution (grey line) underestimates the experimental (blue and red dotted lines) range of about 2 mm. The overall bulge extension is significantly underestimated. For radial distances over 15 mm from the apex, the three load distributions are difficult to distinguish.

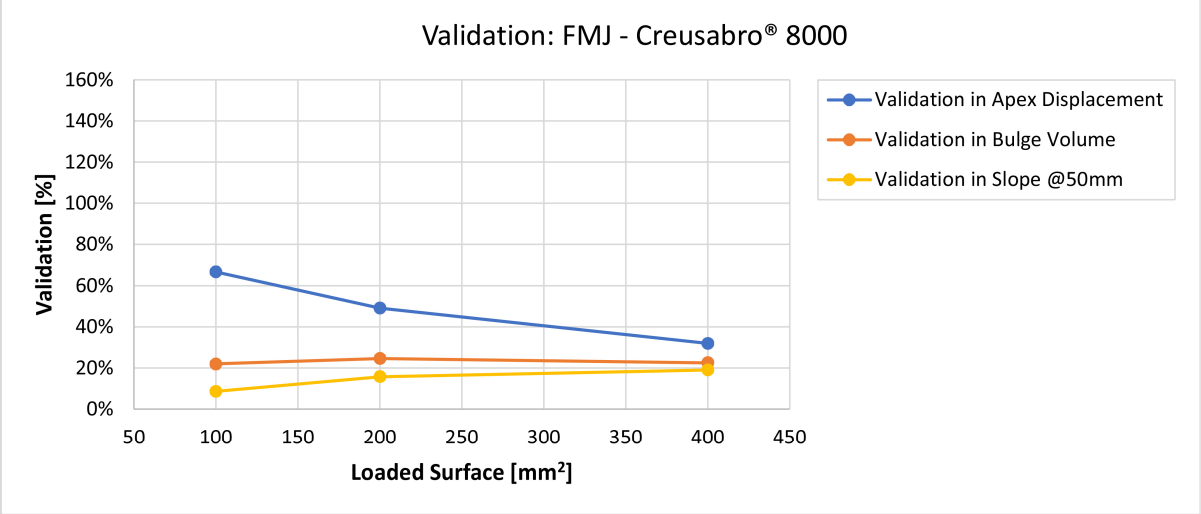

Figure 32. Validation for FMJ on Creusabro® 8000. Validation of the calculated residual displacements fields in terms of apex displacement (blue), total bulge volume (red), and slope at 50 mm (yellow). In abscissa the loaded area of the three arbitrary distributions. In terms of apex displacement, the 100 mm^2 distribution gives the best estimation (67%), while the 200 mm^2 and 400 mm^2 give 49% and 32%. The bulge volume predictions are consistent between 22% and 25%. The slope predictions increase from 9% (100 mm^2) to 19% (400 mm^2).

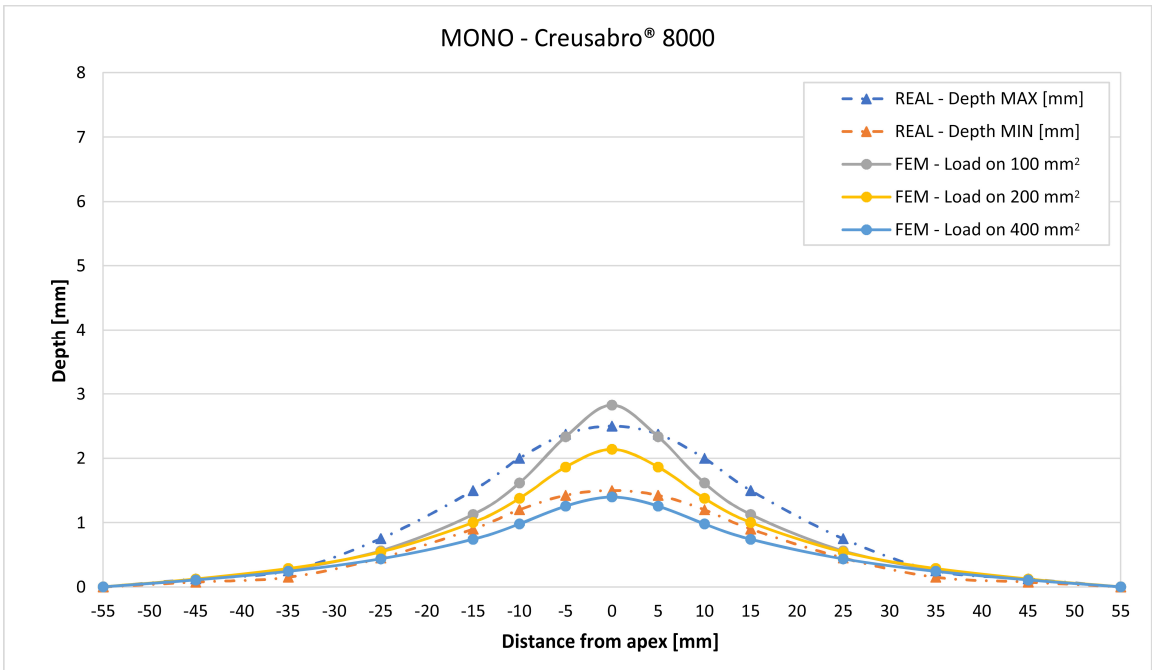

Figure 33. Residual displacements caused by the Monolithic bullet on Creusabro® 8000 plates. The predicted apex displacement for the 100 mm^2 distribution (grey line) exceeds the maximum experimental value (blue dotted line) by 0.3 mm. The predicted apex displacement for the 200 mm^2 distribution (yellow line) almost coincides with the middle range of the experimental values (blue and red dotted lines). The predicted apex displacement for the 400 mm^2 distribution (light blue line) coincides with the minimum experimental value. The radial extension of the bulge is well estimated. For radial distances over 35 mm from the apex, the three load distributions are impossible to distinguish.

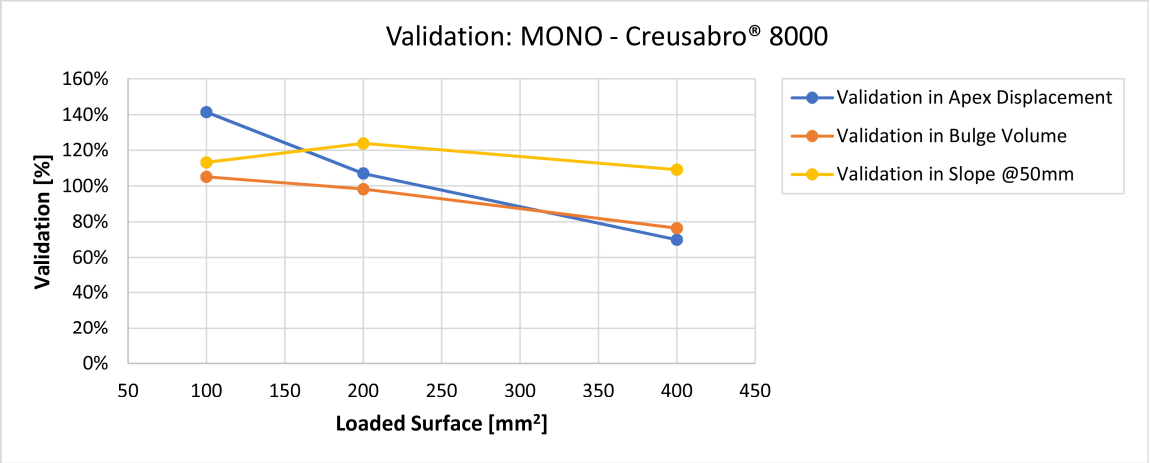

Figure 34. Validation for MONO on Creusabro® 8000. Validation of the calculated residual displacements fields in terms of apex displacement (blue), total bulge volume (red), and slope at 50 mm (yellow). In abscissa the loaded area of the three arbitrary distributions. In terms of apex displacement, the 200 mm^2 distribution gives the best estimation (107%), while the 100 mm^2 and 400 mm^2 give 141% and 70%. The bulge volume predictions decrease with the area, from 113% to 76%. The slope predictions are more consistent, between 109% and 123%.

4. Discussion

All the observed shots showed massive fragmentation of the bullets, with no full penetration of the 8 mm thick targets. However, evidence of non-complete fragmentation was reported on both FMJ bullets: a large solid part of the bullet, with dimensions comparable with the caliber, was found bouncing back after the shot on Creusabro® 8000 (Figure 16), and a significant volume of filler material together with part of the jacket material was found having penetrated the first plate of Durostat® 400 (Figures 12 and 14). These two cases, therefore, do not satisfy the theoretical hypotheses supporting the formula for the load history estimation demonstrated in Section 2.4, For this reason both FMJ shots should be considered control cases to evaluate the effectiveness of the method when its applicability conditions are not verified.

Considering the fields of residual displacement, the simulation and the experimental results diverge significantly for both FMJ bullet cases. The predicted displacement fields are being consistently and significantly underestimated, particularly so in terms of bulge volume and slope, for which the best estimations for FMJ impacts are, respectively, 33% and 40% on Durostat® 400 and 25% and 19% for Creusabro® 8000 (Figures 23, 24, 31 and 32). The relevant underestimation in the fields of residual displacement in these two cases is due to the force peaks needed to decelerate the relevant solid parts of the bullets instead of gradually deflecting their mass as happens during the ideal bullet splash. In the case of the partial penetration of the Durostat® 400 plate, the local reduction in the stiffness of the target due to the loss of integrity of the front plate and the direct impact of parts of the bullet onto the back plate should also have an effect in increasing the real back plate deformation.

The experimental verifications have instead confirmed that, on the contrary, the SP, HP, and MONO cases are fully compliant with the bullet-splash theoretical hypotheses; the comparisons between the predicted and experimental residual displacement fields for these cases are therefore considered significant for the validation of the load histories estimated with the proposed method.

The validation was performed on the results obtained by simulating the impacts on the three different arbitrary load distributions considered representative of the extension of the marks left on the plates after the impacts. The 100 mm^2 and 200 mm^2 distributions were considered representative of the minimum and maximum observed areas where the interaction between bullet and target is mainly compressive, causing the formation of the

fragments and their 90-degree, almost instantaneous, deflection. The 400 mm^2 distribution area, instead, includes approximately the entire extension of the interaction areas observed on the plates, including the peripheral area where the radial marks show that the interaction between bullet and target only consisted in a sliding contact of the already formed and deflected fragments. This last distribution was therefore expected to be less representative of the local compressive phenomena, but still relevant as a sensitivity test case of the effects of the pressure distributions on the deformation fields.

The comparisons between the simulated and experimental fields of residual displacements (Figures 19, 21, 23, 25, 27, 29, 31 and 33) show that the effects of the load distributions are significant only within 25 to 35 mm from the apex. The differences in terms of residual displacement at the apex are due to the fact that the three distributions apply pressure intensities that are inversely proportional to their loaded areas to guarantee that the integration of the pressure fields is equivalent to the load history for all the arbitrary distributions. To apply the same force, the pressure applied on the 100 mm^2 area must be, respectively, two and four times higher than the intensity applied by the 200 mm^2 and 400 mm^2 uniform distributions; therefore, the loaded elements must withstand proportionally higher stress and consequently encounter higher fields of plastic strain compared to the same elements loaded with lower intensity distributions. This explains the local differences in terms of maximum residual displacement at the apex between the three force-equivalent distributions as well as the almost indistinguishable effects over 25 to 35 mm from the apex, since the peripheral elements encounter approximately the same stress waves for all the distributions. In fact, the differences in radial extension between the three loaded areas are very limited compared to the distance covered by a mechanical signal during the duration of the considered impulses, therefore the stress waves propagating from the 100 mm^2 distribution have a duration that is less than 3% shorter than the 400 mm^2 one, which has neglectable engineering effects.

The validation graphs (Figures 20, 22, 24, 26, 28, 30, 32 and 34) demonstrate that the estimated load histories applied on the 100 mm^2 and 200 mm^2 distributions allow correct predictions of the residual displacements at the apex for all the verified bullet splashes (SP, HP, and MONO), with the sharpest distribution giving percentage validations between 109% and 157% (average 126%) on Durostat® 400 and between 125% and 141% (average 131%) for Creusabro® 8000. Moreover, the 200 mm^2 distribution gives representative validations between 82% and 119% (average 95%) on Durostat® 400 and between 98% and 107% (average 101%) for Creusabro® 8000. It is crucial to notice that even though the two sharpest distributions have a 100% difference in pressure intensity and loaded surfaces, the average difference in the estimations of the maximum residual displacement between the two is limited to 31% (129% vs. 98%). Even the 400 mm^2 distribution gives an average validation in apex displacement of 65%, despite a pressure field intensity equal to 25% of the one imposed by the sharpest distribution.

In all of the cases, the validation in bulge volume is much more consistent between the distributions, with just a modest reduction from the sharpest to the flattest. The sharpest distribution gives average percentage validations of 65% on Durostat® 400 and 85% on Creusabro® 8000, while the 200 mm^2 distribution gives 63% on Durostat® 400 and 81% on Creusabro® 8000; the flattest gives 52% on Durostat® 400 and 65% on Creusabro® 8000. The slight reduction in bulge volume is due to the reduction in local stress that causes the reduction in the maximum residual displacement at the apex, which has a minor effect on the total bulge volume.

The validation in slope at 50 mm from the apex in most of the cases increases from the sharpest to the intermediate distribution and then slightly decreases or remains constant for the flattest: the 100 mm^2 gives an average validation of 54% on Durostat® 400 and 85% on Creusabro® 8000, while the 200 mm^2 distribution gives 66% on Durostat® 400 and 97% on Creusabro® 8000. The 400 mm^2 gives 66% on Durostat® 400 and 90% on Creusabro® 8000. The increase and slight decrease with the extension of the loaded areas is explained by the opposite effects of reducing the load intensity, which decreases the bulge volume,

and reducing the average distance from the load application to the peripheral area where the slope is calculated, which tends to increase the peripheral deformation.

In terms of general bulge shape, the simulations tend to underestimate the half-depth diameter. The calculation of the bulge volumes shows that the simulations of the shots on Durostat® 400 estimate bulge volumes around 35% lower than the reality (Table 11), while on Creusabro® 8000 the estimation is better, with just 15% of underestimation on average between the cases (Table 12). A difference in shape between the plate materials is also observed in terms of slope of the bulge at 50 mm from the apex, with a 46% underestimation on Durostat® 400 plates (Table 11) and a 15% underestimation on Creusabro® 8000 (Table 12), again on average between the cases. These differences are due to the simplification hypotheses introduced with the method, in particular with the hypothesis of a 90-degree deflection of the bullet debris, which is an ideal reference case that is closer to reality when the impact surface keeps its perfect planarity. In reality, after the impact surface gradually bulges, the debris are subjected to a slightly higher deflection angle, interacting on a gradually wider surface on the target. This results in a radial component of the impact force that increases the width of the bulge and a slight increase in the normal force due to the higher angle of deflection of the debris. This is confirmed by the fact that the estimation of the bulge volume and slope is significantly better on Creusabro® 8000 plates, which encounter more contained residual displacements compared to the Durostat® 400 ones, thanks to its higher hardness and tensile strength. This confirms that the proposed method is well suited for targets much harder than the bullets, which represents the interactions between bullets and a perfectly working ballistic protection.

Table 11. Validation comparisons for Durostat® 400. Validation percentages are calculated as numerical simulation results obtained for the 100 mm^2 distribution divided by the experimental results.

	SP	**HP**	**FMJ ***	**MONO**
Validation in Bulge Volume	64.22%	53.31%	31.69%	76.12%
Validation in Apex Displacement	108.90%	156.92%	63.47%	112.62%
Experimental Slope @ 50 mm	−2.00%	−2.00%	−4.00%	−2.00%
Numerical Slope @ 50 mm	−1.20%	−0.91%	−0.70%	−1.15%
Validation in Slope @ 50 mm	60.19%	45.26%	17.50%	57.43%

* Not compliant with bullet-splash hypotheses.

Table 12. Validation comparisons for Creusabro® 8000. Validation percentages are calculated as numerical simulation results obtained for the 100 mm^2 distribution divided by the experimental results.

	SP	**HP**	**FMJ ***	**MONO**
Validation in Bulge Volume	75.48%	74.98%	21.95%	105.05%
Validation in Apex Displacement	127.73%	125.00%	66.62%	141.36%
Experimental Slope @ 50 mm	−1.50%	−1.50%	−4.50%	−1.00%
Numerical Slope @ 50 mm	−1.22%	−0.90%	−0.39%	−1.13%
Validation in Slope @ 50 mm	81.11%	60.00%	8.69%	113.26%

* Not compliant with bullet-splash hypotheses.

5. Conclusions

The study verified the effectiveness of the proposed simplified formula to estimate the load history due to bullet-splash in predicting the resultant interaction forces due to semi-jacketed, full metal jacket and monolithic .308 Winchester bullets impacting on double 4 mm-thick plates of Durostat® 400 and Creusabro® 8000 hard steels.

The experimental analyses reported that the SP, HP and MONO impacts were compliant with the bullet-splash theory, while both the FMJ cases failed to meet the theoretical hypotheses due to partial penetration of the target and partial fragmentation. None of the targets were fully penetrated.

The validation of the method was performed by comparing the experimental results, in terms of fields of residual displacement measured on the impacted plates, with the results of finite element explicit simulations to predict the residual deformations of the plates subjected to the load histories estimated according to the proposed theory. Sensitivity tests were conducted to verify the influence of the extension of the load distribution on the numerical results.

The validation in terms of residual displacements at the apex confirm the effectiveness of the method for all the shots fully compliant with the bullet-splash hypotheses (SP, HP, MONO). On the contrary, the simulations applying the load histories estimated for the FMJ bullets significantly underestimated the residual deformation fields, confirming that the effectiveness of method strictly depends on the validation of its theoretical hypotheses.

The validation in terms of bulge volume and slope at 50 mm from the apex of the bulges shows an underestimation of the overall residual deformation fields which has been related to the strength of the target: the more the target is deformed under the normal impact forces, the more the debris must be deflected, therefore probably resulting in a wider bulge than expected by considering only a 90-degree deflection as the method hypothesizes. This suggests a possible improvement and generalization of the formula to take into account deflection angles higher than 90 degrees, depending on the specific experimental evidence.

The sensitivity tests conducted to check the effects of the load distributions on the deformation fields demonstrate that even varying the area (or intensity) by two or four times only causes local effects, within 25 to 35 mm from the apex, while the bulge volume and the slope at 50 mm are just slightly influenced. It is worth noting that the results confirm that the two sharpest distributions (100 mm^2 and 200 mm^2) are the most representative, with validations in terms of apex displacements between 82% and 157%. These two distributions were identified as the range of areas subjected to mostly compressive interactions according to the marks left on the plates; this suggests that an equivalent application area could be effectively identified in this range for all the test cases. The consistency of the validation percentages for different bullets with significantly different mechanical and geometrical characteristics further confirms that the real space distribution of the pressure fields has neglectable effects, and therefore the resultant load history approach is appropriate for the purpose of the study.

All the evidence suggests that the method could be properly applied to the assessment of structural systems subjected to ballistic impacts, provided that previous experimental ballistic tests have been analyzed and demonstrated that the target surface is able to completely fragment and deflect the impactor without allowing any penetration. In case of significant deformation of the impact surface, the results suggest that the method should be applied more carefully, with conservative safety margins to be assessed considering the specific outcomes of the experimental tests.

Further developments of the research should therefore investigate the effects of high deflection angles and the influence of the debris dimensions on the intensity of the impulses, with the ultimate goal of identifying possible simplified procedures to generalize the load history approach and to allow the parsimonious simulation of a wider range of ballistic impacts causing partial penetrations and fragmentations or high deformation of the target.

Author Contributions: R.A. and M.Q. conceived the method and conducted all the numerical analyses. A.C. and I.C. conducted the experimental analyses. F.B. supervised the metallurgical characterization of the plates. M.V.B. leads the project. All authors have read and agreed to the published version of the manuscript.

Funding: This research received no external funding.

Informed Consent Statement: The study did not involve humans.

Data Availability Statement: The data presented in this study are available on request from the corresponding author.

Acknowledgments: The ballistic tests were conducted at the shooting range of Fombio (Lodi, Italy) belonging to the Italian national shooting range network (Tiri a Segno Nazionali/TSN); the shots were taken by Giorgio Prandini. A special thanks from the authors is due to Prandini and the whole staff for the invaluable support, expertise, and patience.

Conflicts of Interest: The authors declare no conflict of interest.

References

1. Chang, J.M.; Tyan, T.; El-Bkaily, M.; Cheng, J.; Marpu, A.; Zeng, Q.; Santini, J. Implicit and Explicit Finite Element Methods for Crash Safety Analysis. *SAE Tech. Pap.* **2007**, *116*, 1025–1037. [CrossRef]
2. Jackson, K.E.; Fasanella, E.L.; Boitnott, R.L.; Lyle, K.H. *Full-Scale Crash Test and Finite Element Simulation of a Composite Prototype Helicopter*; National Aeronautics and Space Administration: Washington, DC, USA, 2003; p. 121.
3. Mason, B.H.; Warren, J.E. Finite Element Simulation of Three Full-Scale Crash Tests for Cessna 172 Aircraft. In Proceedings of the 58th AIAA/ASCE/AHS/ASC Structures, Structural Dynamics, and Materials Conference, Grapevine, TX, USA, 9–13 January 2017; pp. 1–22. [CrossRef]
4. Lumassi, D.; Manes, A.; Giglio, M. Protection Effect on a Ballistic Impact of NATO 7.62 Ball Bullet into Helicopter Drive Shaft: Numerical Simulation. *Appl. Mech. Mater.* **2011**, *82*, 710–715. [CrossRef]
5. Andreotti, R.; Leggeri, V.; Casaroli, A.; Quercia, M.; Bettin, C.; Zanella, M.; Boniardi, M.V. A Simplified Constitutive Model for a SEBS Gel Muscle Simulant—Development and Experimental Validation for Finite Elements Simulations of Handgun and Rifle Ballistic Impacts. *Frat. Integrita Strutt.* **2022**, *16*, 176–197. [CrossRef]
6. Bhatnagar, A. *Lightweight Ballistic Composites*; Bhatnagar, A., Ed.; Elsevier: Amsterdam, The Netherlands, 2016; ISBN 9780081004067.
7. Parker, S.P. Bullet Splash. Available online: https://encyclopedia2.thefreedictionary.com/bullet+splash (accessed on 29 May 2021).
8. Edgerton, H.E.; Jussim, E.; Kayafas, G. Stopping Time: The Photographs of Harold Edgerton. Available online: https://www.metmuseum.org/art/collection/search/281953 (accessed on 28 May 2021).
9. Andreotti, R.; Abate, S.; Casaroli, A.; Quercia, M.; Fossati, R.; Boniardi, M.V. A Simplified Ale Model for Finite Element Simulation of Ballistic Impacts with Bullet Splash—Development and Experimental Validation. *Frat. Integrita Strutt.* **2021**, *15*, 223–245. [CrossRef]
10. Andreotti, R.; Casaroli, A.; Quercia, M.; Boniardi, M.V. A Simplified Formula to Estimate the Load History Due to Ballistic Impacts with Bullet Splash. Development and Validation for Finite Element Simulation of 9 × 21 mm Full Metal Jacket Bullets. *Frat. Integrita Strutt.* **2022**, *16*, 602–612. [CrossRef]
11. Andreotti, R.; Casaroli, A.; Quercia, M.; Boniardi, M.V. *International Conference on Structural Integrity and Durability 2022—Book of Abstracts*, 6th ed.; Bozic, Z., Schmauder, S., Vrdoljak, M., Eds.; University of Zagreb Faculty of Mechanical Engineering and Naval Architecture: Dubrovnik, Croatia, 2022.
12. Andreotti, R.; Quercia, M.; Casaroli, A.; Boniardi, M. V Numerical Estimation of the Load History Due to Ballistic Impacts with Bullet-Splash. Parsimonious Modeling and Experimental Validation for Monolithic. 308 Rifle Bullets. Submitted. In Proceedings of the 6th International Conference on Structural Integrity and Durability 2022—Procedia Structural Integrity, Dubrovnik, Croatia, 19–23 September 2022; Elsevier: Amsterdam, The Netherlands, 2022.
13. Studnicki, A.; Szajnar, J. Investigation of Wear Resistant of Low-Alloyed and Chromium Cast Steel. *Arch. Foundry Eng.* **2012**, *12*, 79–84. [CrossRef]
14. Zemlik, M.; Konat, Ł.; Napiórkowski, J. Comparative Analysis of the Influence of Chemical Composition and Microstructure on the Abrasive Wear of High-Strength Steels. *Materials* **2022**, *15*, 5083. [CrossRef] [PubMed]
15. Wesling, V.; Reiter, R.; Müller, T. Hydroabrasive Wear on High Carbide Infiltration Materials. *IOP Conf. Ser. Mater. Sci. Eng.* **2019**, *480*, 012030. [CrossRef]
16. Teker, T.; Günes, A. Microstructure and Mechanical Properties of AISI 304/DUROSTAT 500 Steel Double-Sided TIG Welds. *Mater. Test.* **2022**, *64*, 1162–1171. [CrossRef]
17. Bleck, W.; Guo, X.; Ma, Y. The TRIP Effect and Its Application in Cold Formable Sheet Steels. *Steel Res. Int.* **2017**, *88*, 1700218. [CrossRef]
18. Berrahmoune, M.; Berveiller, S.; Inal, K.; Moulin, A.; Patoor, E. Analysis of the Martensitic Transformation at Various Scales in TRIP Steel. *Mater. Sci. Eng. A* **2004**, *378*, 304–307. [CrossRef]
19. Newby, J.; Mills, K. *American Society for Metals. Metallography and Microstructures*; Vander Voort, G.F., Ed.; ASM International: Almere, The Netherlands, 2004; Volume 9, ISBN 978-1-62708-177-1.
20. *ISO 6892-1:2019(EN)*; ISO 6892-1:2019(EN) Metallic Materials—Tensile Testing—Part 1: Method of Test at Room Temperature. ISO: Geneva, Switzerland, 2019. Available online: https://www.iso.org/obp/ui/#iso:std:iso:6892:-1:ed-3:v1:en (accessed on 6 March 2023).
21. Leng, Y. *Materials Characterization*; ASM International: Almere, The Netherlands, 2019; Volume 2, ISBN 978-1-62708-213-6.
22. Fuller, P.W.W. Some Highlights in the History of High-Speed Photography and Photonics as Applied to Ballistics. In *High-Pressure Shock Compression of Solids VIII*; Springer: Berlin/Heidelberg, Germany, 2005; pp. 251–298.

23. Ma, H.; Chen, P.; Shi, H.; Zhao, J. Measurement of Bullet Velocity Parameter from High-Speed Sequential Images. *J. Phys. Conf. Ser.* **2021**, *1827*, 012027. [CrossRef]
24. LSTC LS-DYNA®. *Keyword User's Manual—Volume 1*; Version R8.0; LSTC LS-DYNA: Livermore, CA, USA, 2015; Volume I, ISBN 9254492507.
25. Pijpers, R.J.M.; Slot, H.M. Friction Coefficients for Steel to Steel Contact Surfaces in Air and Seawater. *J. Phys. Conf. Ser.* **2020**, *1669*, 012002. [CrossRef]
26. LSTC LS-DYNA®. *R8.0 Keyword User's Manual—Volume II—Material Models, Version R8.0*; LSTC LS-DYNA: Livermore, CA, USA, 2015; Volume II, ISBN 9254492507.
27. Boyce, B.L.; Crenshaw, T.B.; Dilmore, M.F. *The Strain-Rate Sensitivity of High-Strength High-Toughness Steels*; Sandia National Laboratories: Albuquerque, NM, USA; Livermore, CA, USA, 2007.

materials

MDPI

Article

Diffusion and Interdiffusion Study at Al- and O-Terminated Al_2O_3/AlSi12 Interface Using Molecular Dynamics Simulations

Masoud Tahani [1,2,*], Eligiusz Postek [2] and Tomasz Sadowski [3,*]

[1] Department of Mechanical Engineering, Ferdowsi University of Mashhad, Mashhad 91779-48978, Iran
[2] Department of Information and Computational Science, Institute of Fundamental Technological Research, Polish Academy of Sciences, Pawińskiego 5B, 02-106 Warsaw, Poland; epostek@ippt.pan.pl
[3] Department of Solid Mechanics, Lublin University of Technology, 20-618 Lublin, Poland
* Correspondence: mtahani@um.ac.ir or mtahani@ippt.pan.pl (M.T.); t.sadowski@pollub.pl (T.S.)

Abstract: The equivalent characteristics of the materials' interfaces are known to impact the overall mechanical properties of ceramic–metal composites significantly. One technological method that has been suggested is raising the temperature of the liquid metal to improve the weak wettability of ceramic particles with liquid metals. Therefore, as the first step, it is necessary to produce the diffusion zone at the interface by heating the system and maintaining it at a preset temperature to develop the cohesive zone model of the interface using mode I and mode II fracture tests. This study uses the molecular dynamics method to study the interdiffusion at the interface of α-Al_2O_3/AlSi12. The hexagonal crystal structure of aluminum oxide with the Al- and O-terminated interfaces with AlSi12 are considered. A single diffusion couple is used for each system to determine the average main and cross ternary interdiffusion coefficients. In addition, the effect of temperature and the termination type on the interdiffusion coefficients is examined. The results demonstrate that the thickness of the interdiffusion zone is proportional to the annealing temperature and time, and Al- and O-terminated interfaces exhibit similar interdiffusion properties.

Keywords: self-diffusion; interdiffusion; diffusion coefficient; Al_2O_3/AlSi12 interface; molecular dynamics

Citation: Tahani, M.; Postek, E.; Sadowski, T. Diffusion and Interdiffusion Study at Al- and O-Terminated Al_2O_3/AlSi12 Interface Using Molecular Dynamics Simulations. *Materials* **2023**, *16*, 4324. https://doi.org/10.3390/ma16124324

Academic Editors: Angelo Marcello Tarantino, Carmelo Majorana, Raimondo Luciano and Michele Bacciocchi

Received: 28 April 2023
Revised: 2 June 2023
Accepted: 7 June 2023
Published: 12 June 2023

1. Introduction

Metal matrix composites (MMCs) are increasingly employed in the automotive, aerospace, and biomedical industries owing to their exceptional specific strength, high stiffness, and remarkable wear resistance [1]. These composites commonly employ aluminum, titanium, or magnesium as matrix materials, while alumina, silicon carbide, or boron carbide are often utilized as reinforcing elements [2,3].

Aluminum oxide (Al_2O_3) is a versatile and widely used ceramic material with various applications due to its excellent properties and attractive price [4]. Some common uses of aluminum oxide include abrasive material used in grinding and polishing tools, high-temperature environment applications such as furnace linings and refractory materials, electrical insulators, dental and medical applications, and as a filter medium [3,5].

The eutectic aluminum–silicon (AlSi12) alloys, widely used in the transportation industry [6] and have high specific properties and good castability, can replace the pure Al metal matrix. AlSi12 alloy is an aluminum alloy that contains 12 wt.% silicon. It is commonly used in casting applications due to its good fluidity and ability to produce castings with fine details [6]. The high silicon content in the alloy also provides it with excellent thermal properties, making it suitable for use in engine parts and other high-temperature applications [2]. This alloy also has a low density and good corrosion resistance, which makes it useful in the aerospace and automotive industries.

Metal–ceramic composites may exhibit improved wear resistance and strength properties compared to the individual materials and can be used in various high-temperature

applications. For example, a composite of Al_2O_3 and AlSi12 alloy can be made by various techniques such as powder metallurgy [6,7], hot pressing, squeeze casting [7], or infiltration [1,7–10]. Interpenetrating phase composites (IPCs) are novel materials with possibly enhanced characteristics compared with traditional composites with discontinuous particles, whiskers, or short fibers [11–15]. The properties and performance of the composite can be tailored by the processing conditions, relative proportions of the two materials, microstructure, proportion of the components, and the interface's properties.

This study investigates the use of α-Al_2O_3 reinforcement in the AlSi12 metal alloy matrix. The Al_2O_3/AlSi12 composite has demonstrated very good wear and abrasion resistance [16,17]. Therefore, this composite material has the potential to be used in brake disks in the automotive industry [7]. The mechanical characteristics of the interface constituents and the nature of the interface determine the general mechanical and failure behavior of MMCs [18–20]. To this end, the interface attributes in MMCs must be thoroughly investigated. Diffusion causes the interface between phases to exhibit a fuzzy region. Hence, the primary step toward deriving the cohesive zone model of the interface is to investigate the diffusion between the two phases.

Oishi and Kingery [21] first measured oxygen self-diffusion in single and polycrystalline Al_2O_3 in 1960. They studied diffusion in temperatures above 1650 °C and observed enhanced diffusion for the polycrystalline specimens. Lagerlof et al. [22] also deduced oxygen self-diffusion coefficients using observations of the shrinking of tiny prismatic dislocation loops in sapphire crystals subjected to prior distortion at a temperature of 1400 °C. The diffusion coefficient was determined, and it was assumed that oxygen lattice diffusion was smaller than aluminum lattice diffusion. Paladino and Kingery [23] determined the self-diffusion coefficient of aluminum in coarse-grain polycrystalline aluminum oxide using aluminium-26 as a tracer in the temperature range of 1670–1905 °C. They found that the diffusivity of aluminum ions is greater than oxygen ions.

Furthermore, Gall et al. [24] measured aluminum self-diffusion in single-crystal α-Al_2O_3 using aluminum-26 as a radioactive tracer in the temperature range of 1540–1697 °C. They obtained very different conclusions regarding the diffusion coefficients compared to Paladino and Kingery [23]. A review of the major diffusion processes in α-Al_2O_3, including aluminum and oxygen lattice diffusion, oxygen grain boundary diffusion, and pipe diffusion, was presented by Heuer [25]. Knowledge regarding the diffusion of aluminum and oxygen in aluminum oxide was found to be insufficient. Using the density functional theory, Milas et al. [26] investigated the diffusion of Al, O, Pt, Hf, and Y atoms on the α-Al_2O_3(0001) surface to study the diffusion mechanisms at the alumina grain boundaries in thermal barrier coatings. They discovered that the Al diffusion is significantly lower than the O diffusion barrier. The literature on the self-diffusion of single crystals and the impurity diffusion of some significant elements in alumina was reviewed by Pelleg [27]. Moreover, they discussed grain boundary diffusion and poly-crystalline alumina diffusion.

Unfortunately, the wettability of ceramic particles with liquid aluminum alloys is often weak. Many technological procedures have been suggested to improve the wetting of ceramic by liquid metal. These include raising the temperature of the metal liquid, pretreatment of ceramic particles or fibers, coating the ceramics, and incorporating some surface-active elements into the matrix. To the authors' knowledge, no previous investigations have been conducted on the diffusion behavior of the α-Al_2O_3/AlSi12 diffusion couple. Therefore, this study aims to explore the self-diffusion and interdiffusion phenomena at the interface by employing the molecular dynamics (MD) method by increasing the system's temperature to the specified level. The Al- and O-terminated interfaces of α-Al_2O_3 with AlSi12 are considered. The influence of annealing temperature, annealing duration, and type of termination at the interface on the diffusion zone and interdiffusion coefficients are studied.

2. Modeling Method and Simulation Technique

Diffusion involves the migration of atoms or molecules from a region of higher concentration to a region of lower concentration. Atoms can diffuse across the interface, resulting in the movement of atoms between the two phases. The diffusion rate depends on several factors, including the temperature, chemical composition of the two materials, and the interface between the two phases. At high temperatures, the diffusion rate will be faster, and the atoms will have more energy to move through the material. It is intended to investigate the effect of raising the temperature on the diffusion region and interdiffusion coefficients at the α-Al_2O_3/AlSi12 interface.

The molecular dynamics method can study basic processes such as diffusion by using Newton's second law to calculate the acceleration of atoms by describing atomic interactions through interatomic potentials. In this study, MD simulations are performed utilizing the open-source MD program LAMMPS version 23Jun2022 (large-scale atomic/molecular massively parallel simulator) [28], and the OVITO version 3.8.4 (open visualization tool) software [29] is utilized to visualize the atomic structure's evolution. The interatomic potential must be precisely quantified because an interatomic potential energy model typically represents atomic interactions. Experimental data or ab initio calculations, such as cohesive energy and elastic modulus, can be used to determine the model parameters. The following section explores the interatomic potentials attributed to aluminum oxide, aluminum, silicon, and the interface.

2.1. Potential Functions

In the Al_2O_3/AlSi12 system, several atomic interactions are possible and should be taken into account during simulations. The atomic interactions between Al particles in an fcc crystal structure differ significantly from those between aluminum oxide ceramic particles. Metal atoms have electron clouds that determine the strength of their bonds, whereas ionic bonding is the primary factor in ceramics. The interface between metal and ceramic, where the atoms tend to create bonds between two dissimilar structures, introduces additional complexity.

The third-generation charge-optimized many-body potential (COMB3) [30] is a type of interatomic potential that can be used to describe interactions between atoms in aluminum–oxygen systems. The COMB3 potential uses a combination of pair potentials and electron density functions to describe the atomic interactions. The potential is fitted to experimental data and ab initio calculations. It has been shown to reproduce a wide range of properties of aluminum–oxygen systems, including the lattice constant, elastic constants, and the deformation of Al and Al_2O_3 under tensile loading. The total energy per atom for the Al-O system, with a charge of q at position r, in the COMB3 potential can be expressed as [30]:

$$U_{tot}(r,\ q) = U_{es}(q,\ r) + U_{short}(q,\ r) + U_{vdW}(r) + U_{corr}(r) \tag{1}$$

where U_{es} denotes the energy required to create an atom's charge, as well as the energies involved in charge–charge interactions, charge–nuclear interactions, and polarizability. Furthermore, U_{short} is the energy of pairwise attractive and repulsive functions, U_{vdW} is long-range van der Waals interactions, and U_{corr} is the correction terms employed to adjust energies associated with specific angles outside the bond order terms.

The Tersoff potential [31], an empirical function composed of two-body terms, is employed for silicon–oxygen interactions. The bonding between atoms i and j in the many-body Tersoff potential can be expressed as:

$$V_{ij} = f_C(r_{ij})\left[f_R(r_{ij}) + b_{ij}f_A(r_{ij})\right] \tag{2}$$

where $f_R(r_{ij})$, $f_A(r_{ij})$, and $f_C(r_{ij})$ are repulsive, attractive, and cut-off potential functions, r_{ij} is the atomic bond length between atom i and j, and b_{ij} is a function that adjusts the attractive interaction, respectively.

The ab initio data gathered by Zhao et al. [32] are consistent with the Morse potential, which best represents aluminum–silicon interactions. The Morse potential function is defined as:

$$V = D_0\left[e^{-2\alpha(r-r_0)} - 2e^{-\alpha(r-r_0)}\right] \quad (3)$$

where D_0, α, r, and r_0 represent the well depth of the potential, the width of the potential, the distance between atoms, and the equilibrium bond length, respectively. The Morse potential with parameters D_0 = 0.4824 eV, α = 1.322 1/Å, and r_0 = 2.92 Å [26] is employed in this study for aluminum–silicon interactions.

The elastic constants of α-Al_2O_3 are determined with previously mentioned potential functions and then compared with the experimental [33], MD simulations [34], and innovative integration of metadynamics and kinetic Monte Carlo simulation techniques ref. [35] in Table 1. The same results for AlSi12 are also presented in this table. The lattice parameters of hexagonal α-Al_2O_3 are $a = b$ = 4.759 Å, c = 12.991 Å, $\alpha = \beta = 90^o$, and $\gamma = 120^o$, and the lattice constant of fcc Al is 4.0495. AlSi12 single-crystal is formed by substituting 12 wt.% of Al atoms with Si atoms. The linear elastic constants C_{ij} are obtained at zero temperature by analyzing the stress–strain relation $C_{ij} = \partial\sigma_{ij}/\partial\varepsilon_{ij}$, where σ_{ij} and ε_{ij} are, respectively, the stress and strain components. General decent agreements between the present results and those of other investigators are observed in Table 1. Consequently, the potential functions utilized here demonstrate an accurate simulation of the interactions between atoms.

Table 1. The elastic constants determined through the current MD simulations and their comparison with values reported by other researchers.

Material	Method	C_{11} (GPa)	C_{12} (GPa)	C_{13} (GPa)	C_{33} (GPa)	C_{44} (GPa)	C_{66} (GPa)
α-Al_2O_3	Present	510	130	138	518	138	165
	Experiment [33]	497	164	111	498	147	167
	MD [34]	537	180	106	509	130	179
	Monte Carlo simulation [35]	666	269	192	520	158	-
AlSi12	Present	268	134	154	214	108	105

2.2. Molecular Dynamics Model

According to high-resolution transmission electron microscopy, it has been observed that the predominant orientation relationship at the Al_2O_3/Al interface is characterized by the parallel alignment of the Al(111) plane and the Al_2O_3(0001) basal plane [36]. Pilania et al. [37] also studied coherent and semi-coherent α-Al_2O_3(0001)/Al(111) interfaces with a mixed metallic–ionic atomistic model using MD simulations. Therefore, in this study, the lattice orientation alignment $(0001)[2\,\bar{1}\,\bar{1}\,0]_{\alpha-Al_2O_3} \parallel (111)[\bar{1}\,\bar{1}\,2]_{AlSi12}$ is taken into account according to the research of other investigators.

The current model comprises a bilayer nanocomposite composed of α-Al_2O_3 and AlSi12. The initial α-Al_2O_3/AlSi12 interface shown in Figure 1 is considered a single crystal of AlSi12 at the bottom and a single crystal of α-Al_2O_3 at the top with an initial gap of 2.0 Å which closely approximates the equilibrium atomic distance at the interface. To examine the impact of alumina terminations on diffusion, two configurations are modeled at the interface: one with Al-termination and another with O-termination. These cases allow a comprehensive exploration to occur of how different terminations affect diffusion behavior. The MD model has a typical size of about 119 × 58 × 184 Å, containing a total of 109,986 atoms.

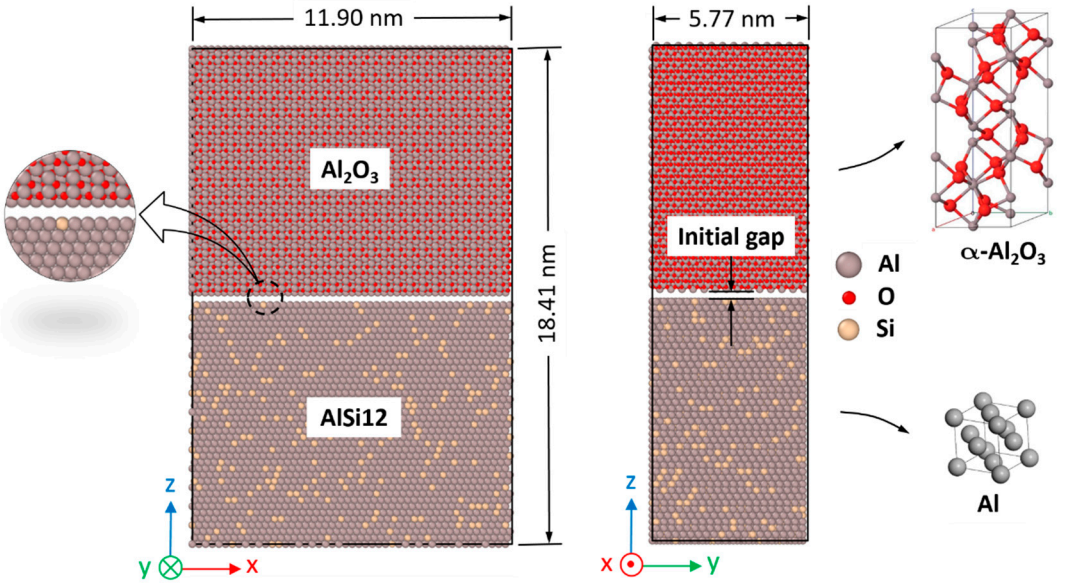

Figure 1. Model of the Al-terminated α-Al_2O_3/AlSi12 interface designed for the MD analyses.

The geometric arrangement of atoms is optimized through the utilization of the conjugate gradient (CG) energy minimization method. First, the *NVT* canonical ensemble (constant number of particles *N*, volume *V*, and temperature *T*) at a constant temperature of 1200 K is imposed on the sample for 10 ps. Second, the *NPT* ensemble (constant number of particles *N*, pressure *P*, and temperature *T*) at zero pressure and a constant temperature of 1200 K is used for 15 ps to regulate the volume and achieve relaxation in the assembled interface system. Subsequently, the sample is subjected to heating at a heating rate of 10 K/ps until it reaches a preset temperature. Finally, the temperature is held constant at the specified value for a duration of 2.0 ns to analyze interdiffusion while monitoring and recording the atomic movements throughout this period. All processes are conducted using the *NPT* ensemble at zero pressure, employing a time-step of 0.2 fs. The simulations are performed at 1500, 1600, 1800, and 2000 K temperatures. Periodic boundary conditions are implemented for the sample in all three directions.

3. Results and Discussion

To study the diffusion properties of the α-Al_2O_3/Al interface, the system is heated to a predetermined temperature and maintained there for 2.0 ns. The development of the interface diffusion for the Al-terminated Al_2O_3/AlSi12 interface after heating it to 2000 K is illustrated in Figure 2. The initial configuration illustrates the sharp interface between Al_2O_3 and AlSi12, considering an initial gap of 2 Å. Furthermore, after maintaining it for 2.0 ns at 2000 K, the system configuration represents the local movement of atoms and the creation of a diffusion zone. The diffusion front is shown in this figure with a dashed line.

3.1. Self-Diffusion

The mean square displacements (MSDs) of Al, O, and Si atoms after maintaining the system for a duration of 2.0 ns at different temperatures of 1500, 1600, 1800, and 2000 K for the Al- and O-terminated α-Al_2O_3/AlSi12 diffusion couples are depicted in Table 2. This table presents the MSD values for Al atoms in α-Al_2O_3, Al atoms in AlSi12, and all Al atoms in the system. As expected, due to the difference in ceramic and metal atomic bonding, the Al atoms in α-Al_2O_3 have a significantly lower MSD than the Al atoms in AlSi12. It is also observed that the MSD of O atoms is smaller than the MSD of Al atoms in α-Al_2O_3. It is observed that the MSD of Al atoms is larger than the MSD of Si atoms, and the MSD of Si atoms is also larger than the MSD of O atoms.

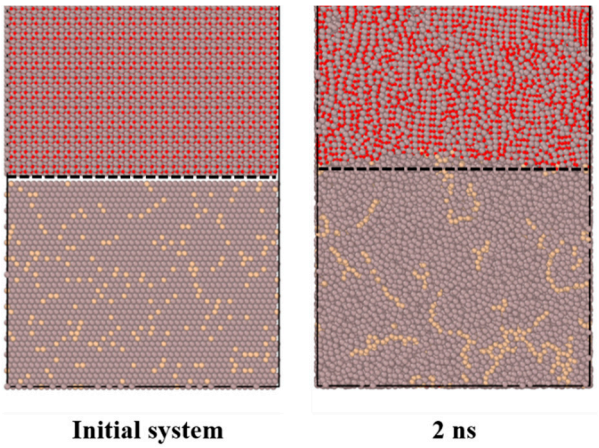

Figure 2. Cross-sections of the atomic configurations of the Al-terminated Al_2O_3/AlSi12 interface. The figure shows the initial atomic structure before relaxation, as well as the configuration after the system is held at 2000 K for 2.0 ns. The dashed line indicates the front of the diffusion region.

Table 2. Mean square displacement (nm^2) of Al, O, and Si atoms at different temperatures for the Al- and O-terminated α-Al_2O_3/AlSi12 diffusion couples.

Diffusion Couple	Temperature (K)	Atom				
		Al (Al_2O_3)	Al (AlSi12)	Al	O	Si
Al-terminated α-Al_2O_3/AlSi12	1500	0.65	24.95	13.46	0.35	2.22
	1600	0.84	32.26	17.45	0.37	2.25
	1800	1.26	47.45	25.51	0.41	2.31
	2000	1.70	63.29	34.01	0.47	2.36
O-terminated α-Al_2O_3/AlSi12	1500	0.50	25.11	13.57	0.34	2.34
	1600	0.64	32.26	17.58	0.38	2.36
	1800	1.04	46.98	25.42	0.45	2.40
	2000	1.67	62.34	33.63	0.50	2.46

The coefficients of self-diffusion for each atom type are obtained by analyzing the slope of the MSDs employing Einstein's relation [38]:

$$D_A = \lim_{t\to\infty} \frac{1}{N_A} \sum_{i=1}^{N_A} \frac{\left\langle \left| \mathbf{r}_i^A(t) - \mathbf{r}_i^A(0) \right|^2 \right\rangle}{6t} \quad (4)$$

where N_A represents the total number of atoms of type A, $\mathbf{r}_i^A$ denotes the position vector of the ith atom belonging to type A, and $\langle \cdots \rangle$ signifies the average calculated across all atoms of the same type. The activation energy Q and pre-exponential factor D_0 of atoms can be obtained by fitting the self-diffusion coefficients to the Arrhenius equation $D = D_0 \exp(-Q/RT)$. The Arrhenius plots of Al, O, and Si atoms for the Al- and O-terminated interfaces are illustrated in Figure 3. Similar to the MSD, Al atoms in Al_2O_3 have a significantly smaller self-diffusion coefficient than the Al atoms in AlSi12 because of the differences in atomic bonding between ceramic and metal. Additionally, the self-diffusion coefficient of O atoms is less pronounced than Al atoms in Al_2O_3. As can be seen, Al atoms have a higher self-diffusion coefficient than Si atoms, and Si atoms also have a higher self-diffusion coefficient than O atoms. Table 3 also displays the outcomes of the atoms' activation energies and pre-exponential factors.

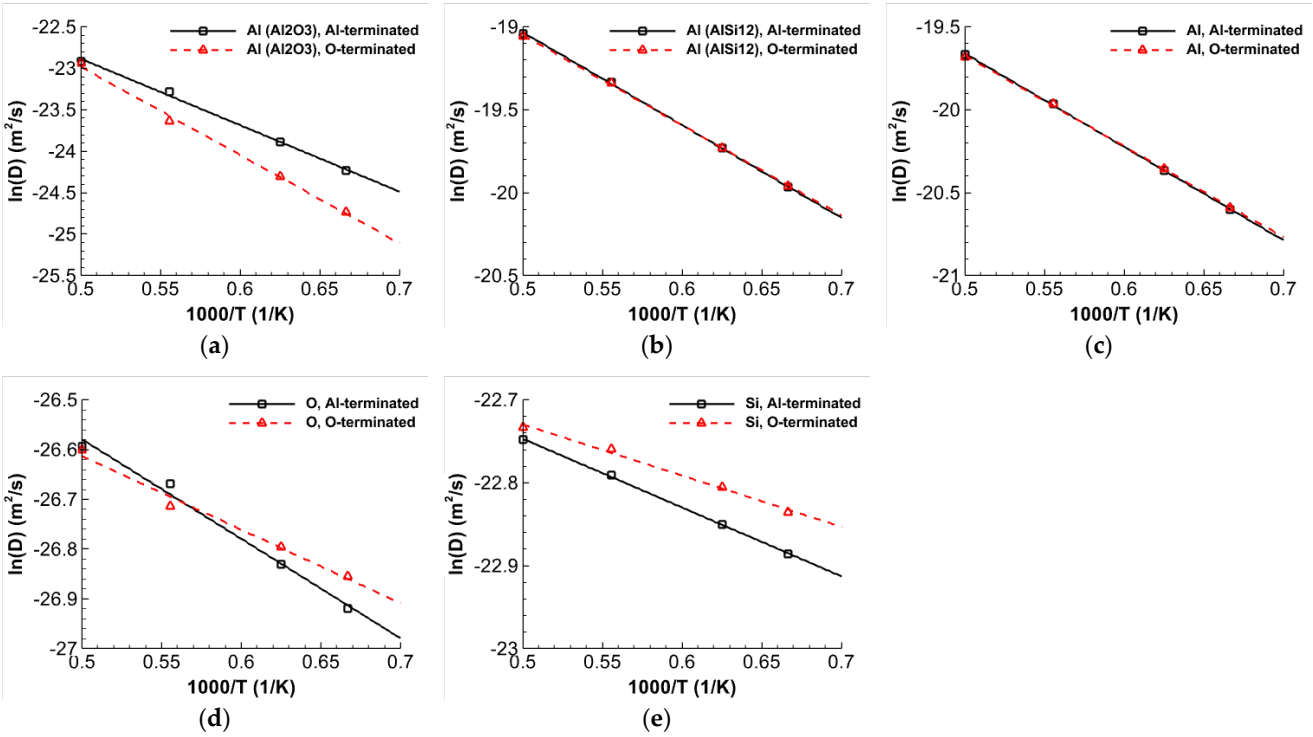

Figure 3. Plots of Arrhenius equation for Al, O, and Si atoms in the Al- and O-terminated α-Al_2O_3/AlSi12 interface. (**a**) Al in Al_2O_3, (**b**) Al in AlSi12, (**c**) Al, (**d**) O, and (**e**) Si atoms.

Table 3. Arrhenius parameters, D_0 and Q, for self-diffusion of Al, O, and Si atoms for Al- and C-terminated α-Al_2O_3/AlSi12 diffusion couples.

Atom	Al-Terminated		O-Terminated	
	Q (kJ/mol)	$D_0 \times 10^{-9}$ (m²/s)	Q (kJ/mol)	$D_0 \times 10^{-9}$ (m²/s)
Al (Al_2O_3)	66.39	6.32	88.15	21.37
Al (AlSi12)	46.56	89.13	45.22	80.82
Al	46.84	48.15	45.54	44.03
O	16.64	0.0078	12.30	0.0058
Si	6.89	0.200	5.14	0.183

3.2. Interdiffusion

The interdiffusion flux of an n-component system is described by the following Onsager's formulation [39,40] of Fick's law:

$$\widetilde{J}_i = -\sum_{j=1}^{n-1} \widetilde{D}_{ij}^{n} \frac{\partial C_j}{\partial z} \tag{5}$$

where $\widetilde{J}_i$, C_i, and $\partial C_i/\partial z$ are the interdiffusion flux, mole fraction, and concentration gradient of component i, respectively. Furthermore, $\widetilde{D}_{ij}^{n}$ is the interdiffusion coefficient. According to Equation (5), the interdiffusion behavior in a ternary system can be described by four independent interdiffusion coefficients: $\widetilde{D}_{11}^{3}$, $\widetilde{D}_{12}^{3}$, $\widetilde{D}_{21}^{3}$, and $\widetilde{D}_{22}^{3}$. The Boltzmann–Matano [41,42] method can determine the interdiffusion coefficients.

In the present research, the average interdiffusion coefficients are determined using the approach proposed by Dayananda and Sohn [41]. The average main interdiffusion coefficients (i.e., $\overline{\widetilde{D}}_{11}^{3}$ and $\overline{\widetilde{D}}_{22}^{3}$) and cross interdiffusion coefficients (i.e., $\overline{\widetilde{D}}_{12}^{3}$ and $\overline{\widetilde{D}}_{21}^{3}$) are evaluated by computing the atomic interdiffusion flux using only the single diffusion couple under study. The concentration curve is fitted using the Gaussian error function for

each component. The interested reader will find detailed explanations about the method in Refs. [42,43].

The variations in Al, Si, and O atom concentrations with respect to the z-coordinate, which is normal to the interface plane, are shown in Figure 4 for a quantitative analysis of the diffusion process in the Al-terminated α-Al_2O_3/Al interface. To obtain the concentration profiles, the diffusion couple is divided into thin slices with a thickness of 2.0 Å along the interface plane. The count of atoms for each type is determined within each slice. Figure 4 shows the initial concentration profiles before diffusion, and the profiles observed after keeping the system at 2000 K for a duration of 2.0 ns. A grey region also depicts the diffusion zone. The variations in atom concentrations for the O-terminated interface, which are not shown here for conciseness, indicate that the diffusion zones in the Al- and O-terminated systems are not significantly different.

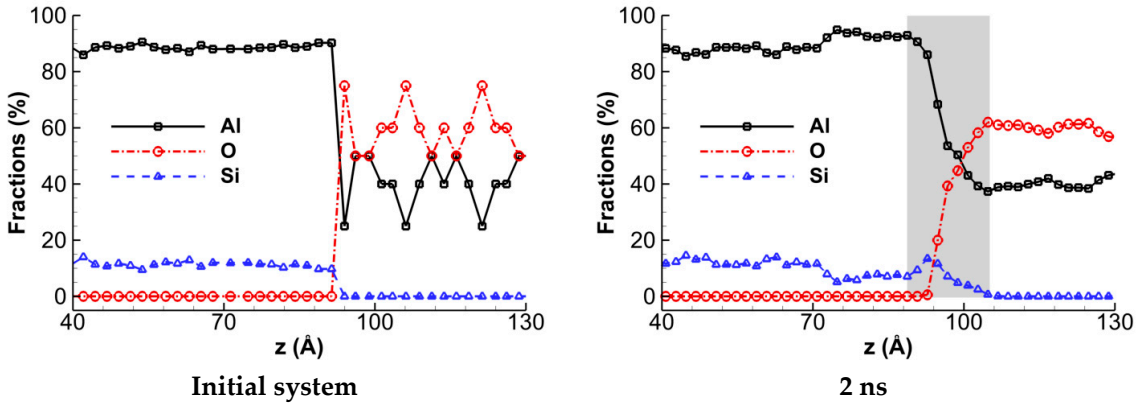

Figure 4. The variations in Al, Si, and O atom concentrations along the z-axis during interdiffusion of the Al-terminated α-Al_2O_3/AlSi12 interface. The initial system before relaxation and after a 2.0 ns maintenance at 2000 K are illustrated. The diffusion zone is depicted by the gray region.

Figure 5 illustrates the variations in the interdiffusion flux $\widetilde{J}$ and $\widetilde{J}(z-z_0)$ for the Al- and O-terminated α-Al_2O_3/AlSi12 diffusion couples after keeping the systems at 2000 K for a duration of 2.0 ns. The position of the Matano plane, denoted by z_0, is also shown in Figure 5 by a vertical dashed line. It is observed that the Matano plane corresponds to the point of highest interdiffusion flux. The independent variables are arbitrarily chosen as the Al and O atoms, while the Si atom is assigned as the dependent variable. The profile variations in the two diffusion couples appear to be very similar. However, it is worth noting that the maximum interdiffusion flux of the Al-terminated interface is slightly higher than that of the O-terminated interface.

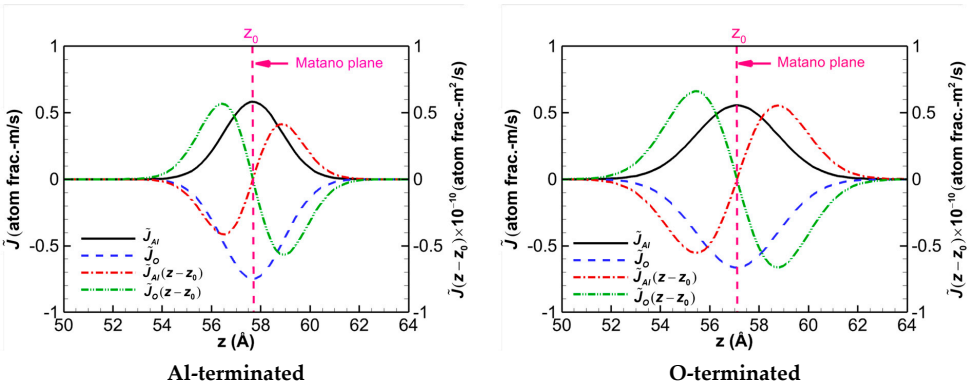

Figure 5. Interdiffusion flux $\widetilde{J}$ and $\widetilde{J}(z-z_0)$ for diffusion systems of the Al-terminated and O-terminated α-Al_2O_3/AlSi12 heated to 2000 K and kept at that temperature for a duration of 2 ns.

Table 4 presents the calculated average values of the main and cross ternary interdiffusion coefficients for the Al- and O-terminated α-Al_2O_3/AlSi12 diffusion couples. The diffusion couples are kept at annealing temperatures of 1500, 1600, 1800, and 2000 K for a duration of 2.0 ns. The coefficients are determined using the composition ranges on the lower and upper sides of the Matano plane. It is observed from Table 4 that the main interdiffusion coefficients increase as the annealing temperature increases, as expected. Furthermore, all cross ternary interdiffusion coefficients are significantly smaller, with at least four orders of magnitude lower than the main interdiffusion coefficients. Hence, the cross ternary interdiffusion coefficients do not significantly influence the current ternary systems. Moreover, based on the findings in this table, it is observed that the diffusivity of Si and O atoms shows a slight increase in the Al-terminated system compared to the O-terminated counterpart. However, generally speaking, there is no appreciable distinction between the average interdiffusion coefficients of the Al- and O-terminated systems.

Table 4. The average interdiffusion coefficients for the ternary systems on either side of the Matano plane. These values are determined after the system is maintained at the preset temperature for a duration of 2 ns.

Diffusion Couple	Temperature (K)	For Composition Range of the Lower Side of Matano Plane $\overline{\overline{D}}^{3}_{ij} \times 10^{-11}$ (m²/s)				For Composition Range of the Upper Side of Matano Plane $\overline{\overline{D}}^{3}_{ij} \times 10^{-11}$ (m²/s)			
		$\overline{\overline{D}}^{Si}_{AlAl}$	$\overline{\overline{D}}^{Si}_{AlO}$	$\overline{\overline{D}}^{Si}_{OAl}$	$\overline{\overline{D}}^{Si}_{OO}$	$\overline{\overline{D}}^{Si}_{AlAl}$	$\overline{\overline{D}}^{Si}_{AlO}$	$\overline{\overline{D}}^{Si}_{OAl}$	$\overline{\overline{D}}^{Si}_{OO}$
Al-terminated α-Al_2O_3/AlSi12	1500	0.489	-4.2×10^{-7}	1.8×10^{-5}	0.584	0.489	2.2×10^{-7}	-2.0×10^{-5}	0.584
	1600	0.518	-6.3×10^{-7}	8.4×10^{-6}	0.623	0.518	5.7×10^{-7}	-9.3×10^{-6}	0.623
	1800	0.608	-7.9×10^{-7}	6.1×10^{-7}	0.845	0.608	-1.2×10^{-6}	-1.9×10^{-6}	0.845
	2000	0.753	1.3×10^{-7}	-6.4×10^{-6}	1.307	0.753	-2.5×10^{-7}	2.8×10^{-6}	1.307
O-terminated α-Al_2O_3/AlSi12	1500	0.429	2.1×10^{-7}	6.3×10^{-6}	0.489	0.429	2.8×10^{-7}	4.1×10^{-6}	0.489
	1600	0.452	-5.4×10^{-7}	-1.3×10^{-6}	0.531	0.452	7.6×10^{-7}	3.8×10^{-6}	0.531
	1800	0.527	-4.9×10^{-7}	-6.9×10^{-6}	0.562	0.527	1.4×10^{-6}	1.7×10^{-6}	0.685
	2000	0.696	4.9×10^{-5}	2.9×10^{-4}	1.012	0.696	-1.3×10^{-4}	9.9×10^{-5}	1.012

4. Conclusions

A molecular dynamics method was employed to investigate atomistic evolutions during the interdiffusion at the α-Al_2O_3/AlSi12 interface. The self-diffusion and interdiffusion coefficients were assessed at 1500, 1600, 1800, and 2000 K annealing temperatures for different diffusion couples. Based on the findings of this study, the following conclusions can be made:

- The self-diffusion coefficient for Al atoms in Al_2O_3 is higher compared to O atoms.
- The average main and cross ternary interdiffusion coefficients were determined for the first time for the Al- and O-terminated Al_2O_3/AlSi12 systems utilizing the concentration profiles of atoms during diffusion.
- The diffusion zone and interdiffusion coefficients increased with the progressive elevation of the annealing temperature and duration.
- No notable distinction of ternary interdiffusion coefficients was observed between the Al- and O-terminated interfaces.

Future studies may utilize the samples after diffusion and cooling to determine the effective mechanical properties of the Al_2O_3/AlSi12 interface through the cohesive zone model and, therefore, the mechanical properties of the MMC.

Author Contributions: All authors contributed to the study's conception and design. Data collection and analysis were performed by M.T. The first draft of the manuscript was written by M.T. and all authors commented on previous versions of the manuscript. The final manuscript was approved by all authors. All authors have read and agreed to the published version of the manuscript.

Funding: This research was funded by the Polish National Agency for Academic Exchange (NAWA) under grant number [BPN/ULM/2021/1/00115/U/DRAFT/00001]. National Science Center, Poland, grant No. UMO 2019/33/B/ST8/01263.

Institutional Review Board Statement: Not applicable.

Informed Consent Statement: Not applicable.

Data Availability Statement: Data available on request due to restrictions, e.g., privacy.

Acknowledgments: E.P. and T.S. acknowledge the National Science Center, Poland, grant No. UMO 2019/33/B/ST8/01263. The calculations were performed at PLGrid national facilities—Academic Computer Centre Cyfronet in Krakow, Academic Computer Centre in Gdańsk, and Interdisciplinary Centre for Mathematical and Computational Modelling, University of Warsaw, Poland.

Conflicts of Interest: The authors declare no conflict of interest.

References

1. Kaczmar, J.W.; Pietrzak, K.; Włosiński, W. The production and application of metal matrix composite materials. *J. Mater. Process. Technol.* **2000**, *106*, 58–67. [CrossRef]
2. Kainer, K.U. *Metal Matrix Composites: Custom-Made Materials for Automotive and Aerospace Engineering*; Wiley: Hoboken, NJ, USA, 2006.
3. Rawal, S.P. Metal-matrix composites for space applications. *JOM* **2001**, *53*, 14–17. [CrossRef]
4. Hermansen, A.E. *Aluminium Oxide: Structure, Production and Applications*; Nova Science Publishers Inc.: New York, NY, USA, 2020.
5. Francis, N.; Leonard, M.; John Baptist, K. Novel applications of aluminium metal matrix composites. In *Aluminium Alloys and Composites*; Kavian Omar, C., Ed.; IntechOpen: Rijeka, Croatia, 2019; Chapter 5.
6. Wang, Z.; Prashanth, K.G.; Chaubey, A.K.; Löber, L.; Schimansky, F.P.; Pyczak, F.; Zhang, W.W.; Scudino, S.; Eckert, J. Tensile properties of Al–12Si matrix composites reinforced with Ti–Al-based particles. *J. Alloys Compd.* **2015**, *630*, 256–259. [CrossRef]
7. Maj, J.; Węglewski, W.; Bochenek, K.; Rogal, Ł.; Woźniacka, S.; Basista, M. A comparative study of mechanical properties, thermal conductivity, residual stresses, and wear resistance of aluminum-alumina composites obtained by squeeze casting and powder metallurgy. *Metall. Mater. Trans.* **2021**, *52*, 4727–4736. [CrossRef]
8. Dobrzañski, L.A.; Kremzer, M.; Nagel, A. Aluminium EN AC—AlSi12 alloy matrix composite materials reinforced by Al_2O_3 porous performs. *Arch. Mater. Sci. Eng.* **2007**, *28*, 5.
9. Gafur, M.; Ahmed, A.; Abrar, R.; Soshi, S. Development and characterization of aluminium-based metal matrix composites. *Mater. Sci. Appl.* **2023**, *14*, 19. [CrossRef]
10. Pasha, M.B.; Kaleemulla, M. Processing and characterization of aluminum metal matrix composites: An overview. *Rev. Adv. Mater. Sci.* **2018**, *56*, 79–90. [CrossRef]
11. Zulfia, A.; Hand, R.J. The production of Al-Mg alloy/SiC metal matrix composites by pressureless infiltration. *J. Mater. Sci.* **2002**, *37*, 955–961. [CrossRef]
12. Liu, J.; Binner, J.; Higginson, R. Dry sliding wear behaviour of co-continuous ceramic foam/aluminium alloy interpenetrating composites produced by pressureless infiltration. *Wear* **2012**, *276–277*, 94–104. [CrossRef]
13. Basista, M.; Jakubowska, J.; Węglewski, W. Processing induced flaws in aluminum–alumina interpenetrating phase composites. *Adv. Eng. Mater.* **2017**, *19*, 1700484. [CrossRef]
14. Maj, J.; Basista, M.; Węglewski, W.; Bochenek, K.; Strojny-Nędza, A.; Naplocha, K.; Panzner, T.; Tatarková, M.; Fiori, F. Effect of microstructure on mechanical properties and residual stresses in interpenetrating aluminum-alumina composites fabricated by squeeze casting. *Mater. Sci. Eng. A* **2018**, *715*, 154–162. [CrossRef]
15. Roy, S.; Stoll, O.; Weidenmann, K.A.; Nagel, A.; Wanner, A. Analysis of the elastic properties of an interpenetrating AlSi12–Al2O3 composite using ultrasound phase spectroscopy. *Compos. Sci. Technol.* **2011**, *71*, 962–968. [CrossRef]
16. Dolata, A.J. Tribological properties of AlSi12-Al_2O_3 interpenetrating composite layers in comparison with unreinforced matrix alloy. *Materials* **2017**, *10*, 1045. [CrossRef] [PubMed]
17. Tomiczek, B.; Kremzer, M.; Sroka, M.; Dziekońska, M. Abrasive wear of AlSi12-Al_2O_3 composite materials manufactured by pressure infiltration. *Arch. Metall. Mater.* **2016**, *61*, 1255–1260. [CrossRef]
18. Kim, J.-K.; Tjong, S.C.; Mai, Y.-W. Effect of interface strength on metal matrix composites properties. In *Comprehensive Composite Materials II*; Beaumont, P.W.R., Zweben, C.H., Eds.; Elsevier: Amsterdam, The Netherlands, 2018; Volume 4, pp. 22–59.
19. Postek, E.; Sadowski, T. Distributed microcracking process of WC/Co cermet under dynamic impulse compressive loading. *Comp. Struct.* **2018**, *194*, 494–508. [CrossRef]
20. Postek, E.; Sadowski, T. Qualitative comparison of dynamic compressive pressure load and impact of WC/Co composite. *Int. J. Refract. Hard Met.* **2018**, *77*, 68–81. [CrossRef]
21. Oishi, Y.; Kingery, W.D. Self-diffusion of oxygen in single crystal and polycrystalline aluminum oxide. *Chem. Phys.* **1960**, *33*, 480–486. [CrossRef]
22. Lagerlof, K.P.D.; Mitchell, T.E.; Heuer, A.H. Lattice diffusion kinetics in undoped and impurity-doped sapphire (α-Al2O3): A dislocation loop annealing study. *J. Am. Ceram.* **1989**, *72*, 2159–2171. [CrossRef]
23. Paladino, A.E.; Kingery, W. Aluminum ion diffusion in aluminum oxide. *Chem. Phys.* **1962**, *37*, 957–962. [CrossRef]
24. Gall, M.L.; Lesage, B.; Bernardini, J. Self-diffusion in α-Al_2O_3 I. Aluminium diffusion in single crystals. *Philos. Mag. A* **1994**, *70*, 761–773. [CrossRef]

25. Heuer, A.H. Oxygen and aluminum diffusion in α-Al2O3: How much do we really understand? *J. Eur. Ceram.* **2008**, *28*, 1495–1507. [CrossRef]
26. Milas, I.; Hinnemann, B.; Carter, E.A. Diffusion of Al, O, Pt, Hf, and Y atoms on α-Al2O3(0001): Implications for the role of alloying elements in thermal barrier coatings. *J. Mater. Chem.* **2011**, *21*, 1447–1456. [CrossRef]
27. Pelleg, J. *Diffusion in Ceramics*; Springer: Berlin/Heidelberg, Germany, 2016.
28. Plimpton, S. Fast parallel algorithms for short-range molecular dynamics. *J. Comput. Phys.* **1995**, *117*, 1–19. [CrossRef]
29. Stukowski, A. Visualization and analysis of atomistic simulation data with OVITO–the Open Visualization Tool. *Model. Simul. Mat. Sci. Eng.* **2010**, *18*, 015012. [CrossRef]
30. Choudhary, K.; Liang, T.; Chernatynskiy, A.; Phillpot, S.R.; Sinnott, S.B. Charge optimized many-body (COMB) potential for Al2O3 materials, interfaces, and nanostructures. *J. Phys. Condens. Matter* **2015**, *27*, 305004. [CrossRef] [PubMed]
31. Munetoh, S.; Motooka, T.; Moriguchi, K.; Shintani, A. Interatomic potential for Si–O systems using Tersoff parameterization. *Comput. Mater. Sci.* **2007**, *39*, 334–339. [CrossRef]
32. Zhao, H.; Chen, N. An inverse adhesion problem for extracting interfacial pair potentials for the Al(0 0 1)/3C–SiC(0 0 1) interface. *Inverse Probl.* **2008**, *24*, 035019. [CrossRef]
33. Wachtman, J.B.; Cannon, W.R.; Matthewson, M.J. *Mechanical Properties of Ceramics*, 2nd ed.; John Wiley: Hoboken, NJ, USA, 2009.
34. Streitz, F.H.; Mintmire, J.W. Molecular dynamics simulations of elastic response and tensile failure of alumina. *Langmuir* **1996**, *12*, 4605–4609. [CrossRef]
35. Aschauer, U.; Bowen, P.; Parker, S.C. Oxygen vacancy diffusion in alumina: New atomistic simulation methods applied to an old problem. *Acta Mater.* **2009**, *57*, 4765–4772. [CrossRef]
36. Medlin, D.L.; McCarty, K.F.; Hwang, R.Q.; Guthrie, S.E.; Baskes, M.I. Orientation relationships in heteroepitaxial aluminum films on sapphire. *Thin Solid Films* **1997**, *299*, 110–114. [CrossRef]
37. Pilania, G.; Thijsse, B.J.; Hoagland, R.G.; Lazić, I.; Valone, S.M.; Liu, X.-Y. Revisiting the Al/Al_2O_3 interface: Coherent interfaces and misfit accommodation. *Sci. Rep.* **2014**, *4*, 4485. [CrossRef] [PubMed]
38. Einstein, A. *Investigations on the Theory of the Brownian Movement*; Courier Corporation: Chemsford, MA, USA, 1956.
39. Onsager, L. Reciprocal Relations in Irreversible Processes. I. *Phys. Rev.* **1931**, *37*, 405–426. [CrossRef]
40. Onsager, L. Reciprocal relations in irreversible processes. II. *Phys. Rev.* **1931**, *38*, 2265–2279. [CrossRef]
41. Dayananda, M.A.; Sohn, Y.H. A new analysis for the determination of ternary interdiffusion coefficients from a single diffusion couple. *Metall. Mater. Trans.* **1999**, *30*, 535–543. [CrossRef]
42. Tahani, M.; Postek, E.; Sadowski, T. Molecular dynamics study of interdiffusion for cubic and hexagonal SiC/Al interfaces. *Crystals* **2023**, *13*, 46. [CrossRef]
43. Tahani, M.; Postek, E.; Motevalizadeh, L.; Sadowski, T. Effect of vacancy defect content on the interdiffusion of cubic and hexagonal SiC/Al interfaces: A molecular dynamics study. *Molecules* **2023**, *28*, 744. [CrossRef] [PubMed]

materials

MDPI

Article

A FEM Free Vibration Analysis of Variable Stiffness Composite Plates through Hierarchical Modeling

Gaetano Giunta [1,*], Domenico Andrea Iannotta [1,2] and Marco Montemurro [3]

[1] Luxembourg Institute of Science and Technology, 5 Avenue des Hauts-Fourneaux, L-4362 Esch-sur-Alzette, Luxembourg; domenico-andrea.iannotta@list.lu
[2] Doctoral School in Science and Engineering (DSSE), University of Luxembourg, 2 Avenue de l'Université, L-4365 Esch-sur-Alzette, Luxembourg
[3] Arts et Métiers Institute of Technology, Université de Bordeaux, CNRS, INRA, Bordeaux INP, HESAM Université, I2M UMR 5295, F-33405 Talence, France; marco.montemurro@ensam.eu
* Correspondence: gaetano.giunta@list.lu

Abstract: Variable Angle Tow (VAT) laminates offer a promising alternative to classical straight-fiber composites in terms of design and performance. However, analyzing these structures can be more complex due to the introduction of new design variables. Carrera's unified formulation (CUF) has been successful in previous works for buckling, vibrational, and stress analysis of VAT plates. Typically, one-dimensional (1D) and two-dimensional (2D) CUF models are used, with a linear law describing the fiber orientation variation in the main plane of the structure. The objective of this article is to expand the CUF 2D plate finite elements family to perform free vibration analysis of composite laminated plate structures with curvilinear fibers. The primary contribution is the application of Reissner's mixed variational theorem (RMVT) to a CUF finite element model. The principle of virtual displacements (PVD) and RMVT are both used as variational statements for the study of monolayer and multilayer VAT plate dynamic behavior. The proposed approach is compared to Abaqus three-dimensional (3D) reference solutions, classical theories and literature results to investigate the effectiveness of the developed models. The results demonstrate that mixed theories provide the best approximation of the reference solution in all cases.

Keywords: free vibration analysis; finite element method; variable angle tow plates; Carrera's unified formulation; Reissner's mixed variational theorem

Citation: Giunta, G.; Iannotta, D.A.; Montemurro, M. A FEM Free Vibration Analysis of Variable Stiffness Composite Plates through Hierarchical Modeling. *Materials* **2023**, *16*, 4643. https://doi.org/10.3390/ma16134643

Academic Editors: Angelo Marcello Tarantino, Carmelo Majorana, Raimondo Luciano and Michele Bacciocchi

Received: 17 May 2023
Revised: 14 June 2023
Accepted: 17 June 2023
Published: 27 June 2023

1. Introduction

Over the last decades, composite structures have gained significant attention across diverse application fields, including aerospace, automotive and construction, due to their unique properties. Due to their high stiffness-to-weight ratio, composites help to build light structures with interesting mechanical properties. Despite this, a common thought is that the potential of fiber-reinforced structures could be better exploited by improving the directional properties through the variation of the fiber angle along the in-plane directions. The choice to keep the fiber orientation constant in each layer is particularly restrictive for geometries that present geometrical discontinuities such as cut-outs. VAT plates are characterized by an in-plane variation of fiber angle, helping to expand the design space of a specific structure. This is particularly useful for optimization problems, where a wider design space can positively affect the search of an optimal solution. For example, in the context of vibrational analyses, the maximization of fundamental frequencies can be improved by using curvilinear fibers. VATs were originally obtained through automated tape placement (ATP) and automated fiber placement (AFP). ATP helps the automated placement of composite material tapes with a specific angle in order to reproduce a desired path. AFP is similar to ATP, since the main difference is related to the width of the material that is laid down: while ATP handles a tape with a width between 75 and

300 mm, AFP involves the placement of the material with a typical width between 3.1 and 12.7 mm. By consequence, AFP allows for better control of fiber angles, achieving a wider design flexibility; see Dirk et al. [1]. However, automated processes show some limitations related to manufacturing defects, such as gaps and overlaps, or constraints such as the minimum steering radius. These aspects can be partially overcome due to new technologies such as additive manufacturing (AM), also known as 3D printing. AM involves the layer-by-layer deposition of materials to create a three-dimensional object. In the case of variable angle tow composites, AM techniques are used to deposit and cure layers of composite materials with varying fiber orientations; see Zhuo et al. [2]. VAT composites have diverse applications ranging from aerospace engineering and wind energy to automotive and construction contexts, offering enhanced structural performance, weight reduction, and tailored properties for improved efficiency and functionality in a wide range of industries. For example, these materials can be employed in the optimization of aircraft wings to enhance structural weight and fuel consumption, as presented in Brooks et al. [3]. In the space context, VATs can be used for the design of liquid oxygen in order to reduce the mass and increase the payload of space launchers, as discussed by Gren et al. [4]. Despite the significant advantages associated with curvilinear fiber composites, these materials have limitations from both manufacturing and design perspectives. The production of VAT composites can be more complex in comparison with traditional laminates, since the material behavior is strongly affected by process-induced defects. Moreover, not all fiber patterns can be realized, because of the technological limitations that characterize their production. The complexity of analysis is one of the main disadvantages of VATs, because a greater number of unknowns must be taken into account and unfeasible fiber patterns could be obtained during the optimization process.

Several methods for the study of VAT mechanical responses are available in the literature. In the following text, a brief review of these approaches is presented, with a particular focus on free vibration analyses. To the best of the authors' knowledge, the first works that have been presented on the topic are based on the assumption of a constant fiber angle within each element in a finite element method (FEM) solution. Therefore, the continuous variation of fiber direction was approximated in a step-wise discrete way. This approach can be used in commercial FEM software tools that, at the moment, cannot handle continuous fiber variation. Hyer and Charette [5] and Hyer and Lee [6] used this method to improve the VAT tensile strength and buckling response, respectively. One of the main disadvantages of this step-wise approach is that, as the true variation is continuous, the discrete representation of fiber angle variation imposes a further approximation. A p-version FEM based on the third-order shear deformation theory (TSDT) was applied by Akhavan and Ribeiro [7] to preform vibrational analyses. The results showed that fiber variation helps to increase (or decrease) natural frequencies and that thin plates are more affected by this phenomenon if compared with thick ones. Ribeiro and Akhavan [8] used the p-version FEM approach with elements based on the first-order shear deformation theory (FSDT) to perform non-linear vibration analyses. The advantage of the p-version of the FEM is that the accuracy of the approximation is improved by increasing the order of shape functions over the elements. Vibration analyses were performed on VAT plates with a central circular cut-out considering parabolic fibers by Hachemi et al. [9]. Zhao and Kapania [10] investigated the free vibration of prestressed VAT stiffened plates, where plates and stiffeners were modeled separately through Mindlin plate theory and Timoshenko beam theory, respectively. The compatibility conditions at the interface between the plate and stiffeners were satisfied by using a transformation matrix. Honda and Narita [11] used the classical plate theory within the Ritz method in order to evaluate the natural frequencies and vibrational modes. An experimental approach was used in Rodrigues et al. [12] for the free vibration analysis of a plate with free boundary conditions that was subjected to random excitation via an electromagnetic shaker. Subsequently, the results were compared to the ones obtained through FEM, where a four-node isoparametric element based on the Reissner–Mindlin theory was used. Stodieck et al. [13] showed that curvilinear fibers

can be useful for improving the aeroelastic response of composite wings. The Rayleigh–Ritz method and classical lamination theory were used to develop a 1D beam model, considering the assumption of null chamber deformation of the wing chord-wise section. The aeroelastic response was computed by introducing quasi-static aerodynamic forces in a model developed for the plate structural analysis. A parametric study showed that by using VATs, it is possible to influence wing response both positively and negatively.

Curvilinear fibers can improve the modal response, as shown in several works. Abdalla et al. [14] used the classical lamination theory in combination with a successive approximation method in order to solve an optimization problem. The results showed that curvilinear fibers increased the optimal fundamental frequency in comparison with straight ones. A similar approach was presented in Blom et al. [15], where the maximization of the first natural frequency considering manufacturing constraints was obtained for VAT conical shells. In Carvalho et al. [16], a genetic algorithm and shell elements based on FSDT were used for maximization of the fundamental frequency. The multi-scale two-level (MS2L) approach helps to split the optimization problem in two parts. The composite is modeled as an equivalent homogeneous anisotropic plate in the first step, which aims to find the ideal distribution of the polar parameters that represent the mechanical design variables. The main goal of a second step is to establish the best stacking sequence in relation to the mechanical property distribution that has been obtained in the first step. The MS2L method was applied by Montemurro and Catapano [17] to VAT plates in order to optimize the buckling response. In order to evaluate the polar parameters, B-spline surfaces were introduced, while manufacturing constraints were considered during the second step. More details about the MS2L approach can be found in Catapano et al. [18], Montemurro and Catapano [19] and Fiordilino et al. [20], where both stiffness and buckling optimization problems were solved.

VAT structures have also been studied by using Carrera's unified formulation. CUF is a mathematical framework that helps the derivation of different theories, such as classical lamination plate theory, higher-order shear deformation theories, or LW approaches, within a unique formulation; see Carrera [21,22]. The a priori approximation over the thickness (typical of plates' structural modeling) can also be freely assumed as a generic combination of functions whose number is a free parameter of the formulation. When polynomial functions are used, as in this article, the expansion order along the thickness of the plate is arbitrary in the formulation, and it can be set when performing a specific analysis. This flexibility is beneficial because it helps to tailor the accuracy and computational efficiency of the analysis to the specific requirements of the problem at hand. Carrera et al. [23] used CUF in order to develop a Navier closed-form solution for the static analysis of isotropic plates under several loading conditions. The same approach was used in Carrera and Giunta [24] in order to perform failure analyses on isotropic plates. A further extension of this method was shown in Giunta et al. [25], where a indentation failure analysis of composite sandwich plates was performed. Giunta et al. [26] performed free vibration analyses of composite beams. In Viglietti et al. [27] and Fallahi et al. [28], free vibration and buckling analyses of VATs were performed through the use of a 1D CUF model. Within this framework, shell models were developed as well for VAT cases in order to perform stress analyses; see Sánchez-Majano et al. [29]. In Pagani and Sánchez-Majano [30,31] and Sánchez-Majano et al. [32], manufacturing defects were taken into account by using stochastic techniques. Vescovini and Dozio [33] used the Ritz method within CUF for vibrational and buckling analyses. A generalization of CUF was developed in order to allow for the use of different expansions for every component of the displacement vector. Demasi et al. [34] applied this approach to the study of VAT plates with an ESL model. A further advantage of CUF is that it can be used in combination with different variational statements. An alternative to the classic PVD is represented by the RMVT, where both displacements and transverse out-of-plane stresses are considered as primary variables. RMVT has been widely used within CUF for the study of straight-fiber composite structures.

For example, Carrera and Demasi [35,36] developed RMVT-based CUF models to perform the static analysis of straight fiber plates.

The free vibration analysis is an important problem in engineering (see Babaei et al. [37]), and within this context, CUF has been applied to the study of VATs considering PVD as the main variational statement. For this reason, this work aims to extend this framework with the RMVT formulation in order to develop a family of hierarchical plate finite elements. This will help to better predict the natural frequencies of composite plates characterized by curvilinear fibers. Section 2 shows the theoretical derivation for free vibration problems. Section 3 presents the numerical results where three cases are investigated. Analyses are performed that consider a varying side-to-thickness ratio in order to investigate thin and thick plates, and the differences between models are discussed regarding PVD or RMVT statements. The results are compared to reference solutions for validation. Concluding observations and remarks are presented in Section 4.

2. Carrera's Unified Formulation

A plate is a flat body whose material points lie in the Cartesian closed-point subset

$$\mathcal{P} = \Omega \times \mathcal{H} \tag{1}$$

of the three-dimensional space $\mathbb{R}^3$ where:

$$\begin{aligned} \Omega &= \left\{ (x,y) \ : \ \frac{x}{a}, \ \frac{y}{b} \in [0,1] \right\} \subset \mathbb{R}^2, \\ \mathcal{H} &= \left\{ z \ : \ \frac{2z}{h} \in [-1,1] \right\}, \end{aligned} \tag{2}$$

where a and b are the dimensions along the two in-plane axes, and h measures its thickness along the z-axis, where $z \ll a$ and b. The global reference system and plate geometry are presented in Figure 1.

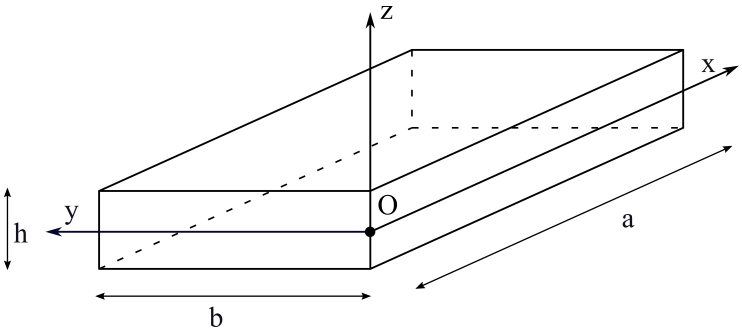

Figure 1. Plate geometry and reference system.

The displacement field is expressed as:

$$\mathbf{u} = \left\{ \begin{array}{c} u_x \\ u_y \\ u_z \end{array} \right\}. \tag{3}$$

The strain tensor components can be written in vector form. Two vectors are obtained, representing the in-plane and out-of-plane components:

$$\boldsymbol{\epsilon}_p = \left\{ \begin{array}{c} \epsilon_{xx} \\ \epsilon_{yy} \\ \epsilon_{xy} \end{array} \right\}, \ \boldsymbol{\epsilon}_n = \left\{ \begin{array}{c} \gamma_{xz} \\ \gamma_{yz} \\ \gamma_{zz} \end{array} \right\}. \tag{4}$$

The hypothesis of small displacements helps to use a linear strain–displacement relation:

$$\begin{aligned} \boldsymbol{\epsilon}_p &= \mathbf{D}_p \mathbf{u} \ , \\ \boldsymbol{\epsilon}_n &= (\mathbf{D}_{n\Omega} + \mathbf{D}_{nz}) \mathbf{u} \ , \end{aligned} \tag{5}$$

where $\mathbf{D}_p$, $\mathbf{D}_{n\Omega}$ and $\mathbf{D}_{nz}$ are the following differential operators:

$$\mathbf{D}_p = \begin{bmatrix} \frac{\partial}{\partial x} & 0 & 0 \\ 0 & \frac{\partial}{\partial y} & 0 \\ \frac{\partial}{\partial y} & \frac{\partial}{\partial x} & 0 \end{bmatrix}, \ \mathbf{D}_{n\Omega} = \begin{bmatrix} 0 & 0 & \frac{\partial}{\partial x} \\ 0 & 0 & \frac{\partial}{\partial y} \\ 0 & 0 & 0 \end{bmatrix}, \ \mathbf{D}_{nz} = \begin{bmatrix} \frac{\partial}{\partial z} & 0 & 0 \\ 0 & \frac{\partial}{\partial z} & 0 \\ 0 & 0 & \frac{\partial}{\partial z} \end{bmatrix}. \tag{6}$$

The stress vector is expressed in a similar manner:

$$\boldsymbol{\sigma}_p = \begin{Bmatrix} \sigma_{xx} \\ \sigma_{yy} \\ \sigma_{xy} \end{Bmatrix}, \ \boldsymbol{\sigma}_n = \begin{Bmatrix} \sigma_{xz} \\ \sigma_{yz} \\ \sigma_{zz} \end{Bmatrix}. \tag{7}$$

Hooke's law reads:

$$\begin{aligned} \boldsymbol{\sigma}_p &= \widetilde{\mathbf{C}}_{pp} \boldsymbol{\epsilon}_p + \widetilde{\mathbf{C}}_{pn} \boldsymbol{\epsilon}_n \ , \\ \boldsymbol{\sigma}_n &= \widetilde{\mathbf{C}}_{np} \boldsymbol{\epsilon}_p + \widetilde{\mathbf{C}}_{nn} \boldsymbol{\epsilon}_n \ , \end{aligned} \tag{8}$$

where the terms $\widetilde{\mathbf{C}}_{pp}$, $\widetilde{\mathbf{C}}_{pn}$, $\widetilde{\mathbf{C}}_{np}$ and $\widetilde{\mathbf{C}}_{nn}$ are subcomponents of a material stiffness matrix $\widetilde{\mathbf{C}}$ according to the stress and strain ordering in Equations (4) and (7), where the fibers lay in Ω and where they are not, in general, aligned with the x-axis. $\mathbf{C}$ stands for the stiffness matrix in the global reference system, and its components can be written in terms of the Young's moduli E_L and E_T, shear moduli G_{LT} and G_{TT} and Poisson's ratios ν_{LT} and ν_{TT}, where subscripts L and T stand for the directions parallel and perpendicular to the fibers, respectively. For further details, see Reddy [38].

2.1. Variable Stiffness Composite Plates

Laminated VAT structures are considered in this work. For this reason, the material stiffness coefficients can change layer-wise along the thickness and pointwise along the in-plane directions. The mapping of $\mathbf{C}$ into $\widetilde{\mathbf{C}}$ reads:

$$\widetilde{\mathbf{C}} = \mathbf{T}\mathbf{C}\mathbf{T}^T \ . \tag{9}$$

Superscript T stands for the transpose operator. The matrix $\mathbf{T}$ represents a rotation matrix that depends on an in-plane rotation angle θ. For the sake of brevity, the components of $\widetilde{\mathbf{C}}$ and $\mathbf{T}$ are not reported here; they can be found in Reddy [38]. In a laminated VAT, the rotation angle θ is a bi-dimensional field in Ω. In this work, two different variation laws are considered for θ, a linear variation law and a parabolic one. The linear law can be expressed according to the following formula:

$$\theta(\alpha) = \Phi + T_0 + \frac{T_1 - T_0}{d} |\alpha| \ . \tag{10}$$

The angle Φ describes the original direction along which θ varies, and α is a generic spatial variable defined as:

$$\alpha = x' \cos(\Phi) + y' \sin(\Phi) \ . \tag{11}$$

x' and y' denote a generic in-plane reference system used for describing a fiber path, where θ is measured. The introduction of a new reference system is useful in order to represent the local fiber orientation independently from the global reference system identified by axes x and y. T_0 and T_1 are the angles between the α-axis and the tangent to a fiber for α equal to zero and d, respectively; see Figure 2.

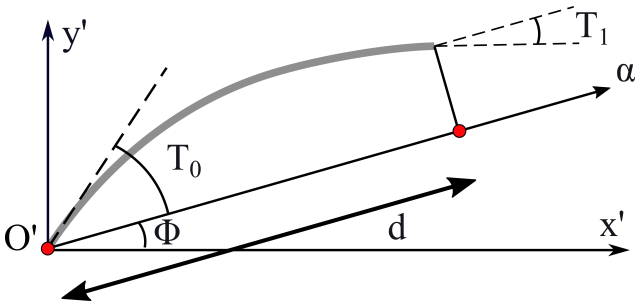

Figure 2. Example of in-plane fiber orientation.

As shown in the Figure 2, the fiber angle is always measured with respect to the x'-axis, and it can change along a generic direction α, defined as a combination of x' and y' depending on the angle Φ. Further details about the fiber linear variation law can be found in Gürdal et al. [39]. The parabolic law can be expressed according to the following equation:

$$\theta(\alpha) = \Phi + T_0 + \tan^{-1}\left(\gamma \frac{\alpha}{d}\right) . \tag{12}$$

The parameter γ is used to control the shape of the parabola, and it is related to the final fiber angle T_1 as $T_1 = \tan^{-1}(\pm\gamma)$. More details about the parabolic fiber path can be found in Hachemi et al. [9] and Honda et al. [40]. The following notation, based upon the above introduced parameters, is used in order to describe the in-plane linear and parabolic fiber behavior: $\Phi < T_0, T_1 >$.

2.2. Variational Statements

PVD and RMVT variational statements are considered to derive the governing equations for the free vibration problem for a laminated VAT plate. The fundamental distinction is that the RMVT considers the vector of the out-of-plane stresses $\boldsymbol{\sigma}_n$ as a primary unknown, whereas the PVD considers only displacements as primary variables. For the PVD case, the following variational statement applies:

$$\int_\Omega \int_\mathcal{H} \left(\delta \boldsymbol{\epsilon}_{pG}^T \, \boldsymbol{\sigma}_{pH} + \delta \boldsymbol{\epsilon}_{nG}^T \, \boldsymbol{\sigma}_{nH} \right) dz \, d\Omega + \delta \mathcal{L}_{in} = 0 , \tag{13}$$

where the subscript G refers to the components obtained from the geometrical relations in Equation (5), and subscript H refers to the components obtained from Hooke's law in Equation (8). $\mathcal{L}_{in}$ is the virtual work of the inertial forces, and δ stands for a virtual variation. For the RMVT case, the variational statement is:

$$\int_\Omega \int_\mathcal{H} \left[\delta \boldsymbol{\epsilon}_{pG}^T \, \boldsymbol{\sigma}_{pH} + \delta \boldsymbol{\epsilon}_{nG}^T \, \boldsymbol{\sigma}_{nM} + \delta \boldsymbol{\sigma}_{nM}^T (\boldsymbol{\epsilon}_{nG} - \boldsymbol{\epsilon}_{nH}) \right] dz \, d\Omega + \delta \mathcal{L}_{in} = 0 . \tag{14}$$

The M subscript refers to the transverse stress components considered as primary unknowns in the mixed formulation. For the RMVT formulation, Hooke's law is rewritten as follows:

$$\begin{aligned} \boldsymbol{\sigma}_{pH} &= \hat{\mathbf{C}}_{pp} \boldsymbol{\epsilon}_{pG} + \hat{\mathbf{C}}_{pn} \boldsymbol{\sigma}_{nM} , \\ \boldsymbol{\epsilon}_{nH} &= \hat{\mathbf{C}}_{np} \boldsymbol{\epsilon}_{pG} + \hat{\mathbf{C}}_{nn} \boldsymbol{\sigma}_{nM} , \end{aligned} \tag{15}$$

where $\hat{\mathbf{C}}_{pp}$, $\hat{\mathbf{C}}_{pn}$, $\hat{\mathbf{C}}_{np}$ and $\hat{\mathbf{C}}_{nn}$ are (see Carrera and Demasi [35]):

$$\begin{aligned} \hat{\mathbf{C}}_{pp} &= \widetilde{\mathbf{C}}_{pp} - \widetilde{\mathbf{C}}_{pn} \widetilde{\mathbf{C}}_{nn}^{-1} \widetilde{\mathbf{C}}_{np} , \\ \hat{\mathbf{C}}_{pn} &= \widetilde{\mathbf{C}}_{pn} \widetilde{\mathbf{C}}_{nn}^{-1} , \\ \hat{\mathbf{C}}_{np} &= -\widetilde{\mathbf{C}}_{nn}^{-1} \widetilde{\mathbf{C}}_{np} , \\ \hat{\mathbf{C}}_{nn} &= \widetilde{\mathbf{C}}_{nn}^{-1} . \end{aligned} \tag{16}$$

The superscript "-1" indicates the inverse of a matrix. The inertial work can be expressed as:

$$\delta \mathcal{L}_{in} = \int_{\Omega} \int_{\mathcal{H}} \delta \mathbf{u}^T \rho \, \ddot{\mathbf{u}} \, d\Omega \, dz \, , \tag{17}$$

where ρ is the plate material density, and $\ddot{\mathbf{u}}$ represents the acceleration vector.

2.3. Kinematic Assumptions

CUF uses an axiomatic approach along the through-the-thickness direction to represent the primary unknowns; see Carrera [22]. The generic unknown component $f = f(x, y, z)$ is approximated as:

$$f(x, y, z) = F_\tau(z) g_\tau(x, y) \, , \quad \tau = 0, \, 1, \, \ldots, \, N \, , \tag{18}$$

where f is a displacement component in a formulation derived from the PVD, but it can also be an out-of-plane stress component when a RMVT formulation is considered. F_τ is an approximation function in $\mathcal{H}$, and g_τ is an unknown two-dimensional function in Ω. According to Einstein's notation, a twice-repeated index implies a sum over the index range. Finally, N is the approximation order. Both N and F_τ are a priori defined. This feature of CUF helps to obtain multiple theories in the same formulation. Within CUF, ESL or LW models can also be obtained depending on the support of F_τ. In an ESL model $F_\tau : \mathcal{H} \mapsto \mathbb{R}$, whereas for a LW model $F_\tau : \mathcal{H}^k \mapsto \mathbb{R}$ where $\mathcal{H}^k = \left\{ z^k \, : \, \dfrac{2z^k}{h^k} \in [-1, 1] \right\}$ such that $\mathcal{H} = \bigcup_{k=1}^{N_l} \mathcal{H}^k$ and $\mathcal{H}^k \cap \mathcal{H}^{k'} = \emptyset$ for $k \neq k'$ with $k, k' = 1, \, 2, \, \ldots, \, N_l$, where N_l is the total number of laminae, and h^k is the thickness of a generic k lamina such that $k = \sum_{k=1}^{N_l} h^k$. The number of unknowns in the ESL case is independent of the number of layers in the lamination since the approximation is imposed globally over $\mathcal{H}$. The total stiffness contributions can be seen as a weighted average of each layer stiffness along the thickness. Maclaurin's series approximation is considered for the ESL models as a linear combination of the power functions:

$$F_\tau(z) = z^\tau \, , \quad \tau = 0, \, 1, \, \ldots, \, N \, , \tag{19}$$

where N is the expansion order. The computational cost of ESL models depends on N only, and for a given N, it is lower than a LW model since this latter model depends on the total number of layers in the lamination. ESL models are suitable for relatively thick laminates. However, they are unable to accurately predict the behavior of thick plates with a high degree of anisotropy. ESL models have C^∞-continuity over $\mathcal{H}$ because of the used approximation functions, whereas laminated composites present a C^0-continuity since the interface between the two consecutive layers of the different materials introduces a change in the slope of the displacements (also known as zig-zag displacement through-the-thickness variation). This behavior can be accommodated within an ESL theory by means of Murakami's function. This approach is not considered here; for more details, refer to Carrera [41]. In an LW model, the kinematics of each layer are formulated independently:

$$f^k(x, y, z) = F_b(z) g_b^k(x, y) + F_r(z) g_r^k(x, y) + F_t(z) g_t^k(x, y) \, , \quad r = 2, \, \ldots, \, N \, , \tag{20}$$

where subscripts b and t stand for the bottom and top layers, respectively. Congruence at the interface is retrieved via a through-the-thickness assembly procedure similar to that used in the finite element method. For this reason, Lagrange polynomials (which ensure partition of unity), or the following linear combination of Legendre polynomials, which are represented as:

$$F_t\Big(z(\xi^k)\Big) = \frac{P_0 + P_1}{2}, \quad F_b\Big(z(\xi^k)\Big) = \frac{P_0 - P_1}{2}, \quad F_r\Big(z(\xi^k)\Big) = P_r - P_{r-2}, \quad r = 2, \, \ldots, \, N \tag{21}$$

are typically used as approximation functions over $\mathcal{H}^k$. The use of Lagrange or Legendre polynomials along the thickness changes according to the used model, and this is specified at the end of the next subsection. In Equation (21), $\xi^k = \dfrac{2z^k}{h^k} \in [-1, 1]$ and $P_i = P_i\left(\xi^k\right)$ are an i-order Legendre polynomial. Equation (21) creates a base where F_t and F_b are the two linear Lagrange polynomials, and F_r is a kind of p-version-enriching function since it does not contribute to a base linear combination for $\xi^k = \pm 1$, being, by definition, $F_r(\pm 1) = 0$. Since LW base functions have local support, inter-layer C^0-continuity for layers made of different materials is ensured, but the computational costs are higher than for ESL models.

2.4. Acronym System

An acronym system is used in order to identify all the derived theories. Figure 3 shows this system.

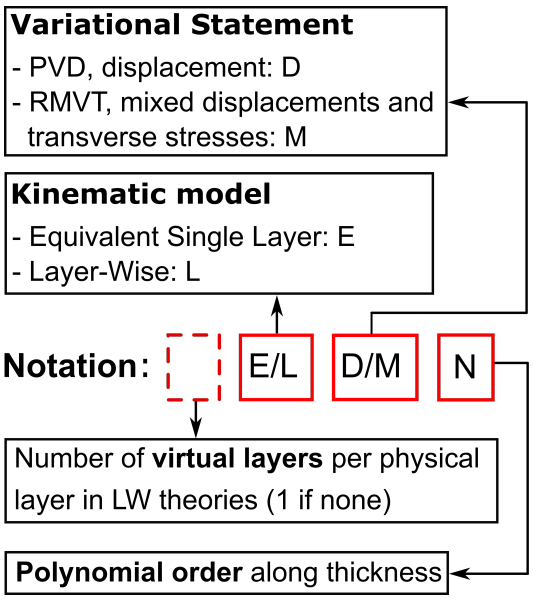

Figure 3. Acronym system.

The first letter addresses the approximation level that is applied: 'E' denotes the ESL models, whereas 'L' denotes the LW models. The second letter denotes the variational statement: PVD or RMVT are denoted by 'D' or 'M', respectively. The last number is the order of expansion along the plate thickness. A number at the beginning of the acronym, when present, indicates how many virtual layers have been used to approximate each physical layer in an LW model to improve the results for a given approximation order. If this number is not present, only one virtual layer has been used to represent each physical layer.

As an example, in EDN models, the displacement field can be expressed as:

$$\begin{aligned} u_x &= u_{x0} + u_{x1}z + u_{x2}z^2 + \cdots + u_{xN}z^N \,, \\ u_y &= u_{y0} + u_{y1}z + u_{y2}z^2 + \cdots + u_{yN}z^N \,, \\ u_z &= u_{z0} + u_{z1}z + u_{z2}z^2 + \cdots + u_{zN}z^N \,. \end{aligned} \tag{22}$$

In vector form:

$$\mathbf{u} = F_0\mathbf{u}_0 + F_1\mathbf{u}_1 + \cdots + F_N\mathbf{u}_N = F_\tau\mathbf{u}_\tau \,, \quad \tau = 0,\ 1,\ \ldots,\ N \,, \tag{23}$$

where $F_\tau = z^\tau$ and $\mathbf{u}_\tau = \mathbf{u}_\tau(x, y)$. Additionally, classical theories can be taken into account. Classical lamination theory (CLT) and first-order shear deformation theory are obtained as a particular case of a first-order ESL theory. FSDT is obtained through the penalization of the uz_1 term, while for CLT, transverse shear stresses are disregarded by using a fictitiously

high value of the material shear moduli. The material stiffness matrix needs to be reduced in a plane-stress sense to overcome thickness locking.

For LDN solutions, only displacements are considered as the primary variables:

$$\mathbf{u}^k = F_0\mathbf{u}_0^k + F_1\mathbf{u}_1^k + \cdots + F_N\mathbf{u}_N^k = F_\tau\mathbf{u}_\tau^k\ , \qquad \tau = 0,\ 1,\ \ldots,\ N\ ,\ k = 1,\ 2,\ \ldots,\ N_l\ . \quad (24)$$

For LMN solutions, transverse stresses are treated as primary variables. The transverse stress field can be expressed as:

$$\boldsymbol{\sigma}_n^k = F_0\boldsymbol{\sigma}_0^k + F_1\boldsymbol{\sigma}_1^k + \cdots + F_N\boldsymbol{\sigma}_N^k = F_\tau\boldsymbol{\sigma}_\tau^k\ , \qquad \tau = 0,\ 1,\ \ldots,\ N\ ,\ k = 1,\ 2,\ \ldots,\ N_l\ . \quad (25)$$

It can be observed that ESL theories can be considered as a particular case for LW theories. While in the first case the integration along the thickness is performed in order to represent composite properties through a unitary layer, for the second case, the integration is computed layer by layer. This helps to represent the kinematics of each layer separately for LW models. LDN solutions are obtained with Lagrange polynomials with equally spaced nodes, whereas LMN ones are obtained with Legendre polynomials.

2.5. FE Stiffness Matrices

As far as a FEM solution is concerned, the in-plane domain is discretized into N_e subdomains such as $\Omega = \bigcup_{e=1}^{N_e} \Omega_e$ and $\Omega_e \cap \Omega^{e'} = \emptyset$ for $e \neq e'$. Shape functions are then introduced for the approximation of the variation over Ω_e. In the case of a bi-dimensional model, Equation (18) becomes:

$$f(x,y,z) = F_\tau(z)N_i(x,y)g_{\tau i}\ , \quad \tau = 0,\ 1,\ \ldots,\ N\ , \quad i = 1,\ \ldots,\ N_n\ , \quad (26)$$

where N_i stands for the shape functions, and N_n is the number of nodes in the used finite element. Classical Lagrange shape functions are used. They are not presented here for the sake of brevity, but they can be found in Bathe [42]. FE stiffness matrices are obtained by the weak form of the variational principles. In the PVD case, considering Equation (26), the displacement field can be written as:

$$\mathbf{u} = F_\tau N_i \left\{ \begin{array}{c} q_{x\tau i} \\ q_{y\tau i} \\ q_{z\tau i} \end{array} \right\} = F_\tau N_i \mathbf{q}_{\tau i}\ . \quad (27)$$

Through the substitution of Equations (5), (8) and (27) into Equation (13), the weak PVD form can be obtained:

$$\begin{array}{l} \int_{\Omega_e} \delta\boldsymbol{q}_{\tau i}^T \left[\mathbf{D}_p^T(N_i\mathbf{I})\widetilde{\mathbf{Z}}_{pp}^{\tau s}\mathbf{D}_p\left(N_j\mathbf{I}\right) + \mathbf{D}_p^T(N_i\mathbf{I})\widetilde{\mathbf{Z}}_{pn}^{\tau s}\mathbf{D}_{n\Omega}\left(N_j\mathbf{I}\right) + \mathbf{D}_p^T(N_i\mathbf{I})\widetilde{\mathbf{Z}}_{pn}^{\tau s_{,z}}\left(N_j\mathbf{I}\right)\right. \\ +\mathbf{D}_{n\Omega}^T(N_i\mathbf{I})\widetilde{\mathbf{Z}}_{np}^{\tau s}\mathbf{D}_p\left(N_j\mathbf{I}\right) + \mathbf{D}_{n\Omega}^T(N_i\mathbf{I})\widetilde{\mathbf{Z}}_{nn}^{\tau s}\mathbf{D}_{n\Omega}\left(N_j\mathbf{I}\right) + \mathbf{D}_{n\Omega}^T(N_i\mathbf{I})\widetilde{\mathbf{Z}}_{nn}^{\tau s_{,z}}\left(N_j\mathbf{I}\right) \\ \left.+(N_i\mathbf{I})\widetilde{\mathbf{Z}}_{np}^{\tau_{,z}s}\mathbf{D}_p\left(N_j\mathbf{I}\right) + (N_i\mathbf{I})\widetilde{\mathbf{Z}}_{nn}^{\tau_{,z}s}\mathbf{D}_{n\Omega}\left(N_j\mathbf{I}\right) + (N_i\mathbf{I})\widetilde{\mathbf{Z}}_{nn}^{\tau_{,z}s_{,z}}\left(N_j\mathbf{I}\right)\right] \\ \boldsymbol{q}_{sj}d\Omega = -\int_{\Omega_e} \delta\boldsymbol{q}_{\tau i}^T(N_i\mathbf{I})\rho E_{\tau s}\left(N_j\mathbf{I}\right)\ddot{\boldsymbol{q}}_{sj}d\Omega\ , \end{array} \quad (28)$$

where:

$$\left(\widetilde{\mathbf{Z}}_{wr}^{\tau s}, \widetilde{\mathbf{Z}}_{wr}^{\tau_{,z}s}, \widetilde{\mathbf{Z}}_{wr}^{\tau s_{,z}}, \widetilde{\mathbf{Z}}_{wr}^{\tau_{,z}s_{,z}}\right) = \left(\widetilde{\mathbf{C}}_{wr}E_{\tau s}, \widetilde{\mathbf{C}}_{wr}E_{\tau_{,z}s}, \widetilde{\mathbf{C}}_{wr}E_{\tau s_{,z}}, \widetilde{\mathbf{C}}_{wr}E_{\tau_{,z}s_{,z}}\right):\ w,r = p,n\ , \quad (29)$$

$$\left(E_{\tau s}, E_{\tau_{,z}s}, E_{\tau s_{,z}}, E_{\tau_{,z}s_{,z}}\right) = \int_{\mathcal{H}} \left(F_\tau F_s, F_{\tau_{,z}}F_s, F_\tau F_{s_{,z}}, F_{\tau_{,z}}F_{s_{,z}}\right)dz\ . \quad (30)$$

An axis coordinate as comma-preceded subscript stands for a derivative in that coordinate direction. In compact vector form, Equation (28) reads:

$$\delta\boldsymbol{q}_{\tau i}^T\mathbf{K}^{\tau sij}\boldsymbol{q}_{sj} = -\delta\boldsymbol{q}_{\tau i}^T\mathbf{M}^{\tau sij}\ddot{\boldsymbol{q}}_{sj}\ , \quad (31)$$

where $\mathbf{K}^{\tau sij}$ and $\mathbf{M}^{\tau sij} \in \mathbb{R}^{3\times3}$ are fundamental nuclei (FN) of the stiffness and mass matrices, respectively. Through the cycles on the indices τ, s, i and j, it is possible to build the stiffness and mass matrices of a finite element. The components of the stiffness FN for the PVD case can be written as:

$$
\begin{aligned}
K_{xx}^{\tau sij} &= \int_{\Omega_e} \left(\widetilde{Z}_{pp11}^{\tau s} N_{j,x} N_{i,x} + \widetilde{Z}_{pp16}^{\tau s} N_{j,y} N_{i,x} + \widetilde{Z}_{pp16}^{\tau s} N_{j,x} N_{i,y} + \widetilde{Z}_{pp66}^{\tau s} N_{j,y} N_{i,y} + \widetilde{Z}_{nn44}^{\tau_{,z} s_{,z}} N_j N_i \right) d\Omega \,, \\
K_{xy}^{\tau sij} &= \int_{\Omega_e} \left(\widetilde{Z}_{pp12}^{\tau s} N_{j,y} N_{i,x} + \widetilde{Z}_{pp16}^{\tau s} N_{j,x} N_{i,x} + \widetilde{Z}_{pp26}^{\tau s} N_{j,y} N_{i,y} + \widetilde{Z}_{pp66}^{\tau s} N_{j,x} N_{i,y} + \widetilde{Z}_{nn45}^{\tau_{,z} s_{,z}} N_j N_i \right) d\Omega \,, \\
K_{xz}^{\tau sij} &= \int_{\Omega_e} \left(\widetilde{Z}_{pn13}^{\tau s_{,z}} N_j N_{i,x} + \widetilde{Z}_{pn36}^{\tau_{,z} s} N_j N_{i,y} + \widetilde{Z}_{nn44}^{\tau_{,z} s} N_{j,x} N_i + \widetilde{Z}_{nn45}^{\tau_{,z} s} N_{j,y} N_i \right) d\Omega \,, \\
K_{yx}^{\tau sij} &= \int_{\Omega_e} \left(\widetilde{Z}_{pp12}^{\tau s} N_{j,x} N_{i,y} + \widetilde{Z}_{pp26}^{\tau s} N_{j,y} N_{i,y} + \widetilde{Z}_{pp16}^{\tau s} N_{j,x} N_{i,x} + \widetilde{Z}_{pp66}^{\tau s} N_{j,y} N_{i,x} + \widetilde{Z}_{nn45}^{\tau_{,z} s_{,z}} N_j N_i \right) d\Omega \,, \\
K_{yy}^{\tau sij} &= \int_{\Omega_e} \left(\widetilde{Z}_{pp22}^{\tau s} N_{j,y} N_{i,y} + \widetilde{Z}_{pp26}^{\tau s} N_{j,x} N_{i,y} + \widetilde{Z}_{pp26}^{\tau s} N_{j,y} N_{i,x} + \widetilde{Z}_{pp66}^{\tau s} N_{j,x} N_{i,x} + \widetilde{Z}_{nn55}^{\tau_{,z} s_{,z}} N_j N_i \right) d\Omega \,, \\
K_{yz}^{\tau sij} &= \int_{\Omega_e} \left(\widetilde{Z}_{pn23}^{\tau s_{,z}} N_j N_{i,y} + \widetilde{Z}_{pn36}^{\tau_{,z} s} N_j N_{i,x} + \widetilde{Z}_{nn45}^{\tau_{,z} s} N_{j,x} N_i + \widetilde{Z}_{nn55}^{\tau_{,z} s} N_{j,y} N_i \right) d\Omega \,, \\
K_{zx}^{\tau sij} &= \int_{\Omega_e} \left(\widetilde{Z}_{nn44}^{\tau s_{,z}} N_j N_{i,x} + \widetilde{Z}_{nn45}^{\tau_{,z} s} N_j N_{i,y} + \widetilde{Z}_{np13}^{\tau_{,z} s} N_{j,x} N_i + \widetilde{Z}_{np36}^{\tau_{,z} s} N_{j,y} N_i \right) d\Omega \,, \\
K_{zy}^{\tau sij} &= \int_{\Omega_e} \left(\widetilde{Z}_{nn45}^{\tau s_{,z}} N_j N_{i,x} + \widetilde{Z}_{nn55}^{\tau_{,z} s} N_j N_{i,y} + \widetilde{Z}_{np23}^{\tau_{,z} s} N_{j,y} N_i + \widetilde{Z}_{np36}^{\tau_{,z} s} N_{j,x} N_i \right) d\Omega \,, \\
K_{zz}^{\tau sij} &= \int_{\Omega_e} \left(\widetilde{Z}_{nn44}^{\tau s} N_{j,x} N_{i,x} + \widetilde{Z}_{nn45}^{\tau s} N_{j,y} N_{i,x} + \widetilde{Z}_{nn45}^{\tau s} N_{j,x} N_{i,y} + \widetilde{Z}_{nn55}^{\tau s} N_{j,y} N_{i,y} + \widetilde{Z}_{nn33}^{\tau_{,z} s_{,z}} N_j N_i \right) d\Omega \,.
\end{aligned}
\tag{32}
$$

The mass FN can be written as:

$$
\mathbf{M}^{\tau sij} = \int_{\Omega_e} (N_i \mathbf{I}) \rho E_{\tau s} \left(N_j \mathbf{I} \right) d\Omega \,. \tag{33}
$$

It is possible to observe that $\mathbf{M}^{\tau sij}$ is a diagonal matrix and that since the plate density is assumed to be constant, the term $\rho E_{\tau s}$ can be placed outside the integral.

In the RMVT case, transverse stresses are a priori approximated:

$$
\boldsymbol{\sigma}_n = F_\tau N_i \left\{ \begin{array}{c} g_{xz\tau i} \\ g_{yz\tau i} \\ g_{zz\tau i} \end{array} \right\} = F_\tau N_i \mathbf{g}_{\tau i} \,. \tag{34}
$$

Through the substitution of Equations (5), (15), (27) and (34) into Equation (14), the RMVT weak form can be obtained:

$$
\begin{aligned}
&\int_{\Omega_e} \delta \boldsymbol{q}_{\tau i}^T \left[\mathbf{D}_p^T (N_i \mathbf{I}) \hat{\mathbf{Z}}_{pp}^{\tau s} \mathbf{D}_p \left(N_j \mathbf{I} \right) \right] \boldsymbol{q}_{sj} + \delta \boldsymbol{q}_{\tau i}^T \left[\mathbf{D}_p^T (N_i \mathbf{I}) \hat{\mathbf{Z}}_{pn}^{\tau s} \left(N_j \mathbf{I} \right) + \mathbf{D}_{n\Omega}^T (N_i \mathbf{I}) (E_{\tau s} \mathbf{I}) \left(N_j \mathbf{I} \right) \right. \\
&\left. + (N_i \mathbf{I}) (E_{\tau_{,z} s} \mathbf{I}) \left(N_j \mathbf{I} \right) \right] \boldsymbol{g}_{sj} + \delta \boldsymbol{g}_{\tau i}^T \left[(N_i \mathbf{I}) (E_{\tau s} \mathbf{I}) \mathbf{D}_{n\Omega} \left(N_j \mathbf{I} \right) + (N_i \mathbf{I}) (E_{\tau s_{,z}} \mathbf{I}) \left(N_j \mathbf{I} \right) \right. \\
&\left. - (N_i \mathbf{I}) \hat{\mathbf{Z}}_{np}^{\tau s} \mathbf{D}_p \left(N_j \mathbf{I} \right) \right] \boldsymbol{q}_{sj} - \delta \boldsymbol{g}_{\tau i}^T (N_i \mathbf{I}) \hat{\mathbf{Z}}_{nn}^{\tau s} \left(N_j \mathbf{I} \right) \boldsymbol{g}_{sj} d\Omega = - \int_{\Omega_e} \delta \boldsymbol{q}_{\tau i}^T (N_i \mathbf{I}) \rho E_{\tau s} \left(N_j \mathbf{I} \right) \ddot{\boldsymbol{q}}_{sj} d\Omega \,,
\end{aligned}
\tag{35}
$$

where:

$$
\left(\hat{\mathbf{Z}}_{wr}^{\tau s}, \hat{\mathbf{Z}}_{wr}^{\tau_{,z} s}, \hat{\mathbf{Z}}_{wr}^{\tau s_{,z}}, \hat{\mathbf{Z}}_{wr}^{\tau_{,z} s_{,z}} \right) = \left(\hat{\mathbf{C}}_{wr} E_{\tau s}, \hat{\mathbf{C}}_{wr} E_{\tau_{,z} s}, \hat{\mathbf{C}}_{wr} E_{\tau s_{,z}}, \hat{\mathbf{C}}_{wr} E_{\tau_{,z} s_{,z}} \right) : \; w, r = p, n \,. \tag{36}
$$

In a compact form:

$$
\begin{aligned}
&\delta \boldsymbol{q}_{\tau i}^T \mathbf{K}_{uu}^{\tau sij} \boldsymbol{q}_{sj} + \delta \boldsymbol{q}_{\tau i}^T \mathbf{K}_{u\sigma}^{\tau sij} \boldsymbol{g}_{sj} = - \delta \boldsymbol{q}_{\tau i}^T \mathbf{M}^{\tau sij} \ddot{\boldsymbol{q}}_{sj} \,, \\
&\delta \boldsymbol{g}_{\tau i}^T \mathbf{K}_{\sigma u}^{\tau sij} \boldsymbol{q}_{sj} + \delta \boldsymbol{g}_{\tau i}^T \mathbf{K}_{\sigma\sigma}^{\tau sij} \boldsymbol{g}_{sj} = 0 \,.
\end{aligned}
\tag{37}
$$

In this case, four fundamental nuclei are obtained. The components of the FN for the RMVT case can be written as:

$$
\begin{aligned}
&K_{uuxx}^{\tau sij} = \int_{\Omega_e} \left(\hat{Z}_{pp11}^{\tau s} N_{j,x} N_{i,x} + \hat{Z}_{pp31}^{\tau s} N_{j,x} N_{i,y} + \hat{Z}_{pp13}^{\tau s} N_{j,y} N_{i,x} + \hat{Z}_{pp33}^{\tau s} N_{j,y} N_{i,y} \right) d\Omega \,, \\
&K_{uuxy}^{\tau sij} = \int_{\Omega_e} \left(\hat{Z}_{pp12}^{\tau s} N_{j,y} N_{i,x} + \hat{Z}_{pp32}^{\tau s} N_{j,y} N_{i,y} + \hat{Z}_{pp13}^{\tau s} N_{j,x} N_{i,x} + \hat{Z}_{pp33}^{\tau s} N_{j,x} N_{i,y} \right) d\Omega \,, \\
&K_{uuyx}^{\tau sij} = \int_{\Omega_e} \left(\hat{Z}_{pp21}^{\tau s} N_{j,x} N_{i,y} + \hat{Z}_{pp31}^{\tau s} N_{j,x} N_{i,x} + \hat{Z}_{pp23}^{\tau s} N_{j,y} N_{i,y} + \hat{Z}_{pp33}^{\tau s} N_{j,y} N_{i,x} \right) d\Omega \,, \\
&K_{uuyy}^{\tau sij} = \int_{\Omega_e} \left(\hat{Z}_{pp22}^{\tau s} N_{j,y} N_{i,y} + \hat{Z}_{pp32}^{\tau s} N_{j,y} N_{i,x} + \hat{Z}_{pp23}^{\tau s} N_{j,x} N_{i,y} + \hat{Z}_{pp33}^{\tau s} N_{j,x} N_{i,x} \right) d\Omega \,, \\
&K_{uuxz}^{\tau sij} = 0 \,, \quad K_{uuyz}^{\tau sij} = 0 \,, \quad K_{uuzx}^{\tau sij} = 0 \,, \quad K_{uuzy}^{\tau sij} = 0 \,, \quad K_{uuzz}^{\tau sij} = 0 \,, \\
&K_{u\sigma xx}^{\tau sij} = \int_{\Omega_e} \left(E_{\tau,zs} N_j N_i \right) d\Omega \,, \quad K_{u\sigma xz}^{\tau sij} = \int_{\Omega_e} \left(\hat{Z}_{pn13}^{\tau s} N_j N_{i,x} + \hat{Z}_{pn33}^{\tau s} N_j N_{i,y} \right) d\Omega \,, \\
&K_{u\sigma yy}^{\tau sij} = \int_{\Omega_e} \left(E_{\tau,zs} N_j N_i \right) d\Omega \,, \quad K_{u\sigma yz}^{\tau sij} = \int_{\Omega_e} \left(\hat{Z}_{pn23}^{\tau s} N_j N_{i,y} + \hat{Z}_{pn33}^{\tau s} N_j N_{i,x} \right) d\Omega \,, \\
&K_{u\sigma zx}^{\tau sij} = \int_{\Omega_e} \left(E_{\tau s} N_j N_{i,x} \right) d\Omega \,, \quad K_{u\sigma zy}^{\tau sij} = \int_{\Omega_e} \left(E_{\tau s} N_j N_{i,y} \right) d\Omega \,, \quad K_{u\sigma zz}^{\tau sij} = \int_{\Omega_e} \left(E_{\tau,zs} N_j N_i \right) d\Omega \,, \\
&K_{u\sigma xy}^{\tau sij} = 0 \,, \quad K_{u\sigma yx}^{\tau sij} = 0 \,, \\
&K_{\sigma uxx}^{\tau sij} = \int_{\Omega_e} \left(E_{\tau s,z} N_j N_i \right) d\Omega \,, \quad K_{\sigma uxz}^{\tau sij} = \int_{\Omega_e} \left(E_{\tau s} N_{j,x} N_i \right) d\Omega \,, \quad K_{\sigma uyy}^{\tau sij} = \int_{\Omega_e} \left(E_{\tau s,z} N_j N_i \right) d\Omega \,, \\
&K_{\sigma uyz}^{\tau sij} = \int_{\Omega_e} \left(E_{\tau s} N_{j,y} N_i \right) d\Omega \,, \quad K_{\sigma uzx}^{\tau sij} = - \int_{\Omega_e} \left(\hat{Z}_{np31}^{\tau s} N_{j,x} N_i - \hat{Z}_{np33}^{\tau s} N_{j,y} N_i \right) d\Omega \,, \\
&K_{\sigma uzy}^{\tau sij} = - \int_{\Omega_e} \left(\hat{Z}_{np32}^{\tau s} N_{j,y} N_i - \hat{Z}_{np33}^{\tau s} N_{j,x} N_i \right) d\Omega \,, \quad K_{\sigma uzz}^{\tau sij} = \int_{\Omega_e} \left(E_{\tau s,z} N_j N_i \right) d\Omega \,, \\
&K_{\sigma uxy}^{\tau sij} = 0 \,, \quad K_{\sigma uyx}^{\tau sij} = 0 \,, \\
&K_{\sigma\sigma xx}^{\tau sij} = - \int_{\Omega_e} \left(\hat{Z}_{nn11}^{\tau s} N_j N_i \right) d\Omega \,, \quad K_{\sigma\sigma xy}^{\tau sij} = - \int_{\Omega_e} \left(\hat{Z}_{nn12}^{\tau s} N_j N_i \right) d\Omega \,, \\
&K_{\sigma\sigma yx}^{\tau sij} = - \int_{\Omega_e} \left(\hat{Z}_{nn21}^{\tau s} N_j N_i \right) d\Omega \,, \quad K_{\sigma\sigma xx}^{\tau sij} = - \int_{\Omega_e} \left(\hat{Z}_{nn22}^{\tau s} N_j N_i \right) d\Omega \,, \\
&K_{\sigma\sigma xz}^{\tau sij} = 0 \,, \quad K_{\sigma\sigma yz}^{\tau sij} = 0 \,, \quad K_{\sigma\sigma zx}^{\tau sij} = 0 \,, \quad K_{\sigma\sigma zy}^{\tau sij} = 0 \,, \quad K_{\sigma\sigma zz}^{\tau sij} = 0 \,.
\end{aligned}
\tag{38}
$$

The mass FN is the same as the PVD case; see Equation (33). Since the in-plane integrals are calculated via Gauss quadrature, it is crucial to consider an appropriate number of Gauss points in accordance with the variational rule of the fiber angle.

3. Results and Discussion

Three cases are analyzed in this work: a cantilever monolayer plate, a clamped multilayer plate and a clamped multilayer plate with a central circular cut-out. For each case, a square geometry is considered ($a = b = 1$ m). Parametric studies are performed considering different side-to-thickness ratios ($a/h = 100, 10, 5$). Material properties are represented in Table 1 for all the considered analyzed cases.

Table 1. Material properties.

Case	E_L (GPa)	E_T (GPa)	$G_{LT} = G_{TT}$ (GPa)	$\nu_{LT} = \nu_{TT}$
1	50.0	10.0	5.0	0.25
2	173.0	7.2	3.8	0.29
3	138.0	9.0	7.1	0.30

Reference solutions are represented by an Abaqus 3D model where quadratic elements (C3D20R) were used. For CUF solutions, nine-node square elements were used. For each case study, a preliminary convergence analysis was carried out to identify the appropriate mesh for both CUF and Abaqus solutions.

3.1. Monolayer Plate

The first case corresponds to a cantilever monolayer plate with density $\rho = 1540\ \mathrm{kg/m^3}$. For this problem, axes x' and y' of the angle reference system are coincident with axes x and y of the plate. This means that the origin of the angle reference system is the same as the global one and that x' and y' are parallel to x and y, respectively. It is assumed that the fiber angle is a linear function of y'; see Equation (10). The length parameter corresponds to $d = b$, while the direction of fiber variation α corresponds to y', which means that $\Phi = 90°$. In this case, $T_0 = 0°$ and $T_1 = 90°$. The fiber orientation changes only along y' from a value of $\theta(0) = \Phi + T_0 = 90°$ to $\theta(b) = \Phi + T_1 = 180°$. The angle variational law in this case can be expressed as $90 < 0, 90 >$, and it is presented in Figure 4.

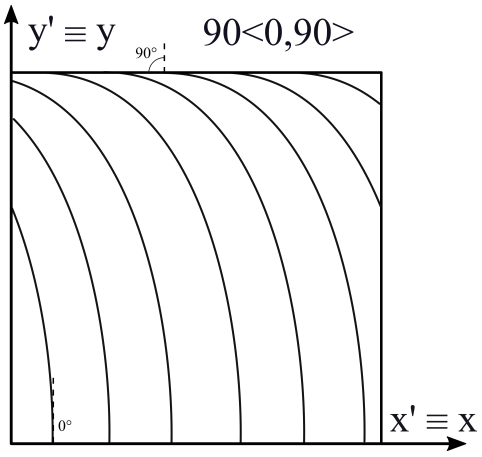

Figure 4. Stacking sequence; case 1.

This law has been taken from Viglietti et al. [27]. The reference solution contains 80 elements along each in-plane side and 12 elements along the thickness. The only clamped side of the plate is the one that lies on the xz plane, corresponding to $y' = 0$. For the CUF results, a 10×10 mesh is considered. Table 2 shows the degrees Of freedom (DOF) for some considered solutions.

Table 2. Degrees of freedom; case 1.

Model	DOF
Abaqus 3D	997,515
3LM4	34,398
2LM2	13,230
3LD4	17,199
2LD2	6615
ED4	6615
ED2	3969
FSDT	2646
CLT	2646

It is possible to observe that higher-order CUF models allow for a DOF reduction of one order of magnitude in comparison with the Abaqus 3D reference solution. Table 3 shows the first five natural frequencies for $a/h = 100$.

Table 3. Natural frequencies (Hz), $a/h = 100$; case 1.

	Mode				
	1	**2**	**3**	**4**	**5**
Abaqus 3D	7.397	16.354	37.158	48.025	63.349
3LM4	7.399	16.334	37.164	47.988	63.310
2LM2	7.398	16.333	37.162	47.986	63.309
3LD4	7.400	16.362	37.179	48.053	63.378
2LD2	7.400	16.362	37.179	48.054	63.379
ED4	7.400	16.362	37.179	48.053	63.378
ED2	7.401	16.368	37.186	48.069	63.399
FSDT	7.398	16.363	37.171	48.054	63.388
CLT	7.403	16.414	37.213	48.175	63.537

For this case, classic and higher-order theories show very good approximations of the reference solution, where the maximum difference from the reference solution is 0.4% for the second natural frequency computed via CLT. Table 4 shows the first five natural frequencies for $a/h = 10$.

Table 4. Natural frequencies (Hz), $a/h = 10$; case 1.

	Mode				
	1	**2**	**3**	**4**	**5**
Abaqus 3D	72.229	151.762	338.517	389.336	431.011
3LM4	72.244	151.751	338.577	389.554	431.004
2LM2	72.233	151.705	338.432	389.546	430.824
3LD4	72.250	151.796	338.625	389.587	431.151
2LD2	72.269	151.906	338.939	389.589	431.577
ED4	72.253	151.810	338.669	389.588	431.207
ED2	72.466	153.069	342.179	389.592	435.990
FSDT	72.437	153.021	342.036	389.510	435.853
CLT	73.825	163.064	365.813	389.510	472.565

It is possible to observe that classical and lower-order ESL theories are now less accurate, especially for the prediction of higher frequencies. For example, CLT, FSDT and ED2 models, corresponding to the third natural frequency, present a percentage error equal to 8.1%, 1.0% and 1.1%, respectively. This can be explained by considering that the side-to-thickness ratio $a/h = 10$ corresponds to a thick plate. In this case, higher-order theories are needed to obtain an accurate approximation. Since a moderately thick plate is considered, transverse shear stresses affect the solution. This is the reason that CLT, which neglects those stresses, is less close to the reference solution. The best approximations of plate natural frequencies are given by 2LM2 and 3LM4 mixed theories, which show a maximum percentage error of 0.1% each for the fourth natural frequency. In particular, it is possible to observe that the 2LM2 solution is globally closer to Abaqus in comparison with the 3LD4 solution, even if the last one is characterized by a higher number of degrees of freedom. Table 5 shows the first five natural frequencies for $a/h = 5$.

Because of the low side-to-thickness ratio, a very thick plate is considered, and lower-order theories do not provide a correct prediction of the natural frequencies. For CLT, the sixth mode is the same as the fifth mode of the reference solution, that is, the order of appearance is swapped. In this regard, mode tracking was performed by visually comparing the modes of each proposed solution with those of the reference solution obtained in Abaqus. The corresponding percentage error is as high as 27.1%. On the other hand, a 3LM4 model matches the Abaqus reference results.

Table 5. Natural frequencies (Hz), $a/h = 5$; case 1.

	Mode				
	1	**2**	**3**	**4**	**5**
Abaqus 3D	136.723	264.080	389.391	556.394	704.284
3LM4	136.742	264.077	389.557	556.404	704.295
2LM2	136.667	263.747	389.550	555.332	703.121
3LD4	136.755	264.119	389.638	556.511	704.442
2LD2	136.875	264.684	389.643	558.145	706.381
ED4	136.774	264.224	389.640	556.855	704.832
ED2	138.015	269.553	389.651	570.563	721.354
FSDT	137.947	269.463	389.510	570.329	721.159
CLT	146.479	319.929	389.510	696.687	895.089

3.2. Multilayer Plate

The second case is taken from Viglietti et al. [27] and corresponds to a multilayer clamped plate with density $\rho = 1540\ \mathrm{kg/m^3}$. The plate is composed of three layers with the same thicknesses. It is assumed that fiber angle is a function of y' only, which means that α is parallel to y' ($\Phi = 90°$). In this case, a linear law is considered for the fiber path, according to Equation (10). For this problem, axes x' and y' of the angle reference system are aligned with axes x and y of the plate, but their origin is placed on the center of the plate $(a/2, b/2)$. In this case, $d = b/2$ is considered as the length parameter in Equation (10). T_0 and T_1 are set for each layer as follows: $T_0^{layer1} = T_0^{layer3} = 0°$, $T_0^{layer2} = -45°$, $T_1^{layer1} = T_1^{layer3} = 45°$, $T_1^{layer2} = -60°$. The lamination of the plate is $90 < 0, 45 >$ for layer 1, $90 < -45, -60 >$ for layer 2 and $90 < 0, 45 >$ for layer 3. The stacking sequence is presented in Figure 5.

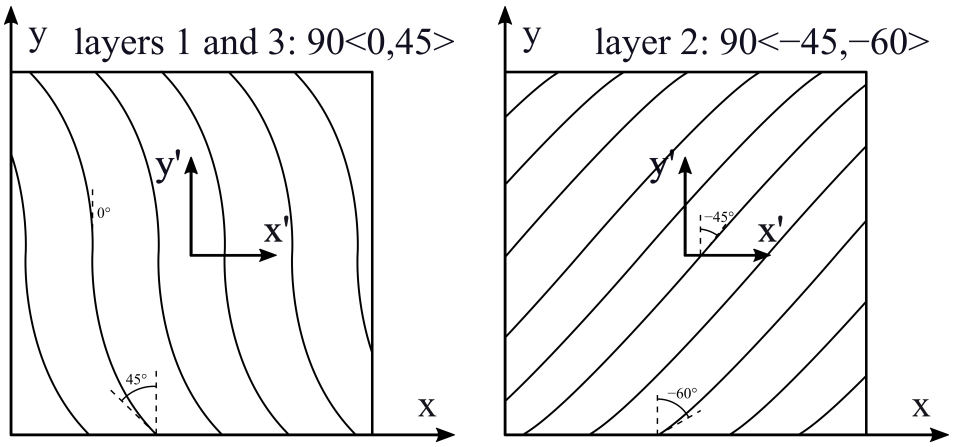

Figure 5. Stacking sequence; case 2.

As for the previous case, the Abaqus reference solution contains 80 elements along each side and 12 elements along the thickness. For the CUF results, a 10×10 mesh is considered. Table 6 shows the first five natural frequencies for $a/h = 100$, together with the results presented in Viglietti et al. [27].

In this case, the best approximation is given by the LM2 and LM4 theories. The LM2 and LM4 models both have a maximum percentage error as high as 0.4% corresponding to the third frequency. In addition, classical and low-order theories provide good results since a thin plate is considered. For this reason, transverse stresses do not play an important role. For example, the maximum error given by CLT is 2.1% for the fifth frequency. The case for $a/h = 10$ is presented in Table 7.

Table 6. Natural frequencies (Hz), $a/h = 100$; case 2.

	Mode				
	1	**2**	**3**	**4**	**5**
Abaqus 3D	92.18	130.68	194.96	237.56	274.60
Ref. [27]	92.90	132.28	198.97	240.46	278.75
LM4	92.35	131.01	195.77	238.25	275.60
LM2	92.34	130.99	195.74	238.23	275.58
LD4	92.36	131.03	195.81	238.30	275.67
LD2	92.36	131.04	195.84	238.31	275.69
ED4	92.37	131.06	195.88	238.32	275.72
ED2	92.49	131.23	196.16	238.97	276.48
FSDT	92.38	131.01	195.75	238.74	276.20
CLT	93.04	131.85	197.00	242.48	280.40

Table 7. Natural frequencies (Hz), $a/h = 10$; case 2.

	Mode				
	1	**2**	**3**	**4**	**5**
Abaqus 3D	606.67	896.70	1208.24	1313.26	1458.25
Ref. [27]	609.79	903.63	1216.00	1328.41	1469.33
LM4	606.90	897.26	1208.80	1314.85	1459.23
LM2	606.33	896.52	1206.86	1313.56	1457.30
LD4	607.22	897.73	1209.64	1315.80	1460.16
LD2	608.65	901.20	1213.06	1322.93	1465.20
ED4	609.84	905.18	1214.60	1331.82	1469.17
ED2	633.68	941.96	1272.39	1396.16	1540.10
FSDT	632.82	940.46	1271.42	1393.96	1538.74
CLT	921.28	1287.71	2368.22	1885.61	2699.22

Here, the CLT model shows that the inversion of the third and fourth modes can be observed by the corresponding values of the frequencies that are not in ascending order as the mode number increases. In comparison with the monolayer plate, in this case, the mode inversions of the CLT model can be seen for higher side-to-thickness ratios and lower frequencies. For the third mode, CLT shows a percentage error of 96.0%, while the best approximation is given by LM4, which has a percentage error of 0.17% for the same mode. Table 8 shows the first five frequencies for $a/h = 5$.

Table 8. Natural frequencies (Hz), $a/h = 5$; case 2.

	Mode				
	1	**2**	**3**	**4**	**5**
Abaqus 3D	794.730	1201.916	1439.956	1701.328	1810.250
LM4	794.760	1202.101	1440.092	1701.788	1811.113
LM2	792.734	1199.331	1433.897	1696.266	1805.942
LD4	795.213	1202.777	1441.080	1702.986	1812.317
LD2	799.063	1209.706	1448.714	1713.982	1820.716
ED4	802.019	1216.744	1450.930	1723.900	1825.405
ED2	845.154	1294.481	1523.246	1847.193	1930.364
FSDT	844.048	1292.846	1522.478	1845.945	1928.631
CLT	1790.121	2411.198	-	-	-

In this case, lower-order theories have an evident loss of accuracy. The CLT model can predict only the first two modes. In addition, the FSDT and ED2 models show non-negligible errors, which become bigger with the increase in frequency. On the other hand, mixed models are able to correctly predict the dynamic behavior of the plate for both low and high frequencies.

3.3. Multilayer Plate with Central Hole

Case 3 is taken from Hachemi et al. [9] and corresponds to a multilayer clamped plate that presents a circular cut-out. The center of the cut-out is placed at the plate center $(a/2, b/2)$, and its radius is $r = 0.2$ m. It is assumed that the fiber angle is a parabolic function of x', which means that α is parallel to x' ($\Phi = 0°$). As in the previous case, the x' and y' axes are parallel, respectively, to x and y, and their origin is placed at the center of the plate. The angle variational law is defined in Equation (12), considering $d = a/2$. The plate is composed of two layers that have the same thicknesses. The values of T_0 and T_1 are set for each layer as follows: $T_0^{layer1} = T_0^{layer2} = 0°$, $T_1^{layer1} = 30°$, $T_1^{layer2} = -30°$. The stacking sequence is $0 < 0, \pm 30 >$; see Figure 6.

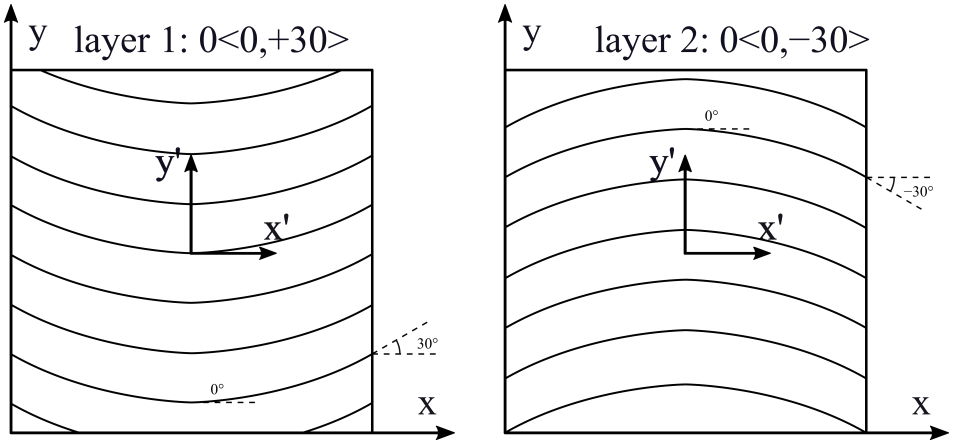

Figure 6. Stacking sequence; case 3.

In this case, the Abaqus reference solution is made of 73728 elements: 4608 elements are defined on the plate plane, and 16 elements are defined along the thickness. For the CUF results, 128 elements are used on the plate plane. The natural frequencies are expressed in the following dimensionless form:

$$\overline{\omega} = \left(\omega a^2\right)\sqrt{\rho h / D_0}\,, \tag{39}$$

$$D_0 = E_2 h^3 / 12(1 - \nu_{LT}\nu_{TL})\,, \tag{40}$$

where ω is the natural frequency, while D_0 represents a reference bending stiffness. Table 9 presents the first five non-dimensional frequencies for $a/h = 100$.

Table 9. Non-dimensional frequencies $\overline{\omega}$, $a/h = 100$; case 3.

	Mode				
	1	**2**	**3**	**4**	**5**
Abaqus 3D	87.079	106.407	147.559	184.034	197.096
LM4	87.281	106.622	147.070	184.554	197.522
LM2	87.259	106.593	147.045	184.500	197.489
LD4	87.327	106.704	147.911	184.789	197.969
LD2	87.336	106.719	147.952	184.821	198.022
ED4	87.331	106.708	147.921	184.798	197.984
ED2	87.364	106.768	148.169	184.931	198.228
FSDT	87.184	106.538	148.047	184.525	198.029
CLT	87.387	106.942	150.080	185.420	199.725

It is possible to observe that the theories show a good approximation of the reference results. In addition, the percentage errors of FSDT and CLT are less than 2%. Mixed theories match the Abaqus results. Table 10 shows the results for $a/h = 10$ in order to compare the

Abaqus reference solution with the one presented in Hachemi et al. [9] and the solutions obtained with CUF.

Table 10. Non-dimensional frequencies $\overline{\omega}$, $a/h = 10$; case 3.

	Mode				
	1	**2**	**3**	**4**	**5**
Abaqus 3D	72.645	86.745	104.279	136.366	140.278
Ref. [9]	72.432	86.626	103.910	135.828	139.747
LM4	72.699	86.830	104.307	136.467	140.408
LM2	72.573	86.700	104.051	136.137	140.143
LD4	72.744	86.888	104.376	136.558	140.516
LD2	73.107	87.263	105.144	137.567	141.231
ED4	72.868	86.990	104.630	136.851	140.725
ED2	73.977	88.609	107.143	140.522	143.556
FSDT	74.075	88.782	107.645	141.221	143.885
CLT	84.751	104.166	143.133	190.321	174.656

As already observed in previous cases, classical theories and, in general, low-order ones are not able to provide an accurate approximation of natural frequencies, because of the low side-to-thickness ratio value. It is also possible that this generates the inversion of modes four and five for the CLT case. On the other hand, the best approximation is given by mixed theories, which are closer to the Abaqus solution for high frequencies. The shapes of the modes are presented in Figures 7–11 for $a/h = 10$. The modal shapes obtained with the LM4 model are compared with those of Abaqus 3D.

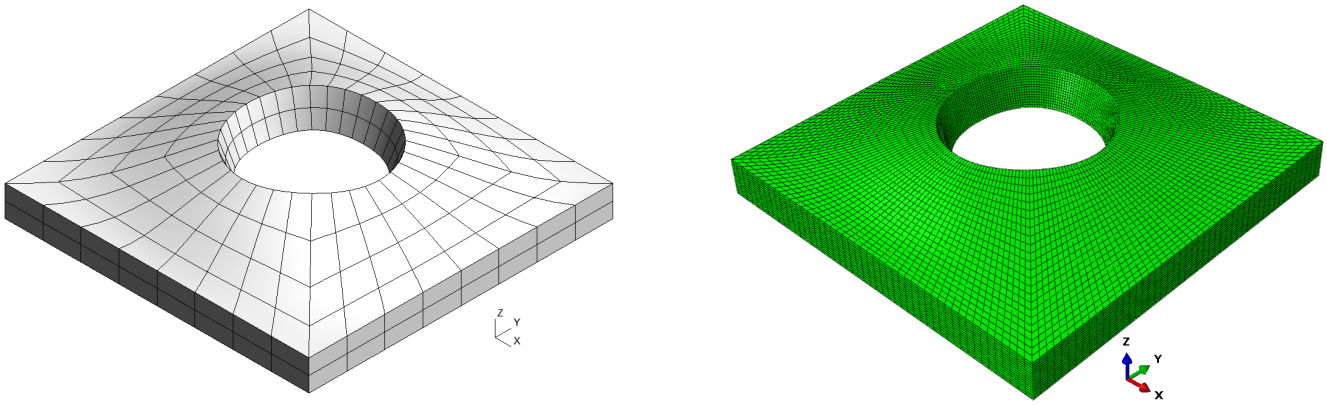

(**a**) LM4 (**b**) Abaqus 3D

Figure 7. Mode 1, $a/h = 10$; case 3.

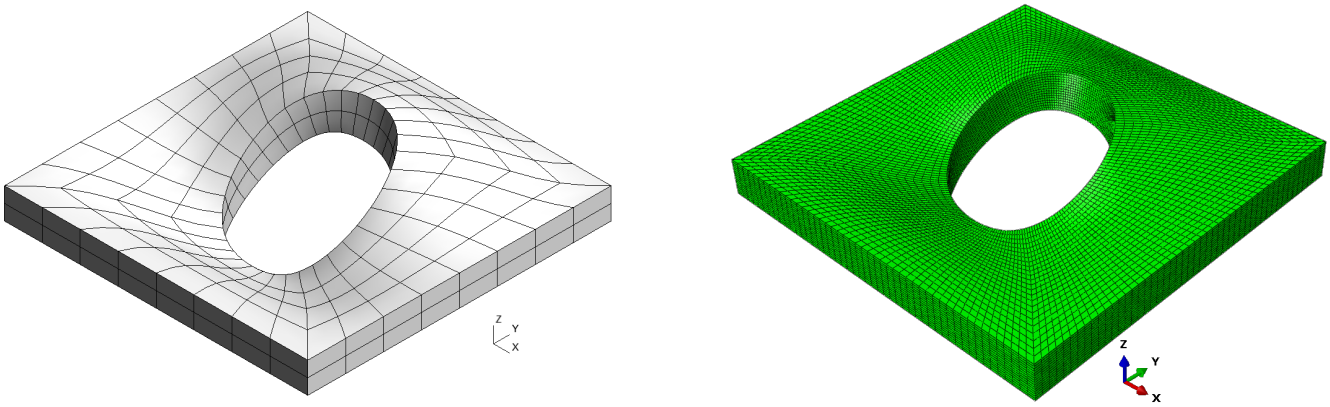

(**a**) LM4 (**b**) Abaqus 3D

Figure 8. Mode 2, $a/h = 10$; case 3.

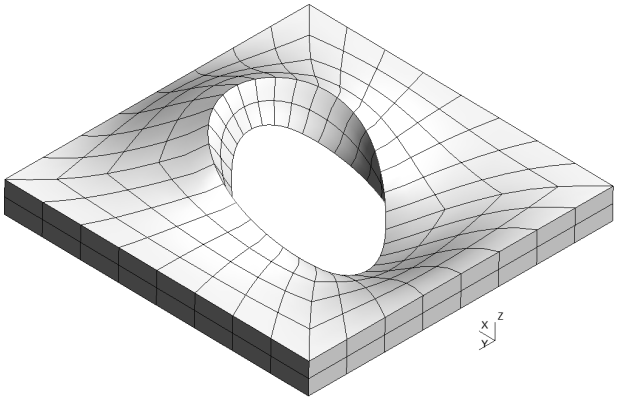

(**a**) LM4

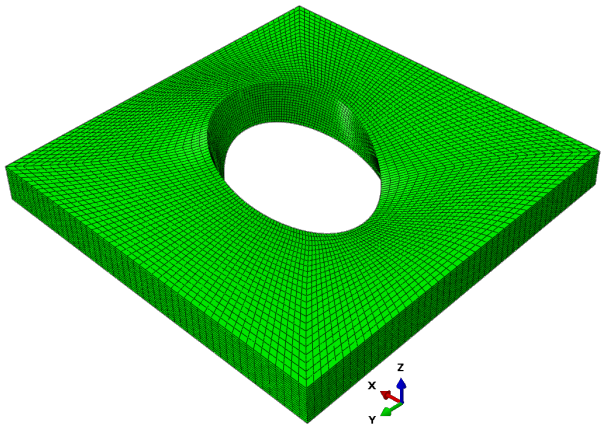

(**b**) Abaqus 3D

Figure 9. Mode 3, $a/h = 10$; case 3.

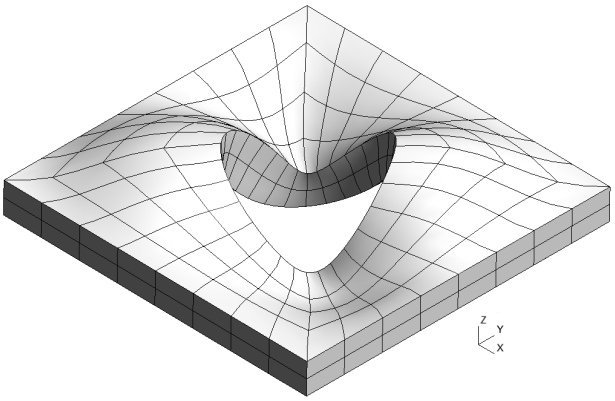

(**a**) LM4

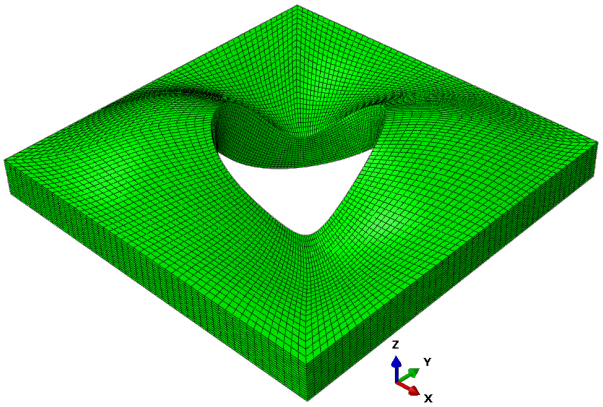

(**b**) Abaqus 3D

Figure 10. Mode 4, $a/h = 10$; case 3.

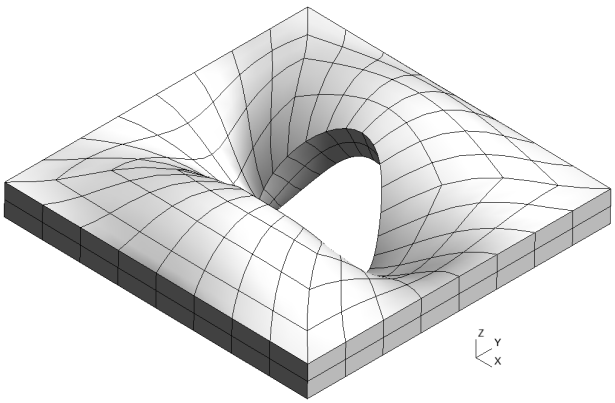

(**a**) LM4

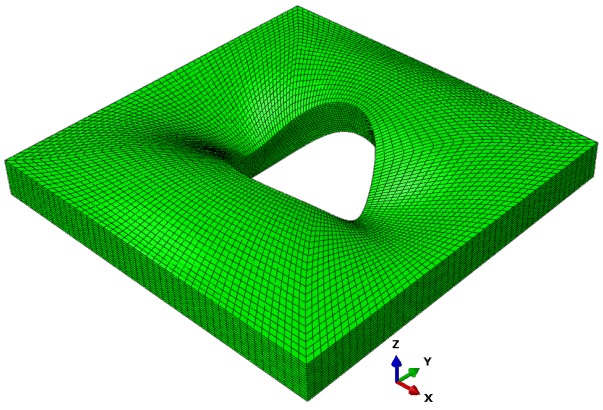

(**b**) Abaqus 3D

Figure 11. Mode 5, $a/h = 10$; case 3.

The first mode shows a simple bending of the plate on the xy plane with a single half-wave along each in-plane direction. The second and the third modes show two half-waves in the y and x directions, respectively. Mode number four shows three half-waves along the plate diagonally between the x and y axes. The fifth mode shows three half-waves along the y direction. Finally, Table 11 shows the frequencies for $a/h = 5$.

Table 11. Non-dimensional frequencies $\overline{\omega}$, $a/h = 5$; case 3.

	Mode				
	1	**2**	**3**	**4**	**5**
Abaqus 3D	54.333	64.456	70.572	90.875	98.086
LM4	54.326	64.456	70.541	90.866	98.098
LM2	54.038	64.201	70.036	90.292	97.612
LD4	54.388	64.514	70.619	90.956	98.191
LD2	54.875	64.963	71.421	91.868	98.955
ED4	54.554	64.623	70.913	91.224	98.408
ED2	56.062	66.756	73.181	94.442	101.535
FSDT	56.253	66.985	73.702	95.219	102.017
CLT	76.928	95.975	119.513	-	-

Since a thick plate is considered, the effect of transverse stresses is not negligible, which causes the classical and lower-order theories to be inaccurate. This can be observed for CLT, which is not able to predict the fourth and fifth modes and has an error as high as 69.4% for the third mode. Considering the FSDT, ED4 and LD4 models, this error can be reduced to 4.4%, 0.5% and 0.1%, respectively.

4. Conclusions

In this paper, a new framework for the dynamic analysis of VAT structures is presented. RMVT is developed within CUF in order to obtain a new family of 2D models for the free-vibration analysis of VAT plates. The results are obtained via either RMVT or PVD and are compared in order to show the effective capabilities of the proposed method in the prediction of VAT plates' natural frequencies. The Abaqus 3D reference solutions and results from Refs. [9,27] are also included to further validate the models proposed in this article. Linear and parabolic laws are both considered in order to describe the in-plane path of fiber variation. The possibility to use a polynomial order defined a priori through CUF and the introduction of the transverse stress field as a primary variable of the problem through RMVT both help to obtain a valid approach for the prediction of VAT dynamic behavior. After the results analysis, the following remarks can be made:

- Classical theories (FSDT and CLT) provide the best trade-off between accuracy and computational costs for thin plates ($a/h = 100$), whereas they are not able to correctly predict the behavior of thicker plates ($a/h = 10$ and 5), specially at high frequencies. The loss of accuracy is more evident for CLT results, since this theory does not consider transverse shear stresses, which become important in thick plates. This error is particularly evident in the second- and third-order theories, where the inversion of modes can be observed.
- The PVD results show monotonic convergence to the reference solution: the lower the DOF number, the higher the frequency value. For a given mode, frequency values decrease when higher-order models are employed, and they move closer to the reference solution.
- In all the cases, layer-wise mixed theories yield the best match of the reference 3D solution, independently from the plate geometry or fiber variational law. This is justified by the fact that RMVT considers both displacements and transverse stresses as primary variables, assuring a better approximation of the transverse stresses field into the problem domain, and improving the overall solution accuracy.
- For a given expansion order, models based on RMVT are more computationally expensive than PVD models. For this reason, the use of LW mixed models is advantageous in the cases where a more precise representation of the through-the-thickness behavior is needed, as in the case of higher frequencies or for thick plates, whereas low-order ESL and classical models are accurate for lower frequencies and thin plates.

In conclusion, the application of RMVT within CUF has demonstrated significant potential for improving the accuracy and efficiency of modeling VAT plates for free-vibration

analyses. The promising results suggest, as future perspectives, the extension to buckling and failure analyses where an accurate and efficient modeling of VAT structures under various loading and operational conditions is required.

Author Contributions: Methodology, G.G., D.A.I. and M.M.; Software, D.A.I.; Validation, D.A.I.; Writing—original draft, D.A.I.; Writing—review & editing, G.G. and M.M.; Supervision, G.G. and M.M.; Funding acquisition, G.G. and M.M. All authors have read and agreed to the published version of the manuscript.

Funding: This research was funded by the Luxembourg National Research Fund (FNR), grant reference INTER/ANR/21/16215936 GLAMOUR-VSC. For the purpose of open access, and in fulfillment of the obligations arising from the grant agreement, the author has applied a Creative Commons Attribution 4.0 International (CC BY 4.0) license to any Author Accepted Manuscript version arising from this submission. M. Montemurro is grateful to French National Research Agency for supporting this work through the research project GLAMOUR-VSC (Global–LocAl two-level Multi-scale optimisation strategy accOUnting for pRocess-induced singularities to design Variable Stiffness Composites) ANR-21-CE10-0014.

Institutional Review Board Statement: Not applicable.

Informed Consent Statement: Not applicable.

Data Availability Statement: Not applicable.

Conflicts of Interest: The authors declare no conflict of interest.

References

1. Dirk, H.J.L.; Ward, C.; Potter, K.D. The engineering aspects of automated prepreg layup: History, present and future. *Compos. Part B Eng.* **2012**, *43*, 997–1009.
2. Zhuo, P.; Li, S.; Ashcroft, I.A.; Jones, A.I. Material extrusion additive manufacturing of continuous fiber reinforced polymer matrix composites: A review and outlook. *Compos. Part B Eng.* **2021**, *224*, 109143. [CrossRef]
3. Brooks, T.R.; Martins, J.R.; Kennedy, G.J. High-fidelity aerostructural optimization of tow-steered composite wings. *J. Fluids Struct.* **2019**, *88*, 122–147. [CrossRef]
4. Grenoble, R.W.; Nguyen, T.; McKenney, M.J.; Przekop, A.; Juarez, P.D.; Gregory, E.D.; Jegley, D.C. Fabrication of a composite tow-steered structure for air-launch vehicle applications. In Proceedings of the AIAA/ASCE/AHS/ASC Structures, Structural Dynamics, and Materials Conference, Kissimmee, FL, USA, 8–12 January 2018.
5. Hyer, M.W.; Charette, R.F. *Innovative Design of Composite Structures: The Use of Curvilinear Fiber Format in Composite Structure Design*; NASA Langley Research Center: Hampton, VA, USA, 1990.
6. Hyer, M.W.; Lee, H.H. Innovative design of composite structures: The use of curvilinear fiber format to improve buckling resistance of composite plates with central circular holes. *Compos. Struct.* **1991**, *18*, 239–261. [CrossRef]
7. Akhavan, H.; Ribeiro, P. Natural modes of vibration of variable stiffness composite laminates with curvilinear fibers. *Compos. Struct.* **2011**, *93*, 3040–3047. [CrossRef]
8. Ribeiro, P.; Akhavan, H. Non-linear vibrations of variable stiffness composite laminated plates. *Compos. Struct.* **2012**, *94*, 2424–2432. [CrossRef]
9. Hachemi, M.; Hamza-Cherif, S.M.; Houmat, A. Free vibration analysis of variable stiffness composite laminate plate with circular cutout. *Aust. J. Mech. Eng.* **2020**, *18*, 63–79. [CrossRef]
10. Zhao, W.; Kapania, R.K. Prestressed vibration of stiffened variable-angle tow laminated plates. *AIAA J.* **2019**, *57*, 2575–2593. [CrossRef]
11. Honda, S.; Narita, Y. Natural frequencies and vibration modes of laminated composite plates reinforced with arbitrary curvilinear fiber shape paths. *J. Sound Vib.* **2012**, *331*, 180–191. [CrossRef]
12. Rodrigues, J.D.; Ribeiro, P.; Akhavan, H. Experimental and finite element modal analysis of variable stiffness composite laminated plates. In Proceedings of the 11th Biennial International Conference on Vibration Problems (ICOVP-2013), Lisbon, Portugal, 9–12 September 2013; Volume 30.
13. Stodieck, O.; Cooper, J.E.; Weaver, P.M.; Kealy, P. Improved aeroelastic tailoring using tow-steered composites. *Compos. Struct.* **2013**, *106*, 703–715. [CrossRef]
14. Abdalla, M.M.; Setoodeh, S.; Gürdal, Z. Design of variable stiffness composite panels for maximum fundamental frequency using lamination parameters. *Compos. Struct.* **2007**, *81*, 283–291. [CrossRef]
15. Blom, A.W.; Setoodeh, S.; Hol, J.; Gürdal, Z. Design of variable-stiffness conical shells for maximum fundamental eigenfrequency. *Comput. Struct.* **2008**, *86*, 870–878. [CrossRef]
16. Carvalho, J.; Sohouli, A.; Suleman, A. Fundamental Frequency Optimization of Variable Angle Tow Laminates with Embedded Gap Defects. *J. Compos. Sci.* **2022**, *6*, 64. [CrossRef]

17. Montemurro, M.; Catapano, A. On the effective integration of manufacturability constraints within the multi-scale methodology for designing variable angle-tow laminates. *Compos. Struct.* **2017**, *161*, 145–159. [CrossRef]
18. Catapano, A.; Montemurro, M.; Balcou, J.-A.; Panettieri, E. Rapid prototyping of variable angle-tow composites. *Aerotec. Missili Spaz.* **2019**, *98*, 257–271. [CrossRef]
19. Montemurro, M.; Catapano, A. A general B-Spline surfaces theoretical framework for optimisation of variable angle-tow laminates. *Compos. Struct.* **2019**, *209*, 561–578. [CrossRef]
20. Fiordilino, G.A.; Izzi, M.I.; Montemurro, M. A general isogeometric polar approach for the optimisation of variable stiffness composites: Application to eigenvalue buckling problems. *Mech. Mater.* **2021**, *153*, 103574. [CrossRef]
21. Carrera, E. Theories and finite elements for multilayered, anisotropic, composite plates and shells. *Arch. Comput. Meth. Eng.* **2002**, *9*, 87–140. [CrossRef]
22. Carrera, E. Theories and finite elements for multilayered plates and shells: A unified compact formulation with numerical assessment and benchmarking. *Arch. Comput. Meth. Eng.* **2003**, *10*, 215–296. [CrossRef]
23. Carrera, E.; Giunta, G.; Brischetto, S. Hierarchical closed form solutions for plates bent by localized transverse loadings. *J. Zhejiang Univ. Sci. A* **2007**, *8*, 1026–1037. [CrossRef]
24. Carrera, E.; Giunta, G. Hierarchical models for failure analysis of plates bent by distributed and localized transverse loadings. *J. Zhejiang Univ. Sci. A* **2008**, *9*, 600–613. [CrossRef]
25. Giunta, G.; Catapano, A.; Belouettar, S. Failure indentation analysis of composite sandwich plates via hierarchical models. *J. Sandw. Struct. Mater.* **2013**, *15*, 45–70. [CrossRef]
26. Giunta, G.; Biscani, F.; Belouettar, S.; Ferreira, A.J.M.; Carrera, E. Free vibration analysis of composite beams via refined theories. *Compos. Part B Eng.* **2013**, *44*, 540–552. [CrossRef]
27. Viglietti, A.; Zappino, E.; Carrera, E. Analysis of variable angle tow composites structures using variable kinematic models. *Compos. Part B Eng.* **2019**, *171*, 272–283. [CrossRef]
28. Fallahi, N.; Viglietti, A.; Carrera, E.; Pagani, A.; Zappino, E. Effect of fiber orientation path on the buckling, free vibration, and static analyses of variable angle tow panels. *Facta Univ. Ser. Mech. Eng.* **2020**, *18*, 165–188. [CrossRef]
29. Sánchez-Majano, A.R.; Azzara, R.; Pagani, A.; Carrera, E. Accurate Stress Analysis of Variable Angle Tow Shells by High-Order Equivalent-Single-Layer and Layer-Wise Finite Element Models. *Materials* **2021**, *14*, 6486. [CrossRef]
30. Pagani, A.; Sánchez-Majano, A.R. Influence of fiber misalignments on buckling performance of variable stiffness composites using layerwise models and random fields. *Mech. Adv. Mater. Struct.* **2022**, *29*, 384–399. [CrossRef]
31. Pagani, A.; Sánchez-Majano, A.R. Stochastic stress analysis and failure onset of variable angle tow laminates affected by spatial fiber variations. *Compos. Part C Open Access* **2021**, *4*, 100091. [CrossRef]
32. Sánchez-Majano, A.R.; Pagani, A.; Petrolo, M.; Zhang, C. Buckling sensitivity of tow-steered plates subjected to multiscale defects by high-order finite elements and polynomial chaos expansion. *Materials* **2021**, *14*, 2706. [CrossRef]
33. Vescovini, R.; Dozio, L. A variable-kinematic model for variable stiffness plates: Vibration and buckling analysis. *Compos. Struct.* **2016**, *142*, 15–26. [CrossRef]
34. Demasi, L.; Biagini, G.; Vannucci, F.; Santarpia, E.; Cavallaro, R. Equivalent Single Layer, Zig-Zag, and Layer Wise theories for variable angle tow composites based on the Generalized Unified Formulation. *Compos. Struct.* **2017**, *177*, 54–79. [CrossRef]
35. Carrera, E.; Demasi, L. Classical and advanced multilayered plate elements based upon PVD and RMVT. Part 1: Derivation of finite element matrices. *Int. J. Numer. Methods Eng.* **2002**, *55*, 191–231. [CrossRef]
36. Carrera, E.; Demasi, L. Classical and advanced multilayered plate elements based upon PVD and RMVT. Part 2: Numerical implementations. *Int. J. Numer. Methods Eng.* **2002**, *55*, 253–291. [CrossRef]
37. Babaei, M.; Kiarasi, F.; Tehrani, M.S.; Hamzei, A.; Mohtarami, E.; Asemi, K. Three dimensional free vibration analysis of functionally graded graphene reinforced composite laminated cylindrical panel. *Proc. Inst. Mech. Eng. Part L J. Mater. Des. Appl.* **2022**, *236*, 1501–1514. [CrossRef]
38. Reddy, J.N. *Mechanics of Laminated Composite Plates and Shells: Theory and Analysis*; CRC Press: Boca Raton, FL, USA, 2003.
39. Gürdal, Z.; Tatting, B.F.; Wu, C.K. Variable stiffness composite panels: Effects of stiffness variation on the in-plane and buckling response. *Compos. Part A Appl. Sci. Manuf.* **2008**, *39*, 911–922. [CrossRef]
40. Honda, S.; Oonishi, Y.; Narita, Y.; Sasaki, K. Vibration analysis of composite rectangular plates reinforced along curved lines. *J. Syst. Des. Dyn.* **2008**, *2*, 76–86. [CrossRef]
41. Carrera, E. On the use of the Murakami's zig-zag function in the modeling of layered plates and shells. *Comput. Struct.* **2004**, *82*, 541–554. [CrossRef]
42. Bathe, K.-J. *Finite Element Procedures*; Prentice Hall: Upper Saddle River, NJ, USA, 2006.

MDPI
St. Alban-Anlage 66
4052 Basel
Switzerland
www.mdpi.com

Materials Editorial Office
E-mail: materials@mdpi.com
www.mdpi.com/journal/materials

MDPI

Academic Open
Access Publishing

mdpi.com

ISBN 978-3-0365-9713-3